

*CR 87
v. 20
for K... ..*

Outer Continental Shelf Environmental Assessment Program

Final Reports of Principal Investigators

Volume 49

December 1986



U.S. DEPARTMENT OF COMMERCE
National Oceanic and Atmospheric Administration
National Ocean Service
Office of Oceanography and Marine Assessment
Ocean Assessments Division
Alaska Office



U.S. DEPARTMENT OF THE INTERIOR
Minerals Management Service
OCS Study, MMS 86-0111

"Outer Continental Shelf Environmental Assessment Program Final Reports of Principal Investigators" ("OCSEAP Final Reports") continues the series entitled "Environmental Assessment of the Alaskan Continental Shelf Final Reports of Principal Investigators."

It is suggested that sections of this publication be cited as follows:

Latham, G. V., H. J. Dorman, and A. -B. K. Ibrahim. 1980. Coordinated ocean bottom seismograph measurements in the Kodiak Shelf area. U.S. Dep. Commer., NOAA, OCSEAP Final Rep. 49(1986):1-28

Lahr, J. C. and C. D. Stephens. 1983. Earthquake activity and ground shaking in and along the eastern Gulf of Alaska. U.S. Dep. Commer., NOAA, OCSEAP Final Rep. 49(1986):29-83

Frohlich, C. and P. Donoho. 1982. Measurement and location of earthquakes in western Alaska, the Gulf of Alaska, and the Bering Sea. U.S. Dep. Commer., NOAA, OCSEAP Final Rep. 49(1986):85-133

Jacob, K. H. and E. Hauksson. 1983. A seismotectonic analysis of the seismic and volcanic hazards in the Pribilof Islands - eastern Aleutian Islands region of the Bering Sea. U.S. Dep. Commer., NOAA, OCSEAP Final Rep. 49(1986):135-367

Pulpan, H. and J. Kienle. 1984. Seismic risk studies, western Gulf of Alaska. U.S. Dep. Commer., NOAA, OCSEAP Final Rep. 49(1986):369-434

Kienle, J. and S. E. Swanson. 1980. Volcanic hazards from future eruptions of Augustine Volcano, Alaska. U.S. Dep. Commer., NOAA, OCSEAP Final Rep. 49(1986):435-574

OCSEAP Final Reports are published by the U.S. Department of Commerce, National Oceanic and Atmospheric Administration, National Ocean Service, Office of Oceanography and Marine Assessment, Ocean Assessments Division, Alaska Office, Anchorage, and primarily funded by the Minerals Management Service, U.S. Department of the Interior, through interagency agreement.

Requests for receipt of OCSEAP Final Reports on a continuing basis should be addressed to:

NOAA-OMA-OAD
Alaska Office
701 C Street
P.O. Box 56
Anchorage, AK 99513

OUTER CONTINENTAL SHELF
ENVIRONMENTAL ASSESSMENT PROGRAM
FINAL REPORTS OF PRINCIPAL INVESTIGATORS

Volume 49

December 1986

U.S. DEPARTMENT OF COMMERCE
National Oceanic and Atmospheric Administration
National Ocean Service
Office of Oceanography and Marine Assessment
Alaska Office

U.S. DEPARTMENT OF THE INTERIOR
Minerals Management Service
Alaska OCS Region
OCS Study, MMS 86-0111

Anchorage, Alaska



The facts, conclusions, and issues appearing in these reports are based on research results of the Outer Continental Shelf Environmental Assessment Program (OCSEAP), which is managed by the National Oceanic and Atmospheric Administration, U.S. Department of Commerce, and funded (wholly or in part) by the Minerals Management Service, U.S. Department of the Interior, through an Interagency Agreement.

Mention of a commercial company or product does not constitute endorsement by the National Oceanic and Atmospheric Administration. Use for publicity or advertising purposes of information from this publication concerning proprietary products or the tests of such products is not authorized.

Content of these reports has not been altered from that submitted by the Principal Investigators. In some instances, minor grammatical, spelling, and punctuation errors have been corrected to improve readability; some figures, charts, and tables have been enhanced to improve clarity in reproduction.

Outer Continental Shelf Environmental Assessment Program

Final Reports of Principal Investigators

VOLUME 49

DECEMBER 1986

C O N T E N T S

G. V. LATHAM, H. J. DORMAN, and A. -B. K. IBRAHIM: Coordinated ocean bottom seismograph measurements in the Kodiak Shelf area	1
J. C. LAHR and C. D. STEPHENS: Earthquake activity and ground shaking in and along the eastern Gulf of Alaska.	29
C. FROHLICH and P. DONOHO: Measurement and location of earthquakes in western Alaska, the Gulf of Alaska, and the Bering Sea.	85
K. H. JACOB and E. HAUSSON: A seismotectonic analysis of the seismic and volcanic hazards in the Pribilof Islands - eastern Aleutian Islands region of the Bering Sea.	135
H. PULPAN and J. KIENLE: Seismic risk studies, western Gulf of Alaska.	369
J. KIENLE and S. E. SWANSON. Volcanic hazards from future eruptions of Augustine Volcano, Alaska	435

**COORDINATED OCEAN BOTTOM SEISMOGRAPH MEASUREMENTS
IN THE KODIAK SHELF AREA**

by

**Dr. Gary V. Latham,
Principal Investigator**

**Dr. H. James Dorman and Dr. Abou-Bakr K. Ibrahim,
Co-Investigators**

**The University of Texas Marine Science Institute
Galveston Geophysics Laboratory**

**Final Report
Outer Continental Shelf Environmental Assessment Program
Research Unit 579**

March 1980

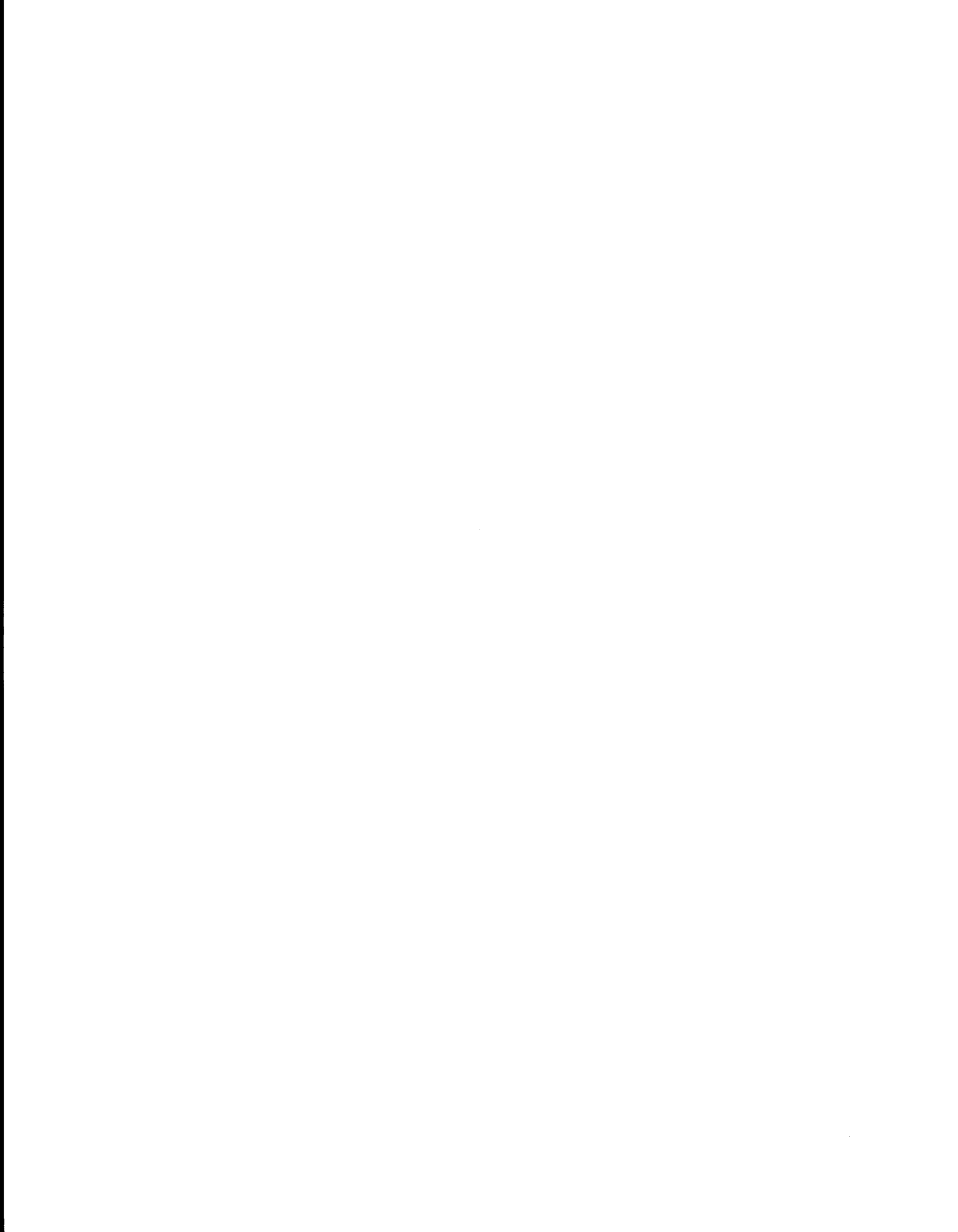


TABLE OF CONTENTS

List of Figures	5
Introduction	7
History of Program to Date	8
Brief Description of Instrumentation	10
Brief Summary of Results to Date	17
Field Operations and Construction Plans	22
1. Strong-motion measurements	22
2. Microearthquake measurements	26
3. Construction of six strong-motion stations for use on land ...	26
Data Processing and Analysis Plans	27
1. Microearthquake (high gain OBS) data analysis	27
2. Strong-motion data analysis	28
References	28



LIST OF FIGURES

- Figure 1. Map showing locations of ocean bottom seismic stations installed in June, 1979. Strong-motion and high-gain stations of the University of Alaska network on Kodiak and adjacent islands are also shown. Repeat installation of high-gain stations at sites marked 1-8 is proposed for the summer program of 1980.
- Figure 2. A strong-motion seismic station as it would appear on the sea floor.
- Figure 3. Photograph of a strong-motion seismic station, with preload system, prepared for launch.
- Figure 4. Sketch of the major elements of the strong-motion ocean bottom seismography system.
- Figure 5. Typical earthquake recorded from high-gain OBS #5 off Kodiak. Identified arrivals are the compressional wave (P) and the shear wave (S).
- Figure 6. Locations of epicenters of earthquakes recorded by the combined land and ocean bottom seismic network during the summer of 1979.
- Figure 7. Number of events believed to be of biological origin detected by various high-gain OBS stations versus station depth.
- Figure 8. Map showing the distribution of earthquakes of magnitude greater than 5 that have occurred in the Alaska zone during the past decade. Major sedimentary basins of the region are also indicated.
- Figure 9. Map showing recommended distribution of an initial 10-station network of strong-motion OBS stations. One or two additional stations would be placed in Norton Sound during the second and succeeding years of the program.



COORDINATED OCEAN BOTTOM SEISMOGRAPH MEASUREMENTS
IN THE KODIAK SHELF AREA

Introduction

Many special working groups and panels have pointed out the need for measurements of sea floor accelerations caused by potentially damaging earthquakes in offshore zones of oil and gas potential. The Alaska continental shelf is currently the most important example of such a zone within U. S. Territory. There is also a need for recording micro-earthquakes to increase the data set available for earthquake risk assessment and to delineate active faults that may transect zones of economic interest.

A low-cost seismic station for recording earthquakes on the sea floor has been developed at the University of Texas, Marine Science Institute, and has been used extensively over the past four years.

A system for recording strong-motions of the sea floor caused by earthquakes has also been developed and field tested as part of a collaborative effort between Exxon Production Research Company (EPR), the University of Texas-Marine Science Institute (UT-MSI), and the National Oceanic and Atmospheric Administration (NOAA). Operational systems can be constructed at relatively low-cost (less than \$10,000 per station), can operate on the sea floor for one year or more with minor modification, and can be deployed and retrieved from relatively small vessels. A recoverable preload system designed to imbed a set of vertical spikes attached to the base of the frame that serves as a pier for the ocean bottom station, has also been developed. Theoretical and experimental studies show that the ocean bottom station is capable of recording

ground accelerations of up to about 1 g, in the 0.1 Hz to 10 Hz frequency band, with good fidelity (Steinmetz et al., 1979).

Field operations using a combination of microearthquake and strong-motion seismograph stations during the first year of the present program (1979-1980), and initial results, are described in the following sections of this report.

History of Program to Date

The design and testing of various types of ocean bottom seismic (OBS) stations has been a principal activity of the University of Texas-Marine Science Institute since its beginning in 1972. In 1978, the Exxon Production Research Company (EPR) awarded a contract to MSI to begin development of a 3-axis digital system capable of recording strong-motions of the sea floor. Members of the EPR research staff undertook the task of investigating techniques for obtaining adequate ground coupling in marine sediments.

Three prototype stations were installed off Kodiak, Alaska in the fall of 1978. These were successfully recalled by acoustic command after about 1 month of operation. Five additional strong-motion stations were constructed during the spring of 1979 with the financial support of Exxon. During the following June (1979), under the sponsorship of the NOAA/OCSEAP program, all of the 8 strong-motion OBS stations, and 11 high-gain (microearthquake) OBS stations were deployed off Kodiak Island from the NOAA ship DISCOVERER at locations shown in Figure 1. Three additional strong-motion stations, modified for land use, were installed on neighboring islands in close proximity to the offshore network. The stations of the high-gain network were recovered in August of 1979. Several of the strong-

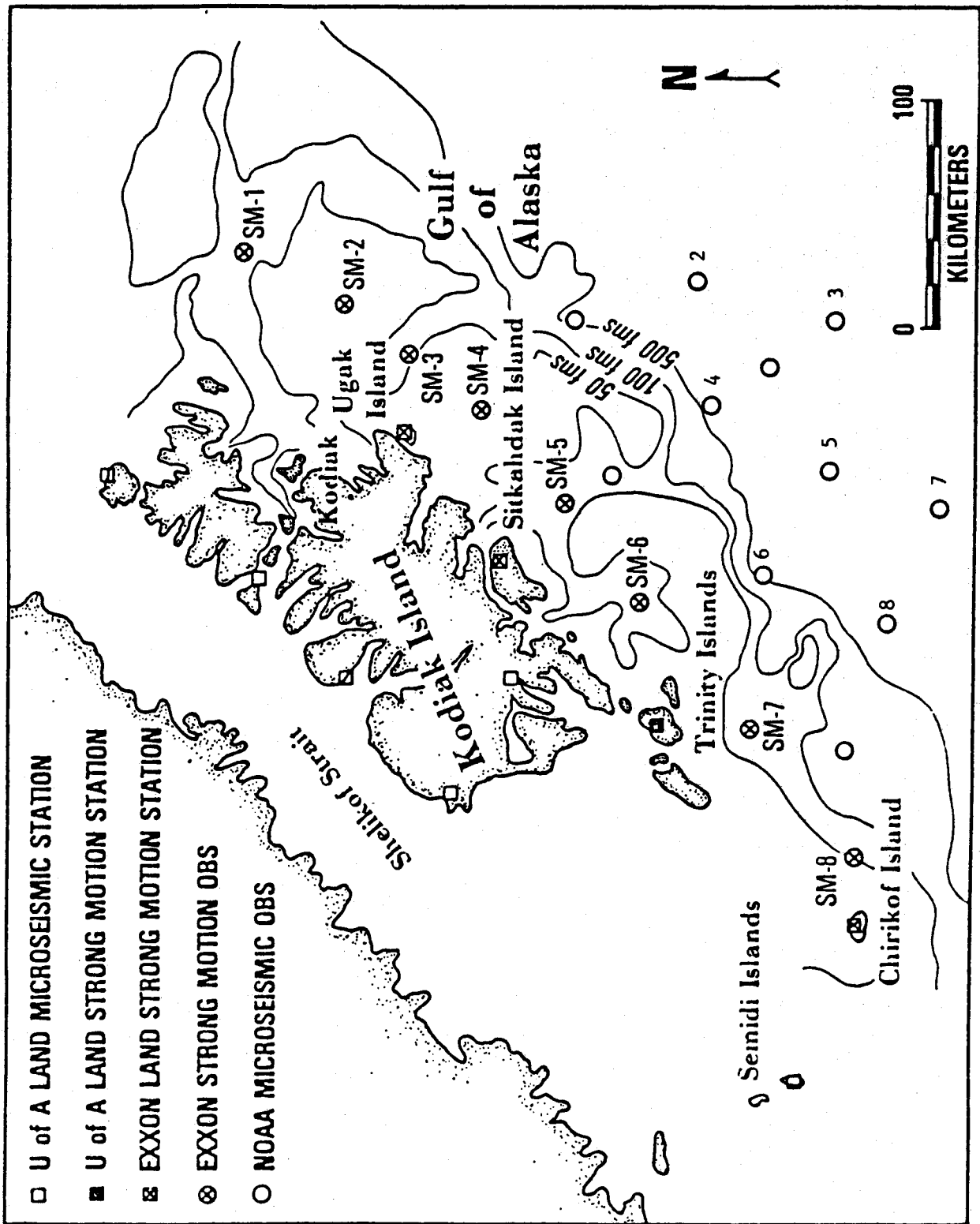


Figure 1. Map showing locations of ocean bottom seismic stations installed in June, 1979. Strong-motion and high-gain stations of the University of Alaska network on Kodiak and adjacent islands are also shown. Repeat installation of high-gain stations at sites marked 1-8 is proposed for the summer program of 1980.

Figure 1

motion stations were recovered and redeployed during cruises in August and October, 1979. In the October exercise, 4 strong-motion stations were left on bottom to be recovered the following spring. These were recovered in March of 1980. Thus, 12 successful recoveries of strong-motion station have been achieved out of 15 attempts. Of the three losses, 2 were sustained at sites with hard clay sediments. Damage to the stations on impact is suspected as the cause of their failure to return to the surface. Two premature releases have occurred, and this may account for the disappearance of the third station.

Despite these losses, we now feel that enough progress has been made toward understanding and eliminating design defects, that we can enter the program planned for 1980-81 with a high level of confidence.

Brief Description of Instrumentation

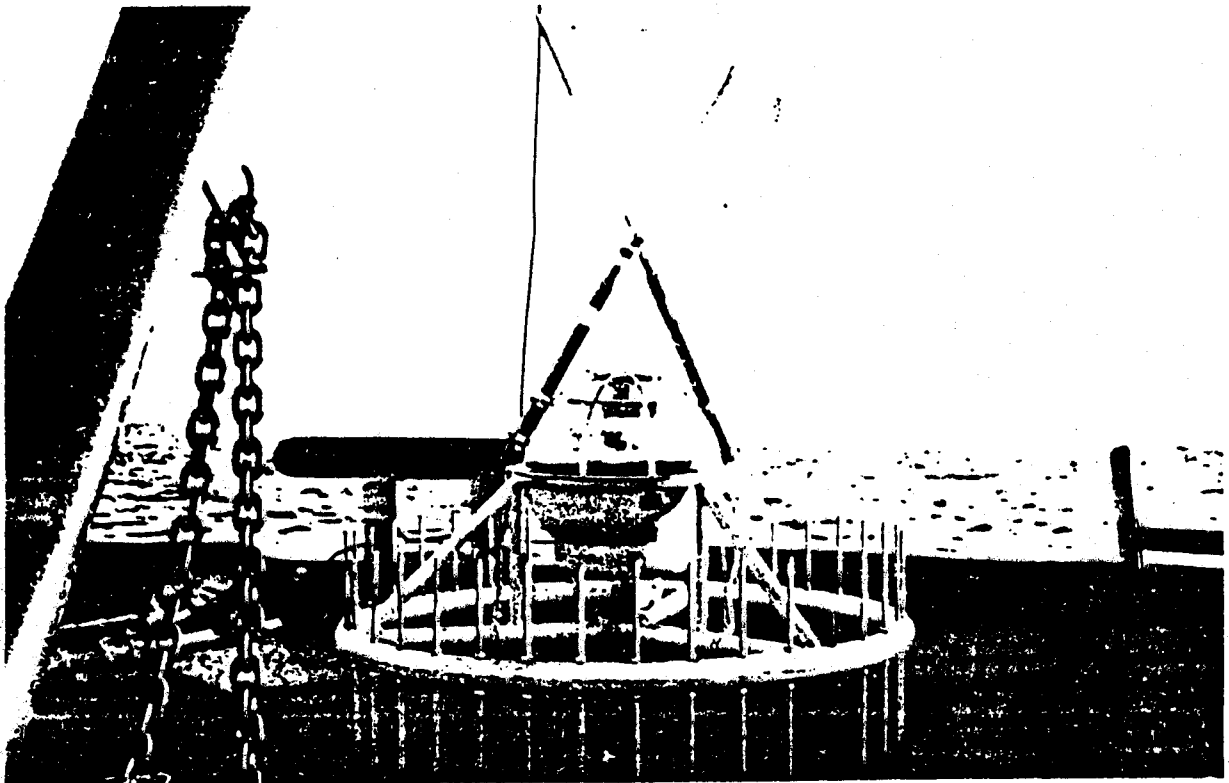
The UT/Exxon strong-motion OBS is described in recent papers by Steinmetz et al. (1979, 1980). The high-gain station used in refraction studies and normal earthquake recording has been described by Latham et al. (1978).

We wish to emphasize at this point that the primary goals of the design effort for the strong-motion OBS stations were threefold: (1) to keep system cost low enough that deployment of extensive networks of stations would be feasible; (2) to minimize power drain to the point that operational life times of one year or more could be achieved on internal battery supplies; and (3) to keep size and weight to levels that would permit the use of small vessels in the deployment and retrieval operations. The first goal is paramount. It is evident that the probability of acquiring useful strong-motion data will increase with the number of stations deployed. Also, since the radiation pattern from an earthquake

focus is not uniform, measurements over a range of distances and azimuths are needed to properly define the spatial distribution of ground accelerations related to a given earthquake.

An ocean bottom seismometer station, in sea floor configuration, is shown in Figure 2. The complete system ready for deployment, including the preload system described below, is shown in Figure 3. The primary system elements are shown schematically in Figure 4.

The circular, spiked frame is 1.2 m in diameter and the complete station without preload, weighs 81.6 kg in air. The electronic subsystems, tape recorder, battery pack, and triaxial geophone accelerometers, are contained in a single, spherical pressure vessel made of a high strength glass capable of withstanding pressures of 700 kg/cm^2 (10,000 psi). The sphere is 43 cm in diameter and has a net positive buoyancy of 6.8 kg. The bottom hemisphere of the pressure vessel fits snugly into a molded plastic cap. Two small radio beacons, used in recovery, are mounted externally on the sphere. The geophones are mounted in the bottom of the sphere. The pressure vessel, with its plastic bottom cap, recovery radios, and internal components are retrievable and redeployable and are referred to as the return capsule. When deployed, the return capsule is firmly attached to the circular steel frame footing by a spring-loaded loop of stainless steel wire, as shown schematically in Figure 4. This wire is electrolytically dissolved on acoustic command (or clock timer) releasing the return capsule which then ascends to the ocean surface from its own positive buoyancy. The new mechanical link provides enough tension between the instrument package and support frame that 1.0 g of ground acceleration in both the vertical and horizontal directions can be experienced without relative movement between the frame and package.



STRONG MOTION OCEAN BOTTOM SEISMOMETER

Figure 2. A strong-motion seismic station as it would appear on the sea floor.

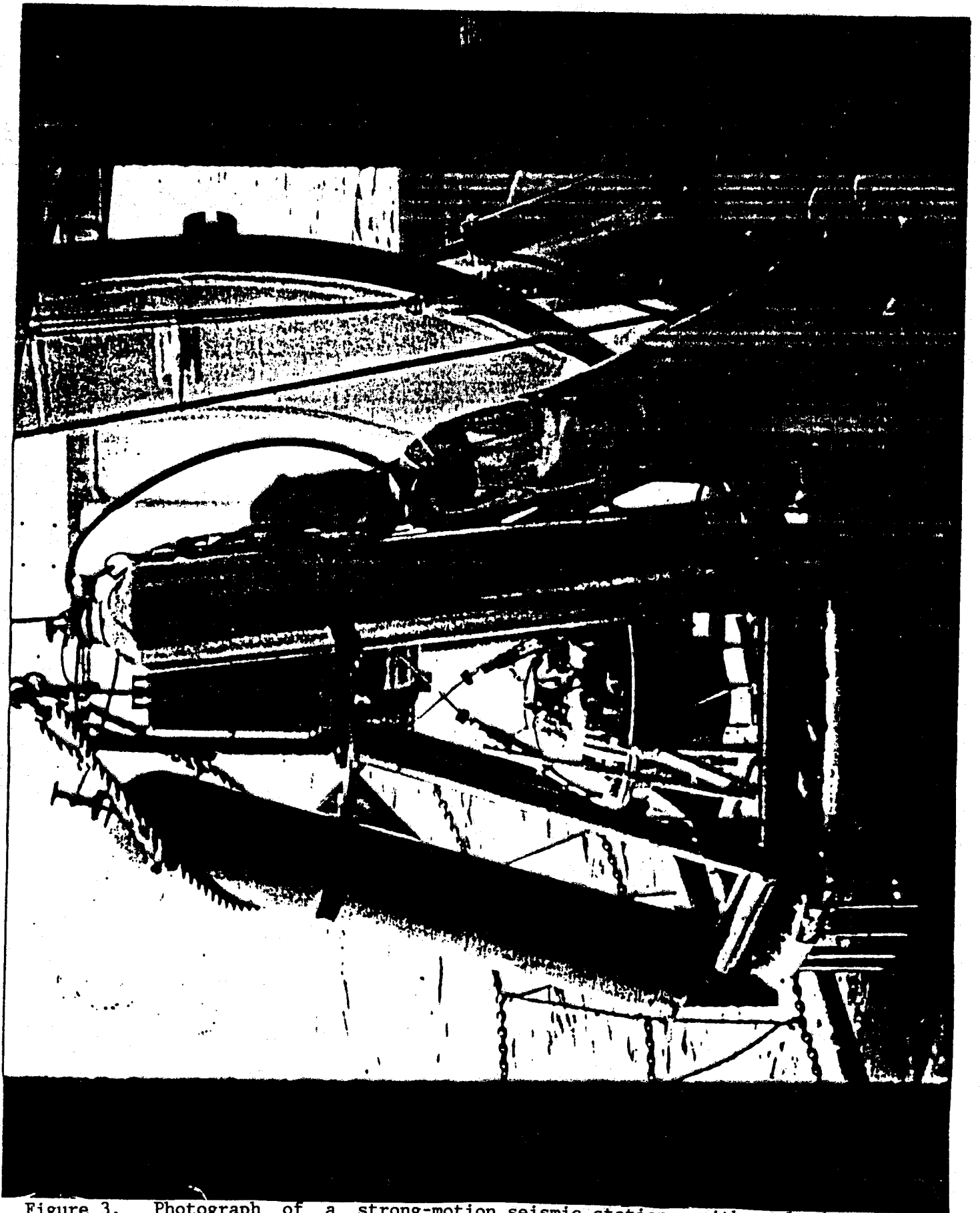
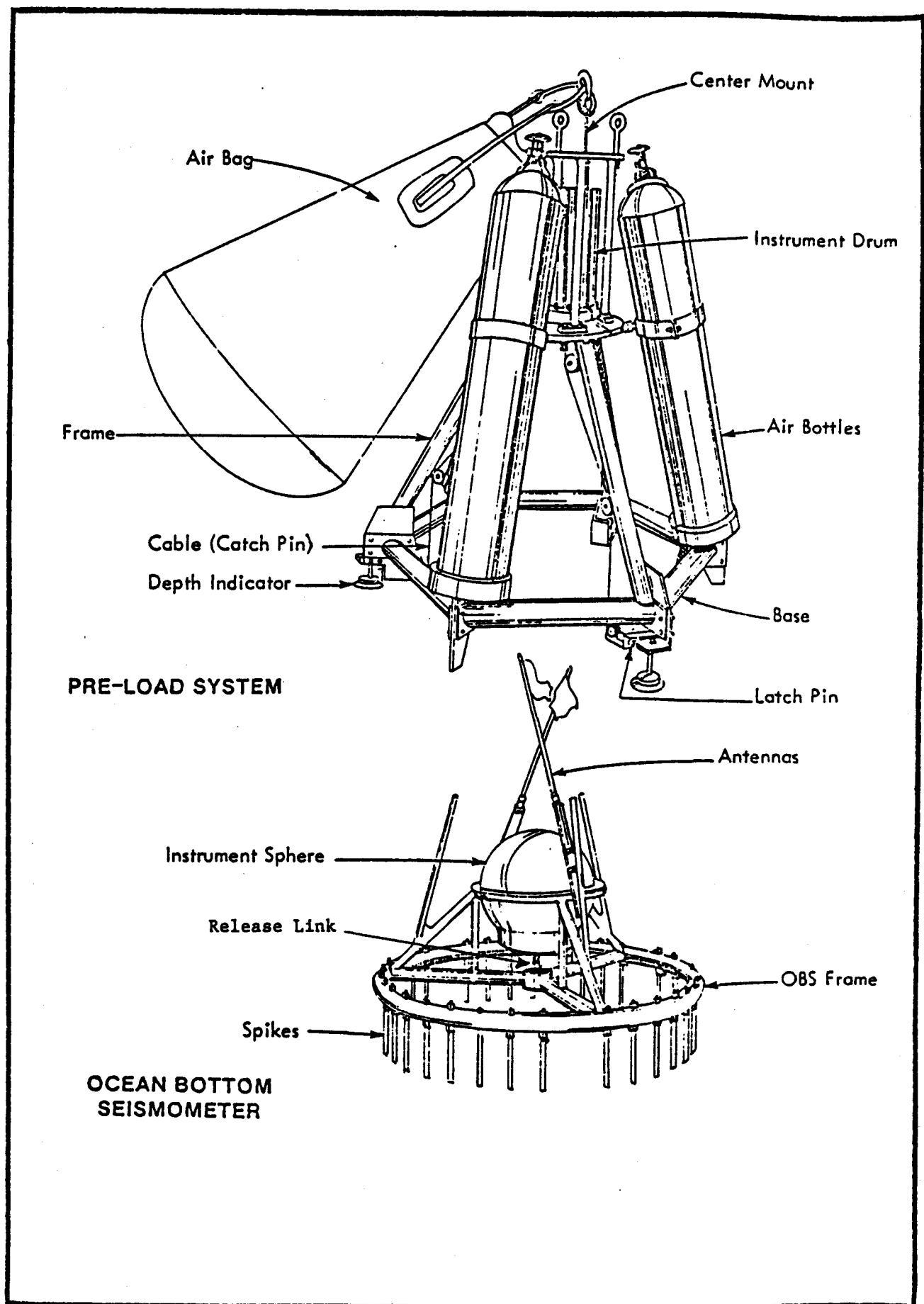


Figure 3. Photograph of a strong-motion seismic station, with preload system, prepared for launch.



McCLELLAND
ENGINEERS

PLATE 1

Figure 4. Sketch of the major elements of the strong-motion ocean bottom seismography system.

Up to 33 adjustable spikes are affixed to the base ring to penetrate the sea floor. A large 680 kg tripod device; used as a preload, fits over the sphere with its base locking into the base of the steel footing. This is used to increase the terminal free fall velocity and mass of the system to achieve full penetration and seating of the footing into the sea floor. The preload is decoupled and retrieved after sensor deployment to avoid the undesirable dynamic effects of the additional preload mass. Following bottom impact, a timer initiates release of gas into the air bag shown in Figure 4. High pressure air displaces water within the bag, increasing buoyancy. When sufficient lift is achieved, the preload frame is decoupled and floats to the surface. A gyrocompass, attached to the preload frame, records the azimuthal orientation of the horizontal component sensors. A more detailed discussion of this device is given by Steinmetz et al. (1980).

The electronics subsystem of the SM-OBS consists of gain-ranging sensor amplifiers, shaping filters to give geophone outputs flat to ground acceleration, analog-to-digital converter, and two microprocessors with memory to perform the functions of event detection, data transfer to magnetic tape in digital format, and tape recorder control. The recording system is "triggered" on when the signal amplitude from any of the three geophones exceeds a preset acceleration threshold (usually 10^{-3} g). First data recorded corresponds to data entered into memory 5 sec before the trigger instant. This ensures preservation of the onset of the signal that produced the trigger. Data will continue to be recorded until the acceleration threshold is not exceeded in any 5-sec time-window. A crystal controlled clock provides time words incorporated into the header

of each recorded data block. Date/time groups are entered into memory and compared with clock time to initiate such functions as system turnon, activation of the transponder for possible recall by acoustic command, and release of the return capsule at the preset clock release time. A second, less accurate clock, operating on an independent battery supply, is also set to the desired release time as a backup to the master clock. The overall system dynamic range is 96 db.

Every effort has been made to minimize system power drain. At present, a station can operate on the sea floor for about 6 months using 22 D-size lithium cells mounted within the pressure vessel. By screening components for low power consumption and increasing the number of cells in the battery pack, we expect to obtain a useful lifetime of one year.

A major concern in making strong-motion measurements offshore is the dynamic behavior of the soil-instrument system. Because ocean bottom soils near the mudline can be very soft, achievement of adequate ground coupling for strong-motion measurements is a significant design problem. An extensive experimental and analytical study of this problem (see Steinmetz et al., 1979) was conducted to insure that the fidelity of the measurements were acceptable at accelerations of up to 1.0 g over the frequency range of 0.1 Hz to 10 Hz. Based on this study, it was concluded that the present system responds accurately in very soft, cohesive soils with shear strengths on the order of 490 to 975 kg/m² (100 to 200 psf). Having shown this, the accuracy of the system in stiffer soils is assured if adequate penetration of the base spikes can be achieved. The study did point out, however, that it is necessary to insure that the footing is well seated so that the base ring maintains full contact with the soil. This led to the decision to develop a means for preloading the footing

to insure adequate seating, without adding permanently to the system mass.

Brief Summary of Results to Date

The initial 6-week period of operation of the high-gain OBS network (June-August, 1979, 11 stations) was one of unusual quiescence off Kodiak. Also, faulty tape recorder operation resulted in partial loss of data from 5 of the high-gain stations. Nevertheless, sixty earthquakes were recorded by two or more OBS stations. A typical seismogram from a local earthquake recorded by one of the high-gain OBS stations is shown in Figure 5. Arrival times for all earthquake phases identified in the OBS records were transmitted to Dr. Hans Pulpan for comparison with readings from the University of Alaska land station network. Thus far, it has been possible to locate 89 earthquakes using data from the combined onshore-offshore network. The preliminary epicenter locations for these earthquakes are shown in Figure 6. The focal depths range from less than 10 km to about 200 km. Much of the activity during the period of the 1979 experiment was located beneath the Lower Cook Inlet. The hypocenters of the detected events are concentrated along the inclined (Benioff) zone associated with the subduction of the Pacific plate beneath western Alaska.

Since we plan to repeat the microearthquakes experiment off Kodiak during the summer of 1980, we defer further comment on the seismicity of the region until the much larger data set that we anticipate, can be assembled. We point out, however, that the location accuracy, particularly depth estimates, for the earthquakes that occurred between Kodiak and the trench axis during the 1979 experiment is much greater than would have been possible without the OBS network.

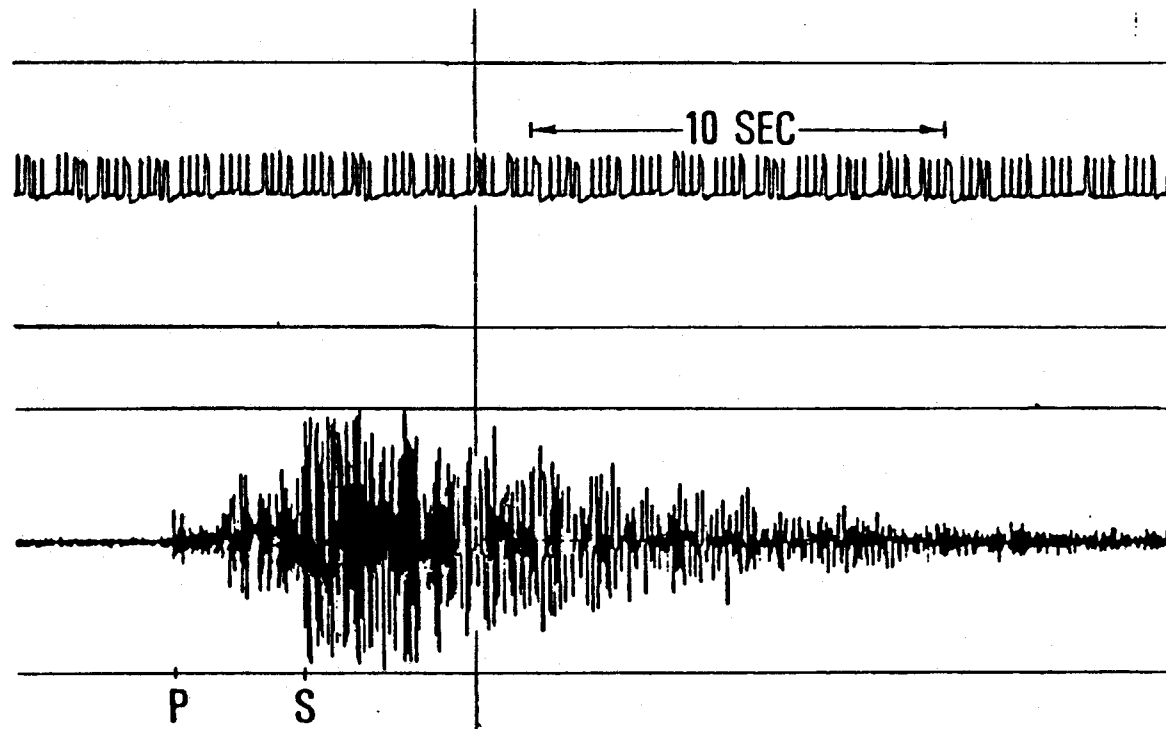


Figure 5. Typical earthquake recorded from high-gain OBS #5 off Kodiak. Identified arrivals are the compressional wave (P) and the shear wave (S).

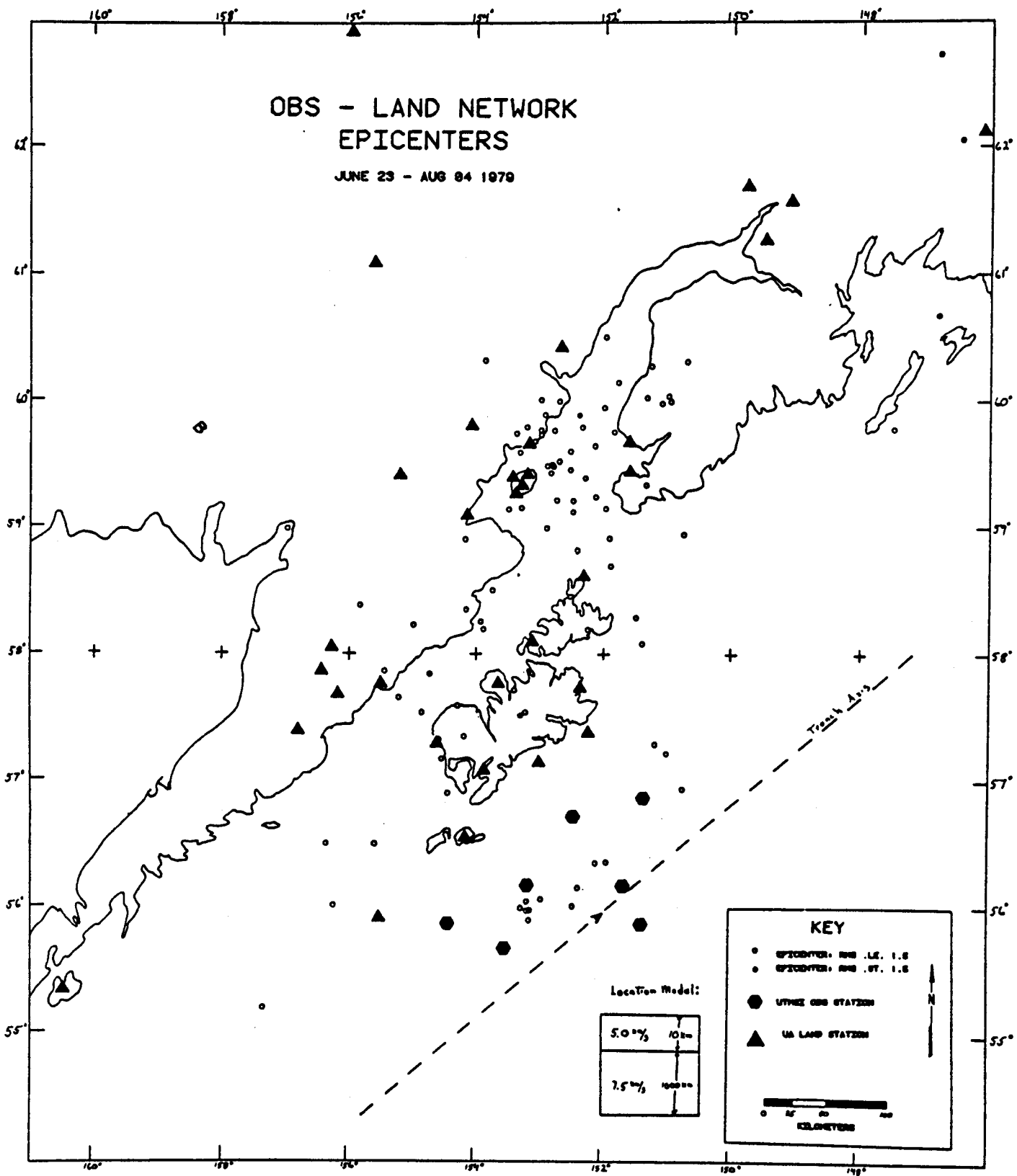


Figure 6. Locations of epicenters of earthquakes recorded by the combined land and ocean bottom seismic network during the summer of 1979.

Concerning the strong-motion portion of the program, no earthquakes large enough to produce meaningful strong-motion data have occurred in the Kodiak zone since monitoring operations were begun under this program.

An important new research opportunity may emerge from the data set obtained from the high-gain OBS stations off Kodiak during 1979. For years we have been puzzled as to the origin of a set of distinctive seismic signals that have been recorded in every OBS experiment in widely ranging locations. These were much more numerous in the Kodiak experiment than had previously been encountered. The Kodiak experiment was the first one in which we deployed the ocean bottom stations over a large range of water depths. A plot of the daily rate of occurrence of these events, versus station depth, is shown in Figure 7. It is evident that the rate of occurrence diminishes rapidly with increasing depth until a depth of about 1500 m is reached. Also, the sources are local, i.e., a given event is never recorded at more than one station. Hence, the distribution of sources with depth is as shown in Figure 7. Finally, these same signals are recorded in zones of no known seismic activity, e.g., the Gulf of Mexico. Taken together, these facts are almost indisputable evidence that the strange events are of biological origin. If so, the important point of Figure 7, is that the activity does not diminish to zero at abyssal depths, but remains at a fairly high level (14 to 35 events per day). By adding a bottom camera capable of imaging the OBS station at the time of each trigger, we may have discovered a new method of surveying benthic sea life.

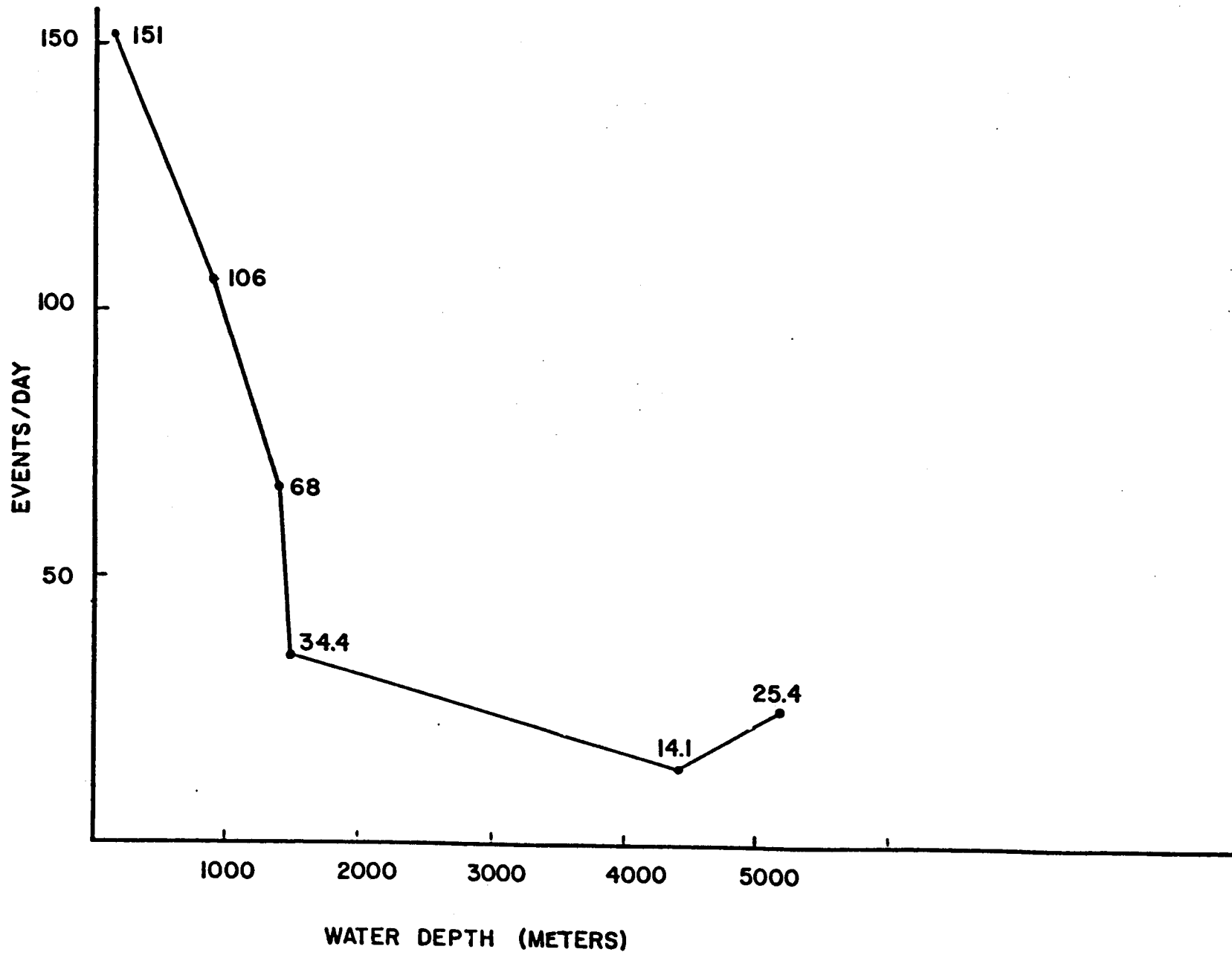


Figure 7. Number of events believed to be of biological origin detected by various high-gain OBS stations versus station depth.

Field Operations and Construction Plans

1. Strong-motion measurements. Industry support has been obtained for the construction of 12 additional strong-motion stations over the next two years. Briefly, our present plan for field operations and construction is the following:

- (a) Deploy the four existing stations in the Kodiak shelf zone in June, 1980.
- (b) Construct six additional stations. Deploy these new stations plus the balance of the present stations, at the approximate locations shown in Figure 8, in September, 1980. Recover these stations in June, 1981.
- (c) Construct six additional stations. Deploy these new stations plus the balance of the previously constructed stations at the earlier sites, and install at least 1 station at a new site in Norton Sound, in June-July, 1981. Recover and redeploy all stations in June-July, 1982.

The selection of sites for installation of strong-motion stations proposed here is based upon a combination of factors including: (1) regional seismicity, (2) the locations of sedimentary basins of possible interest to the oil industry, and (3) the need to obtain data that will permit testing and refinement of the earthquake risk assessments derived in the Offshore Alaska Seismic Exposure Study (OASES).

Obviously, the probability of obtaining strong-motion data is highest within the belts of highest seismicity. However, site specific data, i.e., measurements obtained on the specific sediment types to be encountered in future production operations, is also required. Finally, we prefer a combination of sites that will record signals from earthquake sources

that follow raypaths that traverse the major structural elements of the offshore Alaska provinces.

As shown in Figure 8, the seismically active belt of greatest concern extends along the Aleutian Trench, past Kodiak Island, and into interior Alaska along a N-S trend. A weaker trend extends in an E-W direction into Norton Sound. Two "gaps" in seismic activity have been identified within the major seismic belt: one in the northern Gulf of Alaska and one centered on the Shumagin Islands. The term seismic gap has taken on a variety of meanings in recent scientific literature. Here, we mean the region bordered by major rupture zones (as defined by aftershocks) of earlier earthquakes. Presumably, these gaps are the most likely candidates for future large earthquakes; although, this point is not well established.

During the first year of the program, we propose to concentrate the strong-motion stations along the OCS regions of the western Gulf of Alaska and Aleutian Islands, with several stations located behind the Island Arc in the Bristol and St. George Basins of the Bering Sea. A suggested distribution is shown in Figure 9. A total of ten stations is indicated in the network. This assumes that we have 4 stations remaining after recovery in October, 1980 of the network now operating off Kodiak, and that six additional stations can be constructed during the summer of 1980. Note that we have included stations in the vicinity of the Shumagin Gap.

In the second and following years of the program, we propose to extend the network northward with at least one station operating in Norton Sound. The stations of the proposed network span a large segment of the Aleutian seismic belt. In the event of a large earthquake within this belt, the raypaths of recorded signals will traverse the major structural

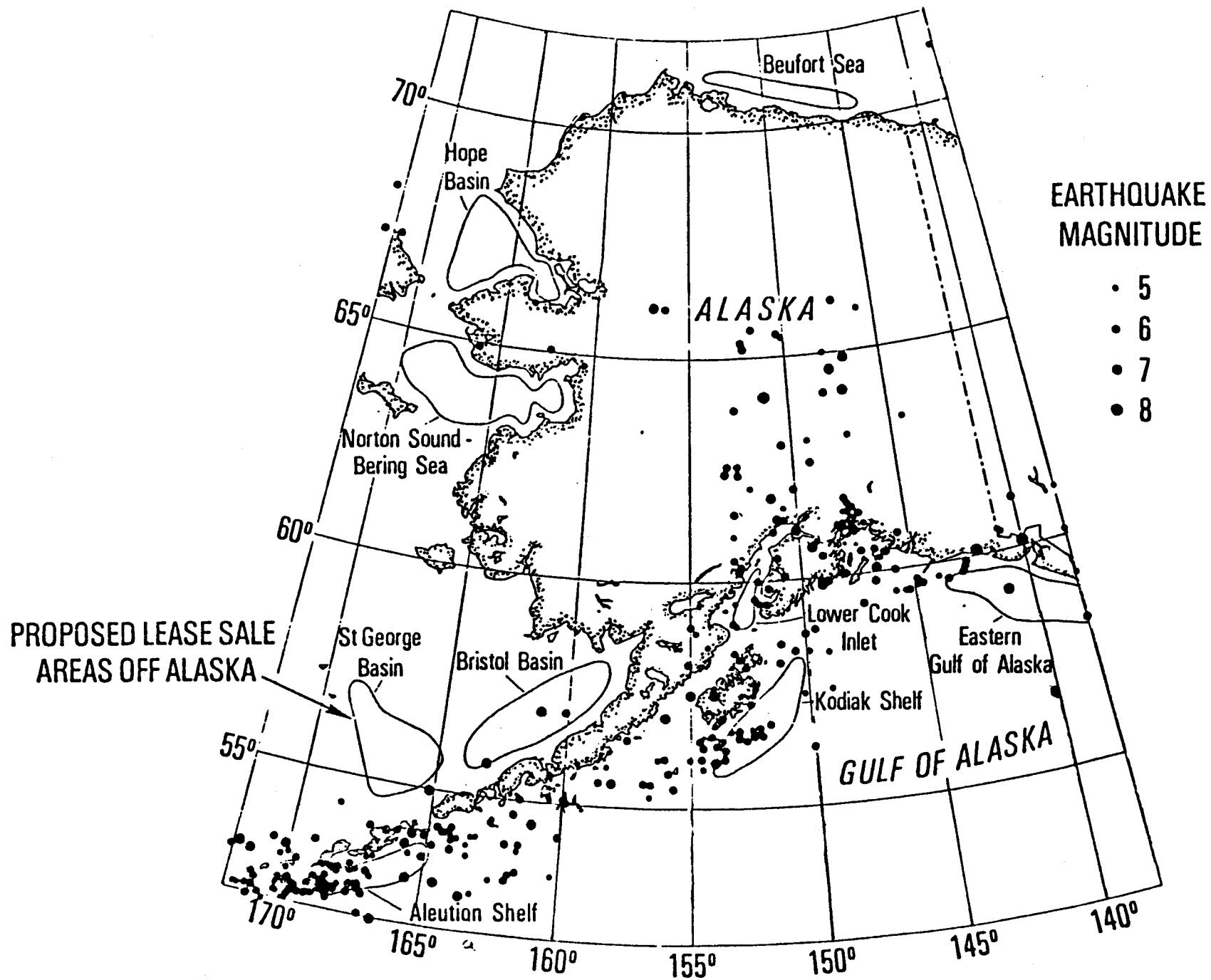


Figure 9. Map showing recommended distribution of an initial 10-station network of strong-motion OBS stations. One or two additional stations would be placed in Norton Sound during the second and succeeding years of the program.

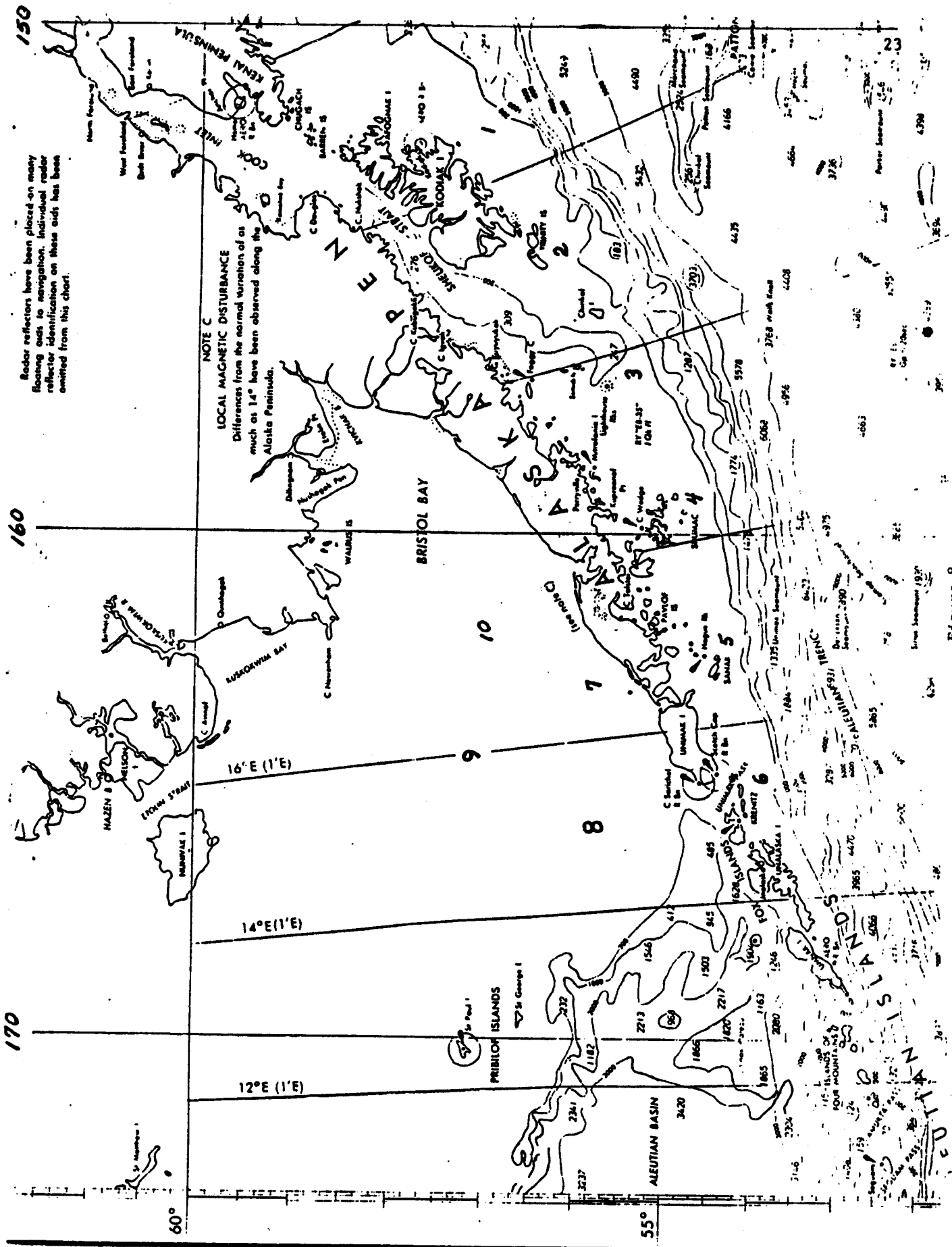


Figure 8. Map showing the distribution of earthquakes of magnitude greater than 5 that have occurred in the Alaska zone during the past decade. Major sedimentary basins of the region are also indicated.

elements of the region: (1) forearc shelf, (2) island ridge, and (3) backarc basin. These data will contribute importantly to the refinement of model parameters, particularly attenuation, assumed in the OASES study. In addition, they will provide the first records of the actual waveforms of sea bottom accelerations.

We wish to point out that site surveys (precision depth profile and sonobuoy refraction lines) and sediment cores will be needed to properly interpret any strong-motion data eventually obtained. We propose that such surveys be deferred until useful strong-motion data are obtained at a given site.

2. Microearthquake measurements. Owing to the limited success of the microearthquake measurements program in 1979, we plan to return to the Kodiak zone during the summer of 1980 with 8 of our high-gain OBS stations to repeat the experiment. Suggested station locations are numbered 1-8 in Figure 1. Three additional high-gain stations will be constructed during 1980 to increase the total number available to thirteen.

Improvements in station design are proposed in two areas: (1) Improve tape recorder reliability by installing new drive motors, and eliminating the optical end of tape sensor which has failed to operate properly in many cases; and (2) increase the reliability of the acoustic recall system so that it can serve as the primary recovery method.

3. Construction of six strong-motion stations for use on land. Six additional strong-motion stations for use on land will be constructed in 1980. These will be installed and operated by personnel of the University of Alaska as part of their existing network of radio-telemetering seismic stations.

Data Processing and Analysis Plans

1. Microearthquake (high gain OBS) data analysis. A series of tasks will be accomplished jointly with the University of Alaska. (a) First we will generate a list of readings of times of first arrivals for all events recorded on OBS playouts. (b) These data will be used by the University of Alaska in their standard quarterly bulletin calculations. The University of Alaska presently has the capability of producing a seismological bulletin with earthquake origin times, locations, depths, magnitudes and statistical parameters about one month after receipt of data. Their existing system will be able to absorb the additional station locations and additional arrival time readings without serious impact. A subset of well-recorded earthquakes from the final bulletin list will be selected for (c) focal mechanism studies, and (d) crust-mantle structural analyses. Secondary phases and frequency content will be analyzed. It seems likely that progress can be made in identifying tectonic units characterized by particular seismic velocities, in elastic absorption, and focal mechanism patterns. These problems will be of interest to both groups, and copies of original data on these events will be exchanged. (e) The same data will also be of use in more detailed studies of wave propagation characteristics over the joint network. Surface wave data will be studied by normal mode methods, and a comprehensive effort will be made to understand the details of generation and propagation of waves in these well-recorded events. In particular, short period surface waves generated by moderate to large earthquakes in the region will provide waveforms which can be interpreted in terms of rigidity profiles for the upper sedimentary layers of the continental shelf. These results will ultimately be useful to platform design engineers.

Seismic bulletins will be distributed as at present by the University of Alaska.

2. Strong-motion data analysis. Strong-motion data will be reformatted to produce computer compatible 9-track data tapes. These, along with analog playouts and supporting documentation (locations, calibrations, available information on sub-bottom structure, and source parameters) will be distributed to NOAA and the industrial sponsors.

REFERENCES

- Latham, G., P. Donoho, K. Griffiths, A. Roberts, and A. K. Ibrahim, The Texas Ocean-Bottom Seismograph: Proceedings of the 10th Annual Offshore Technology Conference, Houston, Texas, May 8-11, 1978, pp. 1467-1476.
- Steinmetz, R., P. Donoho, J. Murff, and G. Latham, Soil Coupling of a Strong-motion, Ocean Bottom Seismometer: Proceedings of the 11th Annual offshore Technology Conference, Houston, Texas, April 30-May 3, 1979, pp. 2235-2249.
- Steinmetz, R., J. Murff, G. Latham, A. Roberts, P. Donoho, L. Babb, and T. Eichel, Seismic Instrumentation of the Kodiak Shelf: accepted for publication in Marine Geotechnology, 1980.

**EARTHQUAKE ACTIVITY AND GROUND SHAKING
IN AND ALONG THE EASTERN GULF OF ALASKA**

by

John C. Lahr and Christopher D. Stephens

**Office of Earthquakes, Volcanoes, and Engineering
U.S. Geological Survey**

**Final Report
Outer Continental Shelf Environmental Assessment Program
Research Unit 210**

1983

This study was supported by the Bureau of Land Management through interagency agreement with the National Oceanic and Atmospheric Administration, under which a multi-year program responding to needs of petroleum development of the Alaskan Continental Shelf is managed by the Outer Continental Shelf Environmental Assessment Program Office.

This report is preliminary and has not been reviewed for conformity with U.S. Geological Survey editorial standards and stratigraphic nomenclature. Any use of trade names is for descriptive purposes only and does not imply endorsement by the USGS.

TABLE OF CONTENTS

	List of Figures	33
	List of Tables	35
I.	SUMMARY OF OBJECTIVES, CONCLUSIONS, AND IMPLICATIONS WITH RESPECT TO OCS OIL AND GAS DEVELOPMENT	37
	A. Objectives	37
	B. Conclusions	37
	C. Implications	37
II.	INTRODUCTION	37
	A. General Nature and Scope of Study	37
	B. Specific Objectives	38
	C. Relevance to the Problem of Petroleum Development	38
III.	CURRENT STATE OF KNOWLEDGE	38
IV.	STUDY AREA	40
V.	METHODS AND RATIONALE OF DATA COLLECTION	40
	A. High-Gain, High-Frequency Seismograph Network	40
	B. Earthquake Locations	40
	C. Magnitude Determination	40
	D. Strong-Motion Network	42
VI.	RESULTS AND DISCUSSION	43
	A. Proposed Kinematic Model for Pacific-North American Interaction	43
	1. Plate and Block Boundaries	43
	2. Plate Motions in Model	45
	3. Historical Seismic Record	45
	B. Seismicity During 1974 - 1981	59
	C. Estimation of Recurrence Times for Major Earthquakes	72
	D. Strong-Motion Recordings	78
VII.	CONCLUSIONS	79
VIII.	NEEDS FOR FURTHER STUDY	79
IX.	ACKNOWLEDGMENTS	80
X.	REFERENCES	81

1000

1000

1000

1000

1000

1000

1000

1000

1000

1000

1000

1000

1000

1000

1000

1000

1000

1000

1000

1000

LIST OF FIGURES

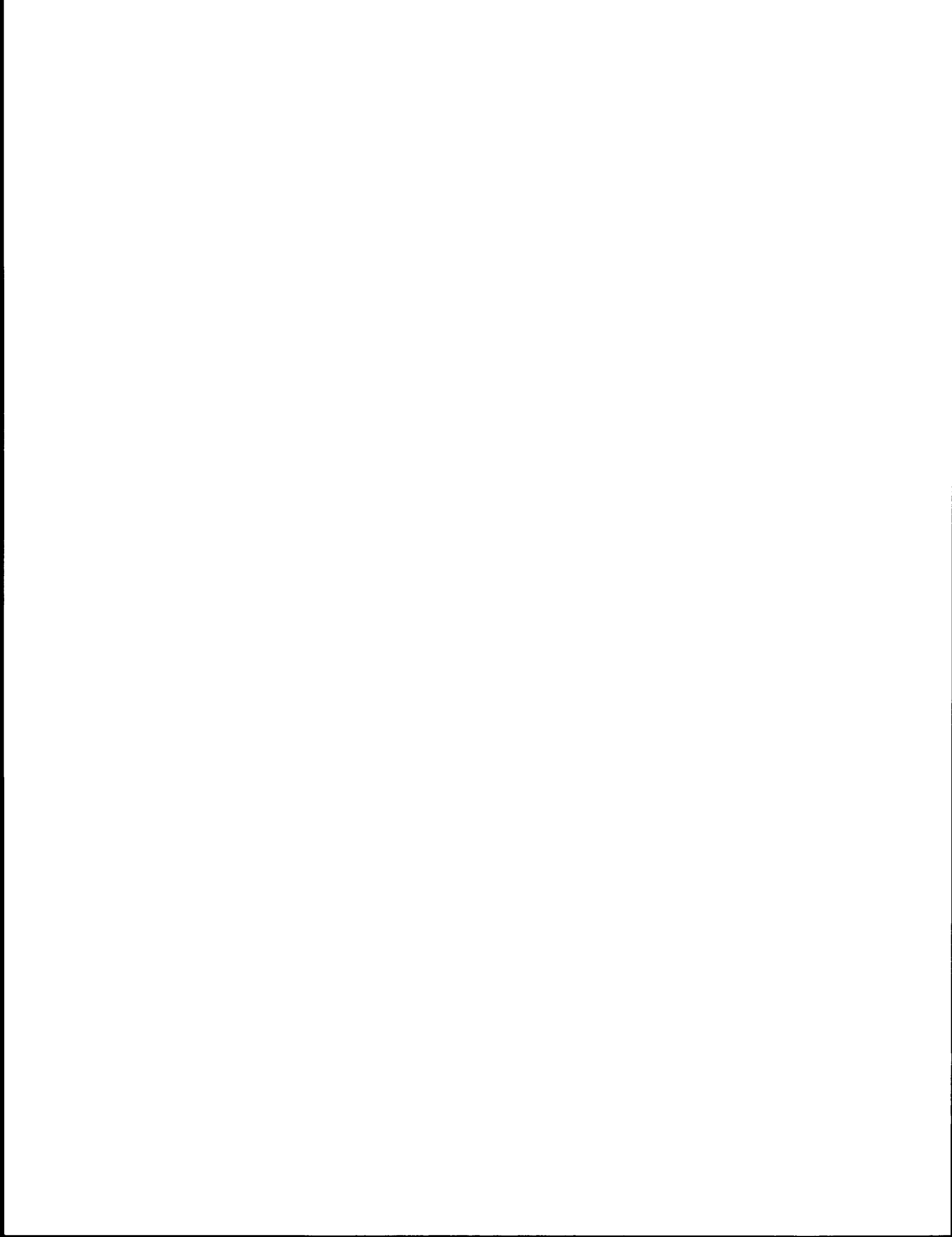
- Figure 1. Map of southern Alaska and western Canada emphasizing the principal regional tectonic features. Faults after Clague (1979) and Beikman (1978).
- Figure 2. High-gain vertical-component seismic stations operated in the NEGOA and adjacent areas during 1974 through 1981.
- Figure 3. Location of USGS strong-motion instruments in southern Alaska showing year(s) of installation (and removal). Stations which were maintained at least in part with OCSEAP funds are indicated by solid circles. For Anchorage and Valdez, the year of the earliest installation is given.
- Figure 4. Proposed model for present crustal deformation along Pacific-North American plate boundary in southern and southeastern Alaska. Circled numbers give rate of motion (centimeters per year) of Pacific plate, Yakutat block (YB), St. Elias block (SE), and Wrangell block (WB) relative to North American plate. Numbers next to paired vectors give rate of motion across indicated zone. Stippled bands mark surface outcrops of major zones of deformation and faulting. A-B, location of cross section shown in Figure 5.
- Figure 5. Diagrammatic structure along plane A-B of Figure 4.
- Figure 6a. Map of epicenters for 80 historic earthquakes that occurred between January 1, 1900 and March 28, 1964. Numbers next to epicenters indicate total number of events in cases where more than one event occurs at the same location with the same magnitude. Filled symbols mark the more accurate epicenters, and are repeated in Figure 7. Symbol size is proportional to magnitude as indicated at the upper right.
- Figure 6b. Historic epicenters, as in Figure 6a, except year and magnitude are indicated for events greater than or equal to 6.0.
- Figure 7. Epicenters of 24 relocated earthquakes (Tobin and Sykes, 1966; Tobin and Sykes, 1968; Sykes, 1971) that occurred between 1954 and 1959 (solid symbols) with a line extending to the location given in the Earthquake Data File.
- Figure 8. Epicenter map of the 19 events that occurred within two weeks of the July 10, 1958 earthquake on the Fairweather fault. 1958 rupture zone after McCann and others (1980). Filled symbols are relocated events from Tobin and Sykes (1966, 1968) and Sykes (1971).

- Figure 9a. Map of epicenters for 155 earthquakes that occurred between March 28, 1964 and April 12, 1964, the first two weeks following the 1964 Alaska earthquake. Symbols and labels same as Figure 6a.
- Figure 9b. Epicenters during first two weeks following the 1964 earthquake, as in Figure 9a. The eastern boundary of the 1964 rupture zone, as defined by McCann and others (1979), is shown.
- Figure 10a. Epicenter map of 453 earthquakes that occurred between April 13, 1964 and September 30, 1974. Symbols and labels same as Figure 6a.
- Figure 10b. April 13, 1964 through September 30, 1974 epicenters, as in Figure 10a.
- Figure 11. Plot of EDF body-wave magnitude (m_p) versus coda magnitude calculated from local stations.
- Figure 12a. Epicenter map of 42 earthquakes with coda magnitudes greater than or equal to 3.5 that occurred between October 1, 1974 and September 31, 1981. Labels same as Figure 6a. Note change in symbol values from previous figures.
- Figure 12b. October 1, 1974 through September 30, 1981 epicenters, as in Figure 12a.
- Figure 13a. Epicenter map of 2015 earthquakes located by the local seismograph network between October 1, 1974 and February 28, 1979 just prior to the St. Elias earthquake. Labels same as Figure 6a. Note that symbol values are larger than in previous figures.
- Figure 13b. October 1, 1974 through February 28, 1979 epicenters, as in Figure 13a.
- Figure 14a. Epicenter map of 287 earthquakes located by the local seismograph network starting with the St. Elias earthquake on February 28, 1979 through March 20, 1979. Labels same as Figure 6a.
- Figure 14b. February 28, 1979 through March 20, 1979 epicenters, as in Figure 14a.
- Figure 15. Epicenter map of 3534 earthquakes located by the local seismograph network between October 1, 1979 and September 30, 1980. Labels same as Figure 6a.
- Figure 15b. October 1, 1979 through September 30, 1980 epicenters, as in Figure 15a.

- Figure 16. Epicenter map of 3811 earthquakes located by local seismograph network between October 1, 1980 and September 30, 1981. Labels same as Figure 6a.
- Figure 16b. October 1, 1980 through September 30, 1981 epicenters, as in Figure 16a.
- Figure 17a. Epicenter map of 643 earthquakes with coda magnitude greater than or equal to 2.4 located by the local seismograph network between October 1, 1974 and September 30, 1981. Labels same as Figure 6a.
- Figure 17b. October 1, 1974 through September 30, 1981 epicenters, as in Figure 17a.
- Figure 18. Principal rupture zones of NEGOA region and possible extent of Yakataga seismic gap (dashed). Approximate location of 40 km isobath of Wrangell Benioff zone given by heavy solid line.

LIST OF TABLES

- Table 1. Estimated recurrence times for two principal seismic sources in the eastern Gulf of Alaska region.
- Table 2. Preliminary strong-motion results.



I. SUMMARY OF OBJECTIVES, CONCLUSIONS, AND IMPLICATIONS WITH RESPECT TO OCS OIL AND GAS DEVELOPMENT

A. Objectives

The objective of this research has been to develop information necessary for improved assessment of the hazards posed by earthquakes to development of oil and gas within the northeast Gulf of Alaska (NEGOA) and adjacent onshore areas.

B. Conclusions

The NEGOA region lies along the boundary of the North American and Pacific lithospheric plates and is seismically active due to the relative motion of these plates. A kinematic model has been developed which specifies the slip rates on the principal faults that accommodate the relative plate motion, and this model allows an estimate to be made of the long-term rate of seismicity on each fault. Based on this model and on the theory of seismic gaps, the coastal zone between Icy Bay and Kayak Island is thought to be a likely site for a magnitude 8 or larger earthquake within the next two or three decades. The model also suggests that infrequent great ($M_s > 8$) earthquakes could occur on the low-angle megathrust zone which is thought to underlie the entire continental shelf between Cross Sound and Kayak Island.

In addition to the hazard from infrequent great events, moderate and large-size earthquakes ($5.5 < M_s < 8$) could occur throughout the entire coastal zone and pose a more localized hazard. This type of event could occur along the underlying megathrust zone or on faults within either of the interacting lithospheric plates. The source regions for such events are not limited to areas that are currently experiencing relatively high rates of microearthquake activity.

C. Implications

The northeast Gulf of Alaska lies within an active tectonic region which will continue to be subjected to the effects of earthquakes. In addition to generating strong ground shaking, earthquakes could trigger tsunamis, seiches, submarine slumping, and surface faulting, any of which could be hazardous to offshore and coastal structures. Careful consideration must clearly be given to these potential seismic hazards in developing oil and gas resources within the northeast Gulf of Alaska.

II. INTRODUCTION

A. General nature and scope of study

The purpose of this research has been to investigate the earthquake potential in the NEGOA and adjacent onshore areas. This was accomplished by reviewing the historical seismic record as well as by collecting new and more detailed information on both the distribution of current seismicity and the nature of strong ground motion resulting from large earthquakes.

B. Specific objectives

1. Review historical record of earthquakes in the NEGOA.
2. Record the locations and magnitudes of all significant earthquakes within the NEGOA area.
3. Prepare focal mechanism solutions to aid in interpreting the tectonic processes active in the region.
4. Identify both offshore and onshore faults that are capable of generating earthquakes.
5. Assess the nature of strong ground shaking associated with large earthquakes in the NEGOA.
6. Evaluate the average recurrence time for large events within and adjacent to the NEGOA.

C. Relevance to the problem of petroleum development

It is crucial that the seismic potential in the NEGOA be carefully analyzed and that the results be incorporated into the plans for future petroleum development. This information should be considered in the selection of tracts for lease sales, in choosing the localities for oil pipelines and land-based operations, and in setting minimum design specifications for both coastal and offshore structures.

III. CURRENT STATE OF KNOWLEDGE

The current relative motions of the rigid plates that constitute the earth's outer shell (lithosphere) have been well-established based on many lines of geological and geophysical evidence, including the pattern of ocean-bottom magnetic anomalies, the orientation of major strike-slip faults, the global distribution of earthquakes, and earthquake focal mechanisms (see, for example, Minster and Jordan, 1978). The Aleutian trench, located south of the Aleutian arc and the Alaska Peninsula and extending as far east as the Gulf of Alaska, forms part of the near-surface expression of the Pacific-North American plate boundary. The boundary also follows the Queen Charlotte Islands fault along southeastern Alaska and Canada. The relative motion of these two plates results in SE-NW convergence along the Aleutian megathrust and right lateral strike-slip motion on the Queen Charlotte Islands fault (Figure 1). Direct evidence for this convergent motion today comes from studies of large earthquakes along sections of the Pacific-North American plate boundary adjacent to the NEGOA. For example, the 1964 Alaska earthquake resulted from low-angle, dip-slip motion of about 12 m (Hastie and Savage, 1970) on the section of the Aleutian megathrust extending from beneath eastern Prince William Sound to southern Kodiak Island. While the plate boundary in the source region of the 1964 earthquake and along the Queen Charlotte Islands fault is thought to be relatively simple, the precise manner in which the relative plate motion is accommodated in the intervening NEGOA region is still the subject of investigation. Accurate assessment of the seismic hazard in the NEGOA can only be made when the relative motion between the Pacific and North American plates can be understood in terms of the displacement rates on the faults that accommodate the motion. Toward this end, one of the principal results of this research has been the development of a working model for the kinematics of the NEGOA region.

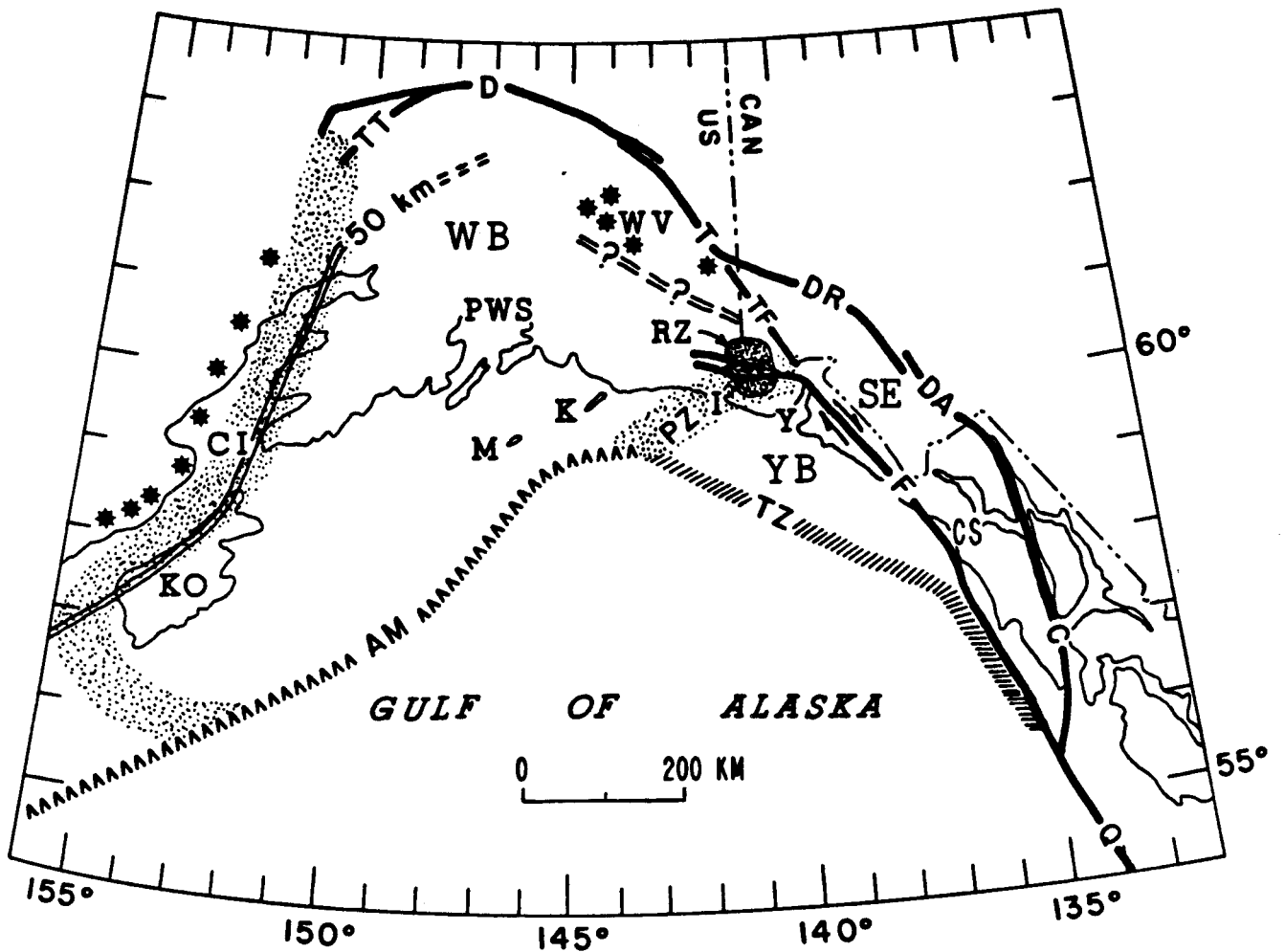


Figure 1. Map of southern Alaska and western Canada emphasizing the principal regional tectonic features. Faults after Clague (1979) and Beikman (1978). KO, Kodiak Island; M, Middleton Island; K, Kayak Island; CI, Cook Inlet; PWS, Prince William Sound; I, Icy Bay; Y, Yakutat Bay; CS, Cross Sound; WV, Wrangell volcanics; RZ, rupture zone of 28 February 1979 earthquake; AM, Aleutian megathrust; TZ, Transition zone; Q, Queen Charlotte Islands fault; C, Chatham Strait fault; DA, Dalton fault; DR, Duke River fault; TF, possible fault connecting the Fairweather and Totschunda faults; T, Totschunda fault; D, Denali fault; TT, unnamed faults; F, Fairweather fault; PZ, Pamplona zone; YB, Yakutat block; SE, Saint Elias block; WB, Wrangell block; double line marks 50 km isobath of Benioff zone, queried where inferred; stippled bands mark surface outcrops of major zones of deformation and faulting.

IV. STUDY AREA

This project is concerned with the seismicity within and adjacent to the eastern Gulf of Alaska continental shelf. The area includes southern coastal Alaska and the adjacent continental shelf region between Prince William Sound and Yakutat.

V. METHODS AND RATIONALE OF DATA COLLECTION

A. High-gain, high-frequency seismograph network

The high-gain, high-frequency seismograph stations operated along the eastern Gulf of Alaska largely with funds from the Outer Continental Shelf Environmental Assessment Program are shown in Figure 2. Single-component stations record the vertical component of the ground motion, while three-component stations have instruments to measure north-south and east-west motions as well. The seismic signals detected by these instruments are transmitted by frequency-modulated radio and telephone links to a central recording facility in Palmer, Alaska, where they are photographically recorded on 16-mm film. The films are sent to Menlo Park, California for data processing and analysis.

Data from these instruments are used to determine the parameters of earthquakes as small as magnitude 1. The parameters of interest are origin time, epicenter, depth, magnitude, and for larger shocks, focal mechanism. These data are required to further our understanding of the regional tectonics, to identify active faults, and to assess rates of seismic activity.

B. Earthquake locations

Earthquakes of interest are selected by scanning the 16-mm films and noting times of occurrence. Timing is done by projecting the seismic traces onto a table such that 1 cm corresponds to 1 sec in time, and then digitizing x,y data pairs corresponding to P- and S-wave arrival times, duration of signal in excess of a given threshold, and period and amplitude of maximum signal. The directions of P-wave first motions are also noted. The digitized data are converted to phase data using the computer program DIGIT3 (written by P. L. Ward and W. L. Ellsworth, U.S.G.S., modified by C. D. Stephens), and then are processed using the program HYPOELLIPSE (Lahr, 1980) to determine hypocenter parameters. The P-wave velocity model used for the NEOGA region features a crust of linearly increasing velocity from 5 km/s at the surface to 7.8 km/s at 32 km depth overlying a half-space of 8.2 km/s. A constant P to S-velocity ratio of 1.78 is assumed.

Details of the operation of the high-gain, high-frequency seismograph network and the processing of the seismic data can be found in published catalogs (for example, Stephens and others, 1982).

C. Magnitude determination

Magnitudes are determined from the maximum trace amplitude or the signal duration. Eaton and others (1970) approximate the Richter local magnitude, which by definition is derived from maximum trace amplitudes recorded on

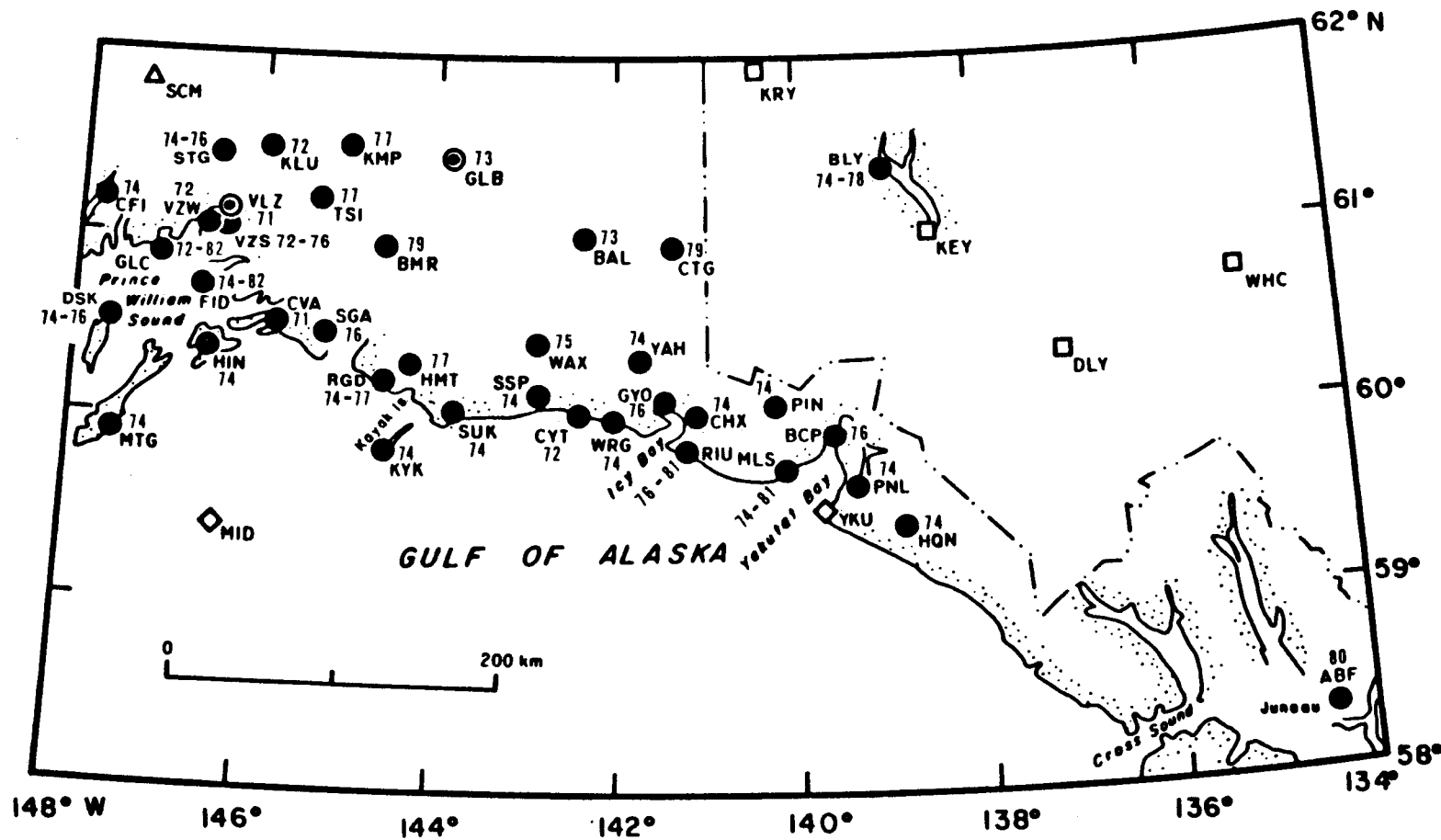


Figure 2. High-gain vertical-component seismic stations operated in the NEGOA and adjacent areas during 1974 through 1981. The symbols are as follows: solid circles--USGS vertical stations; circles with center dot--USGS three-component stations; diamonds--Alaska Tsunami Warning Center stations; triangle--University of Alaska station; squares--stations operated by the Canadian Department of Energy, Mines and Resources. The station at Middleton Island (MID) was not operational between March 1979 and February 1981. For the USGS stations the year(s) of installation (and removal) is given. The stations installed in 1974-1976 were purchased with OCSEAP funds.

standard horizontal Wood-Anderson torsion seismographs, by an amplitude magnitude based on maximum trace amplitudes recorded on high-gain, high-frequency vertical seismographs such as those operated in the Alaskan network. The amplitude magnitude, XMAG, used is based on the work of Eaton and his co-workers and is given by the expression (Lee and Lahr, 1972):

$$\text{XMAG} = \log_{10}A - B_1 + B_2 \log_{10}D^2 \quad (1)$$

where A is the equivalent maximum trace amplitude in millimeters on a standard Wood-Anderson seismograph, D is the hypocentral distance in kilometers, and B_1 and B_2 are constants. Differences in the frequency response of the seismograph systems are accounted for in calculating A. It is assumed, however, that there is no systematic difference between the maximum horizontal ground motion and the maximum vertical motion. The terms $-B_1 + B_2 \log_{10}D^2$ are normalizing terms and equal the logarithm of the trace amplitude for an earthquake of magnitude zero as a function of epicentral distance D. The constants are: $B_1 = 0.15$ and $B_2 = 0.08$ for $D = 1$ to 200 km and $B_1 = 3.38$ and $B_2 = 1.50$ for $D = 200$ to 600 km.

Due to the limited dynamic range of the film recordings the maximum trace amplitude is often offscale. To circumvent this problem, coda duration is also used to estimate the magnitude. For small, shallow earthquakes in central California, Lee and others (1972) express the coda duration magnitude FMAG at a given station by the relationship

$$\text{FMAG} = -0.87 + 2.0 \log_{10}T + 0.0035 D \quad (2)$$

where T is the signal duration in seconds from the P-wave onset to the point where the peak-to-peak trace amplitude on the Geotech Model 6585 film viewer with 20X magnification falls below 1 cm, and D is the epicentral distance in kilometers.

Comparison of XMAG and FMAG estimates from equations (1) and (2) for 77 Alaskan shocks in the Cook Inlet region in the depth range 0 to 150 km and in the magnitude range 1.5 to 3.5 reveals a systematic linear decrease of FMAG relative to XMAG with increasing focal depth. Also, Alaskan earthquakes show no systematic dependence of T on D. The following equation is therefore used, including a linear depth-dependence term, but no distance term:

$$\text{FMAG} = -1.15 + 2.0 \log_{10}T + 0.007 Z \quad (3)$$

where Z is the focal depth in kilometers.

The magnitude preferentially assigned to each earthquake is the mean of the FMAG (equation 3) estimates obtained for USGS stations. The XMAG estimate is used when no FMAG determination can be made.

D. Strong-motion network

Strong-motion instruments are designed to trigger during large earthquakes and give high quality records of large ground motions which are

necessary for engineering design purposes. This type of instrument was first installed in Alaska following the 1964 Alaska earthquake. Between 1974 and 1981 OCSEAP funding supported both the installation and maintenance of additional strong-motion instruments in southern Alaska. Figure 3 shows the locations of instruments, almost exclusively Kinematics SMA-1 accelerographs, operated by the USGS and their dates of installation and removal.

VI. RESULTS AND DISCUSSION

A. Proposed kinematic model for Pacific-North American interaction

A working model has been developed for the Holocene Pacific-North American plate interaction along the Gulf of Alaska (Lahr and Plafker, 1980). In this model deformation within the North American plate is concentrated mainly on the boundaries of three blocks, which are assumed to be relatively rigid. In the following discussion, the plate and block boundaries will be described first, then the motions within the model will be given, and finally the historic seismicity will be discussed and related to the model.

1. Plate and block boundaries

The tectonic setting and major boundaries are illustrated in Figure 1. The Yakutat block (YB), which has been described by Plafker and others (1978), is bounded by the Transition zone (TZ), the Fairweather fault (F), and the Pamplona zone (PZ) which passes through Icy Bay (I). Northwest of the Yakutat block is the Wrangell block (WB). The Wrangell block is bounded on the northeast by the Denali (D), Totschunda (T), and an inferred connecting fault between the Totschunda and Fairweather faults, and on the south by the Pamplona zone (PZ) and the Aleutian megathrust (AM). The northwestern boundary of the Wrangell block is speculative; it is tentatively assumed to diverge southward from the Denali fault, pass through Cook Inlet (CI), around Kodiak Island (KO) and back to the Aleutian megathrust. The St. Elias block (SE) is bounded by the Totschunda-Fairweather system on the southwest and by the Duke River (DR), Dalton (DA), and Chatham Strait (C) faults on the northeast.

The extent and configuration of the Pacific plate underlying Alaska can be inferred, at least partly, from the distribution of subcrustal earthquakes that make up the Benioff zone. These events occur within the underthrust oceanic plate near its upper surface. The 50-km isobath of earthquake foci shown in Figure 1 northwest of the Aleutian megathrust (AM) represents an active Benioff zone (Lahr, 1975).

The continuity of the Pacific plate below the Gulf of Alaska and the hundreds of kilometers of convergence indicated by the Benioff zone northwest of Prince William Sound imply that a similar amount of convergence has taken place in the zone between Prince William Sound and the Queen Charlotte Islands fault. The queried 50-km isobath in Figure 1 is the position for the underthrust Pacific plate suggested by Lahr and Plafker (1980) based on two assumptions: (1) the andesitic Wrangell

STRONG MOTION STATIONS

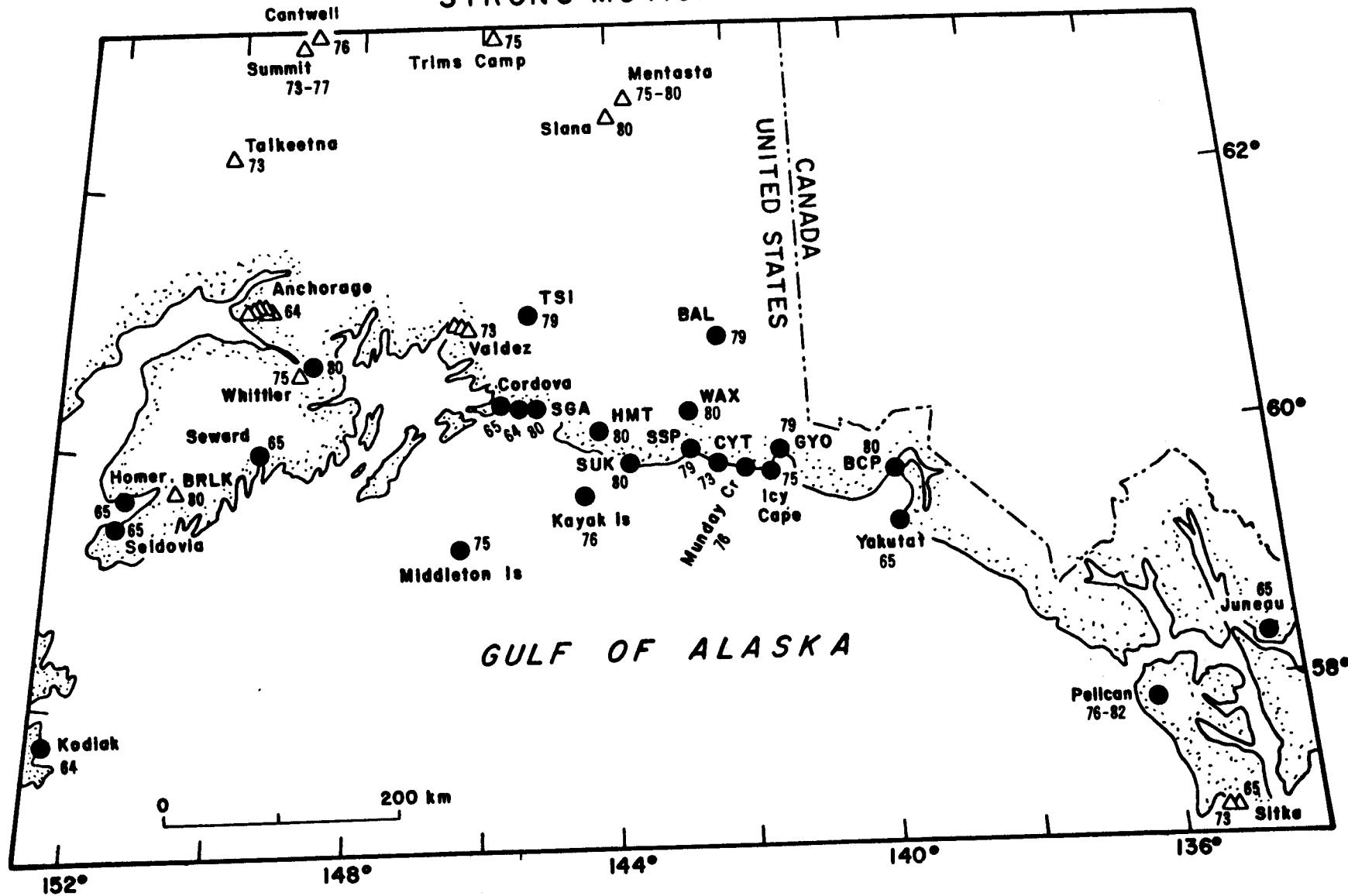


Figure 3. Location of USGS strong-motion instruments in southern Alaska showing year(s) of installation (and removal). Stations which were maintained at least in part with OCSEAP funds are indicated by solid circles. For Anchorage and Valdez, the year of the earliest installation is given.

volcanic rocks (Deninger, 1972; MacKevett, 1978) are situated above the 100-km isobath of the Benioff zone, as is typical for andesitic volcanoes associated with an underthrust plate, and (2) the dip of the plate between 50 and 100 km depth (about 40°) is similar to that observed elsewhere along the Aleutian arc (35° to 45°; Davies and House, 1979). Analysis of seismic data from the local seismic network has since confirmed the presence of a north-northeast dipping Benioff zone south of the Wrangells (Stephens and others, 1983) between 143° and 145° W longitude. Although the deepest event so far located has a depth of only 85 km, extrapolation of the zone to deeper depths would place Mounts Wrangell and Drum above events in the 100 to 125 km depth range. It therefore seems likely that the Pacific plate extends at shallow depths below much of the Yakutat and Wrangell blocks, a configuration that should be conducive to significant coupling between those blocks and the Pacific plate.

2. Plate motions in model

Motions in the kinematic model are relative to the stable parts of the North American plate, and in particular the interior of Alaska. This kinematic model was developed to be as compatible as possible with historical seismicity and known rates of relative plate movement (Lahr and Plafker, 1980).

The Pacific plate rotates relative to North America about a pole in eastern Canada and moves northwestward at 5.8 cm/yr along the Queen Charlotte Islands fault (Figure 4). The relative velocity increases to the southwest as distance from the pole of rotation increases. The Yakutat block moves parallel to the Pacific plate but with a slightly lower relative velocity (5.4 cm/yr). Motion of the Wrangell block is counterclockwise rotation about an axis near Kodiak Island, such that its northeastern edge moves in a right-lateral sense relative to the North American plate with a velocity of approximately 1 cm/yr. The St. Elias block moves roughly parallel to the Pacific plate with a relative velocity of 0.2 cm/yr. A cross section through the model is given in Figure 5.

3. Historical seismic record

The instrumental seismic history of the eastern Gulf of Alaska region, prior to the installation of a local network in 1974, is limited in terms of both completeness and accuracy by the lack of nearby seismograph stations. The record for events larger than 7-3/4 is probably complete only since 1899; for events larger than 6 since the early 1930's; and for events larger than 5 since the 1964 Alaska earthquake (Page, 1975; Horner, in press).

Figure 6 shows the distribution of earthquakes from 1900 through March 28, 1964, the date of the 1964 Alaska earthquake. Most of these data are from the Earthquake Data File (EDF) of NOAA. The magnitude used for scaling in the figures is the maximum of the m_b , M_{other} (usually BRK or PAS magnitude), and M_L (PMR, the NOAA Alaska Tsunami

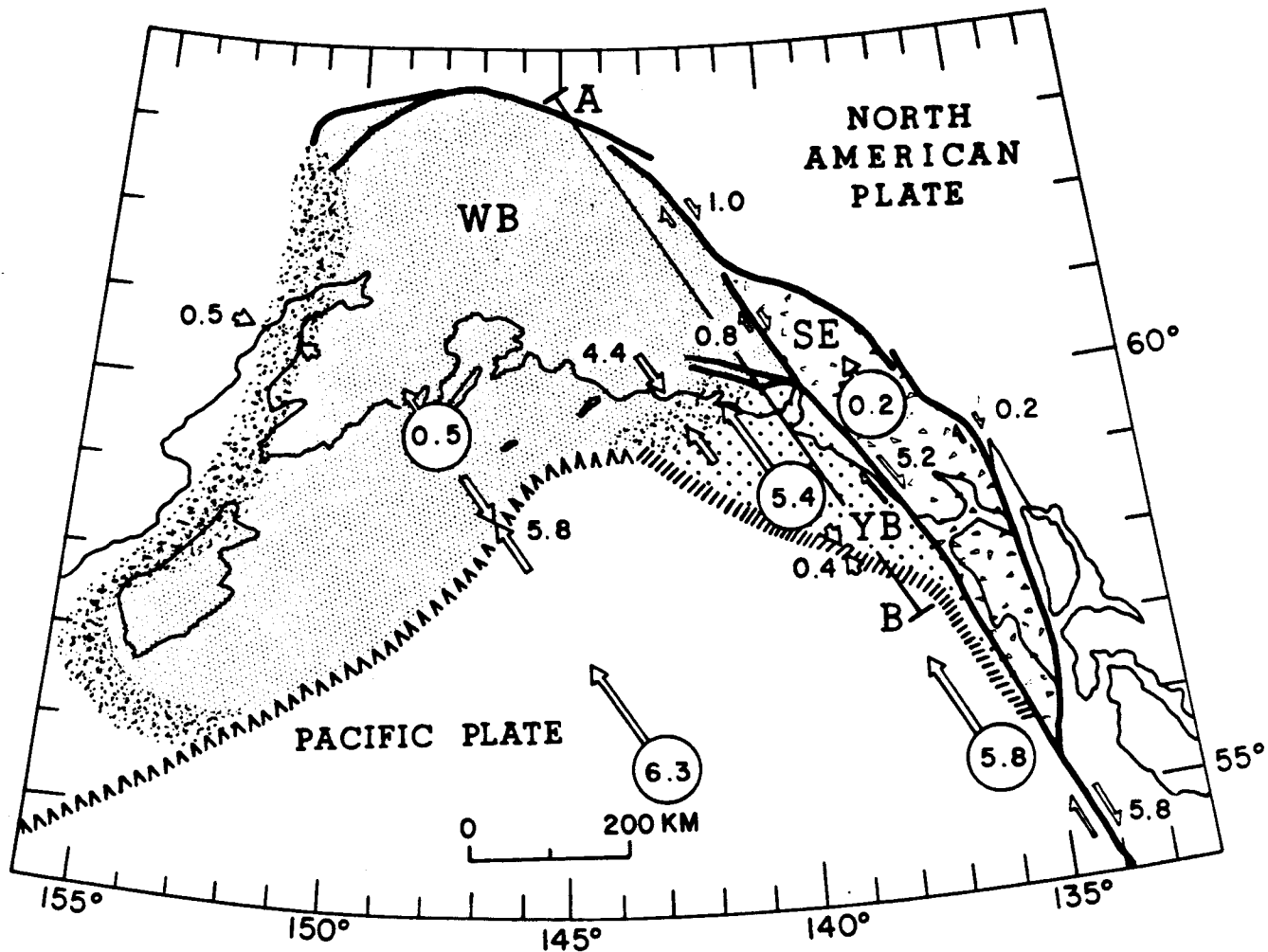


Figure 4. Proposed model for present crustal deformation along Pacific-North American plate boundary in southern and southeastern Alaska. Circled numbers give rate of motion (centimeters per year) of Pacific plate, Yakutat block (YB), St. Elias block (SE), and Wrangell block (WB) relative to North American plate. Numbers next to paired vectors give rate of motion across indicated zone. Stippled bands mark surface outcrops of major zones of deformation and faulting. A-B, location of cross section shown in Figure 5.

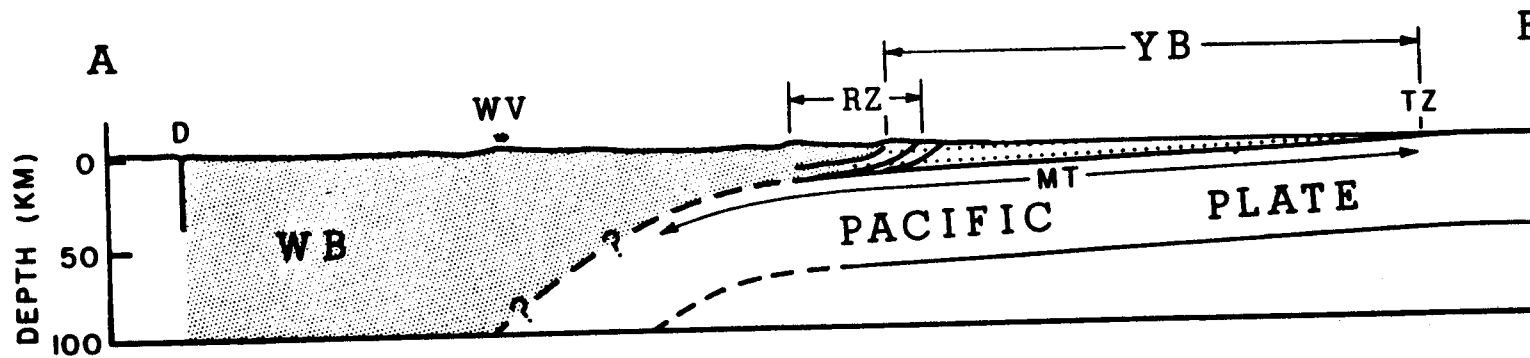


Figure 5. Diagrammatic structure along plane A-B of Figure 4. Abbreviations are: MT - main thrust; WB - Wrangell block; YB - Yakutat block; WV - Wrangell volcanics; D - Denali fault; RZ - rupture zone of February 28, 1979, earthquake; TZ - transition zone. No vertical exaggeration.

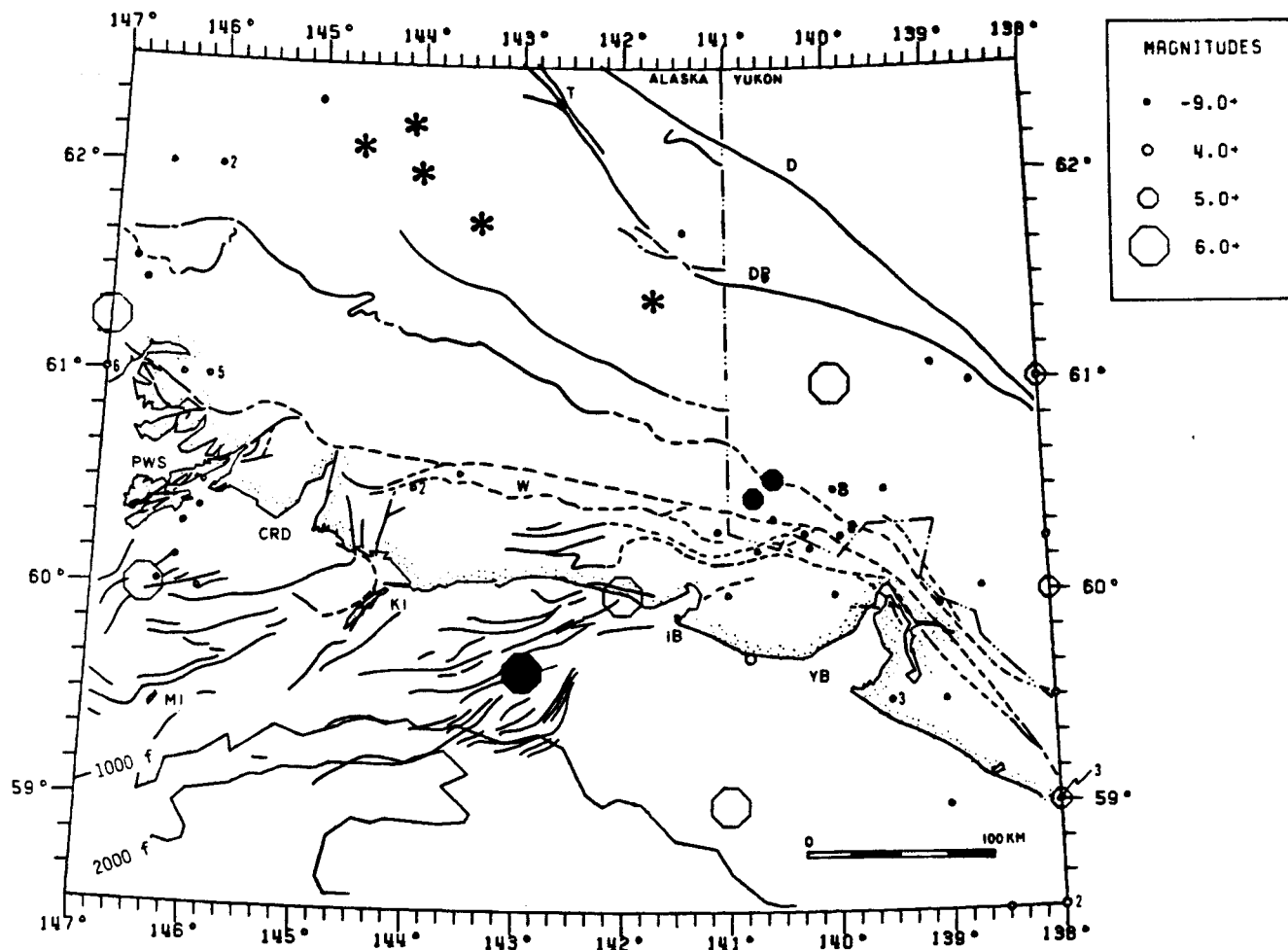


Figure 6a. Map of epicenters for 80 historic earthquakes that occurred between January 1, 1900 and March 28, 1964. Numbers next to epicenters indicate total number of events in cases where more than one event occurs at the same location with the same magnitude. Filled symbols mark the more accurate epicenters, and are repeated in Figure 7. Symbol size is proportional to magnitude as indicated at the upper right. Faults after Beikman (1980), Bruns (1979), and Clague (1979). Volcanic cones (stars) after King (1969). Abbreviations are: CRD - Copper River Delta; D - Denali fault; DR - Duke River fault; IB - Icy Bay; KI - Kayak Island; MI - Middleton Island; PWS - Prince William Sound; W - Waxell Ridge; and YB - Yakutat Bay. All but one of the events indicated to be less than magnitude 4.0 have no magnitude reported, so many of these events are likely to be larger than indicated.

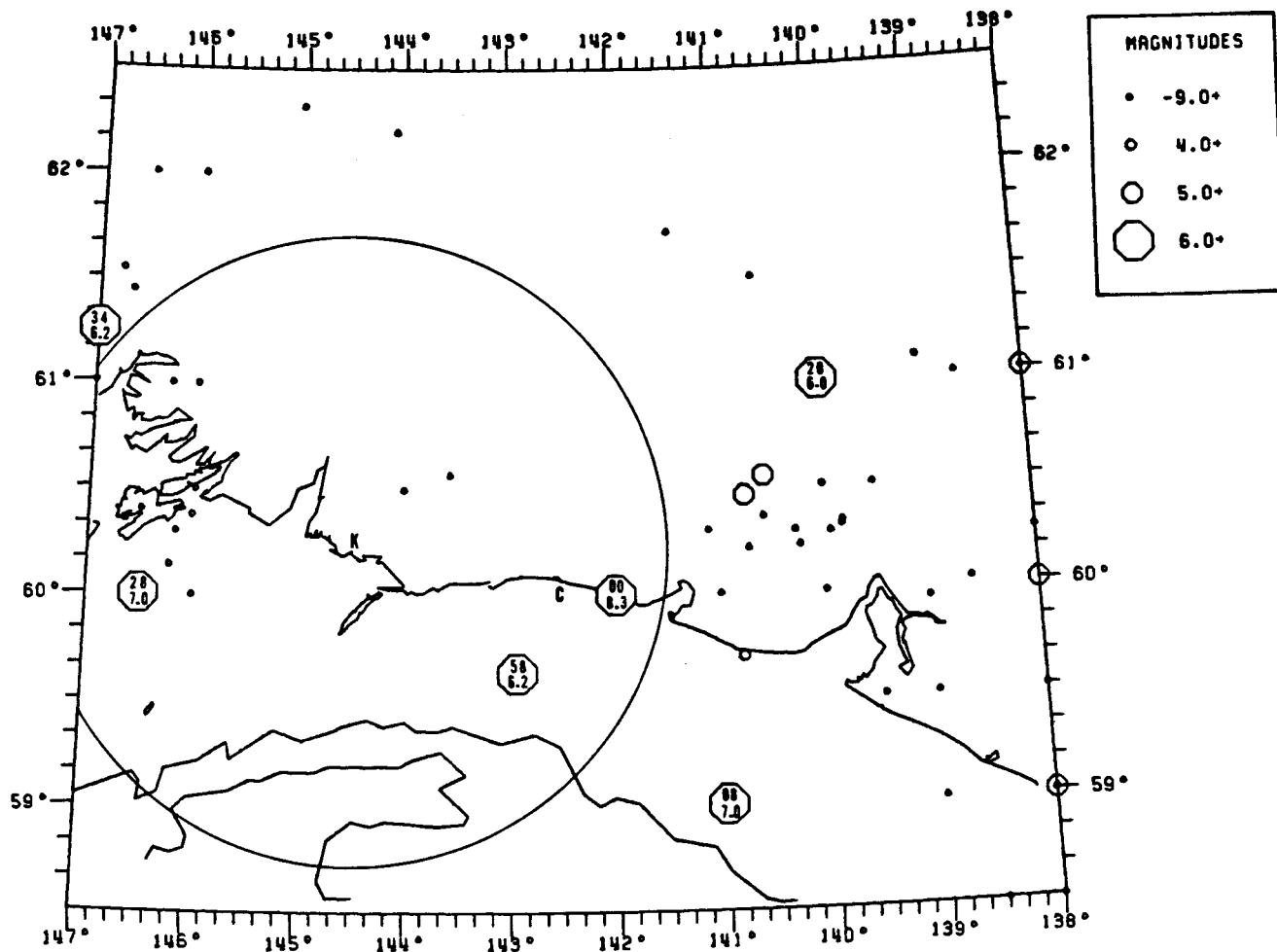


Figure 6b. Historic epicenters, as in Figure 6a, except year and magnitude are indicated for events greater than or equal to 6.0. Abbreviations are: K - Katalla; and C - Cape Yakataga. Circle encloses epicentral location of 1908 event, as inferred from the intensity at Katalla.

Warning Center, formerly Palmer Observatory) magnitude as given in the EDF file. Epicenters for 24 of the events that occurred between 1954 and 1959 are from published relocations (Tobin and Sykes, 1966; Tobin and Sykes, 1968; Sykes, 1971). The 24 relocated events are shown again in Figure 7 along with the location given in the EDF. Tobin and Sykes (1966) estimate that many of the relocated events have epicentral standard errors less than 10 to 20 km as compared to errors as large as 100 km that were common previously. They note, however, that the accuracy of the epicenters could be less than that suggested by the standard errors if there is a regional bias in the locations. Figure 7 gives a graphic indication of the uncertainties in the historic locations.

The large event shown just west of Icy Bay occurred on October 9, 1900, with a magnitude of 8.1 (Richter, 1958; Thatcher and Plafker, 1977). Based on macroseismic effects McCann and others (1980) conclude that this event actually occurred in the vicinity of Kodiak Island, several hundred kilometers southwest of Icy Bay. However, two great (M_s 8) earthquakes that occurred in 1899 produced uplift of as much as 14 m near Yakutat Bay (Tarr and Martin, 1912), and may have ruptured across much of the coast between Yakutat Bay and Kayak Island (McCann and others, 1980). These events occurred within the complex northern corner of the Yakutat block and possibly along the Pamplona zone of thrusting.

The magnitude 7.0 earthquake of 1908 southeast of Icy Bay was located to the nearest degree by Gutenberg and Richter (1954) using arrival times from 11 stations including Sitka (based on Gutenberg and Richter's notes provided by W.H.K. Lee, U.S.G.S.). Gutenberg and Richter's notes include "near Yakataga IX-X", probably reflecting the intensity at Cape Yakataga (C in Figure 6b). The Earthquake History of the United States (1973) includes "At Katalla, there were sharp shocks in rapid succession during which buildings rocked. Rockslides were reported at Yakataga. Felt from Sitka to Seward." The rockslides at Katalla (K in Figure 6b), which may account for the assignment of intensity IX to X, are now thought to be a poor determinant of intensity (Stover and others, 1980). Tarr and Martin (1912) report that the shock was felt slightly at Sitka but generally at Seward. The Katalla Herald newspaper article of May 16, 1908 (Tarr and Martin, 1912) states that the earthquake "set every building in town rocking, moved furniture about rooms, knocked dishes from shelves, and caused many of the people in town, many of whom had retired, to take to the streets." Based on this description, the Modified Mercalli intensity was about VI at Katalla. The 1979 St. Elias earthquake occurred 165 km from Katalla and had a comparable magnitude to the 1908 event. The intensity map of Stover and others (1980) implies that the intensity at Katalla due to the 1979 event was within the V - VI range. Therefore the location of the 1908 earthquake was probably within 165 km of Katalla (see Figure 6b). Due to the location uncertainty it is not possible to determine which fault zone ruptured during the 1908 event.

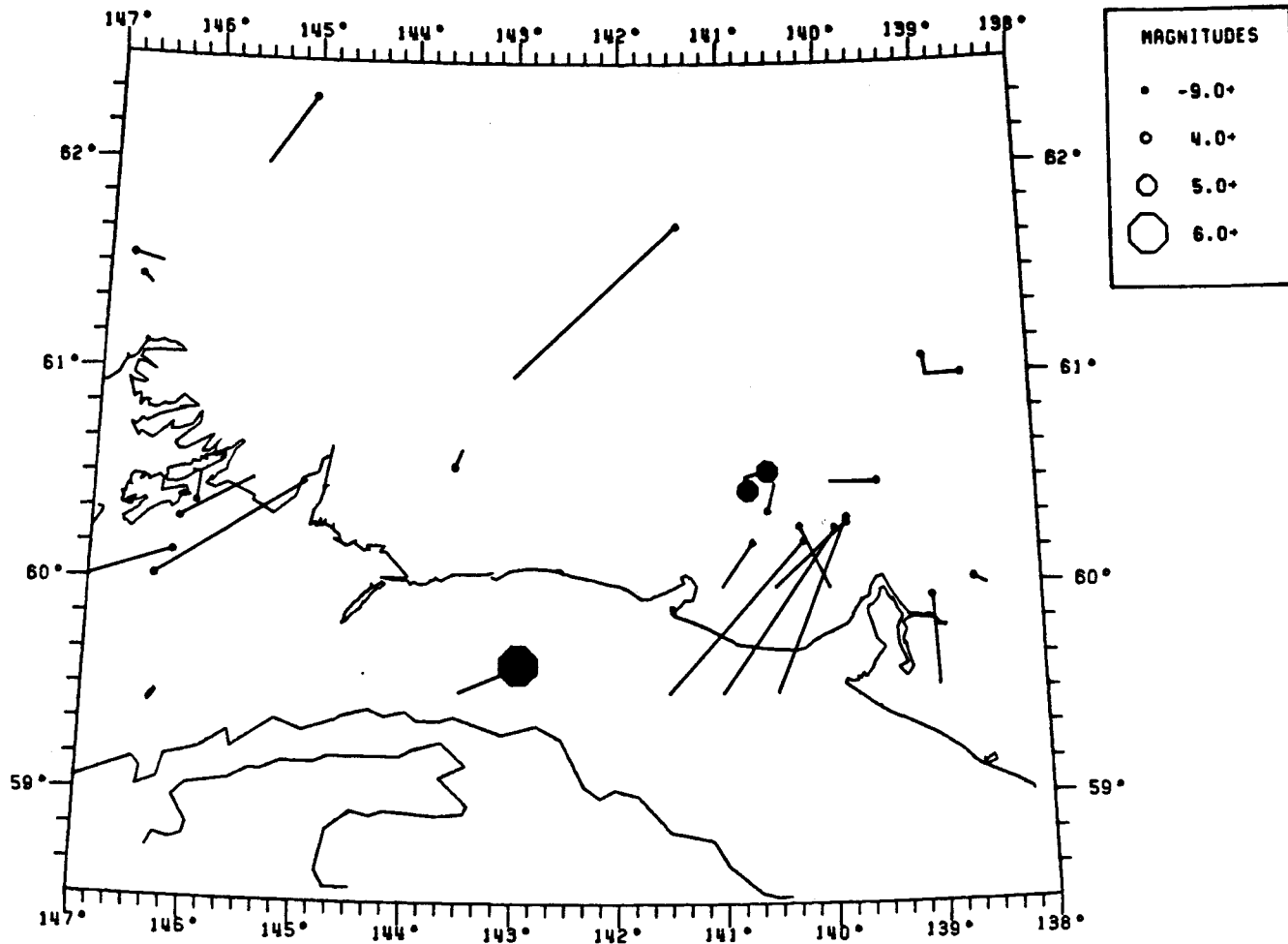


Figure 7. Epicenters of 24 relocated earthquakes (Tobin and Sykes, 1966; Tobin and Sykes, 1968; Sykes, 1971) that occurred between 1954 and 1959 (solid symbols) with a line extending to the location given in the Earthquake Data File.

In 1928 a magnitude 7.0 earthquake occurred south of Prince William Sound, probably on the shallow dipping Aleutian megathrust interface. During the 1964 earthquake secondary faulting occurred within the Wrangell block on the Patton Bay and Montague Island faults. We cannot preclude the possibility that the 1928 event could have been of the latter type. A third possibility, although less likely for an earthquake of this size, is that it occurred within the Pacific plate that is underthrusting the Wrangell block.

Epicenters of events that occurred within 2 weeks of the 1958 earthquake on the Fairweather fault (M_g 7.9; Tobin and Sykes, 1968; Sykes, 1971) are shown in Figure 8. The rupture zone extended from north of Yakutat Bay to Cross Sound, a total distance of about 325 km (Tobin and Sykes, 1968). Fault slip was predominantly right-lateral strike-slip, with the largest offset measuring 6.5 m (Tocher, 1960). The rate of relative motion across the Fairweather fault (which bounds the Yakutat and St. Elias blocks) has probably averaged at least 4.8 and more probably 5.8 cm/yr in a right-lateral sense for at least the past 1,000 years (Plafker and others, 1978). This rate is in reasonable agreement with the model rate of 5.2 cm/yr (Figure 4).

The 1964 Alaska earthquake was one of the largest earthquakes in history, being produced by an average of 12 meters of dip slip motion on a fault plane approximately 200 km wide, 600 km long, and dipping 4° to the northwest (Hastie and Savage, 1970; Page, 1968; Plafker, 1969). Earthquakes that occurred during the first two weeks following the Alaska earthquake are shown in Figure 9.

The severe damage to the coast of south-central Alaska produced by vertical displacements, subaqueous slides, and destructive tsunamis is described by Plafker and Mayo (1965) and is repeated here to illustrate the possible effects of a great earthquake within the eastern Gulf of Alaska region.

"Notable changes in land level occurred over an area in excess of 50,000 square miles [130,000 square kilometers] in a broad northeast-trending belt more than 500 miles [800 kilometers] long and as much as 250 miles [400 kilometers] wide, which lies between the Aleutian Trench and the Aleutian volcanic Arc. The northwest part of this belt, which includes most of the Kenai Peninsula and the Kodiak Island group, sank as much as 7.5 feet [2.3 meters], bringing some roads, rail lines, docks, and settlements within reach of high tides and producing a fringe of salt-water-killed vegetation along the drowned coasts. The area to the southeast, including most of Prince William Sound and the adjacent continental shelf as far south as southern Kodiak Island, rose generally 4 to 8 feet [1.2 to 2.4 meters], and locally at least 33 feet [10.1 meters]. Some beaches and surfcut platforms were permanently raised above the reach of tides, resulting in mass extermination of intertidal faunas and floras and impaired usefulness of harbors, channels, and many shoreline installations."

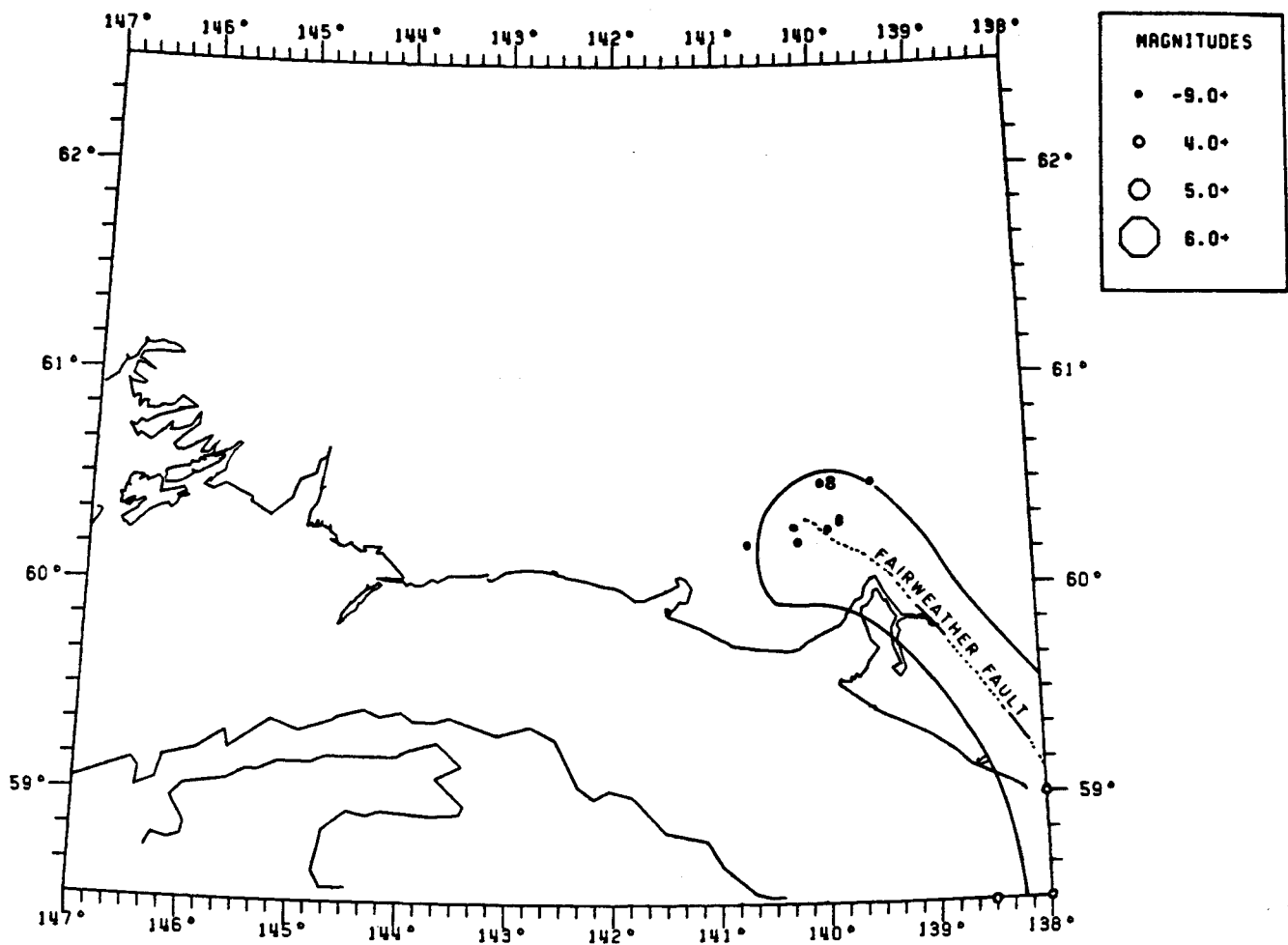


Figure 8. Epicenter map of the 19 events that occurred within two weeks of the July 10, 1958 earthquake on the Fairweather fault. 1958 rupture zone after McCann and others (1980). Filled symbols are relocated events from Tobin and Sykes (1966, 1968) and Sykes (1971).

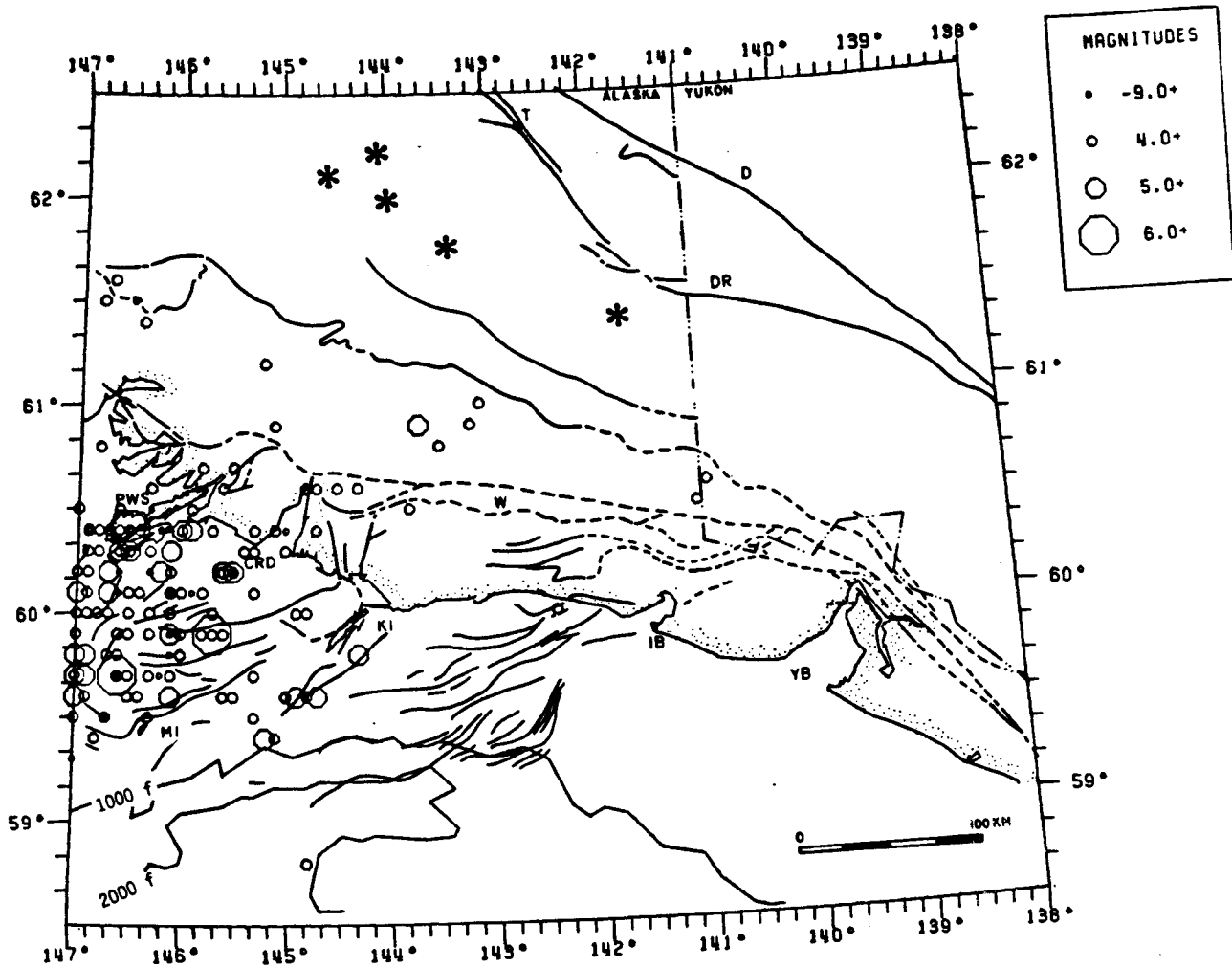


Figure 9a. Map of epicenters for 155 earthquakes that occurred between March 28, 1964 and April 12, 1964, the first two weeks following the 1964 Alaska earthquake. Symbols and labels same as Figure 6a.

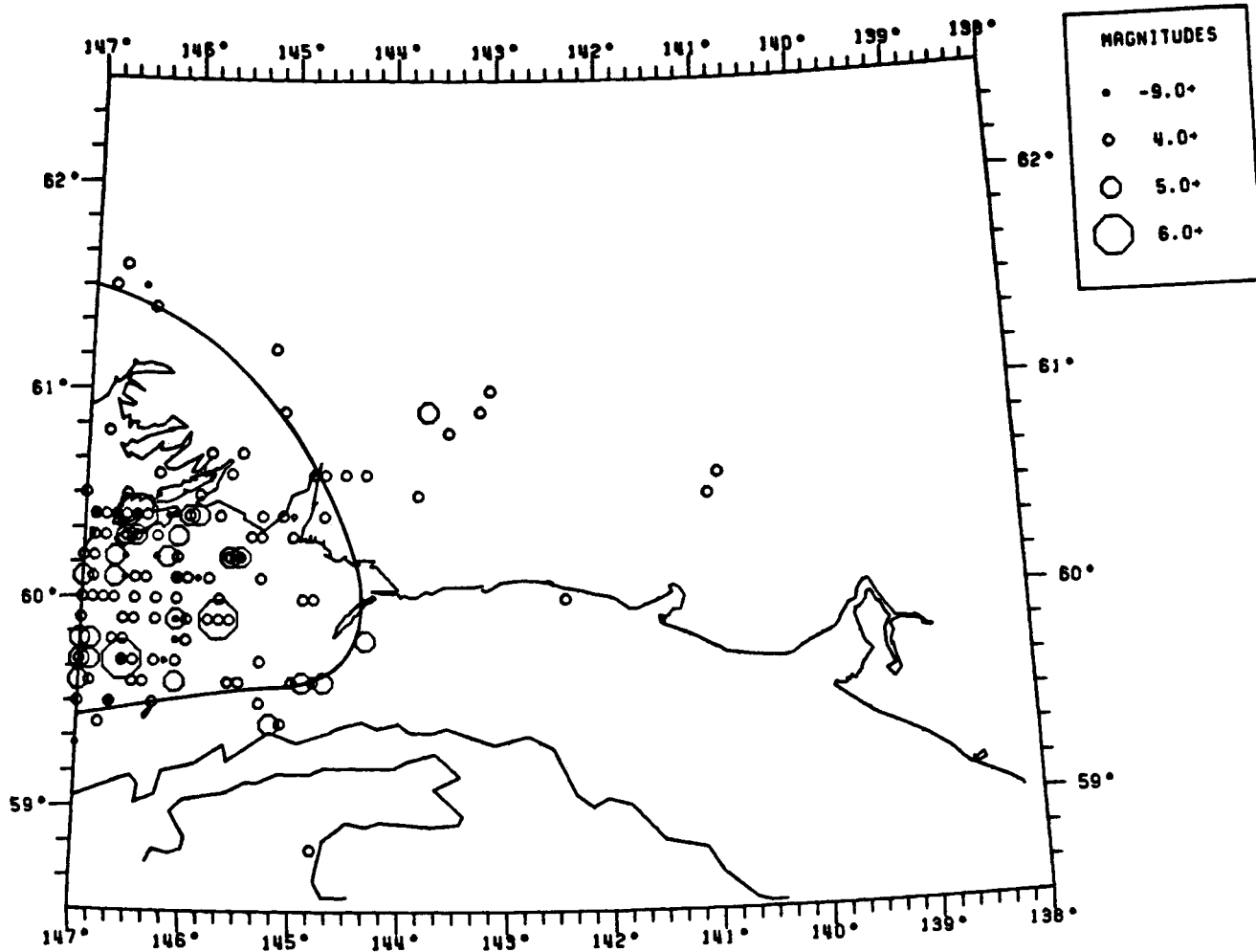


Figure 9b. Epicenters during first two weeks following the 1964 earthquake, as in Figure 9a. The eastern boundary of the 1964 rupture zone, as defined by McCann and others (1979), is shown.

"Surface faulting was confined to Montague Island, and was dominantly vertical and subsidiary to regional uplift. Of the two known faults one has been traced more than 16 miles [26 kilometers] on land and about 15 miles [24 kilometers] in the submarine topography to the southwest of the island. Maximum measured vertical fault displacement on land was 16 feet [4.9 meters] on one fault and about 18 feet [5.5 meters] on the other."

"Submarine uplift of the continental shelf generated a train of long-period large-amplitude seismic sea waves, the first of which struck the outer coasts of the Kenai Peninsula and Kodiak Island between 19 and 30 minutes after the initial shock. The highest waves inundated shorelines locally to elevations of 35 to 40 feet [10.7 to 12.2 meters], causing 20 deaths and damage to property all along the coast of the Gulf of Alaska, especially in those areas that had been lowered relative to sea level by tectonic subsidence. The sea waves were recorded on tide gauges throughout the Pacific Ocean and resulted in casualties and local damage at points as distant as British Columbia, Oregon, and California."

"The earthquake caused widespread subaqueous sliding and sedimentation in Prince William Sound, along the south coast of the Kenai Peninsula, and in Kenai Lake. These slides carried away the port facilities of Seward and Valdez and the small boat harbor at Homer. Local violent surges of water, many of which were generated by known subaqueous slides that occurred during the earthquake, left swash marks as much as 170 feet [51.8 meters] above water level and caused heavy damage and took 85 lives at Seward, Valdez, Whittier, Chenega, and several smaller communities in Prince William Sound."

The seismicity during the ten years following the 1964 Alaska earthquake is shown in Figure 10. Epicenters are from bulletins of the International Seismological Center (ISC) and magnitudes are the maxima of the ISC m_b , EDF m_b , EDF M_{other} (usually M_s at BRK or PAS), and the EDF M_L (Palmer). Activity is dominated by events within and adjacent to the 1964 rupture zone. Offshore activity is approximately bounded on the south and east by the 1000 fathom isobath and the Pamplona zone. Two notable concentrations occur along this boundary, one near 145° W and the other along the Pamplona zone. The rate of activity near 145° W was highest just following the 1964 earthquake. The rate decreased steadily to a low level by the end of 1965 and remained low except for a sequence in mid-1969 that included three magnitude m_b 5 events. The Pamplona zone activity of Figure 10 occurred during two swarms. The first consisted of ten events ranging up to magnitude m_b 5.3 during April and May 1964, while the second consisted of 13 events during April 1970, the largest event having magnitude M_s 6.8. The temporal clustering of the Pamplona zone shocks contrasts with the more nearly continuous activity within the cluster northeast of Icy Bay.

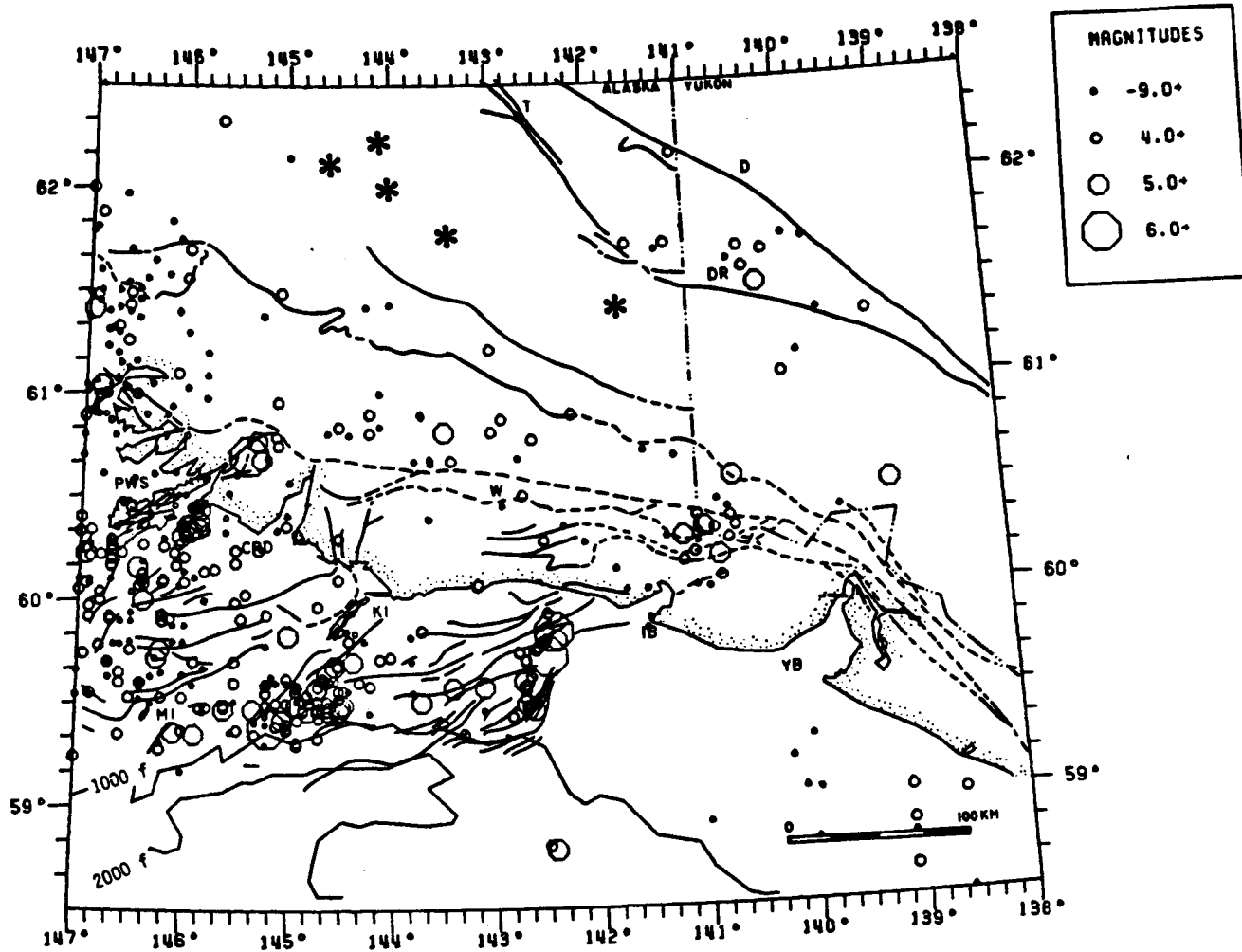


Figure 10a. Epicenter map of 453 earthquakes that occurred between April 13, 1964 and September 30, 1974. Symbols and labels same as Figure 6a.

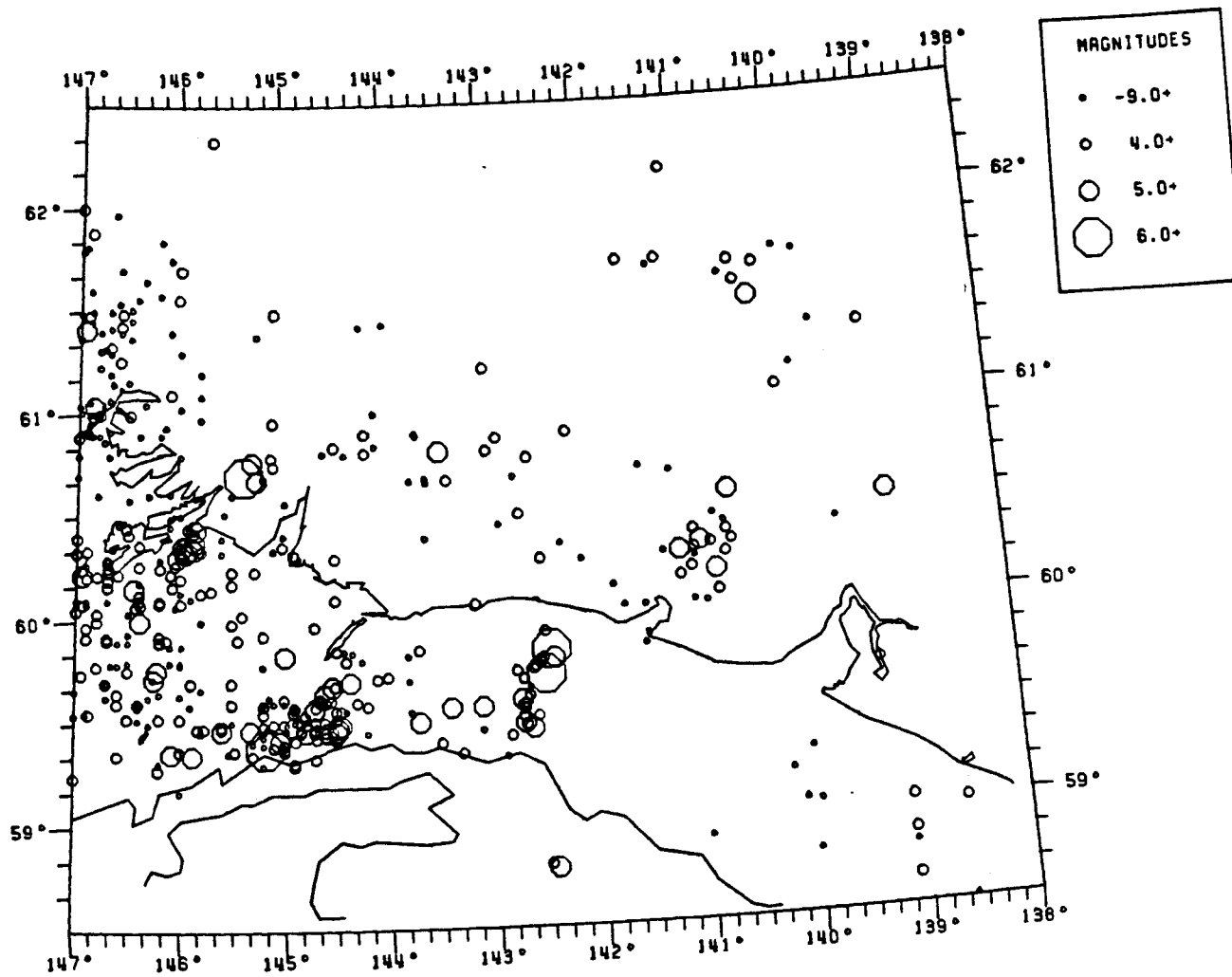


Figure 10b. April 13, 1964 through September 30, 1974 epicenters, as in Figure 10a.

Focal mechanisms were determined for two of these events by Perez and Jacob (1980), and both were consistent with underthrusting on a shallow dipping plane, one in a north-northeast direction and the other in a north-northwest direction. These mechanisms are in general agreement with the proposed model, except that northwest-southeast oriented convergence would be expected between the Yakutat and Wrangell blocks.

B. Seismicity during 1974 - 1981

In September 1974 the seismographic coverage of the eastern Gulf of Alaska was greatly enhanced by the installation of thirteen new stations between Montague Island and Yakutat Bay. This coverage made it possible to routinely monitor seismic activity as small as magnitude 1.0 and to locate events with increased accuracy. Except for gaps that total 1.75 years due to instrumental and operational difficulties, preliminary processing is complete for October 1974 through September 1981. For this period a total of 9647 hypocenters has been determined, which is 14 times greater than the total number located prior to October 1974.

The magnitudes calculated from the local network data are systematically offset to smaller values as compared to the EDF magnitudes. For example, Figure 11 shows the EDF m_b magnitude plotted versus the coda magnitude for events in the region $138^\circ - 147^\circ W$, $58.5^\circ - 62.5^\circ N$ for October 1974 through November 1980. In order to present a complete picture of the most significant earthquakes since 1974, all events with EDF magnitude greater than or equal to 4 were processed using the local network to determine both location and magnitude. Based on the distribution of Figure 11, this sample should contain all events of coda magnitude 3.5 or larger.

In Figure 12, the distribution of events of coda magnitude 3.5 and greater that occurred between October 1, 1974 and September 31, 1981 is shown. Note that, relative to earlier figures, there is a shift of 0.8 magnitude units in the limits chosen for symbol size. This technique was employed so that the earthquakes on this plot would not appear smaller than earthquakes of comparable magnitude in the previous figures. The largest event is the 1979 St. Elias earthquake north of Icy Bay which had a magnitude M_s 7.1 (Buland and Taggart, 1981), and most of the events north and east of Icy Bay in Figure 12 are St. Elias aftershocks. The two next largest events lie offshore near the 1,000 fathom isobath and near the southern limit of seismicity noted in Figure 10.

The seismic data obtained during 1974 - 1981 (Figures 13-17) have provided important constraints for the development of a regional tectonic model. One of the key results from this monitoring is the detailed recording of the aftershock sequence of the large 1979 St. Elias earthquake (Stephens and others, 1980). The depth control provided by the local seismic stations helped to confirm that the rupture from this event was confined to a buried fault or fault system at shallow depth. Focal mechanisms determined from P-wave first-motions for the mainshock and several aftershocks are compatible with a teleseismically determined focal mechanism for the mainshock of low-angle thrusting on a northward-dipping

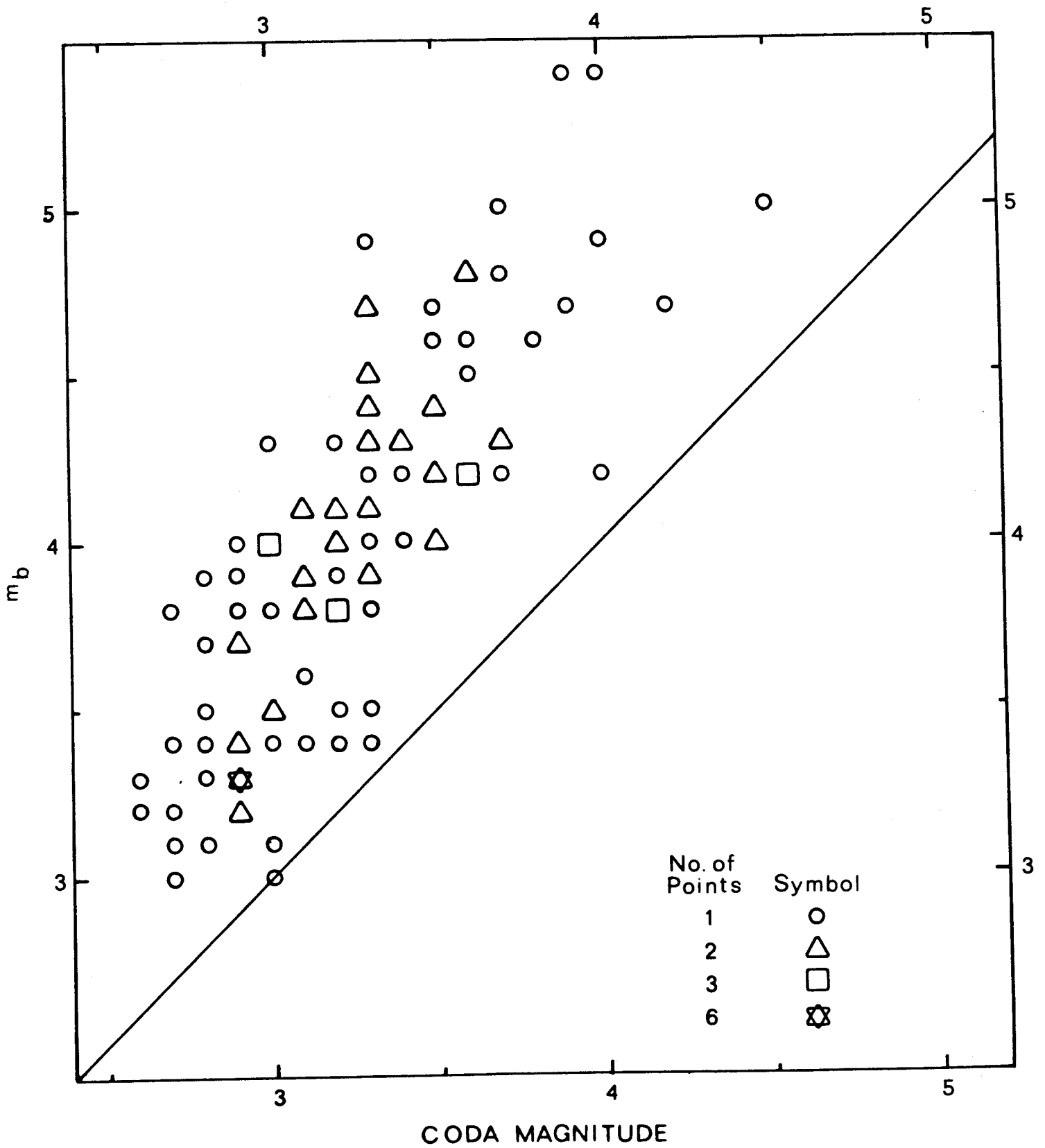


Figure 11. Plot of EDF body-wave magnitude (m_b) versus coda magnitude calculated from local stations.

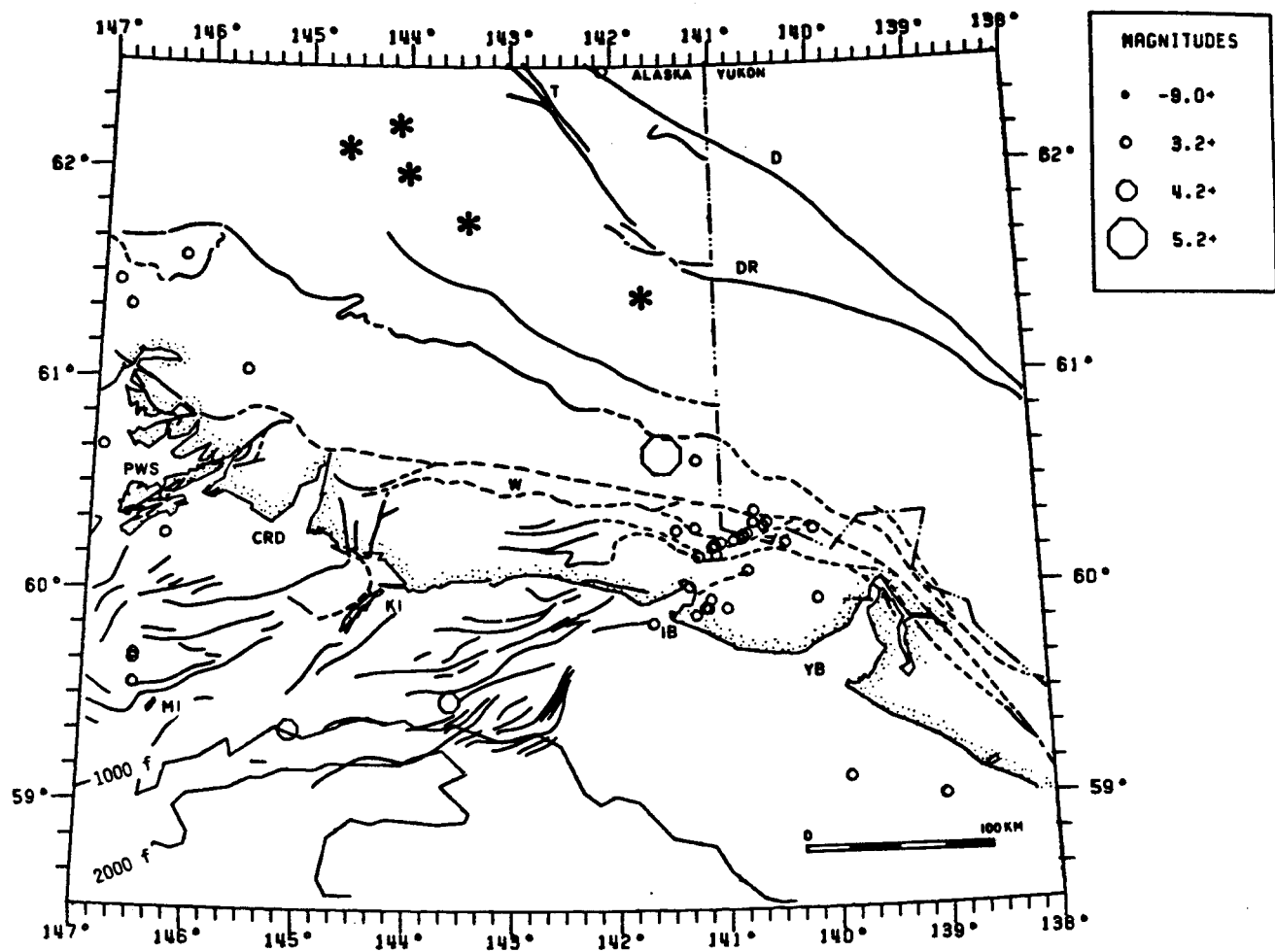


Figure 12a. Epicenter map of 42 earthquakes with coda magnitudes greater than or equal to 3.5 that occurred between October 1, 1974 and September 31, 1981. Labels same as Figure 6a. Note change in symbol sizes from previous figures.

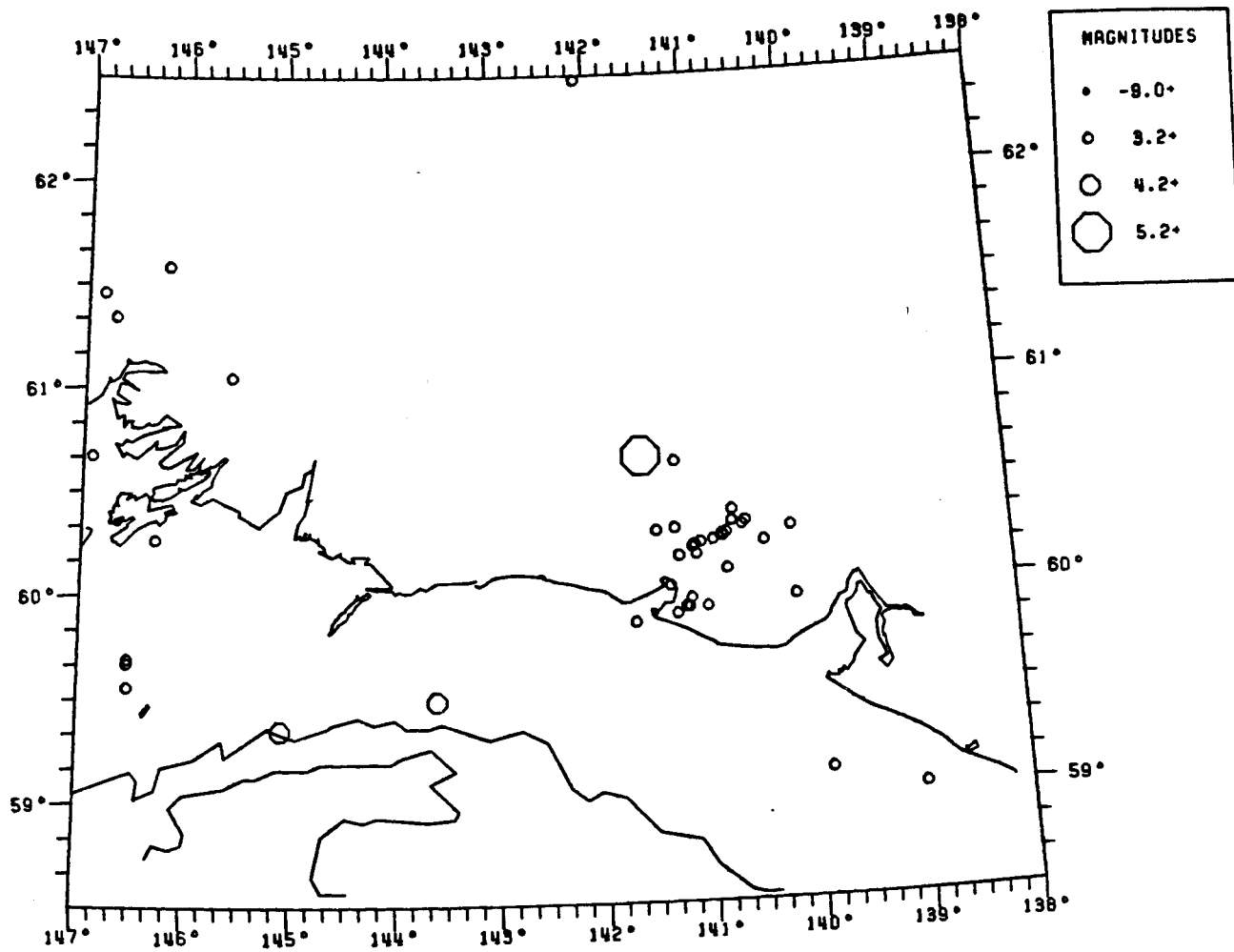


Figure 12b. October 1, 1974 through September 30, 1981 epicenters, as in Figure 12a.

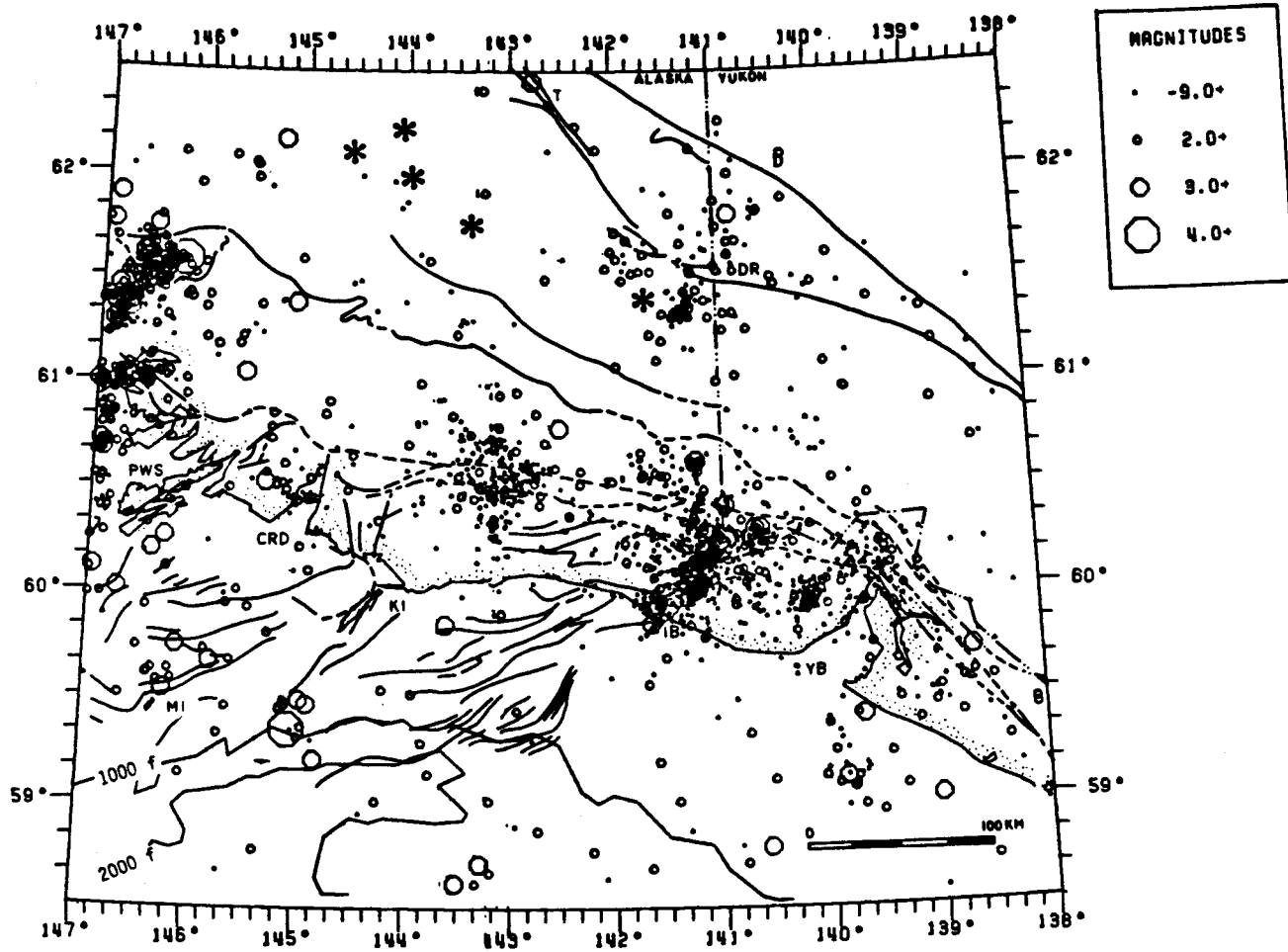


Figure 13a. Epicenter map of 2015 earthquakes located by the local seismograph network between October 1, 1974 and February 28, 1979 just prior to the St. Elias earthquake. Labels same as Figure 6a. Note that symbol sizes are larger than in previous figures.

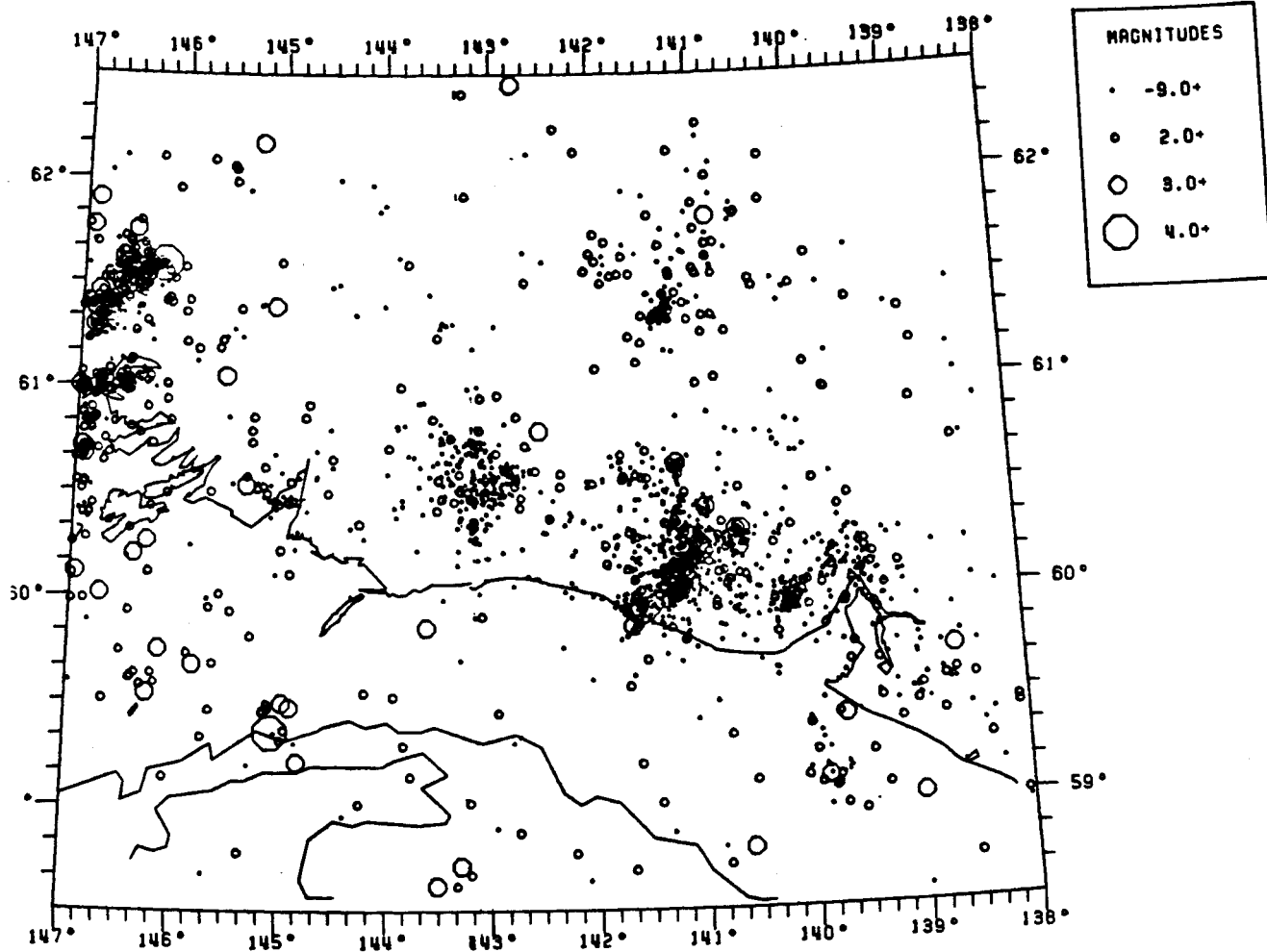


Figure 13b. October 1, 1974 through February 28, 1979 epicenters as in Figure 13a.

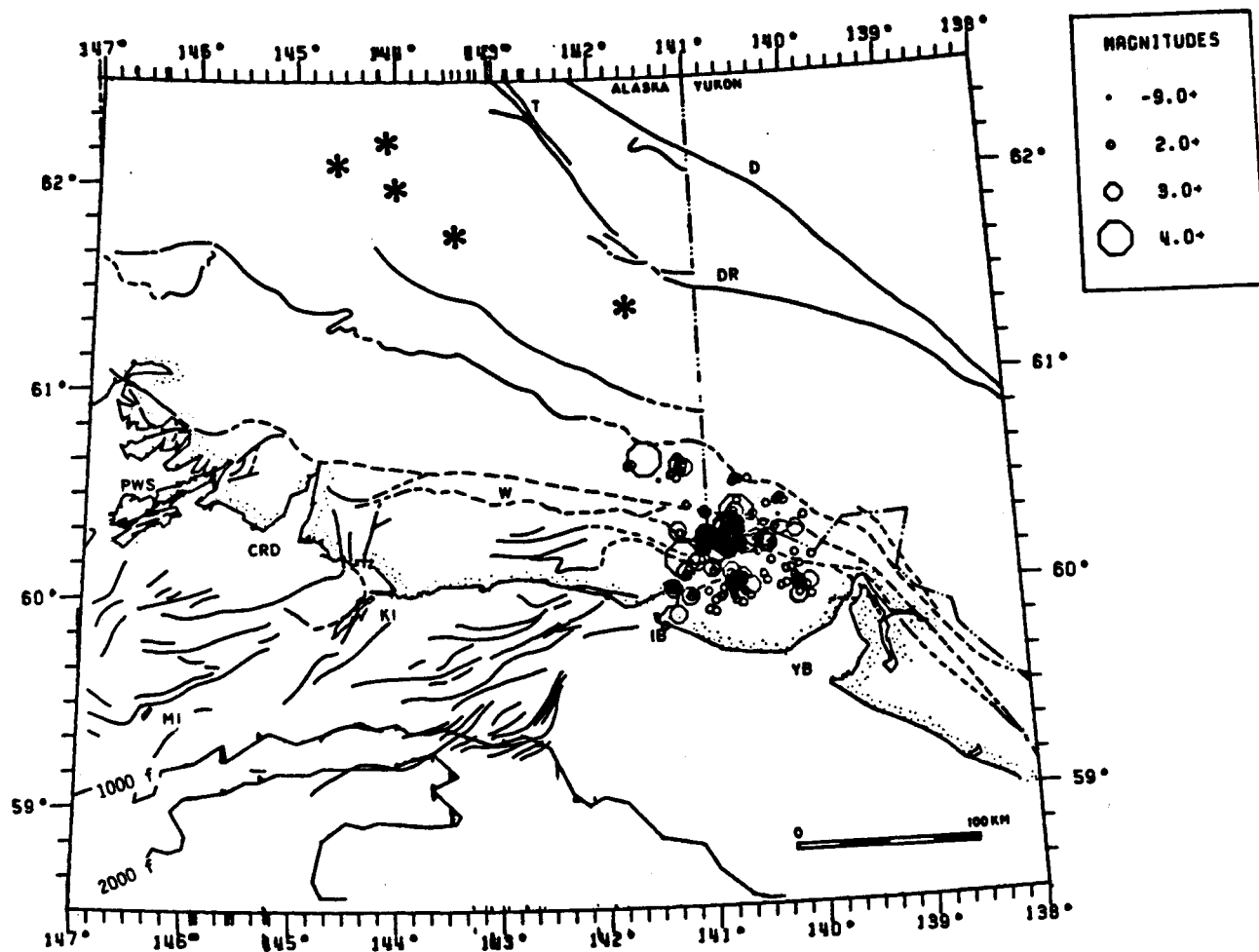


Figure 14a. Epicenter map of 287 earthquakes located by the local seismograph network starting with the St. Elias earthquake on February 28, 1979 through March 30, 1979. Labels same as Figure 6a.

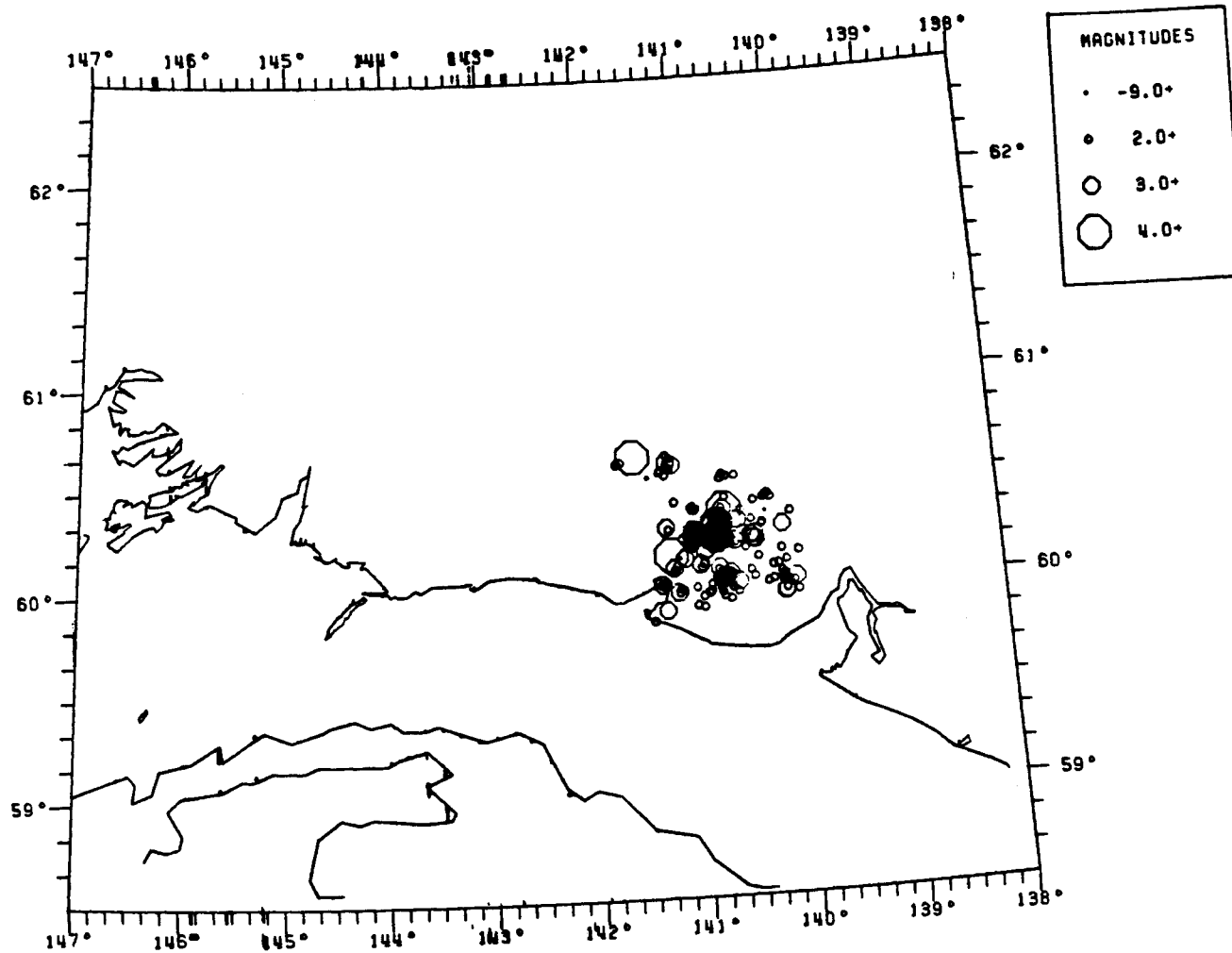


Figure 14b. February 28, 1979 through March 30, 1979 epicenters, as in Figure 14a.

plane. The distribution and depths of the microearthquake activity west of the St. Elias aftershock zone suggest that the same buried fault system that ruptured during the St. Elias earthquake may extend at least 150 km farther to the west.

Another important result is the discovery of a north-northeast-dipping Benioff zone extending to a depth of 85 km south of the Wrangell volcanoes (Stephens and others, 1983). The geometry and orientation of this zone is compatible with the interpretation that the seismicity deeper than about 30 km occurs in the subducted Pacific plate. If this interpretation is correct, then it constrains the northern limit of the Yakataga seismic gap to be south of the 40 km isobath of the Wrangell Benioff zone (Davies and House, 1979). The approximate extent of the Yakataga seismic gap as defined by the rupture zones of the 1964 Alaska earthquake, the 1979 St. Elias earthquake, and the 40 km isobath is shown in Figure 18.

Other areas where notable concentrations of shallow seismicity have been identified include the Copper River Delta, the Waxell Ridge area 100 km northeast of Kayak Island, the Wrangell volcanic massif, and the Denali-Totschunda-Duke River fault system. Relocated hypocenters for the activity beneath the Copper River Delta concentrate in the depth range 20-25 km; many of the events are tightly clustered along a west-northwest-east-southeast trend that is oblique to mapped fault traces at the surface. This activity may be occurring within the subducted Pacific plate. Around Yakutat Bay the pattern of seismicity is more diffuse and may reflect distributed activity on the complex system of mapped strike-slip and inferred thrust faults. Within the seismicity distributed throughout the Wrangell Mountains are distinct sequences of events that are tightly clustered in space and time (see, for example, Stephens and others, 1982). One of these clusters is located near 62° N, 144° W (Figure 16) on the south flank of Mt. Wrangell and may be volcano-related, but in general the clusters have not occurred near the principal volcanoes. Near the strike-slip Denali fault and the Duke River thrust fault system the seismicity is aligned along trends offset to the south from but approximately parallel to the faults. This offset is thought to be the result of systematic errors in locations due to incorrect velocity modeling and large gaps in station coverage, which is confirmed by Horner (1983) who finds little or no offset for earthquakes that have control from nearby Canadian stations. These sections of the Denali and Duke River faults are therefore thought to be active.

The distribution of earthquakes in Figures 13, 15, and 16 is biased by the station distribution (Figure 2) which allows detection and location of smaller events along the coast than offshore or further inland. The study area was divided into six west-northwest-east-southeast striking zones and the magnitude distribution was reviewed for each. While the distribution for the zone extending from the coast to about 100 km inland appeared to be complete for events of about coda magnitude 1.6 and larger, the magnitude level of completeness increased to about 2.4 for the most northerly and

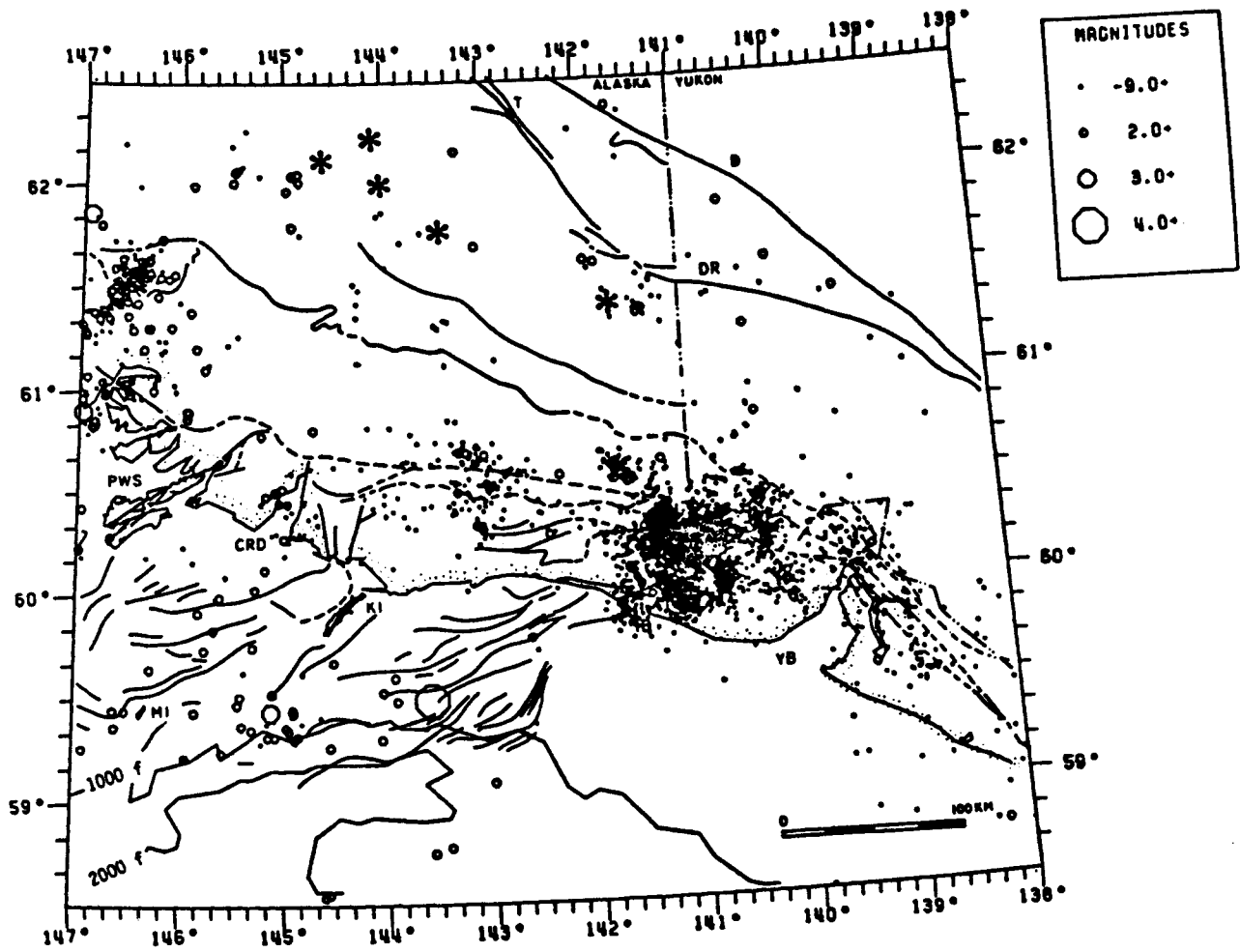


Figure 15a. Epicenter map of 3534 earthquakes located by the local seismograph network between October 1, 1979 and September 30, 1980. Labels same as Figure 6a.

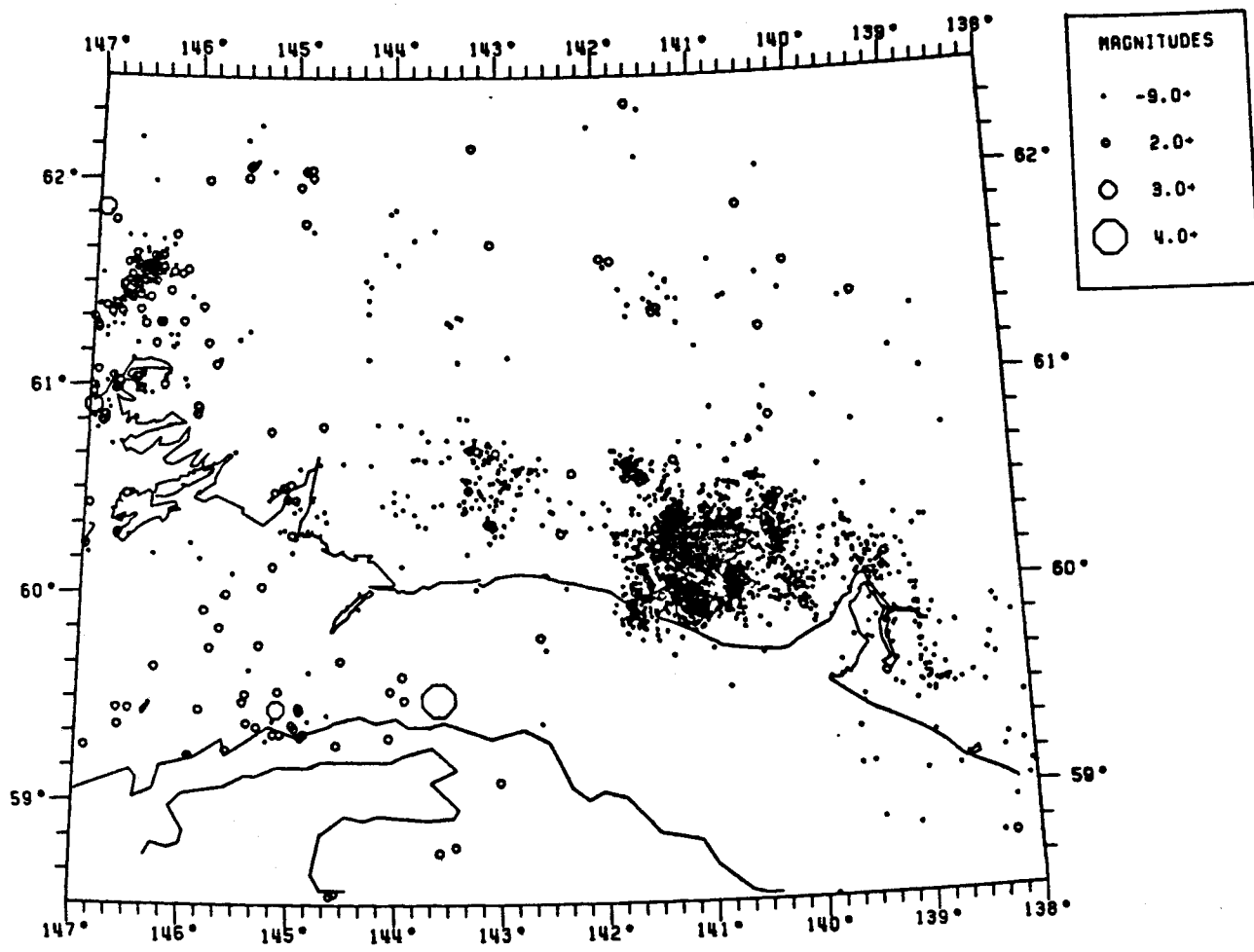


Figure 15b. October 1, 1979 through September 30, 1980 epicenters, as in Figure 15a.

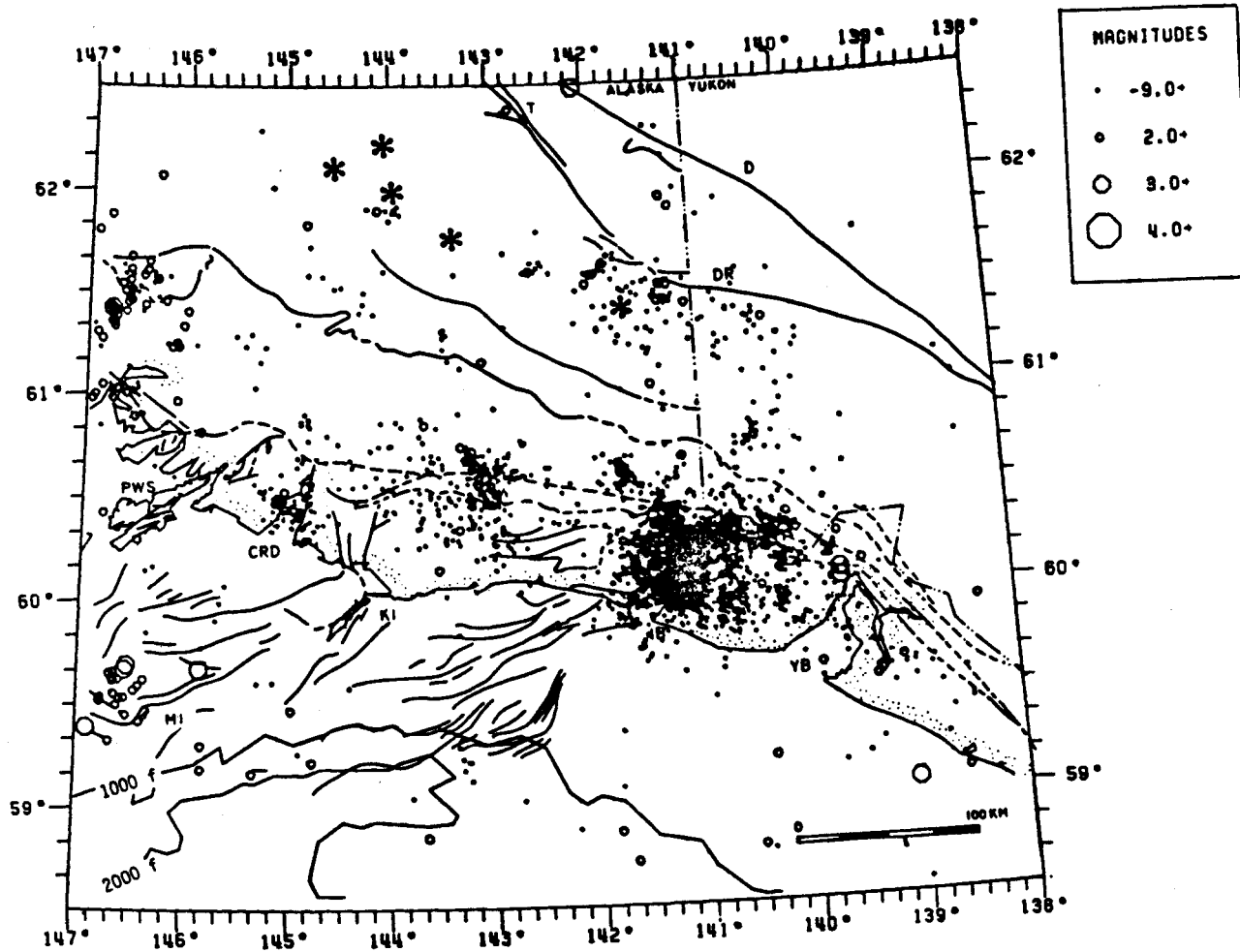


Figure 16a. Epicenter map of 3811 earthquakes located by the local seismograph network between October 1, 1980 and September 30, 1981. Labels same as Figure 6a.

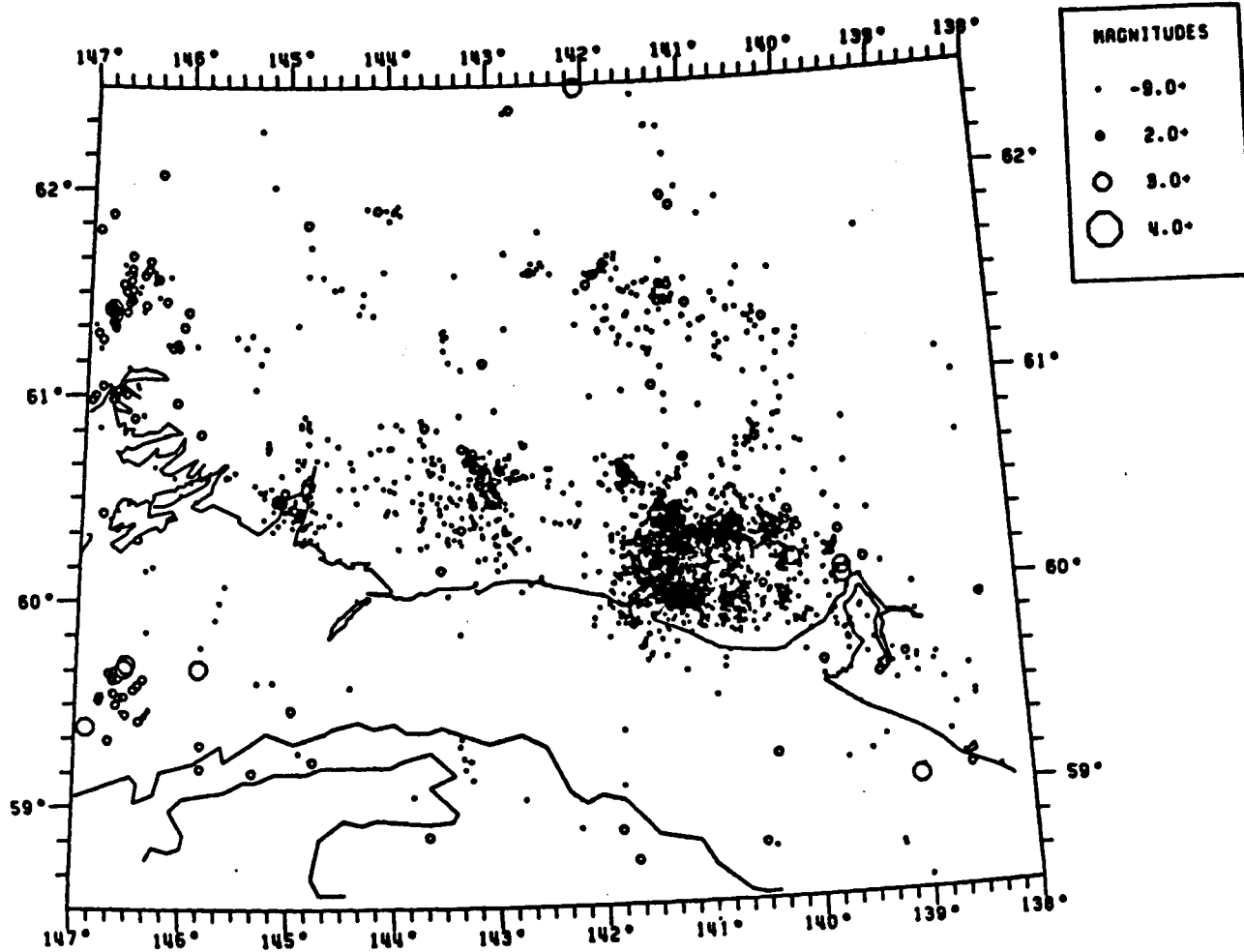


Figure 16b. October 1, 1980 through September 30, 1981 epicenters, as in Figure 16a.

southerly zones. Figure 17 shows the distribution of events with coda magnitude 2.4 and greater for October 1, 1974 through September 31, 1981. Although this figure is not complete in time, due to some gaps in processing, there should be little spatial bias in completeness caused by the station distribution. Some of the areas of high activity, such as near Waxell Ridge and the Copper River Delta, are no longer prominent when events below magnitude 2.4 are excluded, and the seismicity is seen to be much more uniformly spread throughout the region, both onshore and offshore, than in the previous figures (13-16). It is notable that the least active portion of the coast extends from the St. Elias aftershock zone to the Copper River Delta, approximately the same portion of coast identified as the Yakataga seismic gap.

Offshore, concentrations of activity have been identified south of Yakutat Bay (Figure 13) and in several areas west of about $142^{\circ} 30'$ W longitude (Figures 13 through 16). The rates of activity in offshore areas vary considerably with time. For example, little activity has been observed south of Yakutat Bay since 1974 when a prominent swarm of activity occurred. Also, little activity has been observed near the Pamplona Ridge since the network was expanded in 1974, but this had been the site of a sequence of two magnitude 6 earthquakes in 1970 (Figure 10). It is notable that intermediate and larger earthquakes can occur in areas that exhibit relatively low rates of microearthquake activity. For example, a magnitude 5.2 m_b earthquake that occurred near $59^{\circ} 30'$ N, $143^{\circ} 30'$ W in September, 1980 (Figure 15) was the largest event in that area in almost 10 years, but little activity had been located in the same area by the local network in the preceding six years.

C. Estimation of recurrence times for major earthquakes

One of the most critically needed and also most difficult tasks is estimation of the likelihood of major earthquakes, approximately magnitude 7 and larger, that have the potential for causing widespread damage and loss of life. A prerequisite is the understanding of the kinematics of the region including the identification of the major fault boundaries and the slip rate on each. A number of techniques can then be used to estimate the recurrence time for major events on each identified fault.

One possible technique would be to determine the constants A and b in the Gutenberg-Richter magnitude distribution

$$\log N = A - b M \quad (4)$$

where N is the number of events per year with magnitudes greater than or equal to M. Typically data are not available for a long period of time so A and b must be determined on the basis of events with magnitudes between M_{\min} and M_{\max} , where M_{\max} is 2 or more units smaller than the potentially damaging earthquakes of concern. The relationship is then extrapolated to determine the average recurrence time for major earthquakes. This method has the following drawbacks:

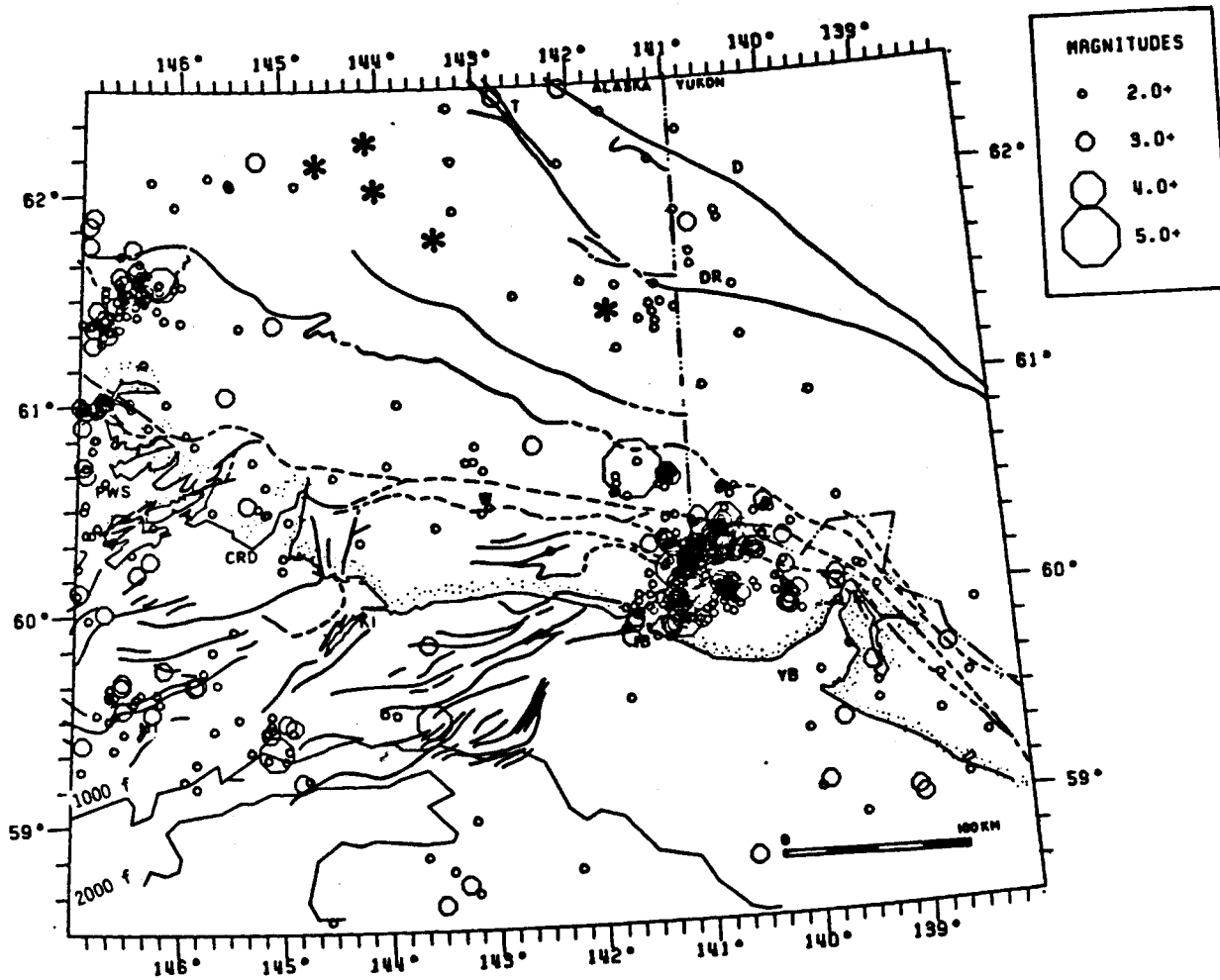


Figure 17a. Epicenter map of 643 earthquakes with coda magnitude greater than or equal to 2.4 located by the local seismograph network between October 1, 1974 and September 30, 1981. Labels same as Figure 6a.

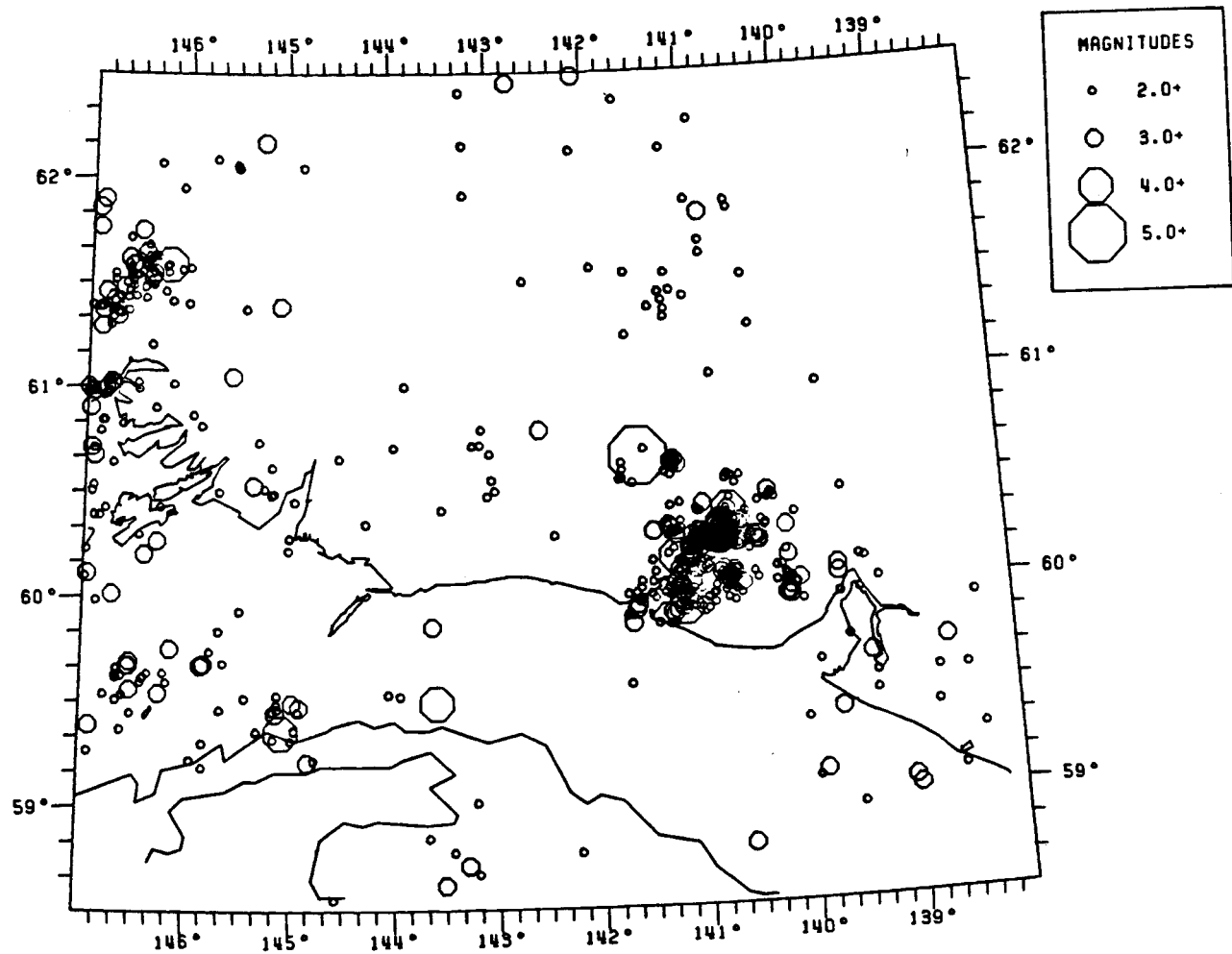


Figure 17b. October 1, 1974 through September 30, 1981 epicenters, as in Figure 17a.

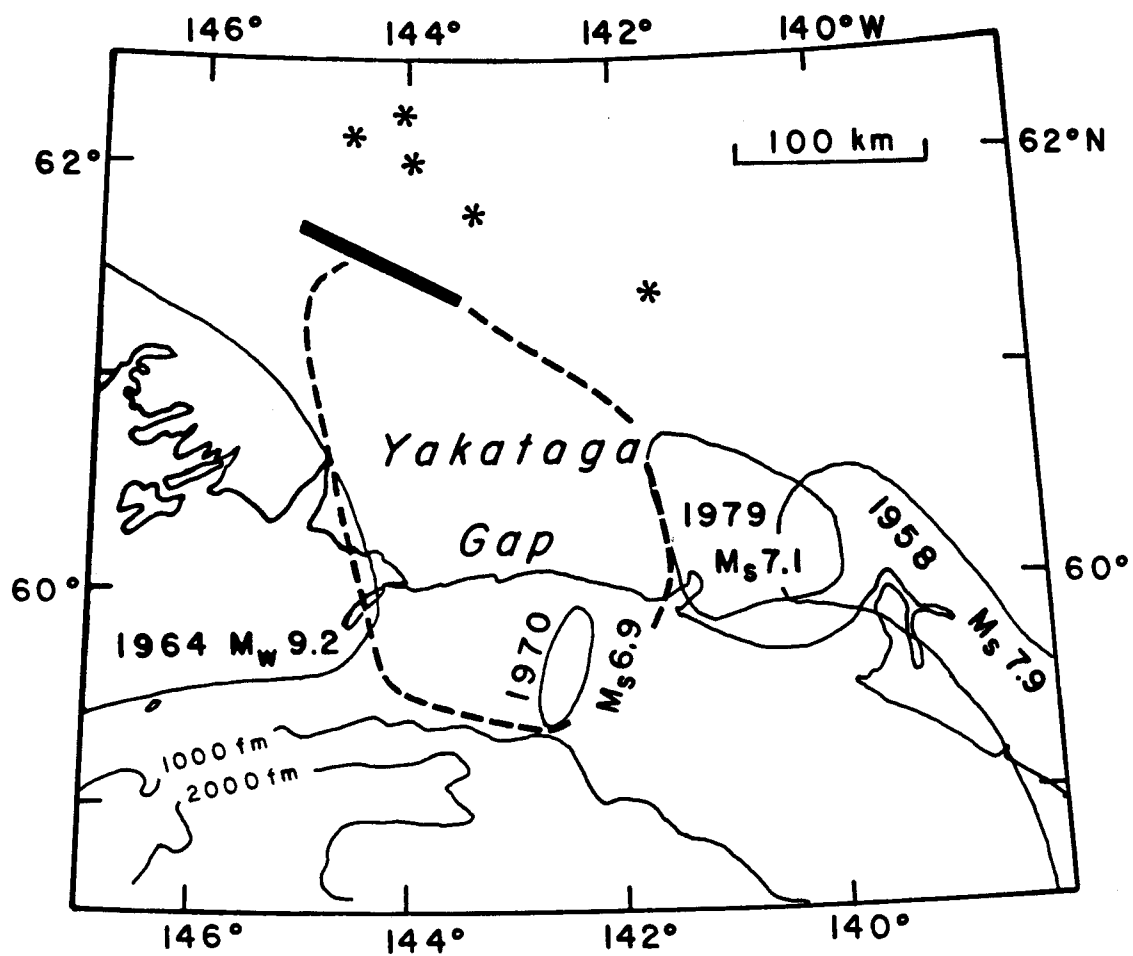


Figure 18. Principal rupture zones of NEGOA region and possible extent of Yakataga seismic gap (dashed). Approximate location of 40 km isobath of Wrangell Benioff zone given by heavy solid line.

- 1) The rate of activity may not be constant in time, so a short time interval may not be representative of the long-term average. Episodic behavior has been suggested by many authors (Tobin and Sykes, 1968; Kelleher, 1970; Sykes, 1971; Davies and House, 1979). This could lead to either over- or under-estimating the recurrence times for major events.
- 2) There is serious question as to the applicability of equation 4 to individual faults, even though the relationship holds well for global and regional scales (Richter, 1958; Anderson and Enrique, 1983). For an individual fault, the number of events near the maximum may be considerably higher than would be predicted from the extrapolation of equation 4 (Lahr, 1982).

An alternative procedure uses the slip rate, fault area and maximum stress drop to estimate the average recurrence interval as a function of magnitude range (Molnar, 1979). This method has the advantage of not relying on a short interval of observations, but like the first technique it assumes that equation 4 is valid for individual faults, and also requires knowledge of the slip rate, fault area and maximum stress drop.

Considering the uncertainties in the proposed kinematic model for the eastern Gulf of Alaska, in the magnitude distribution for individual faults, and in the relative proportion of seismic versus aseismic slip, only an approximate estimate of recurrence times can be offered at this time. An estimate has been made simply by dividing the estimated slip for the largest expected earthquake by the average fault slip rate taken from the model. The estimated recurrence time will be too short to the extent that significant slip occurs aseismically or during smaller earthquakes, and too long to the extent that the estimated slip for the maximum event is too large. Estimates are given in Table 1 for the two principal seismic sources in the eastern Gulf of Alaska region.

<u>REGION:</u>	<u>BOUNDARIES</u>	<u>SLIP RATE</u> (cm/yr)	<u>AREA</u> (km ²)	<u>DISPLACEMENT</u> (cm) ^a	<u>M₀</u> (10 ²⁹ dyne-cm)	<u>M_w</u>	<u>RECURRENCE</u> <u>TIME</u> (yr)
Underthrusting of Yakutat block and Pacific plate below Wrangell block.	Kayak Island, Pamplona zone, Icy Bay, 40 km depth of Benioff zone to north.	4.4	40000	640	1.8	8.8	145
Underthrusting of the Pacific plate below the Yakutat block	Transition zone, Fairweather fault, Pamplona zone.	0.4	22500	640	1.0	8.6	1,600

* The displacement, u, is estimated from

$$u = \frac{3 \Delta \sigma W}{4 \mu} \quad (\text{Molnar, 1979})$$

- assuming: 1) a maximum stress drop, $\Delta \sigma$, of 30 bars (3×10^7 dyne cm^{-2}), typical of the largest events (Kanamori and Anderson, 1975),
 2) $\mu = 7 \times 10^{11}$ dyne cm^{-1} , and
 3) W, the down dip length, is about 200 km in each case.

Table 1. Estimated recurrence times for two principal seismic sources in the eastern Gulf of Alaska region.

D. Strong-motion recordings

From 1974 through 1981 funding was available from OCSEAP to help purchase and maintain Alaskan strong-motion instruments (see Figure 2). During this time interval strong-motion recordings were obtained from three earthquakes in the eastern Gulf of Alaska region. The 1979 St. Elias earthquake triggered 3 of the 6 accelerographs in operation within 250 km of the epicenter. In addition, digital accelerograph data were obtained at Valdez by the Alyeska Pipeline Service Company. The maximum horizontal acceleration recorded from the St. Elias earthquake was 0.16 g (1 g = 980 cm/sec²) at Icy Bay (GYO), located 74 km from the epicenter.

Two earthquakes near Yakutat Bay triggered the nearest instrument at Bancas Point (BCP) in September 1981. Bancas Point is about 12 km from these events and recorded a maximum horizontal acceleration of 0.06 g. In each case, the accelerograph was triggered by the S-wave motion.

The preliminary strong-motion results are summarized in Table 2 below:

Table 2. Preliminary strong-motion results.

Date	EARTHQUAKE			Depth (km)	Recording Station	Epicentral Distance (km)	Max. Horiz. Acc. (g)
	Time (UT)	Magnitude M _{coda} m _b M _s					
02/28/79	21:27	7.1	13	Munday Creek	69	0.06 (1)	
				GYO	74	0.16 (2)	
				CYT	75	No Trigger	
				Yakutat	164	0.09 (2)	
				Kayak Island	181	No Trigger	
				Cordova	222	No Trigger	
				Valdez	225	0.013 (3)	
09/11/81	05:02	3.6 4.0	7	BCP	12	0.06 (4)	
09/17/81	00:18	3.3 3.8	9	BCP	11	0.05 (4)	

Source for accelerations:

- (1) Based on data processed by Kinematics Inc. for Shell Oil Co.
- (2) Porcella (1979). These records have been processed and are available in digital form from NOAA/NGDC, Boulder, Colorado 80303.
- (3) Recorded digitally by Alyeska Pipeline Service Company (Personal communication, R. C. Wahrmond, 1980).
- (4) Personal communication, R. L. Porcella, 1982.

VII. CONCLUSIONS

The eastern Gulf of Alaska region is in a highly active tectonic region and will be subjected to earthquakes from five distinguishable seismic source regions:

- 1) Underthrusting of the Pacific plate below the Wrangell block northwest of the Aleutian megathrust. The 1964 Alaska earthquake ($9.2 M_w$) was of this type and ruptured from about Kayak Island (see Figure 9b) to southern Kodiak Island.
- 2) Underthrusting of the Yakutat block and the Pacific plate below the Wrangell block. This source region extends approximately 200 km northwest from the Pamplona zone. The February 1979 St. Elias earthquake ($7.1 M_s$) noted in Figures 1 and 5 was of this type. The Yakataga seismic gap, between Icy Bay and Kayak Island, is thought to be a likely site for a magnitude 8 or larger earthquake within the next two or three decades (McCann and others, 1980; Lahr and Plafker, 1980).
- 3) Faulting along the northeast boundary of the Yakutat block. Typical of this would be the 1958 earthquake ($7.9 M_s$) which involved dextral strike-slip on the Fairweather fault. Also included would be the Yakutat Bay earthquake ($8.4 M_s$) of September 10, 1899 which involved complex thrust faulting with as much as 14 m of vertical displacement (Thatcher and Plafker, 1977)
- 4) Underthrusting of the Pacific plate below the Yakutat block. Although no historic great earthquake of this type is known to have occurred, it would not be prudent to exclude the possibility of one occurring in the future.
- 5) Moderate and large-size earthquakes ($5.5 < M_s < 8$) occurring anywhere within the Yakutat, St. Elias, and Wrangell blocks. Although the largest earthquakes, in categories 1 through 4, would account for nearly all of the plate motion, smaller events that could occur on smaller geologic structures, few of which are currently known, should also be taken into account.

VIII. NEEDS FOR FURTHER STUDY

Although substantial progress has been made towards understanding the current mode of tectonic deformation in the eastern Gulf of Alaska region, considerable additional research will be required to further develop and verify the current tentative model. Geologic work is essential for problems such as finding the source of the exotic Yakutat block and determining its structure, extent, and the timing of its collision with southern Alaska. Seismic studies, particularly those which provide good depth control for hypocenter determinations, will be useful in mapping the complex geometry of faults that are currently active, including both the main detachment thrust and secondary faults. Inversion of seismic data

from local earthquakes, teleseisms, and refraction shots for improved 3-D velocity structure will give direct insight into the structures present in this region as well as allow for more accurate earthquake locations. Continued direct measurements of crustal deformation and displacements by techniques including leveling (both level lines and tilt meters), trilateration, strainmeters and tide gauges will also provide important constraints on future tectonic models of the region.

IX. ACKNOWLEDGEMENTS

This report has benefited greatly from the thorough reviews of Robert A. Page and James N. Taggart. We are grateful for the contributions of the many people who assisted in this work, both in establishing and maintaining the seismic stations and in processing the data.

We thank Tom Sokoloski and the staff of the NOAA Alaska Tsunami Warning Center for their assistance in maintaining our recording equipment in Palmer, Alaska, as well as for making their seismic data available to us.

This study was supported jointly by the U.S. Geological Survey and by the National Oceanic and Atmospheric Administration, under which a multi-year program responding to needs of petroleum development of the Alaskan continental shelf is managed by the Outer Continental Shelf Environmental Assessment Program (OCSEAP) office.

X. REFERENCES

- Anderson, J. G., and Luco, J. E., 1983, Consequences of slip rate constraints on earthquake occurrence relations: Bulletin of the Seismological Society of America, v. 73, no. 2, p. 471-496.
- Beikman, H. M., 1978, Preliminary geologic map of Alaska: U.S. Geological Survey Map, 1:2,500,000.
- Bruns, T. R., 1979, Late cenozoic structure of the continental margin, northern Gulf of Alaska: in Sisson, Alexander, ed., Proceedings, Alaska Geological Society Symposium, 6th: Anchorage, 1977, Alaska Geological Society, p. 11-130.
- Buland, Ray and Taggart, James, 1981, A Mantle wave magnitude for the St. Elias, Alaska, earthquake of 28 February 1979: Bulletin of the Seismological Society of America, v. 71, p. 1143-1159.
- Clague, J. J., 1979, The Denali fault system in southwest Yukon Territory--a geologic hazard: in Current Research, Part A, Geological Survey of Canada, Paper 79-1A, p. 169-178.
- Davies, J. N., and House, Leigh, 1979, Aleutian subduction zone seismicity, volcano-trench separation and their relation to great thrust-type earthquakes: Journal of Geophysical Research, v. 84, p. 4583-4591.
- Deininger, J. W., Jr., 1972, Petrology of the Wrangell volcanoes near Nabesna, Alaska: University of Alaska, M.S. in Geology, 66 p.
- Eaton, J. P., O'Neill, M. E., and Murdock, J. N., 1970, Aftershocks of the 1966 Parkfield-Cholame, California, earthquake: a detailed study: Bulletin of the Seismological Society of America, v. 60, p. 1151-1197.
- Gawthrop W., Page, R. A., Reichle, M., and Jones, A., 1973, The southeast Alaska earthquake of July 1973: EOS, Transactions of the American Geophysical Union, v. 54, p. 1136.
- Gutenberg, Beno, and Richter, C. F., 1954, Seismicity of the Earth, 2nd ed., Princeton University Press, Princeton, N. J.
- King, P. B., 1969, Tectonic map of North America: Denver, Colorado, U. S. Geological Survey, 2 sheets.
- Hastie, L. M., and Savage, J. C., 1970, A dislocation model for the 1964 Alaska earthquake: Bulletin of the Seismological Society of America, v. 60, p. 1389-1392.
- Horner, R. B., in press, Seismicity in the St. Elias region of northwestern Canada and southern Alaska: Submitted to: Bulletin of the Seismological Society of America.
- Kelleher, John, 1970, Space-time seismicity of the Alaskan-Aleutian seismic zone: Journal of Geophysical Research, v. 75, p. 5745-5746.
- Lahr, J. C., 1975, Detailed seismic investigation of Pacific-North American plate interaction in southern Alaska, Ph.D. dissertation, Columbia University, 141 p.
- Lahr, J. C., and Plafker, George, 1980, Holocene Pacific-North American plate interaction in southern Alaska: Implications for the Yakataga seismic gap: Geology, v. 8, p. 483-486.

- Lahr, J. C., Plafker, George, Stephens, C. D., Fogleman, K. A., and Blackford, M. E., 1979, Interim report on the St. Elias, Alaska, earthquake of 28 February 1979: U.S. Geological Survey Open-File Report 79-670, 35 p.
- Lahr, J. C., and Stephens, C. D. 1982, Alaska seismic zone: Possible example of non-linear magnitude distribution for faults: Earthquake Notes, Eastern Section, Seismological Society of America, v. 53, p. 66.
- Lee, W. H. K., Bennett, R. E. and Meagher, K. L., 1972, A method of estimating magnitude of local earthquakes from signal duration: U. S. Geological Survey Open-File Report, 28 p.
- Lee, W. H. K., and Lahr, J. C., 1972, HYPO71: a computer program for determining hypocenter, magnitude, and first motion pattern of local earthquakes: U. S. Geological Survey Open-File Report, 100 p.
- MacKevett, E. M., Jr., 1978, Geologic map of the McCarthy Quadrangle, Alaska: U. S. Geological Survey Miscellaneous Geological Investigation Map I-1032.
- McCann, W. R., Nishenko, S. P., Sykes, L. R., and Krause, J., 1979, Seismic gaps and plate tectonics: seismic potential for major boundaries: Pure and Applied Geophysics, v. 117, p. 1082-1147.
- McCann, W. R., Perez, O. J., and Sykes, L. R., 1980, Yakataga seismic gap, southern Alaska: seismic history and earthquake potential: Science, v. 207, p. 1309-1314.
- Minster, J. and Jordan, T., 1978, Present-day plate motions: Journal of Geophysical Research, v. 83, p. 5331-5354.
- Molnar, Peter, 1979, Earthquake recurrence intervals and plate tectonics: Bulletin of the Seismological Society of America, v. 69, p. 115-133.
- Page, R. A., 1968, Aftershocks and microaftershocks of the great Alaska earthquake of 1964: Bulletin of the Seismological Society of America, v. 58, p. 1131-1168.
- Page, R. A., 1975, Evaluation of seismicity and earthquake shaking at offshore sites, in Offshore Technology Conference, 7th, Houston, Texas, Proceedings, 3, p. 179-190.
- Plafker, George, 1969, Tectonics of the March 27, 1964, Alaska earthquake: U. S. Geological Survey Professional Paper 543-I, 74 p.
- Plafker, George, Hudson, T., Bruns, T., and Ruben, M., 1978, Late Quaternary offsets along the Fairweather fault and crustal plate interactions in southern Alaska: Canadian Journal of Earth Sciences, v. 15, p. 805-816.
- Plafker, George, and Mayo, L. R., 1965, Tectonic deformation, subaqueous slides and destructive waves associated with the Alaskan March 27, 1964 earthquake: An interim geologic evaluation: U. S. Geological Survey Open-File Report, 19 p.
- Porcella, R. L., 1979, Recent strong-motion records, in U. S. Geological Survey Circular 818-A, pl, Seismic engineering program report January - April 1979.
- Richter, C. F., 1958: Elementary Seismology, W. H. Freeman and Company, San Francisco, 768 p.
- Stephens, C. D., Astrue, M. C., Pelton, J. R., Fogleman, K. A., Page, R. A., Lahr, J. C., Allan, M. A., and Helton, S. M., 1982, Catalog of earthquakes in southern Alaska, April-June, 1978, U. S. Geological Survey Open-File Report 82-488, 36 p.

- Stephens, C. D., Fogleman, K. A., Lahr, J. C. and Page, R. A., 1983, Evidence for a north-northeast dipping Benioff zone south of the Wrangell volcanoes, southern Alaska: (submitted to EOS, Transactions of the American Geophysical Union).
- Stephens, C. D., Lahr, J. C., Fogleman, K. A., and Horner, R. B., 1980, The St. Elias, Alaska, earthquake of February 28, 1979: Regional recording of aftershocks and short-term, pre-earthquake seismicity: Bulletin of the Seismological Society of America, v. 70, p. 1607-1633.
- Stover, C. W., Reagor, B. G., and Wetmiller, R. J., 1980, Intensities and isoseismal map for the St. Elias earthquake of February 28, 1979: Bulletin of the Seismological Society of America, v. 70, p. 1635-1649.
- Sykes, L. R., 1971, Aftershock zones of great earthquakes, seismicity gaps, and earthquake prediction for Alaska and the Aleutians: Journal of Geophysical Research, v. 76, p. 8021-8041.
- Tarr, R. S., and Martin, L., 1912, The earthquakes at Yakutat Bay, Alaska, in September, 1899: U. S. Geological Survey Professional Paper 69, 135 p.
- Thatcher, W., and Plafker, George, 1977, The 1899 Yakutat Bay, Alaska earthquake: IASPEI/IAVCEI Assembly Abstracts with Programs, p. 54.
- Tobin, D. G., and Sykes, L. R., 1966, Relationship of hypocenters of earthquakes to the geology of Alaska: Journal of Geophysical Research, v. 71, p. 1659-1667.
- Tobin, D. E. and Sykes, L. R., 1968, Seismicity and tectonics of the northeast Pacific Ocean: Journal of Geophysical Research, v. 73, p. 3821-3845.
- Tocher, D., 1960, The Alaska earthquake of July 10, 1958: Movement on the Fairweather fault and field investigations of southern epicentral regions: Bulletin of the Seismological Society of America, v. 50, p. 267-292.



**MEASUREMENT AND LOCATION OF EARTHQUAKES IN WESTERN ALASKA,
THE GULF OF ALASKA, AND THE BERING SEA**

by

Cliff Frohlich and Paul Donoho

**Institute for Geophysics
University of Texas at Austin**

**Final Report
Outer Continental Shelf Environmental Assessment Program
Research Unit 579**

May 1982



TABLE OF CONTENTS

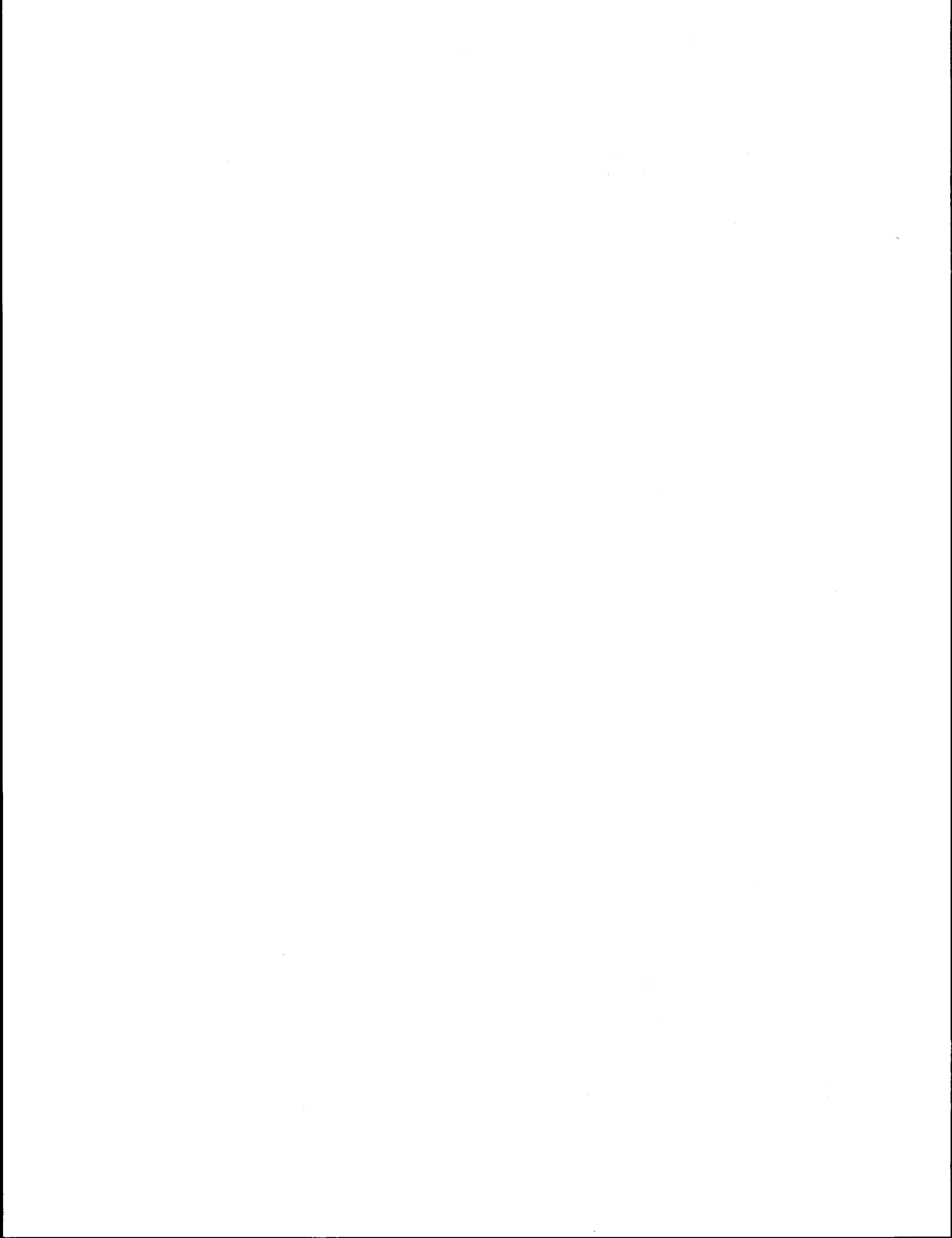
List of Figures	89
List of Tables	89
SECTION I: OBJECTIVES AND PRELIMINARY CONCLUSIONS	91
Objectives	92
Preliminary Conclusions, and Plan of This Report	92
SECTION II: NO LOCAL EARTHQUAKES RECORDED IN BRIEF OBS SURVEY IN THE BERING SEA NEAR AMAK ISLAND, ALASKA.....	95
Acknowledgements	98
References	100
SECTION III: JOINT HYPOCENTER DETERMINATION OF INTERMEDIATE DEPTH EARTHQUAKES NEAR COOK INLET, ALASKA	101
Introduction	102
Methods	103
Selection of Events and Stations	103
Relocation by the Joint Hypocenter Determination Method	103
Results	106
References	115
SECTION IV: JOINT HYPOCENTER DETERMINATION OF TELESEISMICALLY RECORDED EARTHQUAKES ON THE KODIAK SHELF, ALASKA	117
Introduction	118
Methods	118
Difficulties in Relocating Teleseismic Earthquakes	118
Depth Determination	119
Relocation by the joint Hypocenter Determination Method	127
Results and Discussion	132
References	133

LIST OF FIGURES

- Figure I-1. Location map showing where strong-motion OBS instruments have been deployed since 1979.
- Figure II-1. Location map of the Amak-Port Moller area.
- Figure II-2. Seismograms recorded at stations HG1 and HG2.
- Figure III-1. Map of earthquakes located in this study.
- Figure III-2. Vertical cross-section parallel to the Aleutian trench.
- Figure III-3. Vertical cross-section showing locations of cross-sections in subsequent figures.
- Figure III-4. Vertical cross-section of segment 4.
- Figure III-5. Vertical cross-section of segment 5.
- Figure III-6. Vertical cross-section of segment 6.
- Figure III-7. Vertical cross-section of segment 7.
- Figure IV-1. Vertical cross-section of the events relocated by the JHD method in this study.
- Figure IV-2. Short-period seismograms of the event of 22 April 1966.
- Figure IV-3. Short-period seismograms of the event of 22 August 1973.
- Figure IV-4. Vertical cross-section for events with reliable depths.
- Figure IV-5. Map showing locations of earthquakes studied.
- Figure IV-6. Distribution of stations used for JHD relocation.

LIST OF TABLES

- Table II-1. High-gain OBS stations deployed in the Bering Sea in 1981.
- Table III-1. Station corrections determined by the JHD process.
- Table III-2. Velocity model used in this study.
- Table IV-1. Locations determined by the JHD method in this study.
- Table IV-2. Stations and station corrections determined in this study.



SECTION I: OBJECTIVES AND PRELIMINARY CONCLUSIONS

by Cliff Frohlich

OBJECTIVES

As stated in our renewal proposal entitled "Measurement and Location of Earthquakes in Western Alaska, the Gulf of Alaska and the Bering Sea," the specific objectives of our research were:

1. To recover the strong motion OBS instruments deployed in the Gulf of Alaska in 1980, and deploy these and other instruments in the Gulf of Alaska and the Bering Sea.
2. To monitor microseismic activity rates near the Amak Fault Zone and the Port Moller Graben to determine whether these features are currently active, and if so, to determine the level of activity.
3. In collaboration with personnel of the University of Alaska, to apply recently developed sophisticated location methods to the earthquake data that have been collected by the University of Alaska land network. We intend to obtain the most accurate locations possible for events detected by the network.
4. In collaboration with personnel of the University of Alaska, to develop a velocity model and set of station corrections that allow the University of Alaska land network to determine the best possible locations for events that occur within and adjacent to their network. To determine realistically the strengths and limitations of the land network for the determination of earthquake detection and earthquake risk in the offshore area.

PRELIMINARY CONCLUSIONS, AND PLAN OF THIS REPORT

In order to reach these objectives we undertook five more or less separate research projects. Some of these projects were continuations of previous work. These projects were:

1. Recovery, deployment, and analysis of strong motion OBS instruments in the Gulf of Alaska and the Bering Sea. The instruments deployed in 1980 were recovered in June of 1981 from the **Miller Freeman** (see Figure I-1). In September of 1981 new instruments were deployed from the **Alpha Helix**. These will be recovered in July of 1982. Analysis of the data obtained in 1981 is still in progress. Persons interested in these results should contact Dr. Paul Donoho of the Institute for Geophysics at the University of Texas.

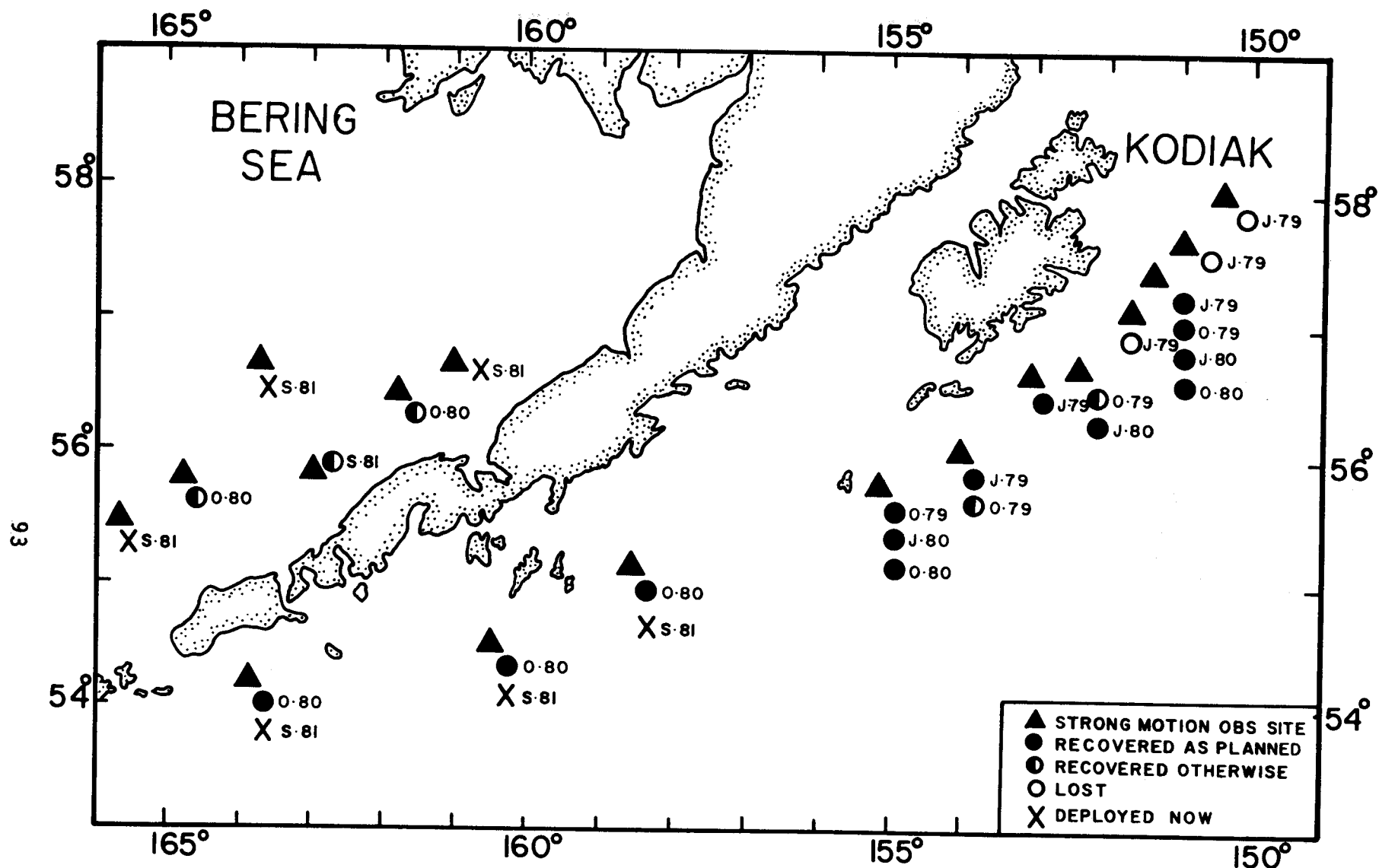


FIGURE I-1: Location map showing where strong motion OBS instruments have been deployed since 1979. Triangles are OBS sites, and symbols below explain recovery situation. Letter and number to the right of recovery symbol are month and year of deployment, e.g., J-79 is July 1979, O-79 is October of 1979, J-80 is June of 1980, O-80 is October of 1980, and S-81 is September of 1981.

2. Deployment and recovery of high gain OBS instruments in the Bering Sea near Amak Island and Port Moller. These instruments were deployed for six days in June of 1981 from the **Miller Freeman**. Analysis of this work is complete, and makes up section II of this report. Although the instruments worked well, no microearthquakes were recorded that occurred within the Bering Sea. Although a six day microearthquake project is by no means definitive for risk determination, the absence of seismicity is consistent with the conclusion that risk from shallow events in the study region is low. Probably risk associated with subduction zone events in the Aleutian Island arc is much greater.
3. Joint Hypocenter Determination (JHD) of regional events with focal depths of 50 km and greater in the Cook Inlet area. Using a JHD program developed specifically for this project, we relocated 178 events with focal depths beneath 50 km in the neighborhood of Cook Inlet. This work makes up section III of this report. These locations are the most accurate locations available at present for this area. The station corrections determined should allow more accurate determination of epicenters in this area in the future using the stations in the UA network. This work corroborates the previous work which suggests that a "double Benioff zone" may exist in the Cook Inlet area.
4. Joint Hypocenter determination of teleseismic events in the Kodiak Shelf region. Using a JHD program developed previously we relocated 34 shallow events which occurred offshore of Kodiak Island. This work makes up section IV of this report. The relocated epicenters form a much less diffuse pattern than the epicenters reported by the International Seismological Center (ISC). In addition, analysis of systematic errors in teleseismic locations suggests that these events are situated on the bathymetric shelf break, rather than about 20 km to the north as reported by the ISC.
5. Joint Hypocenter Determination of regional events in the Kodiak Shelf region. This work is still in progress. For more information, interested persons should contact Dr. Hans Pulpan of the University of Alaska or Dr. Cliff Frohlich of the University of Texas Institute for Geophysics.

SECTION II: NO LOCAL EARTHQUAKES RECORDED IN BRIEF OBS SURVEY
IN THE BERING SEA NEAR AMAK ISLAND, ALASKA

by Cliff Frohlich

Recent hydrocarbon exploration in the Gulf of Alaska and the Bering Sea (Hanley and Wade, 1981) has provided motivation for studying the seismicity in these areas. For this reason, the University of Texas has been engaged in ocean bottom seismograph (OBS) research in these areas since 1978, both with strong motion instruments (Steinmetz et al. 1981) and high gain equipment (Lawton et al. 1982).

Because the NOAA ship **Miller Freeman** planned to visit the Bering Sea for about a week in June of 1981 to recover some strong motion OBS instruments that had been deployed in October of 1980, we decided to undertake a brief microearthquake survey of two basement features in the Bering Sea (Figure II-1). These features were the Amak Fault zone and the Port Moller graben. Since 1960 the National Earthquake Information Service (NEIS) has reported three shallow earthquakes occurring along the Amak Fault zone, and one shallow event along the Port Moller graben. A network operated by Lamont-Doherty observatory of Columbia University has detected a cluster of small shallow events that occurred in 1980 on the peninsula south of Port Moller Bay (Klaus Jacob, personal communication). Davies (1981) presents a more detailed discussion of the historical seismicity in the St. George Basin and adjacent regions.

For this study we deployed four vertical-component high-gain Texas OBS instruments similar in design to those described by Latham et al. (1978). After about six days the **Miller Freeman** recovered three of these instruments (Table II-1). Although we detected a weak radio signal from the fourth instrument it was not recovered at this time. Nevertheless, in October of 1981 a fisherman found it and returned it to the University of Texas. No events of any kind were recorded by the fourth instrument.

Each of the three instruments recovered by the **Miller Freeman** recorded more than a hundred events, however, most of these events did not appear to be earthquakes. All the events looked similar to the events discussed by Buskirk et al. (1981) which are thought to be of biological origin. None of the instruments recorded any events which appear to be local earthquakes.

However, the two stations deployed near Amak Island did record two earthquakes. The first event occurred on 5 June 1981 about 380 km from the OBS instruments (NEIS location: 52.259N 165.186W 11 km 070915.8). No clear first arrival times could be read for this event, as on one OBS the arrival was extremely emergent, and on the other the event occurred during a very noisy portion of the record. A second event occurred on 7 June 1981 about 200 km from the OBS stations (NEIS location: 53.877N 165.086W 14 km 175231.6), and both stations recorded this event clearly (Figure II-2). For the location reported by NEIS, P arrivals at both stations occur about 6.0 sec later than predicted by the JB tables.

Because the OBS survey lasted for only six days, the significance of the absence of any recorded local events is not entirely clear. The fact that two distant events were observed by stations HG1 and HG2 suggests that local events would have been recorded if they did occur.

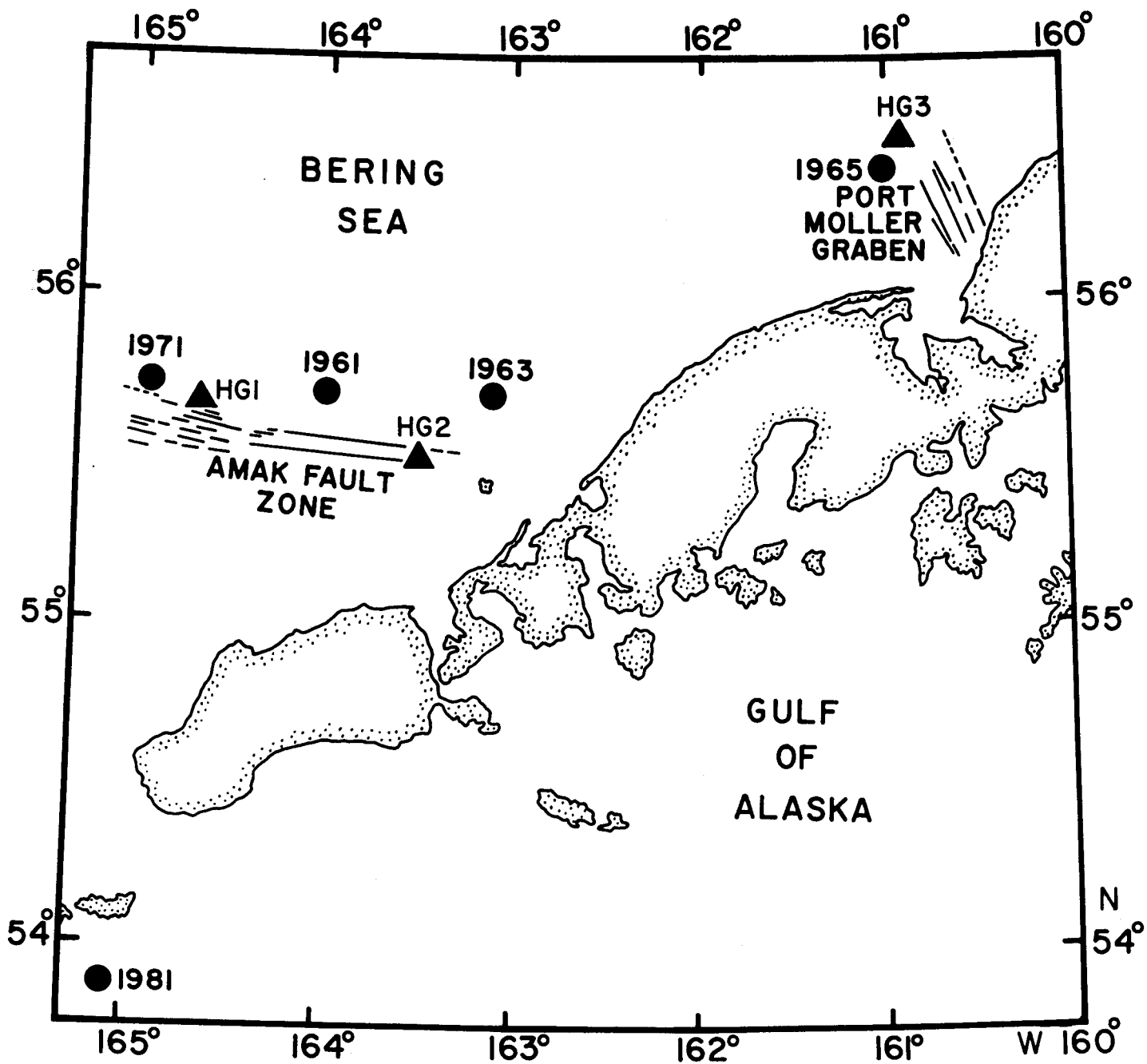


FIGURE II-1: Location map of the Amak-Port Moller area, showing the locations of the OBS stations recovered (filled triangles) and events reported by NEIS in the Bering Sea since 1960 (filled circles, with year of event adjacent). In addition, the map shows the NEIS location of one of the events of 7 June 1981 which was recorded by stations HG1 and HG2.

Three teleseismically recorded events have been reported near the Amak fault zone since 1960 (Figure II-1), one in 1961, one in 1963, and one with magnitude 5.2 in 1971. Assuming a b-value of 1, three events of magnitude 5 will occur as often as 30,000 events of magnitude 1. Thus if one observes 3 magnitude 5 events in 20 years, one should observe about 4 magnitude 1 events each day, or about 25 in the six days that the OBS instruments were deployed. Since no events were observed, either this b-value is too high, or else the events cluster in time. Near Port Moller, the only shallow event reported teleseismically since 1960 occurred in 1965, and had a magnitude of 4.2. However, this event was reported by only 8 stations. As events with focal depths beneath 70 km are known in this area, it is possible that the 1965 event was a deeper event whose focal depth was incorrectly determined.

TABLE II-1: High-gain OBS stations deployed in the Bering Sea in 1981.

<u>STATION</u>	<u>DEPLOYED</u>	<u>LOCATION</u>	<u>WATER DEPTH (fm)</u>	<u>RECOVERED</u>
HG1	03 JUN 0650	55 39.9N 164 39.6W	52f	09 JUN 1330
HG2	03 JUN 0230	55 30.0N 163 30.0W	39f	09 JUN 0730
HG3	02 JUN 1300	56 30.0N 160 50.1W	33f	08 JUN 1300
HG4	02 JUN 0300	58 14.9N 160 39.8W	14f	---

ACKNOWLEDGEMENTS

Paul Donoho, Jeff Lawton, and Phil Roper provided essential field and moral support for this research. We thank Capt. Jack Atwell and the crew of the Miller Freeman for their assistance and their good fellowship.

7 JUNE 1981 1752

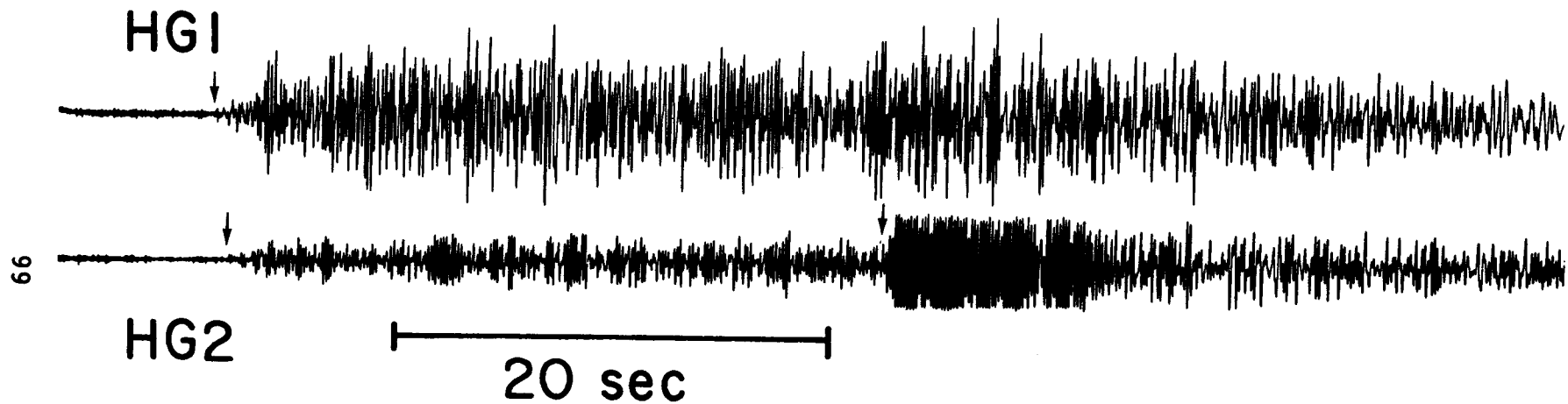


FIGURE II-2: Seismograms recorded at stations HG1 and HG2 for the event of 7 June 1981. The arrows show the author's picks for the P arrival at station HG1, and the P and S arrivals at station HG2. These arrival times were 1753:10.2 (HG1), 1753:10.7 (HG2-P), and 1753:40.7 (HG2-S).

References

- Buskirk, R. E., C. Frohlich, G. V. Latham, A. T. Chen and J. Lawton. Evidence that biological activity affects ocean bottom seismograph recordings. **Mar. Geophys. Res.**, 1981, 5, 189-205.
- Davies, J. N. Seismic and volcanic risk in the St. George Basin and Adjacent Aleutian arc. In **A Seismotectonic Analysis of the Seismic and Volcanic Hazards in the Pribilof Islands-Eastern Aleutian Islands Region of the Bering Sea**. Annual Report NOAA contract 03-50-022-70, 1981.
- Hanley, P. T. and W. W. Wade. New study analyzes Alaska OCS areas. **Oil and Gas Journal**, 1981, 79, 73-79.
- Latham, G., P. Donoho, K. Griffiths, A. Roberts and A. K. Ibrahim. The Texas ocean-bottom seismograph. **Proc. 10th Offshore Tech. Conf.**, 1978, pp. 1467-1473.
- Lawton, J., C. Frohlich, H. Pulpan and G. V. Latham. Earthquake activity at the Kodiak continental shelf, Alaska determined by land and ocean bottom seismograph networks. **Bull. Seismol. Soc. Amer.**, 1982, 72, 207-213.
- Steinmetz, R. L., J. D. Murff, G. V. Latham, A. Roberts, P. Donoho, L. Babb and T. Eichel. Seismic instrumentation of the Kodiak shelf. **Marine Geotechnology**, 1981, 4, 193-221.

SECTION III: JOINT HYPOCENTER DETERMINATION OF INTERMEDIATE DEPTH
EARTHQUAKES NEAR COOK INLET, ALASKA

by

Cliff Frohlich and Hans Pulpan

INTRODUCTION

Although a few seismograph stations have been operated in southwestern Alaska for many years (Lahr, 1975), there has only been a true local network in the region near Cook Inlet since about 1975. This network, capable of locating most earthquakes with magnitudes as small as 2 or below, includes about 30 stations and is operated by the University of Alaska and others (Pulpan and Kienle, 1979). For accurately locating earthquakes occurring in subducted lithosphere, this network is better situated than networks in many subduction zones because of its relatively broad aperture across the arc, including stations as much as 100 km behind the volcanic arc.

However, previous published earthquake locations in this region have not utilized the full location potential of the present network of stations in the Cook Inlet area. For example, Pulpan and Kienle (1979) did not incorporate S-wave observations into their locations in this region. Lahr (1975) only used about 15 stations recording in this region to locate events because these were all that were available at that time. At present, Lahr and his coworkers at the USGS do record data from several stations in the Cook Inlet area, and do use these data when preparing catalogs of earthquakes in southwestern Alaska (e.g., see Stephens et al, 1980).

Several recent studies have focused new interest on locations in subducted lithosphere at depths above 200 km, as they have apparently identified a second less active zone of seismicity beneath the planar Benioff zone. The combination of the usual Benioff zone together with this lower, less active zone are known as a "double Benioff zone." This has been clearly observed in Japan (Hawegawa et al., 1979a; 1978b), and observed less clearly in several other places (Reyners and Coles, 1982; Samowitz and Forsyth, 1981; Veith, 1974). In the Cook Inlet area, Lahr (1975) observed a number of well-located events that were about 20 km beneath the main Benioff zone. However, in spite of the fact that these events possessed most of the features we attribute today to double Benioff zones, Lahr's (1975) work is seldom mentioned in most papers concerning double Benioff zones.

Unfortunately, numerous studies have shown that locations of local networks near subduction zones can be influenced by systematic errors. The use of flat-layered velocity models for determining locations in a region of more complex velocity structure can cause the seismicity pattern to exhibit unusual and apparently spurious features. These phenomena have been studied in the greatest detail in the Central Aleutian arc using data from the Adak network. For example, events which seem to cluster at shallow depths near model velocity increases (Engdahl, 1977) have been found to be distributed over a broad range of depths (Laforge and Engdahl, 1979; Frohlich et al., 1982). Increases in the dip of the Benioff zone disappear when ray tracing is used to locate the events (Engdahl et al., 1977), or when the network geometry is augmented using ocean-bottom seismographs. An initial report of the

existence of a double Benioff zone in the Adak region (Engdahl and Scholz, 1977) was not confirmed by more detailed research (Topper, 1978). Most recently, a number of other detailed investigations have been performed in Adak.

In the present paper we report relocations of events in the Cook Inlet region using all the available data and the joint hypocenter determination method (Douglas, 1967; Dewey, 1972; Frohlich, 1979). These relocations are among the best published locations available in this region at this time.

METHODS

Selection of Events and Stations

Although the University of Alaska (UA) has operated a network of stations in the Cook Inlet area since 1975, S waves have been reported routinely by UA personnel during only three years, 1978, 1980, and 1981. All of the UA stations are vertical component seismographs only, and so all of the reported S-arrivals were read from vertical component records. Restricting our attention to the region between 59 and 60.5°N and between 151.6 and 154°W, there existed about 400 events for which one or more S waves were available. Of these, 178 had two or more S readings, a gap of 170 degrees or less, and a rms location residual of 0.5 sec or less (Figure III-1).

There exist more than 50 stations operating in southern and southwestern Alaska, however, not all of them are close enough to the Cook Inlet area to improve our locations. For this reason, 30 stations were selected for use in this study. Although phases from all of these stations were used in the locations, in practice only 15 of the stations reported arrivals for more than 30 per cent of the events (Table III-1).

As an aid in evaluating the quality of the data to be used in the relocation, we graded all of the earthquakes in terms of three parameters (see caption to Figure III-1). These were the number of S observations reported, the "gap" in station coverage (the largest azimuthal gap for which no P-wave observations were available), and the rms residual of the preliminary location reported by the UA network. As noted above, of the approximately 400 events with focal depths beneath 50 km in the study area, there were 72 events with $Q = 1$, 106 events with $Q = 2$, and the remainder with $Q = 3$.

Relocation by the Joint Hypocenter Determination Method

For groups of earthquakes observed by a network of seismic stations the JHD location program used simultaneously determines hypocenters and station corrections so as to minimize the sums of residuals of travel

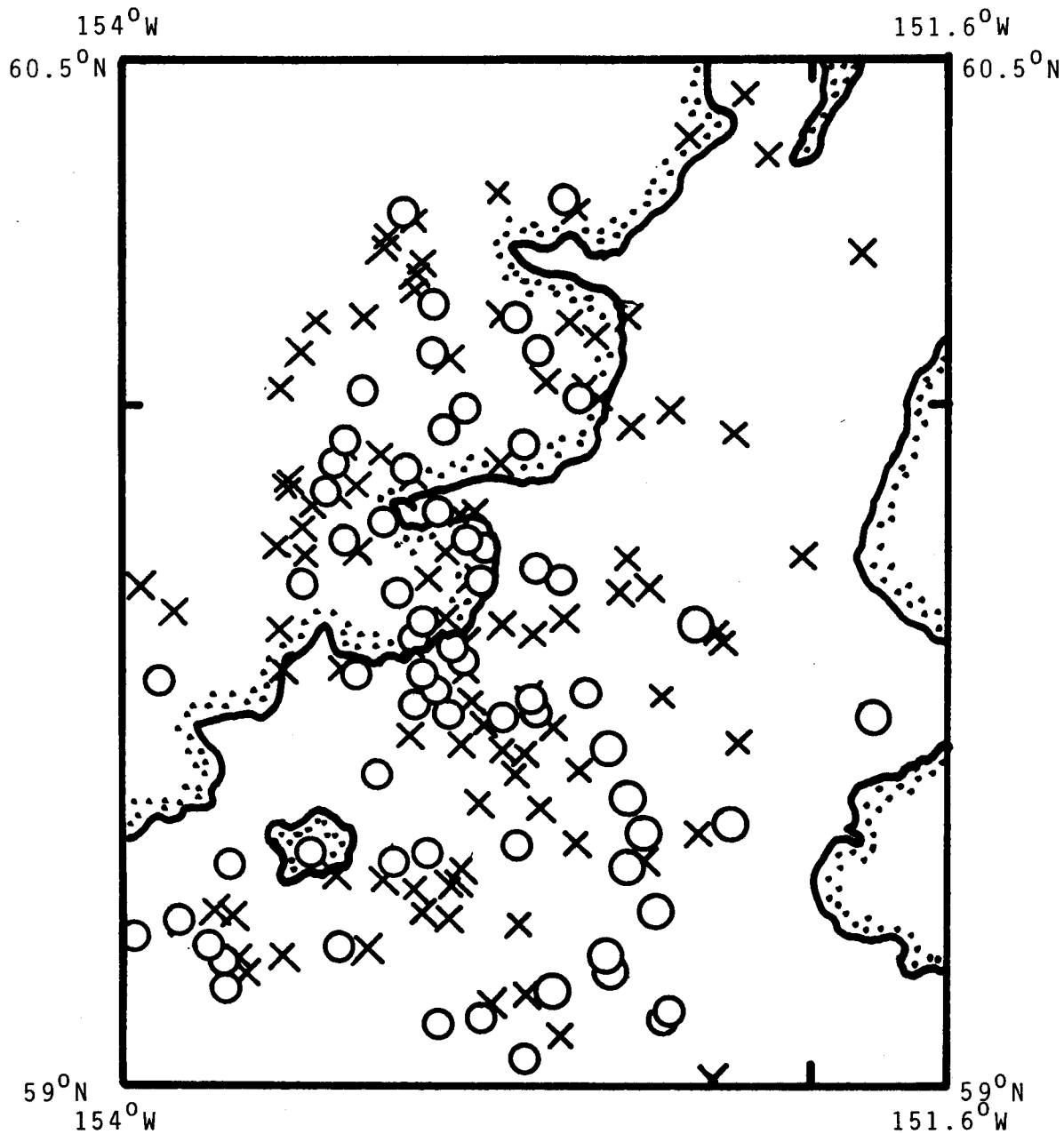


FIGURE III-1 Map of earthquakes locate in this study
 Circles are quality $Q = 1$ events (3 or more S observations, gap of 130° or less, and rms residual of 0.4 sec or less).
 Crosses are quality $Q = 2$ events (2 S observations, gap of 170° or less, and rms residual of 0.5 sec or less).
 Events with one S observation (not shown) were quality $Q = 3$ events.

TABLE III-1: Station corrections determined by the JHD relocation process for each of 15 stations that recorded 30 per cent or more of the seismic events. The six relocations were; I - Q = 1 events only (72 earthquakes), P and S wave residuals used to determine station corrections; II - Q = 1 events only (72 earthquakes), P waves only used to determine station corrections; III - Q = 1 and Q = 2 events (54 earthquakes), focal depth beneath 100 km in northeast section, P waves only used for station corrections; IV - Q = 1&2 events (35 earthquakes), focal depth above 100 km in NE, P waves only; V - Q = 1&2 events, (27 earthquakes), focal depth beneath 100 km in SW, P waves only; VI - Q = 1&2 events, (62 earthquakes) P waves only, focal depth above 100 km depth.

STATION	RELOCATION I	RELOCATION II	RELOCATION III	RELOCATION IV	RELOCATION V	RELOCATION VI
AUI	0.16 sec	0.15	0.35	0.16	0.10	0.24
AUM	0.31	0.31	0.35	0.31	0.32	0.46
BGM	-0.25	-0.23	-0.06	-0.30	-0.20	-0.42
CDA	-0.20	-0.16	-0.16	-0.32	-0.10	-0.18
CKK	-0.04	-0.04	-0.09	0.11	-0.08	-0.15
HOM	0.42	0.35	0.45	0.36	0.37	0.43
KDC	-0.35	-0.27	-0.56	-0.75	-0.38	-0.14
MCN	0.11	0.15	0.24	-0.07	0.17	0.11
OPT	0.08	0.08	0.20	0.16	-0.01	0.13
PDB	-0.07	-0.10	0.14	-0.06	-0.07	-0.16
RAI	-0.12	-0.01	-0.28	0.05	-0.13	-0.05
RED	-0.28	-0.33	-0.22	-0.23	-0.47	-0.34
SHU	0.13	0.16	0.29	0.27	0.10	0.04
SLV	-0.19	-0.22	-0.20	-0.35	-0.23	-0.13
SVW	-0.09	-0.14	-0.30	-0.37	-0.15	-0.16

times for a particular flat-layered velocity model. The program used was developed by the author specifically for this project although it should prove generally useful for local network relocations. Unlike the method of, e.g., Spencer and Gubbins (1980), this program does not attempt to adjust the velocity model during relocation. For our relocations we used the velocity model determined by Lahr (see Stephens et al, 1980) which is reproduced in Table III-2.

The JHD program developed for this project is considerably more efficient than the programs used in most previous investigations. During each iteration of a relocation of N events observed at M stations, many JHD programs typically solve a system of $4N + M$ equations in $4N + M$ unknowns. This often makes it impractical to relocate jointly more than about 40 events in each group. However, using the method outlined by Frohlich (1979), during each iteration the program used in this project instead solves N systems of 4 equations in 4 unknowns, and thus literally hundreds or thousands of events can be relocated jointly.

As discussed by Douglas (1967) and Frohlich (1979), JHD methods must specify at least one additional constraint equation in addition to the condition that the sum of residuals be minimized. The most common additional equations are to fix one event (the "master event") or alternatively to specify some condition concerning the station corrections, such as making the sum of the station corrections zero. We have used the latter approach in this work. As shown by Frohlich (in preparation), if reasonable care is taken in the selection of the station network, the difference in the relative locations of events by the two methods is negligible.

For most teleseismic JHD relocation schemes, compressional wave observations only are used, and thus a single station correction is determined for each station. Numerous studies have shown that for most networks more reliable locations can be determined if S-wave observations are used (e.g., Buland, 1976). Thus for local network JHD relocations, it would be possible to determine separate station corrections for P and S waves. However, because the majority of the events studied in this project had three or fewer S waves, a single station correction was determined for each station and used to adjust both P and S residuals.

Results

To investigate the dependence of station corrections on the events located, we performed six different JHD relocations on events in the Cook Inlet area (see Table III-1 and Figure III-2). Two JHD relocations concentrated on 72 $Q = 1$ events, using both P and S residuals to determine station corrections for relocation I, and using P residuals only for relocation II. The station corrections thus determined were remarkably similar, as the station corrections determined in these two trials differed by more than 0.1 sec for only one of the fifteen

TABLE III-2: Velocity model used by Lahr and his coworkers (see Stephens et al., 1980), and also used for JHD relocations in this study.

<u>VELOCITY</u>	<u>DEPTH</u>
2.75 km/sec	0 - 2 km
5.3	2 - 4
5.6	4 - 10
6.2	10 - 15
6.9	15 - 20
7.4	20 - 25
7.7	25 - 33
7.9	33 - 47
8.1	47 - 65
8.3	65 - --

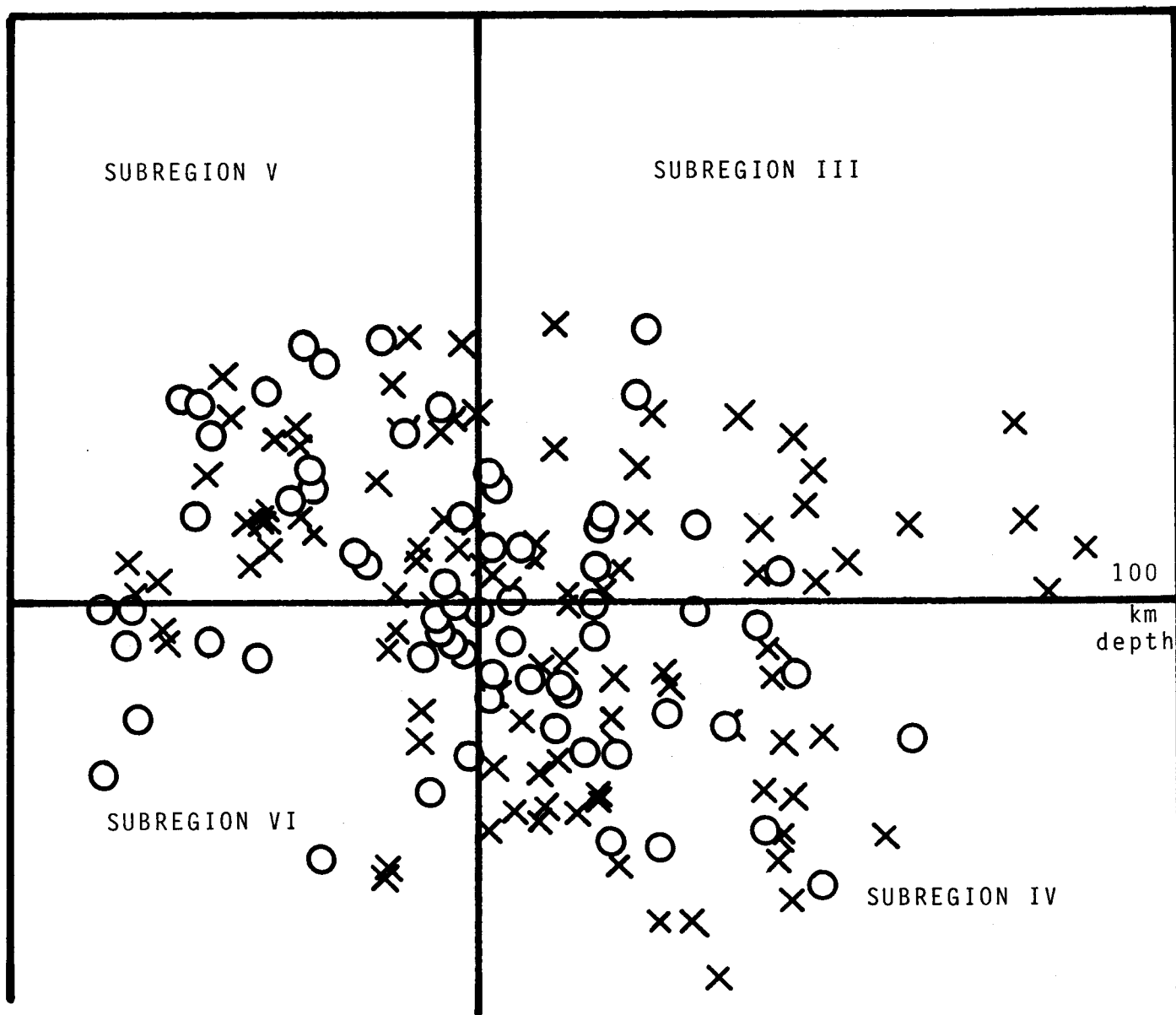


FIGURE III-2 Vertical cross section parallel to the Aleutian trench (azimuthal trend of 32° E of N) showing the events relocated in this study. All $Q = 1$ events (circles) were relocated in relocations I and II (see table III-1). Both $Q = 1$ and $Q = 2$ events (crosses) in the subregions III, IV, V, and VI shown were relocated in relocations III, IV, V, and VI.

stations observing more than fifteen events (Table III-1).

To study the effect of depth and geographic location on the station corrections, we also undertook four additional JHD relocations (Figure III-2) for events with $Q = 1$ or $Q = 2$ which occurred above 100 km depth in the southwest, below 100 km depth in the southwest, above 100 km in the northeast, and below 100 km depth in the northeast. Although the station corrections determined in these relocations differed more than those determined in the relocations I and II, for all but three stations the corrections were within 0.2 sec of those determined in the first relocation. Analysis of the station corrections determined in the six JHD relocations revealed that the corrections determined in relocation I were among the median values (the third or fourth largest of the six values determined) for eleven of the fifteen stations. For these reasons, these corrections were used in the relocation process for all of the events that follow, including those of quality $Q = 2$, and including events at all focal depths deeper than 50 km (Figure III-1).

Cross sections of the relocations of $Q = 1$ and $Q = 2$ events clearly delineate the Benioff zone in the Cook Inlet area (Figures III-3, III-4, III-5, III-6 and III-7). The zone appears to extend to a depth of 160 km, with a dip angle of about 45 degrees and a thickness of 10 to 20 km or less. Two features of the data are worthy of note:

- There appear to be several well located events which lie distinctly beneath the main Benioff zone. For example, in the cross section of Figure III-5 two events are separated from the main Benioff zone by about 15 - 20 km. Both of these events are well recorded and should be accurately located, in fact, the location of the deeper event used 13 P and 6 S observations. Altogether these events form a so-called "double Benioff zone."
- The cross sections suggest that the dip of the Benioff zone changes between the southwest and the northeast. In these data the dip is slightly larger in the northeast.

These results are comparable to those reported by Lahr (1975) for events in this region. Using a slightly different location technique and a geometrically less extensive network, Lahr (1975) also detected the presence of events beneath and apparently separate from the Benioff zone. He also found a change in the dip from northeast to southwest in the Cook Inlet region, however, unlike the present work Lahr (1975) found that the dip of the Benioff zone was slightly less in the northeast than in the southwest.

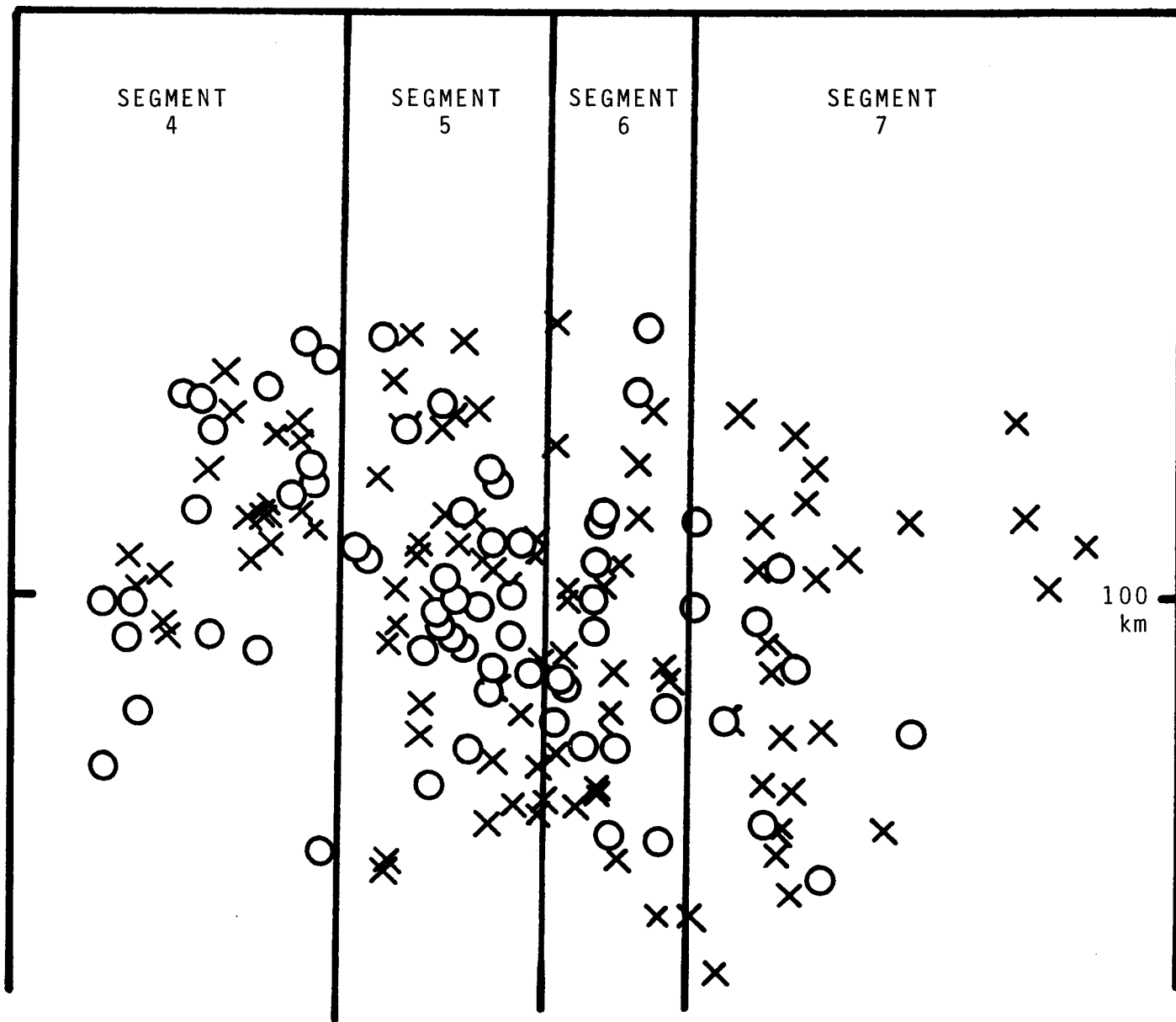


FIGURE III-3. Vertical cross section showing locations of cross sections in subsequent figures. Vertical lines separate segments 4, 5, 6, and 7, showing the events plotted in the cross sections in Figures III-4, III-5, III-6, and III-7.

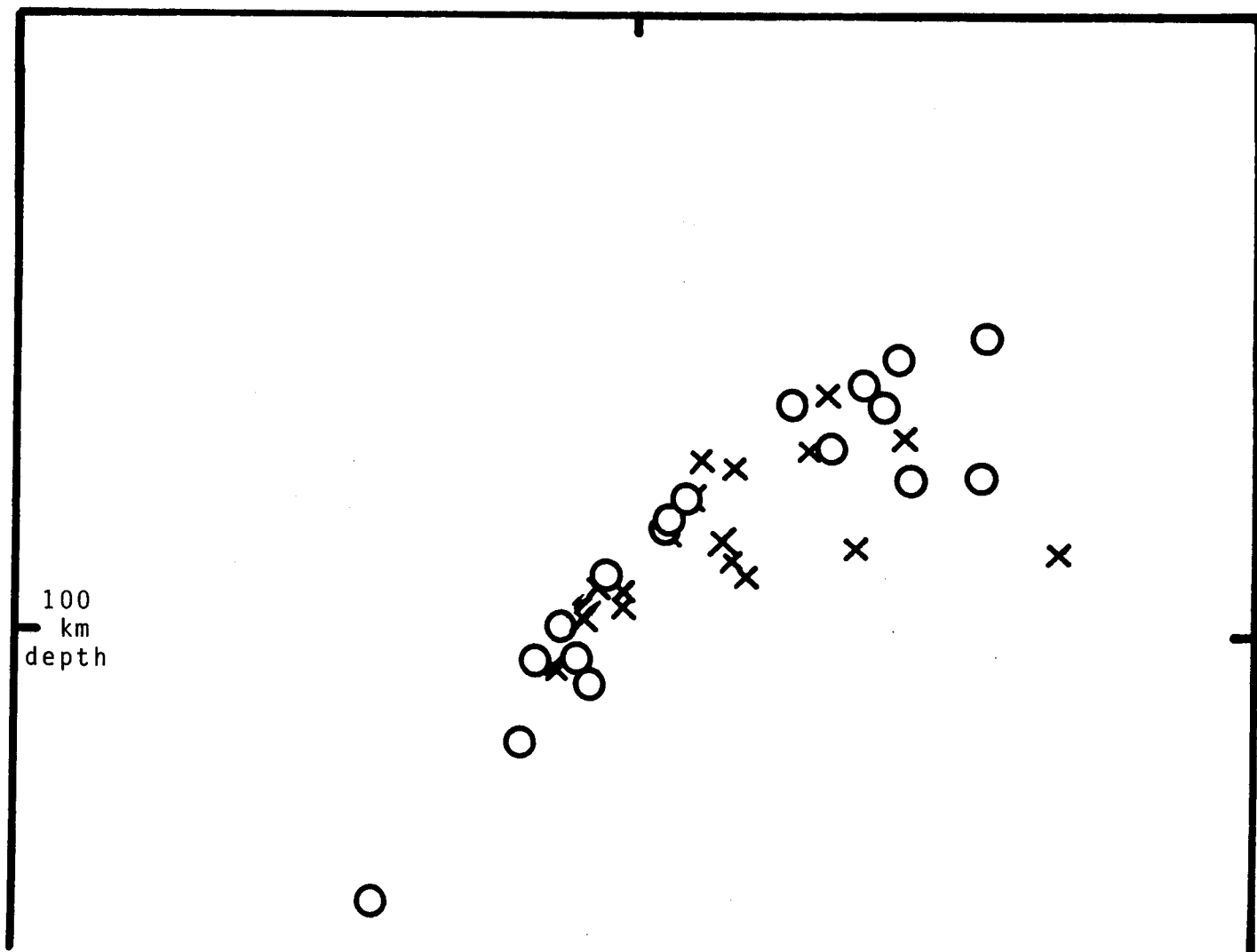


FIGURE III-4 Vertical cross section of segment 4 perpendicular to the Aleutian trench, and perpendicular to the cross sections in Figures III-2 and III-3 (azimuthal trend of 122°E of N) showing the events relocated in this study. See Figure III-3 for location of this cross section, and Figure III-1 for explanation of symbols.

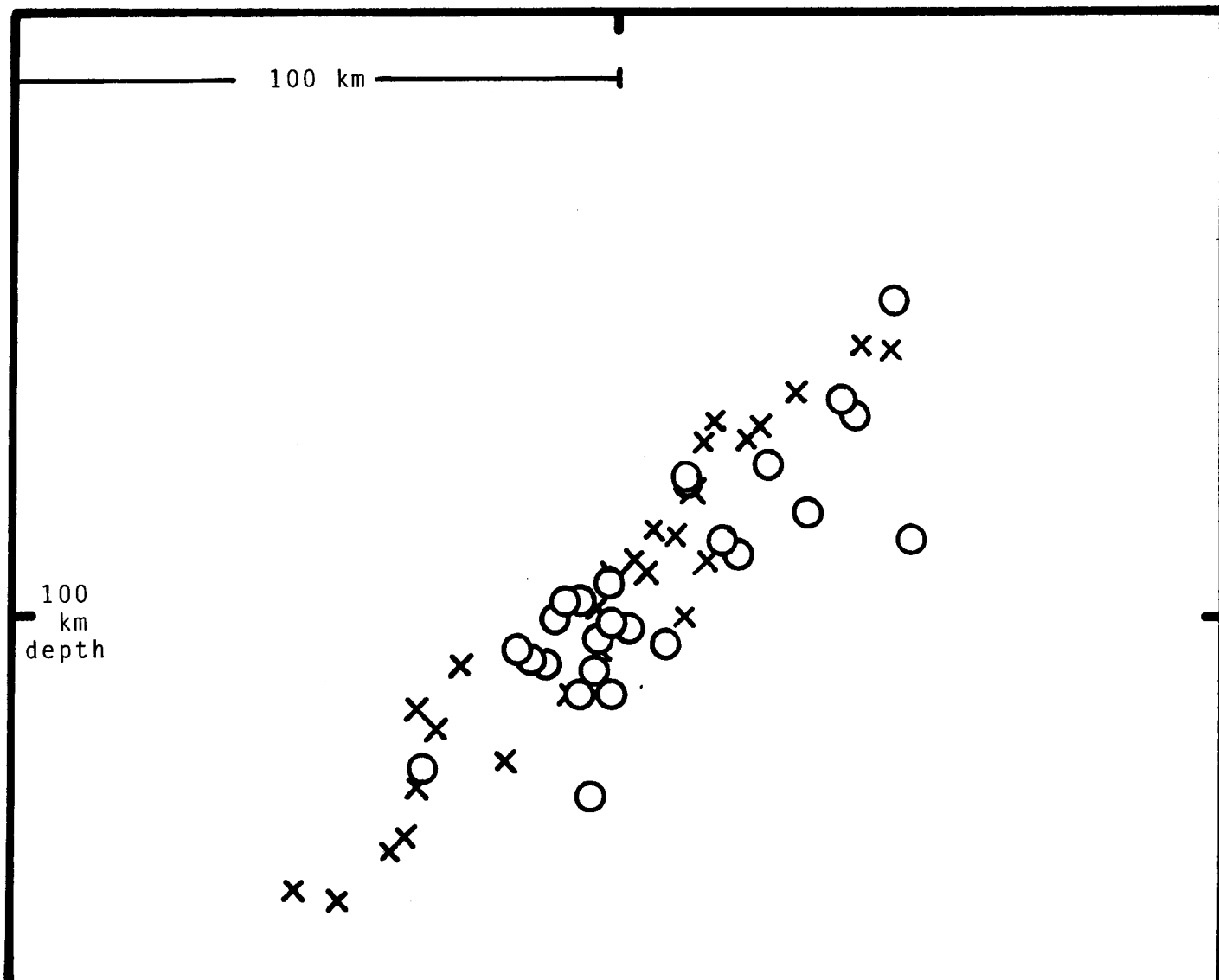


FIGURE III-5 Vertical cross section of segment 5 (see caption to Figure III-4).

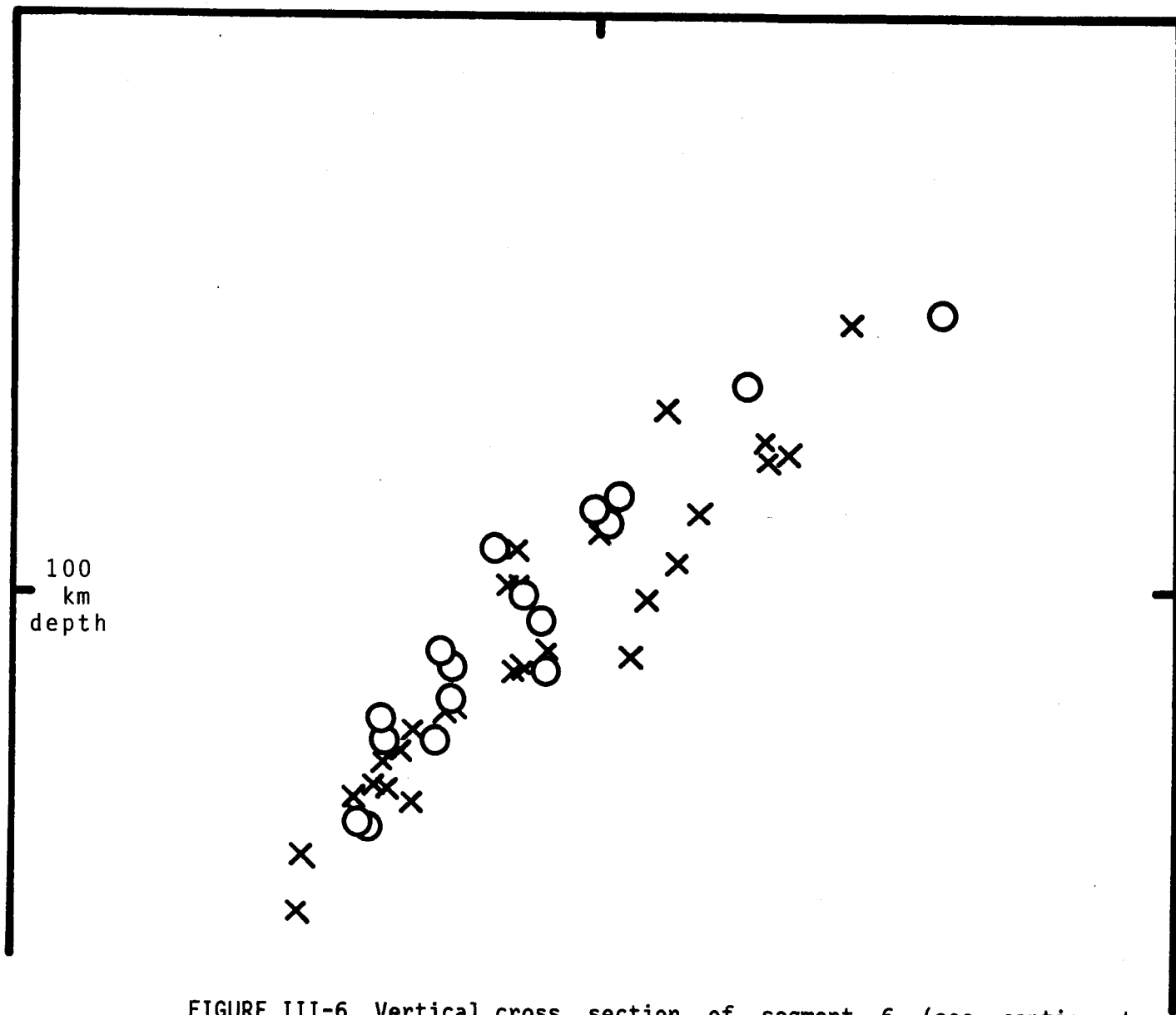


FIGURE III-6 Vertical cross section of segment 6 (see caption to Figure III-4).

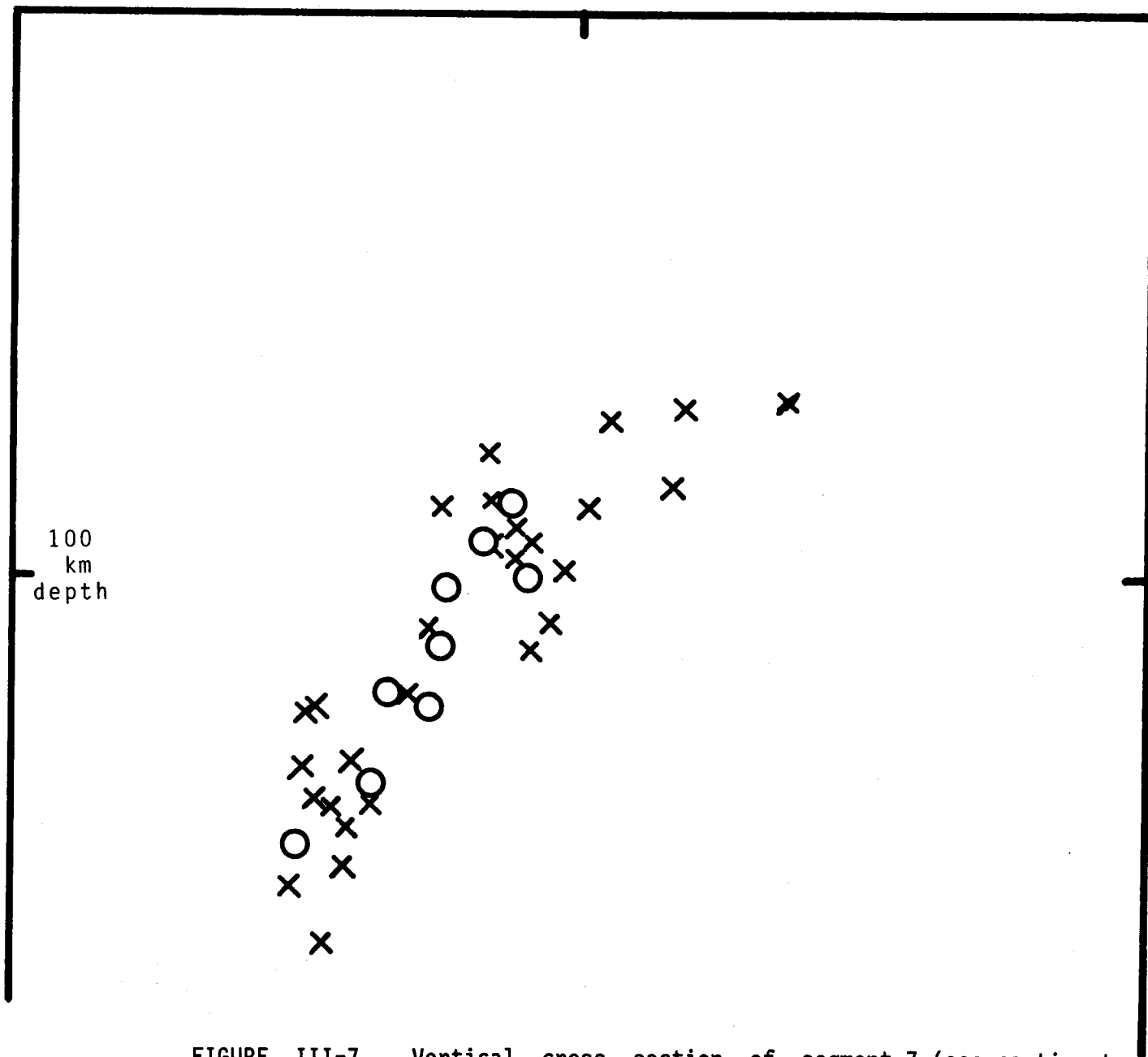


FIGURE III-7 Vertical cross section of segment 7 (see caption to Figure III-4).

References

- Buland, R. The mechanics of locating earthquakes. *Bull. Seismol. Soc. Amer.*, 1976", 66, 173-187.
- Dewey, J. W. Seismicity and tectonics of western Venezuela. *Bull. Seismol. Soc. Amer.*, 1972, 62, 1711-1751.
- Douglas, A. Joint epicenter determination. *Nature*, 1967, 215, 189-205.
- Engdahl, E. R. Seismicity and plate subduction in the central Aleutians. In *Island Arcs, Deep Sea Trenches, and Back Arc Basins*. Amer. Geophys. Union, 1977.
- Engdahl, E. R. and C. H. Scholz. A double Benioff zone beneath the Central Aleutian Islands, an unbending of the lithosphere. *Geophys. Res. Let.*, 1977, 4, 473-476.
- Engdahl, E. R., N. H. Sleep and M. T. Lin. Plate effects in north Pacific subduction zones. *Tectonophysics*, 1977, 37, 95-116.
- Frohlich, C. An efficient method for joint hypocenter determination for large groups of earthquakes. *Computers & Geosciences*, 1979, 5, 387-389.
- Frohlich, C., S. Billington, E. R. Engdahl, and A. Malahoff. Detection and location of earthquakes in the central Aleutian subduction zone using land and ocean bottom seismograph stations. *J. Geophys. Res.*, 1982. in press.
- Hasegawa, A., N. Umino and A. Takagi. Double-planed structure of the deep seismic zone in the northeastern Japan arc. *Tectonophysics*, 1978 a, 47, 43-58.
- Hasegawa, A. N. Umino and A. Takagi. Double-planed deep seismic zone and upper mantle structure in the Northeast Japan Arc. *Geophys. J.*, 1978b, 54, 281-296.
- Laforge, R. and E. R. Engdahl. Tectonic implications of seismicity in the Adak Canyon region. *Bull. Seismol. Soc. Amer.*, 1979, 69, 1515-1532.
- Lahr, J. C. **Detailed seismic investigation of Pacific-North American plate interaction in southern Alaska**. Doctoral dissertation, Columbia University, 1975.
- Pulpan, H. and J. Kienle. Western Gulf of Alaska seismic risk. In *Proc. 11th. Offshore Tech. Conf.*. OTC, 1979.

- Reyners, M. and K. S. Coles. Fine structure of the dipping seismic zone and subduction mechanics in the Shumagin Islands, Alaska. *J. Geophys. Res.*, 1982, **87**, 356-366.
- Samowitz, I. R. and D. W. Forsyth. Double seismic zone beneath the Mariana island arc. *J. Geophys. Res.*, 1981, **86**, 7013-7021.
- Spencer, C. and D. Gubbins. Travel time inversion for simultaneous earthquake location and velocity structure determination in laterally varying media. *Geophys. J.*, 1980, **63**, 95-116.
- Stephens, C. D., K. A. Fogleman, J. C. Lahr, S. M. Helton, R. S. Cancilla, R. Tam and J. A. Freiberg. **Catalogs of earthquakes in southern Alaska January-March 1980** (open file report 80-1253). U. S. Geol. Surv., 1980.
- Topper, R. E. **Fine structure of the Benioff zone beneath the central Aleutian arc.** Master's thesis, University of Colorado, 1978.
- Veith, K. F. **The relationship of island arc seismicity to plate tectonics.** Doctoral dissertation, Southern Methodist University, 1974.

SECTION IV: JOINT HYPOCENTER DETERMINATION OF TELESEISMICALLY RECORDED
EARTHQUAKES ON THE KODIAK SHELF, ALASKA

by

Hans Pulpan and Cliff Frohlich

INTRODUCTION

Recent hydrocarbon exploration offshore of Kodiak Island (Fisher, 1980; Hanley and Wade; 1981) provides new motivation for evaluating the potential for large earthquakes in this area. High seismic risk has been associated with the Kodiak region for at least 200 years (Hansen and Eckel, 1971). In 1964 Kodiak Island was strongly affected by the great Alaskan earthquake (Plafker, 1972), one of the largest earthquakes ever recorded. Because of the spatial limitations of land networks (local and teleseismic) in determining accurate earthquake locations at convergent margin continental shelves, it is desirable to relocate these events using the best methods available.

In the present study we have relocated a number of teleseismically recorded earthquakes that occurred offshore of Kodiak Island since 1964. Most of these events can be considered to be aftershocks of the 1964 Good Friday earthquake. The work reported here is an extension of the work of Lawton et al. (1982), who investigated the seismicity of this region using data from ocean bottom seismograph stations and the network of land stations operated by the University of Alaska (Pulpan and Kienle, 1979).

METHODS

Difficulties in Relocating Teleseismic Earthquakes

Precise determination of earthquake hypocenters in the Kodiak shelf area is difficult for several reasons. The seismicity of the area occurs at shallow focal depths, and reliable depth values for shallow events are notoriously difficult to establish unless the depth of the events is comparable to the distance to the closest observing stations. Thus the land based network operated by the University of Alaska on Kodiak Island (Pulpan and Kienle, 1979) will not provide reliable depth estimates for shelf events (Lawton et al., 1982). With the area of interest lying outside that network, the poor azimuthal station coverage results sometimes in rather poor constraints on the epicentral parameters.

In addition, teleseismically determined epicentral parameters are affected by the high velocity subducting slab upon rays that travel through it for a considerable distance. A further problem is the uneven azimuthal distribution of recording stations, with the Pacific Ocean producing a large gap. Reasonable depth estimates for shallow events can only be achieved with the help of depth phases, but routinely reported teleseismic depth phases are subject to considerable error for such events (Forsyth, 1982).

Depth Determination

All depth values given by the ISC for the events studied here were based on reported depth phases. The large scatter in depth seen in Figure IV-1, which represents a projection of the events onto a vertical plane striking perpendicular to the trench axis, may be due to phase misidentification.

Mistaking pW and pP does not constitute a problem in this study, since the results of the relocation indicate that the shallow water depth associated with the events (less than 1 km) causes pP and pW to arrive at nearly the same time on short period records. However, pP may be buried in the coda of P , especially in the case of larger events. In addition the complexity of upper crustal structure near either the source or the receiver can cause secondary phases easily mistaken for true depth phases. Differentiating pP from sP can also present problems if no additional information about the event is available.

Precise depth determination is of considerable importance for the identification of seismic source zones for purposes of seismic hazards assessment. We therefore scrutinized many teleseismic records for each of the 34 events in search of well defined depth phases. An additional three shallow events (events 35 - 37 of Table IV-1) located somewhat outside the source area of the relocated events were also investigated since bulletin reports indicated consistent depth phases. In the case of 28 of the above events we could not interpret the later arrivals as depth phases in any convincing fashion. Reported late arrivals for two events (numbers 37 and 33) were interpreted as foreshock-mainshock sequences, leaving only eight that permitted depth determination based on secondary arrivals.

Figure IV-2 shows some records for an event that occurred on 22 April 1966 at 57.37 N, 152.27 W (event 37). A very clear phase arrives about seven seconds after P at many US and some European stations. The amplitude ratio between the two phases is very similar for a wide range of azimuths on both short period and long period records, suggesting that the two phases are a foreshock-mainshock sequence. In the absence of a focal mechanism solution for this event the above interpretation is here however to be considered tentative.

Figure IV-3 shows an example of an event that occurred on 22 August 1973 at 57.09 N, 154.12 W. This event is representative of those events where a depth determination could be made with reasonable confidence. A prominent phase arrives at several European stations about 10 seconds after P . A weaker later phase can also be observed on some of these stations approximately 15 seconds after P . This later phase is very prominent at some US stations and one Asian station. These phases can be interpreted as pP and sP respectively, and correspond to a depth of 36 km for this event.

The depths calculated from later arrivals are based on a

KODIAK SHELF - JHD LOCATIONS

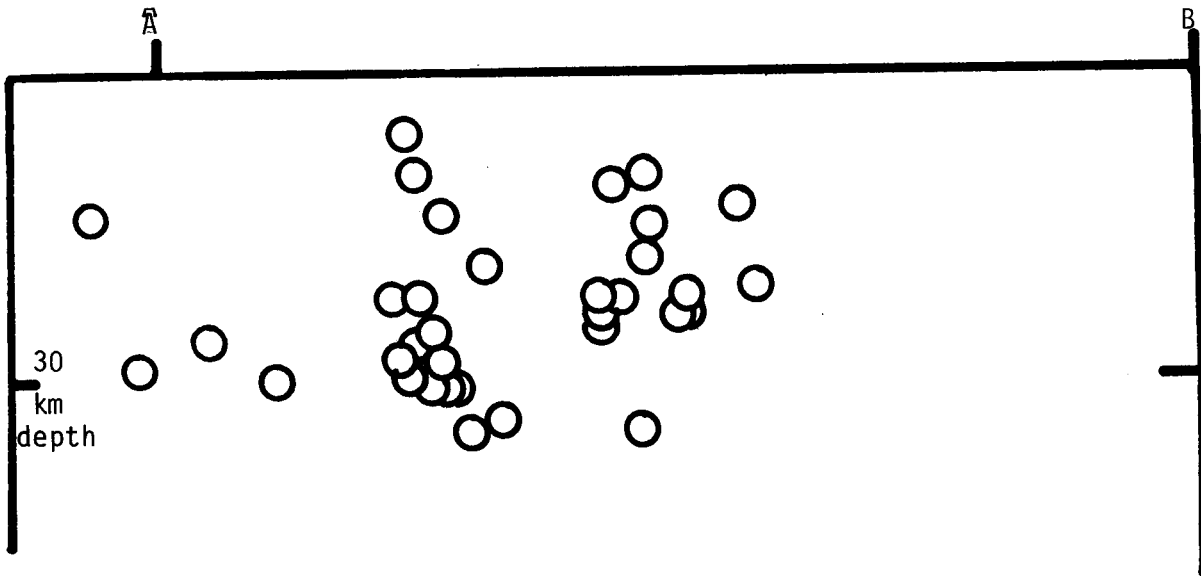


FIGURE IV-1: Vertical cross section of the events relocated by the JHD method in this study. Depths were determined from late arrivals reported in the ISC bulletins, and in some cases from inspection of seismograms recorded at selected WWSSN stations.

TABLE IV-1: Locations determined by the JHD method of 34 events relocated in this study. In addition, the table reports two additional events (#35 - 36) for which reliable depth phases occur as determined from seismograms recorded at WWSSN stations.

<u>NUMBER</u>	<u>DATE</u>	<u>LATITUDE</u>	<u>LONGITUDE</u>	<u>DEPTH</u>	<u>ORIGIN TIME</u>	<u>MAGNITUDE</u>	<u>RELIABLE DEPTH PHASES</u>
1	30 Mar 1964	56.59 N	153.00 W	22.0	0218:05.28	5.8	-
2	30 Mar 1964	56.64 N	152.27 W	18.0	1609:26.99	5.7	-
3	04 Apr 1964	56.60 N	152.75 W	19.0	0840:29.82	5.3	-
4	04 Apr 1964	56.92 N	153.01 W	14.0	0910:54.6	5.8	-
5	05 Apr 1964	56.35 N	153.48 W	30.0	0122:13.90	5.6	YES
6	05 Apr 1964	56.28 N	153.60 W	27.0	0141:43.06	5.4	-
7	12 Apr 1964	56.67 N	152.33 W	22.0	0124:30.41	5.8	-
8	16 Apr 1964	56.51 N	153.04 W	25.0	1926:56.08	5.5	-
9	17 Apr 1964	56.53 N	153.00 W	14.0	0449:28.20	5.5	-
10	06 May 1964	56.64 N	152.27 W	15.0	1526:35.99	5.5	-
11	12 May 1964	56.64 N	152.35 W	11.0	1816:42.10	5.4	-
12	27 Sep 1964	56.60 N	152.10 W	21.0	1550:53.41	5.4	-
13	23 Jun 1964	56.64 N	152.79 W	31.0	1109:15.10	5.7	-
14	22 Jan 1966	56.02 N	153.98 W	34.0	1427:07.09	5.7	YES
15	08 Apr 1966	56.69 N	152.65 W	31.00	2210:56.07	5.0	-
16	11 Apr 1966	56.65 N	152.16 W	24.00	2300:22.41	5.0	-
17	09 May 1967	56.53 N	152.60 W	22.00	1236:36.24	5.0	YES
18	13 May 1967	56.51 N	152.71 W	23.00	0518:54.21	5.0	-

<u>NUMBER</u>	<u>DATE</u>	<u>LATITUDE</u>	<u>LONGITUDE</u>	<u>DEPTH</u>	<u>ORIGIN TIME</u>	<u>MAGNITUDE</u>	<u>RELIABLE</u>	<u>DEPTH</u>	<u>PHASES</u>
19	29 Jan 1968	56.32 N	153.51 W	6.0	2052:20.75	5.2		-	
20	22 Dec 1968	56.39 N	154.07 W	29.0	1644:43.81	5.4	YES		
21	20 Nov 1969	56.61 N	153.23 W	30.0	2346:10.57	5.2		-	
22	21 Nov 1969	56.31 N	153.56 W	22.0	0014:10.71	5.1	YES		
23	24 Nov 1969	56.17 N	153.77 W	28.0	2251:48.47	5.4		-	
24	12 Jan 1970	56.71 N	152.13 W	35.0	0454:31.93	5.3		-	
25	20 Sep 1971	56.45 N	153.15 W	30.0	0644:13.65	5.1		-	
26	18 Jan 1972	56.75 N	153.12 W	26.0	0017:44.95	5.1	YES		
27	01 Aug 1974	56.56 N	152.36 W	23.0	0555:36.11	5.1		-	
28	01 Aug 1974	56.55 N	152.58 W	22.0	0759:54.92	5.1		-	
29	01 Aug 1974	56.56 N	152.45 W	10.0	0507:59.81	5.3		-	
30	07 Aug 1974	56.62 N	152.75 W	35.00	0823:36.26	5.0		-	
31	22 Oct 1976	56.17 N	153.42 W	24.0	1835:25.19	5.5		-	
32	10 Aug 1977	56.63 N	152.89 W	28.0	0935:57.55	5.1		-	
33	12 Apr 1978	56.62 N	152.87 W	10.0	0342:03.51	5.7		-	
34	12 Apr 1978	56.52 N	152.43 W	22.0	0522:29.90	5.0		-	
35	11 Mar 1970	57.39 N	153.97 W	42.0	2238:32.4		YES		
36	22 Aug 1973	57.09 N	154.12 W	36.0	1814:36.6		YES		

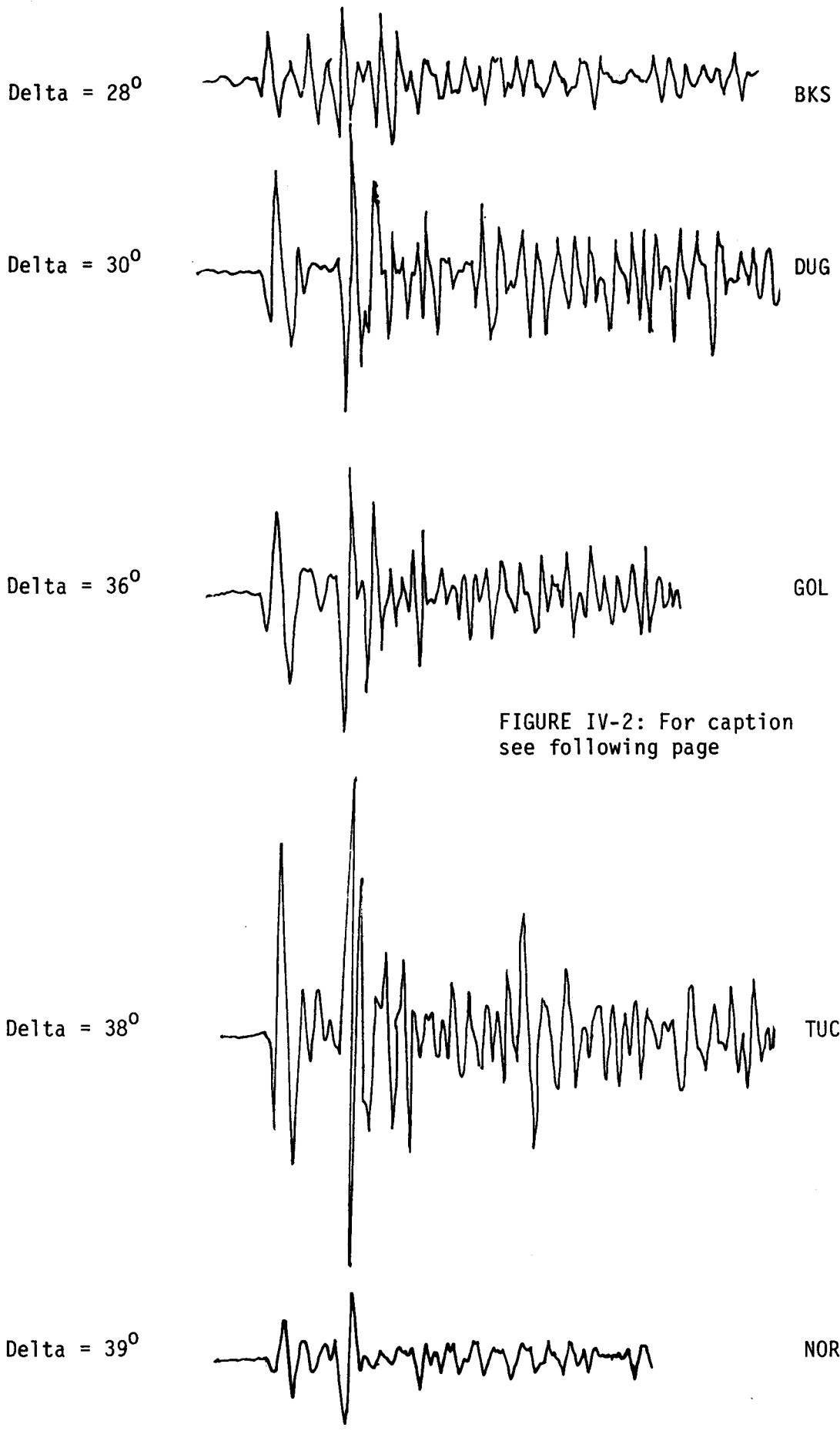


FIGURE IV-2: For caption see following page

Delta = 53°



KEV

Delta = 62°



NUR

FIGURE IV-2: Short period seismograms (vertical component) at several WWSSN stations for the event which occurred on 22 April 1966 (see Table IV-1). Note the clear phase arriving on most records about 7 sec after the initial P arrival.

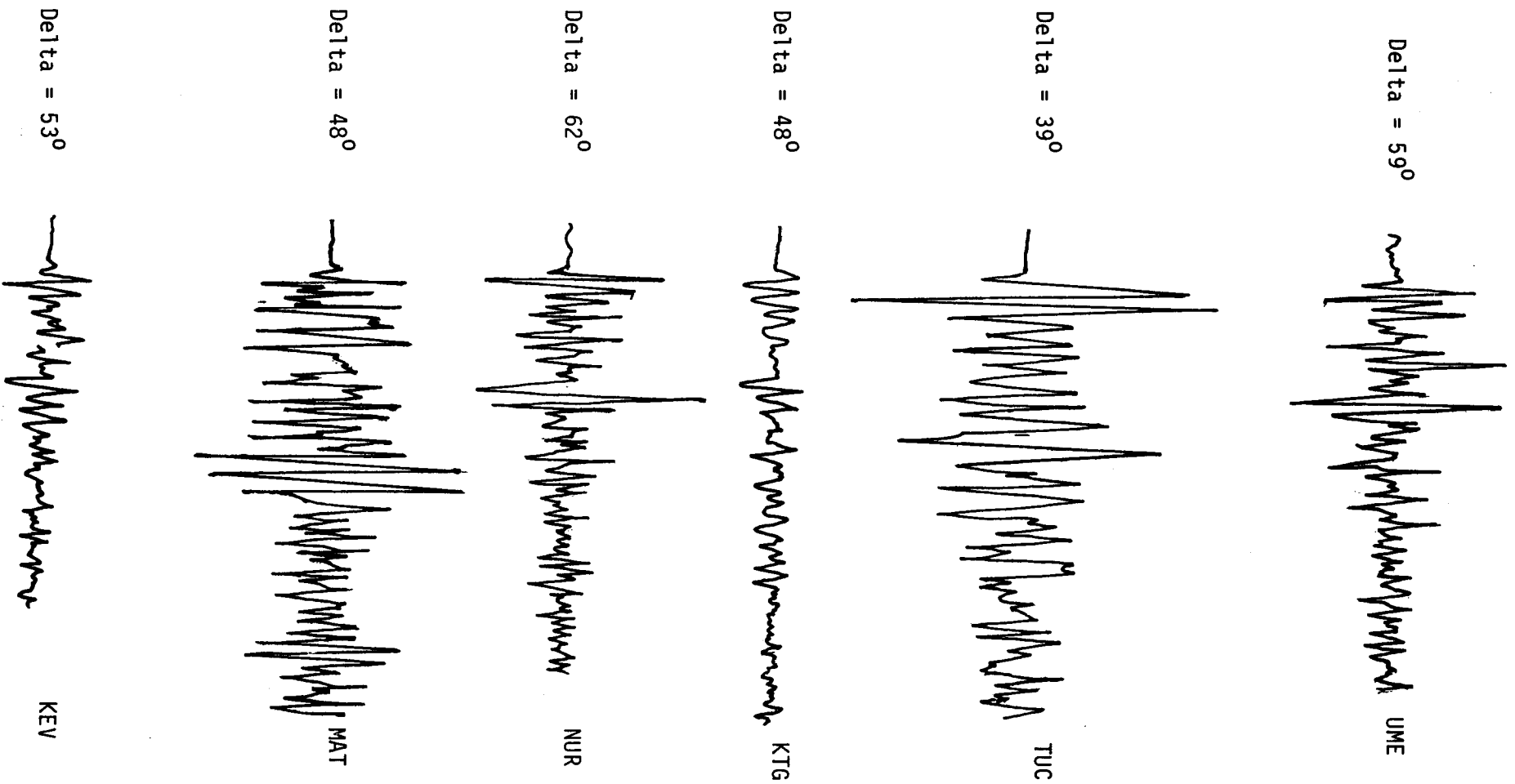
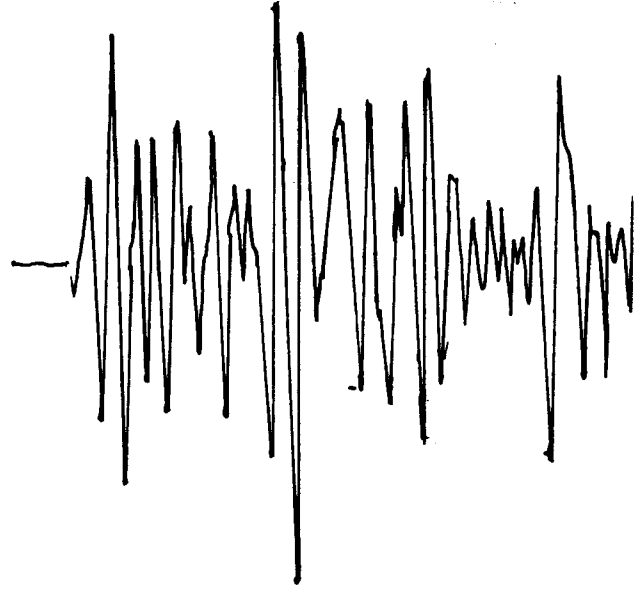


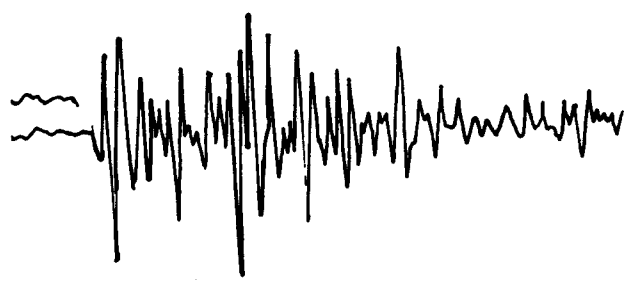
FIGURE IV-3: Short period seismograms (vertical component) at several WWSSN stations for the event which occurred on 22 August 1973 (see Table IV-1).

Delta = 22°



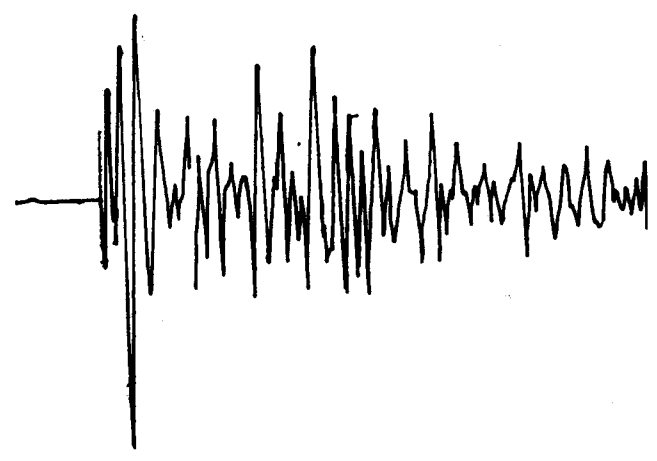
LON

Delta = 63°



KON

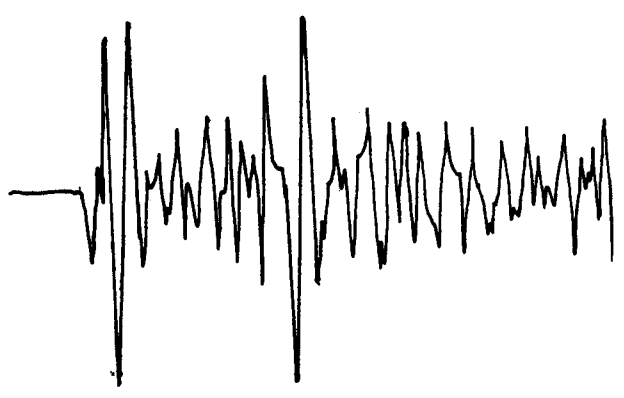
Delta = 45°



JCT

FIGURE IV-3: For caption see preceding page.

Delta = 39°



ALQ

Jeffreys-Bullen earth structure and thus do not take into account differences between the J-B structure and the local crustal structure. However, the resulting error is within the limit of accuracy with which later phases can be timed, and the depths would be shifted only a few km if an appropriate local structure were used. The depths derived here are likely to be more reliable than those reported in the ISC bulletins.

If viewed in cross section (Figure IV-4) there is a much smaller scatter apparent in the depth distribution. This is due in part to the smaller number of events, since a few events are considerably shifted from their reported ISC depths. Our locations are the result of a more rigorous approach towards assessing and relocating teleseismic recorded events than has been used routinely in this area previously. Thus the present locations provide a better basis for speculating on the seismotectonics of the area.

Relocation by the Joint Hypocenter Determination Method

There exist several methods which attempt to improve earthquake locations. Three dimensional ray tracing (e.g., Engdahl and Lee, 1976) can directly account for lateral inhomogeneities and provide accurate locations if the three dimensional velocity structure is well known a priori. The large number of calculations associated with this method, however, prevents its extensive use.

The Joint Hypocenter Determination (JHD) method (Douglas, 1967; Dewey, 1972; Frohlich, 1979) solves for hypocentral parameters and station corrections simultaneously for a group of earthquakes under the assumption that the station corrections are the same for each event of the group. This requires the events to be distributed over a limited volume. In this case JHD will generally provide a considerable improvement in the relative location of the events.

We applied the JHD method of Frohlich (1979) to a group of 34 earthquakes covering an approximately 100 X 150 km area (Figure IV-5). Body wave magnitudes of the events ranged from 5.0 to 5.8. Ten WWSSN stations at teleseismic distances were selected to provide good azimuthal coverage (Figure IV-6) and also clear arrivals from the lower magnitude events. The azimuth of one of these, COL, is such that rays to it will travel to a large extent through the high velocity subducting slab. To somewhat offset this the station ADK was used. Rays to ADK also will travel predominantly through the slab which undergoes an approximate 60 degree azimuthal bend in the Kodiak-Lower Cook Inlet area. The station KDC, operated by NOAA, was used as a nearby station (distance about one degree). Thus a total of 12 stations was used for relocation purposes (Table IV-2). About 80 per cent of the arrival times were reread by the authors. Only where copies of the original records were unavailable did we use readings reported from the bulletins.

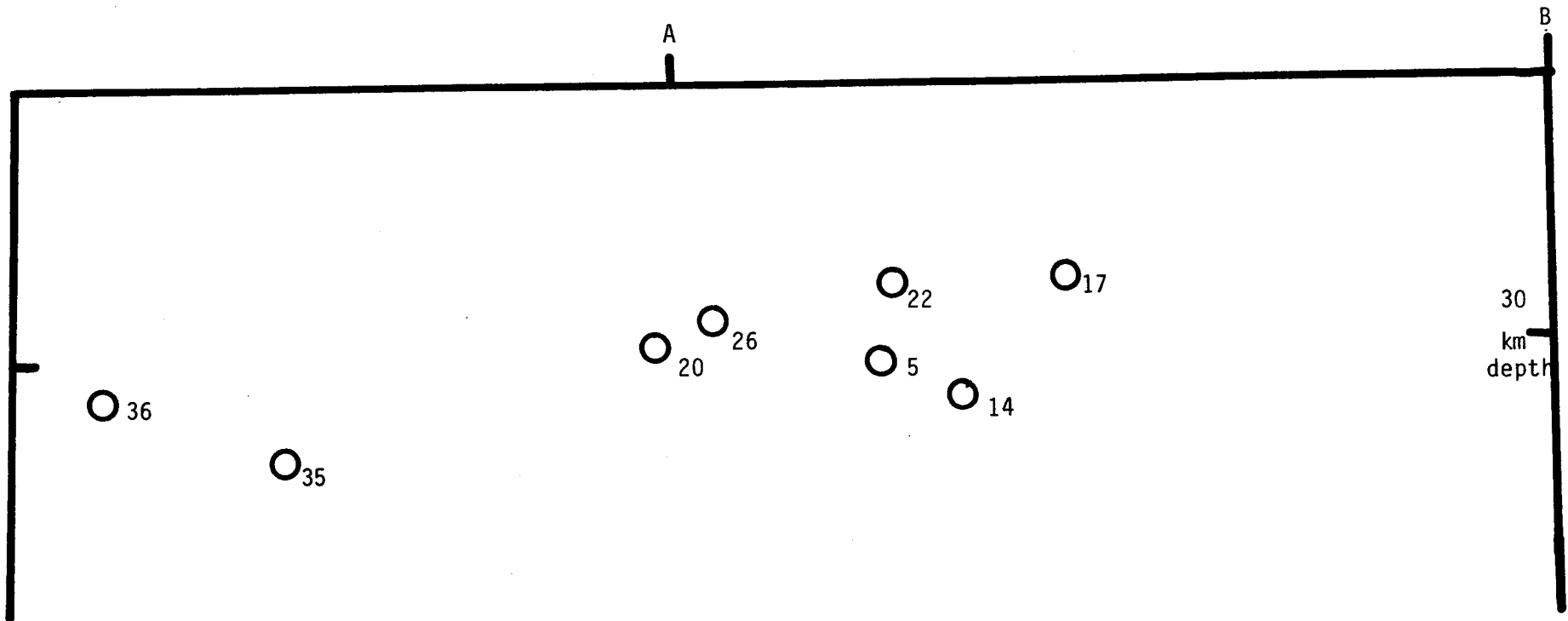
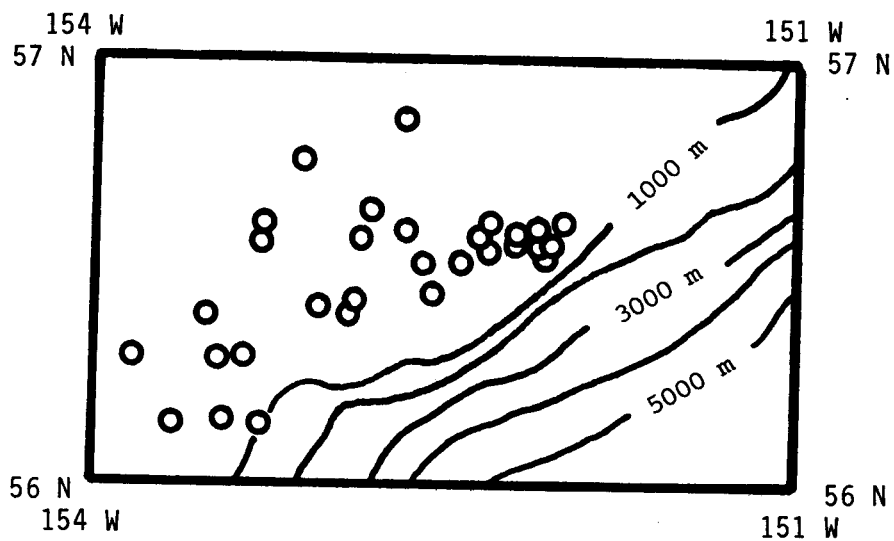


FIGURE IV-4: Vertical cross section of the events for which depths were determined from inspection of seismograms recorded at selected WSSN stations. Numbers adjacent to each event are the event numbers in Table IV-1. Points A and B are as in Figure IV-1

KODIAK SHELF - ISC LOCATIONS



KODIAK SHELF - JHD LOCATIONS

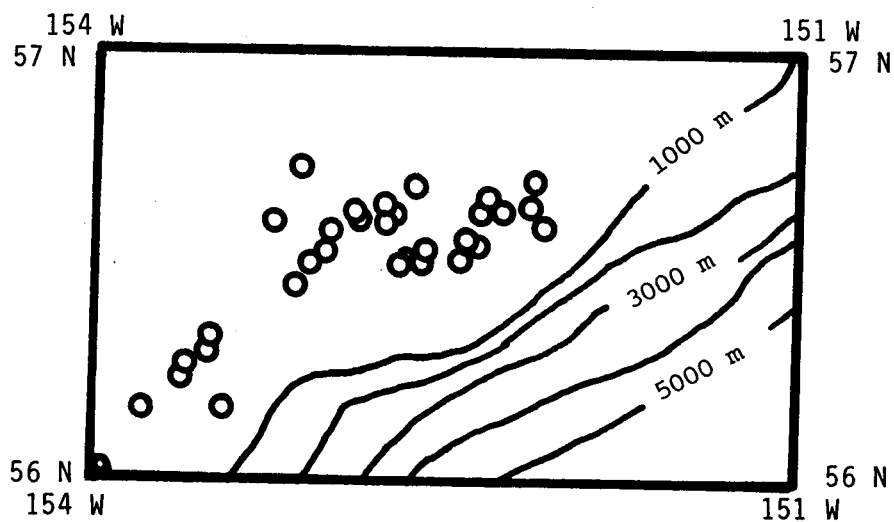


FIGURE IV-5: Map showing the location of 34 earthquakes relocated in this study using the JHD method. Top - locations reported by the ISC; Bottom - same events after relocation by the JHD method.

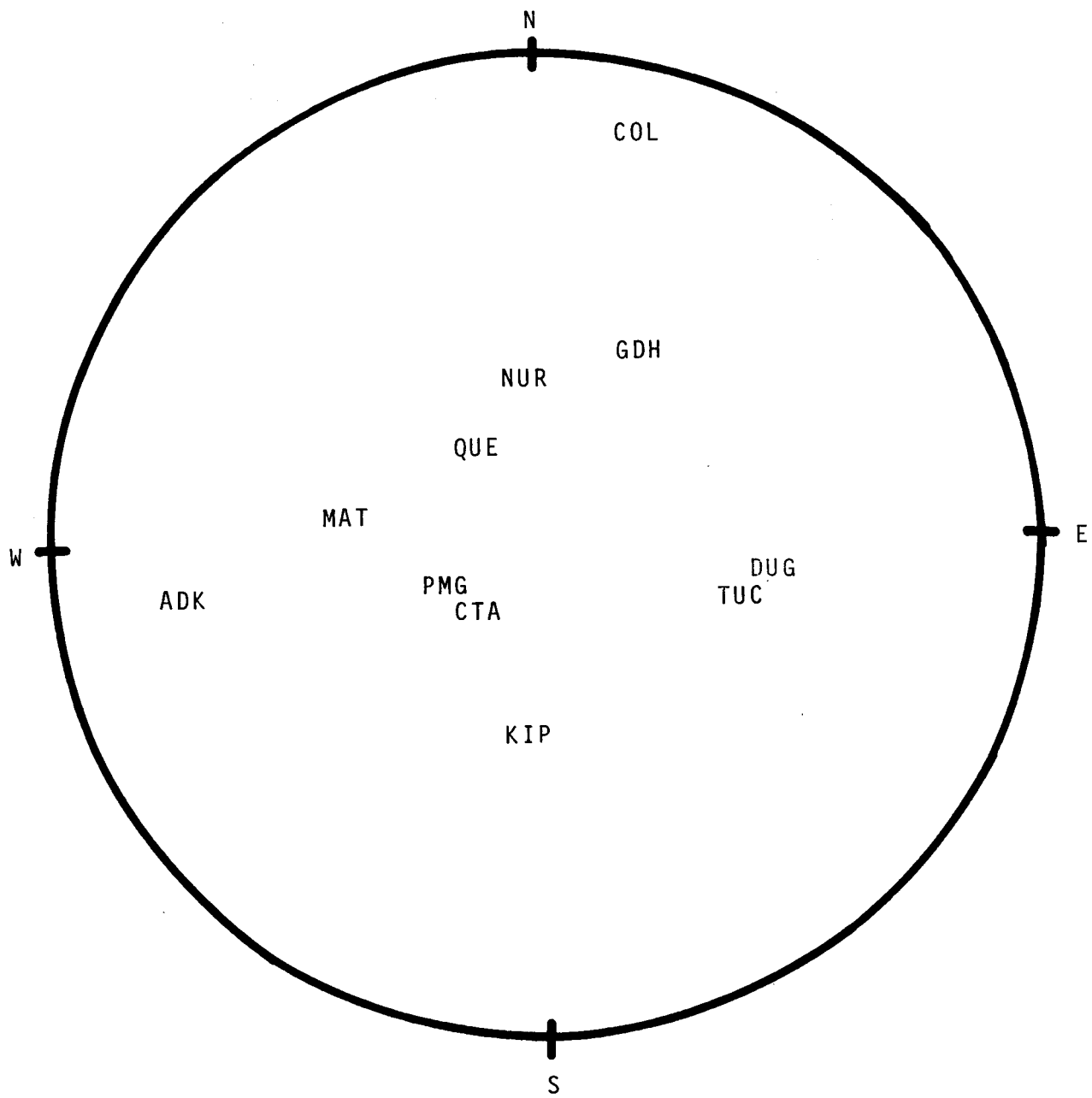


FIGURE IV-6: Distribution on a focal sphere of the stations used in the JHD relocation. One station (KDC) is not shown because its position on the focal sphere depends critically on the velocity model used.

TABLE IV-2: Stations used for JHD relocation of the 34 events in Table IV-1, and stations corrections determined during the JHD relocation.

<u>STATION CODE</u>	<u>CORRECTION</u>
KDC	1.19 sec
COL	-1.81
ADK	-2.73
NUR	0.10
GDH	1.54
TUC	-0.25
DUG	-0.98
KIP	0.06
MAT	-0.33
PMG	0.30
QUE	1.65
CTA	1.27

RESULTS AND DISCUSSION

Upon relocation by the JHD method, the originally diffusely distributed events collapse into two fairly narrow, subparallel groups of events, with only a few events falling outside these groups (Figure IV-4). Before speculating about the implications of this, we will discuss the probably effect of systematic errors in location which affect all the events in the same fashion.

While the relocation provides reliable relative locations for these events, the locations may still be biased as a whole. Four of the relocated events were teleseismically recorded as well as recorded by the UA regional network. The location of these three events is on the average 22 km to the south and 3 km to the west of the corresponding JHD locations. This result is in agreement with the results of Lawton et al. (1982), who compared locations in this area determined by a combined OBS-land-based network with ISC locations.

The OBS study also indicated that well recorded events which are located using stations of the landbased network shift only slightly when data from a combined OBS-land network is used for location. Thus the actual location of the relocated teleseismic events is probably about 20 km south from the locations in Table IV-1. Such a shift puts the events approximately along the shelf break (1000 m bathymetric contour).

Hampton et al. (1979) map a series of faults along the shelf break, some of them offsetting the seafloor by as much as 10 m. There is probably no direct relationship between the relocated events and these faults. The rigidity of the accreted sediments is probably too low to permit brittle fracture at the scale indicated by the magnitude of the events. Focal mechanism solutions available for 11 of the relocated events (Stauder and Bollinger, 1966) all indicate these events to be associated with thrusting on a gently dipping plane. Although the ambiguity in first motion fault plane solutions also permits dip slip faulting on a steeply dipping plane, the direction is opposite to that generally inferred along the imbricate faults of the accretionary wedge, which appears to be aseismic (Chen et al., 1982). However, the relationship between the activity along the main thrust and observed faults might be along the model suggested by Fukao (1979).

The majority of the events relocated in this study are part of the aftershock sequence of the 1964 Good Friday Alaskan earthquake. The relatively narrow belt of aftershock seismicity evident from our relocations probably reflects the release by brittle fracture of stress concentration penetrating the leading seaward edge of the shallow dipping rupture zone associated with the main shock. Since according to Fukao's (1979) model, the main rupture did not propagate further towards the trench along the interface between the overriding and underthrusting plates, the wedge-shaped region of sediments between the trench axis and the leading edge of the rupture zone will be heavily stressed. Thus stresses will be relieved mostly in a ductile manner along slip lines bending from the tip of the rupture zone upwards and emerging at steep dip angles from the ocean floor, producing the mapped seafloor offsets noted by Hampton et al. (1979).

References

- Chen, A. T., C. Frohlich and G. V. Latham. Seismicity of the forearc marginal wedge (accretionary prism). *J. Geophys. Res.*, 1982, **87**, 3679-3690.
- Dewey, J. W. Seismicity and tectonics of western Venezuela. *Bull. Seismol. Soc. Amer.*, 1972, **62**, 1711-1751.
- Douglas, A. Joint epicenter determination. *Nature*, 1967, **215**, 189-205.
- Engdahl, E. R and W. H. K. Lee. Relocation of local earthquakes by seismic ray tracing. *J. Geophys. Res.*, 1976, **81**, 4400-4406.
- Fisher, M. A. Petroleum geology of Kodiak shelf, Alaska. *Am. Assoc. Pet. Geol. Bull.*, 1980, **64**, 1140-1157.
- Forsyth, D. W. Determinations of focal depths of earthquakes associated with the bending of oceanic plates at trenches. *PEPI*, 1982, **00**, 00-00. in press.
- Frohlich, C. An efficient method for joint hypocenter determination for large groups of earthquakes. *Computers & Geosciences*, 1979, **5**, 387-389.
- Fukao, Y. Tsunami Earthquakes and subduction processes near deep-sea trenches. *J. Geophys. Res.*, 1979, **84**, 2303-2314.
- Hampton, M. A., A. H. Bouma, H. Pulpan and R. von Huene. Geo-environmental assessment of the Kodiak Shelf, western Gulf of Alaska. In *Proc. 11th Offshore Tech. Conf.. OTC*, 1979.
- Hanley, P. T. and W. W. Wade. New study analyzes Alaska OCS areas. *Oil and Gas Journal*, 1981, **79**, 73-79.
- Hansen, W. R. and E. B. Eckel. Setting and effects of the earthquake. In *The Great Alaska Earthquake of 1964*. National Research Council; National Academy of Sciences, 1971.
- Lawton, J., C. Frohlich, H. Pulpan and G. V. Latham. Earthquake activity at the Kodiak continental shelf, Alaska determined by land and ocean bottom seismograph networks. *Bull. Seismol. Soc. Amer.*, 1982, **72**, 207-213.
- Plafker, G. Alaskan earthquake of 1964 and Chilean earthquake of 1960: implications for arc tectonics. *J. Geophys. Res.*, 1972, **77**, 901-925.
- Pulpan, H. and J. Kienle. Western Gulf of Alaska seismic risk. In *Proc. 11th. Offshore Tech. Conf.. OTC*, 1979.
- Stauder, W. and G. A. Bollinger. *The S wave project for focal mechanism studies: the Alaska earthquake sequence of 1964* (Tech. Rep. AFCRL-66-572). Air Force Cambridge Research Laboratories, 1966.



**A SEISMOTECTONIC ANALYSIS OF THE SEISMIC AND VOLCANIC
HAZARDS IN THE PRIBILOF ISLANDS - EASTERN ALEUTIAN
ISLANDS REGION OF THE BERING SEA**

by

Dr. Klaus H. Jacob and Dr. Egill Hauksson

**Lamont-Doherty Geological Observatory
Columbia University in the City of New York**

**Final Report
Outer Continental Shelf Environmental Assessment Program
Research Unit 16**

1983

.135



TABLE OF CONTENTS

List of Figures	139
List of Tables	145
Acknowledgments	147
1. ABSTRACT AND SUMMARY OF MOST IMPORTANT RESULTS	148
2. INTRODUCTION	150
3. DATA ANALYSIS	154
3.1 Seismicity Recorded by the Shumagin Network 1973-1982	154
3.2 Teleseismic Data 1973-1982	171
3.3 Strong-Motion Data	177
3.4 Historic and Instrumental Large Earthquakes, 1788 to Present	190
3.5 Historical Eruptive Activity of Pavlof, Akutan, and Makushin Volcanoes	237
3.6 Geology and Geodetic Surveys	247
3.7 Seismicity Recorded by the Unalaska Array 1980-1982	252
3.8 Tsunami Data	256
4. RESULTS	259
4.1 Seismic Hazards	259
4.2 Volcanic Hazards	264
5. CONCLUSIONS	279
6. UNRESOLVED PROBLEMS	281
7. APPENDICES	282
7.1 Earthquake Data Processing Methods	282
7.2 Magnitude Determinations	291
7.3 Annual Plots of Shumagin Network Seismicity 1973-1982	300
7.4 Shumagin Network Status 1973-1982	315
7.5 Seismic and Eruptive Activity of Pavlof Volcano, 1973-1982 ...	325
7.6 Preliminary Risk Assessment in the St. George Basin	335
7.7 List of Publications Supported by Contract NOAA-03-5-022-70 ..	357
8. REFERENCES	359



LIST OF FIGURES

Figure 2.1 - Approximate regions (boxes) in which L-DGO collected data by operating seismic stations or networks in St. Paul (SNP), Dutch Harbor (DUT) on Unalaska Island, and in the Shumagin Islands with central recording at Sand Point (SAN)

Figure 3.1.1 - Map of epicenters showing all the seismicity located by the Shumagin network eastern Aleutians, Alaska, from 1973-1981

Figure 3.1.2 - Map of epicenters showing all the shallow seismicity (depth less than 30 km) located by the Shumagin network, eastern Aleutians, Alaska, from 1973-1981

Figure 3.1.3 - Map of epicenters showing all the intermediate depth and very deep seismicity (depth greater than 40 km) located by the Shumagin network, eastern Aleutians, Alaska from 1973-1981

Figure 3.1.4 - Histogram of number of earthquakes located by the Shumagin seismic network, eastern Aleutians, Alaska

Figure 3.1.5 - Cumulative number of all local earthquakes located by the Shumagin network from 1978 to 1982

Figure 3.1.6 - Both cumulative number and number of earthquakes as a function of magnitude for the whole data set recorded by the Shumagin network from 1977 to 1981

Figure 3.1.7 - Both cumulative number and number of earthquakes as a function of magnitude for all shallow earthquakes (depth less than 30 km) recorded by the Shumagin network from 1977 to 1981

Figure 3.1.8 - Map of epicenters where seismicity lineaments are emphasized by drawing straight lines by eye through clusters that appear to form linear alignments

Figure 3.1.9 - Cumulative number of seismicity lineaments from Figure 3.8 versus length of seismicity lineament

Figure 3.1.10 - Magnitude versus source dimension relationship

Figure 3.1.11 - Recurrence relation for the Gulf of Alaska random sources

Figure 3.2.1 - Map of epicenters showing teleseismically located earthquakes from the PDE bulletin from 1973-1981

Figure 3.2.2 - The vertical bars indicate the occurrence and the magnitude of teleseismically located earthquakes from the PDE bulletin

Figure 3.2.3 - Cumulative number of earthquakes located by the PDE from 1973 to 1982 in the Shumagin Islands region

Figure 3.2.4 - Both cumulative number and number of earthquakes as a function of magnitude for the PDE data from 1973 to 1981 located in the Shumagin Islands region

Figure 3.3.1 - Comparison of peak horizontal accelerations for Alaska with empirical attenuation laws obtained by Joyner and Boore (1981) by regression of mostly western U.S. strong motion data

Figure 3.3.2 - Comparison of Alaska peak horizontal accelerations with type-A attenuation relations proposed by Woodward-Clyde (1982) for shallow, non-Benioff zone earthquakes

Figure 3.3.3 - Comparison of Alaska peak horizontal accelerations with B-type attenuation relations proposed by Woodward-Clyde (1982) for Benioff-zone earthquakes

Figure 3.4.1 - Location map of presently existing seismic gaps and of rupture zones of the most recent sequence of major earthquakes since 1938

Figure 3.4.2 - Major earthquakes in the Alaska-Aleutian region for the instrumental period 1898 to 1982

Figure 3.4.3 - Seismicity of the Aleutian arc versus time for the instrumental period 1898 to 1982

Figure 3.4.4 - Histogram of all major earthquakes for which magnitudes were available, plotted in $M_w = 0.1$ -intervals

Figure 3.4.5 - Logarithmic frequency plots for the instrumental seismicity 1898 to 1982 for the Alaska-Aleutian arc

Figure 3.4.6 - Same as Figure 3.4.5 with number of events n as solid line and cumulative number of events N as broken line

Figure 3.4.7 - Arc-wide seismic moment release for the Aleutian arc during the period 1898 to 1982

Figure 3.4.8 - Space-time plot of instrumental (1898 to 1982) and historical (1788 to 1897) seismicity of the Aleutian arc considering great earthquakes only

Figure 3.4.9 - Statistical properties of recurrence periods

Figure 3.4.10 - Same as Figure 3.4.9 except that a normal (rather than a log-normal) distribution is fitted to observed recurrence times distribution which consists of a reduced number of samples

Figure 3.5.1 - The number of reported eruptions per decade vs. time

Figure 3.6.1 - Maps showing level lines and tide gauges in the Shumagin Islands

Figure 3.6.2 - Data from those level lines in the Shumagins that have been levelled at least twice

Figure 3.7.1 - Dutch Harbor Array, Eastern Aleutians, operated by Lamont-Doherty Geological Observatory

Figure 3.7.2 - Number of earthquakes recorded per day by the Dutch Harbor Array in 1980 and 1981

Figure 3.7.3 - Number of earthquakes recorded per day by the Dutch Harbor Array in 1982

Figure 3.8.1 - Diagram showing tsunami run-up heights and inferred earthquake source region of the 1788 event(s)

Figure 4.1.1 - Map view of arc with instrumental seismicity since 1898

Figure 4.2.1 - Volcano hazards map for the Western Alaska Peninsula

Figure 4.2.2 - Volcano hazards map for the Eastern Aleutian Islands

Figure 4.2.3 - Distribution of volcanic ash layers in North Pacific deep-sea cores

Figures 4.2.4a,b - Sample locality maps in Shumagin Islands and adjacent peninsula

Figures 4.2.5a,b - Examples of volcanic ash layers in cores taken on marine terraces in summer 1979

Figure 4.2.6 - \log_{10} of the cumulative number of eruptions of a given size per hundred years per volcano vs. the \log_{10} of the volume of eruptive products

Figure 4.2.7 - Maximum ash thickness in cm vs. distance from the vent

Figure 7.1.1 - A block diagram showing how the routine developer data processing was carried out for the Shumagin seismic network

Figure 7.1.2 - A block diagram showing how the routine digital data processing is carried out for the Shumagin seismic network

Figure 7.1.3 - A summary display of seismic traces from the program ping

Figure 7.1.4 - A sample seismogram from station CNBZ

Figure 7.1.5 - A sample output from HYPOINVERSE

Figure 7.1.6 - A sample output from the program dplt2

Figure 7.2.1 - Sensor responses and recorder responses shown as a function of frequency for seismic stations in the Shumagin network

Figure 7.2.2 - Magnification curves for a typical high gain short-period station (NGI at 48 db Amp/VCO gain)

Figure 7.2.3 - Comparison between magnitude values determined by the Shumagin network and values published by NEIS

Figure 7.3.1 - Seismicity located by the Shumagin network during 1973

Figure 7.3.2 - Seismicity located by the Shumagin network during 1974

Figure 7.3.3 - Seismicity located by the Shumagin network during 1975

Figure 7.3.4 - Seismicity located by the Shumagin network during 1976

Figure 7.3.5 - Seismicity located by the Shumagin network during 1977

Figure 7.3.6 - Seismicity located by the Shumagin network during 1978

Figure 7.3.7 - Seismicity located by the Shumagin network during 1979

Figure 7.3.8 - Seismicity located by the Shumagin network during 1980

Figure 7.3.9 - Seismicity located by the Shumagin network during 1981

Figure 7.3.10 - Seismicity located by the Shumagin network from January-June 1982

Figure 7.3.11 - Seismicity located by the Shumagin network from 1973-1981

Figure 7.4.1 - The Shumagin seismic network, Alaska

Figure 7.4.2 - Operational status of the Shumagin network in 1973 and 1974

Figure 7.4.3 - Operational status of the Shumagin network in 1975 and 1976

Figure 7.4.4 - Operational status of the Shumagin network in 1977 and 1978

Figure 7.4.5 - Operational status of the Shumagin network in 1979 and 1980

Figure 7.4.6 - Operational status of the Shumagin network in 1981 and 1982

Figure 7.5.1 - Map showing stations of the Pavlof seismic array

Figure 7.5.2 - Types of seismic signals recorded on helicorder from station PVV

Figure 7.5.3 - Number of B-type earthquakes and explosions per day

Figure 7.5.4 - Number of B-type earthquakes and explosions per day

Figure 7.5.5 - Number of B-type earthquakes and explosions per day

Figure 7.5.6 - Number of B-type earthquakes and explosions per day

Figure 7.5.7 - Number of B-type earthquakes and explosions per day

Figure 7.6.1 - Earthquake epicenters, greater St. George Basin area, 1925 through 1978

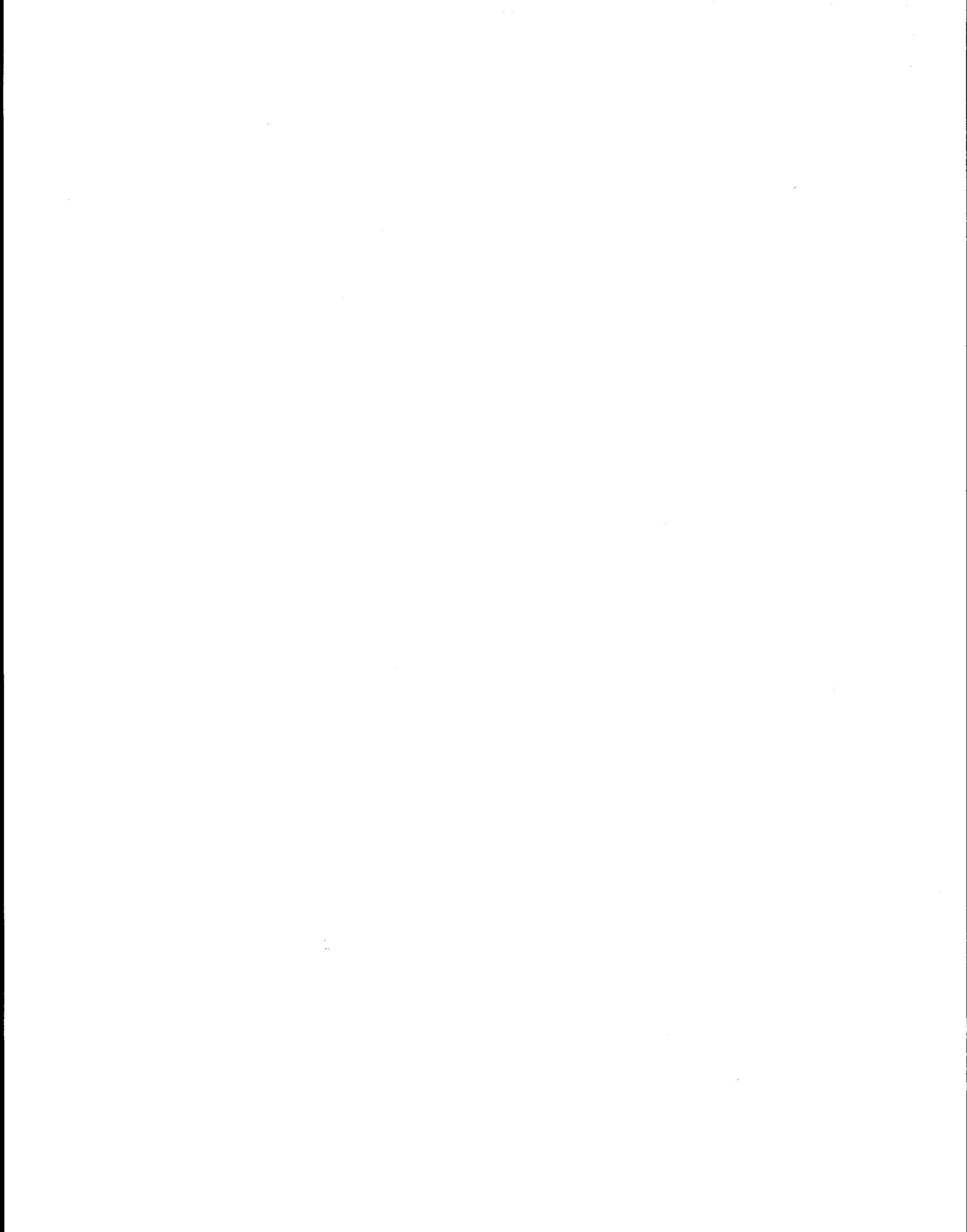
Figure 7.6.2 - Epicenters of shallow earthquakes, limited St. George Basin area, 1957 through 1978

Figure 7.6.3 - Earthquakes per year for the greater and the limited St. George Basin region

Figure 7.6.4 - Logarithm cumulative number of earthquakes vs. magnitude for the limited St. George Basin region during the period 1957 through 1978

Figure 7.6.5 - Peak acceleration vs. distance for some western U.S. earthquakes and eastern Aleutian earthquakes

Figure 7.6.6 - Detection threshold for St. Paul Seismic station (SNP)



LIST OF TABLES

- Table 3.3.1 - Alaska-Aleutian Strong Motion Data
- Table 3.4.1 - List of 116 Large Earthquakes in the Alaska-Aleutian Arc
- Table 3.4.2 - Estimates of Minimum-, Average-, and Maximum Recurrence Times Derived from the b-Value Plot for the Entire Arc
- Table 3.4.3 - Comparison of A and b Values and Recurrence Times T_R for $m = 5.0$ Events Using Different Data Sources
- Table 3.4.4 - Parameters for Plate-Kinematic Model of Seismic Moment Release
- Table 3.4.5 - Recharge Status of Rupture Zones or Gaps Since Last Significant Event
- Table 3.4.6 - List of Great Historic Events and Inferred Source Parameters Based on the 'Time Predictable' Model
- Table 3.4.7 - Moment Balance (expressed in equivalent M_w) Since 1760
- Table 3.4.8 - Observed or Computed Recurrence Times for Rupture Zones Which Broke During the Historic and Instrumental Period 1788 to 1965
- Table 3.4.9 - Probabilities P(%) for Recurrence Periods T_R (years)
- Table 3.4.10 - Cumulative, Conditional, and Annual Probabilities for Great Earthquakes in 1983, 1993 and 2003
- Table 3.4.11 - Cumulative, Conditional, and Annual Probabilities for Great Earthquakes in 1983, 1993 and 2003, for Major Aleutian Rupture Zones Assuming Normally Distributed Recurrence Periods
- Table 3.5.1 - Pavlof Sister
- Table 3.5.2 - Pavlof
- Table 3.5.3 - Akutan
- Table 3.5.4 - Makushin
- Table 3.5.5 - Data on Eruptive Activity of Alaska and Aleutian Volcanoes
- Table 4.2.1 - Carbon 14 Dates and Number of Volcanic Ash Layers for Marine Terrace Cores
- Table 7.2.1 - Earthquakes Located by Both the Shumagin Network & PDE
- Table 7.3.1 - Number of Earthquakes Located by the Shumagin Network and NEIS/PDEE Bulletin Per Year in the Region 52° - 57° N and 156° - 165° W. 161

LIST OF TABLES (con't.)

Table 7.3.2 - Flat-Layered P-Velocity Model for the Shumagin Islands Array Region

Table 7.4.1 - Eastern Aleutian Regional Networks Operated by Lamont-Doherty Geological Observatory, 1973-1982

Table 7.5.1 - Preliminary List of Pavlof Volcano Eruptions, 1973-1983, Deduced from Seismicity

Table 7.6.1 - All Events in the Greater St. George Basin Region for the Period 1925 Through 1978

Table 7.6.2 - Shallow Events in the Limited St. George Basin Region for the Period 1957 Through 1978

Table 7.6.3 - Frequency of Occurrence by Magnitude

Table 7.6.4 - Reports of Volcanic Activity in the Eastern Aleutian Arc from Okmok Volcano, Umnak Island to Pavlof Volcano, Alaska Penn

Table 7.6.5 - Probability for Acceleration to Exceed 0.2 or 0.5 g in 40 Years for a Site Within the St. George Basin Region

Table 7.6.6 - Events Detected at SNP in a Distance Range Such That Origin in St. George Basin is Possible

ACKNOWLEDGMENTS

This study was funded in part by the Bureau of Land Management through interagency agreement with the National Oceanic and Atmospheric Administration, (contract NOAA-03-5-022-70) as part of the Outer Continental Shelf Environmental Assessment Program in the eastern Aleutians, Alaska. The broad seismotectonic aspects of this work were also supported by the U.S. Department of Energy (contract DE-AS02-76ERO-3134).

Dr. John N. Davies, Alaska State Seismologist, who installed the Shumagin Network in 1973 was in charge of this project until July 1981. John's enthusiasm and unceasing efforts are the basis of the results presented in this report.

Thanks to Margaret Eubank for running the seismic recording station in Sand Point and to Bill Eubank for providing logistics support and accommodation at Sand Point. Also, thanks to Beverly Wiggers and William Tcheripanoff, Jr., for running the seismic recording stations in Dutch Harbor and on St. Paul Island, respectively.

Technical work was performed by Laszlo Skinta, Douglas Johnson, David Lentricchia, Fred England, Robert Steuer, Warren Leonard, Larry Shengold, George Gunther, and Tom Ray.

Data reduction and analysis were done by Mary Ann Luckman, Stephan Rosen, John Armbruster, Jim Mori, John Peterson, Jeff Hauptman, Mike Hamburger, Steve Hickman, Leigh House, Janet Krause, and Phil Lelyveld.

We would like to thank our contract monitors at NOAA in Juneau, Rodney A. Combellick and Laurie Jarvela, for their excellent cooperation. George LaPiene and Mike Albertson of NOAA organized the helicopter schedule every year and thanks to the generous help of the NOAA helicopter crews we managed to keep the seismic networks operating through the years.

We owe special thanks to Elvonne Wellmon, who carried out the administration of the contract and proofread this report. Lynn Niebour typed the manuscript and Kazuko Nagao and Mary Ann Luckman drafted the figures.

1. ABSTRACT AND SUMMARY OF MOST IMPORTANT RESULTS

This report presents and summarizes seismic and volcanic data collected by Lamont-Doherty in the eastern Aleutian arc and adjacent Bering Sea between 1973 and 1982. The data were collected with support by the NOAA-OCSEA Program during the period 1975-1982. Seismic networks were operated by Lamont-Doherty in the Shumagin Islands, Unalaska Island, and Pribilofs. The network data are analyzed in combination with teleseismic and historic (preinstrumental) data to: 1) obtain a tectonic model of the subduction process; 2) give a comprehensive definition of seismic and volcanic sources; and 3) determine the probabilities for the occurrence of earthquakes and of volcanic eruptions where the data allow such determinations.

Most of the newly collected data originate from earthquakes in sections of the eastern Aleutian arc and directly adjacent Bering Sea regions close to the following three lease sale planning regions: 'St. George Basin', 'North Aleutian Basin' and 'Shumagin Basin'. Some results regarding great earthquakes concern hazards in the more distant 'Kodiak', 'Lower Cook Inlet' and 'Eastern Gulf of Alaska' lease sale planning regions. The main results are:

1) Mean recurrence times for great earthquakes ($M_w \geq 7.8$) at any given segment in the Aleutian arc are approximately 70 years but have very large uncertainties.

2) Probabilities for the occurrence of great earthquakes ($M_w \geq 7.8$) especially near the Shumagin Islands, Unalaska Island and perhaps near the 1938-rupture zone SW of Kodiak Island are high during the next 20 years and virtually approach certainty (in the first two segments only) for a 40 year planning period (1983-2023). Therefore, future off- or near-shore installations near the seismogenic regions need to be designed for the effects of great earthquakes.

3) Tsunami heights on shorelines with south-facing Pacific Ocean exposures have in the past reached local run up heights of up to about 30 meters (90 feet). Future events can be expected to behave similarly. The Bering Sea side is less prone to tsunami effects.

4) Volcanic hazards are generally of lesser importance than seismic hazards except within close range of volcanoes.

5) Presently there is a general scarcity of strong motion data from Alaska-Aleutian subduction zone earthquakes and a complete global absence of strong motion data from any great ($M_w \geq 7.8$) earthquake. Until such data are collected and analyzed for incorporation into seismic exposure mapping, the latter can only produce tenuous results that may or may not correctly predict future groundmotions from great earthquakes at or near the lease sale regions of interest.

6) The single most important recommendation for future action resulting from this study is to maintain or upgrade a strong motion recording capability in seismic gaps of the Alaska-Aleutian arc and subduction zone so as to collect the urgently required strong motion data at the earliest possible time.

2. INTRODUCTION

This report summarizes the seismic and volcanic data collected from local seismic networks (Figure 2.1) that were operated by Lamont-Doherty in the Shumagin Islands, on Unalaska Island and St. George Island (Pribilofs). We assess the significance of these newly collected data for seismicity and volcanicity in the context of a tectonic model and integrate these results together with globally collected data of instrumental and historic (i.e., preinstrumental) periods from the eastern Aleutian arc and the adjacent Bering Sea to arrive at quantitative probabilistic descriptions of seismicity and volcanicity. Therefore, this report is primarily concerned with a quantitative description of the sources for seismic and volcanic hazards rather than their final effects on hazards exposure.

To complete the assessment of seismic and volcanic hazards exposure, at least two additional steps would therefore be required that are not covered under this project. For instance, from seismology one needs to obtain some empirical attenuation laws that prescribe the groundmotions as a function of distance from, and as a function of the magnitude of, the seismic source. Reliable empirical laws for groundmotions for moderate-sized Alaskan earthquakes do not exist at present in sufficient numbers, and do not exist at all, even on a global scale, for earthquakes with magnitudes ($M_w \geq 7.8$). We discuss extensively the problems caused by this paucity of empirical groundmotion data. We conclude that without the necessary groundmotion data and related attenuation laws, the third and final step, i.e., the computation and mapping of parameters at certain prescribed probability levels of non-exceedence for given periods of interest, cannot be meaningfully completed.

Various attempts in the past have nevertheless been made to compute and map seismic exposure for Alaska offshore regions. One of the first important and comprehensive studies in this category was the so-called 'OASES' Project (Woodward-Clyde Consultants, 1978) that was commissioned by the Oil Industry with interests in Alaska. That study provided a first complete overview but suffered from a number of deficiencies some of which are related to: 1) an inadequate

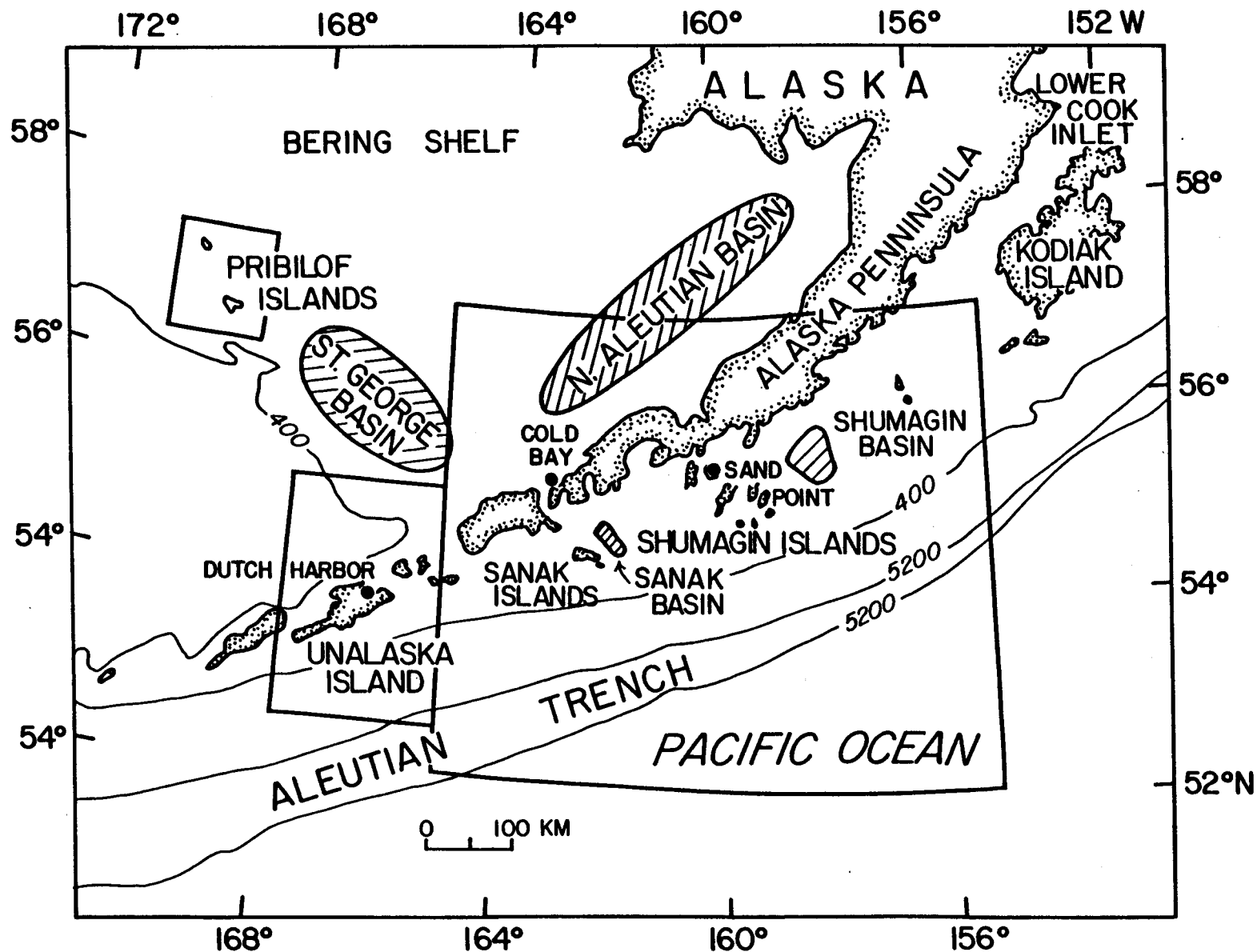


Figure 2.1. Approximate regions (boxes) in which L-DGO collected data by operating seismic stations or networks in St. Paul (SNP), Dutch Harbor (DUT) on Unalaska Island, and in the Shumagin Islands with central recording at Sand Point (SAN). Also labeled are the Lease Sale Planning regions 'St. George Basin', 'North Aleutian Basin', 'Shumagin Isl.' and 'Lower Cook Inlet'.

assessment of the occurrence of great subduction zone events ($M_w \gg 7.8$) which may have the most destructive potential in some regions; 2) poorly constrained strong groundmotion attenuation laws for the Alaska tectonic setting, especially those applicable to great earthquakes.

Therefore as part of the OCSEA Program a revision of the analysis applied in the OASES-project was solicited, to specifically incorporate:

- 1) A provision for the concept of seismic gaps that recognizes that the probability for the occurrence of a great earthquake in any arc segment is time-dependent and somehow is related to the time since the last great event that occurred in the segment;

- 2) A revised source definition with arc segmentation related to the historic record of great earthquakes; and

- 3) Usage of updated or modified groundmotion attenuation laws suitable for the Alaska-Aleutian subduction zone setting.

Results of these revisions and software development are summarized in the Final Report to NOAA-OCSEAP prepared by Woodward-Clyde Consultants (1982, and herein referred to as WCC).

In our opinion the following additional improvements should be incorporated in future efforts or at least need further consideration:

- 1) Integration of the historic seismicity record for great earthquakes ($M_w \geq 7.8$) presented in this report (chapter 3.4) for the purpose of specifying the initial "state" of arc segments in the model of the Markov-process for great earthquakes as defined in Section 4.1 of Volume I of WCC (1982), provided the Markov-model is to be used.

- 2) A critical assessment of whether the Markov-model yields similar results for conditional probabilities for great earthquakes as those presented in chapter 4.1 (Figure 4.1.1) of the present report.

- 3) A test of the transition-probabilities p_{ij} and of holding times h_{ij} (defined in WCC, 1982) using the data set of Table 3.4.8 of the present study.

- 4) A westward extension of the "thrust-and-Benioff seismic source" beyond those sources shown in Figure 2, Volume 2 of WCC (1982) to incorporate the entire 1946-rupture zone, Unalaska Gap, and the 1957 rupture zone. These source regions will contribute to

seismic exposure particularly in the southern portions of the St. George Basin. They will clearly affect adjacent regions of potential future interest (i.e., Umnak-Plateau, Unalaska Island).

5) A redefinition of the presently ill-defined 'Yakutat Gap' and 'Yakataga Gap' thrust zone sources (Figure 2, Volume 2 of WCC, 1982).

6) Comparison of "Random Source 1" and "Deformed Source 1" outlined in Figure 2, Volume 2 of WCC (1982) with regard to level and spatial distribution discussed in chapters 3.1 and 3.2 of the present study (i.e., see Figure 3.1.4). Clearly these sources must be extended to the S-W in order to avoid a fictitious southwesterly decrease of expected groundmotion levels as produced by preliminary maps based on WCC (1982).

7) Probably the single most important future improvement for seismic hazards assessment in the eastern Aleutian arc may come from a new strong motion data set to be collected in the Alaska-Aleutian subduction zone environment. The problems arising from the virtual absence of such a data set are discussed throughout this report but are specifically addressed in chapter 3.3 of this study.

In summary: previous studies have made important contributions to improve the methods of quantitative hazards assessment. The present report provides the data base, that can now be used as input into existing programs for computing and mapping of hazards. Furthermore, we show where the data base needs to be improved before reliable hazards assessments can be made. We also point to incomplete or erroneous data that have been used in the past.

3. DATA ANALYSIS

3.1 Seismicity Recorded by the Shumagin Network 1973-1981

Introduction. Since 1973 L-DGO has operated a short-period, high gain seismic network in the Shumagin Islands region, eastern Aleutians, Alaska. The purpose of operating the network is to collect data that can be applied for analysis of seismic and volcanic hazards as well as for basic seismotectonic studies. The specific tasks related to the analysis of hazards consist of: 1) to determine the hypocenter and magnitude of all locatable earthquakes; 2) to develop frequency of occurrence versus magnitude relationships; and 3) to correlate the shallow seismicity with possible geologic faults.

The details of how the earthquake data were processed are described in Appendix 7.1. The hypocenter locations are determined by the computer program HYPOINVERSE (Klein, 1978). Using P- and S-wave arrivals from more than three stations the program calculates geographical coordinates and depth of the hypocenter as well as uncertainties in arrival times and spatial coordinates. These uncertainties are relative to the flat-layered velocity model and hence, do not include possible systematic biases in the earthquake locations.

For most of the earthquakes recorded since 1977 either coda length or amplitude magnitudes were determined. Prior to 1977 neither amplitudes nor coda lengths had been read. Moreover, since not all the instrument constants and gains are known for this earlier period, it is not possible to determine with any certainty magnitudes for the old data before 1977. A further description of the computations of magnitudes of the earthquakes is included in Appendix 7.2.

As an initial step toward analysis of seismic hazard in the region we evaluate below: 1) the spatial distribution of seismicity; 2) the rate of seismicity; and 3) the linear alignments in the seismicity. The objective of this analysis is to identify the main features in the data that can play a crucial role in identifying the seismic sources for the construction of a seismic exposure map for the eastern Aleutians.

Seismicity distribution and tectonics. In the Shumagin Islands-Cold Bay region the rate of occurrence of small to moderate size earthquakes ranges from 350 to 800 earthquakes per year. This seismicity is associated with the subduction of the Pacific Plate underneath the North American Plate, which takes place at an average convergence rate of about 7.5 cm/yr (Minster and Jordan, 1978).

In Figure 3.1.1 we have plotted all the earthquakes located by the Shumagin network from 1973 to the end of 1981. The symbol type indicates within which depth range the earthquake is located and the actual symbol size is proportional to magnitude. If no magnitude is available for a particular earthquake a symbol size equivalent to magnitude one is plotted. Data from the seismic stations that are shown as triangles were used to calculate both the hypocenters and magnitudes. (See also Appendix 7.4 regarding station status during 1973-1982.)

The axis of the Aleutian Trench is defined by the 5000 m bathymetric contours in Figure 3.1.1 and its orientation is almost perpendicular to the direction of plate convergence, north 30° west. The region that extends from the axis of the Aleutian Trench approximately 100 to 150 km to the north north-east and constitutes the expected rupture zone of great plate-boundary earthquakes, is presently almost aseismic. The bulk of the shallow seismicity in Figure 3.1.1 is located close to the down-dip end of the main thrust zone and is associated with deformation of the upper plate.

Figure 3.1.2 shows only the shallow seismicity where we have plotted high quality solutions as open circles and low quality solutions as y's. The general pattern consists of high-quality solutions (open circles) within the network and low-quality solutions (y's) outside the network extending across the trench. The largest clusters of shallow activity are located on the Shelf between the inner wall of the trench and the Alaska Peninsula. These clusters cut across both the Shumagin Islands and the Sanak Basin forming an approximate east-west trend that coincides with the down dip edge of the main thrust zone. In addition, several significant lineaments of shallow seismicity are found throughout the region.

The seismicity at depths ranging from 40 to 250 km is shown in Figure 3.1.3 where we have excluded the seismicity that is shallower

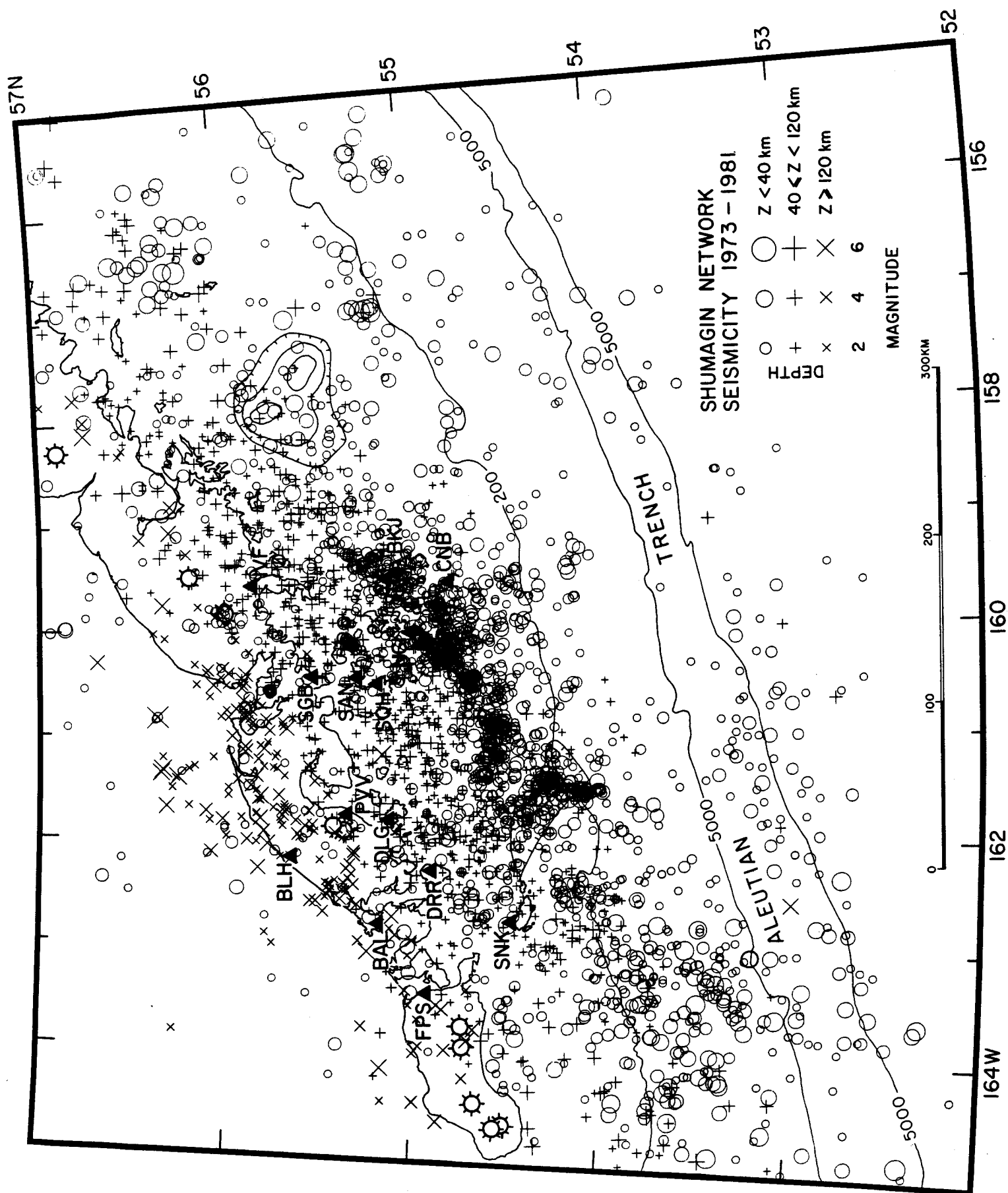


Figure 3.1.1. Map of epicenters showing all the seismicity located by the Shumagin network eastern Aleutians, Alaska, from 1973-1981. The symbol type indicates depth and symbol size is proportional to magnitude. The filled triangles are high-gain short-period seismic stations. The heavy circles (⊗) on the Alaskan Peninsula indicate the location of active volcanoes.

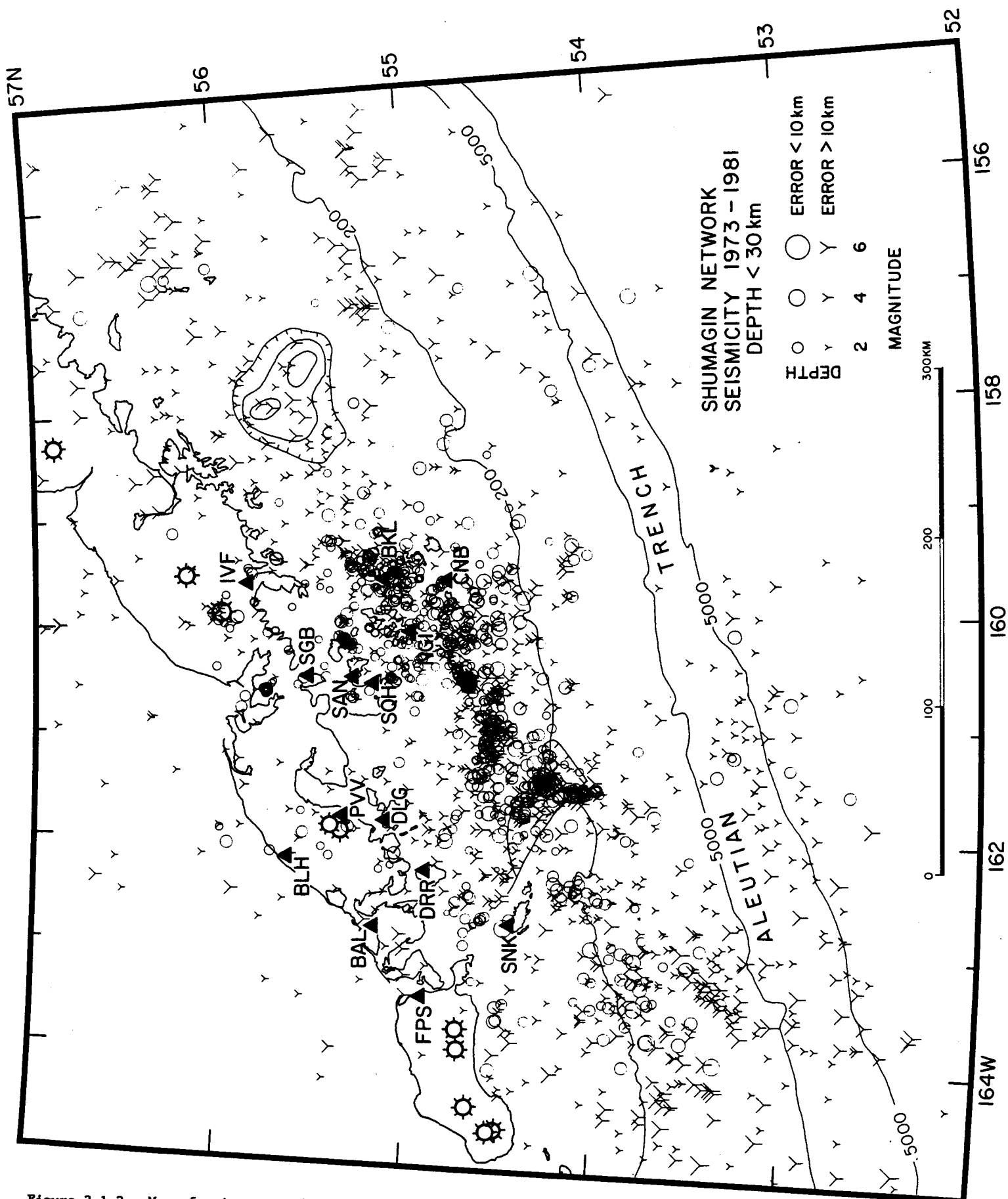


Figure 3.1.2. Map of epicenters showing all the shallow seismicity (depth less than 30 km) located by the Shumagin network, eastern Aleutians, Alaska, from 1973-1981. Open circles are high-quality solutions and y-symbols are low-quality solutions.

than 40 km. This seismicity defines the Benioff zone, which outlines the subducted part of the Pacific Plate. A striking feature of the deep seismicity is the fairly uniform spatial distribution of activity extending from the CNB-station toward north north-west beyond the volcanic axis. Both toward west and east of the network the locatable activity tapers off because small earthquakes are no longer being detected. In Appendix 7.4 we have included annual maps and cross sections of Shumagin seismicity from 1973 to 1982, which give a detailed picture of temporal and spatial variations in the seismicity.

Rates of seismicity. An important step in establishing recurrence relations for moderate size earthquakes is to evaluate whether the available seismic data are complete and cover a long enough time period. To ensure that all recorded moderate size or large earthquakes are included we cross checked the Shumagin catalogue of earthquakes with the PDE-bulletin. The next step consisted of checking how continuous the data are through time and if the rate of seismicity is anomalously low or high during the period on which the calculation of the recurrence relation is based.

The continuity of data recorded by the Shumagin network varies considerably through time as is shown in Figure 3.1.4. Hence, it is difficult to make meaningful statements about the rate of seismic activity from 1973 to 1978, based on the Shumagin network data alone.

During the first half of 1974 and second half of 1975 the level of seismic activity, however, appears to be somewhat higher than the average level observed until the end of 1977 (see Figure 3.1.4). The increase in activity in April 1974 consist in part of an aftershock sequence following a pair of large earthquakes of magnitude 5.8 and 6.0 that occurred near the Nagai Island.

Since early 1978 to present the data recording has been almost continuous (Figure 3.1.4). The temporal distribution of the seismicity since 1978 is illustrated in Figure 3.1.5 where we have plotted the cumulative number of earthquakes located by the Shumagin network since 1978 to present. The data shown in Figure 3.1.5 demonstrate that the seismicity rate in the Shumagin region was higher during 1978 and 1979 than it has been during 1980 to 1982. Anomalously high levels of both shallow and deep seismicity contributed to the burst in activity during 1978 and 1979.

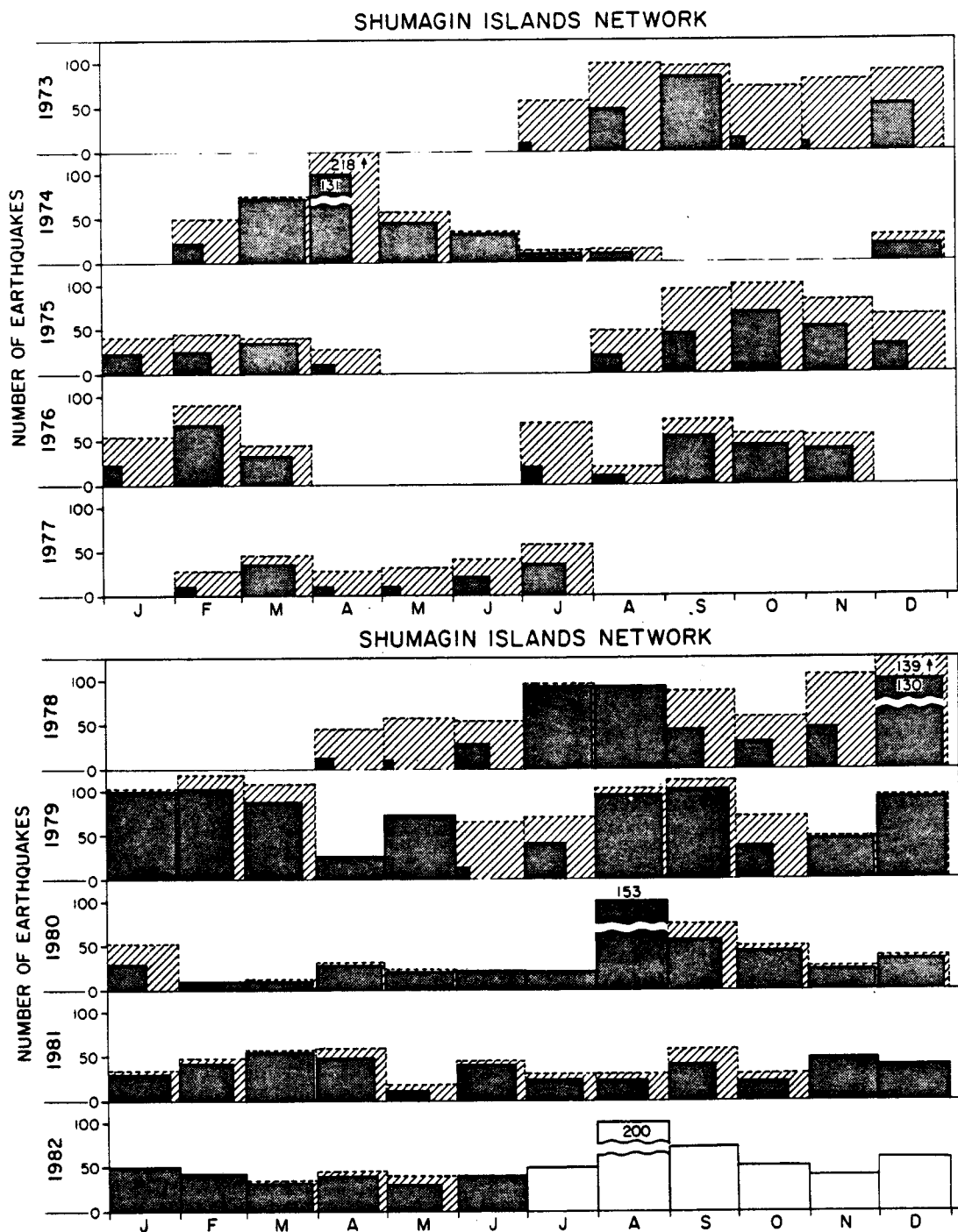


Figure 3.1.4. Histogram of number of earthquakes located by the Shumagin seismic network, eastern Aleutians, Alaska. The dark, stippled rectangles represent total number of events versus number of days in a month during which data was recorded. The hatched rectangles represent the monthly number of events, which is estimated from the stippled rectangles.

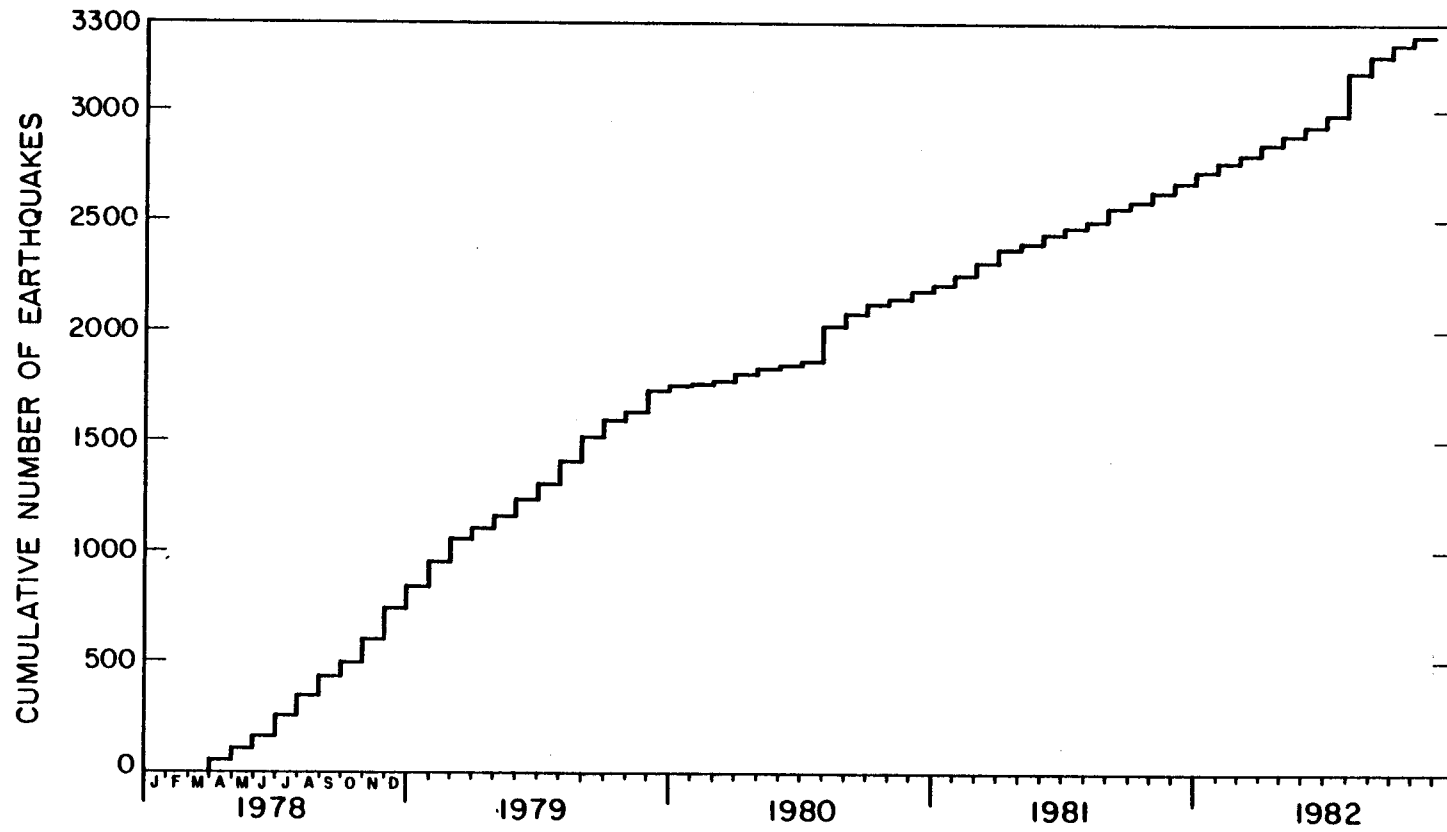


Figure 3.1.5. Cumulative number of all local earthquakes located by the Shumagin network from 1978 to 1982.

We conclude that the time period from 1977 to end of 1981 is probably representative of the long-term seismicity rates of background activity in the eastern Aleutians. Especially, since this time period contains a burst in activity and a following period of average activity it is unlikely that we are underestimating the rate of earthquake occurrence.

b-values. A fundamental part of evaluating seismic hazard consists of determining repeat times for large and possibly damaging earthquakes. Calculations of repeat times for a region that is not located exactly along a plate boundary but rather adjacent to it, such as the Shumagin Shelf, often are based on the Gutenberg-Richter relation,

$$\log N = a - bM$$

where N is the number of earthquakes with magnitude greater than or equal to M, a and b are empirical constants. If representative values of a and b are known for a region, one can calculate N per unit time and unit area for a given maximum magnitude using the equation above.

We have applied the Shumagin data from 1977 to 1981 to determine values of a and b using the method of maximum likelihood as described by Page (1968) (see Figures 3.1.6 and 3.1.7). It is worth pointing out that the cumulative number of earthquakes in Figures 3.1.6 and 3.1.7 levels off at smaller magnitudes because distant smaller earthquakes are not recorded or included in the analysis. In a similar way the cumulative curve may drop off more rapidly at larger magnitudes, if the period of observation is too short compared to the repeat time of the larger earthquakes.

In Figure 3.1.6 we have included in the b-value calculation all the earthquakes since 1977 for which magnitude values are available. The a and b-values were calculated for the magnitude intervals 2.5-6.0 and 3.0-5.5 to test for a possible absence of smaller earthquakes. The two b-values of 0.75 ± 0.06 and 0.85 ± 0.09 fall within the approximate 95 percent confidence limits of each other. These b-values are in the same range (0.8 to 0.9) as determined by Page (1968) for aftershocks following the Great Alaskan 1964 earthquake.

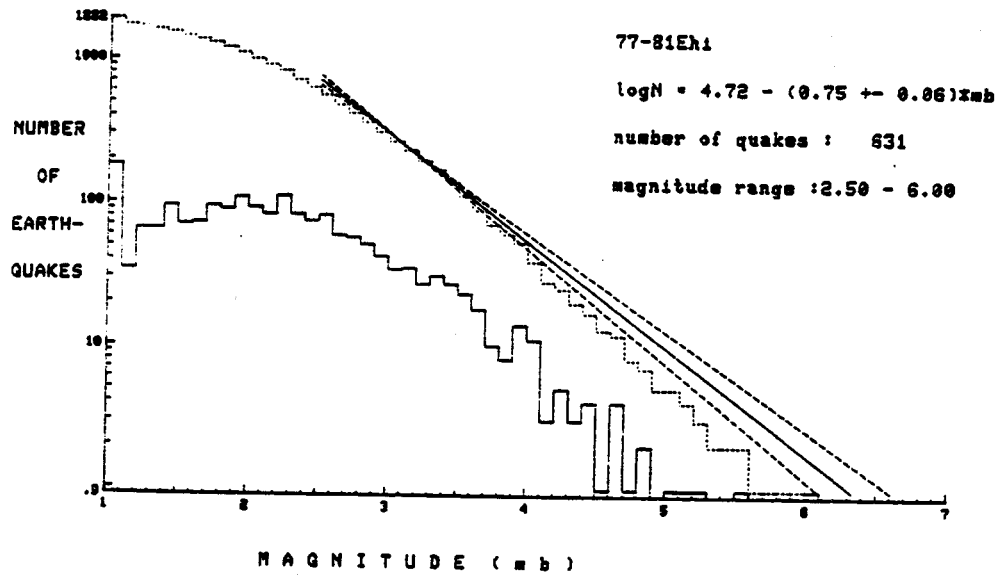
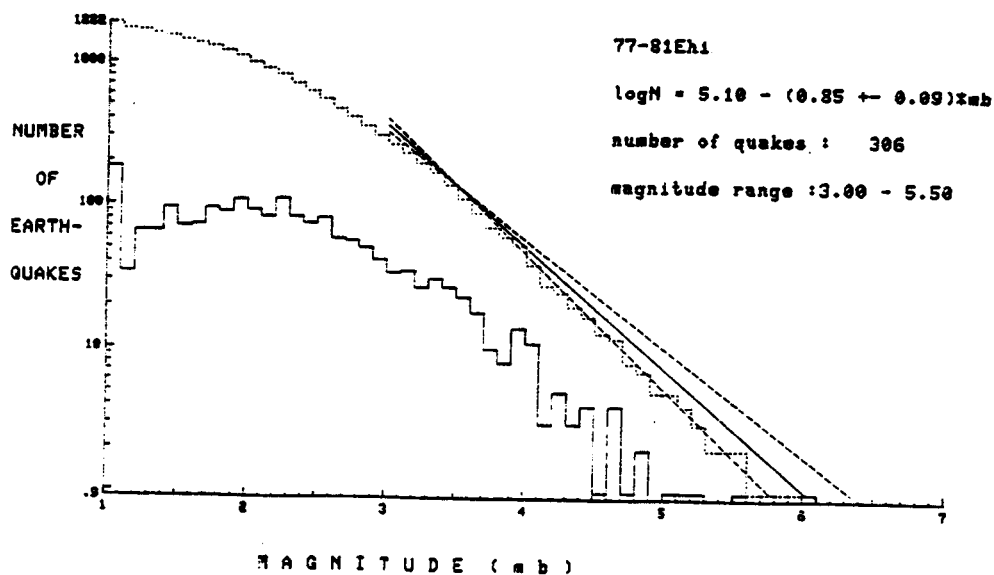


Figure 3.1.6. Both cumulative number and number of earthquakes as a function of magnitude for the whole data set recorded by the Shumagin network from 1977 to 1981. (above) magnitude range is 2.5-6.0; (below) magnitude range is 3.0-5.5. Note that maximum, minimum and average b-value slopes are plotted.



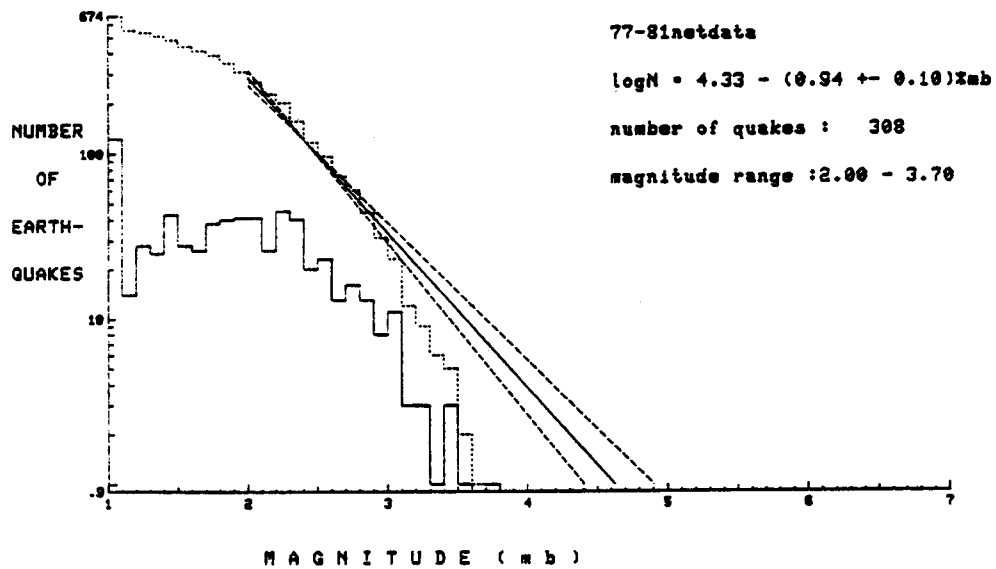
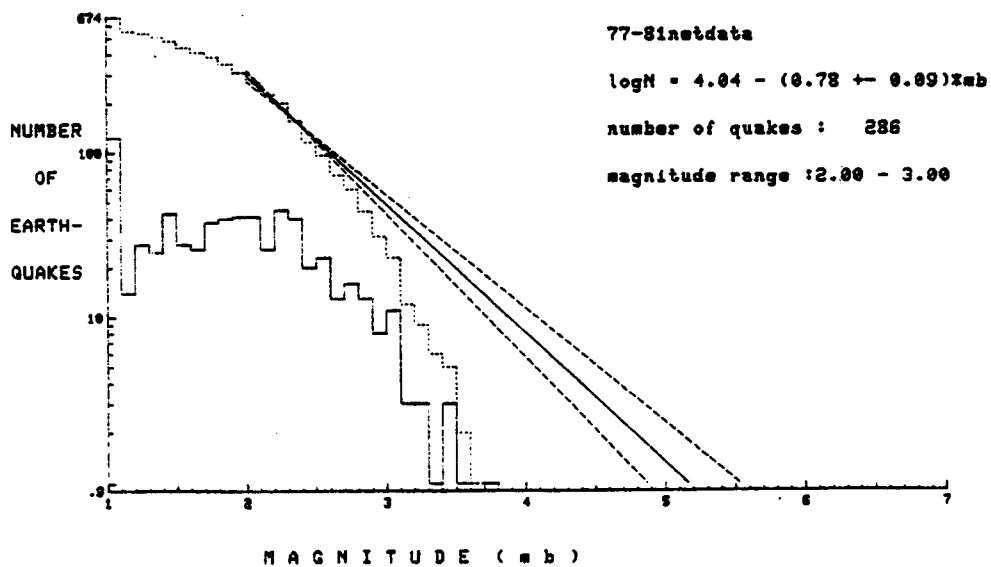


Figure 3.1.7. Both cumulative number and number of earthquakes as a function of magnitude for all shallow earthquakes (depth less than 30 km) recorded by the Shumagin network from 1977 to 1981. (above) magnitude range is 2.0-3.7; (below) magnitude range is 2.0-3.0.



To investigate, if the seismicity shallower than 30 km has a- and b-values that differ from the values calculated for the whole data set, we have determined separately a- and b-values for the shallow seismicity (see Figure 3.1.7). (The shallow seismicity also is plotted separately in Figure 3.1.2.) We note that the number of earthquakes of magnitude greater than 3.1.5 is much smaller than in Figure 3.1.6. The b-values estimated from the data in Figure 3.1.7 fall within the same range as the values estimated from the whole data set. The a-values in Figure 3.1.7 are somewhat smaller since the data set of only shallow earthquakes is smaller than the whole data set. The smaller a-values and the lack of moderate size earthquakes suggest that a longer monitoring period might provide more reliable a- and b-values for the eastern Aleutians.

In conclusion, the a- and b-values that result from this study are inherently more reliable than previously published values, since those were usually based on much smaller data sets (e.g., Page, 1968; Utsu, 1962).

Lineaments of seismicity. To estimate the size of the maximum expected earthquake in a given region some knowledge of the distribution of possible geological fault lengths is needed. On land such information is gained through geologic mapping, but in submarine areas expensive seismic reflection studies are needed to map the fault structure. In both cases seismicity data can be used to identify presently active faults.

Although seismic reflection data were collected in the Shumagin region in October 1982, no results are available yet. Hence, we have attempted to use seismicity lineaments to evaluate the approximate distribution of fault lengths in the region. In Figure 3.1.8 seismicity lineaments are identified by visual inspection of the shallow (less than 30 km) seismicity. In all the cases where dense, linear clustering of seismicity occurs we have drawn a line that represents the observed linear alignment of epicenters. The results of this method, which only yield an approximate estimate of the distribution faults, can be improved in the future by applying relative master-event location techniques and by constructing fault plane solutions for the shallow seismicity.

A histogram of number of lineament lengths is presented in Figure 3.1.9. Lineament lengths of 10 to 30 km appear to be most common. The lineaments shorter than 10 km are probably under-represented because the scale of the Figure 3.1.8 makes it difficult to resolve those. It is a somewhat surprising result that only a very few lineament lengths from 30 to 100 km length are identified.

Presuming that the most commonly occurring source dimension is 30 km or less, we can apply known source dimension versus magnitude relationships to estimate the maximum magnitude of the earthquake that corresponds to the particular source size (see Figure 3.1.10). The particular relationships that are shown in Figure 3.1.10 are based on: 1) data from California (Wyss and Brune, 1968); 2) data from Japan (Wesnousky et al., 1982); and 3) a general relationship established by Wyss (1979). Furthermore, we have also plotted data from two source parameter studies in the Shumagins by House and Boatwright (1980) and Hauksson (1982). The relationships in Figure 3.1.10 indicate that a source dimension of 30 km can be associated with an earthquake magnitude of 5.6-7.1. Hence, a prudent approach would be to assume that the maximum size of a random source within the Shumagin Shelf can be associated with a magnitude 7.0 earthquake.

A general recurrence relation for the Gulf of Alaska, which was established during the early stages of the OCSEA program is plotted in Figure 3.1.11. This general relation is based on a maximum earthquake source of 7.0 which is in agreement with our studies of the length of seismicity lineaments. The relative rate of recurrence of the maximum random source, however, may be underestimated by as much as a factor of 6 for shallow sources or a factor of 30 when all possible random sources are included.

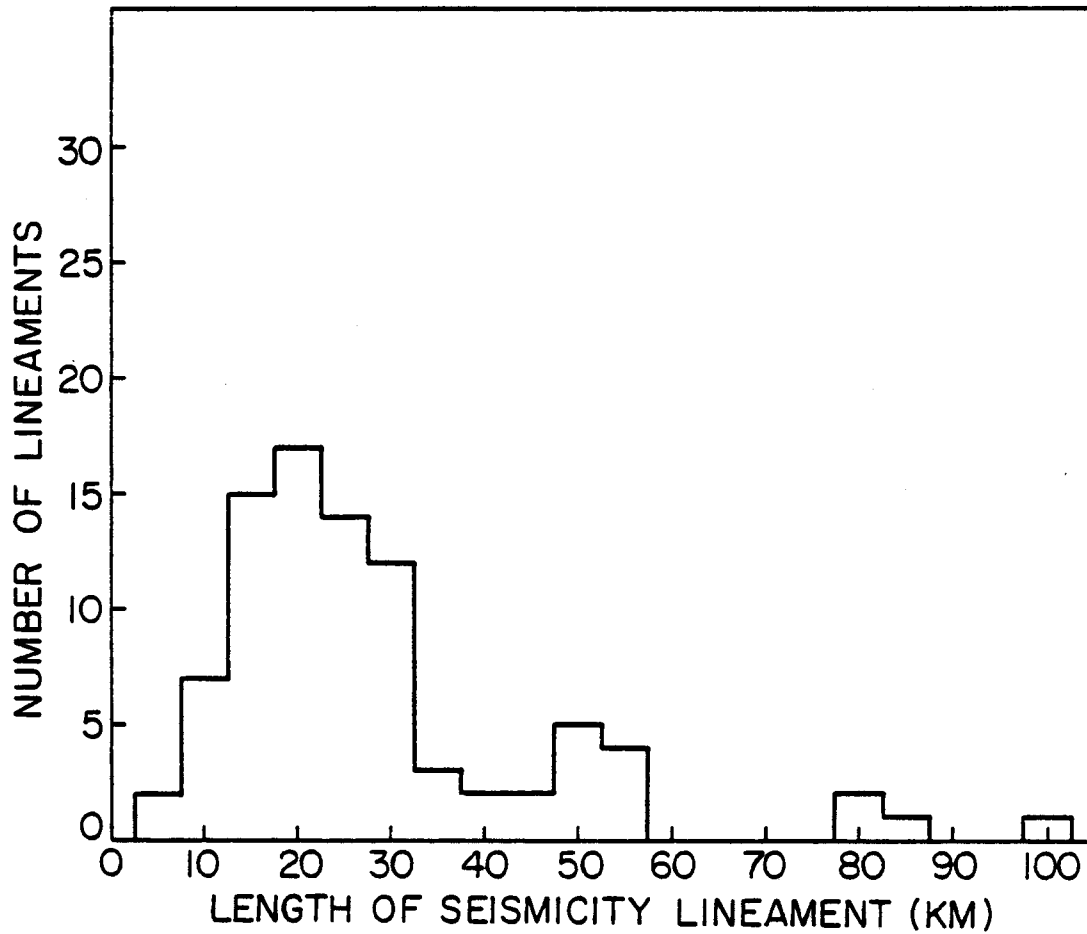


Figure 3.1.9. Cumulative number of seismicity lineaments from Figure 3.1.8 versus, length of seismicity lineament. Note the lack of lineaments in the range from 30 to 100 km.

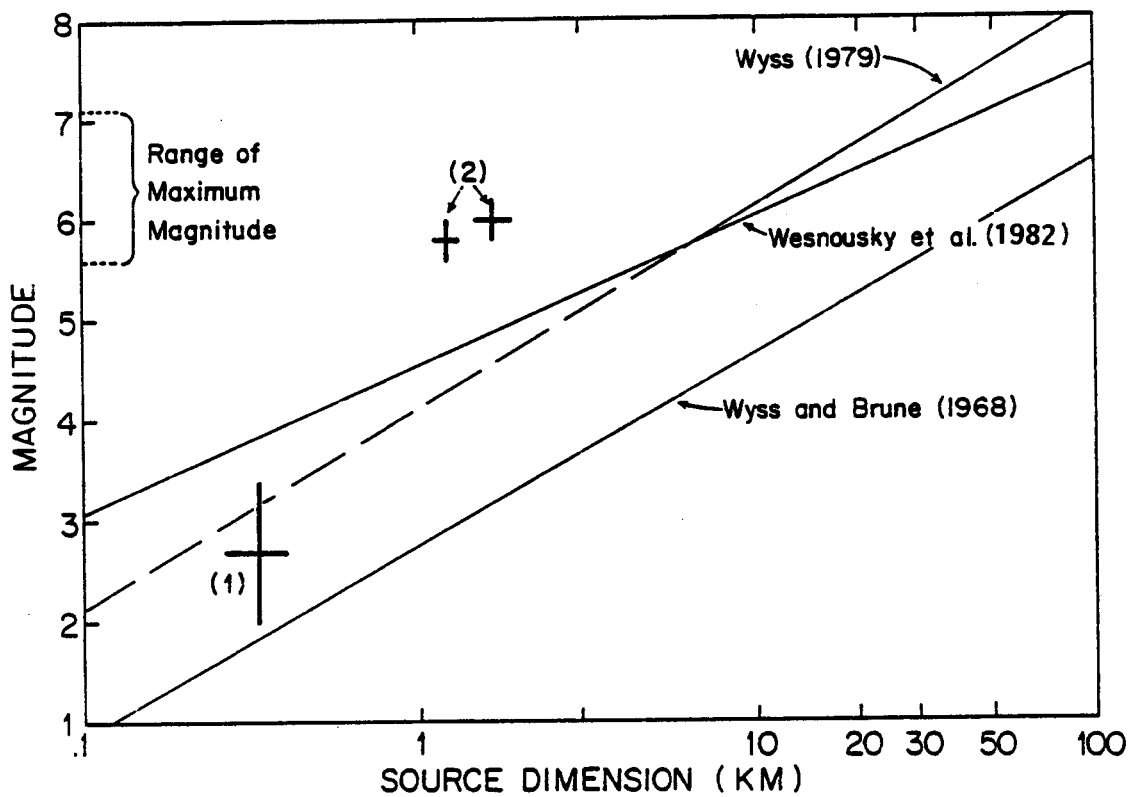


Figure 3.1.10. Magnitude versus source dimension relationships. The data points: 1) is from Hauksson (1982); and 2) is from House and Boatwright (1980); see also the text. The probable range of maximum magnitude is indicated on the left.

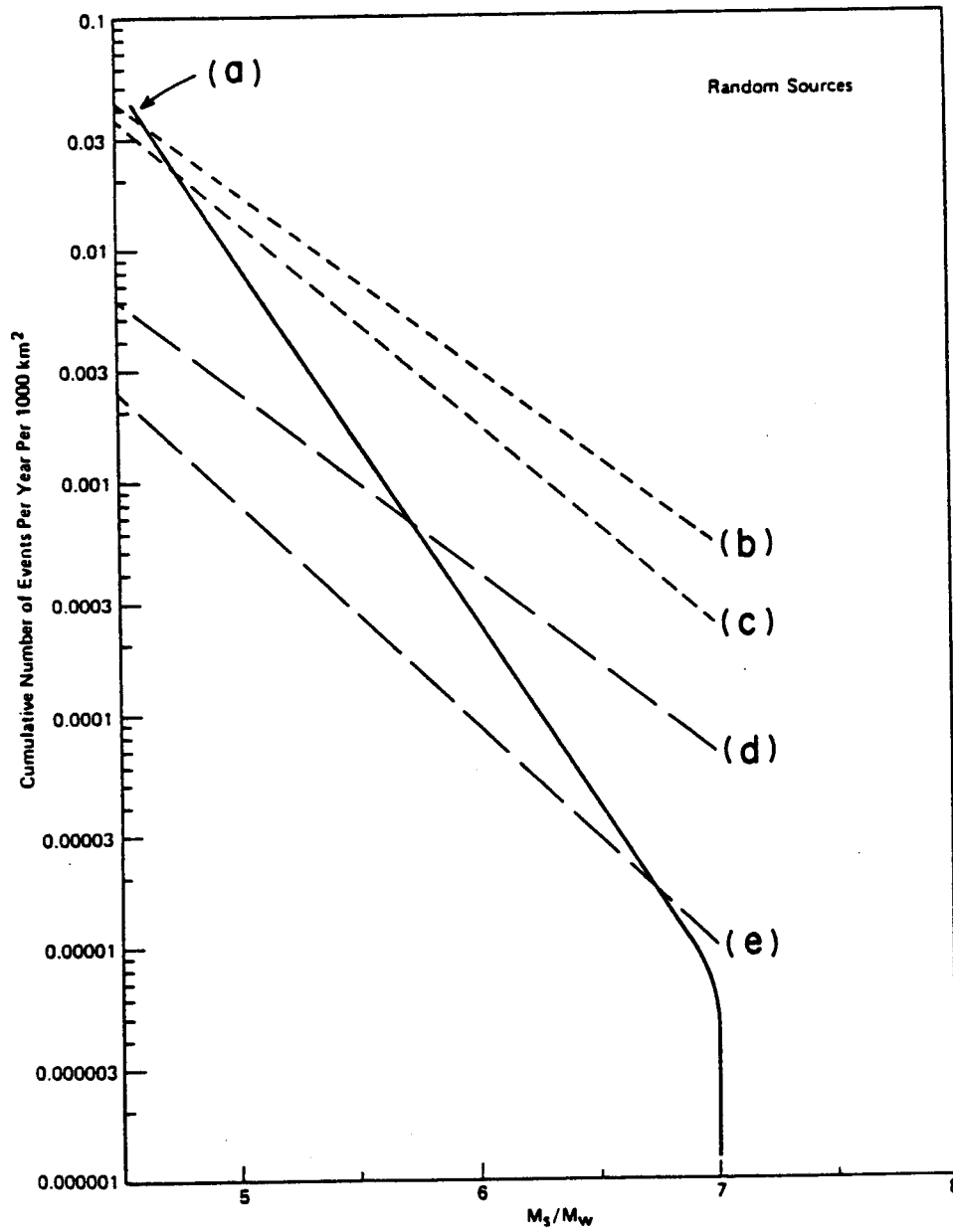


Figure 3.1.11. Recurrence Relation for the Gulf of Alaska Random Sources. a) the initial curve; b) curve based on b-value for all sources in Figure 3.6 (above); c) curve based on b-value for all sources in Figure 3.6 (below); d) curve based on b-value for only shallow sources in Figure 3.7 (above); and e) curve based on b-value for only shallow sources in Figure 3.7 (below).

3.2 Teleseismic Data 1973-1982

As an independent means of verifying the results of the data from the Shumagin network, we have analyzed seismic data from the Shumagin region recorded by the National Earthquake Information Service (NEIS) at teleseismic distances. These teleseismic data are published in the Preliminary Determination of Epicenters (PDE) Bulletin.

The PDE data are considered to be continuous in time and in most cases PDE magnitudes for larger earthquakes ($M > 4.0$) are more homogeneous than magnitudes from local networks. The major drawbacks with PDE data are that they have a rather high minimum magnitude threshold of detection ($M \approx 4.5$ in the Shumagins) and epicentral locations may be systematically biased in island arc regions by as much as 20-40 km away from the trench.

Figure 3.2.1 is an epicentral map of the teleseismic data located within the Shumagin region from 1973 to 1981. When comparing Figures 3.1.1 and 3.2.1 we see that there is a substantial difference in the level of activity and many of the patterns seen in the Shumagin network data are almost absent. The region of high activity west of the station, SNK (Sanak Island) coincides with the aftershock zone of a major earthquake in 1946 as described by Sykes (1971). Another cluster is observed south of the Shumagin Basin (latitude 55.5°N and longitude 157°W) and consist of a 6.5 magnitude main shock-aftershock sequence in 1979. As also demonstrated by the Shumagin network, shallow earthquakes appear to be more common on the Shelf than between the Shelf and the trench axis.

The temporal rate of occurrence of earthquakes located using teleseismic data is illustrated in Figure 3.2.2. We have plotted a bar with a length proportional to magnitude for each earthquake and next to it we show the depth of the earthquake in kilometers. It is worth noting that the rate of occurrence of teleseismically located earthquakes is fairly uniform in time, except for the burst in activity during 1978 and 1979. In the last 10 years six earthquakes of magnitude 6.0 or greater have occurred in the Shumagin region. The cumulative number of teleseismically located earthquakes within the Shumagin region show a similar trend as the seismicity located by the

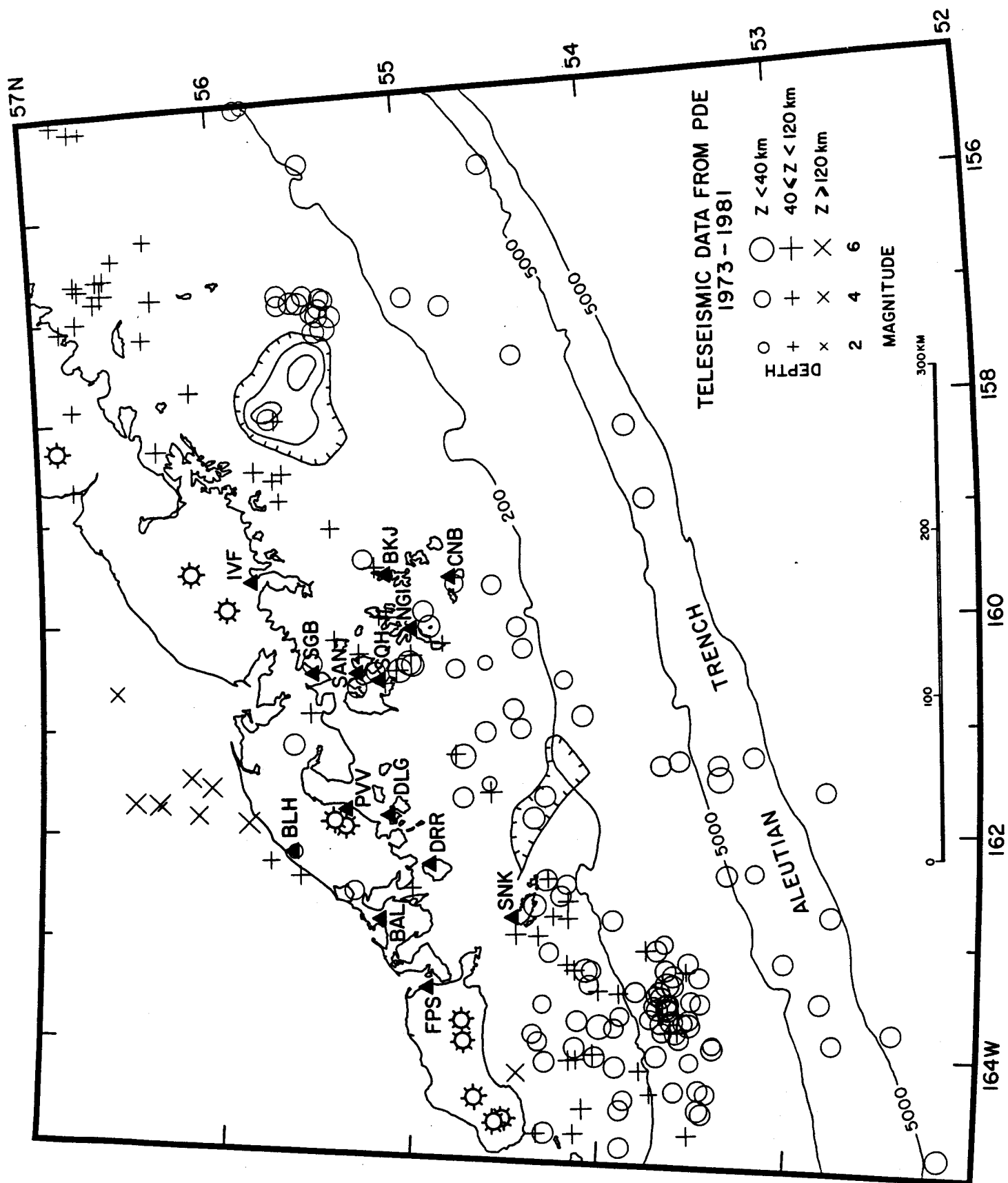


Figure 3.2.1. Map of epicenters showing teleseismically located earthquakes from the PDE bulletin from 1973-1981. The symbol type indicates depth, and symbol size is proportional to magnitude. The filled triangles are high-gain short-period seismic stations in the Shumagin network. The heavy circles (⊗) on the Alaskan Peninsula indicate the location of active volcanoes.

Shumagin network, with a burst in activity during the latter half of 1978 and 1979 (see Figure 3.2.3).

The more subtle or smaller changes in the rate during 1973-1975 compared to during 1975-1979, however, are considered to be changes in the teleseismic detection threshold (Habermann, 1983).

The b-value ($b = 0.92 \pm 0.10$, see Figure 3.2.4) for the teleseismic data is similar to what was observed for the Shumagin network data (compare Figures 3.1.6, 3.1.7 and 3.2.4). Although the Shumagin network data are somewhat discontinuous in time, the similar b-values indicate that both the teleseismic and the network data sets are fairly homogeneous.

In conclusion, when comparing teleseismic and Shumagin data we have found: 1) a fairly steady rate of occurrence of earthquakes in the magnitude range 4.5 to 6.0 during the last 10 years; 2) the temporal increase in the rate of occurrence of earthquakes appears in both data sets; and 3) both data sets show similar b-values although the network b-value is based on the magnitude range 2.0-6.0 and the b-value of teleseismic data is based on the magnitude range 4.4-6.3.

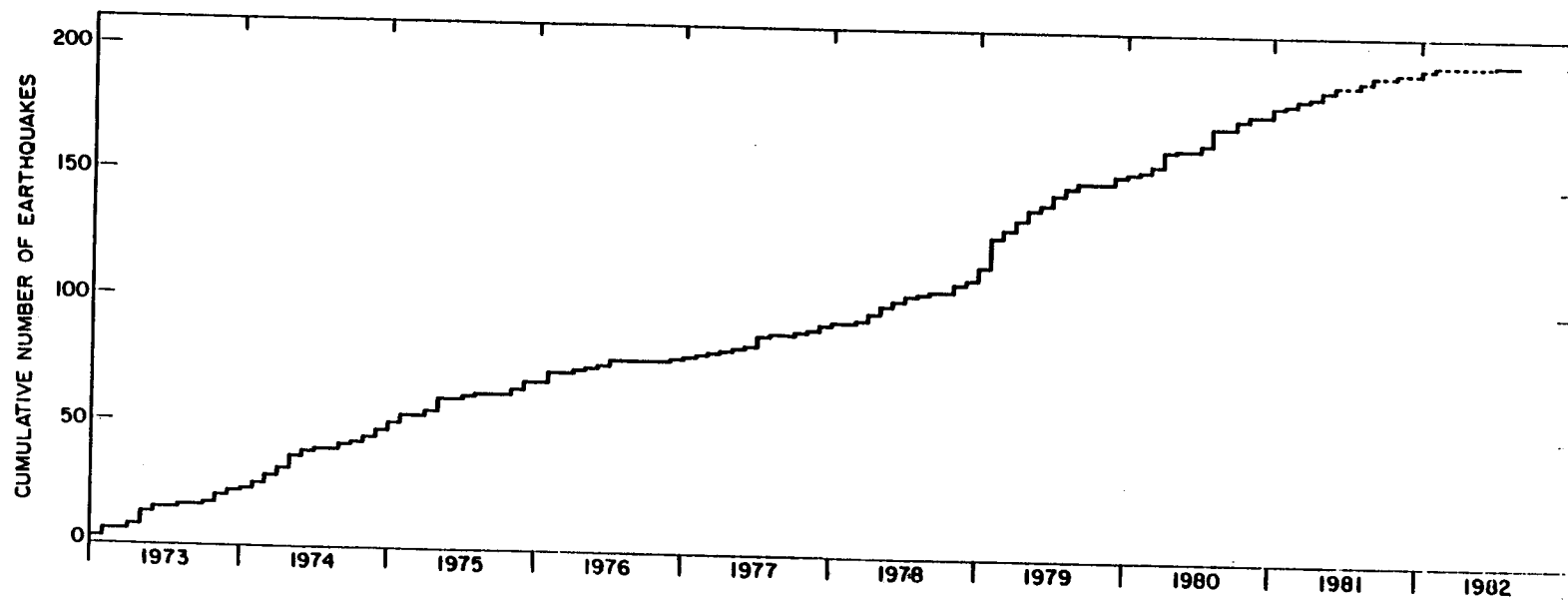


Figure 3.2.3. Cumulative number of earthquakes located by the PDE from 1973 to 1982 in the Shumagin Islands region. (The region chosen is 52°N to 57°N and 156°W to 165°W).

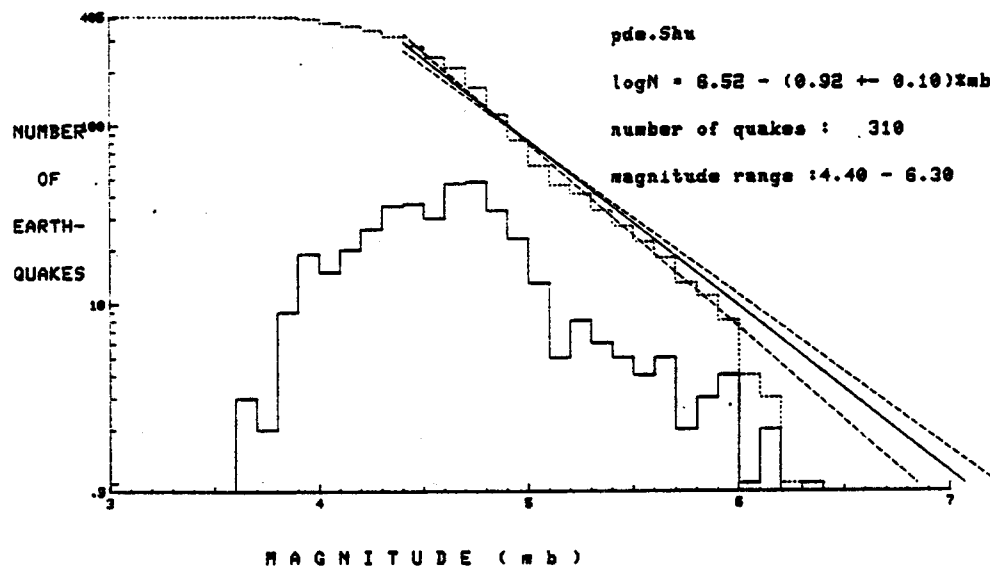
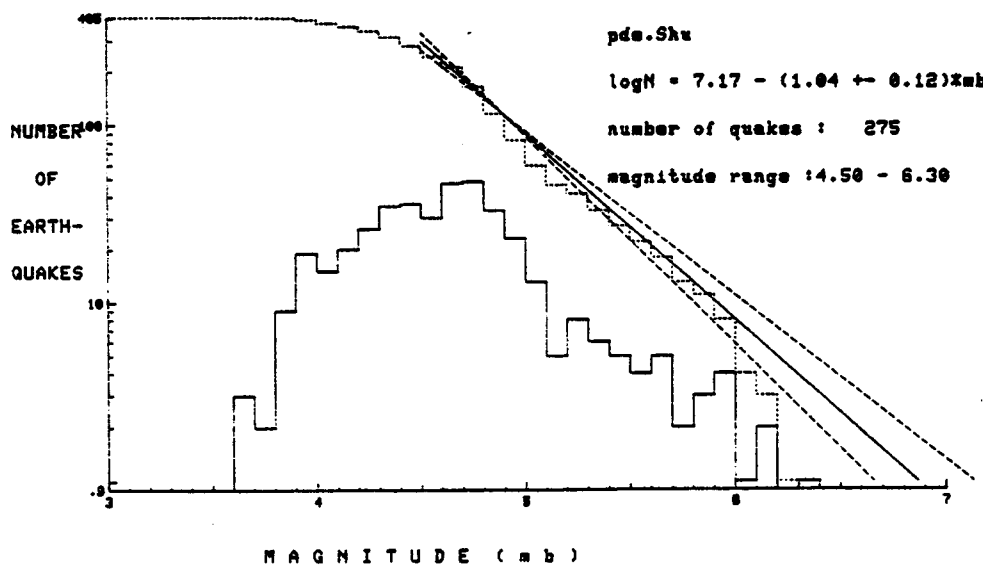


Figure 3.2.4. Both cumulative number and number of earthquakes as a function of magnitude for the PDE data from 1973 to 1981 located in the Shumagin Islands region. (above) magnitude range is 4.4-6.3; (below) magnitude range is 4.5-6.3. Maximum, minimum and average b-value slopes are plotted.



3.3 Strong Motion Data

3.3.1 Historic overview: a subject of neglect. The near-absence of a sufficient strong-motion data base in Alaska is probably the weakest element in any seismic hazards assessment for Alaskan OCS regions. Historic, and still persisting factors have contributed to this severe deficiency. Remedies are urgently needed. Some of the contributing factors are:

1) Large portions of Alaska have lacked until recently in major civil engineering projects such as major highways, bridges, dams, (nuclear) power plants, etc. The Alaska Pipeline, several airports and a few military installations and communication links are but some notable exceptions. The deployment of strong motion accelerographs (SMA-s) has been traditionally linked to major existing engineering projects, rather than being guided by seismological priorities or long-term land-use considerations, planning ahead of actual developments. Because of the few structures of principal engineering interest, the U.S.G.S. (or its cognizant predecessor agencies, i.e., U.S.C.G.S.) operated only one or at most two dozen strong motion instruments distributed throughout the 4000 km long seismic belt stretching from Shemya to Ketchikan, not counting interior Alaska. No state program is (as yet) in existence. Most strong motion instruments were installed after(!) the great Prince William Sound earthquake ($M_w = 9.2$) of 1964, mostly in buildings in Anchorage and a few other municipalities or communication centers. (In comparison, over a smaller and less seismic, but more populated region along the California West Coast, more than a thousand instruments are operated by federal, state and local agencies and/or the private sector.) With an average spacing of several hundred miles between instruments - as is the case in most of Alaska - one can hardly collect strong motion data that can be analyzed in a sensible way.

2) Alaska's subduction-zone tectonic setting is unique in the U.S. in that it exposes any structures to earthquakes (with magnitude M_w up to 9.2) that are among the largest on earth. Their ruptures extend in length up to many hundreds of kilometers and result in rupture durations of one to three minutes and severe shaking that can

easily last twice as long. Nowhere on earth has such an earthquake been recorded by strong motion accelerographs, not in Alaska, not (yet) in Japan, nor anywhere else. The likelihood that future or existing structures near the Shumagin (i.e., St. George and North Aleutian Basins) and Yakataga gaps will be exposed to shaking from such giant earthquakes is very high during the next few decades (chapter 3.4). And so is the chance to monitor such motions. Large or tall structures such as off-shore drilling rigs or production platforms, or oil storage tanks at ship or pipe-line terminals with their often low ($f_0 \approx 1$ Hz) natural eigenfrequencies must be designed to safely survive the long periods and long durations of strong ground motions that are particular to these giant earthquakes. Since no strong motion record from any earthquake larger than $M_w = 7.8$ to 8 is presently available from anywhere on earth, the design of such structures is based on expert judgement and not on hard strong motion data in existence.

3) At an early stage of the OCSEA Program this deficiency of a local SMA data base became clear, and two of the research units (RU 210 in the Yakataga gap, and this project, RU 16, in the Shumagin gap) installed each about a dozen strong motion instruments (mostly with USGS funding for instruments) in both high-probability regions. Both SMA networks became fully operational only until the final 1 or 2 years of the OCSEA Program--much too late to collect a significant number of SMA recordings. Since termination of the OCSEA Program in both regions, SMA operation is jeopardized (e.g., requests to NSF and USGS for continued support of the Shumagin SMA network have been declined to date). Under this circumstance SMA operation at least in the Shumagin seismic gap could cease in summer 1983 despite the potential for a great earthquake in that gap. We urge that federal, state, scientific, and engineering institutions work together to reverse this historic trend of neglect and ensure that the proper strong motion data base will be established. Without this data base, engineers will not be able to cost-efficiently safeguard in their designs against excessive losses from great subduction earthquakes.

The remainder of this section summarizes the strong motion data that presently exist and some of their characteristics.

3.3.2 Peak horizontal accelerations - the Alaska data set.

We have systematically searched through the U.S.G.S. data files and original-record archives collecting both unpublished original data and derivative information accessible from the U.S.G.S. strong motion computer data banks (SMIRS). We were able to compile a list of recorded peak accelerations that include those from our own processed Shumagin records, for which the associated earthquakes and their magnitudes, epicenters and depths are well known. The list of compiled peak accelerations and pertinent parameters are shown in Table 3.3.1. In compiling the earthquake source parameters we have attempted to use the most reliable sources. For example, for earthquakes in the Shumagin Islands region we chose the local-network location parameters rather than PDE (N.E.I.S.-U.S.G.S.) teleseismic determinations. For magnitudes we attempted to use what we perceive the closest approximation to a uniform moment-magnitude scale (i.e., M_w). For this purpose we used $M_w = M_s$ if $m_b \geq 6.0$ and M_w known (usually for $5 \leq M_s \leq 7.5$); $M_w = M_L$ if M_L known ($3 \leq M_L \leq 7$); $M_w = M_s = 1.8 m_b - 4.3$ if no M_s or M_L available (usually for $m_b \leq 6.0$); and $M_w = 2/3 \log M_0 - 10.7$ if moment M_0 (dyn cm) is known.

The formulations for a computed M_s from m_b (PDE) are based on empirical regression curves by Wyss and Haberman (1982) valid for the period 1963-1980. In some instances where several readings of one magnitude type (i.e., M_s (PAS), M_s (BRK), M_s (NEIS)), or where different magnitude types (i.e., M_s , m_L , m_b) gave vastly differing M_w values, we either averaged or had to subjectively decide which value of M_w would best describe the source process as we understand it. Therefore, in some instances the M_w values quoted in Table 3.3.1 may differ in minor aspects from some other author's assessments.

Peak-accelerations are only of limited value in hazards assessment--particularly for giant earthquakes where much of the damage is often related to long durations of severe shaking at low frequencies, rather than peak values. Since information other than peak acceleration is presently rarely available for Alaskan strong

TABLE 3.3.1. Alaska-Aleutian Strong Motion Data.

Record Number	Date	Epicenter	Depth (km)	Magnitude	Station	Distance (km)		Peak Acceleration (g)	
						At Surface	Inclined		
1	4/03/64	22:33	61.62N 147.39W	41	6.0	2718 Anchorage	136	142	.049
6	6/05/64	22:06	58.14N 152.18W	13	4.7	2710 Kodiak	47	49	.026
7	5/11/65	17:37	61.33N 149.52W	61	5.6	2702 Anchorage	21	65	.050
8	5/11/65	17:37	61.33N 149.52W	61	5.6	2704 Anchorage	23	65	.033
11	9/04/65	14:32	58.29N 152.50W	30	6.8	2710 Kodiak	60	67	.017
12	12/22/65	19:41	58.35N 153.13W	38	7.0	2710 Kodiak	72	86	.046
13	12/22/65	19:41	58.35N 153.13W	38	7.0	2719 Seldovia	146	151	.016
14	12/29/65	02:06	54.09N 164.28W	19	6.0	2705 Cold Bay	161	162	.009
17	8/30/66	20:20	61.34N 147.44W	45	6.1	2704 Anchorage	132	139	.018
18	8/30/66	20:20	61.34N 147.44W	45	6.1	2702 Anchorage	132	139	.031
20	6/21/67	18:04	64.91N 147.59W	15	5.4	2721 Fairbanks	13	20	.055
22	10/29/68	22:16	65.46N 150.07W	7	6.7	2707 Fairbanks	125	125	.120
24	12/17/68	12:02	60.15N 152.82W	82	6.3	2719 Seldovia	101	130	.042
27	3/11/70	22:38	57.39N 153.97W	16	6.3	2710 Kodiak	97	98	.050
28	4/18/70	08:50	59.82N 152.79W	89	6.0	2713 Seward	190	210	.020
29	4/18/70	08:50	59.82N 152.79W	89	6.0	2719 Seldovia	74	116	.010
30	6/12/70	02:59	61.54N 151.79W	80	5.6	2703 Anchorage	113	138	.020
32	8/18/70	17:52	60.70N 145.38W	30	5.8	2706 Cordova	27	40	.020
36	5/02/71	06:08	51.42N 177.21W	38	6.8	2701 Adak	67	77	.190
38	7/30/72	21:45	56.77N 135.91W	29	7.5	2714 Sitka	45	53	.110
39	7/30/72	21:45	56.77N 135.91W	29	7.5	2708 Juneau	145	148	.010
41	8/03/72	04:40	51.20N 178.13W	24	6.2	2701 Adak	131	133	.010
42	8/15/72	21:39	65.05N 148.70W	20	4.2	2707 Fairbanks	46	50	.030
a	4/06/74	01:53	54.87N 160.29W	37	5.6	2744 Sand Point	54	65	.100
b	4/06/74	03:55	54.90N 160.29W	40	5.8	2744 Sand Point	51	65	.120
43	8/13/74	03:46	51.49N 178.11W	47	6.1	2701 Adak	114	123	.040
44	11/11/74	05:17	51.59N 178.08W	69	6.1	2701 Adak	108	128	.050
45	12/29/74	18:24	61.57N 150.60W	65	5.8	2704 Anchorage	54	84	.010
46	12/29/74	18:24	61.57N 150.60W	65	5.8	2703 Anchorage	54	84	.030
47	12/29/74	18:24	61.57N 150.60W	65	5.8	2702 Anchorage	60	88	.030
48	12/29/74	18:24	61.57N 150.60W	65	5.8	2716 Anchorage	54	84	.010
50	1/13/75	00:31	61.40N 150.58W	68	4.4	2704 Anchorage	42	80	.010
51	1/13/75	00:31	61.40N 150.58W	68	4.4	2716 Anchorage	42	80	.010
53	5/18/75	15:42	63.17N 150.25W	108	5.4	2727 Talkeetna	97	145	.020
54	7/25/75	10:40	55.04N 160.41W	1	5.6	2705 Cold Bay	148	148	.010

TABLE 3.3.1 (con't.)

Record Number	Date	Epicenter	Depth (km)	Magnitude	Station	Distance (km)		Peak Acceleration (g)
						At Surface	Inclined	
c	7/25/75 10:40	55.04N 160.41W	1	5.6	2744 Sand Point	33	33	.018
55	2/05/75 09:36	59.98N 149.27W	28	4.9	2713 Seward	17	33	.030
56	1/01/75 03:55	61.92N 149.72W	58	6.0	2727 Talkeetna	47	75	.090
57	1/01/75 03:55	61.92N 149.72W	58	6.0	2716 Anchorage	79	98	.080
58	1/01/75 03:55	61.92N 149.72W	58	6.0	2716 Anch. (roof)	79	98	.140
59	1/01/75 03:55	61.92N 149.72W	58	6.0	2702 Anchorage	81	100	.090
60	1/01/75 03:55	61.92N 149.72W	58	6.0	2703 Anchorage	81	100	.070
61	1/01/75 03:55	61.92N 149.72W	58	6.0	2704 Anchorage	79	98	.050
63	2/22/76 07:21	51.57N 176.81W	61	4.7	2701 Adak	38	72	.050
68	9/17/77 21:25	64.81N 147.60W	20	4.0	2707 Fairbanks	12	23	.030
69	9/22/77 10:25	51.72N 175.93W	65	3.6	2701 Adak	48	81	.010
d	1/27/79 18:57	54.79N 160.64W	53	6.2	2744 Sand Point	62	82	.018
e	2/13/79 05:34	55.17N 156.94W	47	6.5	2744 Sand Point	227	232	.030
70	2/28/79 21:27	60.64N 141.59W	13	7.3	2728 Yakutat	92	93	.090
71	2/28/79 21:27	60.64N 141.59W	13	7.3	2723 Icy Bay	25	28	.160
f	2/28/79 21:27	60.64N 141.59W	13	7.3	Shell, Monday Creek	33	35	.064

motion records we, nevertheless, use this set of peak accelerations for a brief comparison. Note that most (but not all) of the reported peak values are raw readings from the unprocessed records without instrument corrections applied. Also, a few values may be contaminated by building response.

A common practice in strong motion seismology is to plot the respective strong motion parameter versus distance to determine its empirical "attenuation" properties, further parameterized by magnitude of the generating earthquake. Such a plot of the Alaskan peak acceleration data versus distance is shown in Figure 3.3.1 and is superimposed on peak acceleration curves derived by Joyner and Boore (1981) from a multivariate regression of a large data set dominated by observations in the western U.S. strike-slip tectonic regime. The Joyner and Boore regression yielded

$$\log A = -1.02 + 0.249M - \log r - 0.00255 r + 0.26P$$
$$\text{with } r = (d^2 + 7.3^2)^{1/2} \text{ for } 5.0 \leq M \leq 7.7$$

where A is peak horizontal acceleration in g, M is moment magnitude, d is the closest distance to the surface projection of the fault rupture in km, and P is zero for 50-percentile values and unity for the 84-percentile values. The curves drawn in Figure 3.3.1 are those for P = 0 (i.e., 50%-iles) and must be uniformly raised by the amount indicated by the bar (upper right corner of figure) to yield 85%-ile curves.

Several aspects become immediately apparent from this comparison of the Alaskan data set with the attenuation relationship derived by Joyner and Boore (1981):

- 1) There may be both a DC shift in the Alaska data set compared to the Joyner-Boore curves as well as a much larger scatter in the Alaska data. For instance the Joyner-Boore 50%-ile curve for M = 6.5 exceeds only 19% of the Alaska data in the magnitude range $6 \leq M \leq 6.9$, and the 84%-ile curve (not plotted) still exceeds only 38% of the Alaska data for the same magnitude bracket. Thus, at a given distance from an earthquake of given magnitude, the range of likely peak

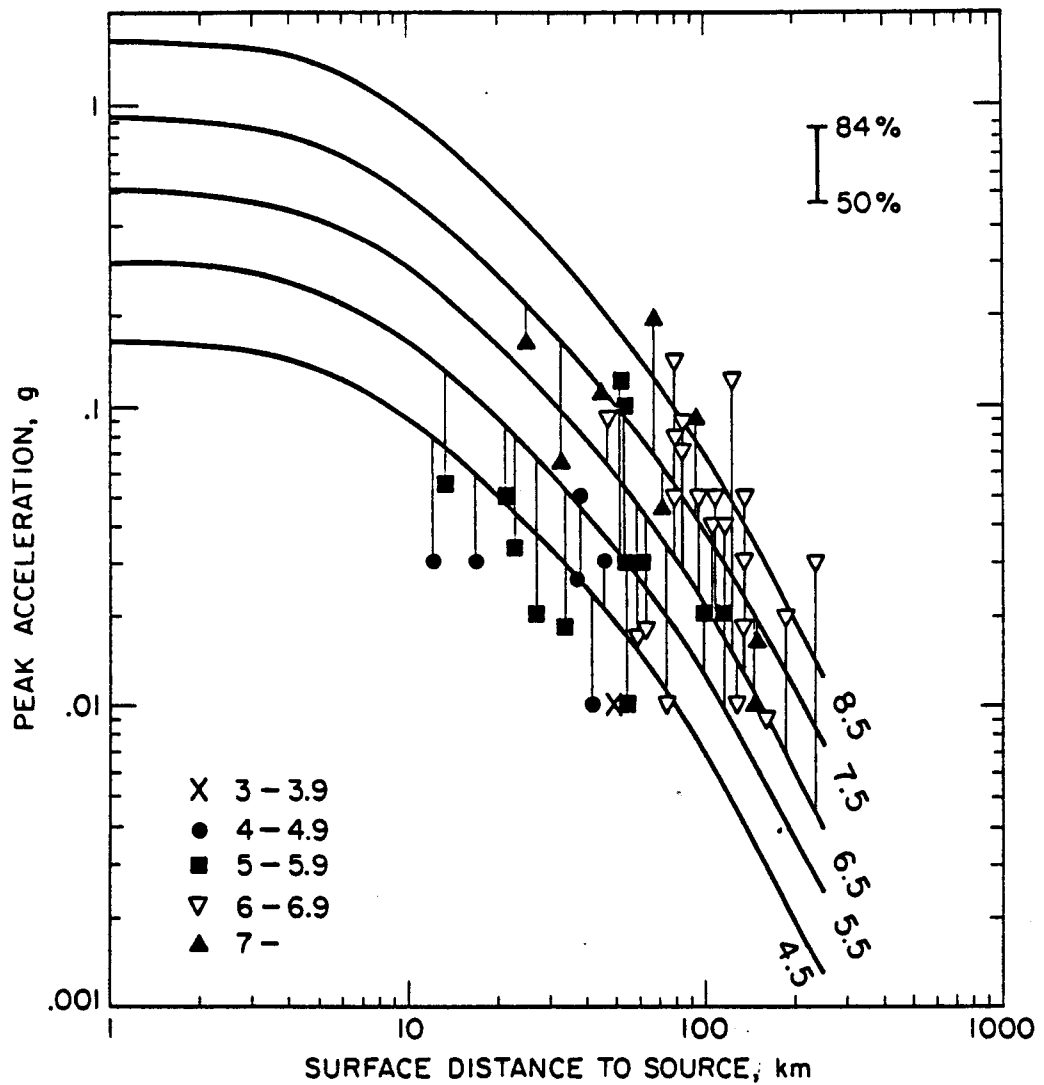


Figure 3.3.1. Comparison of peak horizontal accelerations for Alaska with empirical attenuation laws obtained by Joyner and Boore (1981) by regression of mostly western U.S. strong motion data. The continuous curves correspond to the 50-percentile level of non-exceedence; 84%-ile curves would be offset to a higher level by a constant amount shown in the upper right corner. Symbols represent magnitude ranges M_w as indicated in lower left corner.

accelerations appears much larger for Alaska than that for the western U.S.

2) The slopes of the Joyner-Boore curves appear to be steeper than the Alaskan data would suggest: i.e., at surface distances larger than about 50 km most of the Alaska data seem to yield higher peak values while at shorter distances they tend to yield smaller values. This would suggest that attenuation is stronger in the western U.S. tectonic setting than it is in the Alaska subduction zone environments.

Both features, scatter and slope, may, however, only be an artifact that largely stems from plotting the data versus horizontal surface distance from the source, rather than inclined distance between source and receiver. Since Joyner and Boore used mostly data from shallow earthquakes whose depths rarely exceeds 10 or 15 km, they may have well been justified to carry out their analysis assuming a constant fault depth of 7.3 km, as they did. A quick inspection of Table 3.3.1 shows, however, that in the subduction zone environment where Benioff-zone subcrustal events are common, this approach is not valid since horizontal distance may occasionally be only a fraction of the depth. In these instances, plotting the acceleration at the horizontal rather than the inclined (=hypocenter) distance will be totally misleading. Data points to which this applies are for instance those of record numbers 7, 8, 53, 63, 69, and d (see Table 3.3.1).

Another, physically important difference may lie in the variability of stress drops, which we suspect is much larger in subduction zones than it is in strike-slip tectonic settings. House and Boatwright (1980) have determined stress drops of more than one half kbar for two Shumagin Islands earthquakes of magnitudes $M_w = 5.6$ and 5.8 , respectively (events associated with strong motion records a and b of Table 3.3.1). The associated peak accelerations at Sand Point exceed those of the 50%-curve of Joyner and Boore for a $M_w = 7.5$ earthquake at the same surface distance. Since stress drop is theoretically expected to scale linearly with peak-acceleration we suggest that the Joyner-Boore (1981) regression for peak-acceleration versus distance, parameterized by magnitude and percentile of

non-exceedence, do not apply in the subduction zone tectonic setting, not only for geometrical reasons, but also because of inherent differences in stress drop variations and related source properties.

We, therefore, test the Alaska data set of Table 3.3.1 against attenuation laws that were specifically designed to suit the needs of Alaska OCS seismic hazards assessment. Woodward-Clyde (1982) proposed in its contribution to the NOAA-OCSEA Program two different attenuation laws for peak-accelerations. Their type-A (non Benioff-zone earthquakes depth < 20 km and for stiff rock sites) is:

$$A_{\max} \text{ (median value)} = 191 (e^{0.823M_w}) \times (r + C)^{-1.56}$$

where A_{\max} is the median value of the maximum acceleration in cm/sec², r is the closest distance in km to the rupture plane, C is a magnitude-dependent distance-normalizing parameter with

$$C = 0.864 e^{0.463M_w}$$

Note that for normally or other symmetrically distributed acceleration data ensembles the median value corresponds to the 50%-ile value of non-exceedence.

Their type-B attenuation relationship (Benioff zone, all source depth >6 km, stiff rock sites), that is somewhat modified from their former OASES-study to account now for sites as close as 6 km (instead of 20 km) proximity to the source, is as follows:

$$A_{\max} \text{ (median value)} = 210 (e^{0.5M_w}) \times (r + C)^{-0.85}$$

In Figures 3.3.2 and 3.3.3 we compare the Alaska peak-acceleration data with these A- and B-type attenuation curves, respectively. Note that the abscissa now represents the inclined distance (r) to the nearest portion of the rupture plane, rather than distance at the surface. We find that 16 out of 23 data points (i.e., 70%) in the magnitude bracket $6 \leq M_w \leq 6.9$ exceed the $M_w = 6.5$ type A curve (Figure 3.3.2), while 11 out of 23 (i.e., 48%) exceed that for the

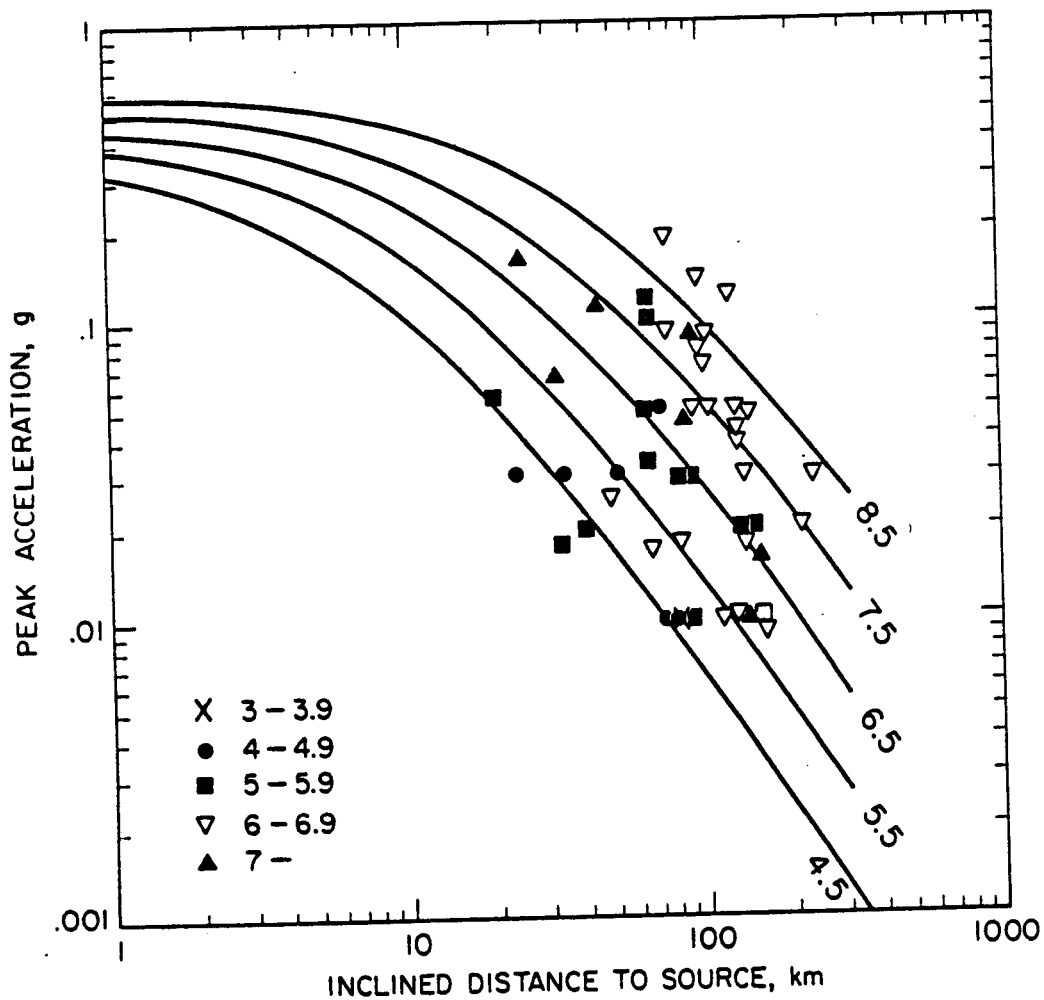


Figure 3.3.2. Comparison of Alaska peak horizontal accelerations with type-A attenuation relations proposed by Woodward Clyde (1982) for shallow, non-Benioff zone earthquakes. The curves apply to stiff rock sites and represent the median in a statistical distribution. The discrete data for Alaska apply to any type of site and in a few instances may be contaminated with effects of building response.

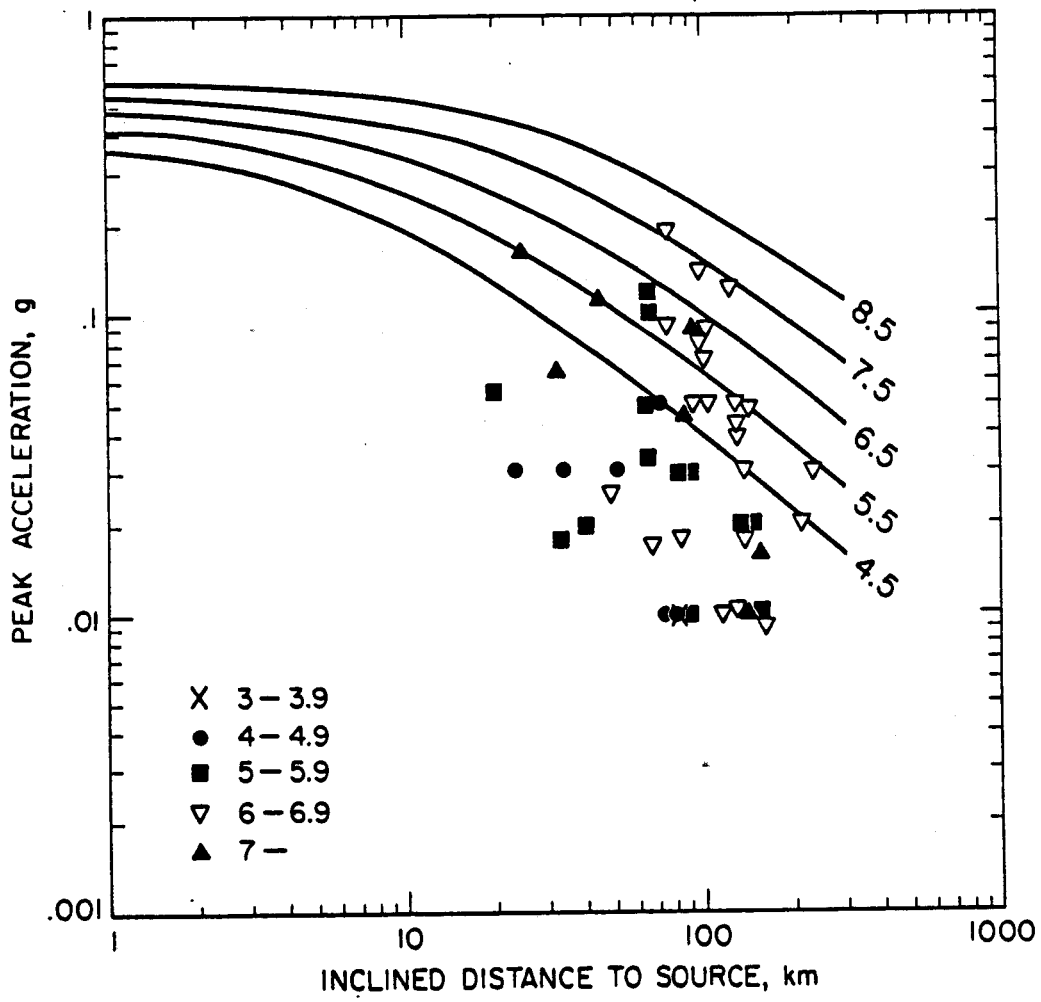


Figure 3.3.3. Comparison of Alaska peak horizontal accelerations with B-type attenuation relations proposed by Woodward Clyde (1982) for Benioff-zone earthquakes. Curves are for stiff sites and represent the median. For other details compare legends of Figures 3.3.1 and 3.3.2.

$M_w = 7.5$ type-A curve that applies to shallow, non-Benioff zone events.

For comparison (Figure 3.3.3), only 3 out of 23 points (i.e., 13%) in the same magnitude bracket ($6 \leq M_w \leq 6.9$) exceed the $M_w = 6.5$ type B-curve (proposed for Benioff zone events) and only one ($\approx 4\%$) exceeds the $M_w = 7.5$ curve.

Thus, we conclude: despite the fact that Alaska peak accelerations may have a wide scatter (high variance probably due to large variations in stress drops), the B-type curves are sufficiently conservative to correctly account for the Alaskan strong motions, and may satisfy the data probably even at a higher percent level of non-exceedence than median value ($\approx 50\%$ -ile if symmetrically distributed).

Ideally we would have liked to carry out a regression analysis on the Alaskan data set similarly to that done by Joyner and Boore (1981) for the western U.S. data. This is not justified, however, for two reasons: 1) the data set is rather small (a total of 51 points, see Table 3.3.1), and 2) there are few earthquakes with more than one recording per event (because of insufficiently dense spacing of SMA's). In cases where multiple recordings exist there are usually not more than two or three recordings and at similar distances. Hence, during regression analysis we would not be able to decouple magnitude (or other source effects) from distance effects as was the main point of the Joyner-Boore analysis.

This conclusion points again toward the urgent need to operate a sufficiently dense SMA network at least in a few selected regions, where the necessary data can be obtained as soon as possible, especially for large events ($M_w > 7.8$) for which a single strong motion record has yet to be collected.

The above data set (Table 3.3.1 and Figures 3.3.1 to 3.3.3) included observations from events in both, subduction zone and strike-slip regimes in Alaska. A data set better suited to the southern Bering Sea and Gulf of Alaska-Aleutian OCS regions could be obtained by selecting only the subduction zone events and combining them with those collected by EXXON Production Research Company (Wildenstein-Mori and Crouse, 1981) which they obtained by processing

original Japanese strong motion records, many of them subduction zone events. Such an improved and enlarged data set for subduction zone strong motions may also permit the magnitude-distance decoupling procedure introduced by Joyner and Boore (1981). Results from such a proposed analysis could serve as a temporary substitute until empirical attenuation laws based on locally recorded Alaskan strong motions become available. However, even the suggested substitute data set is still limited to events with only moderately large events since the Japanese data also do not yet contain recordings from any great subduction earthquakes ($M_w > 7.8$). The strong motion network in the Shumagin seismic gap may provide at present an almost unique opportunity to obtain these urgently needed records of a truly great or giant earthquake.

3.4 Historic and Instrumental Large Earthquakes, 1788 to Present

3.4.1 Overview. Because the destructive potential is greatest for large ($M \geq 7$) and great ($M \geq 7.8$) earthquakes, we need to know the probability of their future occurrence. Two kinds of data are available to assess the occurrence of large events in the past: a) instrumentally recorded data since about 1898, and b) historically reported events for the pre-instrumental period 1788 to 1898. Prior to 1788 no events are known for the Aleutians since no written records were kept prior to establishing the first Russian settlements at Iliuliuk on Unalaska Island at latest by 1776 and on Kodiak Island in 1784. Some indirect evidence for earlier significant earthquakes is of course preserved in the geologic record, e.g., by uplifted marine terraces. But this record is still poorly known for most portions of the Aleutians and many parts of southern Alaska.

The instrumental record of large earthquakes in the Alaska-Aleutian arc has been previously discussed by Sykes (1971), Kelleher (1970) and was later combined with information from the historic record (Sykes et al., 1980 and 1981) to yield a first qualitative assessment of the seismic potential of the eastern Aleutian arc with special emphasis of the Shumagin Islands seismic gap (Davies et al., 1981). The conclusions of these combined studies can be summarized as follows:

- 1) The entire Alaska-Aleutian plate boundary is capable of producing great earthquakes. Virtually each arc segment has been broken by large or great earthquakes at least once during historic times.

- 2) The slip released during the large and great events accounts for a large portion of the relative plate motion between the Pacific and North American plates. Hence, if aseismic slip occurs at the plate interface it is less significant than the portion of plate motion that is released seismically.

- 3) Typical recurrence time between great earthquakes (at the same arc segment) varies along the arc primarily because of variations (a) in the width of the plate contact and (b) in rates of relative plate motions. A typical recurrence time for great events in the

Alaska-Aleutian arc is of the order of 100 years but may vary between about 50 and 200 years or--in few instances--perhaps more.

4) Arc segments with a lack of great earthquakes during the last 30 years or more are identified as 'seismic gaps'. They are very likely to break in a great earthquake much sooner than those that have participated in a great inter-plate earthquake since 30 years or less. In the U.S. portion of the Alaska-Aleutian arc (for the purpose of this study limited between 169°E and 140°W) three seismic gaps have been identified (Figure 3.4.1): the Shumagin gap (Davies et al., 1981); the Yakataga gap (McCann et al., 1980; Lahr et al., 1980; Perez and Jacob, 1980); and the probable Unalaska gap (House et al., 1981).

To further assess the seismic potential for future great events in these three seismic gaps, and of the arc segments in between, we combine these earlier evaluations with one that is based on the history of seismic moment release. Since it is difficult to estimate seismic moments for events during the pre-instrumental period we begin with the instrumental period 1898 to present. We proceed by testing the instrumental seismic moment release against one based on plate kinematic arguments, and then attempt some limited inferences on possible moments that were associated with events during the period of historically documented events, 1788 to 1898. Finally we address some of the problems associated with the difficult questions of where and when great earthquakes may occur next, and the consequences for hazards assessment in the OCS region under study.

3.4.2 Instrumental seismic record. To document thoroughly the large ($M \geq 7$) and great ($M \geq 7.8$) earthquakes along the Alaska-Aleutian arc since world-wide commencement of seismic instrumentation at about 1898, we examined a large number of existing catalogues. The sources we consulted are: Gutenberg and Richter (1949), Duda (1965), Rothé (1969), Tobin and Sykes (1968), Richter (1958), Sykes (1971), Kanamori and Abe (1979), Abe (1981), Abe (1979), Meyers (1976), Meyers et al. (1976), Glover and Meyers (1981), Meyers and Hake (1976), Glover (1980), Glover and Meyers (1982), Davis and Echols (1961), BCIS, ISS, the chronological and regional files of the ISC catalogues, PDE and EDR files of the USGS and predecessors, the

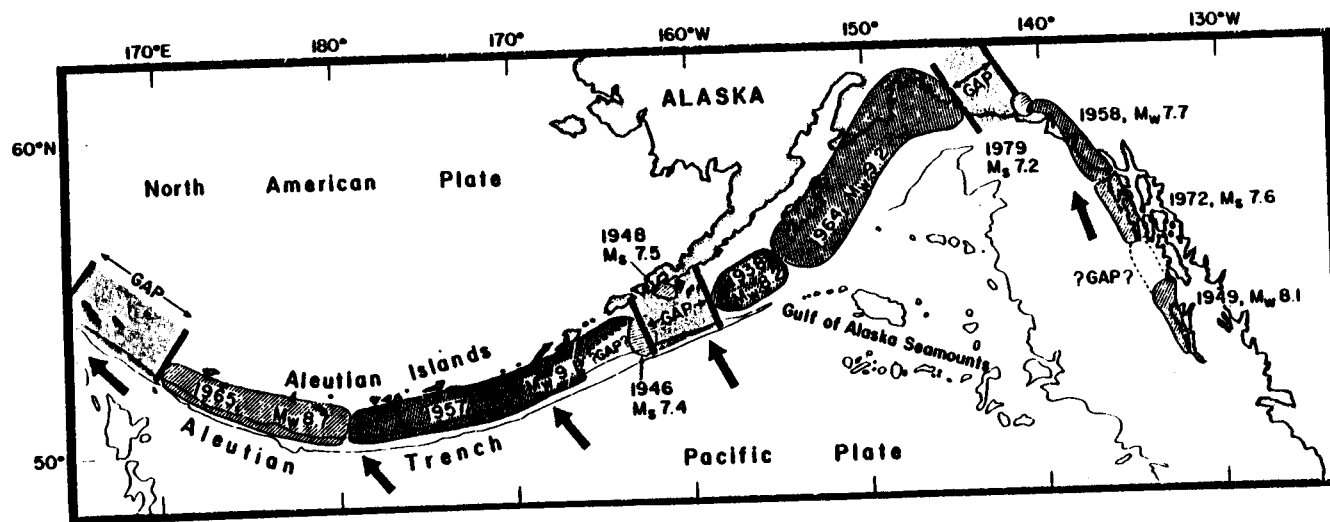


Figure 3.4.1. Location map of presently existing seismic gaps and of rupture zones of the most recent sequence of major earthquakes since 1938. Only the subduction segments of the plate boundary west of 140°W are analyzed in the remainder of this study. The seismic gaps along that portion of the plate boundary are, from east to west: Yakataga gap (near 143°W), Shumagin gap (~160°W), the possible Unalaska gap (queries near 165°W), and the Kommandorski gap (~170°E). The magnitudes indicated are those used by Sykes et al. (1981), House et al. (1981), and Davies et al. (1981) some of which will be modified in the course of this study (see Figure 3.4.8). Solid arrows indicate directions of motion of the Pacific relative to the North American plate (after Sykes et al., 1981).

NEIS-NOAA event-tape-file, and the "Seismological Notes" published in the Bulletin of the Seismological Society of America. For each event a filing card was established and all parallel entries of source parameters noted to detect inconsistencies, printing errors, or systematic variations in determination of source parameters. After careful consideration of all sources we chose a set of parameters. The resulting list of 116 large events along the arc is shown in Table 3.4.1. These and some additional events outside the arc segment studied (169°E to 140°W) are plotted in Figure 3.4.2.

For locations and origin times we adopt the parameters from the first source available when progressing in the following sequence of priority: Sykes (1971), Tobin and Sykes (1968), ISC catalogue, Gutenberg and Richter (1956) and any others. Many of the earliest events (1898-1903) are based on locations determined by Gutenberg or Milne, and are derived from only a few global station readings (see Kanamori and Abe, 1979). After 1904, the world-wide number of stations is generally sufficient to yield reasonably good locations (errors $< 1^{\circ}$) for most events. However, uncertainties in locations for several crucial events remain unresolved. Following McCann et al. (1980), Perez and Jacob (1980), Sykes et al. (1981) and Davies et al. (1981), we place the October 10, 1900 ($M = 8.1$) event somewhere (58°N , 150°W) between Kodiak and Seward based on intensity and aftershock reports, although Richter (1958, p. 710) after Gutenberg (1956), and practically every secondary source thereafter, have placed it probably erroneously at 60°N , 142°W .

The location of the $M = 7.7$ event of July 14, 1899, is noted as 'Arctic near Alaska' in several sources probably after Milne as reported by Gutenberg (1956, Table 3) and as commented on by Kanamori and Abe (1979, Table 4, p. 6136), but the coordinates given (60°N , 150°W) by all these sources suggest a location at the Kenai Peninsula. Sykes et al. (1981) and Davies et al. (1981) note that Tarr and Martin (1912) list felt reports from Unalaska and Unga Islands at the time of this poorly located event of 1899 and thus argue that it may have been located in or near the Unalaska or

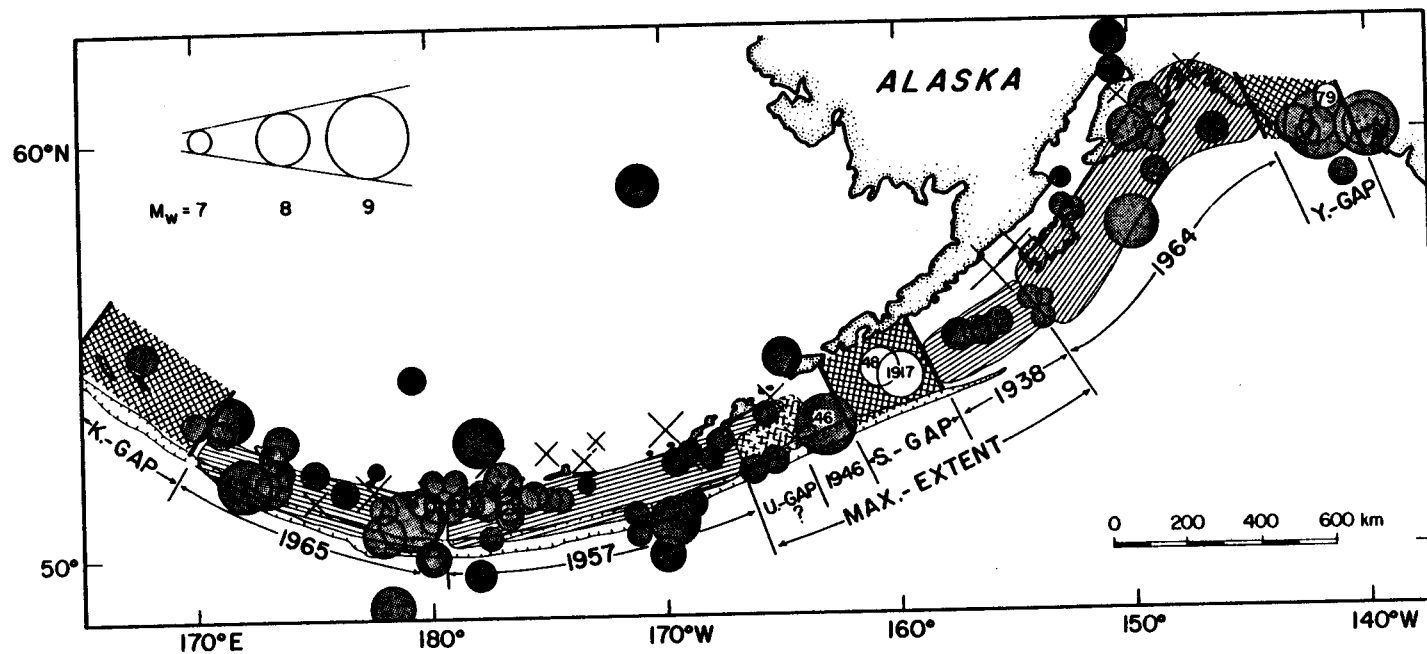


Figure 3.4.2. Major earthquakes ($M_w \sim 7$ and larger) in the Alaska-Aleutian region for the instrumental period 1898 to 1982. All shallow earthquakes ($h < 60$ km) are plotted as circles, except those of the four great earthquakes of 1964, 1938, 1957 and 1965 with magnitudes $M_w = 9.2, 8.4, 9.0$ and 8.7 , respectively, for which rupture zones are indicated by arc-parallel hatching. The Yakataga (Y), Shumagin (S), Kommandorski (K) and possible Unalaska (U?) seismic gaps are indicated by cross hatching. Intermediate depth earthquakes ($h > 60$ km) are shown as crosses. Symbol size indicates magnitude M_w (upper left insert). The 6000-m bathymetric contour outlines the Aleutian trench.

Shumagin seismic gaps. We have retained the 'instrumental' location near Kenai but emphasize how tenuous it is.

One event, that of 31 May 1917 ($M = 7.8$), is of special interest. Its only published source can be traced back to a catalog prepared by T. Usami printed in 1975 in the Science Almanac of the Tokyo Astronomical Observatory and was reproduced by Glover and Meyers (1981). Since this event had not been reported by Gutenberg and Richter (1956) or any other western source prior to 1981, it went unnoticed by Davies et al. (1981) in their assessment of the Shumagin gap despite the fact that the epicenter coordinates place it within the Shumagin gap. This new finding requires corrections to some of the statements by Davies et al. (1981) or Sykes et al. (1981) regarding the duration of quiescence for events larger than $M = 7.5$, and measured recurrence times of great events in the Shumagin gap, however, it only inconsequentially alters these author's assessments of the gap's seismic potential for a future large earthquake.

For magnitudes we adhere as closely as possible to a uniform scale and choose those magnitude values from different sources and methods of determinations that--within the limits of available data--appear to represent most closely the moment magnitude M_w proposed by Kanamori (1977). It relates moment M_0 (dyn cm) to magnitude M_w by

$$\log_{10} M_0 = 16.1 + 1.5 M_w$$

under the assumption of constant and complete stress drop (≈ 50 bar) and a ratio of $\Delta\sigma/\mu = 10^{-4}$ (that is $\mu = 5 \times 10^{11}$ dyn/cm²) regardless of event size. The latter assumption may not be fully valid (Kanamori, 1977; Purcaru and Berckhemer, 1978; Sykes and Quittmeyer, 1981).

For events between 1898 and 1903 (inclusive) we use the magnitude determinations of Kanamori and Abe (1979), except for the September 4, 1899, event which is adopted from Thatcher and Plafker (1977). For most events between 1904 and 1980 we rely on the magnitude determinations by Abe (1981) except for those largest events where

either Abe (1979), Kanamori (1977), Purcaru and Berckhemer (1978) or Sykes and Quittmeyer (1981) have determined or discussed a moment magnitude M_w using information from either long-period seismograms, aftershock zone dimensions, or tsunami heights. Three great events need special mention: we reduce the M_w from 9.1 to 9.0 for the March 9, 1957, event because of a possible reduction of aftershock dimension in the Unalaska region (House et al., 1981). We adopt (after Purcaru and Berckhemer, 1978), a $M_w = 8.3$ for the highly tsunamigenic ($M_T = 9.3$) 1946 earthquake near Unimak (Abe, 1979). We are forced to use $M_w = 7.8$ (Glover and Meyers, 1981) for the 1917 Shumagin gap earthquake without knowing the method of its magnitude determination. At least these three events need further analysis of original instrumental records.

Where several of the magnitude sources give different values (i.e., m_b , M_S , M_L , M_T , M_W , M_E , M_{100}) we often (but not always) tend to choose a value towards the upper limit, to represent M_w , while systematically avoiding the upward revised surface-wave magnitudes \underline{M} of Gutenberg cited by Richter (1958) and quoted as M_S by Sykes (1971), Sykes et al. (1981), and Davies et al. (1981). A more detailed justification and documentation is in preparation (Jacob et al., 1983).

Note that we first adopt the magnitude M_w and then calculate (or recalculate) the moment M_0 (Table 3.4.1) using

$$\log_{10} M_0 = 16.1 + 1.5 M_w$$

Thus, the moments listed in Table 3.4.1 may be in error by as much as 20 to 30% compared to those moments given in the original sources. This is largely due to the fact that round-off to the nearest 0.1- M_w -value can result in this large an error. (Since the difference of a $M_w = 9.20$ and a $M_w = 9.25$ corresponds to a moment increase that in itself is equivalent to a magnitude $M_w = 8.72$, these rounding errors are not trivial for the largest events. For magnitudes $M_w > 7.9$, and for certain purposes, it may therefore be in order to carry a second decimal position through all M_w calculations.)

TABLE 3.4.1. List of 116 Large Earthquakes in the Alaska-Aleutian Arc (169°E to 140°W)
for the Period 1898-1982 for which at Least One Source Reported a Magnitude $M \geq 7$

Columns indicate Date (Y,M,D), Origin Time (H,M,S), Latitude and Longitude (°), Depth (km), Magnitude (M_s), and Equivalent Moment (dyne cm).

Date	Time	Lat	Lon	D	M_s	M_0	Date	Time	Lat	Lon	D	M_s	M_0
980629	1836	52.00	172.00	0	8.00	1.1259e+29	440727	4 23.00	54.00	155.50	70	7.10	1.5623e+27
981211	1637	50.00	180.00	0	7.40	1.1585e+28	441212	417 18.00	51.50	179.50	0	7.10	1.5623e+27
990714	1332	60.00	150.00	0	7.70	1.4467e+28	460112	2025 40.20	59.11	148.97	56	7.20	1.7943e+27
990904	904	60.00	142.00	0	8.50	1.7079e+29	460401	1228 56.00	53.32	163.19	0	8.30	1.3548e+29
990904	440	60.00	142.00	0	7.40	1.1585e+28	461101	1114 24.00	51.50	174.50	40	7.20	1.5623e+27
990910	1704	60.00	140.00	0	7.30	1.0310e+28	480514	2231 43.40	54.71	160.00	0	7.50	1.2239e+28
990910	2141	60.00	140.00	0	8.40	1.5012e+29	490202	1741 29.00	53.00	173.00	20	6.80	1.1995e+27
990923	1104	60.00	143.00	0	7.40	1.1585e+28	490927	1530 45.00	59.75	149.00	50	7.00	1.3901e+27
990923	1250	60.00	143.00	0	7.50	1.2239e+28	510213	2212 53.00	55.55	156.35	0	7.10	1.5623e+27
001009	1220	50.00	150.00	0	8.10	1.1770e+29	521129	2346 27.00	56.30	153.00	0	6.75	1.1679e+27
011231	092	52.00	177.00	0	7.50	1.2239e+28	530105	748 21.60	53.32	171.04	0	7.10	1.5623e+27
020101	520	55.00	165.00	0	7.50	1.2239e+28	540417	2010 37.00	51.50	179.00	0	6.75	1.1679e+27
030117	1605	50.00	170.00	0	7.40	1.1585e+28	541003	1110 45.90	60.71	150.52	73	6.75	1.1679e+27
030602	1317	57.00	156.00	100	8.30	1.3548e+29	550314	1312	52.50	173.50	75	7.00	1.3901e+27
050214	046	53.00	170.00	0	7.90	1.0912e+29	550620	1207 25.00	51.50	180.00	0	6.80	1.1995e+27
050322	330	50.00	180.00	0	7.20	1.7943e+27	570102	312 52.00	52.51	160.10	0	7.20	1.3901e+27
051210	1236	50.00	180.00	0	7.00	1.3901e+27	570102	340 47.00	52.50	160.03	0	7.00	1.3901e+27
060017	10	51.00	179.00	0	8.20	1.2512e+29	570309	1422 27.00	51.53	175.41	0	9.20	1.3901e+28
070002	1601	52.00	173.00	0	7.80	1.0310e+28	570309	2039 16.50	52.43	169.50	0	7.10	1.5623e+27
080515	021	50.00	141.00	0	7.10	1.5623e+27	570311	312 42.00	51.00	177.13	0	6.80	1.1995e+27
090900	1649	52.00	169.00	90	7.00	1.3901e+27	570311	950 44.40	52.66	169.00	0	7.00	1.3901e+27
090919	2000	60.00	149.00	0	7.10	1.1585e+28	570311	1455 19.50	51.54	170.55	0	7.10	1.5623e+27
100909	113	51.50	176.00	0	7.10	1.5623e+27	570312	720 40.30	51.09	172.42	0	6.75	1.1679e+27
110917	326	51.00	180.00	0	7.00	1.3901e+27	570312	1144 53.30	51.10	176.73	0	7.10	1.5623e+27
110922	501	50.50	149.00	50	6.90	1.2010e+27	570314	1447 44.00	51.32	176.70	0	7.10	1.5623e+27
111113	1613	52.00	173.00	0	7.30	1.3901e+27	570316	234 17.00	51.47	170.70	0	7.00	1.3901e+27
120104	1546	52.00	179.00	25	7.00	1.3901e+27	570322	1421 5.50	53.61	165.76	0	7.00	1.3901e+27
120131	2011	61.00	147.50	00	7.00	1.3901e+27	570410	1129 50.20	55.34	153.00	0	7.00	1.3901e+27
120610	1606	59.00	153.00	25	6.90	1.2010e+27	570419	2219 30.00	52.20	165.30	50	7.10	1.5623e+27
121010	1140	54.60	179.20	0	7.10	1.5623e+27	570613	1040 30.00	51.50	175.00	0	7.00	1.3901e+27
121107	740	57.50	155.00	90	7.30	1.1122e+28	600703	2020 50.00	50.50	177.50	0	7.00	1.3901e+27
121205	1227	57.50	154.00	90	6.90	1.2010e+27	601113	920 32.00	51.23	160.00	32	7.10	1.5623e+27
130331	340	49.50	170.00	0	7.30	1.1122e+28	611230	39 27.10	52.30	177.60	56	6.80	1.1995e+27
130622	1349	48.00	170.00	0	7.20	1.7943e+27	640205	1307 21.10	55.75	155.79	0	7.10	1.5623e+27
160206	2151	40.50	170.50	0	7.70	1.4467e+28	640320	336 13.00	61.10	147.60	20	9.20	1.7943e+28
160410	401	53.25	170.00	170	7.40	1.1585e+28	640404	1746 9.00	56.30	154.40	24	7.00	1.3901e+27
170531	047	54.50	160.00	0	7.80	1.0310e+28	650204	501 21.00	51.30	170.60	40	8.70	1.1413e+28
230504	1626	55.55	156.75	0	7.10	1.5623e+27	650204	040 42.00	51.40	179.60	40	7.00	1.3901e+27
261013	1900	51.63	175.65	0	7.10	1.5623e+27	650330	227 7.20	50.60	177.90	51	7.60	1.3162e+28
280021	1027	60.00	146.50	0	7.30	1.1122e+28	650702	2050 30.00	53.00	167.50	40	7.00	1.3901e+27
290307	134	50.00	169.71	0	7.90	1.0912e+29	650729	029 22.00	51.10	171.30	18	7.00	1.3901e+27
290705	1419	51.42	170.34	0	7.00	1.3901e+27	650904	1432 50.00	50.30	152.50	30	7.00	1.2010e+27
290707	2123	51.60	177.07	0	7.40	1.1585e+28	651222	1941 23.00	50.40	153.00	50	7.00	1.3901e+27
291217	1050	53.67	171.46	0	7.00	1.0310e+28	650704	1033 30.70	51.99	179.97	16	7.00	1.3901e+27
320225	2350	62.50	152.50	25	6.90	1.2010e+27	660007	213 4.10	50.57	171.22	29	7.00	1.3901e+27
330427	236	61.25	150.75	0	7.10	1.5623e+27	670120	1352 50.30	52.40	169.54	41	6.70	1.1413e+27
340504	426	61.25	147.50	0	7.10	1.5623e+27	690514	1932 55.00	51.20	179.35	22	7.00	1.3901e+27
350222	1705	52.25	175.00	0	7.10	1.5623e+27	690912	057 5.00	51.27	179.17	30	7.00	1.3901e+27
370003	1040	52.50	177.50	0	7.20	1.7943e+27	700220	1042 31.20	52.70	175.00	15	7.00	1.3901e+27
301110	2010	55.40	150.37	0	8.40	1.5012e+29	720416	533 10.20	59.06	142.43	0	7.00	1.3901e+27
301117	354	55.45	157.55	0	7.30	1.1122e+28	710207	229 29.10	51.47	176.01	40	7.00	1.3901e+27
400207	1716	51.50	175.00	0	7.00	1.3901e+27	710502	600 26.90	51.42	177.21	30	7.10	1.5623e+27
400415	607	52.30	173.50	0	7.10	1.5623e+27	750202	043 39.90	53.00	173.50	10	7.40	1.1585e+28
400416	643	52.60	173.25	0	7.10	1.5623e+27	770219	2234 5.40	53.54	169.46	44	7.10	1.5623e+27
400714	552	51.75	177.50	0	7.40	1.1585e+28	770904	1724 46.60	51.31	177.01	24	7.10	1.5623e+27
400022	327	52.41	165.37	0	7.20	1.7943e+27	790220	2127 6.00	60.60	141.50	15	7.00	1.3901e+27
420909	125	53.00	154.50	0	6.90	1.2010e+27	800324	359 51.30	52.97	167.67	33	7.10	1.5623e+27
431103	1432	61.90	150.04	0	7.40	1.1585e+28	810130	052 44.10	51.74	176.27	33	7.10	1.5623e+27

3.4.3 Magnitude-time distribution for entire arc, and mean occurrence. Before analyzing the data for their time-space distribution and its consequences for seismic potential in seismic gaps, it is of interest to analyze the overall-properties of the data ensemble disregarding any systematic spatial patterns.

Figure 3.4.3 (A through E) displays the major seismicity of the arc (169°E to 140°W) as a function of time. All events ($M_w \geq 7$) within 300 km lateral distance of the arc are included, regardless of depth or focal mechanism. Several features can be discerned from these graphs: Whenever one or more great ($M_w \geq 7.8$) earthquakes occur in any given year (curve B), the number of large events ($M_w \geq 7$) generally is also higher for the same year (see curves A and D). This is consistent with the notion that some great earthquakes trigger large aftershocks, (notably the 1899, 1957, and 1965 sequences). Two kinds of exceptions exist: a) there are times of increased seismicity ($M \geq 7$) without great events (1912 ± 1 y, 1940), and b) there are great events with few reported large aftershocks (1964, 1938, 1917, 1907, 1906). The 1912 'swarm' may represent some volcanically induced seismicity culminating in the 1912 Katmai eruption; interestingly much of it is associated with intermediate-depth earthquakes (60-250 km) that occur probably in the descending Pacific slab beneath the volcanic axis. This volcano-seismic sequence may have started with the great ($M_w = 8.3$) event of 1903 which reportedly (Gutenberg and Richter, 1956) occurred at a depth of ≈ 100 km [The magnitude 8.3 quoted is one of the few events in Table 3.4.1 for which only a revised magnitude \underline{M} is available (after Gutenberg, 1956) (see also Richter, 1958, p. 714)].

A second feature in Figure 3.4.3 is that the rate of significant seismicity is high around the turn of the century (1898-1908) and around 1960 ± 5 y, and low in between. This trend is apparent in both large ($M_w \geq 7$, curves A and D) and great earthquake ($M \geq 7.8$, curve B) activity. To emphasize the energy release dominated by the larger and greatest events we have plotted cumulative excess magnitude above $M_w = 7$ as a function of time in curve C. Excluding the high release before 1901, one can draw an upper and lower envelope to the data in this plot. The envelopes contain a span of about 5 excess units above

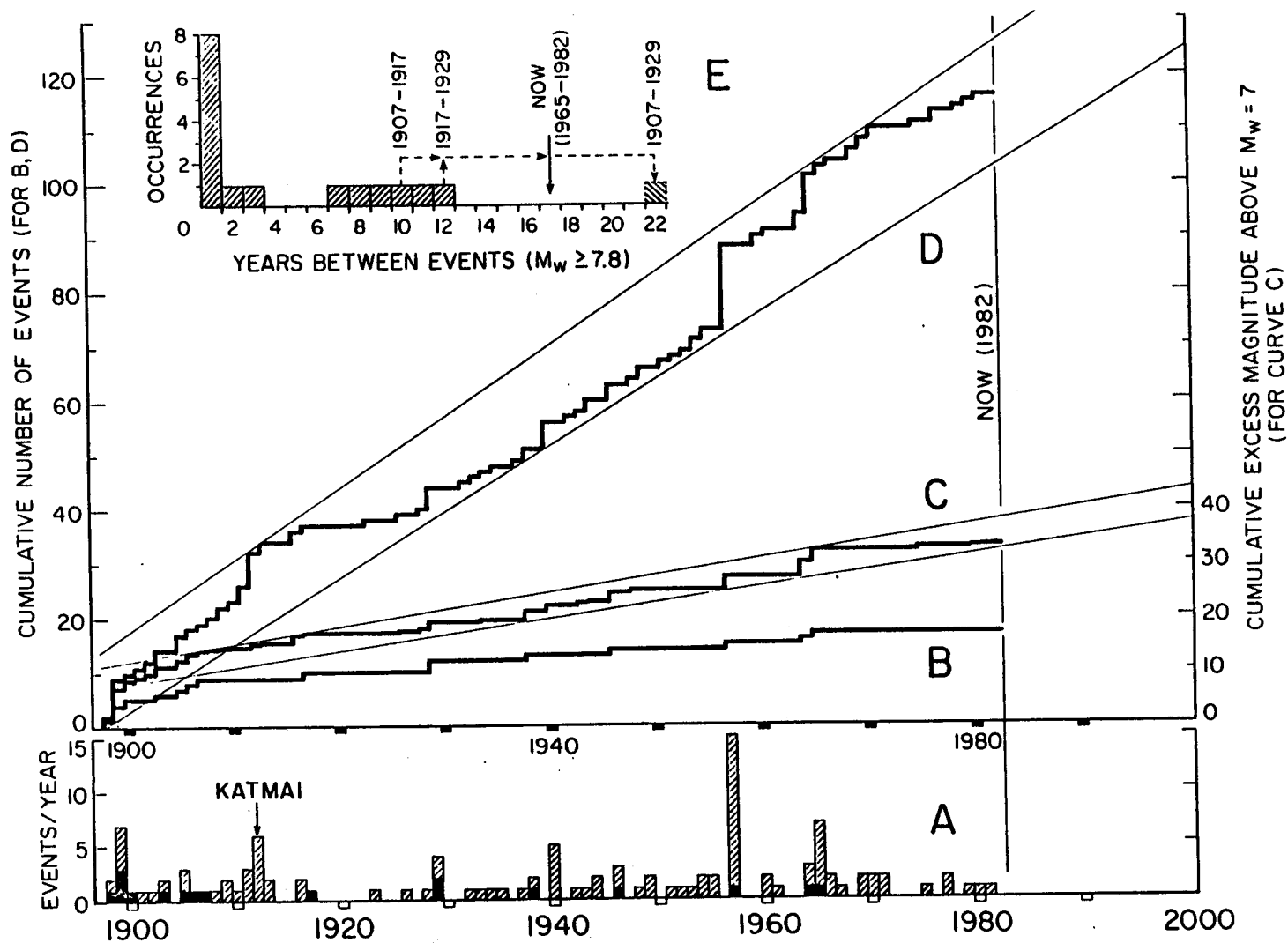


Figure 3.4.3. Seismicity ($M_w \geq 7$) of the Aleutian arc (140°W to 169°E) versus time for the instrumental period 1898 to 1982. The occurrence of events per year (curve A) is differentiated for great ($M_w \geq 7.8$) and large ($M_w < 7.8$) events by solid and hatched symbols, respectively. Cumulative number of events for all major events (curve D) and for great events ($M_w \geq 7.8$) only (curve B) use left-hand scale, cumulative excess-magnitude above $M_w = 7$ (curve C) uses right-hand scale of abscissa. Insert E shows the histogram for the periods (years) between subsequent great earthquakes ($M_w \geq 7.8$) along the arc. Note the long recent period of quiescence of 17 years.

magnitude $M_w = 7$ (i.e., two $M_w = 9$ plus one $M_w = 8$, or five $M_w = 8$ events, etc.). Since 1965 no great earthquake has occurred and from the graph follows that some major activity is due in the Alaska-Aleutian arc by at latest 1985 provided such a representation has any physical significance. Of course no statement can be made from such a presentation where the seismicity would take place within the arc.

Another way to present the same temporal aspect of seismicity is shown in Figure 3.4.3, insert E. There we have plotted for only great events ($M_w \geq 7.8$) the frequency distribution for time intervals between consecutive events (anywhere between 169°E and 140°W). An outstanding feature of this distribution is the strong peak of occurrences of mutliplet events in the same or two consecutive years (i.e., $\Delta t < 2$ years). The 1900 ± 1 y sequence contributes half of the occurrences in this spike, the 1905-07, 1929, and 1964/65 bursts contribute the other half. Note that we have excluded from this study the SE-Alaska strike-slip boundary. Otherwise the 1958 Lituya Bay-Fairweather event would have added another occurrence in 1957/58 to this strong clustering of great events. This clustering occurs mostly in time (1964/65), but sometimes also in time and space (1899). The occurrence of great events in the arc gives the appearance that stress release is communicated over large distances. A physically plausible explanation may be that episodic large-scale plate motions may be the common cause to events that can be large distances apart, rather than one event 'triggering' the other.

Apart from this 'burst'-like clustering in insert E at $\Delta t < 2$ years, another aspect needs to be reiterated that we commented on earlier. In the past 85 years there is no occurrence of a time period longer than 12 years (represented by events in 1917 and 1929) in which no great event has occurred bewteen 169°E and 140°W , except for the ongoing period 1965 to present (i.e., $\Delta t \geq 17$ years). This is to say that the last 17 years have been unusually quiescent and represent a statistically possible but unlikely situation. Even if we remove the questionable event of 1917 whose magnitude $M_w = 7.8$ may in fact not have been as high as reported, than the longest quiescent interval in the last 85 years may have measured 22 years (1907 to 1929), and the

recent quiescence of 17 years is still remarkable. In either interpretation, one can expect soon an arc-wide increase of major seismicity, if the distribution of Figure 3.4.3-E is representative of long-term seismicity. Again, no consideration of depth, location, or nature of faulting (thrusting on the subduction zone, normal faulting at the trench, and some strike-slip in the Near Islands) has been given in this examination of the likelihood of future increased activity.

One can make some simple estimates of average occurrence for significant earthquakes from the presentations A-E of Figure 3.4.3. Of the total of 116 considered events, 102 events had magnitudes $M_w \geq 7$. They occurred during the last 85 years over a 3600 km long arc distance. From these figures we obtain an average occurrence of one large event ($M \geq 7$) about every 10 years within a 300 km long arc segment. The total of 17 great events yields an average occurrence of one great earthquake ($M_w \geq 7.8$) about every 60 years within any 300-km distance along the arc. Because of clustering associated with the seismic cycle, and because of systematic variations in the rates of plate motion and of boundary width (see later sections), the actual values may deviate substantially from these mean values of 10 and 60 years, respectively, in any given 300-km arc segment. We will compare these estimates with those derived by other methods and find some important systematic discrepancies that will be discussed later.

3.4.4 Recurrence estimates from b-values for the entire arc.

The distribution of occurrences of large events per 0.1- M_w -intervals for the entire Alaska-Aleutian arc (169°E to 140°W) is shown in Figure 3.4.4. A more commonly used method in seismology is to plot the logarithm of the cumulative number $N(M_w)$ of events at and above a magnitude M_w as a function of this variable lower boundary M_w , and then find some function

$$\log_{10} N = A - bM_w$$

that in a specifically defined way (say maximum likelihood or least-squares sense) approximates the observed distribution over a limited magnitude range. Figure 3.4.5 (bottom) shows the data set of

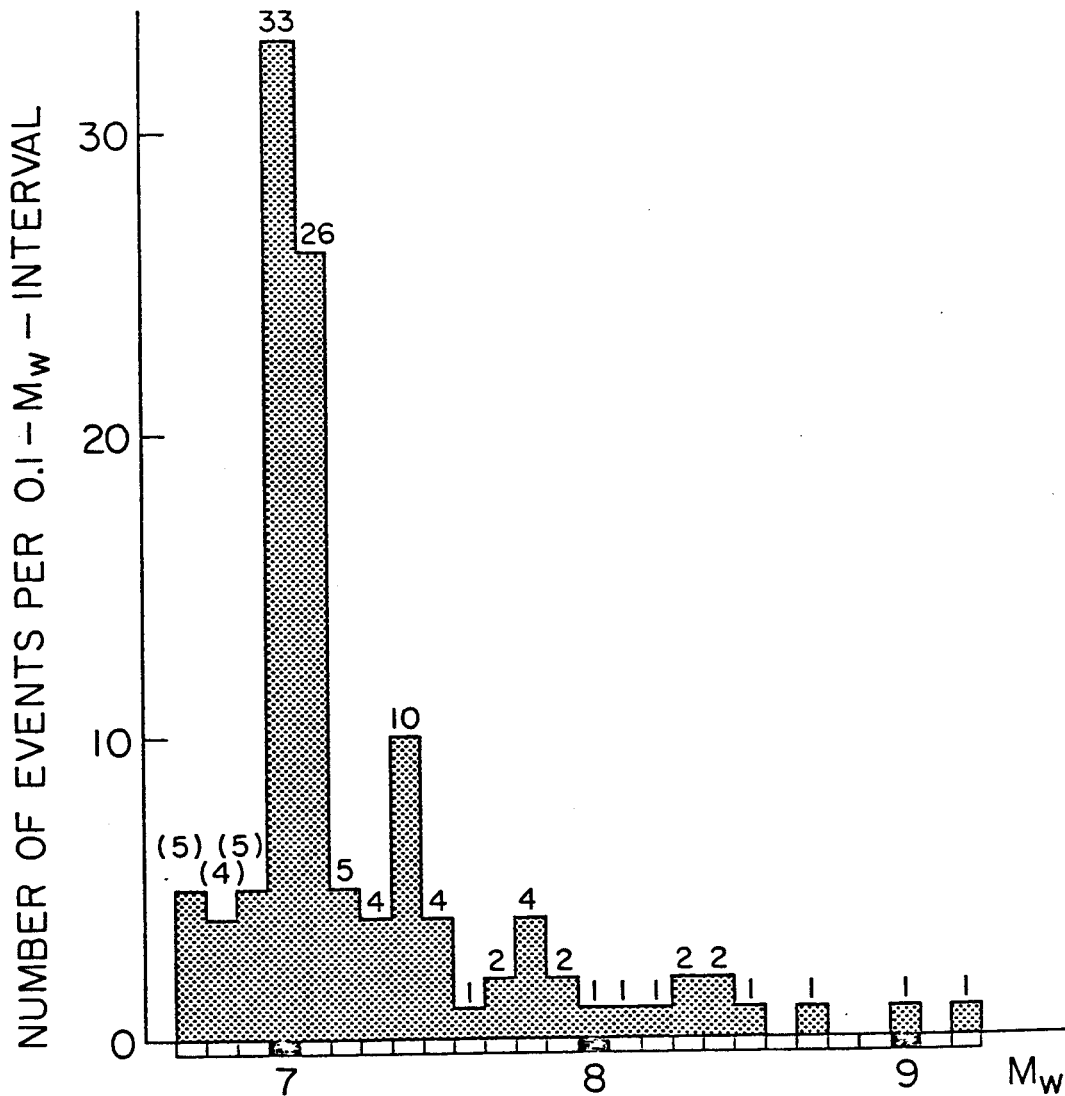


Figure 3.4.4. Histogram of all major earthquakes for which magnitudes were available, plotted in $M_w = 0.1$ -intervals. Note that several earthquakes (a total of 14 events) for which at least one source reported a magnitude 7 or larger, were reassigned to magnitudes $M_w < 7$.

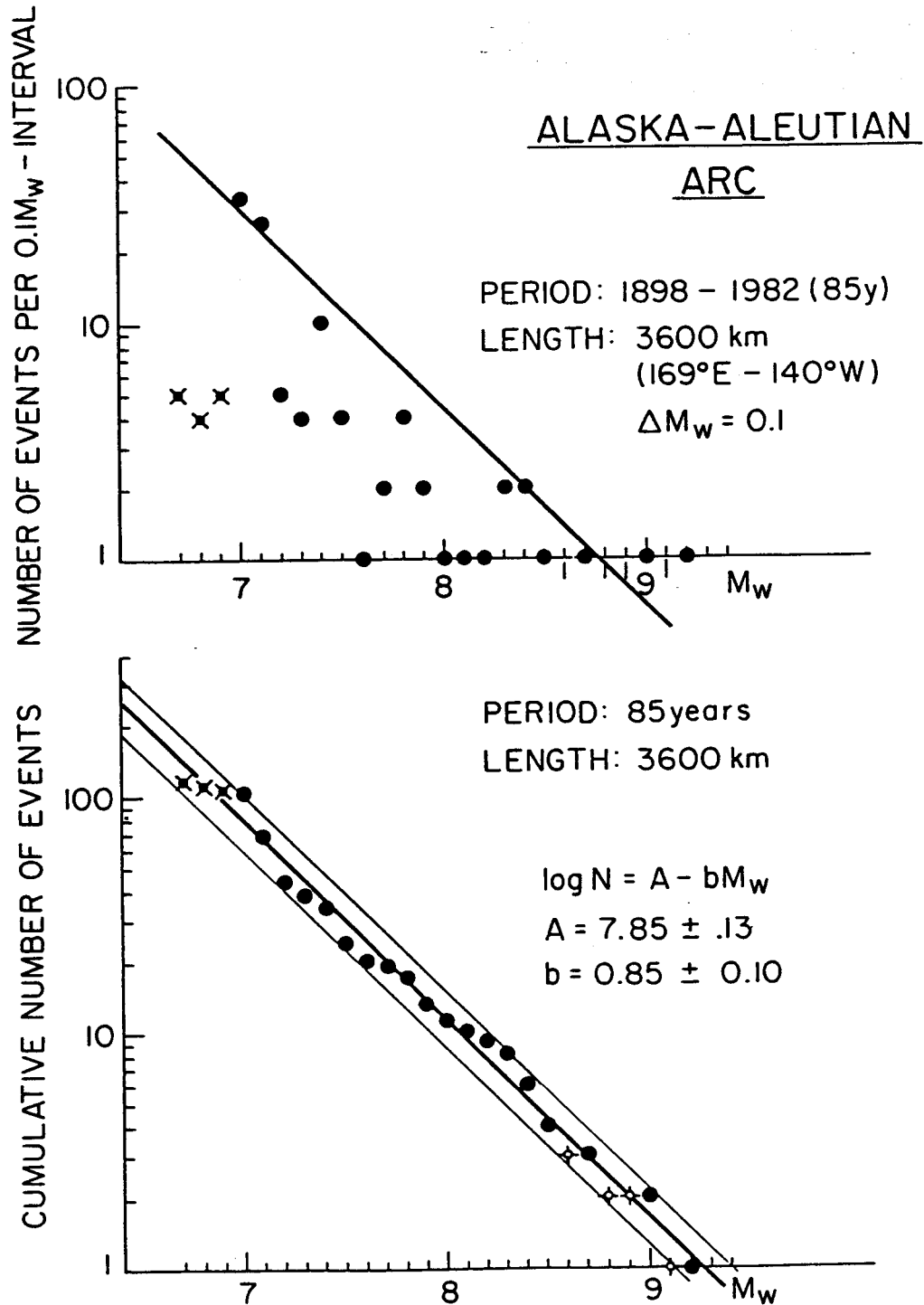


Figure 3.4.5 . Logarithmic frequency plots for the instrumental seismicity 1898 to 1982 (85 years) for the Alaska-Aleutian arc (total arc length 3600 km). Top: number of events n (on logarithmic scale) per 0.1- M_w -interval vs. magnitude M_w . Bottom: cumulative number N of events (on log-scale) with magnitudes M_w and larger vs. M_w . Heavy line represents the relation $\log N = A - bM_w$ with $A = 7.85$ and $b = 0.85$; light lines represent error $\Delta A = \pm 0.13$.

Table 3.4.1 represented in this form. Depending on the method of curve-fitting one obtains different A and b values and associated errors with them. Maximum likelihood methods (Figure 3.4.6) emphasize the slope and absolute number of events close to the average magnitude which is very close to the lower bound of considered magnitudes in the data sample. Because of the importance of the great events (in terms of strain energy or moment release) we have (against common practice) given here more weight towards a regular straight-line least-squares regression and/or 'eye-ball fit' with assigning errors (ΔA and Δb) for the constants such that not a single observation in the range $6.7 \leq M_w \leq 9.2$ falls outside the regression and assigned error range. With this approach we obtain

$$\log_{10} N = (7.85 \pm .13) - (0.85 \pm 0.10) M_w$$

shown as straight lines in Figure 3.4.5 (bottom).

Clearly, the total number in the data-sample is too small to attach great significance to any of these fits when extrapolating to magnitudes outside the observational range. Disregarding, however, this warning we nevertheless proceed to derive recurrence time estimates from this relationship. To do so, we have to keep in mind that the data comprise a time period $T_0 = 85$ years and arc-length $L_0 = 3,600$ km. To scale the number of cumulative occurrences $N(L_0, T_0, M_w)$ to another arc length L and time period T , a vertical shift of the (logarithmic) intercept from $A(L_0, T_0, M_w=0)$ to a new intercept $A(L_0, T_0, M_w=0) + \log(L \cdot T / L_0 \cdot T_0)$ must be performed. Choosing arc length $L = 300$ km for all magnitudes $M_w \leq 8.5$, and larger values of L for the greatest earthquakes ($M \geq 9.0$) because they require larger rupture zones; and setting $T = 1$ year, we calculate, first, the number (or fractional number) of occurrences per year by using T and L in

$$\log_{10} N(L, T, M_w) = A(L_0, T_0) + \log_{10} (L/L_0 \cdot T/T_0) - bM_w$$

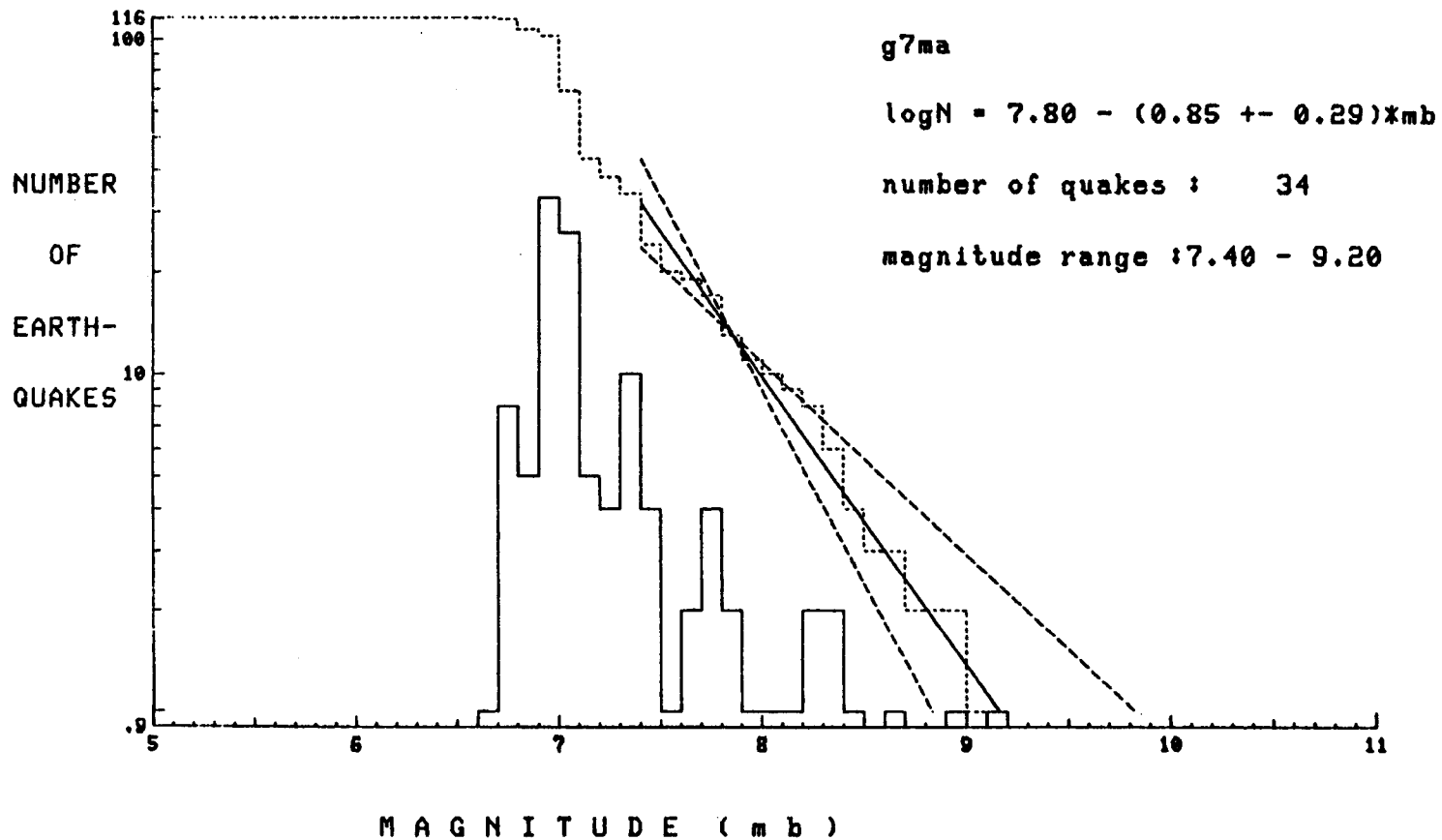


Figure 3.4.6 . Same as Figure 3.4.5 with number of events n as solid line and cumulative number of events N as broken line. Straight-line fits $\log N = A - bM_w$ are calculated by the maximum likelihood method and yield $A = 7.85$ and $b = 0.85$, virtually identical to that for linear regression, but the error $\Delta b = +0.29$ is much larger. Only magnitudes $7.4 \leq M_w \leq 9.2$ were used in the calculation. Maximum likelihood straight-line fits to the data with cut-off magnitudes lower than 7.4 yield poor representation of the observations for high magnitudes.

Having calculated the number of events per year, then the inverse of this number yields recurrence times, i.e.,

$$T_R = N^{-1} (L, T=1, M_w)$$

The results of these calculations are summarized in Table 3.4.2, where the recurrence times T_{avr} , T_{min} , T_{max} refer to the usage of $A(L_0, T_0) = 7.85$, and of the marginal values $A \pm \Delta A$, respectively, where $\Delta A = 0.13$.

The recurrence times derived from the exponential relation (Table 3.4.2) for magnitudes $M_w \approx 7$ and $M_w = 7.8$ agree well with those earlier determined from the mean occurrence rates (chapter 3.4.2) which measured about 10 and 60 years, respectively. The so-calculated recurrence times for the greatest events ($M_w \geq 9.0$), measure up to several hundred years.

Extrapolation to smaller magnitudes than those covered by this data set (i.e., to $M_w < 7$) yield recurrence times for events in a 300-km long arc-segment that are very close to those derived from network data (Figure 3.1.6) or those from teleseisms (Figure 3.2.4). Normalizing the different log-linear relationships derived from the different data sets to a 300-km arc length and a 1-year period yields the values summarized in Table 3.4.3. The different relationships give recurrence times (when extrapolated, for instance, to a common magnitude $m = 5.0$) that all lie within a factor of 2 to 3.5. This variation is remarkably small considering that both the magnitude range covered ($2 \leq m \leq 9.2$) and the method of magnitude determination vary strongly among those data sets.

3.4.5 Arc-wide, instrumentally determined seismic moment release, 1898-1982. Moment M_0 (dyn cm) is related to moment magnitude M_w by the relationship

$$\log M_0 = 16.1 - 1.5 M_w$$

assuming a constant and complete stress drop ($\Delta\sigma \approx 50$ bar) and constant shear modulus ($\mu \approx 5 \times 10^{11}$ dyn cm^{-2}) (Kanamori, 1977). Because moment magnitudes are known for all events listed in Table

TABLE 3.4.2. Estimates of minimum-, average-, and maximum recurrence times derived from the b-value plot for the entire arc. The times are scaled to represent the occurrence of one event of magnitude M_w within a sector of length L along the arc.

M_w	L (km)	T_{min} (years, except for m = months)	T_{av}	T_{max}
5	300	2m	3m	4m
6	300	1.3	1.8	2.4
7	300	9.5	13	17
7.8	300	45	61	82
8	300	67	91	123
8.5	300	180	240	380
9	600	240	320	430
9.2	800	260	360	480
9.5	1000	380	510	690

TABLE 3.4.3. Comparison of A and b values and recurrence times T_R for $m = 5.0$ events using different data sources.

Source	Observed Magnitude Range	Number of Events	$A(L_0, T_0)$	$\frac{L}{L_0} \times \frac{T}{T_0}$ (km/km) x (y/y)	$A(L=300, T=1)$	b	$T_R(m=5.0)$ (years)
Shumagin network, all depth, (1977-1981)	2.5-6.0	631	4.72	$\frac{300}{400} \times \frac{1.0}{4.5}$	3.94	0.75 ± 0.06	0.643
Shumagin network, all depth, (1977-1981)	3.0-5.5	306	5.10	$\frac{300}{400} \times \frac{1.0}{4.5}$	4.32	0.85 ± 0.09	0.848
Teleseismic, all depths (1973-1981)	4.4-6.3	310	6.52	$\frac{300}{600} \times \frac{1.0}{9.0}$	5.26	0.92 ± 0.10	0.216
Teleseismic, all depths (1973-1981)	4.5-6.3	275	7.12	$\frac{300}{600} \times \frac{1.0}{9.0}$	5.86	1.04 ± 0.12	0.216
Large equ., all depths (1898-1982)	6.7-9.2	116	7.85	$\frac{300}{3600} \times \frac{1}{85}$	4.84	0.85 ± 0.10	0.256
Average of above	(2.5-9.2)	---	----	-----	4.847	0.882	0.366

3.4.1, we can calculate the cumulative moment for the Aleutian arc as a function of time from 1898 to 1982. The individual moments so calculated from M_w are listed in Table 3.4.1 and their cumulative values are plotted in Figure 3.4.7.

The features of activity, earlier discussed on the basis of seismicity rates, are amplified by this seismic moment vs. time plot: a rapid moment release lasting from 1898 to about 1907 is followed by a period of slow moment release from 1907 to about 1957, when a major sequence of events commences that lasts from 1957 to 1965. Since 1965, seismic moment release has again been extremely low and has remained so for the last 17 to 18 years.

The cumulative seismic moment released during the last 85 years measures 1.75×10^{30} dyn cm (equivalent to a single $M_w = 9.43$ event). The mean-rate for the entire 85-year period amounts to $\dot{M}_0 \approx 2 \times 10^{28}$ dyn cm y^{-1} (equivalent to one $M_w = 8.14$ per year).

These numbers and Figure 3.4.7 demonstrate several seismicity features very clearly:

- 1) Moment release is almost completely dominated by the largest events.

- 2) Seismic activity throughout the Aleutian arc appears to occur periodically, with two peaks of activity during the last 85 years that are about 60 years apart.

- 3) During the quiescent interval (≈ 50 years) few great earthquakes occur contributing to an average rate of moment release that is only about 3×10^{27} dyn cm y^{-1} (equivalent to one $M_w = 7.6$ event per year), or one to two orders of magnitude lower than in the short intervals (≈ 15 y) of very high moment release (8.6×10^{28} dyn cm y^{-1} , equivalent to one event of about $M_w = 8.5$ per year).

3.4.6 Plate-kinematic strain accumulation rates. To compare the observed seismic moment release with one derived from a simple plate-kinematic model we make the following assumptions:

- 1) Seismicity that actually occurs spread out over a volume at and near the plate boundary, is assumed to be released on a single brittle fault contact of area $A = L \times W$ (km^2) that takes up the entire relative plate motion \dot{u} (cm/y) by periodic seismic slip events (i.e., seismic efficiency $\alpha = u_{\text{seismic}}/u_{\text{total}} = 1$).

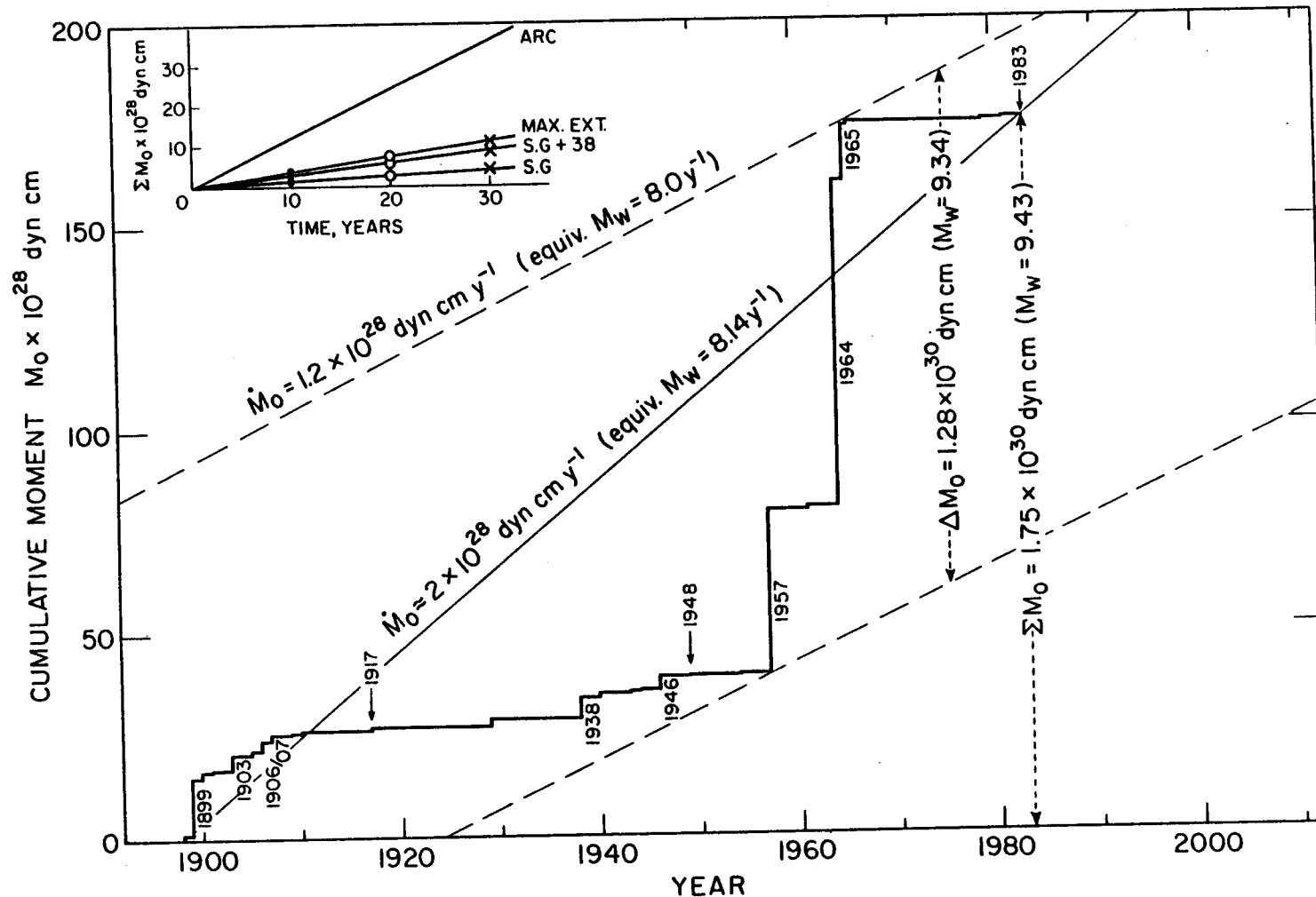


Figure 3.4.7. Arc-wide seismic moment release (heavy solid line) for the Aleutian arc during the period 1898 to 1982 (inclusive). Note periods of high moment release around the turn of century and approximately 60 years later. Fine solid line represents average moment release for 1898 to 1982 ($\dot{M}_0 = 2 \times 10^{28} \text{ dyn cm y}^{-1}$). Broken lines straddling the upper and lower bounds represent the rate ($\dot{M}_0 = 1.2 \times 10^{28} \text{ dyn cm y}^{-1}$) inferred from the plate-kinematic model discussed in the text. Note that this plate-kinematic rate represents only 60% of the mean rate observed during the last 85 years. Upper left insert: shows the moments that accumulate in 10, 20, and 30 years (dots, circles, crosses), respectively, for the entire arc, the maximum credible rupture extent indicated in Figure 3.4.2, for the Shumagin Gap (SG) alone, and combined with that of the 1938 rupture zone (SG + 38). Note that for some rates and moments the equivalent values in magnitude M_w are given.

2) Outside the brittle fault contact, slip of the plates past one another and relative to the mantle occurs entirely ductile and aseismic ($\alpha = 0$).

3) The downdip width W (km) of the dipping fault contact that is assumed to have a full seismic efficiency of $\alpha = 1$, is only a portion of the entire arc-trench distance. Estimates of this seismic width W_i are obtained for individual arc segments i with lengths L_i by measuring the updip distances between the 'aseismic front', generally located at a depth of about 40 km, and the 'seismic front', generally at a depth of about 10 km along the 'main thrust zone' (for definition of these terms, see House and Jacob, 1983; Davies and House, 1979; Yoshii, 1975).

With these assumptions, we calculate the plate-kinematic moment rates

$$\dot{M}_{0i} = \mu \cdot L_i \cdot W_i \cdot \dot{u}_i$$

for each arc segment of length L_i , and from their sum

$$\dot{M}_0 \text{ arc} = \sum \dot{M}_0 i$$

the arc-wide moment release is obtained.

We assume a constant shear modulus of $\mu = 5 \times 10^{11}$ dyn cm^{-2} for the elastic properties of the plates near the fault contact; selecting the fault widths W_i for arc segments of length L_i , and the rates of relative motion \dot{u}_i between the North American and Pacific plates (after Minster and Jordan (1978), as indicated in Table 3.4.4), one obtains respective moment rates \dot{M}_{0i} listed in the same table, and a total moment rate for the arc. This arc-wide rate is

$$\dot{M}_0 \text{ arc} \approx 1.2 \times 10^{28} \text{ dyn cm y}^{-1}$$

It corresponds to one event with magnitude $M_w = 8.0$ per year if it were released at such an unrealistically even mode.

The calculated rate, based on plate kinematic assumptions, yields only 60% of the seismic moment that is instrumentally observed as

TABLE 3.4.4. Parameters for plate-kinematic model of seismic moment release.

Zone	Slip Rate \dot{u} (cm y ⁻¹)	Length L (km)	Width W (km)	Area A (10 ⁴ km ²)	Moment Rate \dot{M}_0^3 (10 ²⁶ dyn cm y ⁻¹)	$\dot{M}_0/100$ km (10 ²⁶ dyn cm y ⁻¹ /100 km)	Stress Rate $\dot{\sigma}$ (bar/y)
Yakutat- Yakataga	6.0	200	100	2.0	6.0	3.00	0.30
1964-rupture	6.5	800	180 (200-150)	14.4	46.8	5.85	0.18
1938-rupture	7.0	350	120	4.2	14.7	4.20	0.29
Shumagin Gap	7.5	300	100	3.0	11.25	3.75	0.38
1946-rupture	7.5	150	80	1.2	4.5	3.00	0.47
Unalaska Gap	8.0	200	60	1.2	4.8	2.40	0.68
1957-rupture	8.0	800	50	4.0	16.0	2.00	0.80
1965-rupture	8.5	700	50	3.5	14.875	2.125	0.85
Entire Arc	7.1 ¹	3500 ^{2,4} 3600	95.7 ¹	33.5 ²	118.925 ²	3.398 3.303	0.37 ¹

¹Weighted average.

²Sum over arc segments.

³Assuming $\mu = 5 \times 10^{11}$ dyn cm⁻².

⁴Sum of zone lengths falls short of total arc length (3,600 km) because of minor under-lap.

⁵Stress rate $\dot{\sigma} = \mu\dot{u}/W$.

mean-rate during the last 85 years (Figure 3.4.7). Either the model underestimates fault width, plate motion, or shear modulus by that much, or their product by some combination of either. Alternatively, one may conclude that the calculated rate of $\dot{M}_0 \text{ arc} = 1.2 \times 10^{28} \text{ dyn cm y}^{-1}$ is a correct lower bound for a long-term average, but that the sequence of great events between 1957 and 1965, including the giant 1964 event, was unusually seismogenic and released a larger moment than the arc typically does during one of its regular seismic cycles.

Using the plate-kinematic moment rates for each individual arc segment as listed in Table 3.4.4 and the moments for the last sequence of great earthquakes, we can calculate hypothetical recharge periods, i.e., the time required to accumulate by plate motion the moment that was released during the last great event. Furthermore, we can calculate the percentage of the full recharge time that has passed between the year of that event and now (1983). That value is >100% if the recharge date has been exceeded and <100% if it will be reached in the future. The results of these calculations are summarized in Table 3.4.5. They show that the Shumagin gap and the 1938-rupture zone are 'overcharged', i.e., they have stored seismic moment far beyond that released during their last significant events. Next in that sequence rank the 1946 rupture zone and the Yakataga gap which have restored less than half of their moment released last. In contrast, the 1964-, 1957-, and 1965-rupture zones have recovered less than 10 to 20% of their moments released in their last great events.

Note that for the purpose of these calculations we placed the 1903 ($M_w = 8.3$) event in the Shumagin Gap although there is little reason to believe it ruptured (the shallow or any portion of) the Shumagin Gap. Hence, the Shumagin gap may be charged more than here indicated from the instrumentally recorded events alone. We therefore consider the next historical record to see when in fact this gap had experienced some major strain relief prior to 1898.

3.4.7 Estimates of moment release associated with historic earthquakes. The Shumagin and probably the potential Unalaska seismic gaps experienced very little or virtually no moment release from truly great earthquakes during the instrumental period since 1898. We therefore consider the historic seismic record of the Aleutian Arc

TABLE 3.4.5. Recharge Status of Rupture Zones or Gaps Since Last Significant Events.

Arc Segment	Year of Event	M_w	Recharge Period (years)	Time Lapsed (years)	Due Date	Years Left	Years Overdue	P Percentage of Recharge
Yakutat-Yakataga Gap	1899	8.68 ¹	221	84	2120	137	--	38%
1964-zone	1964	9.2	170	19	2134	151	--	11%
1938-zone	1938	8.4	34	45	1972	---	11	132%
Shumagin Gap	1948	7.5	2	35	1950	---	33	>1000%
Shumagin Gap	1917	7.8	6	66	1926	---	57	>1000%
Shumagin Gap	1903 ²	8.3 ²	31	80	1934	---	49	258%
Shumagin Gap	1847/1788	8.78 ^{1,3}	136/195 ³	136/195 ³	1983 ³	0 ³	0 ³	100% ³
1946-zone	1946	8.3	79	37	2025	42	--	47%
Unalaska Gap	1878	8.4 ³	105 ³	105 ³	1983 ³	0 ³	0 ³	100% ³
1957-zone	1957	9.0	249	26	2206	223	--	10%
1965-zone	1965	8.7	95	18	2060	77	--	19%
Kommand.-Gap	1849/59	8.69 ^{1,3}	125 ³	129 ³	1983 ³	0 ³	0 ³	100% ³

¹Composite value of several events.

²Did probably not rupture Shumagin Gap.

³Computed value if event would recur in 1983.

that (at present) dates back to about 1784 (Sykes et al., 1980, 1981; Davies et al., 1981). Because for historic events no instrumentally determined moments or magnitudes are directly available, and because intensity reports are spatially very incomplete due to low population density, we have essentially only a few means to assess the sizes of events. For a few events their rupture lengths can be inferred from sparse intensity reports or tsunami reports at widely spaced localities for the same day. Another and new method, which we will apply here systematically, is the concept of the 'time-predictable' model (Shimazaki and Nakata, 1980). It postulates that the time ΔT (of seismic quiescence) between two great earthquakes on the same plate boundary segment is proportional to the moment release M_0 of the first of the two events, and they are related to the long-term plate-tectonic slip-rate \dot{u} (cm/y) by the relation

$$M_0 = \mu W L \dot{u} \Delta T$$

If we know the rupture length L for the event preceeding the time interval ΔT between two great events, and use the same parameters W , \dot{u} , μ as before (see chapter 3.4.6) then we can calculate a rough moment estimate for the event that preceeds the period ΔT (Table 3.4.6).

Note that the above equation can also be solved for

$$L = M_0 / (\mu W \dot{u} \Delta T)$$

We use this relation for those post-1898 events for which a moment and succeeding time-interval ΔT is known but no rupture-length is known because of poor aftershock coverage. We use this formula to estimate rupture length for seven great events ($M_w \geq 7.8$) that occurred between 1898 and 1929 and for which either no or only insufficient intensity reports exist. Applying this relation we find that between 1898 and 1929 about 60% of the 700 km long arc segment that broke in the single 1965 $M_w = 8.7$ event, had broken by a sequence of smaller events with magnitudes $7.8 \leq M_w \leq 8.2$ (Figure 3.4.8).

TABLE 3.4.6. List of great historic events and inferred source parameters based on the 'time predictable' model.

Date	M_w	M_0 (10^{28} dyn cm)	L (km)	W (km)	$\Delta\sigma_s^{1,2}$ (bar)	ΔT^3 (y)	Participating Zones ⁷
7/1788	8.76	17.88	650	130(100-180)	16	56,59	64,38,SG
8/1788	8.63 to 8.77	11.09 to 18.00	150 to 300	111(100-120)	50	158,195	SG,46
1792	8.4	5.01	150	180	10	62	64
1844	8.6	10.00	150	180	21	120	64
1847	8.7 ⁶	14.13 ⁶	500	114(100-120)	22 ⁶	1,70,91,136 ⁶	38,SG
1848	8.0 ⁴	1.26 ⁴	86 ⁵	86 ⁵	20 ⁵	32	38
1849	8.5 ⁶	7.08	250	50	110 ⁶	134 ⁶	KG
1854	8.6	10.00	150	180	10	110	64
1859	8.5 ⁶	7.08	250	50	110 ⁶	124 ⁶	KG
1878	8.4 ⁶	5.01	200	60	70 ⁶	105 ⁶	UG
1880	8.0 ⁴	1.26 ⁴	86 ⁵	86 ⁵	20 ⁵	23	38
Column Averages	8.47	8.43	245	112	41 (27.43)	92	

¹Simple stress drop' $\Delta\sigma_s = M_0 L^{-1}W^{-2}$ ²Note that 10^6 dyn cm^{-2} = 1 bar³ ΔT are the years until the succeeding event(s) on the same rupture zone.⁴Magnitude is estimated, not calculated from 'time-predictable model'.⁵Source parameters inferred by assuming $\Delta\sigma_s = 20$ bar.⁶Minimum value which increases if succeeding event occurs later than 1983.⁷Zones coded by year, i.e., 64 = 1964 rupture zone. SG = Shumagin Gap, KG = Kommandorski Gap, UG = Unalaska Gap.⁸Calculated from average M_0 , L, W.

We emphasize that for all these and the following calculations the same idealized assumptions apply that were used earlier: no aseismic slip must occur within the width W of the fault and the slip released in the quakes constitutes the entire plate motion when averaged over long periods of time (i.e., over many seismic cycles).

In many instances, we don't know the rupture length of historic events very well. To compute at least some very rough moment estimates we assume their spatial limits from whatever limited information is available. These assumptions are depicted in Figure 3.4.8 and closely agree, except for some minor details, with those of Sykes et al. (1980, 1981) and Davies et al. (1981). Where these authors left lateral extent of events undetermined, we arbitrarily made ruptures terminate at the nearest boundary of a tectonic subdivision. The Figure 3.4.8 shows the moments derived for historic events based on these assumptions and on the plate kinematic and time-predictable models. The calculated moments and magnitudes should not be taken as real, but as an indication whether our models and assumptions produce magnitude values that are at least plausible. In that sense they provide a test of the model assumptions.

Several remarkable results emerge from this exercise. None of the magnitudes M_w calculated from the inferred moments M_0 (these magnitudes M_w are shown in parentheses() in Figure 3.4.8) are unreasonably large for any of the historic events. The largest events considered, i.e., those in 1847 and 1788, are all smaller in magnitudes than those of the great 1957 and 1964 events, i.e., none of the calculated magnitudes are required to exceed $M_w = 8.9$. This finding may not necessarily support, but also does not contradict our earlier notion that the 1957-, 1964-, 1965-event sequence of truly great earthquakes may have been somewhat exceptional.

Furthermore, we have calculated hypothetical moment magnitudes M_w for unreported events that might have occurred, say, at about 1760. Using the arc-specific moment rates and the time-predictable model these hypothetical events serve to justify the long periods of apparent quiescence for which no important events are reported during both Russian and early U.S. ownership of Alaska. These hypothetical maximum-size events (assumed at 1760) are indicated near the bottom of

Figure 3.4.8 by unbracketed magnitude symbols M_w . For instance, except for the $M_w = 7.9$ event in 1905 and a normal faulting event $M_w = 7.9$ near the trench in 1929, virtually no great event has been reported in the 1957-zone since 1760, when Russian fur-trade and hunting expeditions in the arc near Amchitka and Attu were well underway, albeit without continuous Russian settlements. Nevertheless, the magnitude $M_w = 8.93$ that is required in order to be succeeded by such an extended quiescence - whether real or not - is still smaller than that of $M_w = 9.0$ for the 1957 event. We conclude that, while this quiescence since at least 1760 may not be real, it is permissible without requiring an unrealistically gigantic earthquake to precede it just prior to the arrival of Russian traders. Similarly, the 139-year long 'quiescence' between 1760 and 1899 in the Yakataga gap requires 'only' a $M_w = 8.55$ event at or prior to 1760; this magnitude is smaller than one derived from the combined moments of the 1899 Yakutat-Yakataga sequence.

As pointed out by Sykes et al. (1980, 1981) the historic record near the Shumagins and Kodiak is probably more complete than elsewhere along the arc. This applies to events since 1788 because of permanent Russian presence at Unalaska, Unga, Sanak, and Kodiak from at latest 1784 onward. Whether the more frequent reports of great events there reflect simply a difference in recurrence times (say 60 to 100 years) compared to more than 200 years in the 1957 zone cannot be resolved at present. The magnitudes and recurrence times permit either a true difference along the arc, a regular variance from one seismic cycle to the next, or incomplete historic records for large arc segments. If the latter is the case, the 1957 and 1964 events should be followed by above-average (quiescent) recurrence periods.

If the 1847 event with an inferred $M_w = 8.7$ ruptured only the eastern half of the Shumagin gap and not also the western half, and if the same applies to the July 22, 1788 event (inferred $M_w = 8.76$), then the event of August 7, 1788, can be calculated to have had a magnitude of at least $M_w = 8.63$ to cause the near-quiescence of the Shumagin gap lasting until now (1983). Should that event also have ruptured the entire 1946-zone then the inferred minimum magnitude for the August 1788 event increases to $M_w = 8.77$. Either magnitude

would be consistent with the tsunami effects at Sanak and the Alaska Peninsula described by historic reports (Sykes et al., 1980, 1981; Davies et al., 1981).

Because the hypothetical moment release for the August 1788-event may come from only a 150 to 300 km long segment it may have required rather high stress drops and/or stiffer elastic plates (increased μ) and thus may signify the Shumagin gap as a hard-to-break asperity. If the Shumagin gap constitutes such an anomaly, recurrence times for major events to break the gap could be prolonged over those of adjacent arc portions (i.e., the 1938 zone where they may measure as short as 60 years). Barring any misinterpretations during the instrumental period it seems that the western and eastern half portions of the Shumagin Gap were quiet for truly great events ($M_w > 8.0$) for 195 and 136 years, respectively.

On the other hand, as shown earlier (Table 3.4.5), the expected, ongoing quiescent periods (or recharge periods) in the 1957 and 1964 zones could last for 249 and 151 years, respectively, if the proposed plate-kinematic and time-predictable model is correct. Therefore the Shumagin gap may not be anomalous, but reflects the regular variations in the same segment of arc that may occur between different seismic cycles.

The 'time-predictable model' can be viewed as one extreme model which is contrasted by the 'slip-predictable' model (Shimazaki and Nakata, 1980). In the latter case the slip (and thus moment) of the earthquake succeeding the quiescent period is proportional to the duration ΔT of that period. If this model were valid we can calculate the magnitude of future great earthquakes breaking any given arc segment. For instance given the virtual quiescence (for $M_w > 8$) of 136 and 195 years of the eastern and western halves of the 300 km long Shumagin seismic gap we obtain a hypothetical magnitude $M_w = 8.72$ for the year 1983 in that gap, that would increase by small amounts each year. We have calculated these hypothetical magnitudes for the year 1983 for each arc segment. They are indicated near the top of Figure 3.4.8 (at year 1983) by the inverted brackets $)M_w($. Reinterpreting these magnitudes $)M_w($ by the 'time-predictable' model implies, that wherever they are less than the magnitude of the

previous great earthquake in the same arc segment a great earthquake is not yet likely. Where they exceed the magnitude of the preceding event, a great event is overdue but may have a magnitude different from the one indicated by M_w . Note that the highest value among the magnitudes M_w has been determined for the Shumagin gap, despite its associated short arc length of only 300 km. This indicates the implied readiness of that gap for a great event, whatever its actual magnitude may be. In fact the adjacent rupture zone of the $M_w = 8.4$ event of 1938 shows a value $M_w = 8.48$ which exceeds that of 1938 and thus may break together with the Shumagin gap in an event that could measure as great as $M_w = 8.8$ to 8.9. Similarly the probable Unalaska gap shows a high value $M_w = 8.4$ for its small (200 km) arc length provided it has not or was only partially ruptured in 1957.

Finally, we can make a present-day balance between the stored cumulative moment that is generated by the plate-kinematic process from a certain year onward up to date, and the cumulative moment released by great, historically and instrumentally reported earthquakes. We choose the arbitrary limits of this period to be 1760 and 1983. The results from this balance are indicated in Table 3.4.7. Assuming all underlying assumptions are correct, which most likely they are not, it shows that the 1964, 1946, and 1957 zone may have 'overspent' some of the (inferred) available moment (or slip), while the 1938, Shumagin and Unalaska Gaps, and, surprisingly, the 1965 zone would be capable of significant events at this time. In this assessment, the Yakataga gap would have just recently reached a moment balance. Note that the arc as a whole is nearly balanced by having to spare not more than the equivalent of a $M_w = 8.8$ to 8.9 at present. Since a balance in each arc segment depends highly on the accuracy of the instrumentally determined magnitudes and completeness of historic record as well as the choice of starting (1760) and termination (1983) of the period considered, little credibility should be attached to the moment balances for some of the arc segments with poor data quality.

3.4.8 Statistics of recurrence times and probabilities for great earthquakes. Figure 3.4.8 shows that since 1788 several of the arc

TABLE 3.4.7. Moment Balance (expressed in equivalent M_w) since 1760.

Arc Segment	Largest M_w	Moment Balance (measured in equiv. M_w)	Years Left	Years Overdue
Yakataga Gap	8.68 ¹	+7.32	--	2
1964 zone	9.2	-8.49	15	---
1938 zone	8.4	+8.29	--	23
Shumagin Gap	8.78 ^{1,2}	+8.29	--	31
1946 zone	8.3	-7.80	14	---
Unalaska Gap	8.4 ²	+8.44	--	118
1957 zone	9.0	-8.40	31	---
1965 zone	8.7	+8.70	--	94
Kommandorski Gap	8.69 ^{1,2}	+8.60	--	95
Entire Arc		+8.86		18.8

¹Composite of several events.

²Computed from time-predictable model.

segments broke more than once in great events. For instance, the 1938 rupture zone broke in 1847 and also in 1788; similarly, various subsections of the 1965 rupture zone broke around the turn of the century. Taking all observations of repeated ruptures of arc segments, and combinations or subdivisions thereof, we can make a list of recurrence intervals between all lead and successor events that bracket the recurrence intervals. Such a listing is compiled in Table 3.4.8. There are 11 observed recurrence intervals with lead events between 1788 and 1880, during the historic period. To those 11 data, a set of five minimum recurrence intervals can be added assuming that a successor event would occur in 1983 or later (see Footnote 1 of Table 3.4.8). This brings the total to 16 recurrence periods following 11 historic lead events (see also Table 3.4.6). There are 8 observed recurrence periods from as many lead events during the instrumental period 1898-1982 to which 5 'observations' of minimum-periods can be added if we assume that the Shumagin (1917) and Yakataga gaps (1899) and the 1938 rupture zone will break in 1983 or some time soon. Note that according to the plate-kinematic calculations, these zones, except for the Yakataga gap (see Table 3.4.5), have recovered their moments since their last event sequences, and hence this assumption is--within the plate kinematic model--marginally permissible.

Furthermore, there are the four great earthquakes of 1946, 1957, 1964 and 1965 that occurred too recently to have ruptured again. For these we can estimate recurrence periods from the 'time-predictable' model (see 'recharge-periods' in Table 3.4.5). These estimates are likely maximum values compared to most others since they are associated with lead events with rather large moments.

In summary, Table 3.4.8 contains a total of 33 data points of which 19 are observed, and 14 are computed values. We can rank the order of recurrence periods of Table 3.4.8 by their increasing magnitude (duration) and then assess the statistical properties of this data sample. In doing so we obtain:

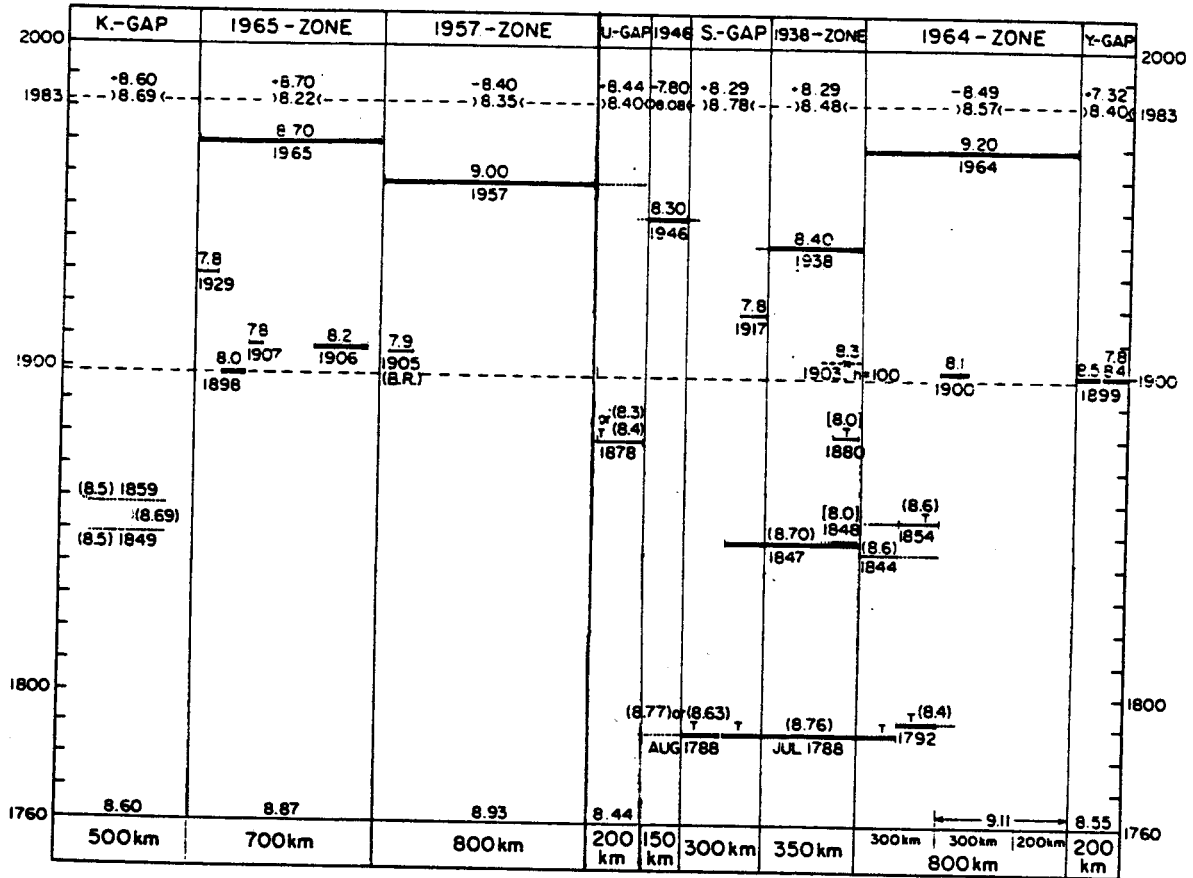


Figure 3.4.8. Space-time plot of instrumental (1898 to 1982) and historical (1788 to 1897) seismicity of the Aleutian arc considering great earthquakes ($M_w \geq 7.8$) only. Note that we have omitted from this plot a $M_w = 7.9$ event in 1929 that occurred presumably as normal faulting in the trench near the eastern end of the 1957 rupture zone. Each event is labeled by year, M_w , and (where applicable for historic events only) any tsunamis reported (T). Magnitudes computed for historic events from the 'time-predictable', plate-kinematic models are indicated in parenthesis. For hypothetical magnitudes plotted near 1760 and those indicated by M_w (at 1983, see text). The magnitudes plotted just above 1983 represent the theoretical moment balance (in equivalent M_w) for each arc segment. Positive values imply moments (measured in M_w) available for release, negative values imply that recent events have 'overspent' the moment and require a quiescent period of plate-motion-driven moment accumulation. Uncertain rupture zones are indicated by broken lines.

TABLE 3.4.8. Observed or computed recurrence times for rupture zones which broke during the historic and instrumental period 1788 to 1965.

Lead Event Year	M _w	Successor Event Year	M _w	Recurrence Period (years)
1788	8.8	1844	8.6	56
1788	8.8	1847	8.7	59
1788	(8.7) ¹	(1983)	?	(195)
1788	8.7	1946	8.3	158
1792	8.4	1854	8.6	62
1844	8.6	1964	9.2	120
1847	8.7	1848	8.0	1
1847	8.7	1938	8.4	91
1847	8.7	1917	7.8	70
1847	(8.7)	(1983)	?	(136)
1848	8.0	1880	8.0	32
1849	(8.5)	(1983)	?	(134)
1854	8.6	1964	9.2	110
1859	(8.5)	(1983)	?	(124)
1878	(8.4)	(1983)	?	(105)
1880	8.0	1903	8.3	23
1898	8.0	1965	8.7	67
1899	8.5	(1983)	?	(84)
1899	8.4	(1983)	?	(84)
1899	7.8	(1983)	?	(84)
1900	8.1	1964	9.2	64
1903	8.3	1938	8.4	35
1905	7.9	1957	9.0	52
1906	8.2	1965	8.7	59
1907	7.8	1965	8.7	58
1917	7.8	(1983)	?	(66)
1929	7.9	1957	9.0	28
1929	7.8	1965	8.7	36
1938	8.4	(1983)	?	(45)
1946	8.3	[2025] ²	?	[79]
1957	9.0	[2206]	?	[249]
1964	9.2	[2134]	?	[170]
1965	8.7	[2060]	?	[95]

¹The values in parentheses () are minimum values which increase if the successor event is not occurring in 1983 but at a later time.

²The values in brackets [] are likely to be maximum values and are calculated by the 'time-predictable' model from the magnitude M_w of the lead-event.

Number of data points: 33
 Smallest value: 1 year
 Largest value: 249 years
 Median value: 70 years
 Mean value: $\mu = 86$ years
 Standard Deviation: $\sigma = \pm 53$ years
 Mean + Standard Deviation: $\mu + \sigma = 139$ years
 Mean - Standard Deviation: $\mu - \sigma = 33$ years

The median and mean values should coincide if the sample population follows a normal distribution; the above results show, however, that this is not the case for these data. Therefore, we search for other distributions that provide a better approximation to the data. Eliminating the lowest value $T_R = 1$ year, we find that the remainder of the data are nearly log-normally distributed. Therefore we plot a histogram of the occurrences of the logarithm of recurrence times (i.e., $y = \log T_R$) in Figure 3.4.9 (bottom). This sample of data has the following properties:

Number of data points: 32
 Smallest value: 23 years
 Largest value: 249 years
 Median value: 74 years
 Logarithmic mean: $\mu_y = 1.88$ (i.e., $T_\mu = 76$ years)
 Standard Deviation: $\sigma_y = \pm 0.25$ (i.e., $T_{\mu \pm \sigma} / T_\mu = 1.78 \pm 1$)
 Mean + Standard Deviation: $T_{\mu + \sigma} = 135$ years
 Mean - Standard Deviation: $T_{\mu - \sigma} = 43$ years

Thus, after a double coordinate transformation

$$\begin{aligned}
 y &= \log T_R \\
 z &= (y - \mu_y) / \sigma_y
 \end{aligned}$$

we can find a normal (Gaussian) distribution for the scaled variable z that has the new properties (Bendat and Pierson, 1981):

Mean: $\mu_z = 0$
 Standard Deviation: $\sigma_z = 1$
 Variance: $\sigma_z^2 = 1$

The associated probability density function $p(z)$ and (cumulative) probability function $P(z)$ are:

$$p(z) = (2\pi)^{-1/2} e^{-z^2/2}$$

$$P(z) = (2\pi)^{-1/2} \int_{-\infty}^z e^{-\xi^2/2} d\xi$$

The cumulative probability $P(z)$ is plotted as the smooth curve in Figure 3.4.9 (upper frame) in comparison with the cumulative occurrence of observed recurrence periods (incremental curve), both of which have the same logarithmic mean μ , and standard deviation σ from the mean.

The distribution $P(z)$ shows that in the Aleutian arc there is a probability of only about 1% that the area of a great earthquake will rupture again in a great event after only 20 years, a probability of 50% that it will rupture after about 76 years, and of 90% after about 160 years. Table 3.4.9 lists selected values of probability P and associated recurrence periods T_R .

We have plotted in Figure 3.4.9 (near the upper margin) the holding times (up to 1983) for the last major earthquakes in each major arc segment. Projecting down from these values T_R in Figure 3.4.9 to the probability distribution $P(z)$ yields the probability as of 1983 that each arc segment has attained for the occurrence of a great event ($M_w > 7.8$). These probabilities $P(1983)$ are listed in Table 3.4.10. We note, for instance, that the two segments of the Shumagin gap that have last ruptured in 1788 and 1847, respectively, have reached respective probabilities as high as 95 and 85%, whereas the 1938 zone has reached (by 1983) a probability of only 18%.

3.4.9. Conditional probability and annual probability rate of occurrence. While it is interesting to know that the Shumagin gap has not yet broken despite such high cumulative probabilities, it is more important to ask the question: what is the probability that the Shumagin gap will rupture during the next, say 10 or 20 years, given

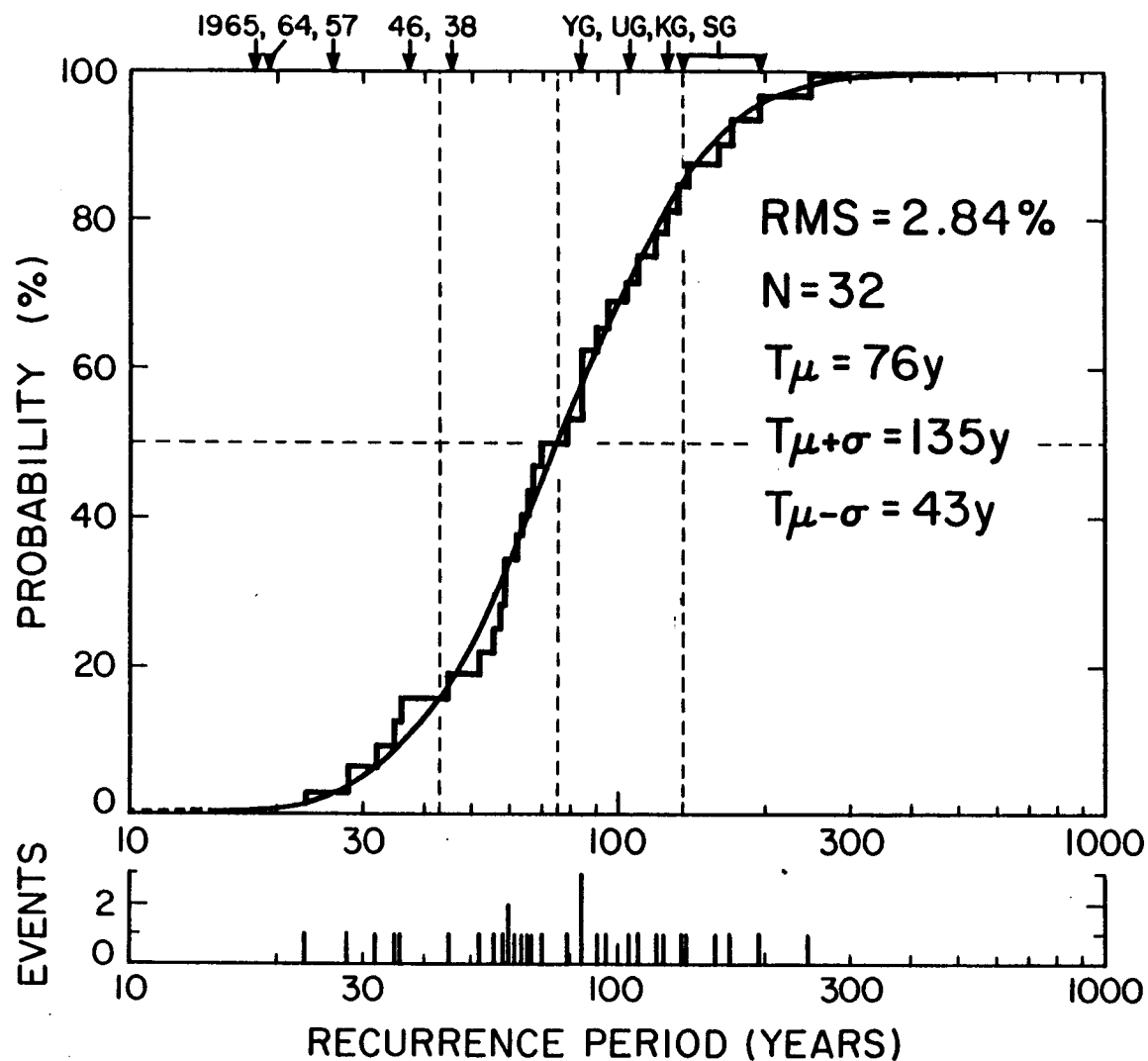


Figure 3.4.9. Statistical properties of recurrence periods. Bottom: Discrete probability density distribution of empirical recurrence periods. Top: Probability (in %) of empirical recurrence periods (incremental curve) and equivalent log-normal probability distribution (smooth curve) with the same logarithmic mean μ ($T_{\mu} = 76$ years) and standard deviation σ . Mean and deviation yield lower and upper values $T(\mu \pm \sigma)$ of 135 and 43 years, respectively (vertical dashed lines). Labels near upper margin of figure indicate the present (1983) holding times since the last great earthquake in each zone. Projecting these times down to the probability curve permits reading of the (cumulative) probability that each zone has attained as of 1983 for a great event with any magnitude $M_w > 7.8$ to recur; e.g., for the Shumagin Gap the probability is 85 to 95%, for the 1938-zone 18%, and only about 1% for the 1964 zone. Note that these cumulative probabilities are distinct from the conditional probabilities of any zone to break in a given future period; see text and Table 3.4.10.

TABLE 3.4.9. Probabilities P(%) for Recurrence Periods T_R (years).

P(%)	T_R (y)
1	20
5	29
10	36
20	47
30	56
40	66
50	76
60	88
70	102
80	123
85	138
90	159
95	195
98	247
99	288
100	∞

the condition that it has not ruptured during the last 136 or 195 years, respectively?

To answer this question we use the concept of the conditional probability defined as

$$P^*(T_R/T_R+\Delta T) = (P(T_R+\Delta T)-P(T_R)) (1-P(T_R))^{-1}$$

It constitutes the probability gain during the interval ΔT (during which the holding time increases from T_R to $T_R + \Delta T$), divided by the remaining probability increment $(1-P(T_R))$ which reflects the assumed certainty ($P=1$) that the gap will break sometime between T_R and $T=\infty$.

We have listed (Table 3.4.10) these conditional probabilities P^* which describe the chances (in percent) that any of the considered gaps or zones will break during the next one or two decades (i.e., during the periods 1983-1993 and 1983-2003, respectively). Note that these conditional probabilities P^* for the next 10 or 20 years vary much less (by a factor ≈ 5) from one region to another than do the probabilities P . Note also that the cumulative probability for the Shumagin gap increases by only $<2\%$ between 1983 and 2003 (from 95.0 to 96.5% for the August 1788 rupture segment), while the conditional probability $P^*_{1983/2003}$ that a great Shumagin event will occur between now (1983) and 2003, measures 30% (amounting to an average annual probability \dot{P}^* of about 1.5% per year). Hence, to maximize the chance for catching a great earthquake, say, for the purpose of monitoring strong motions from a great event, the chances to do so successfully in the next decade is about 4 to 5 times higher in any of the four gaps (Shumagin, Kommandorski, Unalaska, and Yakataga) than, for instance, in the 1964 or 1965 rupture zones. Correspondingly the hazards ratio is similar.

When studying all the particular tectonic and physical properties of a particular gap or arc segment, its specific behavior may very well be explicable partly deterministically. For instance, in the present analysis we have ignored the possible underlying physical causes for some systematic variations in recurrence times T_R . We did not account for the possible systematic effect that the known

variations along the arc of plate rates \dot{u} (cm/y), contact width W and average stress drop $\Delta\sigma$, or the shear modulus μ may have.

The deterministic formulation for recurrence time T_R is of the form (modified after Sykes and Quittmeyer, 1981):

$$T_R = (\Delta\sigma/\mu)/(W/\dot{u}) = M_0/M_0$$

We call $\Delta\sigma = M_0/LW^2$ 'simple stress' by implying that the usually associated geometrical constant C to be of uniform order 1, regardless of fault geometry. Given the dependence of T_R on $\Delta\sigma$, μ , W and \dot{u} , we could have first carried out a multivariate regression of the observed recurrence times (Table 3.4.8), then we could have removed the systematic effects of \dot{u} , W , $\Delta\sigma$, or μ if they existed, and would have obtained a new data set T_R' that presumably would have had a smaller variance σ^2 of the recurrence times from their new mean, provided a significant correlation between the original T_R and local values of \dot{u} , W , $\Delta\sigma$, and μ existed. We have abstained here from using such regression methods which will be reserved for future refinements.

3.4.10. When will the Shumagin Gap break? The key question remains: when will the Shumagin gap (or any of the other gaps) break? According to the deterministic models (that use only a single-value average behavior) the Shumagin gap should have ruptured several decades ago. When treated as part of a random process, it had a probability of about 90% to have broken by now. Given the fact it has not utilized the 90% probability, we can only estimate the probability, rather than a date itself, that it may rupture in, say, the next one or two decades. These conditional probabilities are 'only' about 16 and 30%, respectively, implying a 84 to 70% probability that this gap will not break in the next one or two decades, respectively. It remains to be seen whether the actual behavior of the gap happens to follow more closely the deterministic prediction of overdue imminence, or whether it will ride out the full range of unlikely high, but permissible cumulative probabilities that may be as high as 96% during the next 20 years while the annual probabilities are not exceeding a few percentage points. In all instances, a constant long-term preparedness for a great event is

warranted, that may have to be maintained for more than 2 decades. Shorter-term warnings can only be issued if a variety of seismic and other geophysical earthquake precursors are monitored and identified at a sufficient signal to noise ratio. These precursors can then be used to calculate temporary probability gains (Aki, 1981) that may raise the effective probability rates over and above those of the basic annual probability rates listed in Table 3.4.10 by factors of 30 or more.

Depending on when the Shumagin gap is ready to break, it may have a chance to rupture in a giant event, whose maximum extent (Figure 3.4.2) could include the 1938 rupture zone, the Shumagin gap proper, the Unalaska gap, and even may weakly rerupture the 1946 zone. Such an event, however unlikely, would have a maximum magnitude (calculated from a slip-predictable model) of about $M_w = 8.9$ to 9.0, depending on when it would occur.

3.4.11. Alternative probability model. In section 3.4.8 we have pointed out that a log-normal distribution yields a fit to the recurrence time data that is superior to that obtainable for a normal distribution. This conclusion may be largely due to the fact that we tried to make a statistical statement about recurrence times for the entire arc. Nishenko and Sykes (in preparation) made an analysis of recurrence times on restricted segments of the San Andreas fault and for portions of the Chile subduction zone. They argue that recurrence times for restricted portions of a fault that repeatedly break the same tectonic units are normally distributed. They find also that the standard deviation is only about $1/3$ of the mean recurrence time T , i.e., much smaller than in the case one obtains for the variation of recurrence times along the entire fault system.

Because of a basically different behavior of probabilities in a normally and a log-normally distributed data set for times $T_R \gg T_{\mu} + \sigma$, we present here for completeness an alternative model, the results of which illustrate the great uncertainties that still exist in these assessments when the known seismic history covers at best only 2 to 3 mean recurrence intervals.

For this alternative model we eliminate the smallest ($T_R = 1$ year) and the four largest recurrence times ($T_R = 249, 195, 170$ and

TABLE 3.4.10. Cumulative, conditional, and annual probabilities for great earthquakes in 1983, 1993 and 2003, and intervals in between, respectively, for major Aleutian rupture zones and gaps for log-normally distributed recurrence periods (N = 32; $T_{\mu \pm \sigma} = 76 \times 1.78^{\pm 1}$ years).

Zone	Year of Last Event	Lapsed Time T_R (years) Until 1983	Cumulative Probabilities P(%) ²			Conditional Probabilities P*(%) ³		Annual Rate \bar{P}^* (%/y) ⁴ (10 year avg.) 1983-1993
			1983	1993	2003	1983-1993 ($\Delta T_R=10y$)	1983-2003 ($\Delta T_R=20y$)	
Shumagin	1788	195	95.0	95.8	96.5	16.0	30.00	1.6
Shumagin	1847	136	84.5	87.2	89.5	17.4	32.3	1.7
Kommandorski	1854 ¹	129 ¹	82.2	85.3	88.	17.4	32.6	1.7
Unalaska	1878	105	71.4	76.5	80.7	17.8	32.6	1.8
Yakataga	1899	84	57.1	63.2	71.4	18.9	33.3	1.9
1938-rupture	1938	45	18.2	28.8	39.4	13.0	25.9	1.3
1946-rupture	1946	37	10.6	20.3	30.9	10.9	22.7	1.1
1957-rupture	1957	26	3.1	9.8	19.3	6.9	16.7	0.7
1964-rupture	1964	19	0.8	4.7	18.4	4.0	11.7	0.4
1965-rupture	1965	18	0.6	4.2	11.3	3.6	10.7	0.4

¹Average for 1849/59.

²See curve in Figure 3.4:9.

³ $P^*(1983 \text{ to year } X) = (P_x - P_{1983}) / (1 - P_{1983})$.

⁴ $\bar{P}^* = P^* / \Delta T_R$, with $\Delta T_R = \text{year } x - 1983$.

158 years) from the data set of Table 3.4.8. This yields a new restricted data set with smaller variance, to which we can marginally fit a normal (rather than a log-normal) distribution.

The new data set has the properties:

Number of data points: 28
 Smallest value: 23 years
 Largest value: 136 years
 Median value: 66.5 years
 Mean value: $\mu = 73$ years
 Standard deviation: $\sigma = \pm 32$ years
 Mean + Standard Deviation: $\mu + \sigma = 105$ years
 Mean - Standard Deviation: $\mu - \sigma = 41$ years

The histogram (probability density) of recurrence times T_R and the associated cumulative probability function $P_c(\%)$ are shown in Figure 3.4.10 and the probabilities and conditional probabilities derived for the various arc segments from this normal distribution are summarized in Table 3.4.11. The latter differ from those in Table 3.4.10 (log-normal distribution) in several important ways.

Most prominently, the cumulative probabilities increase to values very close to 100% for gaps whose holding times T_R exceed substantially $T_{\mu+\sigma} = 105$ years (i.e., the Shumagin and Kommandorski gaps). Moreover, the conditional probabilities for a great event to occur during the next 10- or 20-year periods increase monotonically with increasing holding time T_R and measure up to about 5 times higher than those for the log-normal distribution. The same applies of course to the annual probability rates.

The basic reason for these differences lies in the fact that the conditional probability P^* for a fixed small time interval ΔT (into the future) is in the two cases, respectively

normal distribution: $P^* = (p(z)/(1-P(z)))\Delta T/\sigma$

log-normal distribution: $P^* = (p(z)/(1-P(z)))\Delta T/(T\sigma)$

where

$$p(z) = (2\pi)^{-1/2} e^{-z^2/2}$$

$$P(z) = (2\pi)^{-1/2} \int_{-\infty}^z e^{-\xi^2/2} d\xi$$

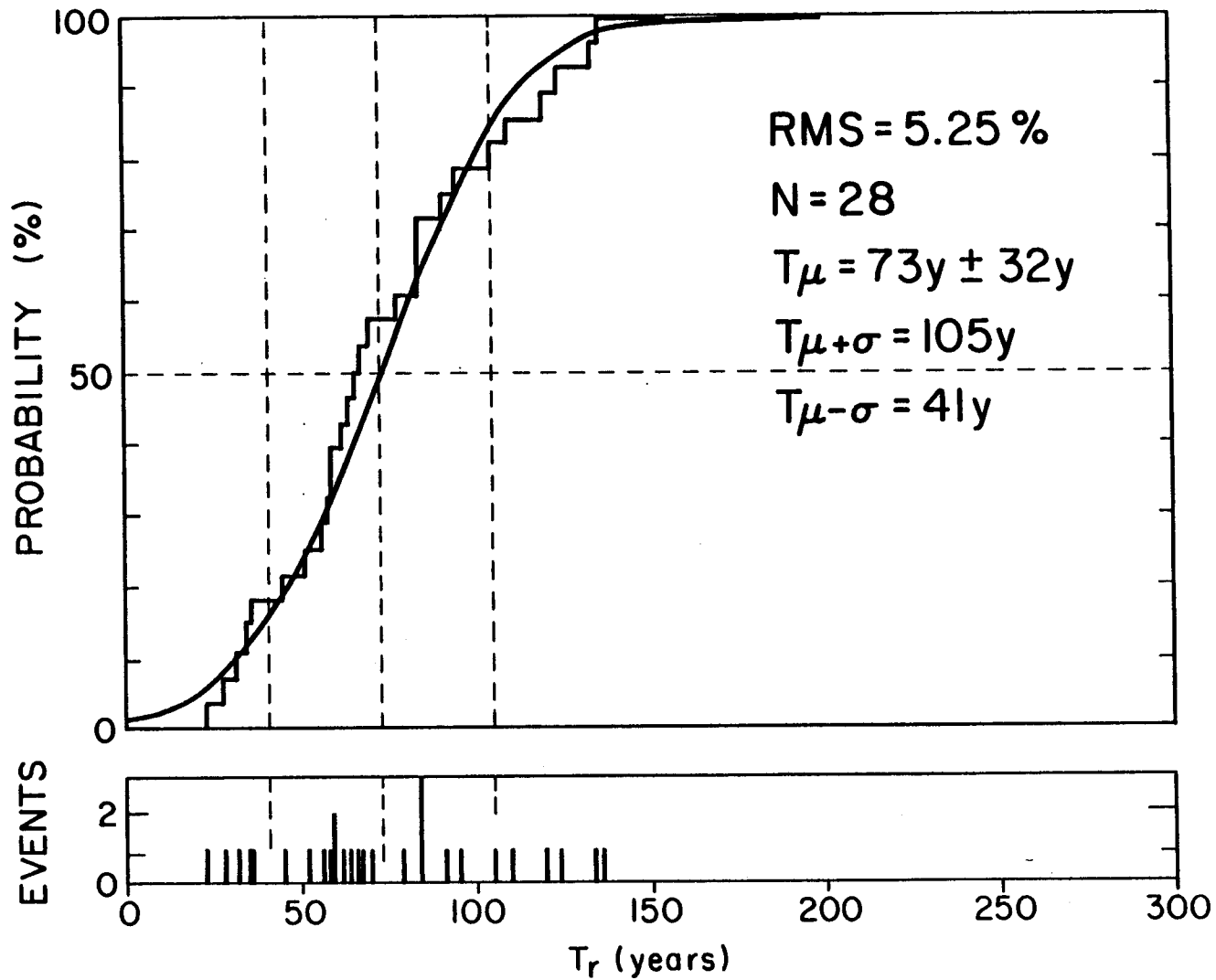


Figure 3.4.10. Same as Figure 3.4.9 except that a normal (rather than a log-normal) distribution (solid line) is fitted to observed recurrence times distribution which consists of a reduced number ($N = 28$) of samples. Note the poorer misfit ($RMS = 5.25\%$) between fitted curve and observations compared to that ($RMS = 2.85\%$) achieved for a log-normal distribution shown in Figure 3.4.9.

TABLE 3.4.11. Cumulative, conditional, and annual probabilities for great earthquakes in 1983, 1993 and 2003, for major Aleutian rupture zones assuming normally distributed recurrence periods ($N = 28$; $T_{\mu \pm \sigma} = 73.5 \pm 32$ years).

Zone	Year of Last Event	Lapsed Time T_R (years) Until 1983	Cumulative Probabilities P(%)			Conditional Probabilities P*(%)		Annual Rate P*(%/y) 1983-1993
			1983	1993	2003	1983-1993 ($\Delta T_R=10y$)	1983-2003 ($\Delta T_R=20y$)	
Shumagin	1788	195	99.99	99.999	99.9999	~90.	~99.	9
Shumagin	1847	136	97.5	98.8	99.5	54.3	80.3	5.4
Kommandorski	1854	129	95.9	98.0	99.1	50.4	77.6	5.0
Unalaska	1878	105	83.8	91.9	94.6	49.7	66.8	5.0
Yakataga	1899	84	62.9	73.9	83.1	29.7	54.4	3.0
1938-rupture	1938	45	18.6	28.2	39.6	11.7	25.7	1.2
1946-rupture	1946	37	12.6	20.4	30.3	8.9	20.3	0.9
1957-rupture	1957	26	6.9	12.1	19.5	5.6	13.6	0.6
1964-rupture	1964	19	4.4	8.1	14.1	4.0	10.1	0.4
1965-rupture	1965	18	4.1	7.7	13.4	3.8	9.6	0.4

σ = standard deviation around mean μ , and T holding time. Note that $z = (T-\mu)/\sigma$ for normal distribution, and $z = (\log T - \mu)/\sigma$ for log-normal distribution.

Thus, with increasing T the values P^* for the log-normal case gradually decrease again, while they monotonically increase for the normal distribution.

The consequences for hazards assessment of these differences in the statistical models are summarized in the pertinent hazards assessment section (Section 4.1).

3.5 Historical Eruptive Activity of Pavlof, Akutan, and Makushin Volcanoes

In order to better understand their eruption styles, we made a detailed, systematic, and thorough search of all available literature pertaining to historic activity of the 4 volcanoes, Pavlof, Pavlof Sister, Akutan, and Makushin¹. Results of the compilation of historic records are shown in Tables 3.5.1-3.5.4. This compilation updates and completes that given in Simkin et al. (1981) (our Table 3.5.5). Symbols are standard symbols used in the Bulletin of Volcanic Eruptions (see figure caption). We find that Pavlof and Akutan volcanoes, with 27 and 28 reported eruptions since 1760, respectively, are two of the most active volcanoes in North America. Figures 3.5.1a,b,c show the number of years per decade with reported eruptions for Pavlof, Akutan, and Makushin from 1760 to the present time. Pavlof and Akutan show more reported eruptions in recent years than in the past, suggesting that the more numerous reports during the past 60 years may represent merely better reporting, rather than a real increase in activity. Makushin, however, appears to be less active today than it was approximately 150 years ago (Figure 3.5.1c).

1973-1982 eruptive activity of Pavlof Volcano. Based on the study of seismicity associated with volcanic activity at Pavlof, we have identified two main eruption styles (McNutt, 1981a,b; McNutt and Beavan, 1981) (see also Appendix 7.5). One is a vigorous effusion of lava lasting 1-2 days accompanied by strong volcanic tremor. Significant amounts of ash are often erupted to heights as great as 37,000' during these eruptions, and lava commonly flows down the flanks of the volcano to distances of 3-4 km. The second eruption style consists of numerous small explosions, as many as 13 per hour, which occur during episodes lasting from several days to about 2 months. The explosions are accompanied by B-type earthquakes (shallow

¹D. Shackelford and S. McNutt completed the job of cross-referencing and verifying all reports as originally compiled by S. Hickman at Lamont-Doherty Geological Observatory in 1978-1980.

emergent events lacking a clear S-phase), which occur in the highest numbers a few days before the onset of explosive activity (McNutt and Beavan, 1981). Examples of the seismicity accompanying each of these eruption types are shown in Appendix 7.5.

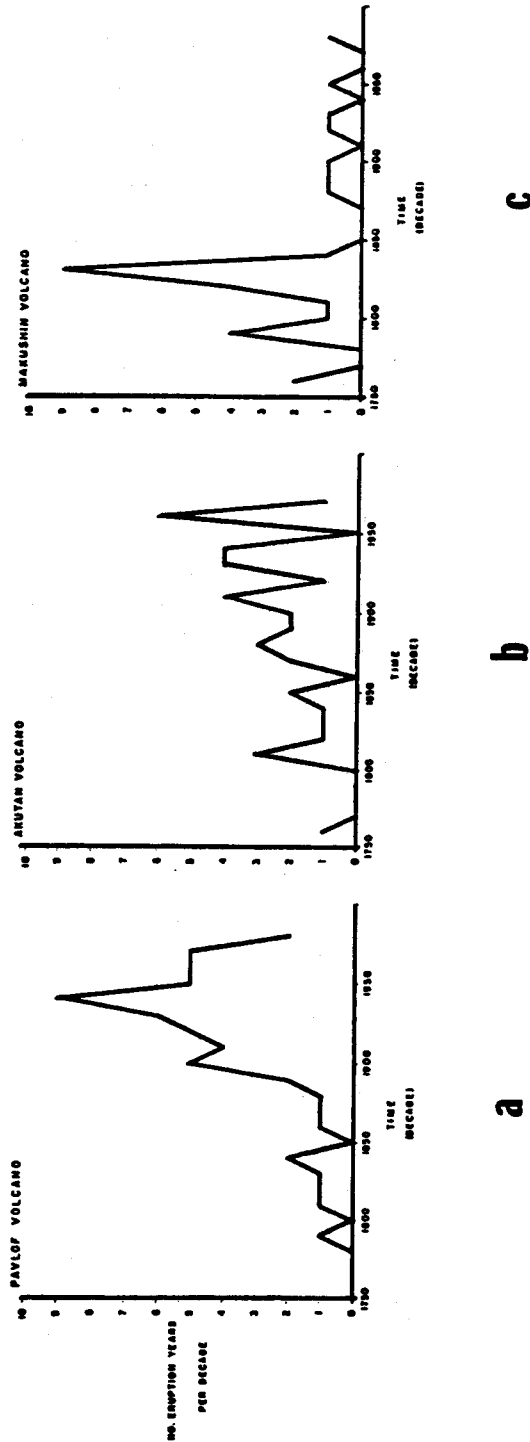


Figure 3.5.1. The number of reported eruptions per decade vs. time. a) Pavlof volcano; b) Akutan volcano; c) Makushin volcano. At Pavlof and Akutan, the apparent increase in activity after 1900 is probably caused by more complete reporting. However, Makushin seems to have had a real increase in activity around 1830.

TABLES 3.5.1-3.5.4. Data from literature search on eruptive activity at Pavlof, Pavlof Sister, Akutan, and Makushin Volcanoes. Compilation by D. Shackelford, S. Hickman, and S. McNutt, 1982, 1980, and 1983, respectively. Symbols used are standard symbols from the Catalogue of Active Volcanoes of the World and the Bulletin of Volcanic Eruptions. Symbols are shown below. (Note: all measurements are given as they appear in the original reports (for example, miles are still miles) to preserve original accuracy.)

CONVENTIONAL SYMBOLS used in the Catalogue and the Bulletin of Volcanic Eruptions

○	Eruption in the central crater	△	extrusion of a spine
◦	eruption in a parasitic crater	↑	phreatic explosions, mud eruptions
◌	eruption in a radial fissure	→	mud flows
=	eruption in a regional fissure	∞	subglacial eruptions
↑	normal explosions	⋈	submarine eruptions
→	eruptions producing nuées ardentes*	★	islets formed by submarine eruptions
⇒	lava flows	≡	tidal waves (tsunamis)
∇	eruptions in a crater lake	‡	solfatara fields, vapours
∩	eruptions in a lava lake	☒	destruction of arable land
△	extrusion of a lava dome	†	casualties

(* including ash flow, pumice flow etc.)

TABLE 3.5.1. Pavlof Sister (55.45°N, 161.87°W)

<u>Date</u>	<u>Activity</u>	<u>Additional Information</u>
1762-1786	(○?) ↑ (∩?)	Eruptive period with strong eruption in 1786. The 1786 eruption accompanied by a strong earthquake (X on Rossi-Forel scale)*. It may be that only 1786 is from Pavlof Sister, the other eruptions may be from Pavlof (identity of active volcano is unclear). Observations in 1928 found fissure or breach on the cone, and there was a summit tholoid. Both features likely formed in 1786, as reports suggest violent activity ("mountain top fell in").

*A recent investigation by Sykes et al. (1981) showed that a strong earthquake occurred on July 22, 1788, yet no mention is made of a strong quake in 1786. Since X is the highest intensity on the Rossi-Forel scale, we infer that the correct date for both the earthquake and the eruption probably should be 1788.

TABLE 3.5.2. Pavlof (55.42°N, 161.90°W)

<u>Date</u>	<u>Activity</u>	<u>Additional Information</u>
1762-1786	↑	With felt earthquake, probably Pavlof Sister (see footnote, TABLE 3.5.1).
1790	↑	
1817	↑	Lapilli falls.
1825	↑?	Eruption of unknown character.
1838	↑ or ⤴	Smoking.
1845, 12 August	↑	Powerful eruption of glowing tephra.
1846, August	○ ↑ ≈	Glowing tephra erupted from vent near summit, ash falling 55 mi. to E (Unga I.) with lava flow down E flank.
1852, early August	⤴	Not an eruption, steaming from vent high on N flank.
1866, 14 March	↑	Identity of volcano uncertain. Ashfall on Kodiak I. (?) left ½" of ash during 15 minute period at ca. 0300.
1886	○	Red glares.
1892	○ ↑	"Fire" at night, from summit.
1894	○ ↑	"Fire" at night, from summit.
1901	↑	
1906-1911	○ ○ ↑ ≈	Continuous minor eruptions from summit from 1906-1911. The most powerful historic eruption of Pavlof took place in December of 1911, most notably 6-7 December. The N flank opened, there was lava flow- age, ejection of large blocks, roarings heard at Unga I. (55 mi. away), and felt earthquakes took place (possible nuees ardentes, too. See 1928).
1914, 06 July	↑	Ash fell on Unga I. between 1430 and 1800. Also, eruptions may have taken place on 15-16 July, but this date is likely to be that of 6 July.
1917, October	↑	Ashfalls, felt earthquake at King Cove.
1922, 24 December-1925	○ ↑	Notable eruptions on 24 December 1922 (glow light up Belkofski vil- lage), in winter 1923, and on 17 January 1924.
1928, 28 June	⤴	Observations by Jaggar found the 1911 fissure still present, with two, concentric and small cinder cones at its upper end at the sum- mit, with surrounding lava field. Evidence of low-angle blast from the summit crater.
1929, March-1931, summer	○ ↑	Period of minor, continuous ash emissions with increased eruptivity in December 1929 and 30 March and 20 May 1931.
1936-1948	○ ↑ ≈	Significant eruptions in 1936, July 1937, and 1942. Lava flow may have been extruded in May 1948. Otherwise, minor, nearly continuous ash emissions. Photo taken in 1942 shows 1911 fissure no longer present (the wound had been healed), and a single cinder cone on upper NE flank (moat between this cone and summit, but flanks of cinder cone merged with Pavlof proper elsewhere).
1950, 31 July- 1953, 25 November	○ ↑	Period of intermittent, occasionally strong ash eruptions. Power- ful eruption on 1 August 1959, with glowing tephra rising 1 km. Strong activity in November 1951, in winter of 1951-1952, and on 25 November 1953 (glow from eruption seen in Pribilof Is.).
1958, 17 May-28 August	○ ↑ ≈	Small eruptions of pumice and dust from vent shifting around the upper NNE flank. Lava flow (rootless?) or lava cascades moved downslope on 17 May.
1960, ca.-1963, ca.	○ ↑ ≈	Mild ash eruptions, especially July 1962-June 1963.
1966, 15 March	○ ↑	Note: during the 1950's and 1960's, the active vent was never exactly located, it shifted around with each eruption high on NE or NNE flank.
1973, 12-13 November	○ ↑ (→?)	Brief, high-amplitude explosive eruption (lava flow may have occur- red) with harmonic tremor. Possible nuees ardentes down NE flank. Ash fell on Cold Bay, 35 mi. away.

1974, 02 September-
1975, 06 January

○ ↑

Moderate ash eruptions, plume rising to max. 6 km a.s.l. Reports of lava flow may be incorrect. Explosions and intermittent tremor recorded.

1974, 14-24 March

○ ↑

Period of probable weak ash emissions. Explosion earthquakes recorded.

1975, 13 September-
1977, March

○ ↑ ≈ (≈?)

Period of generally weak ash emissions, often likened to the chugging of a locomotive. Strong activity 18 September-6 October 1975, 6-12 October 1976, 2-22 November 1976. Both harmonic tremor and explosion earthquakes recorded. Strong explosions, some felt. Short-lived lava flows in October 1975, in February and December 1976, and none in 1977. Some may be lahars, or rootless, spatter-fed lava flows.

1979, July

↑
↑
↑

Summit venting of light steam plume.

1980, early July

Steaming and possible weak ash emission in early July 1980.

1980, 8-13 November

○ ↑ ≈

Seismic activity began 8 November. Strong eruption from 11-13 November from vent on NE shoulder, lava fountaining 300 m high, plumes to 11 km a.s.l., and lava flow down N flank. Harmonic tremor recorded.

1981, 30 March-28 May

○ ↑

Period of probable weak ash emissions. Explosion earthquakes recorded.

1981, 25-27 September

○ ↑ ≈

Strong eruption, with eruptive plumes to 10.5 km a.s.l., lava flow (from vent 100 m below summit on N flank) to 600 m a.s.l. on NNW flank, and glow visible over some distance. Ca. 1 cm of ash fell at Squaw Harbor (Unga I.) as fine sand. Medium-coarse sand fell on Pavlof Bay. The lava flow may have been rootless and spatter-fed. Both B-type earthquakes and harmonic tremor recorded.

TABLE 3.5.3. Akutan (54.13°N, 166.00°W)

Date	Activity	Additional Information
1760's	↑ ?	
1778	Quiet	
1785	Quiet	
1790	⊗ or ↑	
1828-1830	↑ or ⊗	
1838	↑ or ⊗	
1845	⊗ or ↑	
1848, early March	(○ ?) ↑	In the first few days of March, with felt earthquakes.
1852, 01 September	○○↑ (≈?)	Eruption from NW flank (Lava Point or Bight), 5.8 km from summit.
1862	⊗ or ↑	
1865, 04-05 September	↑	Widespread glow visible.
1867	(○ ?) ↑	
1880	⊗	
1883	↑	
1887	↑ ≈	
1892, July-23 September	○ ↑	Explosions audible 30 mi. away. Plumes 1,000' high on 23 September, with felt earthquake.
1894?	○ ↑	This may be the 1892 eruption, or may be active from 1892-1894.
1896	↑	
1907	○ ↑	Year-round explosive activity from the central cone, which appeared to be much lower than present. Felt earthquake on 22 August.
1908, 22 February	↑ ≈	
1911-1912	↑	Ash fall on Akutan village in 1911.
1920's, mid or late	(∞ ?) ↑	Imprecise date of possible eruption on NW flank (Lava Point).
1927-1928	↑	Activity stronger in 1928. Weak, felt earthquakes in 1927.
1929, May-December	○ ↑ ≈ ≈	Possible lava flow in May. Lava flow in December through caldera gorge on NW, generating a mudflow. Earthquakes felt.
1931, May-11 August	○ ↑	Intermittent eruptions from the central cone. Central cone described as 600' tall and uniformly hot. Lake on S or SW floor of caldera; hot on side adjacent to cone.
Sometime between 1942 and summer 1944	none	Central cone still hot (or, perhaps, ash-covered).
1946, December-1947, January	○ ↑ ≈	Lava flow in December 1946, and another in January 1947 from SW base of central cone. The 1947 flow was 3/4 mi. x < 1/2 mi. in extent, confined to caldera, and had ended by 4 January.
1947-1953	○ ↑ (≈?)	In August 1948, central cone ca. 700' tall. Eruption plumes 1 mi. high. The August 1948 observations showed two lakes in the caldera, perhaps recent (post-1931) lava flows had divided the original lake. Lava flow possible in May 1948.
1972, 17 September?-1973, after 22 May	○ ↑	Eruptive plumes to several km in ht.
1974, 11 February	○ or ∞ ↑ (≈?)	Eruption observed at 0900Z. Original report of lava flow appears to be in error. Eruption site originally indicated as NW flank, but this is not clear at present.
1976, Fall-1977, May ?	○ ↑	Periodic Vulcanian eruptions, still erupting on 9 May 1977.
1978, Late September-6 October (or beyond)	○ ↑ ≈	Strong explosions lofted large, glowing (car-sized) blocks 100 m over crater. Probable lava flow into caldera gorge.
1980, July	○ ↑ or †	Small ash eruptions, plumes 0.5 to 1.0 km in ht.

TABLE 3.5.4. Makushin (53.90°N, 166.93°W)

<u>Date</u>	<u>Activity</u>	<u>Additional Information</u>
1760's	↑	
1768-1769	↑	Major explosive eruption.
1778		Not active.
1790, 07 June-1792	↑	Periodic eruptions.
1795	⌵	Off SE coast, identity uncertain.
1802	↑	Major explosive eruption, with great earthquakes.
1816-1817		Quiet.
1818	↑ or ☸	With felt earthquakes.
1826, June-1838	↑ and ☸	Strong explosive eruption in June 1826, with two felt earthquakes, then minor activity ("smoking") into 1838.
1844	☸	Eruption very doubtful.
1845	↑	Eruption from a fissure (site unspecified).
1865	☸	Eruption very doubtful.
1867	☸	Eruption doubtful.
1871-1874	☸	
1880	☸	
1883	↑	Minor ash eruption.
1891	☸	
1892	○ ☸ or ⚡	In July, main vent of central cone showed intense, high-pressure steaming, with occasional subterranean explosions.
1894?	☸	May be 1892.
1895	☸	
1907	○ ☸ (↑?)	Observations on 3 July found strong thermal activity on N portion of central cone, and other areas within the caldera. New crater found within caldera ("Technology crater"), apparently between central cone and N rim of caldera.
1912	☸ or ↑	
1926, 30 December	↑	Eruption of evening of 30 December, with "fire fountains" and slight felt earthquake.
1931		Quiet, no steaming.
1938, October	↑ or ☸	Minor explosive eruption.
1944, September	○ ☸	Strong thermal activity (on N flank?) of central cone, caldera wall, and onto caldera flank.
1951, 20 December	○ ↑ or ⚡	High steam column with ash on snow.
1952	☸ or ↑	Eruption doubtful.
1953, December	☸ or ⚡	Steam plumes, eruption very doubtful.
1980	○ ☸ (⚡)	Observations on 8 July found thermal activity on summit of central cone. Also, just below summit on S flank, a new, small explosion crater with tephra and impact pits extending 60 m to SE from vent.

VOLCANO NAME (SUBREGION)	LAT	LONG	ELEV	TYPE	NUMBER	STATUS	START	STOP	ERUPTIVE CHARACTERISTICS											
									YEAR	M-OY	P	YEAR	M-OY	CERF	SIGC	ENPS	FLOS	FCMT	VEI	
BOGOSLOP (ALEUTIAN IS)	53.93 N	166.03 W	+0046	SUBM	1101-30	HISTORIC														
CASTLE ROCK							1796	05												37
							1804													2
							1806		1823											2
GREWINGK							1883	0927	1895B											3
METCALF CONE, MCCULLOUGH PEAK							1906	0301P	1907	0901										3
TANOMA PEAK							1909	09	1910											2
							1913													2
							1926	07	1928											2
							1931													1
							1951													0
MAKUSHIN (UNALASKA I)	53.90 N	166.93 W	+2036	STRA	1101-31	HISTORIC														
							1788		1788											3+
							1790	0607	1792											3
							1802													3
							1818													3
							1826	06	1838											3
							1844													2
							1865													2
							1887													2
							1883													2
							1907													2
							1912													2
							1926													2
							1938	10												2
							1951	1229												1
							1952													1
							1980	05015												1
AKUTAN (ALEUTIAN IS)	54.13 N	166.00 W	+1303	STRA	1101-32	HISTORIC														
							1790													
							1838													
							1845													
							1848	03												2
NW FLANK, 5.8 KM FROM SUMMIT							1852													2
							1865													2
							1867													2
							1883													2
							1887													0
							1892													2
							1896													2
							1907													0
							1908	0222												2
							1911													2
							1912													2
							1928													2
							1929	05												2
							1931													2
							1946	12	1947	01										2
							1948	10												2
							1951	10												2
							1953													2
							1972	09	1973	06										2
							1974	0211												2
							1976	10150	1977	0509										2
							1978	0925E												2
							1980	07	?											2
GILBERT, MOUNT (AKUN I)	54.25 N	165.85 W	+0819	HYDR	1101-33	FUMAROLIC														
POGROMNI (UNIMAK I)	54.57 N	164.70 W	+2002	STRA	1101-34A	HISTORIC														
							1795													4
							1820													0
							1827													2
							1830													2
WESTDAHL (UNIMAK I)	54.52 N	164.85 W	+1560	STRA	1101-34B	HISTORIC														
							1964	0310	1964	0416										2
							1978	0204	1978	0209										2
FISHER (UNIMAK I)	54.67 N	164.35 W	+1094	STRA	1101-35	HISTORIC														
							1828	1011	1827	01										3
SHISMALDIN (UNIMAK I)	54.75 N	163.97 W	+2857	STRA	1101-36	HISTORIC														
							1775		1778											
							1790													3
							1824													2
							1825													2
							1827													2
							1830	11	1830	12										3
							1838													2
							1842													2
							1865													2
							1880		1881											2
							1883													2
							1887													2
							1888													2
							1889													2
							1901													2
							1912													2
							1922													2
							1925													2

3.6 Geology and Geodetic Surveys

To supplement the seismic monitoring, L-DGO scientists have carried out some geologic mapping and geodetic leveling in the Shumagin Islands region since 1972. Dr. M. A. Winslow was in charge of the geologic mapping that mainly consisted of determining Holocene uplift rates by surveying, sampling, and dating uplifted marine terraces. Dr. J. Beavan was in charge of annual resurveying and expanding the geodetic leveling network up to 9 lines that are located on different islands. The purpose of maintaining the leveling lines is to determine the pre-, co- and postseismic deformation resulting from the forecast great earthquake.

Winslow (1982) presents the results of the geologic surveys and below we have included a summary of the main results.

Holocene uplift. The results on the ages and elevations of marine terraces indicate that the Alaska Peninsula and Inner Shumagin Islands have been uplifting tectonically at an average rate of about 7 mm/year over the past 10,000 years. The Outer Shumagins show a more complex history, possibly involving tectonic subsidence as well as uplift. None of the identified uplifted surfaces could be identified as being the result of one specific earthquake. The presence of large depositional or wave cut surfaces represent relatively long periods of stability near sealevel which were followed by sudden uplift of a sufficient magnitude to raise these features above the inter-tidal zone. Although we were unable to establish recurrence intervals between individual events, the presence of terrace levels can be explained only by sudden emergence due to major earthquakes. Thus, the 7 mm/yr average uplift rate is the slope of a curve which is actually episodic.

Recent faulting. A critical appraisal of aerial photography was done between the 1979 and 1980 field seasons. Two faults on which we suspect Holocene motion have been bracketed with benchmarks in case they are reactivated by a major earthquake. One fault intersects the Korovin level line, and the other is a high angle fault which separates Popof Head from the remainder of Popof Island. Several other recent faults were noted in the area including ones on northwest

Korovin and southeast Unga, and at Zachary Bay, Squaw Harbor (Unga) and Cape Aliaksin (peninsula). Holocene displacements are recognized by abrupt offsets in terrace heights, fault scarps intersecting till, or by development of fault scarps in soft sediment with linear trends of several kilometers. All of these faults are high angle faults striking NNW-SSE or NE-SW. The displacement history is presently unknown on all of these faults. Due to the ratio of water to land and the linear nature of several coasts, it is likely that major faults lie between islands. In fact, the linear segments of some coasts defined by seacliffs of rock and sediment and the lack of a wide shelf all suggest fault control, especially those areas where streams intersect the coast as waterfalls.

The levelling network that is described by Beavan et al. (1983) presently consists of nine short level lines which are measured, annually if possible, to first order standards. The lines vary in length between 600 and 1200 m. Their locations and azimuths are shown in Figure 3.6.1. Line L1 at SQH was established in 1972, line L2 at SPA in 1977 and the others since then. Figure 3.6.2 shows the results from all the lines which have been measured more than once.

The two dots plotted for each year represent the results of the forward and backward runs of levelling. The error bars are standard deviations ($\pm 1\sigma$) calculated from the scatter of several readings of each stadia rod from each tripod position. When the error bars from forward and backward runs overlap we can be more confident that no systematic error or blunder has occurred during the run.

The clearest feature of the SQH data is the trend between 1972 and 1978 which corresponds to tilting downwards towards the trench of $0.9 \pm 0.3 \mu\text{rad}/\text{yr}^{-1}$. It is followed by a tilt reversal of $2.2 \pm 1.0 \mu\text{rad}/\text{yr}^{-1}$ between 1978 and 1980. The agreement from 1978 to 1982 between SQH and SPA lines, which are separated by about 10 km, adds credence to the signal measured by the SQH line. Of the other lines, SMP has been measured most often. It shows no tilt significant at the 95% confidence level, but does show the same general shape of tilt up towards the trench between 1978 and 1980, and tilt down towards the trench between 1980 and 1982. The differences between the SMP and SQH/SPA lines are not surprising in view of the fact that SMP is in a

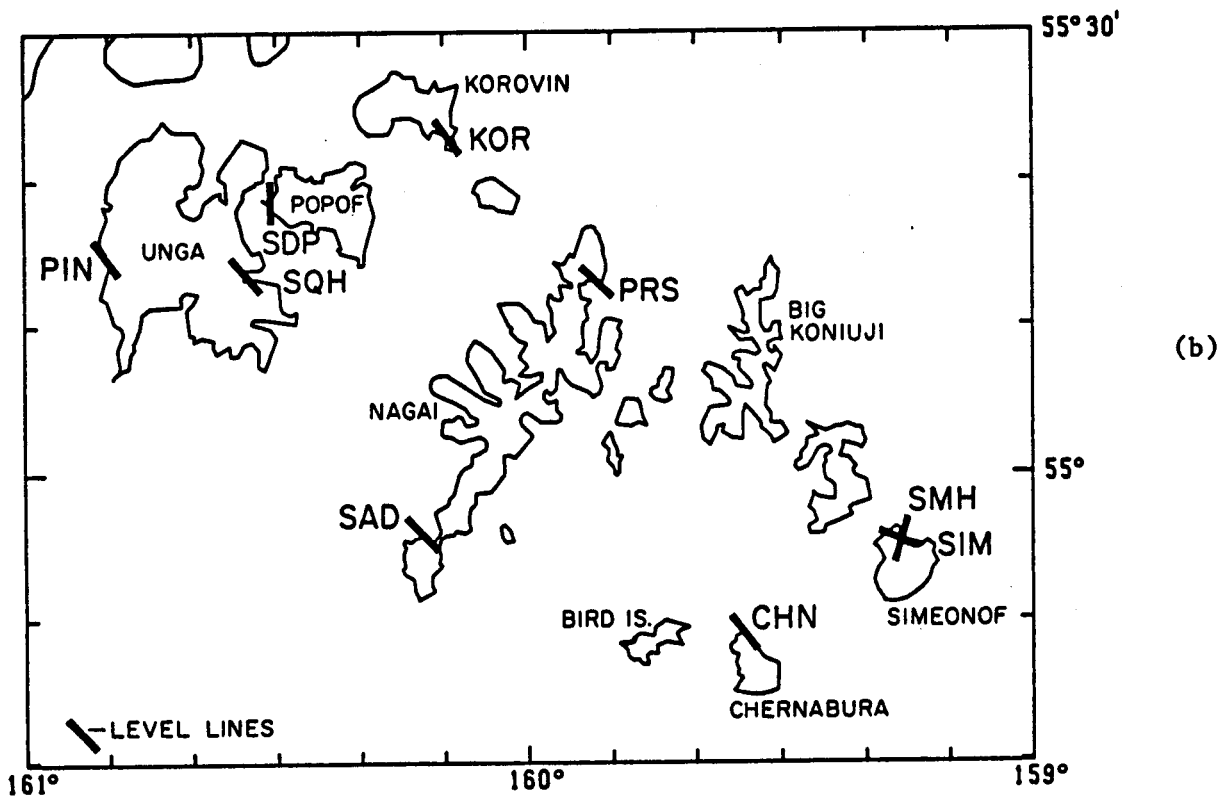
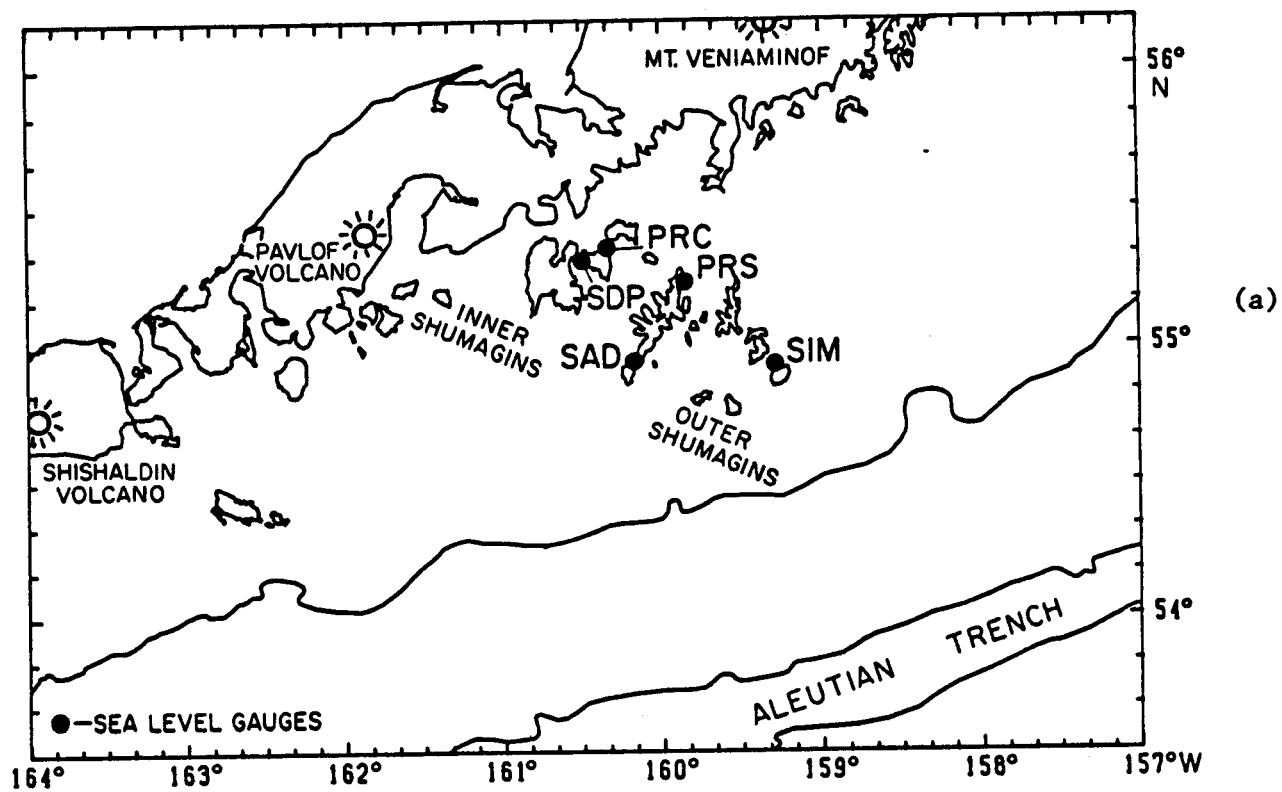


Figure 3.6.1. Maps showing level lines and tide gauges in the Shumagin Islands. The directions of the level lines are indicated by the dark lines. Their lengths vary from 600 to 1200 m.

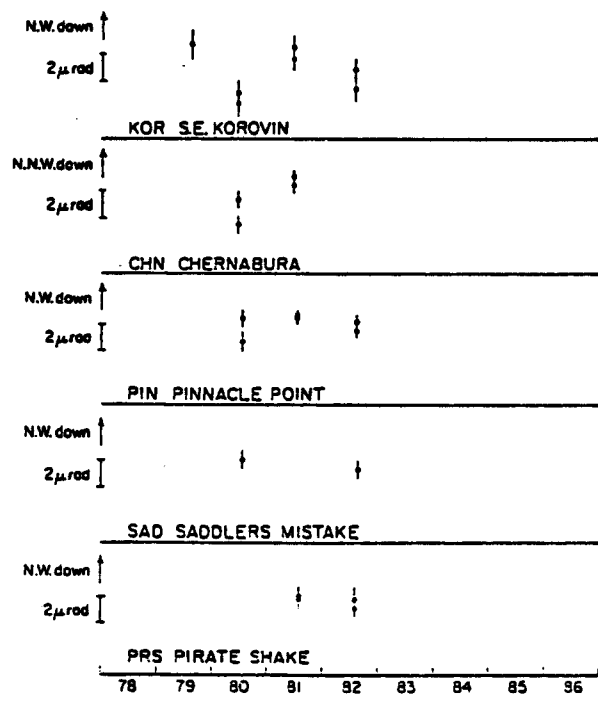
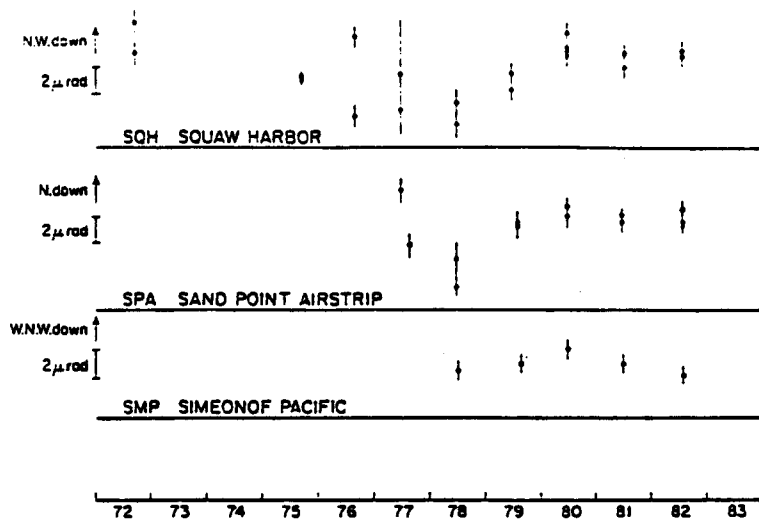


Fig. 3.6.2. Data from those level lines in the Shumagins that have been levelled at least twice. The two dots each year represent forward and backward runs of levelling. The error bars are ± 1 standard deviation based on variations in multiple readings of each station rod from each tripod position. Note particularly the $0.9 \pm 0.3 \mu\text{rad}/\text{year}$ down towards the Aleutian trench between 1972 and 1978 on line L1 (SQH). The tilt apparently reverses ($2.2 \pm 1.0 \mu\text{rad}/\text{year}$) between 1978 and 1980. The L1 data are corroborated by those from line L2 which is about 10 km away. L3, which is much closer to the trench, shows a similar pattern though with tilt rates of different magnitudes. All the other NW-SE oriented lines show a tilt down towards the trench between 1981 and 1982.

quite different part of the arc-trench gap, some 80 km distant from SQH. Winslow (1982) suspects that the two sites are on different crustal blocks. The remaining lines show less consistency of signal, but there is a general trend down towards the trench between 1981 and 1982. The 1979 KOR value is open to question because the line was not reversed. The other lines show a tendency to peak in 1981, as opposed to the 1980 peak shown by SQH, SPA and SMP. The two lines (SMH and a component of PRS) which measure tilt along the trench axis show no significant tilt between 1981, when they were installed, and 1982.

We note that the tilt down toward the trench observed between 1972 and 1978 is of the correct sense to be interpretable as due to loading of the overlying plate by subduction at depth. Conversely the tilt downwards away from the trench between 1978 and 1980 might be interpretable as due to aseismic slip relieving part of the accumulated stress on the Benioff zone beneath the islands.

3.7 Seismicity Recorded by the Unalaska Array 1980-1982

Since 1975 Lamont-Doherty Geological Observatory has operated a small seismic array on Unalaska Island in the eastern Aleutian Islands, Alaska (see Figure 3.7.1). The purpose of operating this array was to monitor the seismic activity of Makushin Volcano and Akutan Volcano as well as to monitor the regional seismicity. Unfortunately, there were never enough funds available to analyze the data collected by this array.

Only an approximate daily event count has been carried out to compare the level of activity with that recorded by the Shumagin network (see Figures 3.7.2 and 3.7.3). These event counts are based on daily records from two helicorders that recorded a short period seismometer and an intermediate period seismometer located at the central recording site. The short period seismometer was usually a remote seismic station such as MAK, SDK or USR (see Figure 3.7.1). The event counts are somewhat discontinuous since the station operator rarely was able to repair minor equipment failures, which resulted in long gaps in the data. Nonetheless, the event counts indicate an average level of activity consisting of approximately 30 events per month with S-P time less than 5 seconds and approximately 60-90 events per month with S-P time between 5 and 50 seconds. This level of activity is considerably higher than the level of activity recorded by the Shumagin network. Although it is not possible to explain this difference without actually locating the earthquakes, one could speculate that some of this activity consists of aftershocks of the 1957 Andreanof-Fox Islands earthquake. It had a magnitude $M_w \approx 9.0$ and ruptured a 1200 km long segment of the plate boundary to the east of Unalaska (House et al., 1981). Some of the earthquake data were also recorded on analog magnetic tapes that will be analyzed in the near future.

In conclusion, the number of earthquakes recorded by the Unalaska array indicates that the level of seismicity is considerably higher in the Unalaska region than the level in the Shumagin seismic gap. Significant microearthquake activity with S-P time less than 5 seconds (or with epicentral distance less than 40 km) is observed by seismic stations located on Unalaska Island.

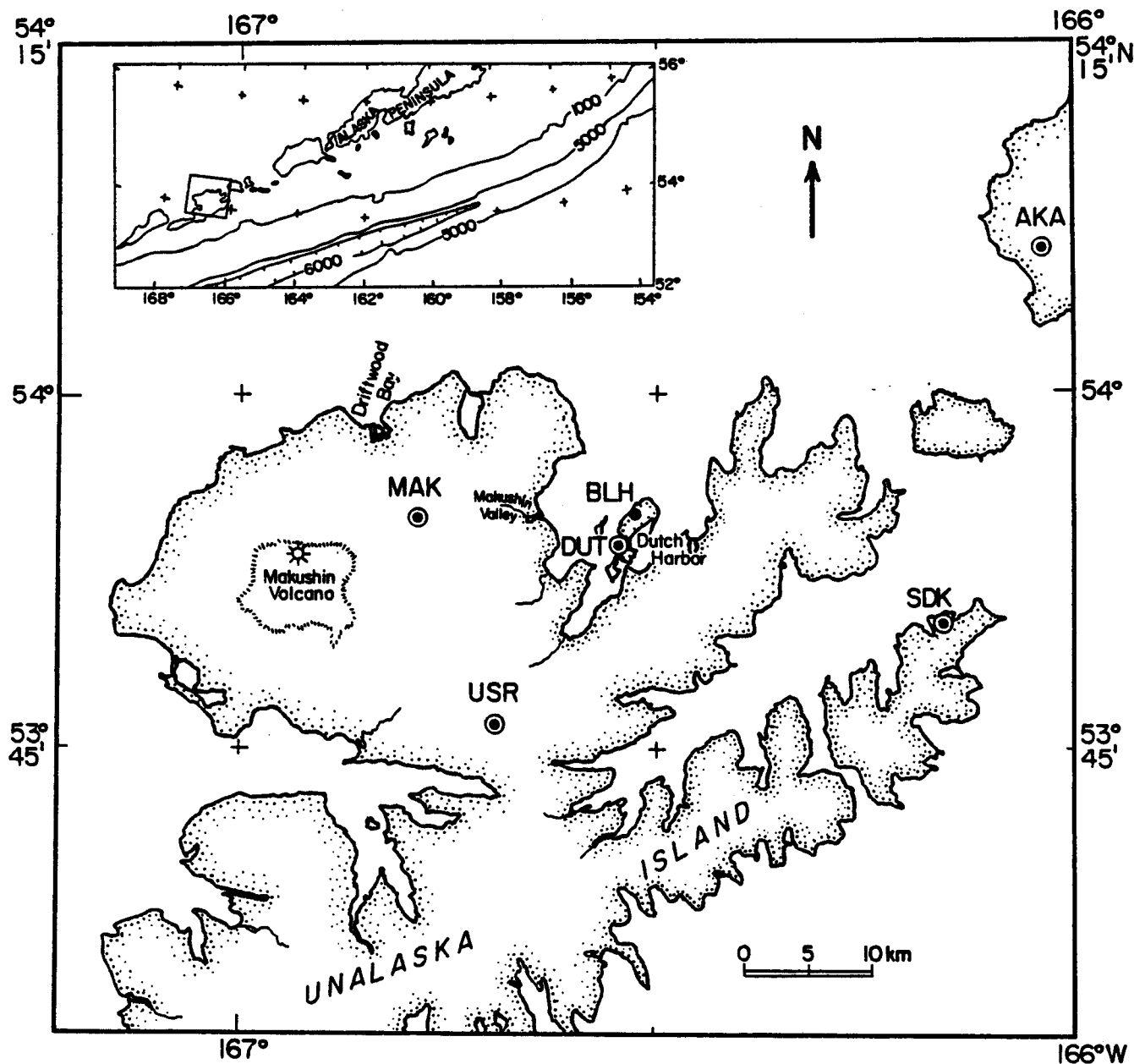
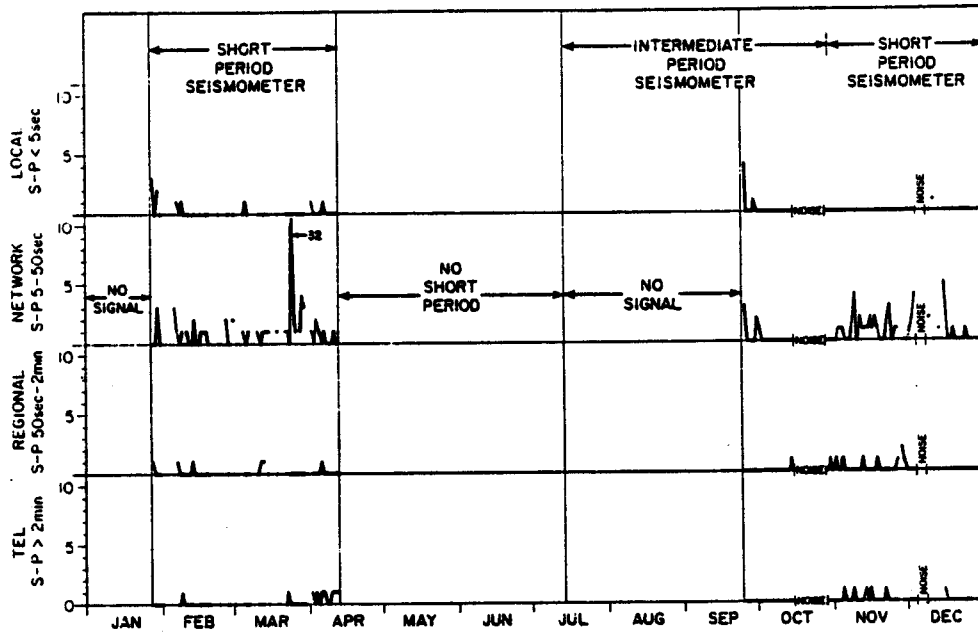


Figure 3.7.1. Dutch Harbor Array, Eastern Aleutians, operated by Lamont-Doherty Geological Observatory. The array consist of four remote stations, MAK, USR, SDK, and AKA with short-period, vertical seismometers. At the central recording station, DUT, a set of two horizontal and one vertical seismometers are operated in addition to an independent strong motion accelerograph (SMA-G1). The BLH is a repeater station for signals that are telemetered from the remote stations and recorded at the central station.

DUTCH HARBOR EVENT COUNT 1980



DUTCH HARBOR EVENT COUNT 1981

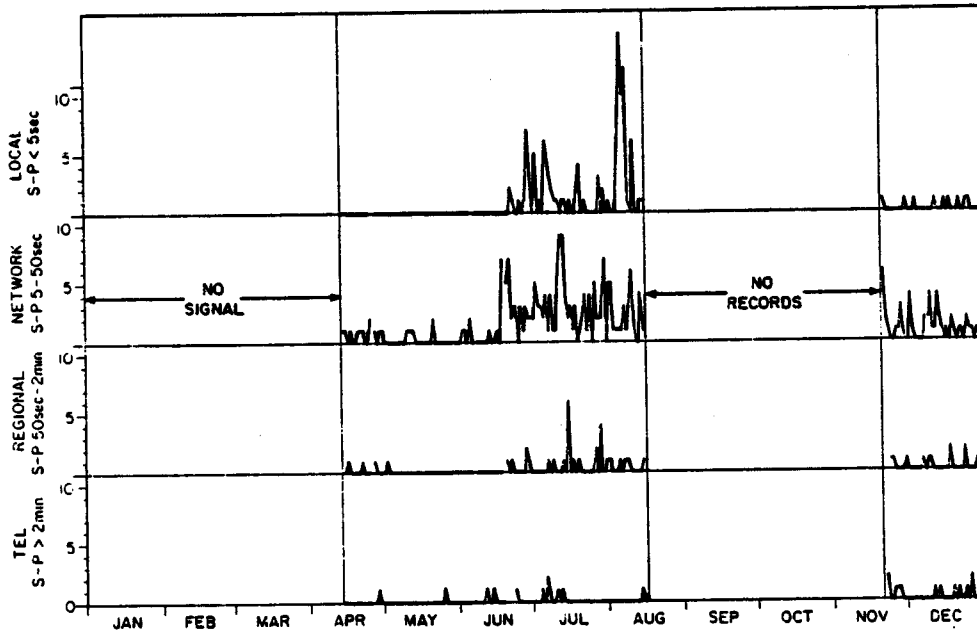


Figure 3.7.2. Number of earthquakes recorded per day by the Dutch Harbor Array in 1980 and 1981. The data are grouped according to S-P travel time.

DUTCH HARBOR EVENT COUNT 1982

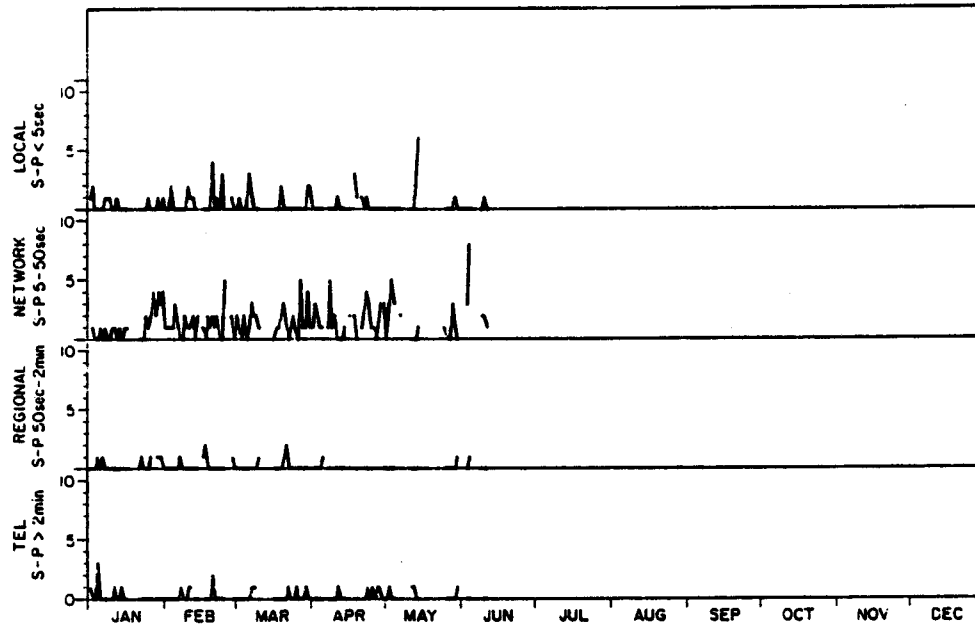


Figure 3.7.3. Number of earthquakes recorded per day by the Dutch Harbor Array in 1982.

3.8. Tsunami Data

Since Cox and Pararas-Carayannis (1976) compiled tsunami data for Alaska, some revisions and additions to this data set (mostly for the historic period prior to 1898) have been made by Davies et al. (1981), Sykes et al. (1980, 1981), McCann et al. (1980), and by House et al. (1981) specifically for the great 1957 event ($M_w = 9.0$).

A thorough analysis of all tsunami data for Alaska is still outstanding. The present report does not alleviate this problem. We merely reproduce here a figure (Figure 3.8.1) taken from Davies et al. (1981) that is based on an assessment of the Sanak-Kodiak tsunami(s) of 1788 by Soloviev (1968). That interpretation may be representative for the kind of tsunami run-up heights that could be expected from a great earthquake rupturing the Shumagin Gap, and perhaps portions of the 1938-rupture zone. Figure 3.8.1 shows that tsunami-run up heights may have been as high as 30 m on particularly exposed, southeasterly-facing shorelines and inlets of the islands on the outer shelf platform, while the inlying SE-facing shorelines of the Alaska Peninsula may have received run up heights of only about 5 meters, although data for the latter are poorly documented. In specific cases tsunami heights on inlying, south-facing shorelines may be much higher as has been dramatically shown by the 1946-tsunami that completely destroyed the Scotch-Cap lighthouse on Unimak Island. The base of the lighthouse was about 10 meters above sealevel, yet tsunami run-up heights may have exceeded 30 meters for this unusually tsunamigenic event ($M_T = 9.3$, Abe (1979)).

Generally tsunami heights on north-facing shorelines and inlets of the Alaska Peninsula and of major islands of the Aleutian chain are substantially smaller for Aleutian subduction-zone events, and rarely seem to exceed 1 m in height. The effects of seiches, however, (standing wave patterns in contained bodies of waters, narrow bays and inlets) should not be neglected since they can produce locally higher waves, particularly as a secondary effect from landslides or volcanic eruptions. In such cases debris may reach bodies of water and partially displace them as transient waves.

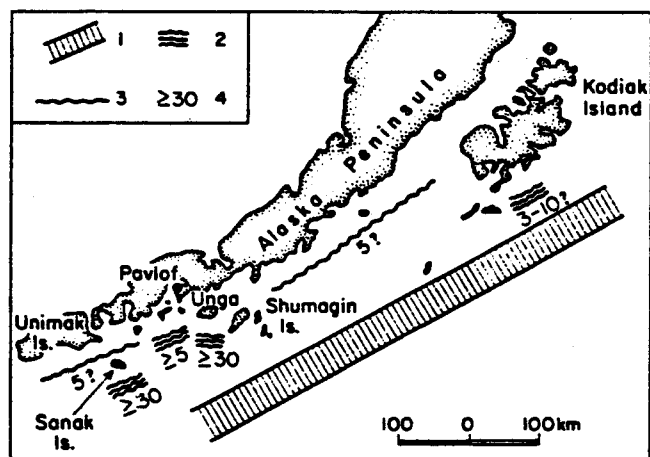


Figure 3.8.1. Diagram (after Davies et al., 1981) showing tsunami run-up heights (in meters) and inferred earthquake source region of the 1788 event(s) as determined by Soloviev (1968). The symbols in the legend imply: 1) hypothetical location of rupture zone, 2) positive known places of appearance of tsunami, 3) probable places of appearance of tsunami, and 4) approximate height of tsunami in meters.

One particular event affecting the Bering Sea side of Unalaska Island is of special interest. We do not have a detailed description of the tsunami of 1878 that apparently destroyed the Aleut settlement in Makushin Bay on Unalaska Island. We assume, however, that run up heights must have exceeded here 5 m, or more, despite the fact that portions of Unalaska shelter the Makushin Bay from a direct southerly exposure. The Bay is located on a northwesterly promontory on the Bering Sea side of Unalaska Island; the bay itself faces, however, west to southwest. It is conceivable that the causative earthquake for this tsunami was located on the Bering-Sea side of the arc rather than on the Pacific side, and may have been induced volcanically. Therefore it is of special interest. It suggests that occasionally the Bering Sea side may be also exposed to tsunamigenic events. This example shows that minimum heights above sealevel exceeding 10 m or more should be required for the base of all critical installations on shores facing the Bering Sea, and probably 30 m or more on shores facing the Pacific ocean. Higher elevations should be sought if technically feasible.

4. RESULTS

4.1 Seismic Hazards

Finite seismic hazards do clearly exist for any future offshore, nearshore, and onshore structures that would be associated with successful exploration and development of oil or gas resources in the three lease-sale planning areas presently known as the "St. George Basin", the "North Aleutian Basin", both located on the Bering Sea side, and the "Shumagin Basin" located on the Pacific side of the Aleutian arc.

We have undertaken a preliminary quantification of the hazard contribution in the St. George Basin that originates from the moderately active local seismic sources on the Bering Sea Shelf itself that lie directly within the region of the St. George Basin (Appendix 7.6). We find from considering the local earthquake sources alone, i.e., excluding contributions from great subduction zone earthquakes near the Aleutian trench, that the probabilities for peak accelerations to exceed 0.2 and 0.5 g (1g = earth's gravitational acceleration) measure about 10 and 2 1/2 percent, respectively, during any 40-year period of interest. These probability values should be taken as only preliminary since the acceleration-vs.-distance curves (attenuation laws) that were used are only poorly constrained and the seismic record is very short and probably incomplete. Moreover, these probabilities do not reflect contributions from great Aleutian thrust zone earthquakes to be discussed next.

At this time, and because of absence of sufficient strong motion data in subduction zones in general and from great earthquakes in particular, we cannot determine with sufficient certainty the probabilities of exceedence of certain levels of groundmotion that will be associated with great earthquakes that occur on the main thrust zone of the Aleutian arc.

Therefore we have limited ourselves to calculating the conditional probabilities for great earthquakes ($M_w > 7.8$) that can be expected to occur in the various segments of the Aleutian arc (including several Aleutian seismic gaps). These probabilities are

shown in Figure 4.1.1 for periods of the next one and two decades. The most important result of this calculation is that probabilities in the Shumagin seismic gap could be as high as $\approx 90\%$ for the 10-year period 1983-1993, and $\approx 99\%$ for the 10-year period 1983-2003. If a 40-year period is envisioned as the likely time of interest for oil exploration in the St. George, North Aleutian, and Shumagin Basin lease planning areas, it should be considered virtually a certainty that in their vicinity a great earthquake will occur either individually in the Shumagin Gap (near 160°W), the Unalaska Gap ($\approx 164^\circ\text{W}$), the 1983-rupture zone ($\approx 156^\circ\text{W}$), or at all of them.

We point out that the probabilities quoted above are those for normally distributed recurrence times and if log-normal distribution of recurrence times applies (see chapter 3.4), than the lower values (shown in solid shading of Figure 4.1.1) would apply.

Which levels and durations of groundmotions would be caused in the three lease-sale planning regions by great earthquakes is at present highly uncertain since strong motion data from any great subduction zone earthquake ($M_w > 7.8$) have never been recorded (see chapter 3.3); moreover, the few strong motion data points for the Alaska subduction-zone environment that have been collected for moderate-sized events (chapter 3.3) have been mostly analyzed only with regard to uncorrected (for instrument response) peak acceleration. Since many tall off-shore platform structures and near-shore oil storage and tanker facilities have their natural modes of response at longer periods (1-10 sec) than those (≈ 0.1 sec) that determine peak accelerations, the most important (i.e., dangerous) aspects of groundmotions from great earthquakes to tall structures at or near subduction-zone environments remains poorly researched and therefore cannot be adequately accounted for in the designs. Until this gap in knowledge (and ground motion data) is filled, no accurate, or at least economic, risk assessment to Alaska-Aleutian offshore structures can be made. The consequence is either costly overdesign of engineering structures or, alternatively, a high risk of loss.

In short, a quantitative seismic hazards assessment in the Alaska-Aleutian setting at or near the subduction zone has progressed to date only to the state of a rather complete and quantitative

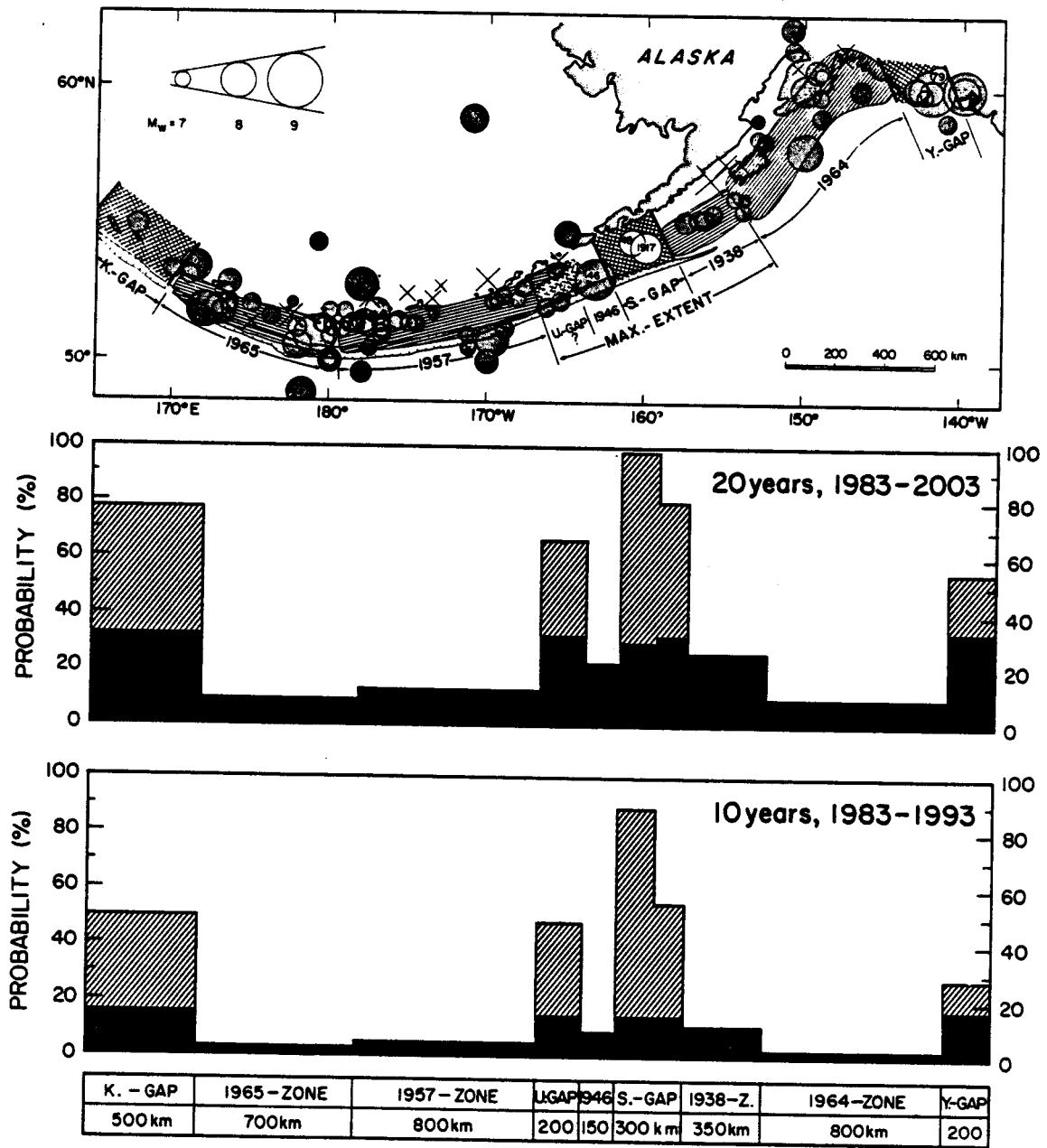


Figure 4.1.1. Top: Map view of arc with instrumental seismicity ($M_w \geq 7.0$) since 1898. Center: Conditional probabilities for the occurrence of a great earthquake to occur in each arc segment during the 20-year period 1983 to 2003. Probabilities computed for normal distribution of recurrence times are in diagonal hatching, and for log-normal distribution in solid shading. Bottom: Same as center but for 10-year period 1983-1993. Box segments on bottom label the arc-segments and their approximate lengths in km.

seismic source definition. Until actual groundmotion measurements become available the hazards assessment cannot be carried beyond this initial stage except by using very tenuous extrapolations of groundmotion attenuation and scaling laws (see chapter 3.3) mostly from other tectonic settings which are unproven for the Aleutian tectonic setting and therefore may or may not apply. The future collection of strong motion data in Alaska from large and great Alaska-Aleutian subduction zone earthquakes emerges as the single most important conclusion from this (negative) assessment.

The early termination of the seismologic components of the NOAA-OCSEAP program severely jeopardizes two such existing efforts to collect the necessary strong motion data (i.e., by Lamont-Doherty in the Shumagin seismic gap, and by the U.S.G.S. in the Yakataga seismic gap). No fully funded substitute programs have yet emerged to date.

Besides the direct seismic hazards associated with groundshaking, indirect seismic effects from soil liquefaction, ice-, rock- and mud-slides, crustal deformation (coastal changes), faulting and tsunamis can be severe and must be accounted for. Effects from changes of coastlines due to crustal deformation and of tsunami can be minimized if coastal structures on the Pacific-facing shorelines have their foundations at elevations not below 30 meters above sealevel (high tide), and on the Bering Sea facing shorelines not below 10 meters above sealevel.

If protective bays, inlets and other narrow bodies of waters at steep coastlines are considered for engineering facilities, site specific studies should be carried out to assess their potential for seiches or surges related to earthquake-induced rock-falls, or to sudden discharges of large volumes of mud, ice, volcanic debris or lakes into such constrained inlets or bodies of water (e.g., surge in Lituya Bay SE-Alaska during 1958 earthquake).

SEABEAM, SEAMARK, bathymetric precision profiler, and single- or multichannel reflection surveys are either still required, or existing ones need to be specifically analyzed for near-surface faulting of the ocean floor, if pipeline routes on the ocean floor will be contemplated at a later stage of development. The near-surface seismicity patterns obtained from the local and regional seismic

network data and reported for the Shumagin segment in chapters 3.1 and 3.2 (e.g., Figure 3.1.8) can be an important guide where such faulting may be expected to be presently active.

4.2 Volcanic Hazards

Introduction

Over 74 active volcanoes are located in the Aleutian Islands/Alaska Peninsula region (Simkin et al., 1981). Of these, ten or more are located in the immediate study areas, including Pavlof, Pavlof Sister, Akutan, and Makushin volcanoes. Their locations are shown in Figures 4.2.1 and 4.2.2. All of these volcanoes are typical andesitic island arc volcanoes.

We have assessed volcanic hazards in two ways: 1) temporally, that is the rate of occurrence of eruptions; and 2) spatially, by delineating the areas of greatest hazard near each volcano. For temporal estimates of eruption rate, we have examined: 1) long-term rates of recurrence as recorded by deep sea ash layers (0-2.8 million years B.P.); 2) intermediate-term eruption rates as recorded by ash layers found in marine terrace deposits (0-10,000 years B.P.); 3) literature search of historic records of eruptions (1760-1982); and 4) documentation of eruptions of Pavlof Volcano from 1973 to the present time based on results of studies of seismicity associated with recent eruptive activity (McNutt and Beavan, 1981; McNutt, 1981a,b; McNutt, 1982a,b; McNutt and Mori, 1982). (Items (3) and (4) above are described in detail earlier in this report.) Spatial zones of greatest hazards are shown in maps (Figures 4.2.1-4.2.2). Delineation of hazard zones is based on study of mapped deposits and eruptions of volcanoes in Alaska and elsewhere. Of special interest is the identification of possible volcanic hazards zones in the Kupreanof area, based largely on results of the seismic monitoring efforts in addition to field observations.

Temporal Hazards Assessment

Long-term eruptions rates. Volcanic ash layers from cores recovered south of the Aleutians and the seaward extent of these ashes are shown in Figure 4.2.3. At least 20 large andesitic eruptions have occurred since 1.8 million years B.P. (Hays and Ninkovich, 1970).

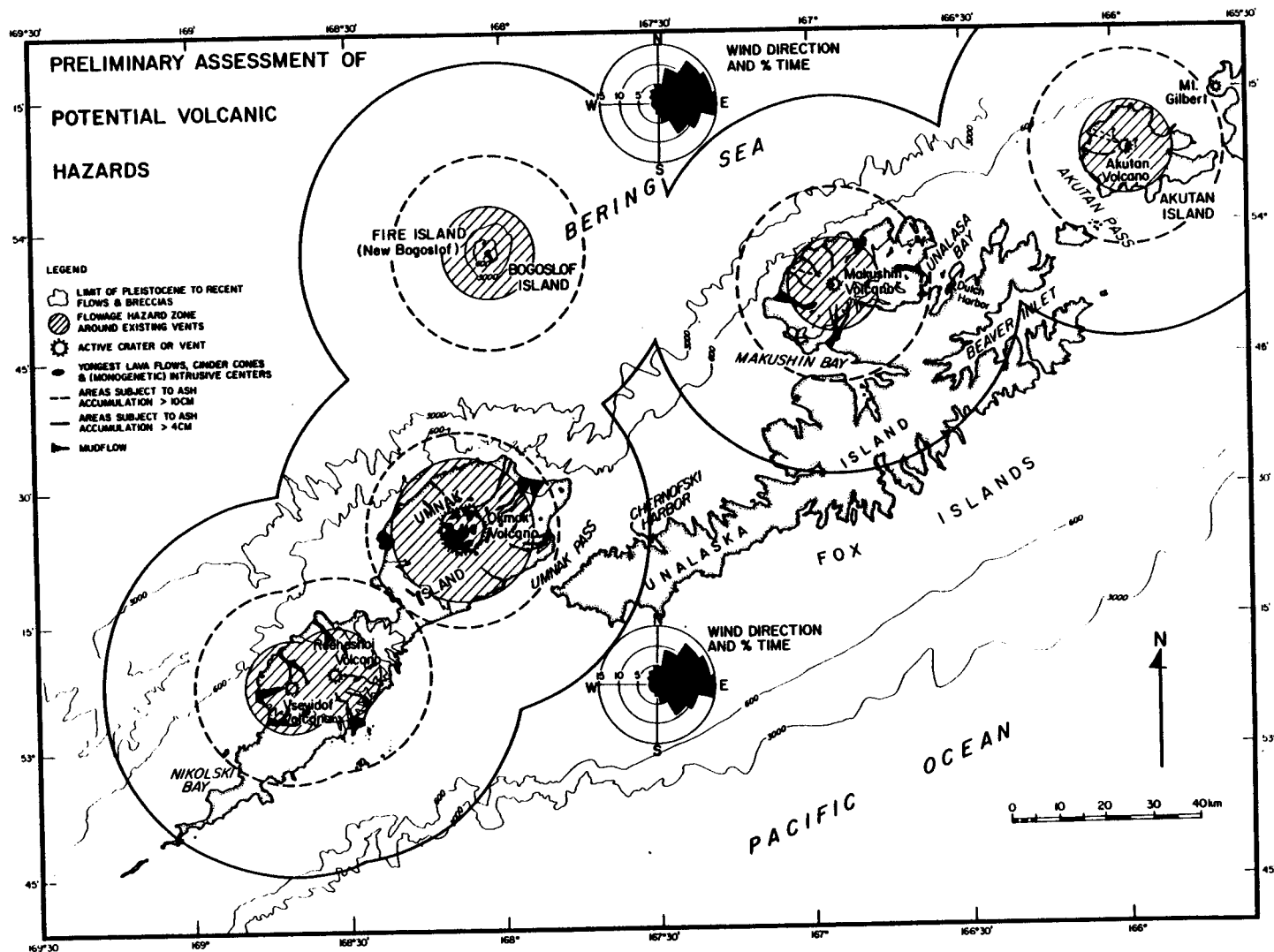


Figure 4.2.2. Volcano Hazards Map for the Eastern Aleutian Islands. Maps show locations of all mapped Holocene and Recent vents, extents of Pleistocene to Recent lava flow and debris flow deposits, flowage hazard zones, mudflow hazard areas, likely extents and ash thicknesses for a once-per-hundred-year eruption, and wind rose diagrams. The rationale for most of these zones is explained in the text. The wind rose diagrams show average wind direction between 5000 and 40,000 feet during all four seasons of the year. Data are from Wilcox (1959). The Unalaska map shows wind data from Dutch Harbor alone. Each sector of the wind rose diagram shows both the direction towards which the wind is blowing and the percentage of the time the wind is blowing in that direction. Average wind speeds are about 35-40 mph. Bathymetric contours are in feet. Map preparation by S. McNutt; drafting by S. McNutt, K. Nagao and M. Luckman.

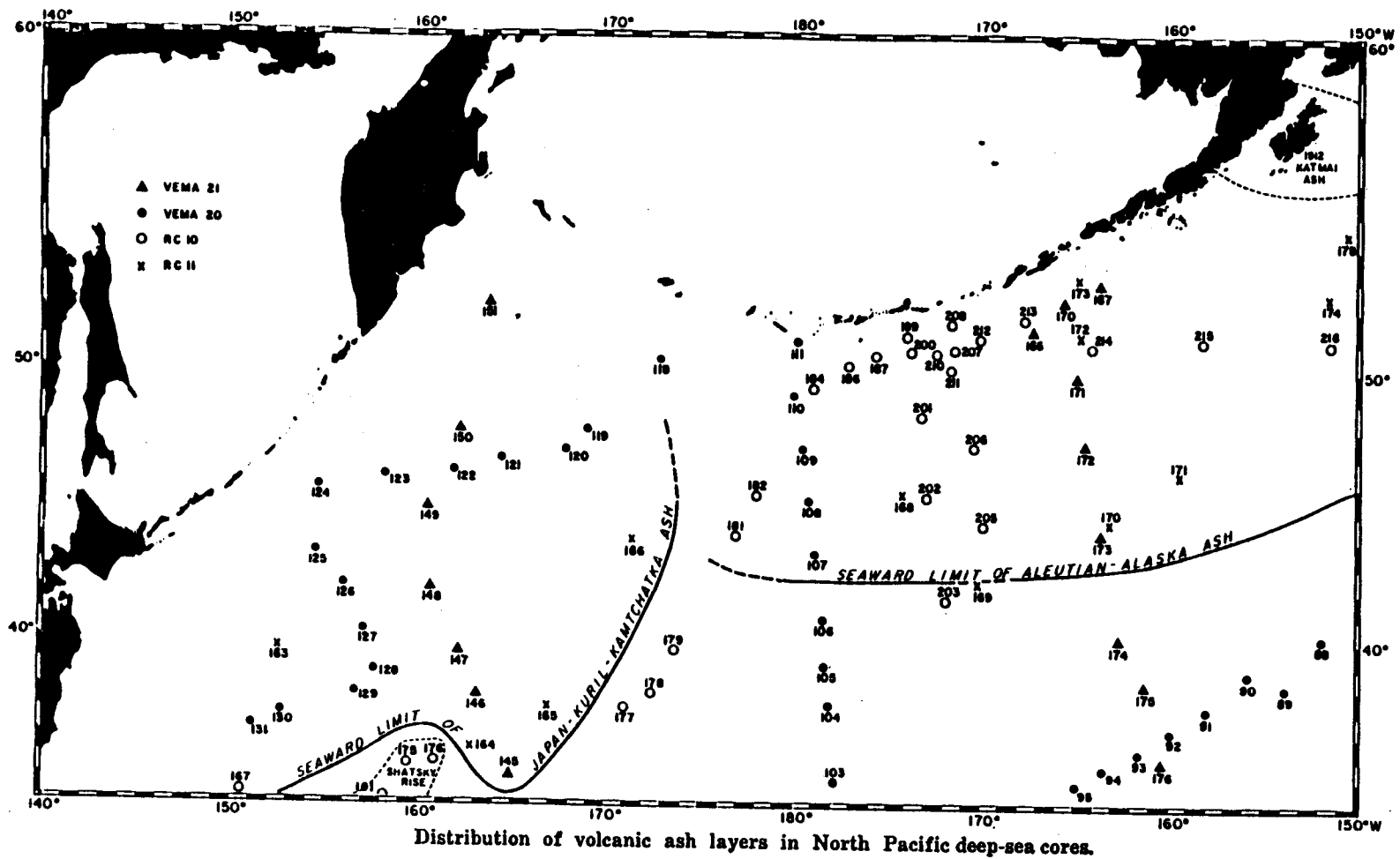


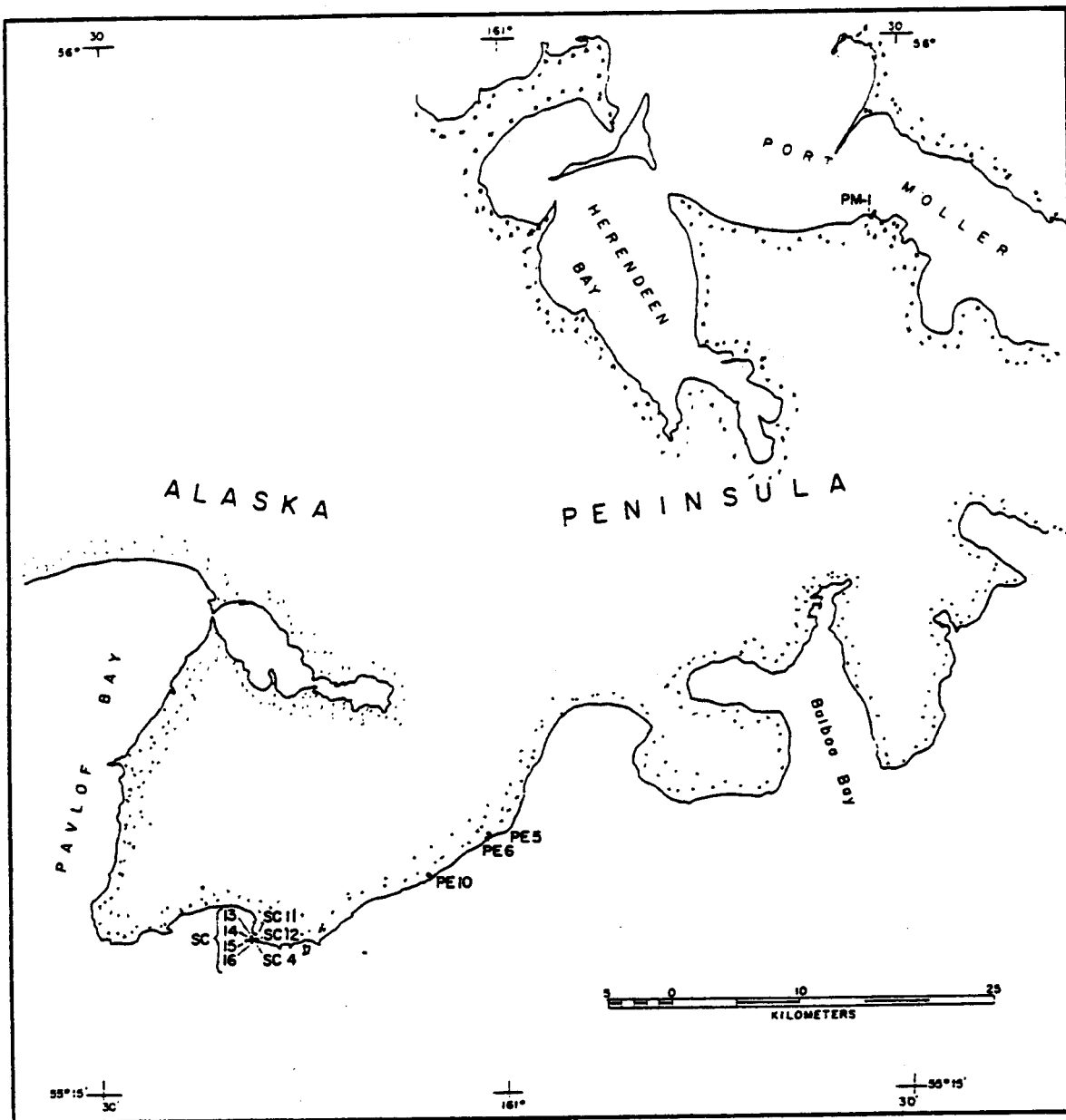
Figure 4.2.3. (Source - Hays and Ninkovich, 1970).

However, cores dating from 1.8 to 2.8 million years B.P. in this area contain no ashes, suggesting that the lower Pleistocene (1.8 m.y. B.P.) was the beginning of the present cycle of volcanism. Donn and Ninkovich (1980) report rates of explosive Cenozoic volcanism in the North Atlantic varying between 3 and 65 eruptions per million years. Based on the northern Pacific data, we estimate that for the entire Aleutian arc an explosive eruption large enough to produce sufficient ash to form a deep-sea ash layer will occur on the average every 90,000 years during the present cycle of activity. Unfortunately the eruptions which deposited the ash layers cannot be attributed to any specific volcano.

Intermediate term eruption rates. Cores were taken in marine terraces in the Shumagin Islands region during the summer of 1980 by M. Winslow, T. Ray, and C. Heusser (personal communication, 1982). Figures 4.2.4a,b are maps showing locations of cores. Peat layers contained in the cores were dated by the Carbon 14 method, and yield a maximum age of 9540 ± 260 years for the oldest and deepest dated layer.

Preliminary study of ash distribution in the cores shows some spatial and/or temporal variation; 2 typical cores are shown in Figures 4.2.5a,b. Based on study of these cores (Table 4.2.1) we estimate the likelihood of an eruption large enough to deposit 1 cm of compacted ash or more in the Shumagin Islands region to be approximately once every 1,900 years. Again, these eruptions cannot be ascribed to any specific volcano in the study area.

Temporal hazards summary. The information from deep sea cores, marine terrace cores, and records of historic eruptive activity have been compiled and plotted on a magnitude vs. frequency of occurrence plot (Figure 4.2.6). The plot shows the \log_{10} of the number of eruptions of a given size per 100 years per volcano versus the \log_{10} of the volume of erupted material. In preparing this plot, we made several assumptions. First, we assumed that each of the 74 active volcanic centers could have been a source for the 20 large eruptions producing deep sea ash cores. We then normalized the result to the



(a)

Figures 4.2.4 a,b. Sample locality maps in Shumagin Islands and adjacent peninsula. Inner Shumagins include Unga, Popof, Korovin, Andronica, Karpa and Henderson Islands. Outer Shumagins include Nagai, Big and Little Koniuji and the islands between them. Simeonof, Chernabura, and Bird Islands are considered to be separate from the Outer Shumagins in this paper. (Source - M. Winslow, written communication, 1982 (used with permission)).

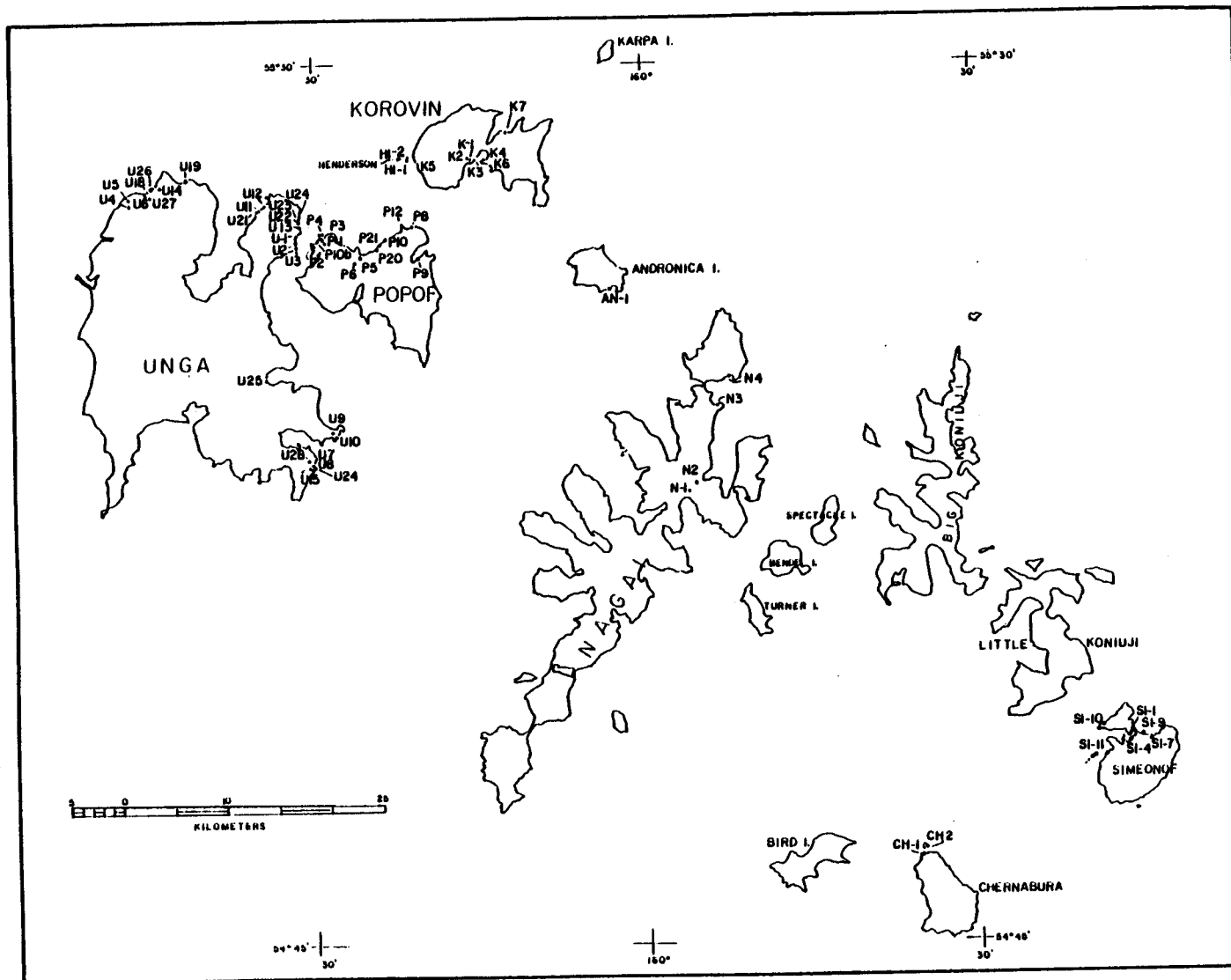
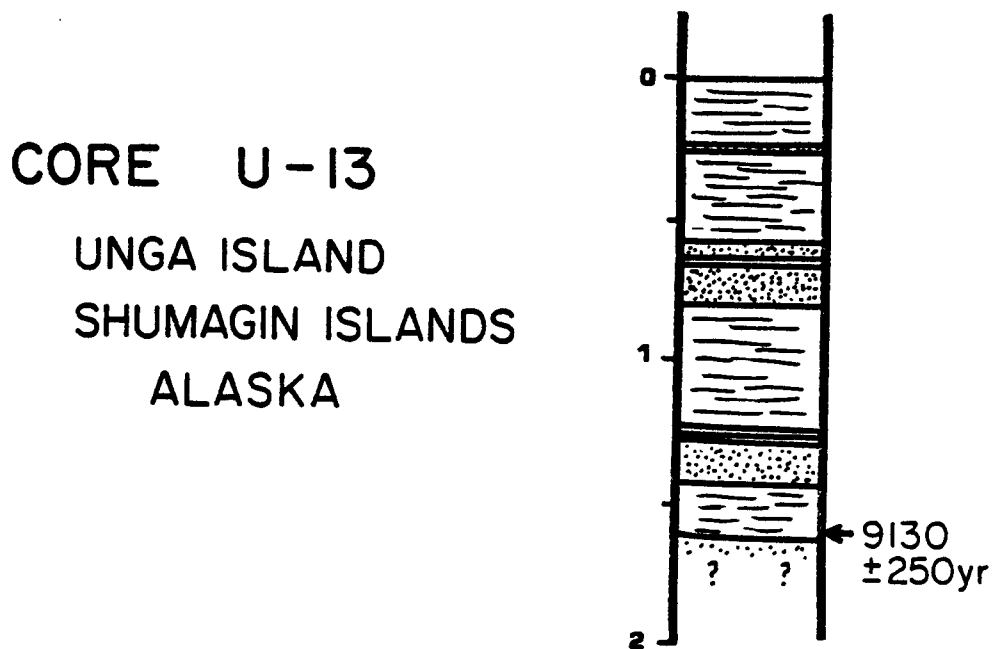
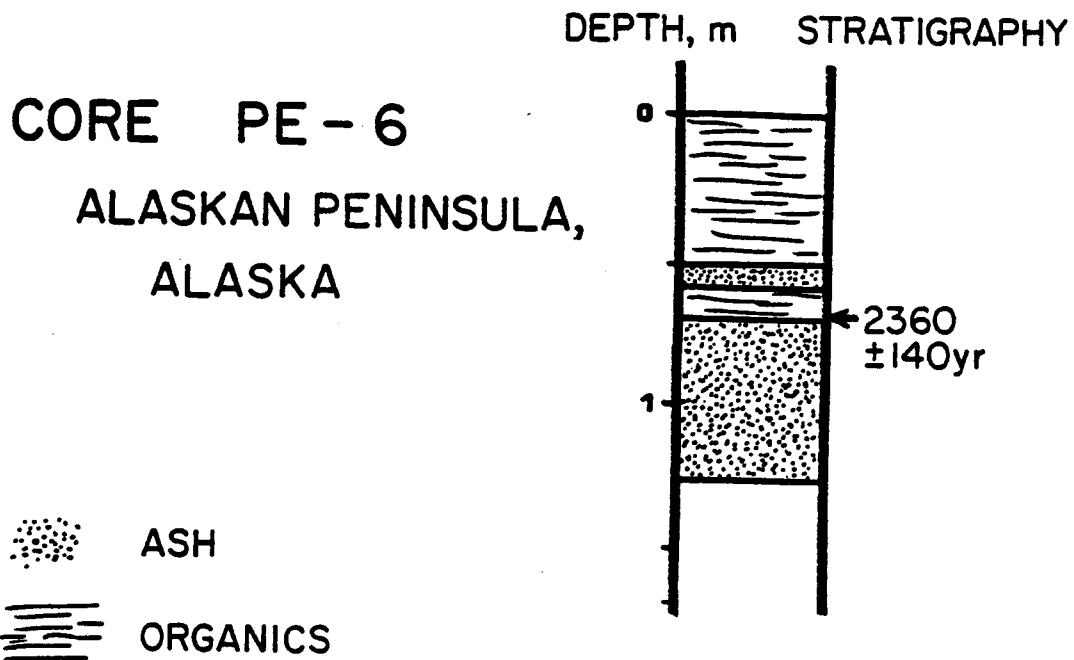


Figure 4.2.4(b). (Source - M. Winslow, written communication, 1982 (used with permission)).



Figures 4.2.5 a,b. Examples of volcanic ash layers in cores taken on marine terraces by M. Winslow, C. Heusser, and T. Ray, summer 1979. The oldest dated peat layer gives a Carbon 14 age of 9540 ± 260 years. The maximum number of ash layers in a core is four (core U-13).

TABLE 4.2.1. Carbon 14 Dates and Number of Volcanic Ash Layers for Marine Terrace Cores.

<u>1979</u>	<u>Samples</u>	<u>Years B.P.</u>	<u># Ash Layers</u>
Andronica Island	AN-1A	460	1
Korovin Island	K-1	7580 \pm 220	1
Nagai Island	N-3	6050 \pm 230	1
Popof Island	P-2	9180 \pm 340	1
Peninsula	PE-5	2970 \pm 170	1
Peninsula	PE-6	2360 \pm 140	3
Peninsula	PE-10	6320 \pm 260	1
Simeonof Island	SI-1	4160 \pm 160	0
Simeonof Island	SI-4	4460 \pm 150	0
Unga Island	U-7	7500 \pm 180	1
Unga Island	U-8	2030 \pm 130	3
Unga Island	U-13	9130 \pm 250	4
Unga Island	U-14	9540 \pm 260	3

(Source - M. Winslow, written communication, 1982)

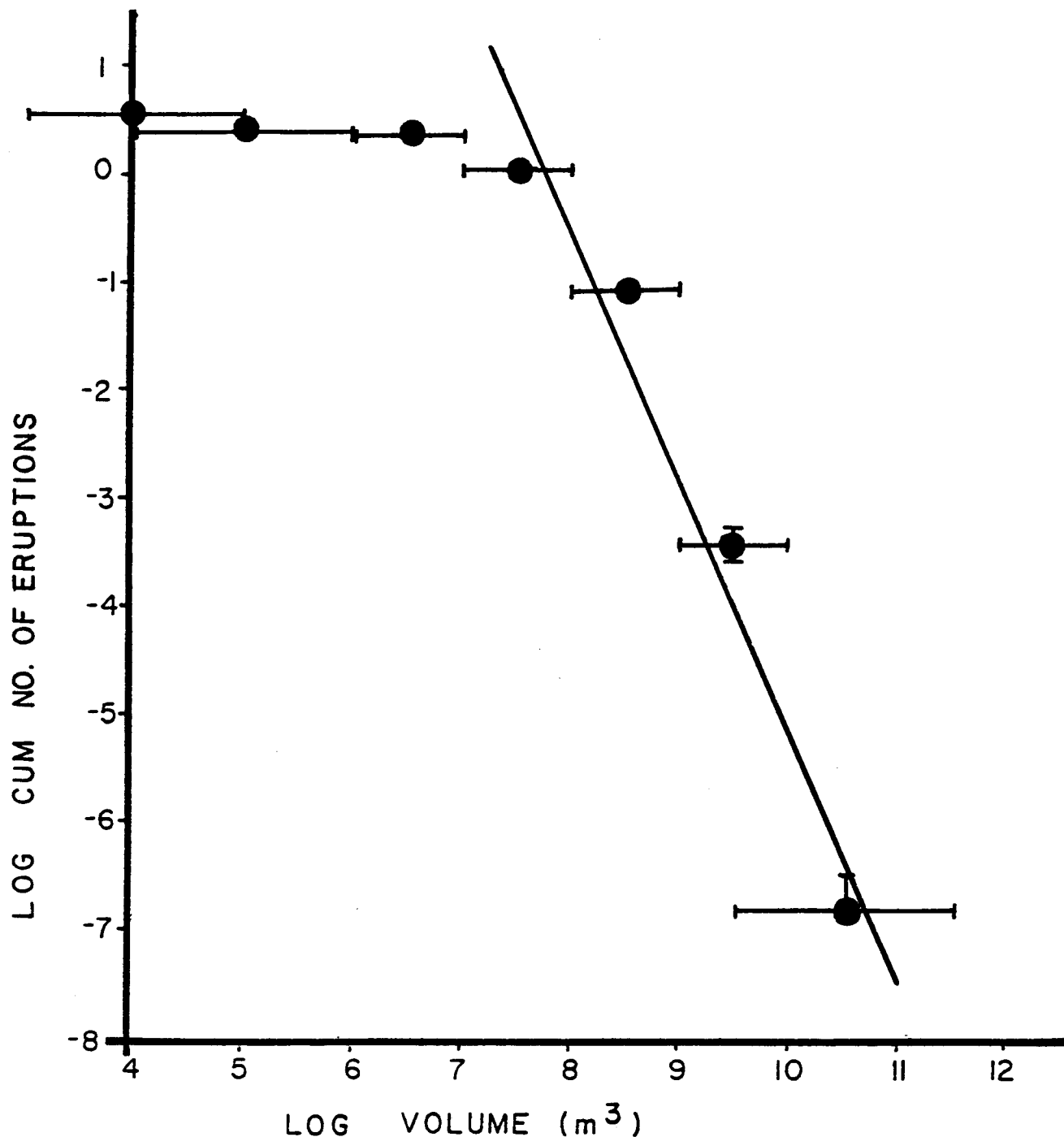


Figure 4.2.6. \log_{10} of the cumulative number of eruptions of a given size per hundred years per volcano vs. the \log_{10} of the volume of eruptive products. The volume is a crude measure of the energy of an eruption. The line is a least squares fit to the 4 data points to the right and has a slope of -2.3. Detection is probably not complete for events smaller than a volume of $3 \times 10^6 m^3$. An eruption of volume $7 \times 10^7 m^3$ is likely to occur at each volcano once per 100 years.

number of such eruptions per 100 years per volcano. If, however, only half the volcanic centers are capable of producing such large eruptions ($10^{9.5} - 10^{11.5} \text{ m}^3$ of ejecta) then the rate of occurrence would be greater by a factor of 2 ($\log_{10} = 0.3$) as shown by the vertical error bar on the plot. The plotted point thus represents a minimum rate of occurrence. The horizontal error bars, one order of magnitude in each direction from a value of $10^{10.5} \text{ m}^3$, indicate that a smaller close-by eruption and a larger but more distant eruption could have the same ash accumulation at a given location. Similarly, we assumed that the eruptions producing the ash layers in marine terrace cores could have originated from any one of 15 ± 5 volcanic centers, with volumes of $10^9 - 10^{10} \text{ m}^3$.

Lastly, we assumed that the recent catalogue of Simkin et al. (1981) (plus 1982 supplement) is complete for Alaska for eruptions > volcano explosivity index 2 (corresponding to volumes $> 10^7 \text{ m}^3$) for the period 1942-1982. Military flights took place almost daily during World War II, and commercial or military flights have occurred almost daily ever since. Thus, we think it unlikely that an eruption with VEI > 2 would have been missed. Further, 3 great earthquakes have occurred in 1957, 1964, and 1965, rupturing a large portion of the Aleutian arc. Since some authors have argued that volcanic activity may be increased both before large earthquakes (Kimura, 1978) and after them (Carr, 1977), we note that the time period since WWII contains nearly as many years prior to a great earthquake as years after a great earthquake, and hence should be free of possible bias. From the plot, we estimate that the largest eruption likely to occur at any volcano in a one-hundred year time interval would have a volume of $7.0 \times 10^7 \text{ m}^3$ of ejecta (\pm a factor of 2). The 1976 eruption of Mt. Augustine roughly corresponds to this volume. The volume estimate then forms part of the basis for our delineation of spatial hazards, as outlined in the next section of this report.

Spatial hazards assessment. Volcanic hazards which can affect life and property in the vicinity of a volcano include: 1) pyroclastic surges, flows and nuees ardentes; 2) lava flows; 3) debris and mud flows and floods; 4) wind blown ash; 5) noxious fumes,

poisonous gases and acid rains; and 6) volcanic earthquakes. The first four of these hazards are displayed on hazards maps of the western Alaska Peninsula, and Unalaska and Umnak Islands (Figures 4.2.1 and 4.2.2). The rationale for each of the mapped hazard zones, as well as the unmapped hazards, are given below.

Pyroclastic surges, flows and nuees ardentes represent the most catastrophic potential hazards. These features generally originate from presently active vents or adjacent vents, hence the positions of all known Quaternary active vents, cinder cones, etc., are also shown on the hazards maps. The main driving force for the pyroclastic surges, flows and nuees ardentes (as well as lava flows) is gravity; generally the material is erupted to some height above the volcano, and the resulting gravitational collapse of the cooling eruption column feeds the flow. Lateral blasts, such as Mt. St. Helens, are not very common. Most known surges and flows are limited to distances of about 10-20 km from the volcanoes, and flows usually die out at the topographic base of the volcanoes (D. Miller, personal communication, 1982; Miller et al., 1982). Hence the smaller volcanoes are assigned a 10 km flowage hazard zone, Okmok Volcano is assigned a 15 km zone, and the largest volcano in the study area, Mt. Veniaminoff, which is substantially larger than the others, is assigned a 20 km flowage hazard zone. The extent of known Pleistocene to Recent lava flows and pyroclastic surge and flow deposits as mapped by Burke (1965), Detterman et al. (1981a,b), Drewes et al. (1961), Waldron (1961), and Byers (1959), are included on the hazards maps, and show good general agreement with the assigned 10 to 20 km flowage hazard zones.

Mudflows, debris flows, and floods represent an important hazard for the Alaskan/Aleutian volcanoes. Most of the volcanoes are covered by glaciers, hence a large amount of water is available to form landslides of mud and debris. Mud and debris flows are generally restricted to valleys except for the uppermost portion of the volcanoes, and the flows can travel great distances--several tens of kilometers--from the volcano. Thus we have identified all major valleys and rivers draining each volcano as likely sites of future mud and debris flows and floods. Mapped holocene mudflows from Mt. Veniaminoff (Detterman et al., 1981) demonstrate the areal extent of this hazard.

Wind blown ash is probably the most common and pervasive volcanic hazard. Some ash is emitted during almost every eruption, but except for large eruptions, most of the ash is deposited quite close to the source. The azimuth of greatest ash thickness is strongly controlled by prevailing wind direction which is highly variable in the Aleutians. Figure 4.2.7 shows the maximum ash thickness vs. distance for a number of large eruptions, including several eruptions of size comparable to our estimated one-per-hundred year eruption, with a volume of $7.0 \times 10^7 \text{ m}^3$ (\pm a factor of 2). As shown in that figure, typically 10 cm of ash can be deposited at a distance of 21 km, and a thickness of 4 cm of ash can be expected at a distance of 40 km. These two ash thicknesses are plotted on the hazards maps. The prevailing wind directions are shown in rose diagrams on the maps. We note that most of the time the wind blows towards the east; however, we have chosen to draw the ash fall hazard zones as circles centered on the volcanoes to emphasize the fact that significant ash accumulation can occur in any direction if the wind happens to be blowing that way during an eruption.

Distribution of noxious fumes, poisonous gasses, and acid rains also depends strongly on wind speed and direction. In general, their distribution will resemble that of the ash fall hazard zones. Again we emphasize that the often strong (up to 100 knots) and highly variable winds typical of the Aleutians make accurate spatial assessment of these hazards very difficult.

Volcanic earthquakes generally occur in high numbers around the times of eruptions. For purposes of this report, there are 3 basic types of volcanic earthquakes (other authors have used many different classification schemes): 1) shallow, low-frequency, tremor-like signals of small magnitude such as the events observed at Pavlof; 2) larger (up to about magnitude 5) events accompanying or preceding large explosive eruptions, for example Mt. St. Helens; and 3) large events probably related to subsurface movements of magma but not necessarily related to eruptions, such as recent earthquakes in Iceland and Hawaii, (e.g., Einarsson and Brandsdottir, 1980; Wyss et al., 1981). Most volcanic earthquakes originate under or in the immediate vicinity of a volcano. Because of their smaller size the

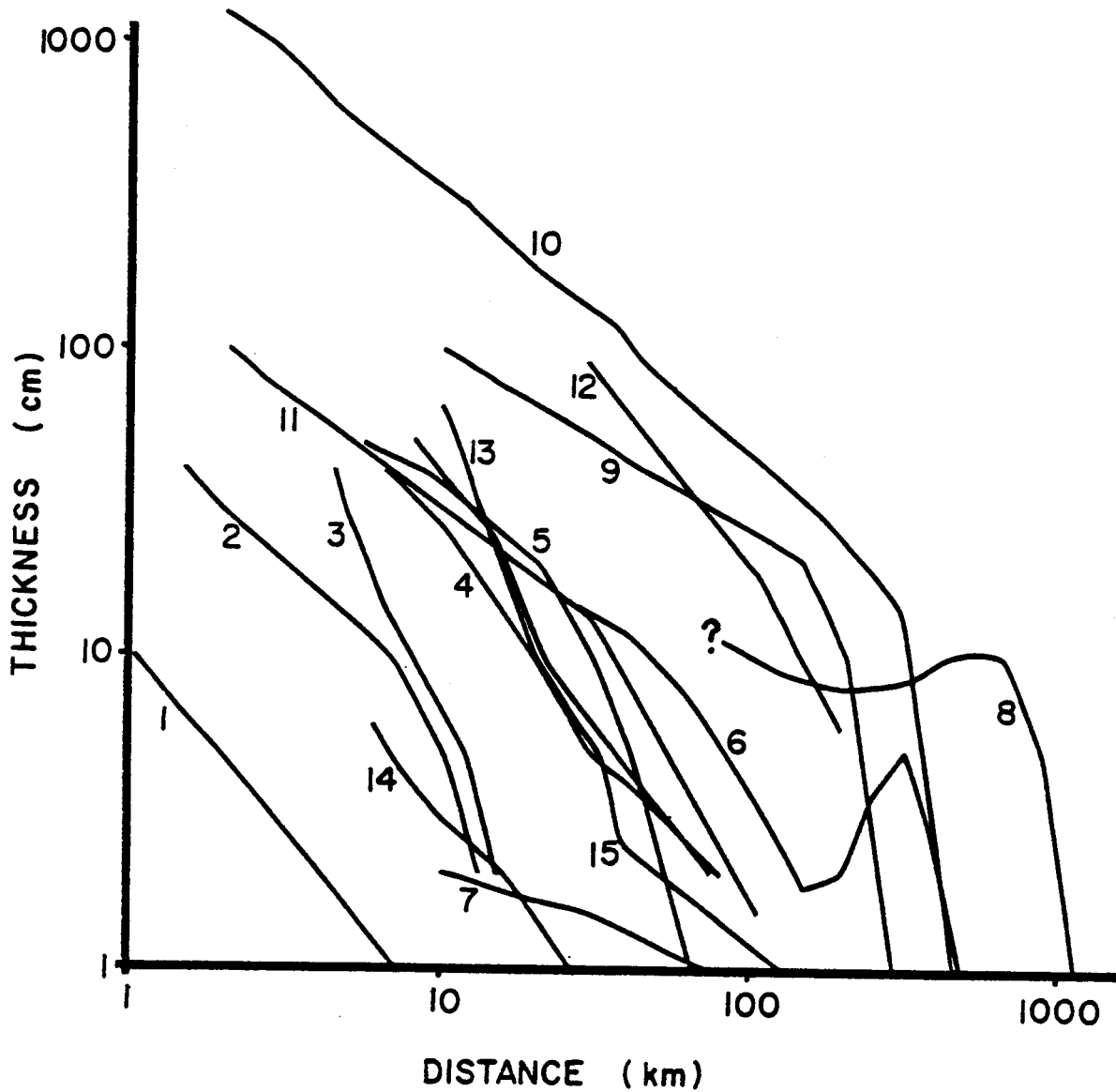


Figure 4.2.7. Maximum ash thickness in cm vs. distance from the vent. Sources of data are given below.

Maximum Ash Thickness vs. Distance

<u># on Plot</u>	<u>Volcano Name and Year of Eruption</u>	<u>Volume</u>	<u>References</u>
1	Paricutin	7.0×10^7	Wilcox, 1959
2	Cerro Negro, 1968	1.7×10^7	Taylor & Stoiber, 1973
3	Cerro Negro, 1971	7×10^7	Rose et al., 1973
4	Fuego, 1971	10^7	Rose et al., 1973
5	Hekla, 1947	1.7×10^8	Rose et al., 1973
6	Mt. St. Helens, 1980, May 18	1.5×10^7	Wilcox, 1959
7	Mt. St. Helens, 1842	10^7	Sarna-Wojcicki et al., 1982
8	Quizapu, 1932	3×10^9	Crandell & Mullineaux, 1978
9	Santa Maria, 1902	5×10^9	Wilcox, 1959
10	Katmai, 1912	3×10^{10}	Rose, 1972
11	Mt. St. Helens, layer T	10^8	Sapper, 1905
12	Mt. St. Helens, layer Yn	10^8	Wilcox, 1959
13	Mt. Shasta, (Layer R.B.)	$1-3 \times 10^9$	Crandell & Mullineaux, 1978
14	Mt. St. Helens, 1980, May 25	10^8	Crandell & Mullineaux, 1978
15	Fuego, 1974 (October)	1.4×10^7	Miller, 1980
		2.1×10^8	Sarna-Wojcicki et al., 1982
			Rose et al., 1978

seismic hazard due to volcanic earthquakes is quite small compared to the seismic hazard from large subduction zone events.

Shallow seismicity along volcanic axis. Shallow seismicity (at depth less than 30 km) recorded by the Shumagin Islands network from 1973-1982 is plotted in Figure 3.1.2. Along the volcanic axis the seismicity is generally low, with the exception of two prominent clusters. One of these is located ~20 km southwest of Kupreanof volcano (lat. 56N, long. 159W). The site is the same location as several sightings of steam emission, fumarolic activity and snow discoloration near the summit of an unnamed mountain at the head of Stepovac Bay.

The second cluster is located at lat. 56N, long. 160W, near Port Moller. This area contains several hot springs, one of whose temperatures was measured at about 140°F during the summer of 1979 (T. Ray, personal communication, 1979). It is interesting to note that the average volcano spacing for this section of the Aleutian arc is about 40 km. However, a gap appears in the Port Moller area. It is possible, but unlikely that a new volcano is being formed here.

While the identification of clusters of seismicity does not alone unambiguously delineate the possible locations of volcanoes, continued geophysical monitoring and more detailed studies may help to establish the extent to which these two areas may be likely sites of future volcanic activity. Further, we note that Pavlof volcano, which has erupted frequently during the last 9 years, has not had such clusters of seismicity located beneath it. Pavlof's seismicity instead includes volcanic tremor, B-type events, and explosions, as outlined elsewhere in this report. Thus, it is likely that any future volcanic activity associated with the two clusters of seismicity may have a different character than the activity observed at Pavlof.

5. CONCLUSIONS

The prime purpose of this study is to attempt a rather complete and up-to-date instrumental and historic data base of the seismic and volcanic activity associated with the Aleutian arc. We include those adjacent regions in the Pacific and Bering Sea Shelves that fall within or affect the Lease Sale Planning regions known as the "St. George Basin", the "North Aleutian Basin" and the "Shumagin Basin". As part of this effort we have operated a telemetered seismic network in the Shumagin Islands segment of the arc (and Alaska Peninsula), and for short periods of time, at Unalaska Island and the Pribilof Islands. The seismic study has lead to a remarkably good spatial seismic source definition and a consistent tectonic model which is important for developing probabilistic predictions of the future space-time behavior of seismicity, especially of great Aleutian subduction-zone earthquakes.

The study has had little opportunity to contribute to solving the open question of severe groundmotions associated with major subduction zone earthquakes. The study clearly points to the fact that this open problem of groundmotions need to be resolved before attempting any further statistical exposure calculations. The merits of such calculations remains doubtful as long as they are not based on solid data of groundmotions of moderate to great subduction zone earthquakes.

Notwithstanding this severe deficiency we conclude that, based only on potential source distributions and on probabilities of occurrences of moderate to great earthquakes in the arc, the seismic hazard near the Shumagin, Unalaska and (to a lesser degree) near the 1938 rupture zone is severe for a forthcoming period of interest, and may decrease to more moderate levels (see Appendix 7.6) in the northern portions of the St. George Basin, where local sources may be an important contributing hazards factor.

Volcanic hazards clearly exist and should be accounted for especially when planning for an operational stage of resource extraction. But, except for local and near-shore conditions, they appear to be a less restrictive regional hazards factor in most offshore regions when compared with the seismic hazards.

Crustal deformation and tsunami effects are expected to be severe on the Pacific side of the Aleutian Arc (including the Alaska Peninsula and outlying islands with pacific exposure). The historically observed tsunami run-up heights of up to 30 m, and coastal vertical level changes approaching 10 m or more should set a guideline for preventive measures.

We have established a comprehensive database for future quantitative exposure mapping in the subject region. The actual quantitative probabilistic mapping is not within the scope of this project and remains to be carried out by taking into account the data presented here.

6. UNRESOLVED PROBLEMS

We have discussed throughout this report a variety of unresolved problems that need to be addressed in future efforts if hazards assessment shall progress from producing qualitative to yielding quantitative results. In order of perceived importance we repeat and list the following items:

1) Collection of strong motion data from moderate to great earthquakes within the Aleutian arc.

2) Thorough, digital analysis of these Aleutian groundmotion data to derive parameterizations of groundmotions (duration, attenuation, etc.) both in the time and spectral domains that are of direct use to engineering design methods. The importance of data from great earthquakes is stressed.

3) Improve the understanding of statistics of recurrence times of great events in the arc to reduce uncertainties in conditional probabilities (i.e., resolve the question whether recurrence time data conform to normal or long-normal distributions?; is the Markov-process a useful model or not?)

4) Develop a quantitative method to characterize volcanic activity (by volume of ejecta, energy, etc.) and of volcanic effects on engineering structures.

5) Continue monitoring seismic, geodetic, sea level and other, tectonic-volcanic data that have a potential to improve medium-to-short term forecasting methods of hazardous events. This phase of data collection has to precede resource production stages by many years in order to establish false-alarm rates. False-alarm rates need to be known in order to not overestimate levels of risk during a 'precursory' phase of observation, preceding a suspected or imminent event. Medium-to-short term forecasting may be useful only to affect operational modes of hazards mitigation. They do not affect the basic long-term hazards assessment important for lease-sale planning and engineering design decisions. Given, however, certain post-lease sale developments and design implementations, such shorter-term measures may considerably reduce damage from an event if preparedness is properly implemented (temporary reduction of storage or production, removal of tanker or service fleets, etc.).

7. APPENDICES

7.1 Earthquake Data Processing Methods

Since 1973 the Shumagin network data have been recorded by several types of instruments. Initially, from July 1973 to August 1975 slow-speed, direct, analog tape recorders that recorded continuously were in use. The develocorder that records the data continuously on film, served as the main recorder from September 1975 until the end of April 1981. Since April 1980 analog, four channel, Teac tape recorders that are event triggered and record FM-modulated signals, have provided data that can be digitized at L-DGO. Such data can be analyzed using the PDP 11/70-UNIX system as any other digital data. Currently, the Teac tape recorders record data only as a back-up to the digital system.

The event triggered, digital data acquisition system (DDAS) that today is the main recording system for the network was installed in December 1980. During most of 1981 we had severe problems with operating the DDAS and the data recovery was less than 30%. In late December it became quite clear that the room temperature at the central station should be kept below 74°F so that the DDAS would function properly. During 1982 we have had almost 100% data recovery from the DDAS. The DDAS was connected to a separate digital event detector in October 1981. The new digital event detector can be accessed (by phone modems) from the L-DGO PDP 11/70-UNIX computer and relevant parameters can be reset. For visual recording the Shumagin network had from the beginning one or two helicorders. During the last three years the number of helicorders was increased from two to five and to eight in October 1981.

Develocorder data processing. Usually, the develocorder data that consisted of continuous seismogram traces from up to 14 stations and two time code channels, were processed in batches. The purpose was to determine hypocenter and magnitude of every locatable earthquake that occurred within 400 km distance and was recorded by the Shumagin network. Initially, the films are scanned for recorded earthquakes and the date and time to the nearest minute of locatable earthquakes are written on a summary sheet (see also Figure 7.1.1). The next step consisted of using a ruler to measure the arrival time

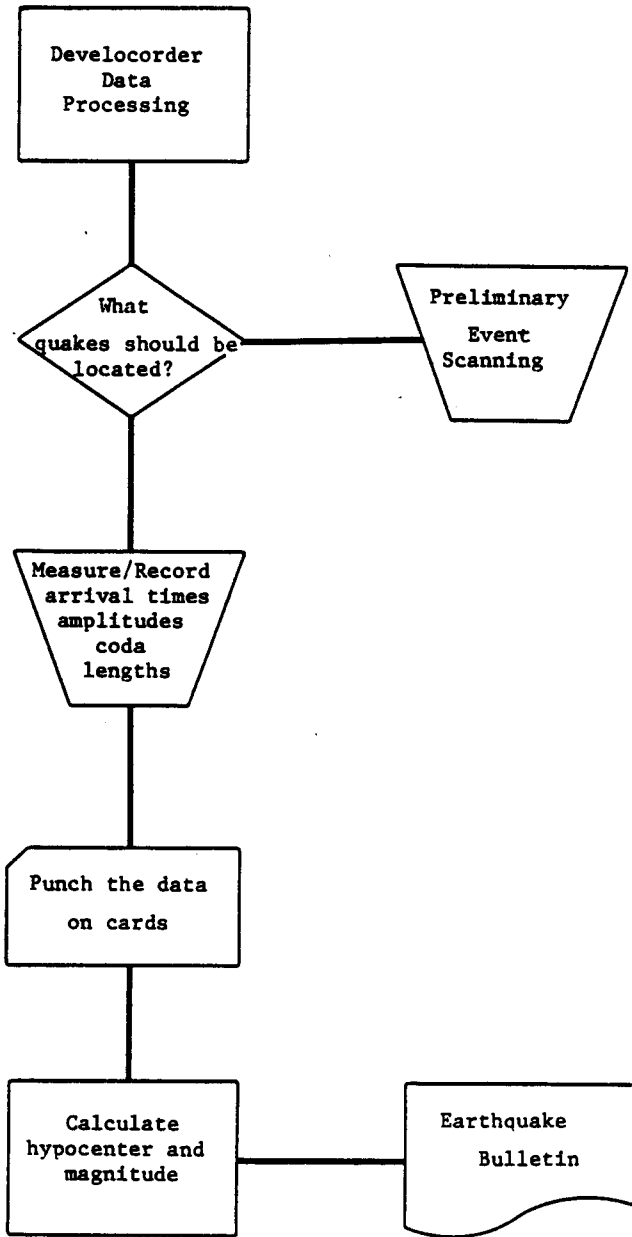


Figure 7.1.1. A block diagram showing how the routine developer order data processing was carried out for the Shumagin seismic network, eastern Aleutians, Alaska.

of P- and S-waves and amplitude information on a developocorder-viewscreen. A batch of arrival times from 40 to 50 earthquakes was punched on computer cards, or later tapes into a computer file from a terminal, for calculating earthquake hypocenter and magnitude. If the calculated hypocenter was found to be of low quality, the arrival times were checked for possible typographical errors or possible erroneous picking of P- or S-wave arrival times. Although this procedure was repeated normally at least three times, often a few "difficult" earthquakes still had low quality hypocenter solutions.

Digital data processing. The purpose of the routine digital data processing also is to determine hypocenter and magnitude of every locatable earthquake. The following description of the data processing is based on the block diagram shown in Figure 7.1.2.

First, the arrival time to the nearest minute and the peak amplitude of all the earthquakes that show up on the helicorder records are recorded in a logbook. The DDAS writes 25 to 30 events on the source tape at Sand Point. The table of content is generated both on site and at L-DGO using a program called trdla. The table of content is compared with the logbook to determine what files on the digital tape are earthquakes and which ones are false triggers or bursts of noise. To facilitate further processing hard copies or seismograms are made of each earthquake. Once the hard copies are available the events are classified as local (within 400 km distance), regional (400-1200 km), teleseismic (greater than 1200 km), volcanic events or calibration pulses.

The local events are demultiplexed and stored temporarily on an rll disk. The interactive program ping is run from a Tectronix 4014 graphics terminal and a data analyst picks arrival times, amplitudes and periods using cursor controls as is shown in Figures 7.1.3 and 7.1.4. The program addchdv adds instrument codes and attenuation settings to the pickfile. The program trgndmn changes amplitude values from digital counts to nanometers of ground motion. The computer program HYPOINVERSE (Klein, 1978) is used to calculate hypocenter and magnitude using the data stored in the pick file. HYPOINVERSE stores the results in four different files as demonstrated in Figure 7.1.5. In Figure 7.1.5 it is shown also how each event is

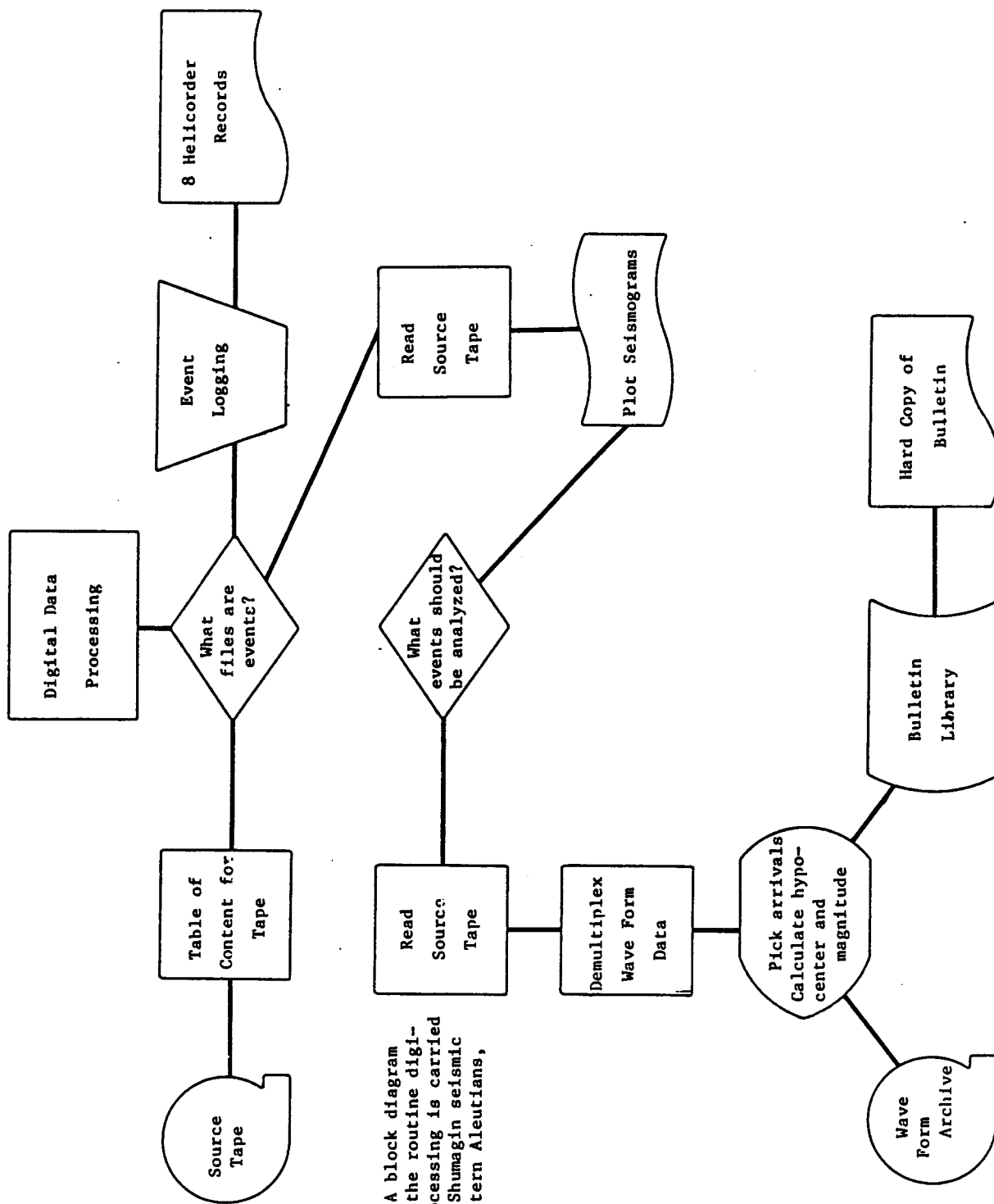


Figure 7.1.2A block diagram showing how the routine digital data processing is carried out for the Shumagin seismic network, eastern Aleutians, Alaska.

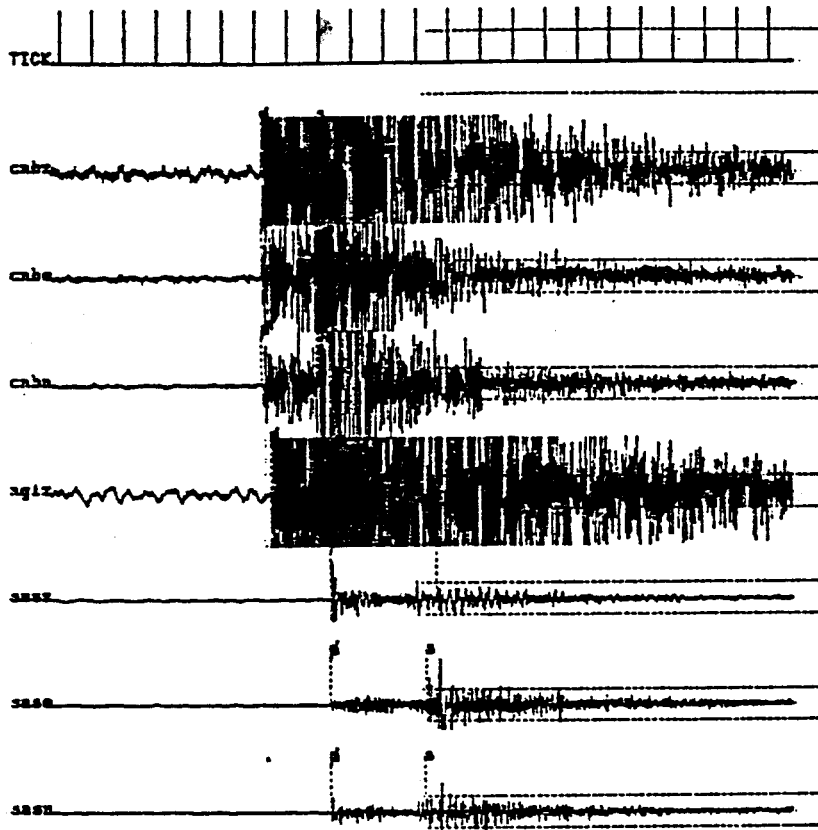


Figure 7.1.3. A summary display of seismic traces from the program ping. The analyst can choose which trace he wants to amplify (see Figure 7.1.4). The data analyst can also compare his P- and S-wave picks at the different stations, and pick coda lengths. Note in this mode the data are shown strongly decimated.

Station: cbs 32.53 - 57.53 - - - - 1981/12/23 11:14:17.00 14

Pick 2 pts with polarity

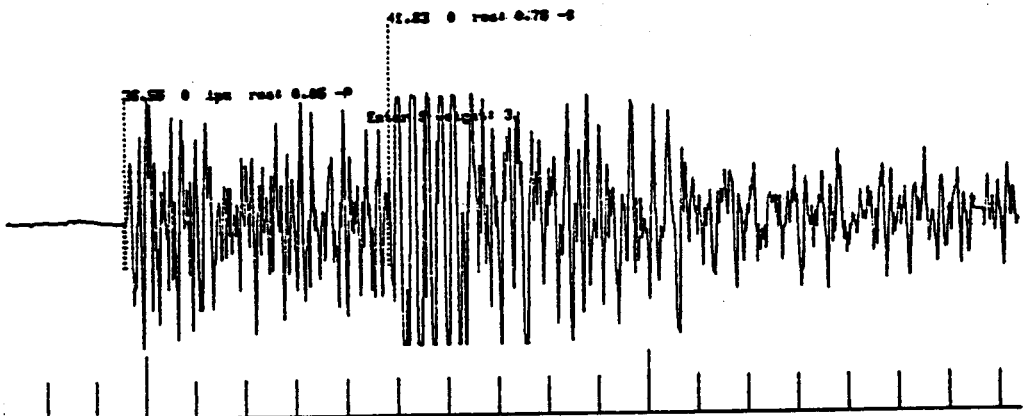
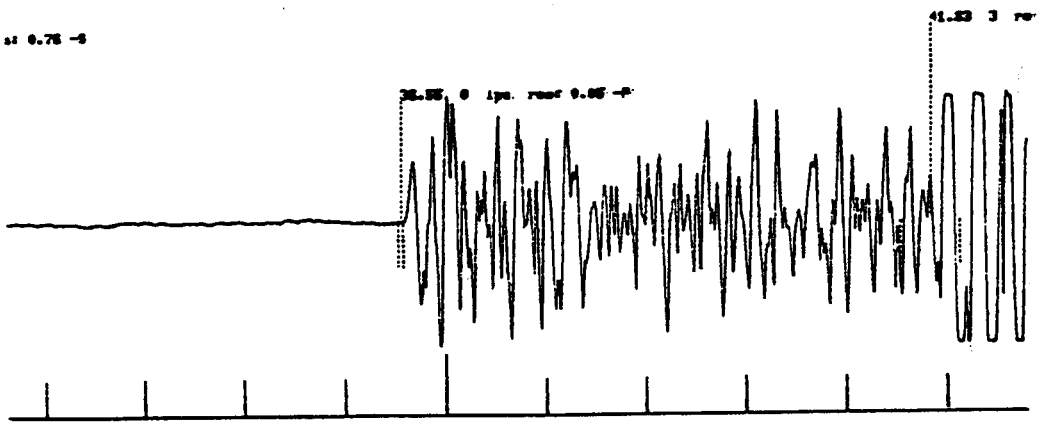


Figure 7.1.4.A sample seismogram from station CNBZ. The distance between tickmarks is 1 second. In this mode the data analyst picks, P-, S-arrivals, amplitude and period. Note that the lower trace is an amplification of the upper trace.

Station: cbs 32.57 - 42.57 - - - - 1981/12/23 11:14:17.00 14

Pick p-amplitude (upper/low):
p-amp 4064
Pick p period (begin/end):
p-per 0.140 7.1 Hz



the 811223.111417e file is:

1 23 dec 81, 11:14 event no. 1

yr	mo	da	origin	lat	lon	u	depth	rms	erh	erz	gap	xmag	fmag		
81	12	23	1114	30.33	54	42.31	159	54.88	31.29	.39	1.50	3.14	205	2.8	
result data itr nrm nrm rms remk q sqd															
.39 24.5 3 9 35 15 cd d c d															
sta	dist	azm	an	p/s	u	sec+ccor	(tobs	-tcal	-dly	*rea	wt	xmg	fmag	r	info
cabz	24.5	58	135	ipu	s	36.58	.00	6.25	6.20	.00	.95	2.03	2.3		.282
					s	41.82	.00	11.49	10.73	.00	.76	.51			.073
					s	36.59	.00	6.25	6.20	.00	.96	2.03			.282
cabz	24.5	58	135	epu	s	41.64	.00	11.31	10.73	.00	.58	.51			.073
					s	36.61	.00	6.28	6.20	.00	.98	2.03			.282
cabz	24.5	58	135	epu	s	41.73	.00	11.40	10.73	.00	.67	.51			.073
					s	37.51	.00	7.18	7.65	.00	-.47	2.03			.239
ngiz	38.4	346	119	ipd	s	43.59	.00	13.26	13.23	.00	.02	.51			.160
					s	42.98	.00	12.65	12.80	.00	-.15	2.03	3.3		.120
saaz	79.7	333	100	epd	s	52.83	.00	22.50	22.14	.00	.35	.51			.063
					s	42.99	.00	12.66	12.80	.00	-.14	2.03			.120
saaz	79.7	333	100	epd	s	51.91	.00	21.58	22.14	.00	-.57	.51			.063
					s	43.01	.00	12.68	12.80	.00	-.12	2.03			.120
sgbe	99.5	340	97	epd	s	51.77	.00	21.44	22.14	.00	-.71	.51			.063
					s	45.76	.00	15.43	15.37	.00	.06	2.03			.212
sgba	99.5	340	97	epd	s	57.38	.00	27.05	26.59	.00	.46	.51			.056
					s	45.70	.00	15.37	15.37	.00	.00	2.03			.212
dlgz	131.9	292	95	epd	s	56.63	.00	26.30	26.59	.00	-.29	.51			.056
					s	49.21	.00	13.78	19.60	.00	-.72	1.52			.216
lvfz	134.6	10	94	epd	s	66.85	.00	36.52	33.91	.00	2.63	.00			.000
					s	50.88	.00	20.55	19.35	.00	.60	1.01	2.8		.227
pvvz	140.7	302	94	epd	s	67.48	.00	37.15	34.51	.00	2.63	.00			.000
					s	51.06	.00	29.73	20.75	.00	-.02	.51	3.1		.015
pa2a	143.1	303	94	epu	s	67.21	.00	36.88	35.90	.00	.98	.51			.057
					s	51.66	.00	21.33	21.07	.00	.26	2.03			.232
pa3z	143.2	303	94	epd	s	69.54	.00	39.51	36.45	.00	3.06	.51			.056
					s	51.54	.00	21.21	21.07	.00	.14	.51	3.2		.014
pa4z	143.3	301	94	epd	s	71.38	.00	41.05	36.45	.00	4.60	.00			.000
					s	51.50	.00	21.17	21.17	.00	.00	.51	3.1		.015
pa6z	152.0	304	94	epd	s	67.84	.00	37.17	36.62	.00	.88	.51			.058
					s	53.53	.00	23.20	22.23	.00	.37	.00			.000
pa7z	153.1	303	94	epd	s	73.68	.00	43.35	38.46	.00	4.89	.00			.000
					s	53.67	.00	23.34	22.38	.00	.96	.00	3.4		.000
drzr	153.7	280	94	epd	s	74.08	.00	43.75	38.72	.00	5.03	.00			.000
					s	51.72	.00	21.39	22.45	.00	-1.06	.00	2.1		.000
pa8z	157.2	302	94	epd	s	69.59	.00	39.26	38.84	.00	.42	.51			.008
					s	53.82	.00	23.49	22.91	.00	.58	.51	3.0		.015
pa4z	159.4	303	93	epd	s	70.05	.00	39.72	39.63	.00	.08	.51			.054
					s	54.35	.00	24.92	23.20	.00	.82	.51	3.2		.014
blhz	175.8	310	93	epd	s	75.31	.00	44.98	40.14	.00	4.84	.00			.000
					s	56.32	.00	25.99	25.35	.00	.64	.51	2.3		.011
saaz	186.0	263	93	epd	s	75.30	.00	44.97	43.88	.00	1.11	.51			.044
					s	56.70	.00	26.47	26.69	.00	-.22	1.01			.277
balz	191.2	287	93	epd	s	80.91	.00	50.58	46.17	.00	4.40	.00			.000
					s	58.99	.00	28.66	27.38	.00	1.28	.51			.030
					s	88.37	.00	52.04	47.37	.00	4.67	.00			.000

the trial solution was:
 8112231114382754 4224159 5456 320329 34206 24 4110066 333 9 0 154 0cd 742315 155 305 811.73

811223.111417p - the original pickfile from ping
 811223.111417c - the condensed output pickfile with converted amplitudes
 811223.111417e - the legible version of 811223.111417c
 811223.111417f - the solution in hypo71 format
 811223.111417h - the solution in hypoinverse format
 SIDCHANect31 is the channels file used

cnbz10u#	8112231114	3658	5282	4182	s3	76495	58	#	#	245135	#	#	58	823	282	73	8.131n	#	-36
cnbz00u#	8112231114	3659	6282	4164	s3	58	58	#	#	245135	#	#	58	823	282	73	8.141qb#	#	-42
cnbz00u#	8112231114	3661	8282	4173	s3	67	58	#	#	245135	#	#	58	823	282	73	8.151qb#	#	-42
ngiz1pd#	8112231114	3751	-47292	4359	s3	2	58	#	#	384119	#	#	246	823	239	150	8.151n	#	-36
saazepd#	8112231114	4298	-15202	5203	s3	35134	58	#	#	797188	#	#	333	833	128	63	5.291b	1	-22
saazep#	8112231114	4299	-14262	5191	s3	-57	58	#	#	797188	#	#	333	823	128	63	5.331b	8	-22
saazepd#	8112231114	4301	-12202	5177	s3	-71	58	#	#	797188	#	#	333	823	128	63	5.311b	8	-22
sgbeep#	8112231114	4876	6282	5738	s3	46	58	#	#	995	97	#	348	823	212	56	3.241qb#	#	-42
sgbepd#	8112231114	4877	8282	5663	s3	-29	58	#	#	995	97	#	348	823	212	56	3.251qb#	#	-42
dlgzep.1	8112231114	4921	-72152	6685	s4	261	58	#	#	1319	95	#	292	823	216	56	3.061n	#	-24
lvfzep.2	8112231114	5088	68101	6748	s4	263198	58	#	#	1346	94	#	18	820	227	56	6.421n	#	-36
pvvzepd3	8112231114	5106	-2	58	6721	s3	98424	58	#	1487	94	#	302	831	15	57	8.761n	#	-42
pa2zepu0	8112231114	5166	26232	6984	s3	386	58	#	#	1431	94	#	333	823	232	56	8.101qb#	#	-36
pa3zep.3	8112231114	5184	14	58	7138	s4	46437	58	#	1432	94	#	333	822	14	5	9.111qb#	#	-42
pa6zep.3	8112231114	5188	58	58	6784	s3	88422	58	#	1439	94	#	331	831	15	50	6.121qb#	#	-36
pa7zep.4	8112231114	5353	97	7368	s4	489	58	#	#	1525	94	#	354	823	11	5	8.201qb#	#	-42
pa7zep.4	8112231114	5367	96	7408	s4	583765	58	#	#	1525	94	#	354	823	11	5	8.211qb#	#	-42
drzzep.4	8112231114	5372	-186	6959	s3	42	31	58	#	1537	94	#	328	821	8	96	6.251n	#	-36
pa7zep.3	8112231114	5382	58	58	7895	s3	8291	58	#	1572	94	#	352	823	15	54	6.221qb#	#	-36
pa4zep.3	8112231114	5435	82	50	7531	s4	484458	58	#	1594	93	#	333	822	14	7	7.191qb#	#	-48
blhzep.3	8112231114	5622	54	58	7520	s3	111	48	58	#	1750	93	#	310	823	11	4413.181n	#	-42
saazep.2	8112231114	5583	-22181	3691	s4	440	58	#	#	1850	93	#	263	823	277	5	8.971n	#	-36
balzep.3	8112231114	5699	109	50	8237	s4	467	58	#	1922	93	#	267	823	38	5	8.841n	#	-48
811223:11420354	4231:59	5488	312929	35285	25	3918266	342	12	8	149	8cd	652315	158	314	911.73				

Figure 7.1.5.A sample output from HYPOINVERSE. Above, the -o file is shown; below the -c file is shown.

given a name that is the date and time, when the digital or analog event detector declared the onset of an event. Currently, all five files, -p, -c, -o, -7, -h, are stored in an event directory (with a suffix -L) within the bulletin library. The seismograms or the demultiplexed waveform data are stored in two files on archive tapes with suffixes -d and -D where -d contains the data and -D contains header information. The pickfile or the -p files are stored also on the archive tape.

Figure 7.1.6 contains a simple but very useful graphical representation of the arrival time data. The programs that create this output from the -c file are described by Nicholson and Simpson (1983). The Wadati and Ruzhichenko diagrams give an independent estimate of the origin time and of the depth of the hypocenter. Further, they also provide an easy way to check for data inconsistencies.

In conclusion, the major advantages of digital data processing can be summarized as follows:

- 1) No measurements done by hand using a ruler are required. The data analyst never needs to copy down by hand such information as, for example, station code, wave type or arrival time. Thus a large source of potential error is eliminated.

- 2) Using the program ping the seismograms can be band-pass filtered and often signals can be restored that without filtering are just white noise. The Tectronix graphics terminal allows the data analyst to amplify or attenuate the data such that the whole dynamic range of 72dB can be exploited. A develocorder record had a typical dynamic range of only 20dB.

- 3) The digital data are processed as single events, and no event is archived until a satisfactory hypocentral solution has been found. The develocorder data were usually batch processed and although 3-5% of the events were not properly located the data processing was terminated, since chasing a few "difficult" earthquakes was not considered worthwhile.

Yr Mo Dy Origin Lat N Lon U Depth Mag RMS Err Ers Nata Gap Dmin Nur Nus Up/Us No.
 81-12-23 1114 30.33 54 42.31 159 54.88 31.29 2.9 0.39 1.50 3.14 20 205 25 35 15 1.73 1

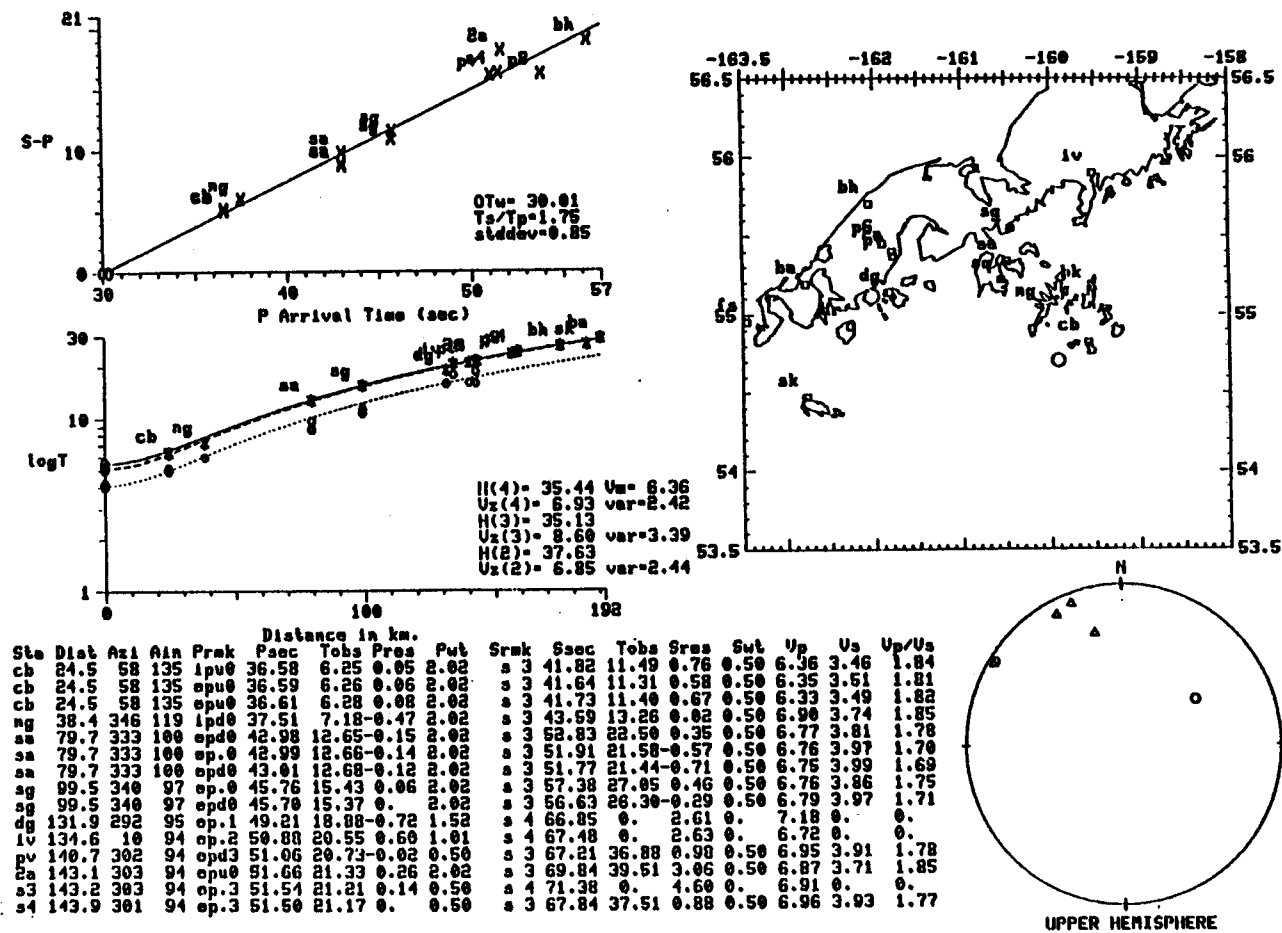


Figure 7.1.6. A sample output from the program dplt2 written by C. Nicholson. Upper-left is the Wadati diagram; lower-left is the Ryznichenko diagram. The epicenter is plotted on the map as an open circle close to the station cb. Lower-right an upper hemisphere focal mechanism; Δ - dilatations; o - compressions; x - are nodal arrivals.

7.2 Magnitude Determinations

Objectives. One of the purposes of operating the Shumagin seismic network is to determine the magnitude of local earthquakes. Either the body wave magnitude or the coda length magnitude for local events can be determined. A body wave magnitude is a more useful measure of the size of a local earthquake since it represents the measured ground motion at the respective seismic station. The coda length magnitude can be more easily determined since no calibrations of the instruments are needed as long as they remain unchanged. The coda length magnitude, however, is not a known function of ground motion and is sometimes dependent on the S-P-arrival time of the local earthquake. Prior to 1980 we determined coda length magnitudes for earthquakes that occurred within our network. Since much of our instrumentation was upgraded in 1980 and 1981 we were faced with the task of redetermining our coda length magnitude scale or to calibrate our instrumentation to facilitate the calculation of body wave magnitudes. We decided to calibrate our instrumentation since that permitted us to use the network to achieve other scientific goals (for example, attenuation studies, calculation of source parameters) in addition to enabling us to determine body wave magnitudes.

The calibration of the seismic network was carried out in two different ways. First, all individual components were calibrated in the laboratory or specifications on instrument characteristics were obtained from the respective manufacturer. This information (see Figure 7.2.1) was combined into a total system response as described below to determine ground motion in nanometers (nm, 10^{-9} m). Second, the seismic stations were calibrated in the field during the October 1981 field trip. A constant-current-square-wave signal of 10 second period was applied to the calibration coil of the seismometer. These calibration pulses can be used to confirm the results obtained using the first method. Further, at 10 seismic stations in the network a calibration signal is generated automatically every 24 hours to check if the station's calibration changes with time.

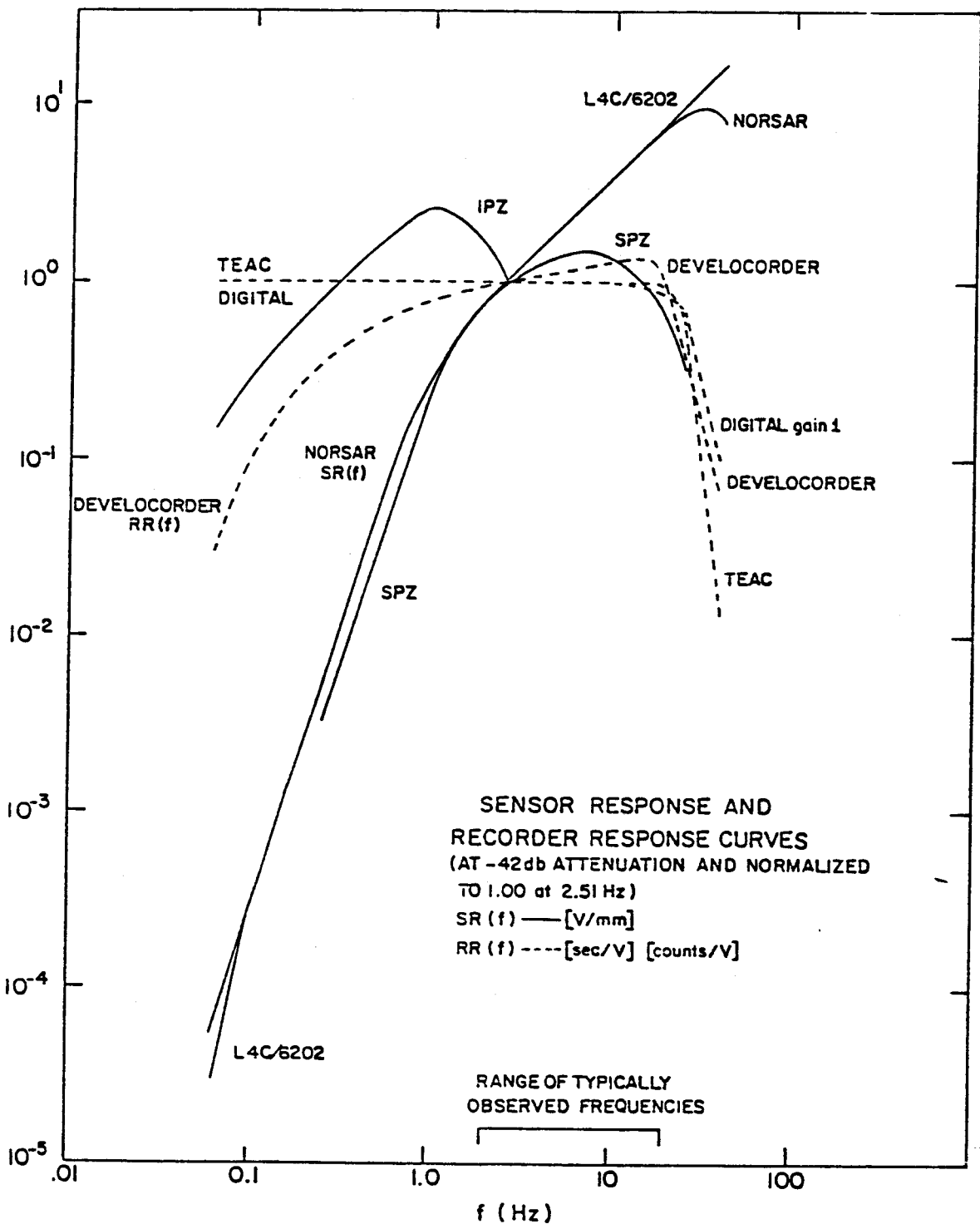


Figure 7.21. Sensor responses and recorder responses shown as a function of frequency for seismic stations in the Shumagin Network. The sensors are short period vertical (SPZ) and intermediate period vertical (IPZ). The SPZ sensors are either NORSAR HS-10 or Mark L4-C/6202, 1B seismometers. The IPZ sensors are broad band (Baby Benioff) seismometers. The recorders are continuous recording on a film (DEVELOCORDER), an event triggered analog tape recorder (TEAC) and an event triggered digital tape recorder (DIGITAL). Above the horizontal axis the range of typically observed frequencies is shown. The sensor and the recorder responses are combined to get the total system response as described in the text.

Calibration of the total system response. The total seismograph system response, TSS(f) at frequency, f, is the product of the sensor response SR(f) and recorder response RR(f) (see Figure 7.2.1).

$$TSS(f) = SR(f) \times RR(f)$$

The sensor response, SR(f), is the product of the seismometer response, S(f), and the amplifier response, A(f), or

$$SR(f) = S(f) \times A(f)$$

The seismometer response as a function of frequency was calculated with the following formula:

$$S(f) = \frac{2\pi f^3 G_E}{[(F_0^2 - f^2)^2 + 4B_t^2 F_0^2 f^2]^{1/2}} \quad [V/mm]$$

where G_E is the effective motor constant [V/mm/sec]

F_0 is the natural frequency [Hz]

B_t is the damping ratio (parallel or series)

The amplifier response vs. frequency (A(f)) was measured during a calibration sequence in the laboratory. This is a relative function that is normalized to 1.0 on the flat portion of its response curve. The sensor response is normalized to a 42 db attenuation of the station amplifier VCO [i.e., total gain is 90 db, (EMTEL 6242), or 120 db (DEVELCO 6202), hence attenuation 42 db is equivalent to gain 48 db or 78 db, respectively) since that is a commonly used value in our network. Since July 1982 the total gain is 72 db for the EMTEL 6242.

Further, the sensor response is normalized to 1.0 at 2.51 Hz for numerical convenience. The actual value of SR (2.51) constitutes the sensor gain G^S , or

$$SR(2.51) = G^S$$

The recorder response function, $RR(f)$ is the product of telemetry gain, $T(f)$ and recording device sensitivity, $R(f)$.

$$RR(f) = T(f) * R(f)$$

The telemetry gain is always set equal to one. The recorder sensitivity is determined by the particular input filters that were calibrated in the laboratory. The recorder response is normalized at 2.51 Hz and the actual value of $RR(2.51)$ constitutes the recorder gain, G^R .

Therefore, the normalized seismogram system response is determined by the $SR(f)$ and $RR(f)$ as shown in Figure 7.2.1. To obtain the total system response these curves have to be multiplied by the sensor gain, G^S and recorder gain G^R . If the VCO attenuation setting differs from -42dB it is taken into account when calculating G^S .

Typical magnification curves for data recorded by the digital data acquisition system are shown in Figure 7.2.2. The purpose of operating the low gain and the ultra-low gain instruments is to enable us to determine magnitudes for larger earthquakes.

Conversion of recorded amplitudes to true ground motion. A program was developed to convert the measured amplitudes to ground motion in nanometers. The appropriate TSS functions are stored for the seismometer, VCO, recorder combinations that are listed below. Also stored are the total gain factors for each TSS and an attenuation look-up file for handling the VCO attenuation setting variability, and extra damping pads.

Geophones

Mark L4-C, 1B
Geospace HS-10 (3 main coil resistances, 3 external dampings)
Norsar HS-10
Broad Band (Baby Benioff) SP, IP

Amplifiers-VCO's

Emtel 6242 (90 db)
Develco 6202 (120 db)

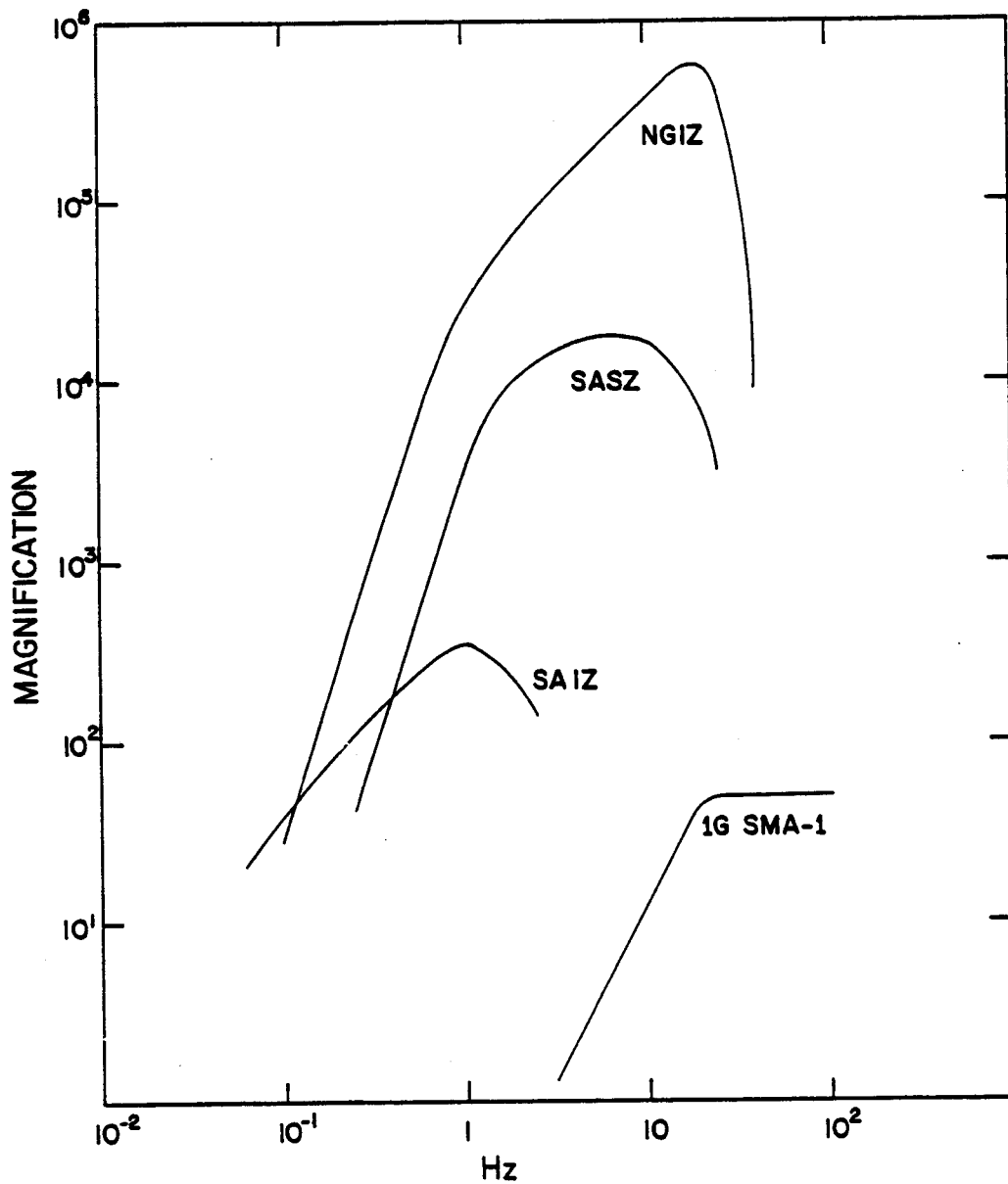


Figure 7.22. Magnification curves for a typical high gain short-period station (NGI at 48 db Amp/VCO gain); the low gain short-period seismometers at Sand Point (SASZ) and the ultra-low gain intermediate period seismometers at Sand Point (SAIZ). The magnification curve for a strong motion accelerograph (1G SMA-1) is shown for comparison.

Recorders

Develocorder
TEAC analog to digital
Digital system (ADC gain 1, 2)
Helicorder
Crown analog tape
Sangamo analog tape

True ground motion is simply the recorded amplitude divided by the product of the total seismograph system response, total gain and attenuation factors.

Calculation of earthquake magnitude. To determine the local magnitude scale such that it is calibrated with respect to the body wave magnitude, m_b published in monthly PDE bulletins, the following approach is taken:

From Richter (1958) we have for a Wood-Anderson instrument

$$M_L = \log A - \log A_0$$

where A is the zero to peak of the largest phase on the record in mm and A_0 is a distance correction. When correcting for the gain of the W-A we obtain

$$M_L = \log (A/2800) - \log A_0 + \log 2800$$

$$M_L = \log (A_q) - 6 + \log 2800 - \log A_0$$

where A_q now is measured ground motion in nanometers (nm). Instead of measuring the largest phase on the record which in our case is most often a surface wave or an S-wave, we measure the largest amplitude in the P-wave train. This permits us to determine a local body wave magnitude as

$$m_b = \log A_{pq} - 2.55 - \log A_0.$$

We prefer to use the largest P-wave amplitude (A_{pq}) since it is less often saturated or clipped than the S- or surface wave amplitudes.

To compare the values of magnitudes determined by the Shumagin network with values published by the National Earthquake Information Service (NEIS) in monthly or weekly PDE bulletins, we have plotted in Figure 7.2.3 magnitudes from PDE against magnitudes from the Shumagin network. The data are tabulated also in Table 7.2.1. We note that nearly all the PDE or PMR magnitudes are greater than 4.0. Unfortunately, this is the range where the Shumagin network starts saturating and amplitudes of earthquakes larger than magnitude 4.0 may be clipped. Nonetheless, the data plotted in Figure 7.2.3 indicate that the Shumagin magnitudes in the range from 3.0 to 5.0 are underestimated by 0.3-0.5 magnitude units. (These Shumagin magnitudes are shown in columns 73-75 in data files submitted to NOAA).

Coda length magnitude. In rare cases we still report coda length magnitudes when a body wave magnitude cannot be determined. The surface wave magnitude, i.e., coda length magnitude, reported (as shown in cols. 61-63 in data files submitted to NOAA) are determined using the FMAG formulation of J.C. Lahr (1980) and his empirical constants derived for Alaska.

$$\text{FMAG} = C_1 + C_2 \log (F_\gamma) + C_3 \Delta + C_4 Z + C_5 (\log (F_\gamma))^2$$

$$\begin{array}{lll} C_1 = -1.15 & C_3 = 0.0035 & C_5 = 0.0 \\ C_2 = 2.0 & C_4 = 0.007 & \end{array}$$

C_5 may be determined in the future with a larger data set "to compensate for the nonlinear relationship of log (coda) and magnitude."

F = F-P time; measured from P onset to 1 cm p-p amplitude cut-off

Δ = epicentral distance (km)

Z = hypocentral depth (km)

γ = station correction (1 used here)

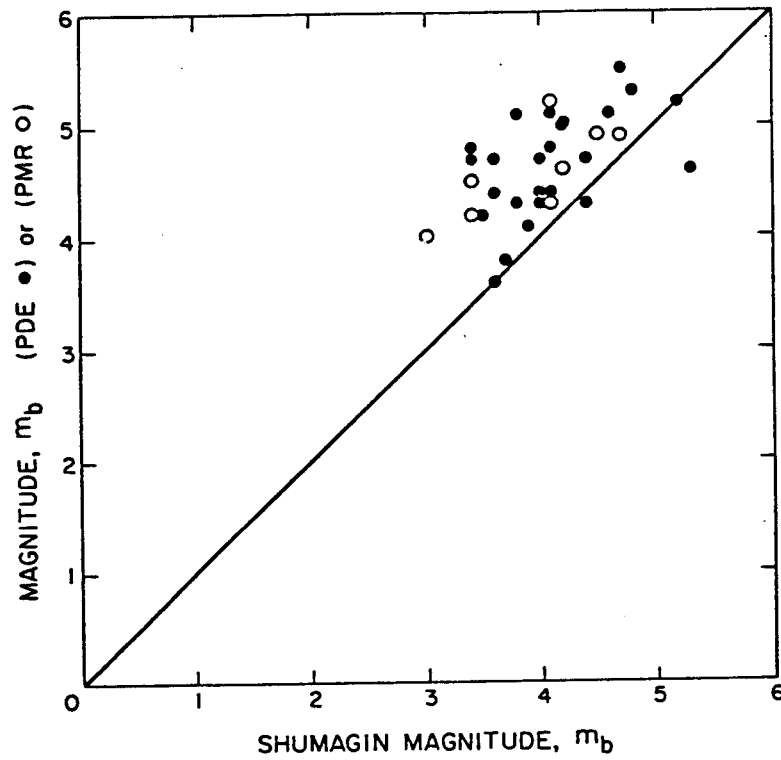


Figure 7.2.3. Comparison between magnitude values determined by the Shumagin network and values published by NEIS in monthly and weekly PDE-bulletins. The straight line has a slope of one. Open circles are PMR magnitudes.

TABLE 7.2.1. Earthquakes Located by Both the Shumagin Network and PDE

The respective magnitudes are plotted in Figure 7.2.3.

Date.Time	Shumagin				PDE			
	Latitude	Longitude	Depth (km)	Xmag.	PMR	MB	Avg.	Msz
810107.165917	55N50	154W41	6*	3.4	4.5m	4.8m	4.8	
810417.232919	57N59	154W06	94*	5.3		4.5w/4.6m	4.6	
810510.225302	56N22	161W21	200	4.0		4.3w/m	4.3	
810524.102339	55N58	159W24	118	3.2				
810605.070951	52N24	164W52	11*	4.7	4.9w/m	5.5w/m	5.5	4.6w
810607.175257	53N24	164W51	17*	4.3	4.6w/m	5.0w/m	5.0	
810613.132129	53N25	163W13	3	4.3		4.9w/5.0m	5.0	4.4w/m
810625.013632	54N50	159W45	31	4.1	5.2w/m	4.8w/m	4.8	
810801.014319	59N21	150W54	160*	5.2		5.1w/5.2m	5.2	
810815.103113	56N06	156W46	77	4.1		5.1w	5.1	
810818.225548	55N39	158W43	39	3.6		4.4w/m	4.4	
810906.132045	56N32	156W09	45*	3.8		4.3w/m	4.3	
810913.201210	54N16	163W43	66	3.0	4.0m			
810927.121347	57N09	153W25	154*	3.6				
811114.004324	53N44	164W30	81	4.6		5.1w/m	5.1	
811118.193511	53N22	163W58	30	3.6		4.7m	4.7	
811209.122304	52N50	154W37	33*	4.5	4.9m	4.9w/m	4.9	
811228.102821	54N44	160W37	30	3.7	3.8w		3.8	
820102.202712	55N35	157W13	13*	4.1	4.3m	4.4m	4.4	
820122.090046	55N49	159W00	84	4.0		4.4w/m	4.4	
820129.140307	53N31	163W55	3	3.4	4.2w/m	4.7w/m	4.7	
820131.112437	58N52	153W31	68*	4.4		4.3w/m	4.3	
820216.180231	54N10	156W21	8	4.0		4.7w/m	4.7	
820219.025102	53N36	164W35	10	4.4		4.7w/4.6m	4.7	
820315.145325	52N42	162W00	4	3.8		5.1w/5.0m	5.1	4.3w/m
820404.234113	52N45	167W15	1*	3.9		4.3w/m	4.3	
820415.162109	54N01	161W28	23*	4.8		5.3w/m	5.3	
820416.084700	53N21	163W09	11*	3.5		4.2w/m	4.2	
820416.084946	53N23	163W06	6	3.6		3.6w/m	3.6	

*Assigned depth of hypocenter; w - weekly, m - monthly PDE Bulletin, Avg. - PDE magnitude plotted in Fig. 7.2.3.

7.3 Annual Plots of Shumagin Network Seismicity 1973-1982

As a necessary step in preparing this report we put a large effort into reorganizing, refining and recompileing all the arrival time data recorded by the Shumagin network and the computed hypocenters since 1973 to the middle of 1982.

First the arrival time data was organized into monthly pickfiles (e.g., files containing all the arrival times of all the events recorded during that month) in a standard HYPOINVERSE format. Then the whole data set was relocated using HYPOINVERSE (Klein, 1978). To choose a reasonable trial depth each month of data was passed through a filter that simulates a Reyners and Coles (1982) cross section. If a hypocenter happened to be located outside of the filter boundaries, several different possible values of trial depth were tried until a consistent solution was found.

The results of this effort are shown below in Figures 7.3.1 through 7.3.11. Table 7.3.1 contains the total number of located earthquakes each year. In Figure 7.3.11 we have plotted all the earthquakes that were located by the Shumagin network from 1973 to 1981. Each year of data, which contains all locatable earthquakes observed during that year, is shown also separately in Figures 7.3.1 through 7.3.10. Although the continuity of data recording varies considerably through time, the annual seismicity maps and cross sections indicate how the seismic activity changes in space from one year to another. Both variations in the scattered background seismicity and temporal occurrence of seismicity clusters can be seen in the annual plots. Each cross section is taken along the line shown on the respective map striking north 30° west. The different symbols indicate within which depth range the earthquake is located, (triangles: 0-40 km; x: 40-120 km; diamonds: 120-250 km; and rectangles: depth greater than 250 km). No magnitude information is included in Figures 7.3.1 through 7.3.11.

We have used the flat-layered earth model that is shown in Table 7.3.2 to locate earthquakes beneath the Shumagin Islands network. Some of the features in the cross sections show linear clusters of hypocenters at constant depths which coincide with the layer

boundaries in this model. This artifact is caused by poor depth control which mainly results from incomplete network coverage in offshore regions.

As an aid for studying Figures 7.3.1 through 7.3.11 we summarize the most important characteristics of each data set below:

- 1973 (Figure 7.3.1). Generally scattered seismicity, similar to the patterns observed in 1975 and 1981. A cluster of seismicity is located below Kupreanof Volcano on the Alaska Peninsula.
- 1974 (Figure 7.3.2). The large cluster located at the southern end of the Nagai Island included two moderate size earthquakes ($m_b = 5.8, 6.0$).
- 1975 (Figure 7.3.3). Generally scattered seismicity similar to the pattern observed in 1981. The Cold Bay link was installed and hence, event detection was improved west and south of Cold Bay and Sanak Island.
- 1976 (Figure 7.3.4). Scattered seismicity and some small clusters near the Nagai Island.
- 1977 (Figure 7.3.5). The seismicity is evenly scattered throughout the Shumagin Islands region.
- 1978 (Figure 7.3.6). Concentrated activity located west of the Shumagin Islands. A cluster of activity near the Korovin Island continues in 1979.
- 1979 (Figure 7.3.7). Several earthquakes deeper than 200 km were observed. High level of activity along and above the lower edge of the main thrust zone accounts for the doubling of number of earthquakes located in 1979. A main shock of magnitude (M_s) 6.5 was located at 55.1°N and 157.0°W .

- 1980 (Figure 7.3.8). The seismicity is less scattered than during 1981. A wide band of seismicity subparallel to the Sanak Basin and concentrated clusters in the Port Moller region and near Nagai Island are prominent features during 1980.
- 1981 (Figure 7.3.9). The seismicity is evenly scattered throughout most of the Shumagin region. A cluster of seismicity appears east of Sanak Island.
- 1982 (Figure 7.3.10). Prominent cluster of shallow activity located west of Deer Island. The lower plane of the Benioff zone is unusually quiescent. High level of activity south and west of Sanak Island.
- 1973-1981 (Figure 7.3.11). Note the high level of activity along the lower edge of the main thrust zone and within the upper plate along the southeastern part of the Shelf. This activity may indicate the existence of possible imbricate thrust faults. The main thrust zone is a region of low level of activity. Horizontal bands of seismicity (seen in the cross section) are caused by the lack of depth control. The upper plane of the Benioff zone has a higher level of seismic activity than the lower plane.

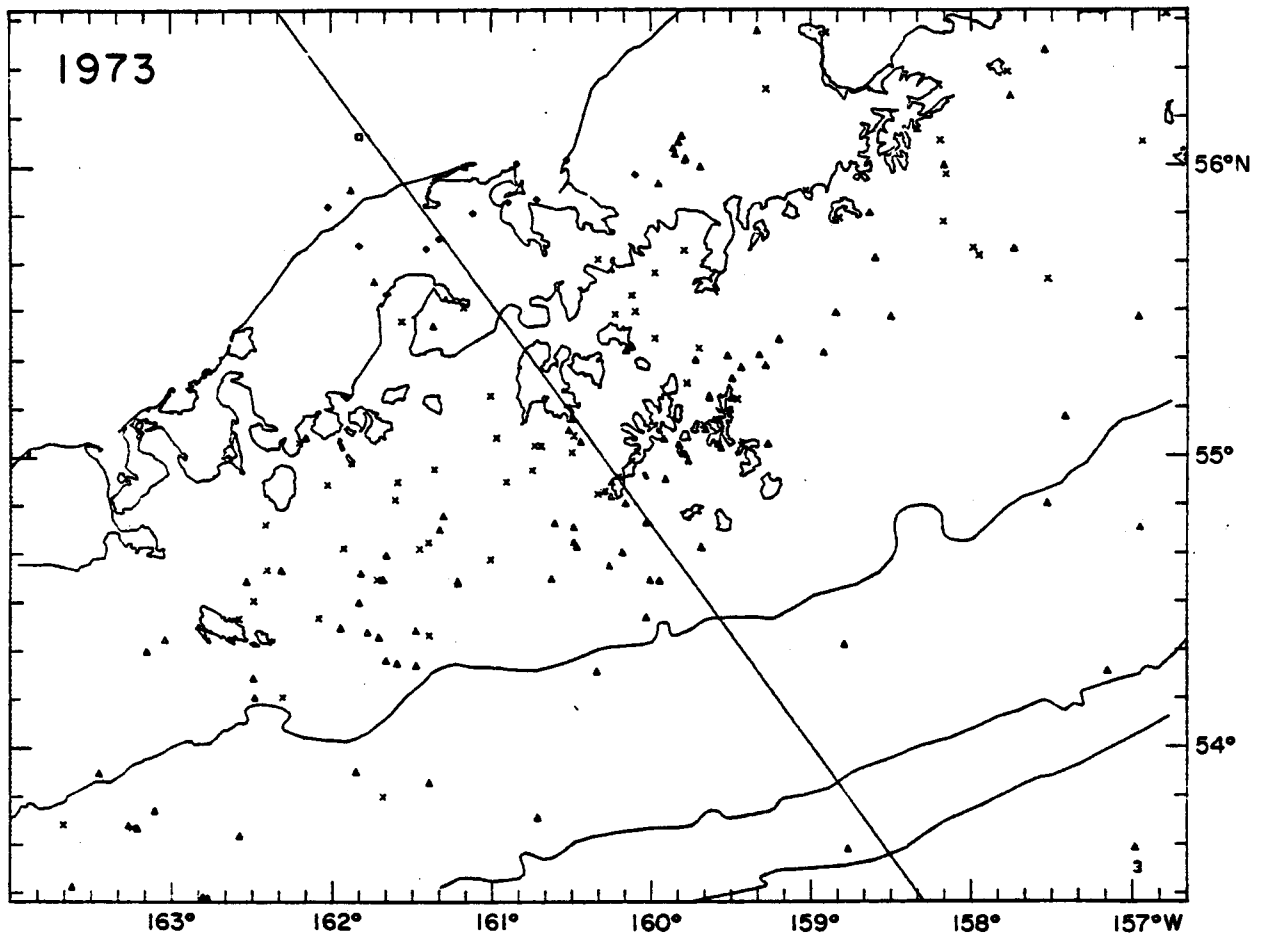
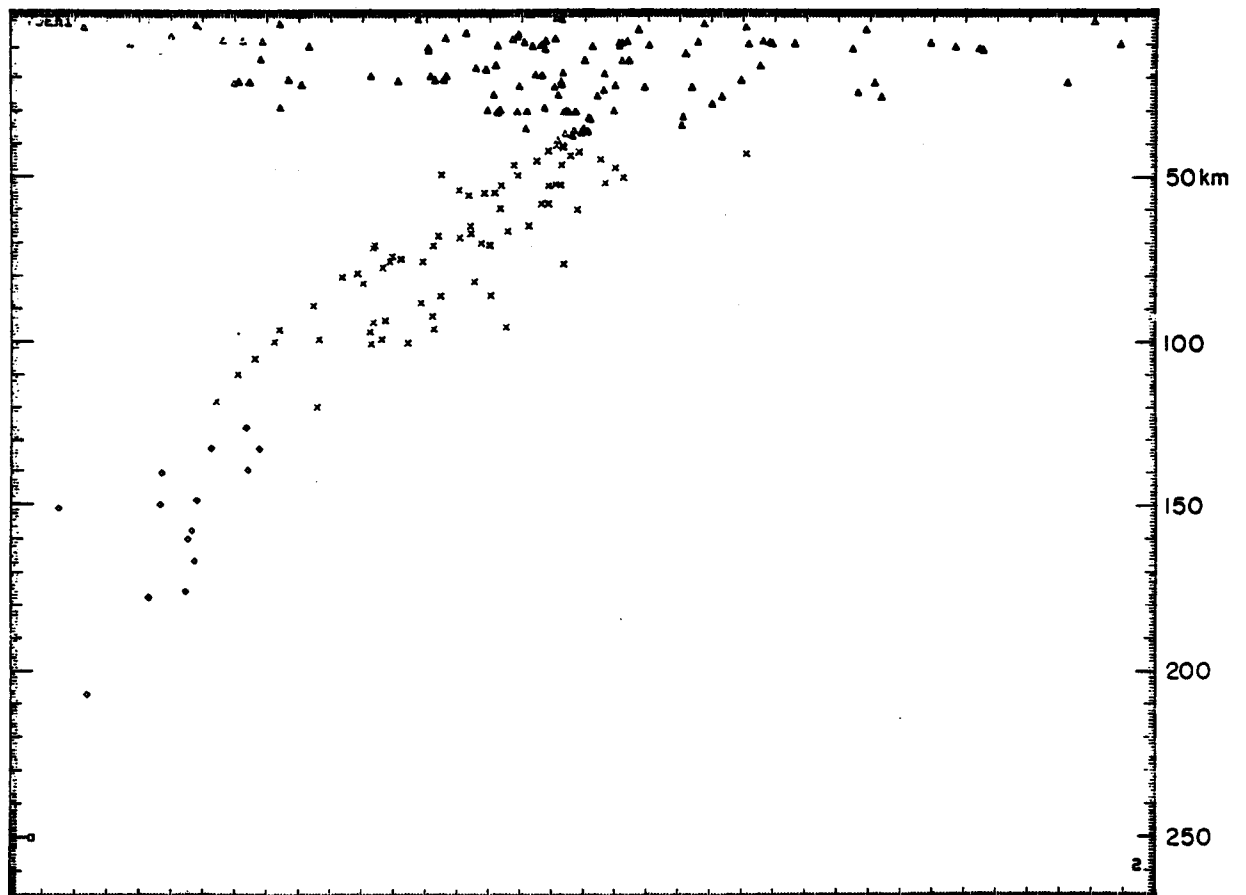


Figure 7.3.1. Seismicity located by the Shumagin network during 1973.



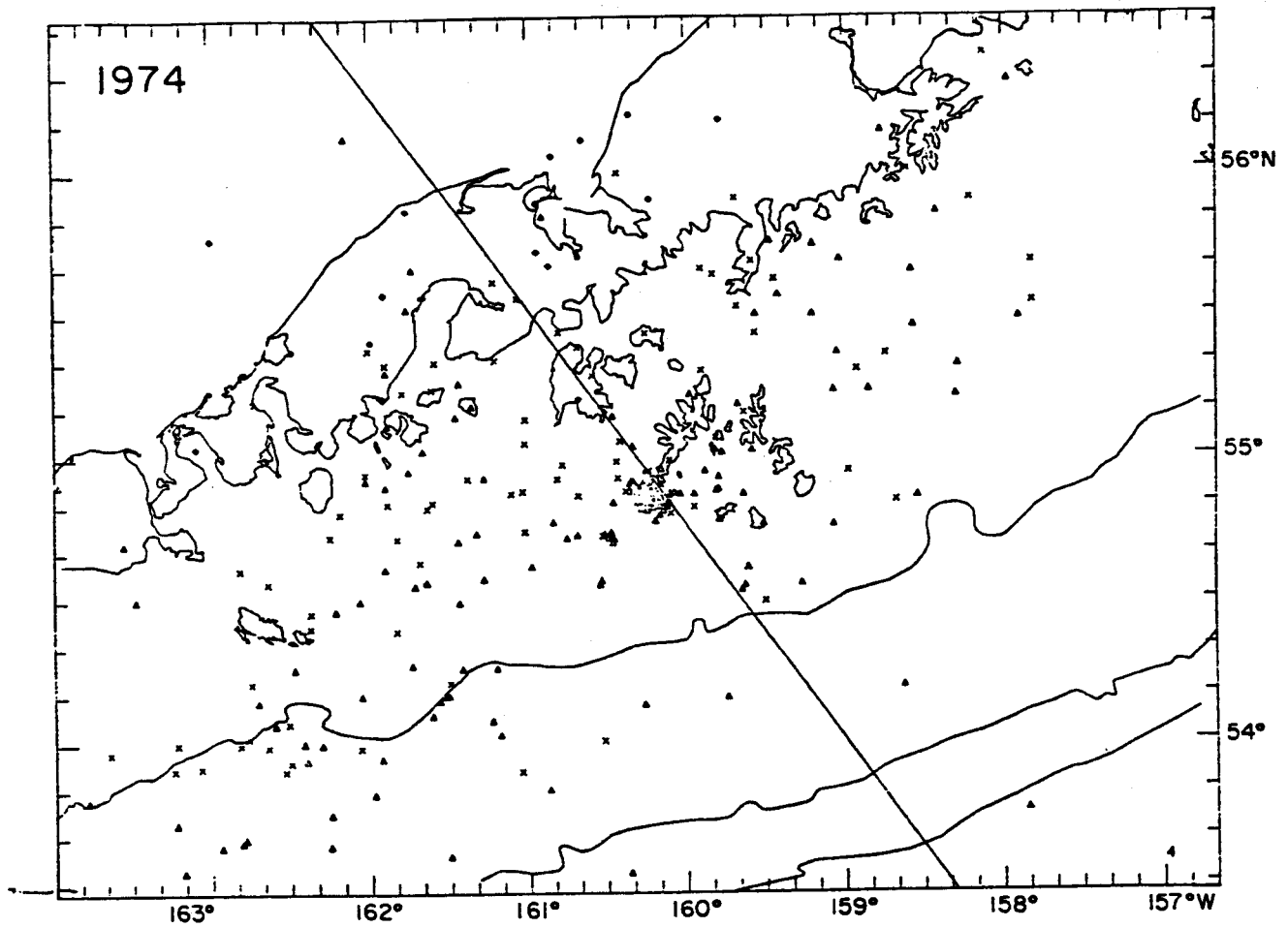
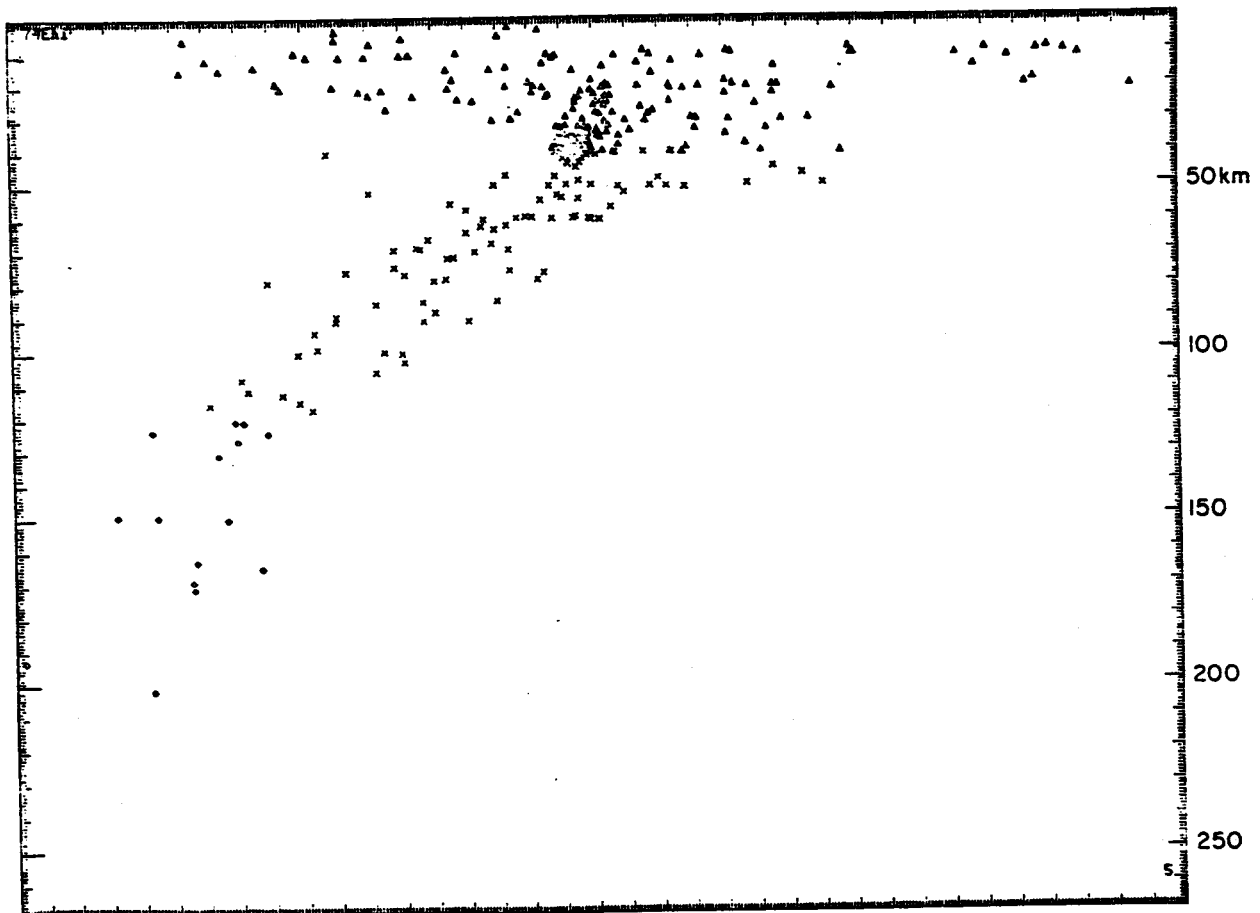


Figure 7.3.2. Seismicity located by the Shumagin network during 1974.



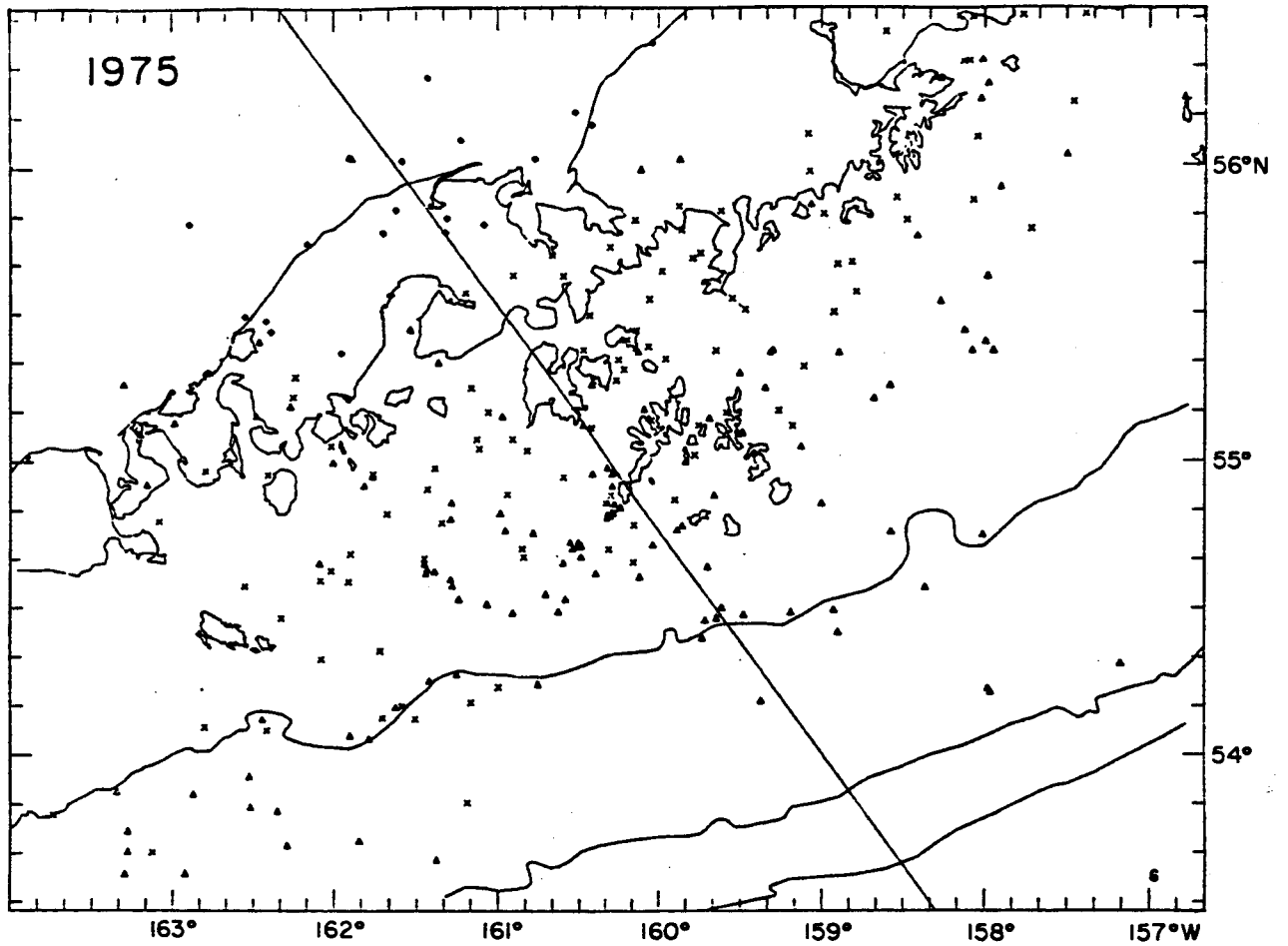
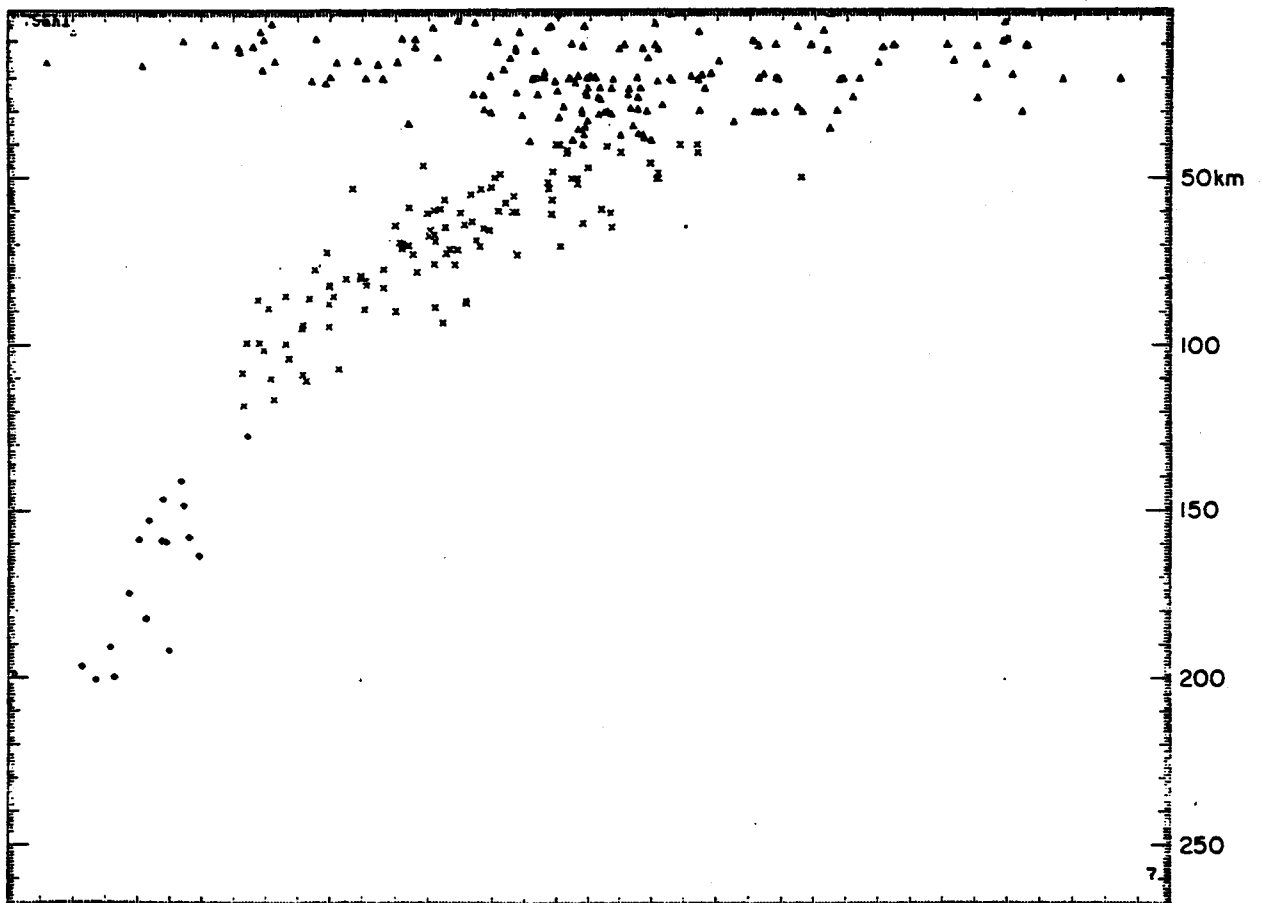


Figure 7.3.3. Seismicity located by the Shumagin network during 1975.



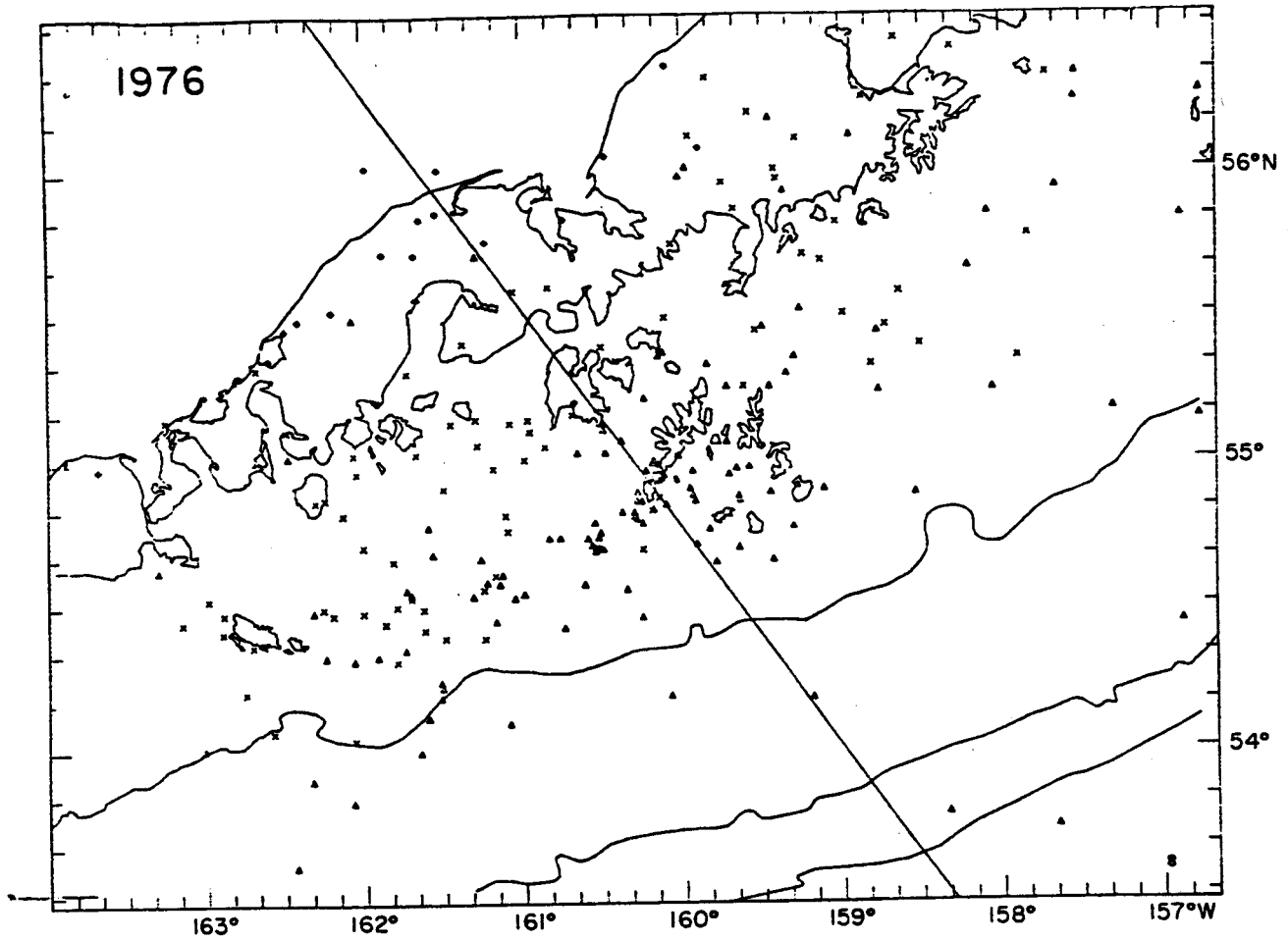
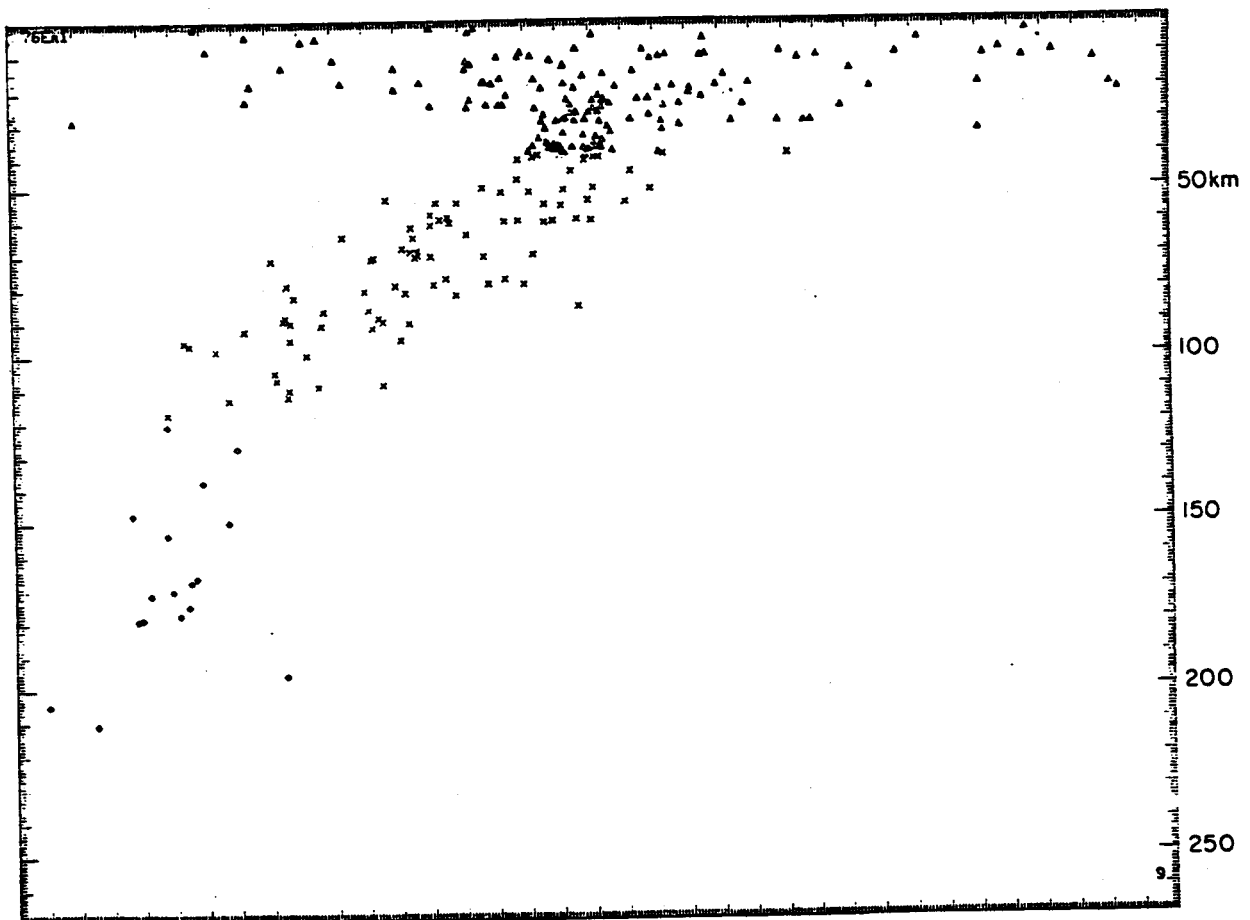


Figure 7.3.4. Seismicity located by the Shumagin network during 1976.



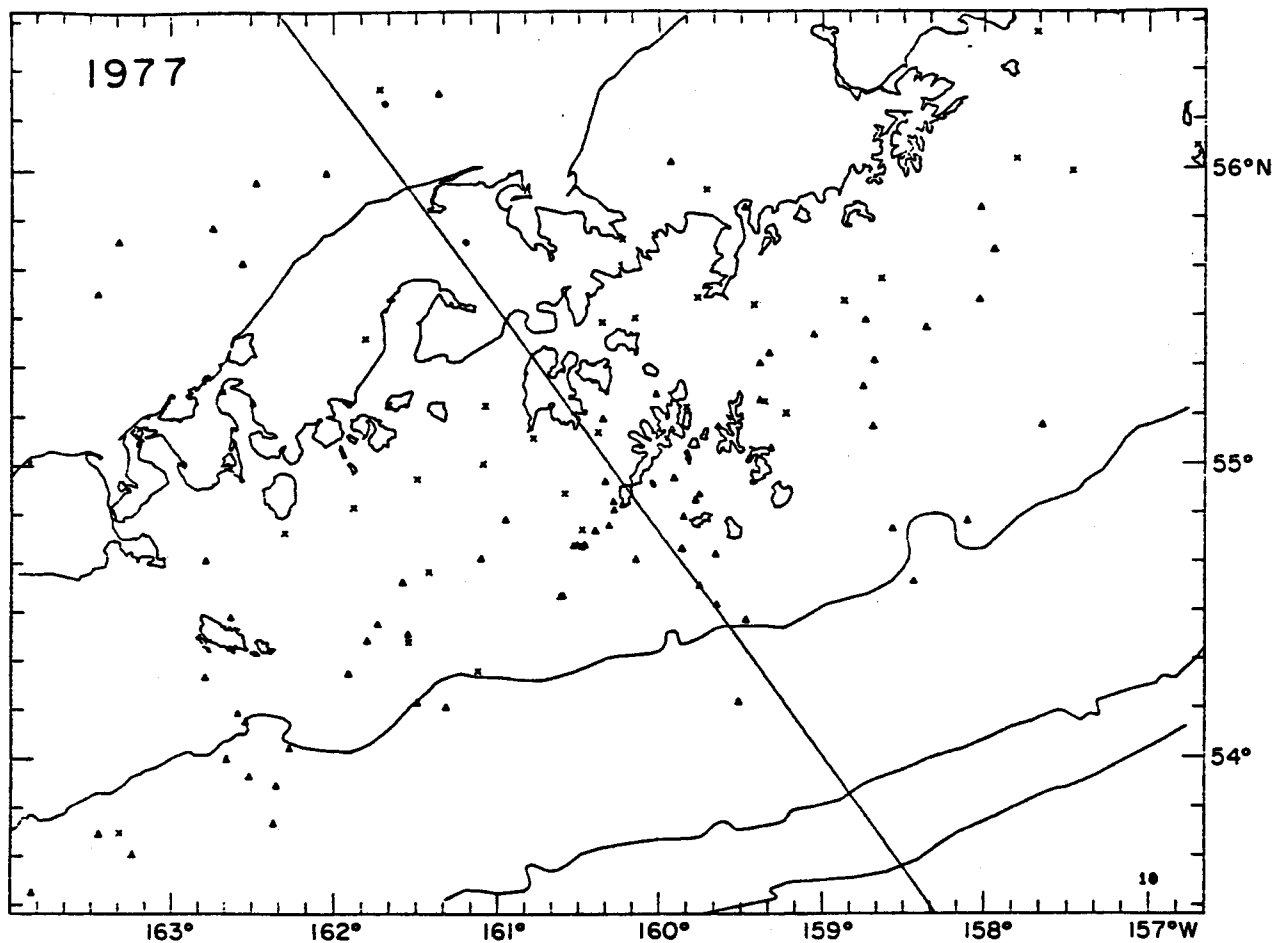
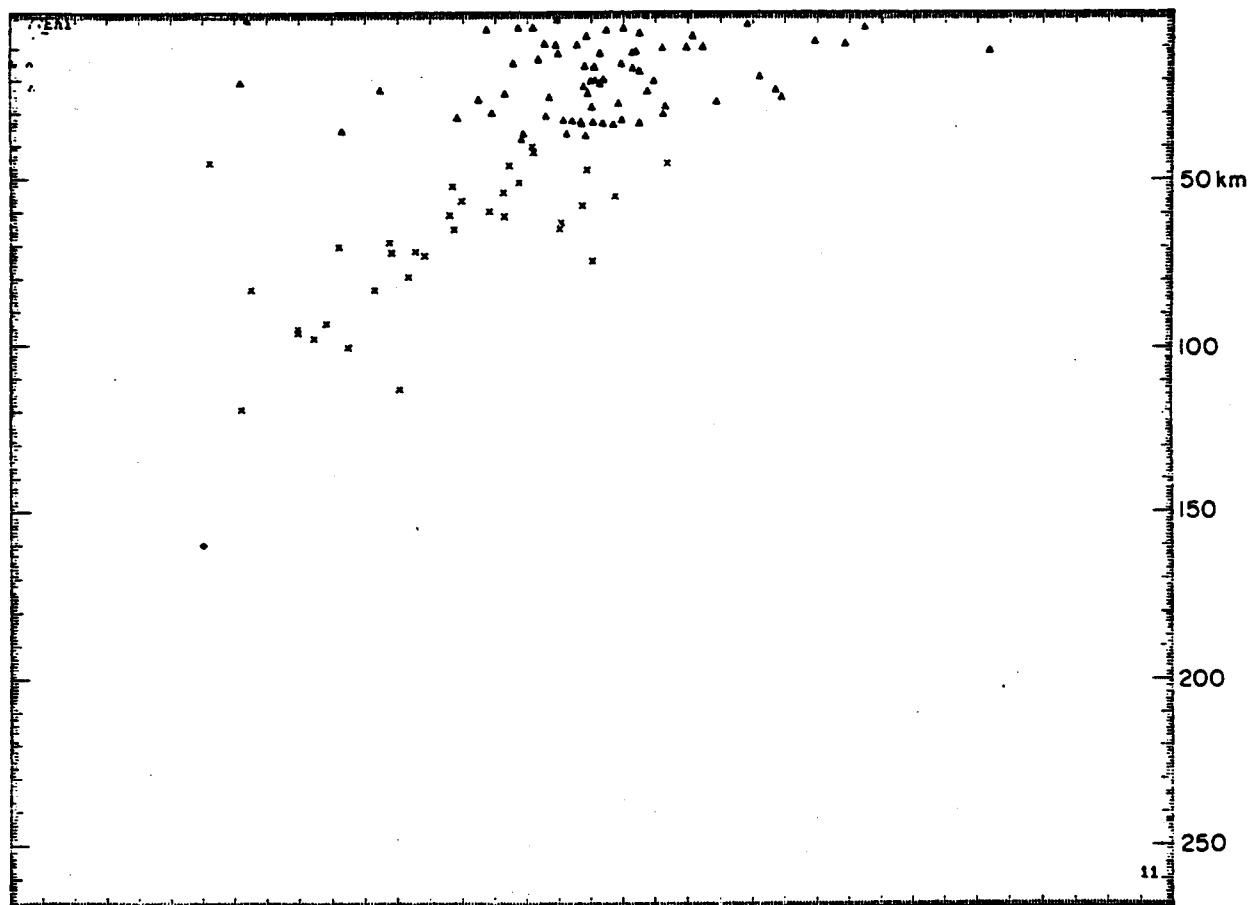


Figure 7.3.5. Seismicity located by the Shumagin network during 1977.



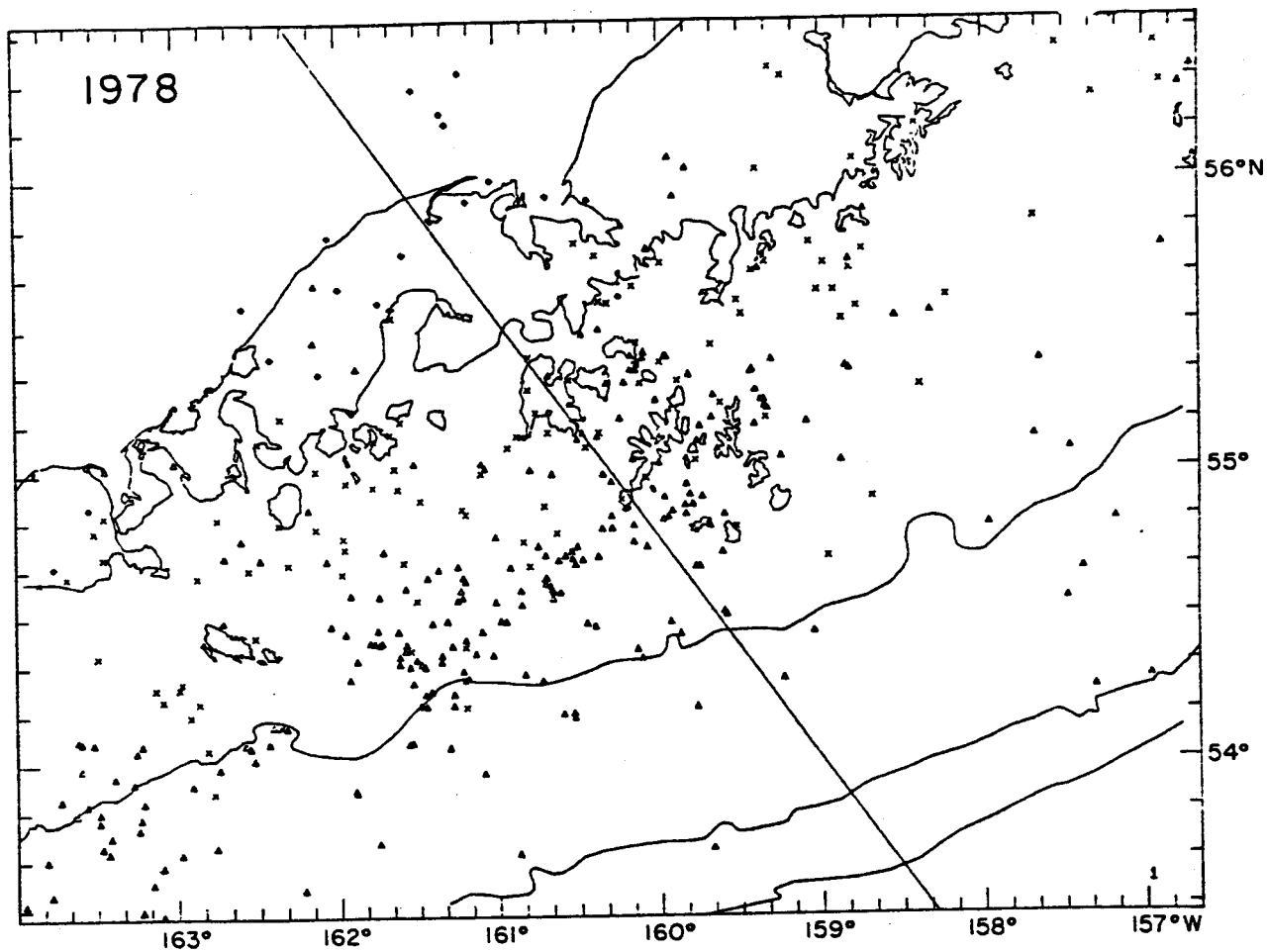
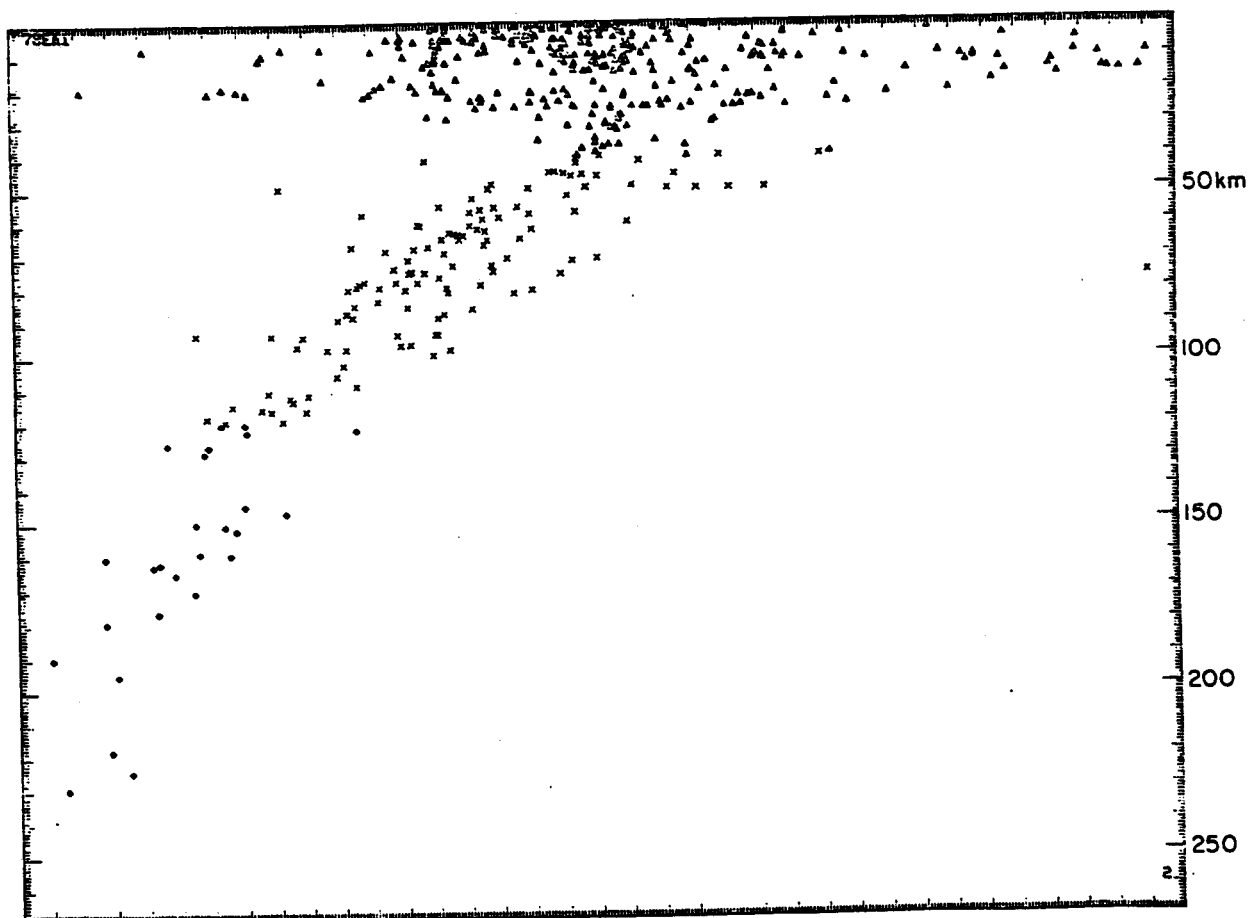


Figure 7.3.6. Seismicity located by the Shumagin Network during 1978.



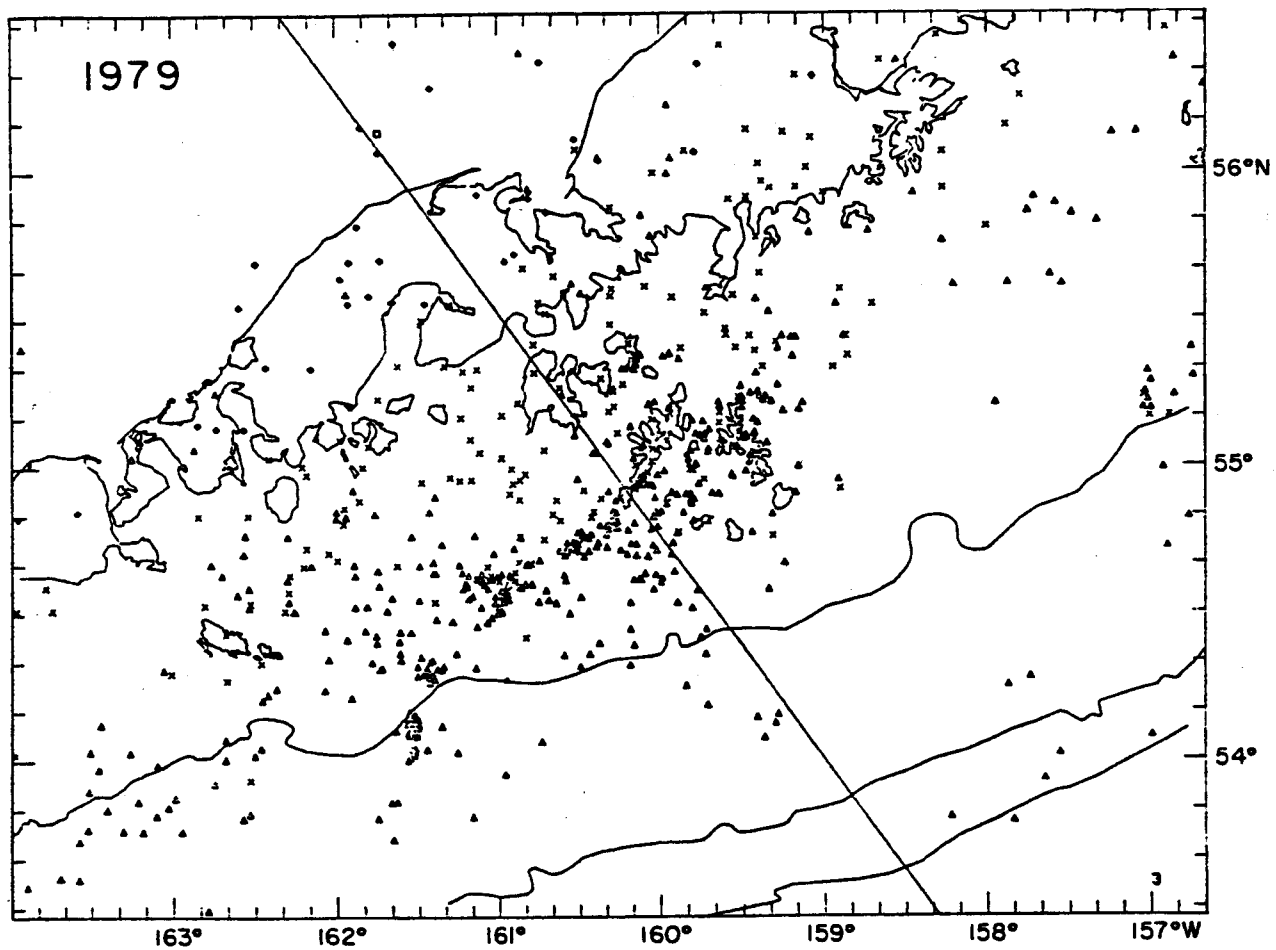
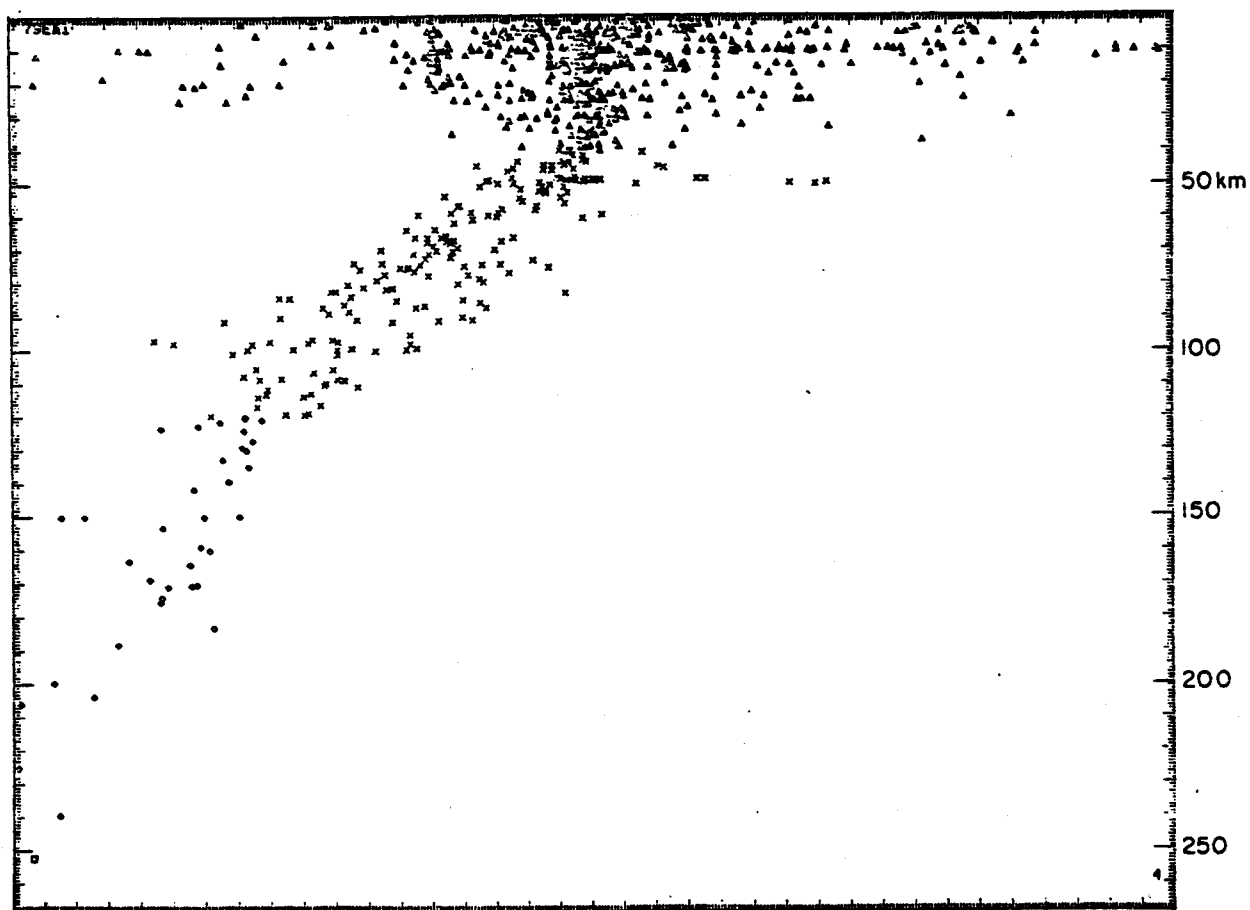


Figure 7.3.7. Seismicity located by the Shumagin network during 1979.



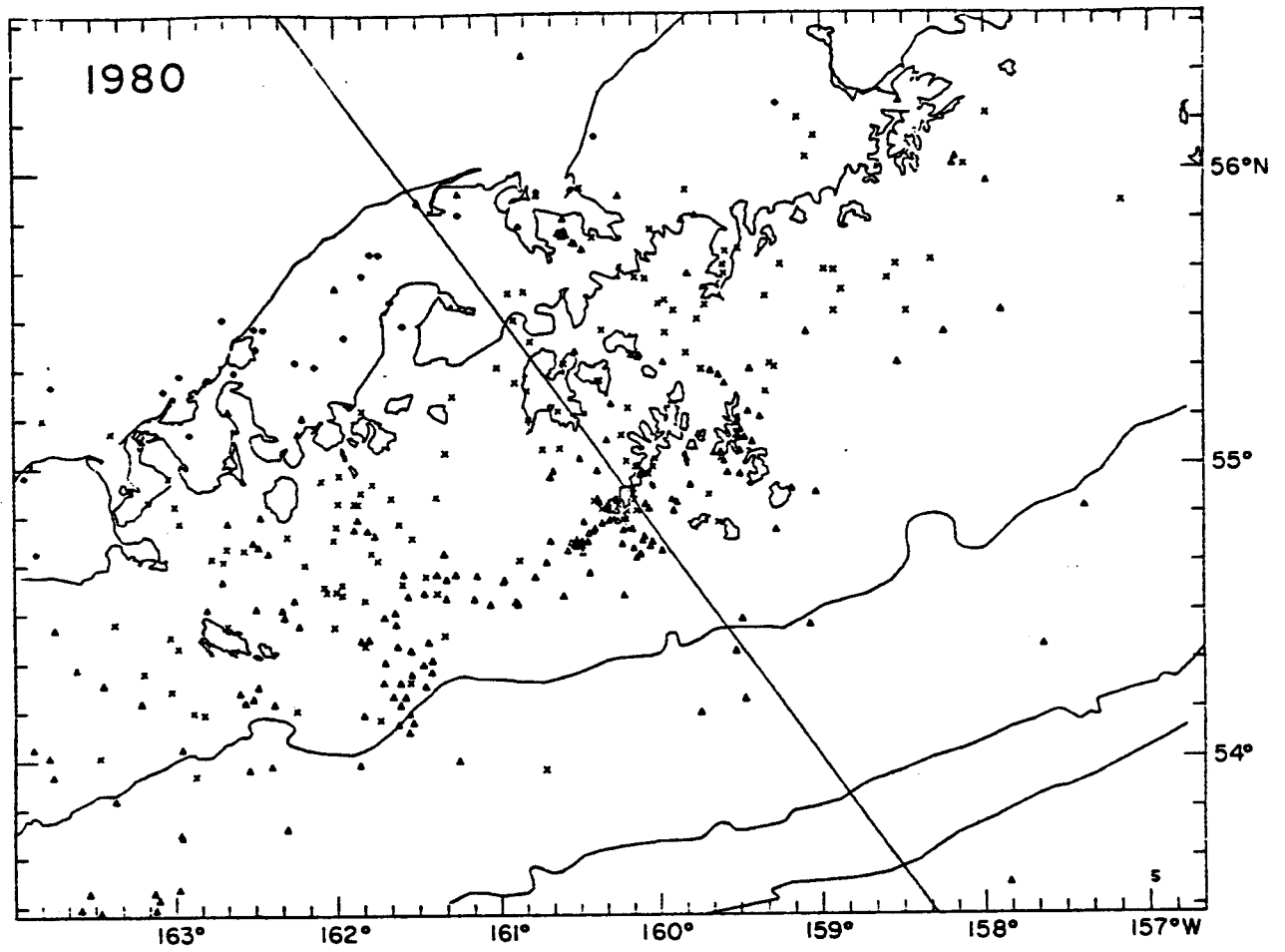
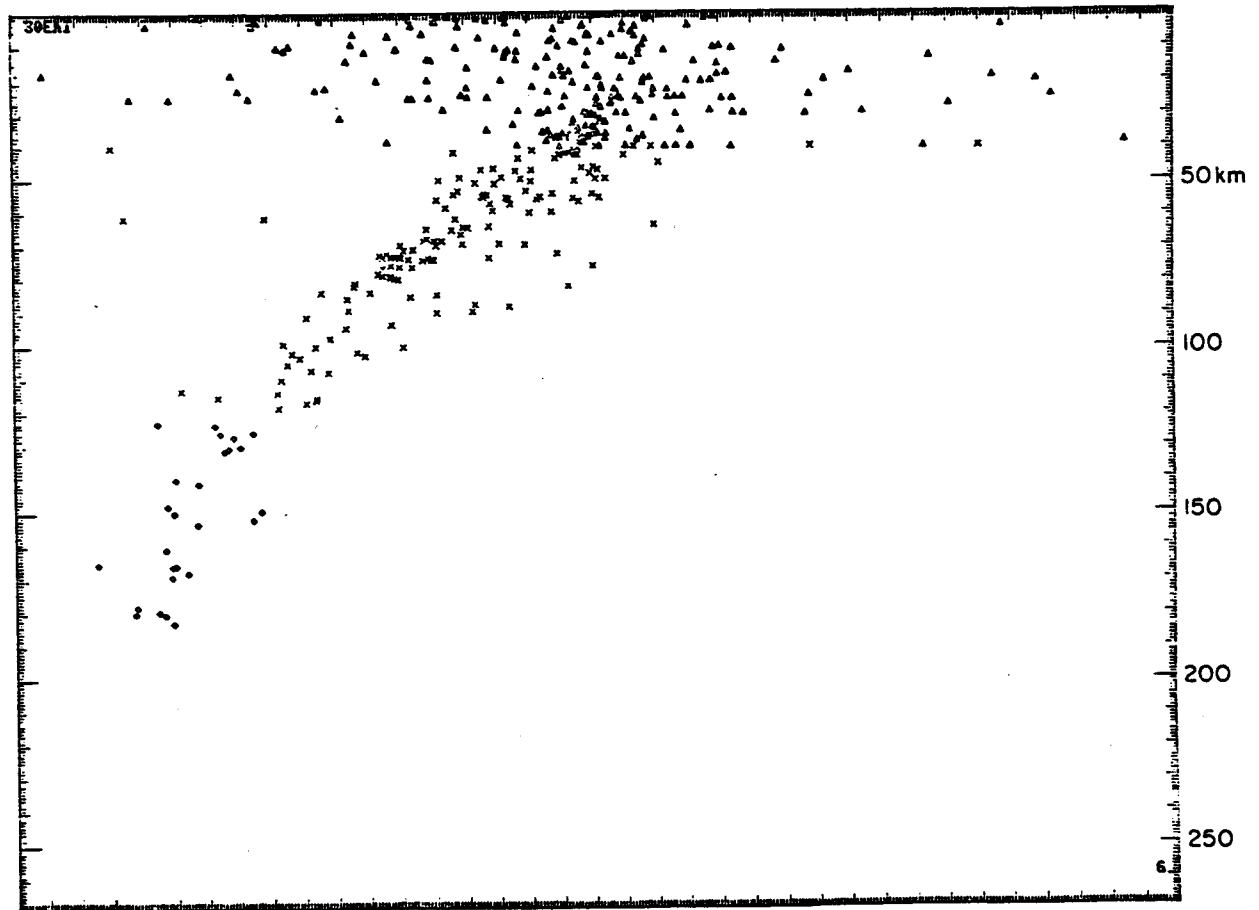


Figure 7.3.8. Seismicity located by the Shumagin Network during 1980.



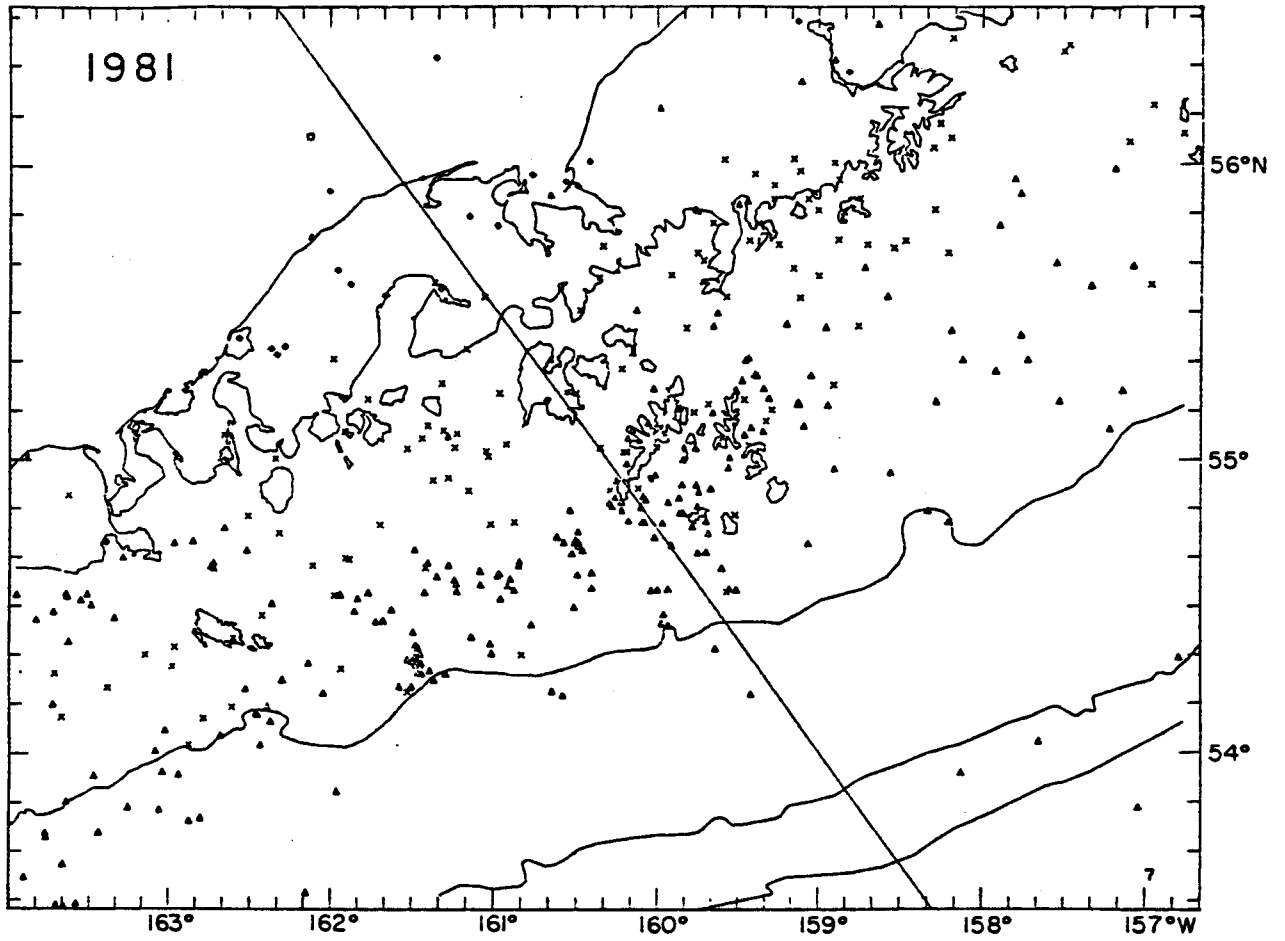
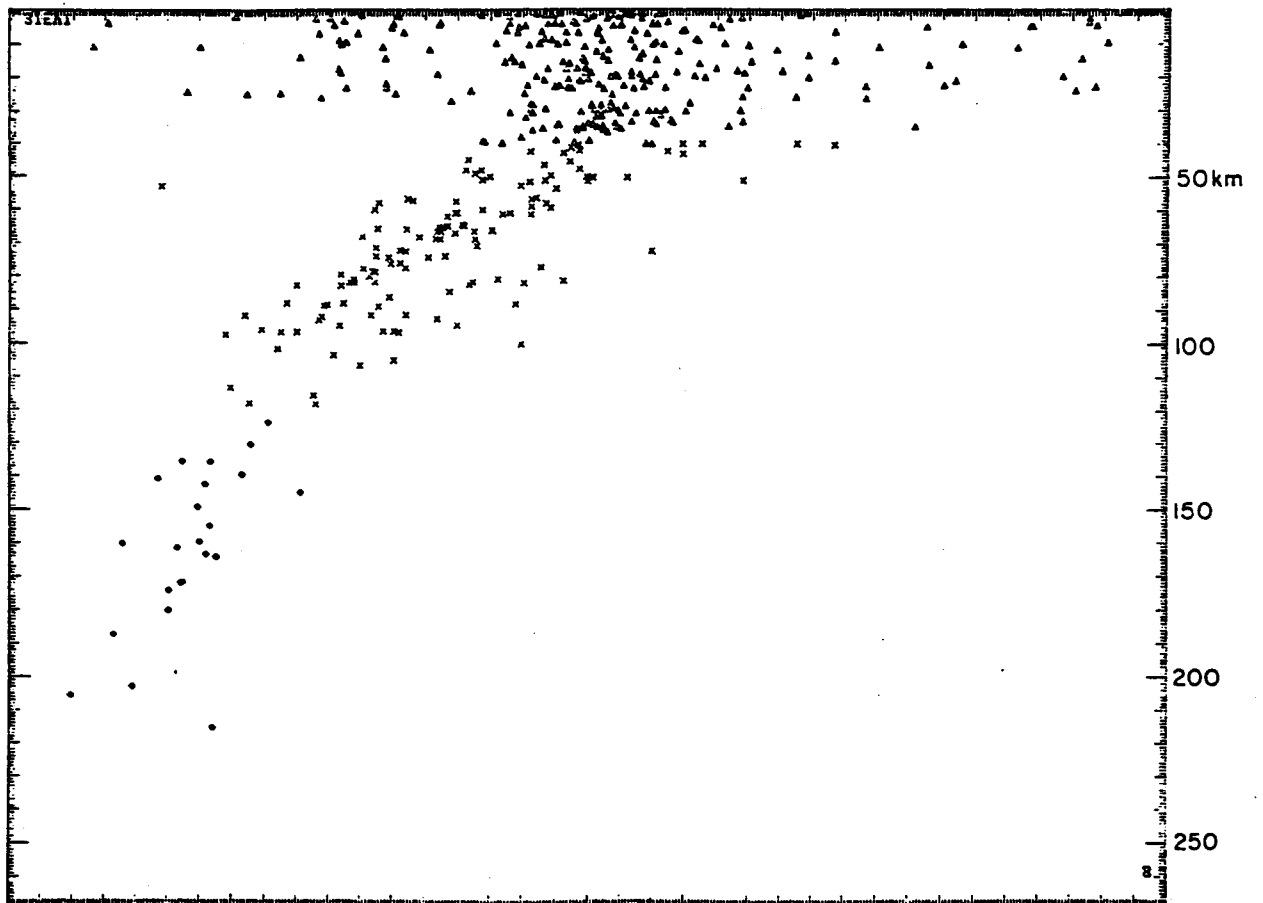


Figure 7.3.9. Seismicity located by the Shumagin Network during 1981.



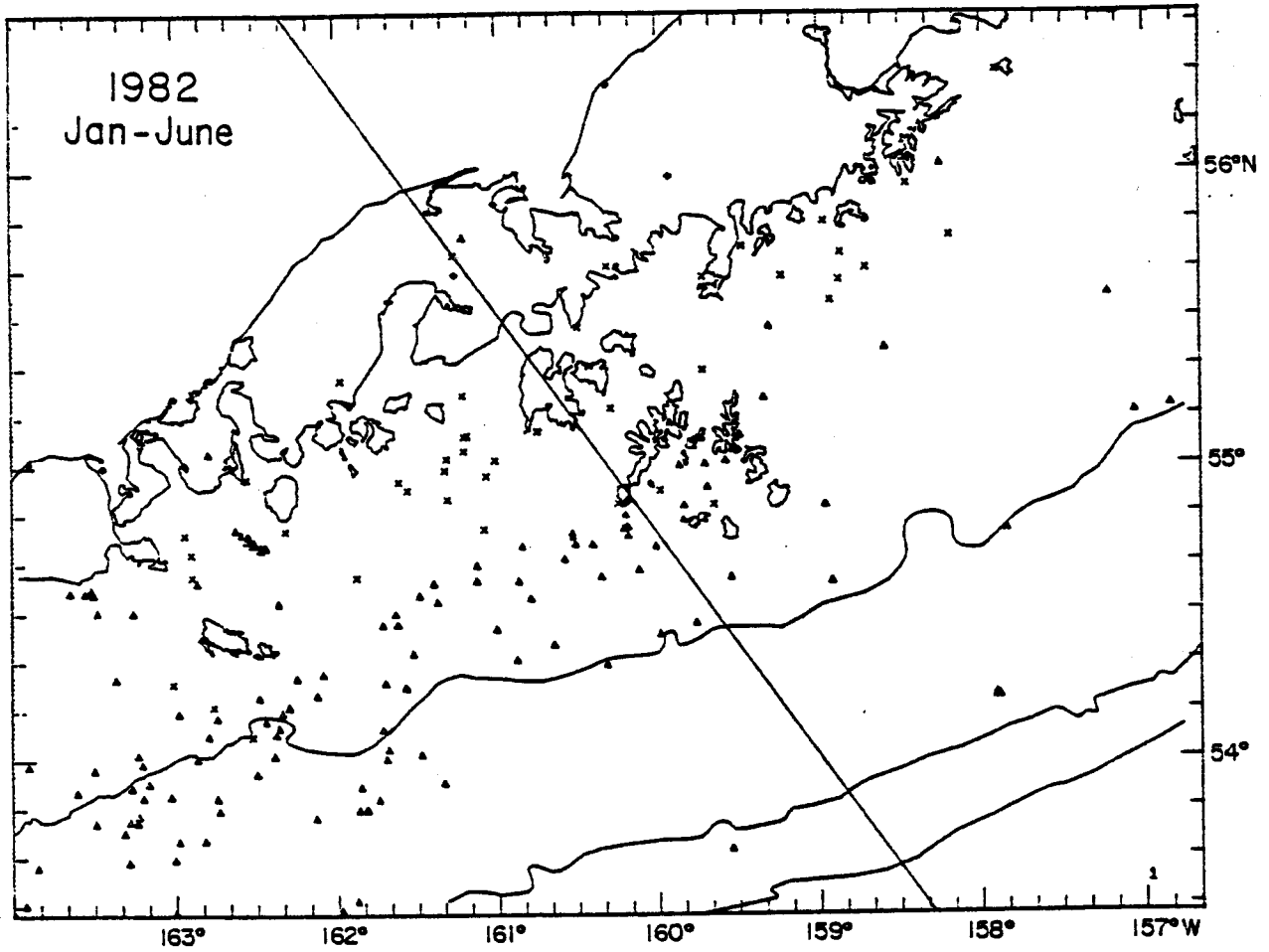
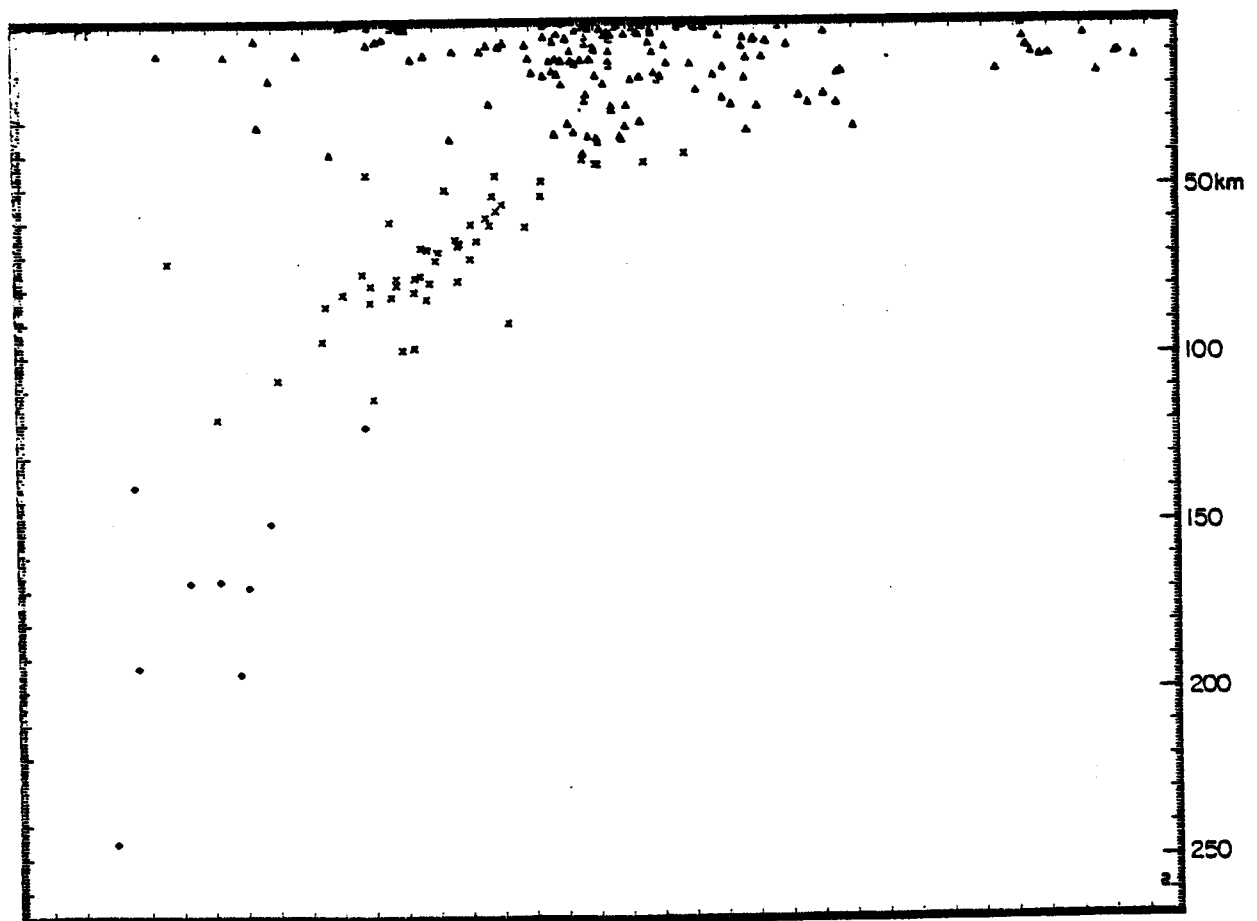


Figure 7.3.10. Seismicity located by the Shumagin network from January-June, 1982.



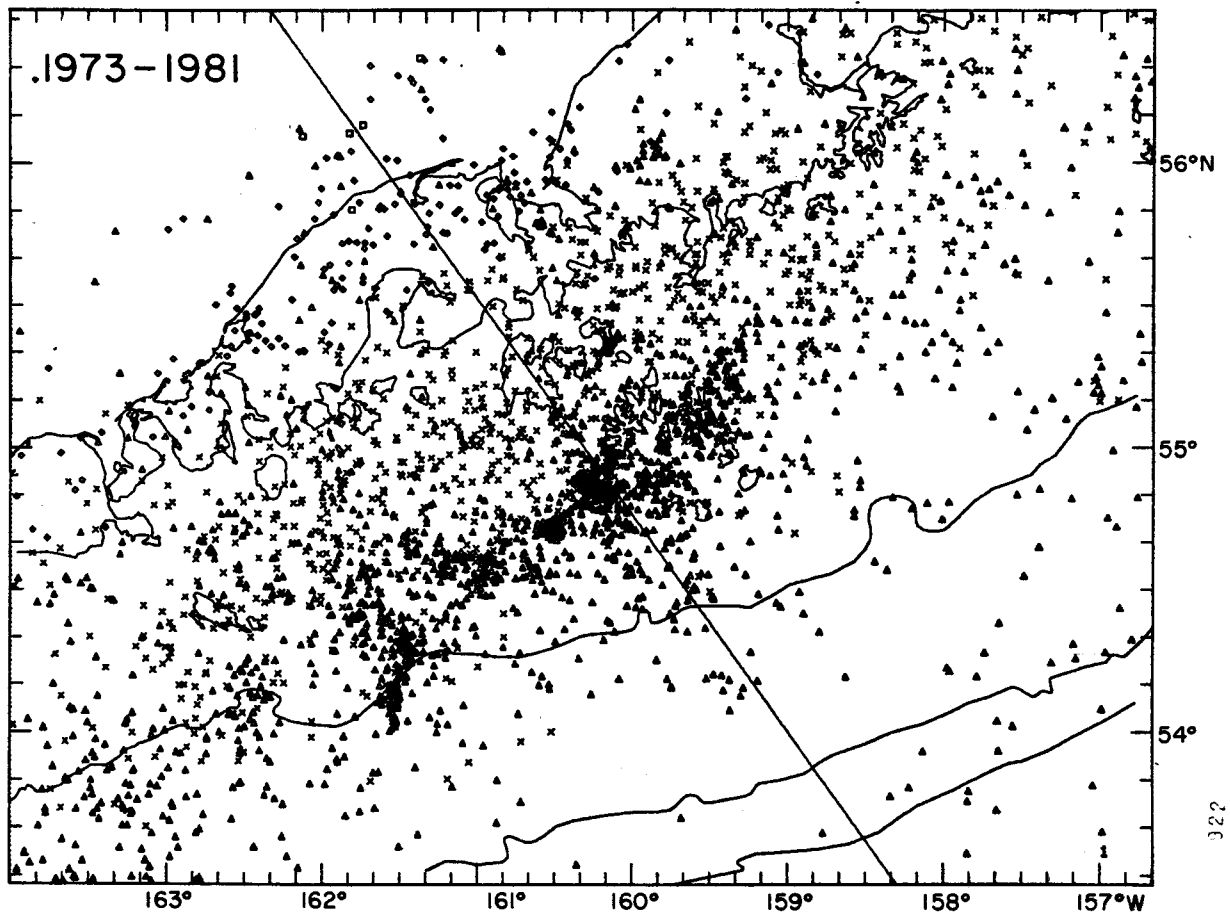


Figure 7.3.11. Seismicity located by the Shumagin network from 1973-1981.

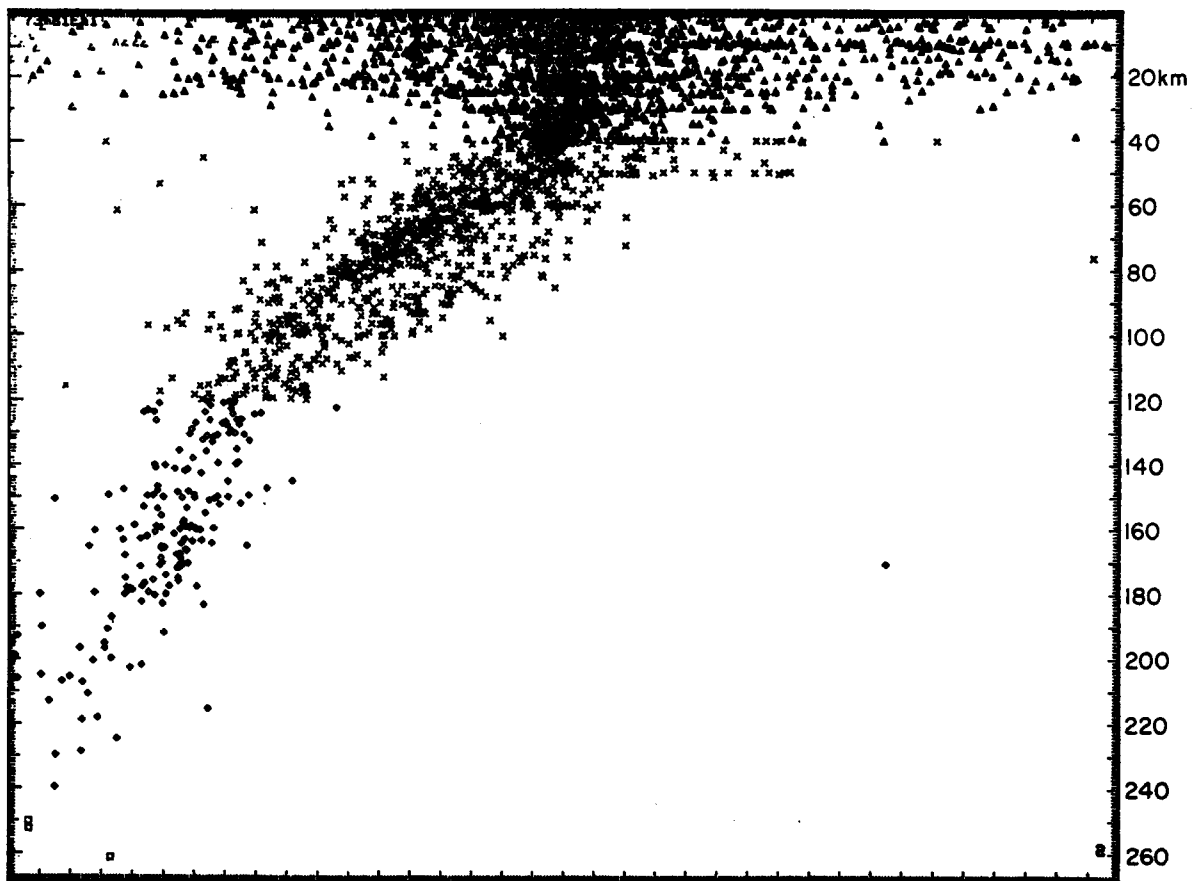


TABLE 7.3.1. Number of Earthquakes Located by the Shumagin Network and NEIS/PDE Bulletin Per Year in the Region 52°-57°N and 156°-165°W

<u>Year</u>	<u>Shumagin Network</u>	<u>PDE Bulletin</u>
1973	211	22
1974	328	25
1975	302	20
1976	279	10
1977	118	15
1978	475	19
1979	808	42
1980	448	25
1981	438	17

TABLE 7.3.2

Flat-Layered P-Velocity Model for the Shumagin Islands Array Region

<u>P-Wave Velocity of Layer (km s⁻¹)</u>	<u>Depth to Top of Layer (km)</u>
3.44	0.00
5.56	1.79
6.06	3.65
6.72	10.18
7.61	22.63
7.90	38.51
8.26	90.19

A ratio of P-wave velocity to S-wave velocity of 1.73 was adopted for all layers.

7.4 Shumagin Network Status 1973-1982

One of the goals of operating a seismic network is to collect a data set that is continuous both in time and space. Such a complete data set is needed to facilitate studies of possible temporal and/or spatial patterns in the seismicity.

Maintaining a seismic network in continuous operation in the hostile environment of the eastern Aleutians, however, has proven to be a challenging undertaking. Both failures of antiquated recording equipment and individual seismic stations have contributed to substantial gaps in the data.

In Figure 7.4.1 we show the 1982 station configuration of the Shumagin network and in Table 7.4.1 we list station names and geographical coordinates. The three station network on St. Paul Island in the Pribilofs was removed in August 1981. Furthermore, in 1982 we closed down the Unalaska network and under a temporary agreement we made the central station equipment in Dutch Harbor available to Dr. John Davies who is now the state seismologist for the State of Alaska.

The continuity of data recording varies considerably through time as is shown in Figures 7.4.2 to 7.4.6. In Figures 7.4.2 to 7.4.6 we use the following notation: 1) a solid bar means the station operated continuously and data were being recorded; 2) a hatched bar means that the station operated intermittently and data were being recorded; 3) an open bar means that the station was not operating although data were being recorded; 4) a gap in the histograms showing no station status indicates that no data was recorded during that time period by the main recording device. One or two helicorders, however, have operated fairly continuously since 1973.

During the early years, 1973-1977, significant gaps in the data were caused by the frequent failures of obsolete equipment such as an aging tape recorder or develocorder, which in some instances lasted for extended periods of time before repairs could be carried out. The number of stations in the Shumagin network has increased through time. Initially, in 1973 seven remote stations were installed. In 1975 the number of stations had increased to 14. In 1976 the

12-station Pavlof subarray was installed. Today, the Shumagin network is trimmed back and consists of 13 stations where five stations are three-component stations and the Pavlof subarray consist of four stations. The data coverage since 1978 has been fairly continuous both in terms of recording, and in terms of station survival rate through the winter. Both quality and continuity of the retrieved data are presently excellent.

TABLE 7.4.1

EASTERN ALEUTIAN REGIONAL NETWORKS OPERATED BY LAMONT-DOHERTY GEOLOGICAL OBSERVATORY, 1973-1982

<u>Network</u>	<u>Station</u>	<u>Code</u>	<u>Components</u>	<u>N. Lat</u>	<u>W. Long</u>	<u>Error(m)*</u>	<u>Elev.(m/f)</u>		
Shumagin	Chernabura Island	CNB	SPZ,E,N	54°49.22'	159°35.30'	50(2)	90	295	
	Nagai Island	NGI	SPZ	55°02.36'	160°04.15'	27(2)	240	787	
	Squaw Harbor	SQH	SPZ,E,N	55°13.20'	160°33.74'	307(2)	360	1181	
	Ivanof Bay	IVF	SPZ	55°73.75'	159°31.80'	22(2)	275	902	
	Big Koniuji Island	BKJ	SPZ	55°09.40'	159°33.53'	30(0)	146	480	
	San Diego Bay	SGB	SPZ,E,N	55°32.75'	160°27.23'	31(2)	275	902	
	West Unga	WUN	SPZ	55°19.87'	160°44.40'		150	492	
	Port Moller	PMA	SPZ	55°58.72'	160°29.83'		320	1050	
	Sand Point	SAN	SPZ,E,N IPZ,E,N	55°20.40'	160°29.83'	22(2)	23	75	
	False Pass	FSP	SPZ	54°57.2'	163°27.4'	30(1)	200	660	
	Baldy Mountain	BAL	SPZ	55°11.593'	162°47.208'	1(6)	360	1180	
	Sanak Island	SNK	SPZ	54°28.44'	162°46.52'	70(6)	159	522	
	Deer Island	DRR	SPZ	54°55.41'	162°16.99'	28(2)	380	1246	
	Dolgoi Island	DLG	SPZ	55°08.46'	161°50.15'	32(2)	367	1204	
	Coal Harbor	CHR	R	55°19.0'	160°44.4'	500(3)	150	492	
	Pavlof Volcano	PVV	SPZ,E,N	55°22.451'	161°47.399'	10(5)	164	538	
	Black Hill	BLH	SPZ,E,N	55°42.15'	162°03.95'	40(6)	390	1279	
	Beaver Bay	BVB	R	55°31.9'	160°59.2'	1000(1)	518	1700	
	Pavlof	Pavlof North-4	PN4	SPZ	55°28.819'	162°01.369'	10(5)	434	1424
		Pavlof North-6	PN6	SPZ	55°27.118'	161°54.888'	10(5)	814	2670
Pavlof North-7		PN7	SPZ	55°26.591'	161°56.781'	10(5)	780	2258	
Pavlof North-8		PN8	SPZ	55°26.623'	162°01.246'	10(5)	605	1984	
Black Hill		BLH	R	55°42.15'	162°03.95'	40(6)	390	1279	
Pavlof South-1		PS1	SPZ	55°25.339'	161°44.173'	10(5)	300	983	
Pavlof South-2A		PS2A	SPZ	55°24.205'	161°48.189'	20(6)	455	1465	
Pavlof South-3		PS3	SPZ	55°23.517'	161°49.014'	10(5)	450	1476	
Pavlof South-4		PS4	SPZ	55°21.238'	161°52.091'	10(5)	520	1707	
Zachery Bay		ZKR	R	55°18.66'	160°44.43'	10(6)	183	600	

TABLE 7.4.1 (con't.)

<u>Network</u>	<u>Station</u>	<u>Code</u>	<u>Components</u>	<u>N. Lat</u>	<u>W. Long</u>	<u>Error(m)*</u>	<u>Elev.(m/f)</u>	
Dutch Harbor	Dutch Harbor	DUT	SPZ,E,N IPZ,E,N	53°53.9'	166°32.2'	1000(3)	60	197
	Ballyhoo	BHR	R	53°54.8'	166°31.9'	2000(8)	427	1400
	Akutan Volcano	AKI	SPZ	54°06.7'	166°03.1'	1000(8)	457	1500
	Makushin Volcano	MAK	SPZ	53°54.9'	166°47.9'	1000(8)	366	1200
	Upper Shaishnikof River	USR	SPZ	53°46.0'	166°41.75'	1000(9)	610	2000
	Sedanka Island	SDK	SPZ	53°40'	166°08'	2000(9)	366	1200

Legend:

R = repeater only, high gain
 SPZ,E,N = short period, high gain vertical,
 horizontal east and north
 IPZ,E,N = intermediate period, low gain vertical,
 horizontal east and north

*Source Codes:

- (0) theodolite survey, Surveyor crew 13 June 1978
- (1) picked from C and GS chart 8802, September 1978
- (2) picked from 1:63K maps, May 1978
- (3) picked from 1:250K maps, May 1978
- (4) taken from October 1975 list of station coordinates
- (5) geodimeter/theodolite survey made June-August 1977
- (6) measured from nearby benchmark, June-August 1977, August 1978
- (7) proposed from C and GS charts 8994,8995
- (8) proposed from 1:250K USGS maps
- (9) proposed from 1:1M Aeronautical Chart CE-13

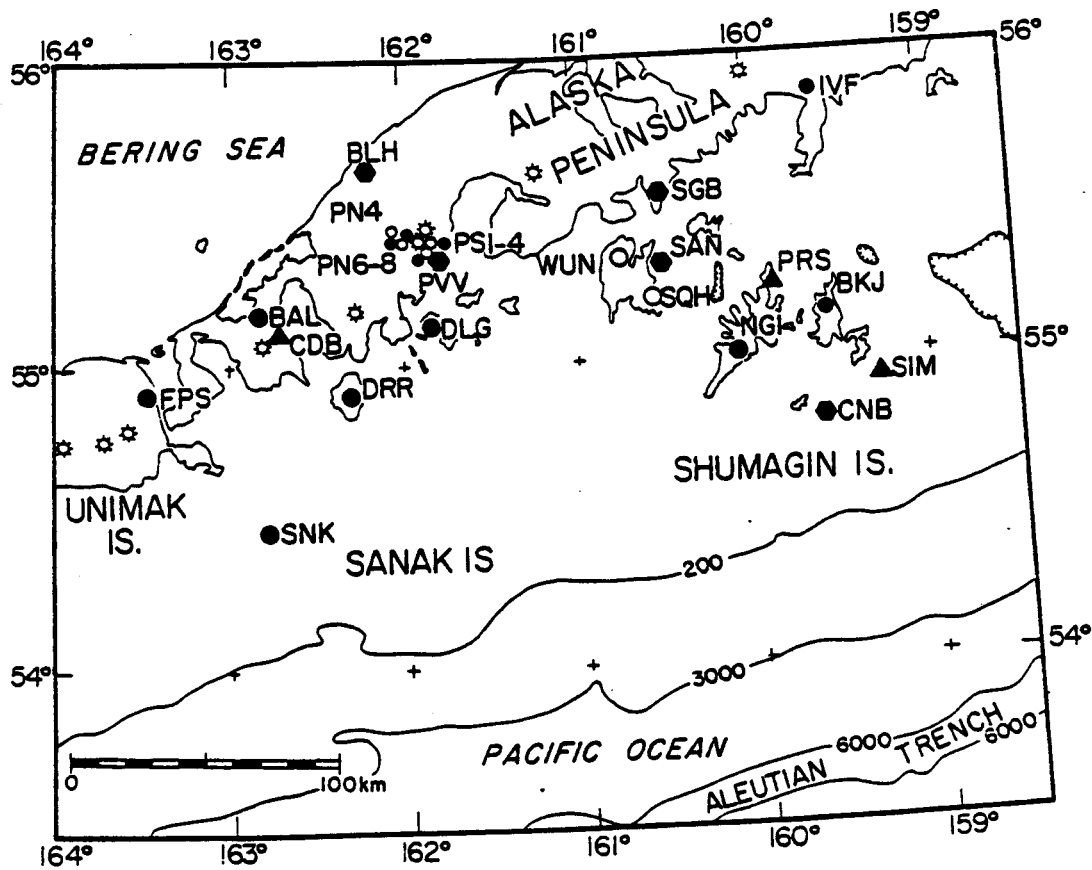


Figure 7.4.1. The Shumagin seismic network, Alaska. Filled circles are short period, single (vertical) component seismic stations. The hexagons are short period, three component seismic stations. Open circles are seismic stations that have been removed. Strong motion accelerographs (SMA-1) are located at the seismic stations SNK, DRR, DLG, SGB, SAN, NGI, BKJ, IVF, and CNB and 3 SMA-1's are located separately at CDB, SIM, and SIM (shown as triangles).

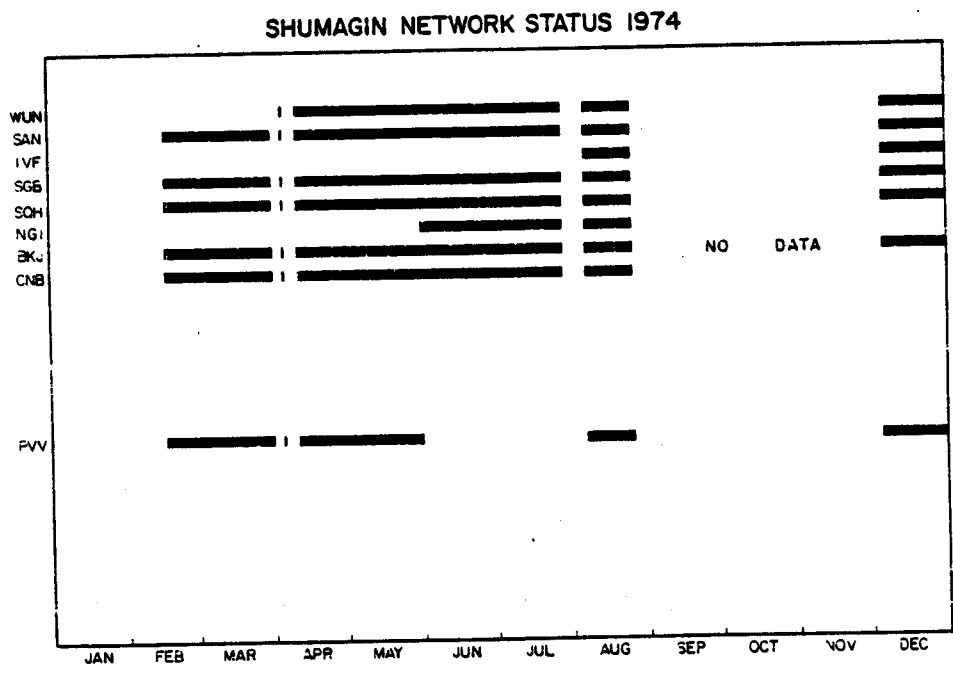
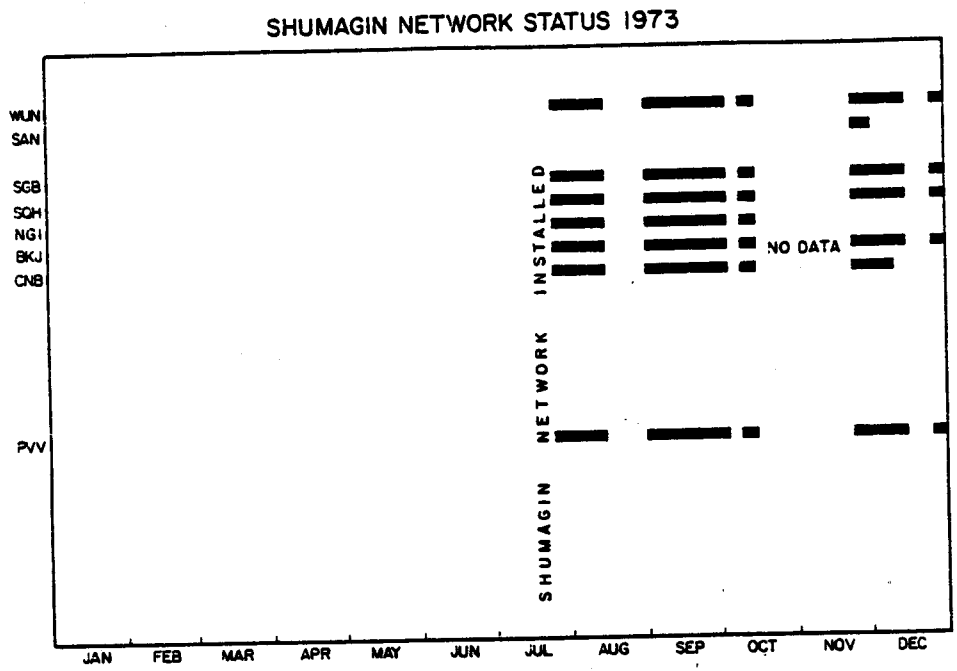
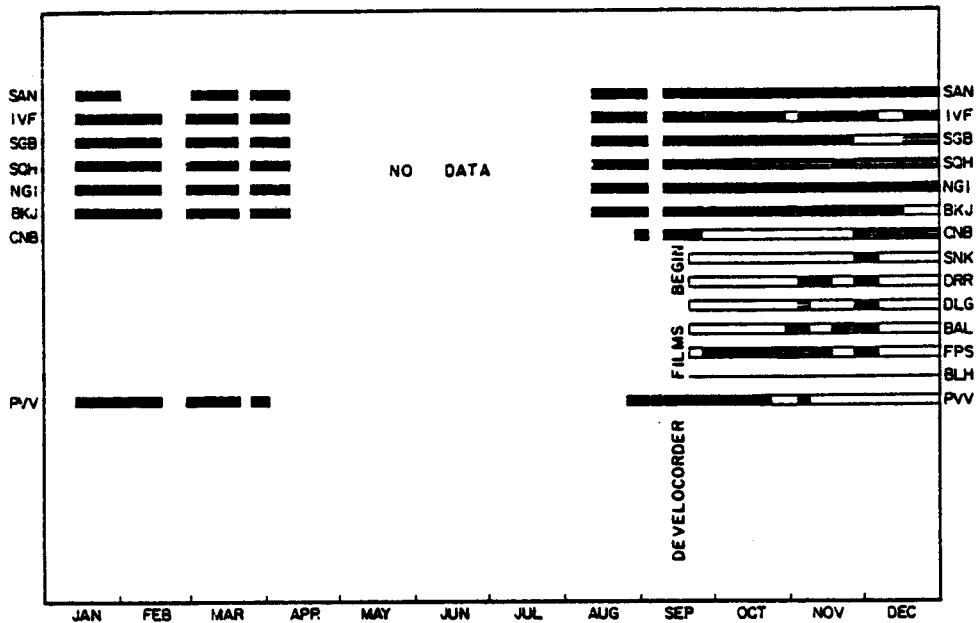


Figure 7.4.2. Operational status of the Shumagin network in 1973 and 1974.

SHUMAGIN NETWORK STATUS 1975



SHUMAGIN NETWORK STATUS 1976

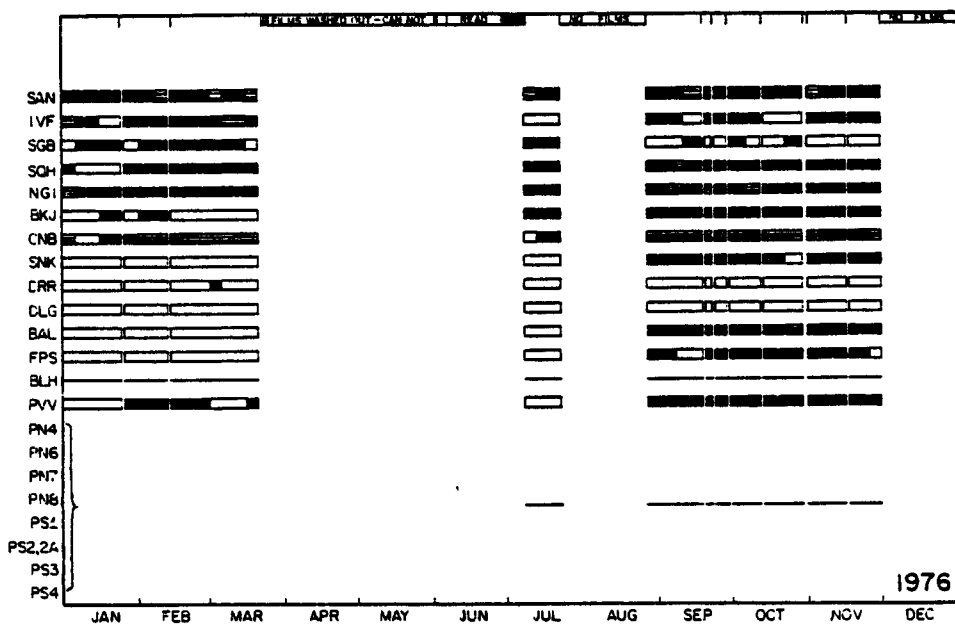
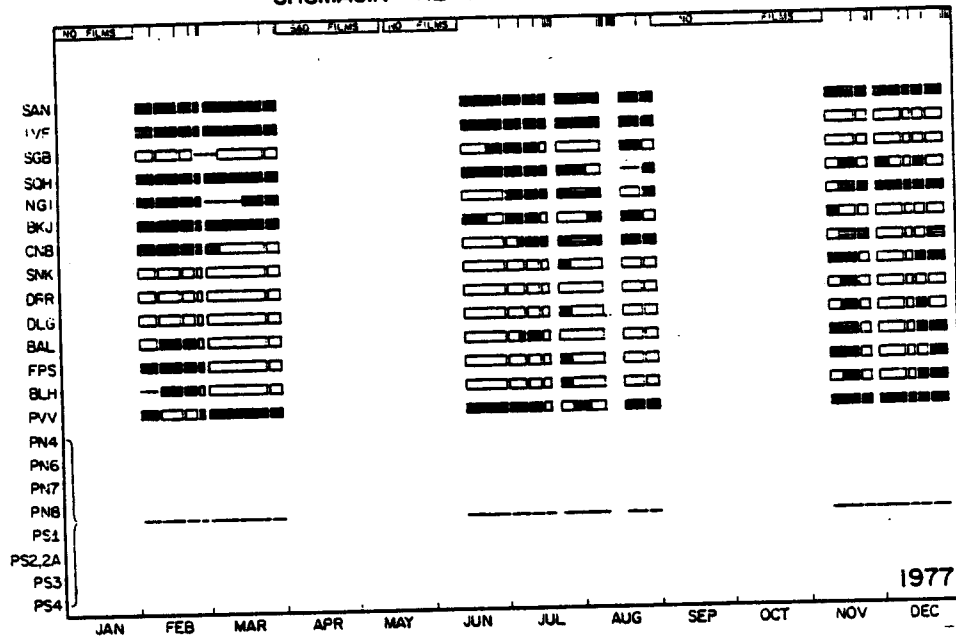


Figure 7.4.3. Operational status of the Shumagin network in 1975 and 1976.

SHUMAGIN NETWORK STATUS 1977



SHUMAGIN NETWORK STATUS 1978

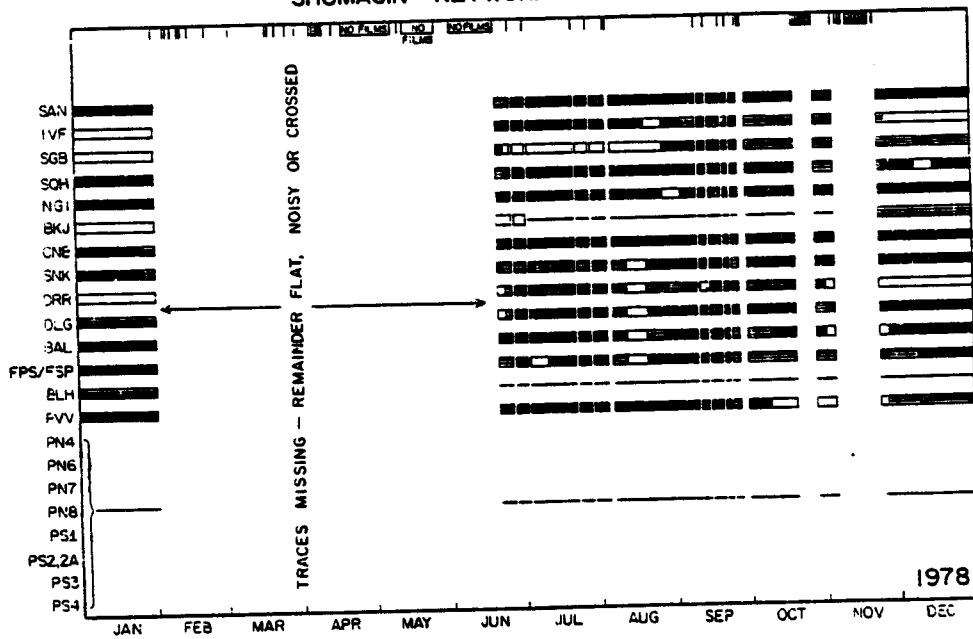


Figure 7.4.4. Operational status of the Shumagin network in 1977 and 1978.

7.5 Seismic and Eruptive Activity of Pavlof Volcano, 1973-1982

Pavlof Volcano has had 5 major eruptions and several episodes of minor explosions since seismic monitoring began in fall 1973. The major eruptions occurred in 1973, 1975, 1976, 1980, and 1981 (Table 7.5.1). Station PVV, 7.5 km to the SE of the volcano's summit (Figure 7.5.1), has been used as the seismic monitoring station. Data have been continuously displayed on helicorder records since fall 1973, except during short periods of time when the station malfunctioned. The station consisted of a single short-period (1 Hz) seismometer from 1973 until 1982; in summer 1982 the station was upgraded to 3 components. (The vertical component is still displayed on the helicorder). An equipment change in 1979 resulted in a gain reduction of about a factor of three. When feasible, other stations of the local network installed in 1976 were displayed on the helicorder if station PVV malfunctioned.

Four types of seismic events of probable volcanic origin have been observed on Pavlof seismograms and are shown in Figure 7.5.2: high-frequency tremors, B-type earthquakes (shallow events with emergent arrivals and no clear S-phase), explosion earthquakes, and volcanic tremor. Magnitudes of B-type events range from -0.2 to 1.0. B-type events have b-values (negative slope of magnitude-frequency relation) ranging between 1.9 and 2.6 (McNutt, 1981a,b; McNutt and Beavan, 1981; McNutt, 1982a,b; McNutt and Mori, 1983). Figures 7.5.3-7.5.7 show the numbers of B-type earthquakes and explosions per day for all data from 1973, 1974, most of 1975, and all of 1981 and 1982. Data for the remainder of 1975, 1976-1980, and 1983 are still being analyzed, however, all records have been scanned. Table 7.5.1 was prepared based on detailed study of reduced data as well as scanning of remaining records. Also, there were virtually no volcanic events recorded from spring of 1977 until fall of 1980, so the data set presented here is actually more complete than it may appear.

During major eruptions with strong lava fountaining the seismicity increases from a background level of several 10's of events

per day to several thousand events per day and/or continuous high amplitude volcanic tremor. This can be seen in Figures 7.5.3, 7.5.5, and 7.5.6. The increase in seismicity and onset of eruption occur quite abruptly, that is on a scale of a few hours. The smaller eruption episodes consisting of numerous explosions are accompanied by increases in seismicity to a level of several hundred events per day (Figures 7.5.4 and 7.5.6). The increase takes place on a scale of 3-4 days, during which time seismicity has been observed to correlate with the solid earth tides (McNutt and Beavan, 1981).

To date, only the two eruption styles and accompanying seismicity described above have been observed. The historic record, however, contains some descriptions of other perhaps more vigorous activity (Table 3.5.2--see years 1845 and 1906-1911). We can only speculate about the seismicity accompanying these eruptions. However, several descriptions of felt earthquakes (which remain to be verified) suggest that perhaps larger shocks than those which have been recorded to date (up to about magnitude 1.0) have occurred at the volcano in the past. We further note that no locatable events have occurred at shallow depths beneath the volcano, and only four located events have occurred within 15 km of the volcano from 1973 to 1982. We speculate that the volcano has erupted so frequently that the conduit has remained open and has not permitted large enough stresses to build up to cause larger earthquakes.

Lastly, the volcano sits roughly in the middle of the Shumagin seismic gap. The historic record gives an indication that some eruptions may have occurred at the time of large nearby earthquakes (Tables 3.5.1 and 3.5.2, see years 1786 and 1917). Thus, we have some reason to anticipate possible eruptive activity accompanying the expected large or great earthquake. We feel we are in an excellent position to compare the seismic and eruptive activity of Pavlof Volcano during the pre-seismic, co-seismic and post-seismic periods of seismicity at the adjacent Pacific-North American Plate boundary.

TABLE 7.5.1. Preliminary list of Pavlof Volcano eruptions, 1973-1983, deduced from seismicity.

<u>Date</u>	<u>Description of Activity</u>	<u>Seismogram Characteristics*</u>	<u>Confirmation</u>
Nov. 13-14, 1973	major magmatic	volcanic tremor	photograph-lava fountain- ing & ash column
Mar. 12-14, 1974	explosive	explosion quakes	
before Sep. 1-21, 1974	explosive	explosion quakes	
Oct. 29 - Nov. 17, 1974	explosive	explosion quakes	
Nov. 25 - Dec. 16, 1974	explosive	explosion quakes	
Dec. 25 - Jan. 06, 1975	explosive	explosion quakes	
Sep. 13-15, 1975	magmatic	volcanic tremor	
before Sep. 18-21, 1975	explosions	explosion quakes	
Sep. 23-24, 1975	magmatic	volcanic tremor	photograph-lava fountain- ing & ash column
Sep. 25 - Oct. 06, 1975	explosions	explosion quakes	
Oct. 06-12, 1976	magmatic(?) & explosive	volcanic tremor & explosion quakes	
Nov. 02-04, 1976	explosive	explosion quakes	
Nov. 10-22, 1976	magmatic	volcanic tremor (note-long duration but low amplitude)	
Nov. 11-12, 1980	major magmatic	volcanic tremor	photograph-lava fountain- ing & ash column
before? Mar. 30 - May 28, 1981	explosive	explosion quakes	
Sep. 26-27, 1981	major magmatic	volcanic tremor	field party-witnessed lava flow

*b-type earthquakes always occur, but in higher numbers during eruptions.

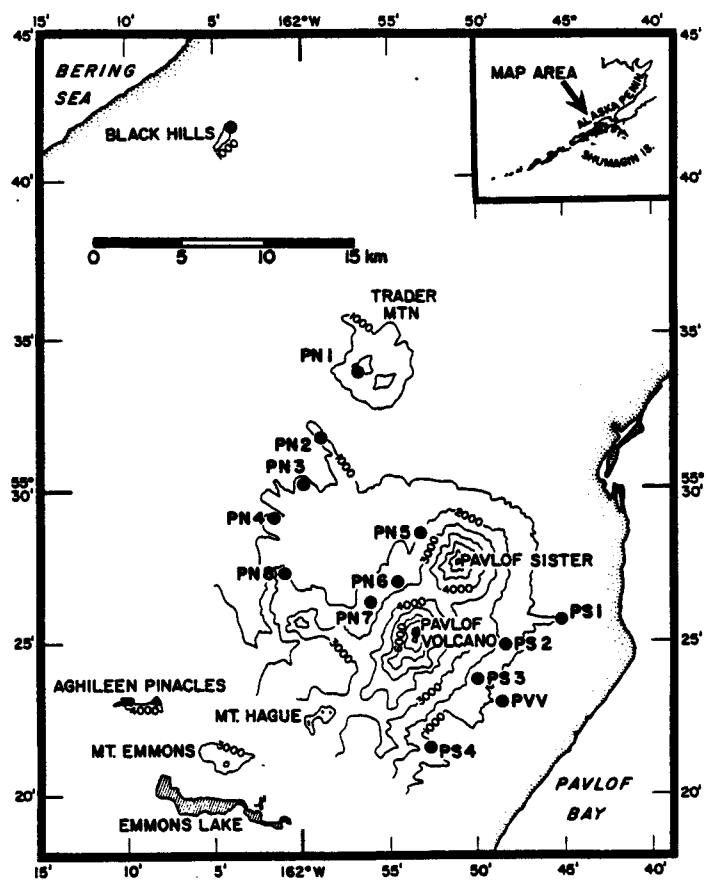
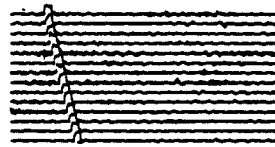
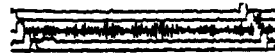


Figure 7.5.1. Map showing stations of the Pavlof seismic array. Station PVV, 7.5 km SE of the volcano's summit, is the monitoring station and was installed in 1973. The remaining stations were installed in 1976; some have been removed in 1981 and 1982.

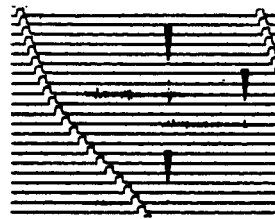
**HIGH FREQUENCY
TREMORS**



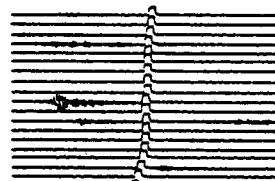
**HARMONIC
TREMOR**



**EXPLOSION
EARTHQUAKES**



**B-TYPE
EARTHQUAKES**



ONE MINUTE

Figure 7.5.2. Types of seismic signals recorded on helicorder from station PVV. Arrows point to air shock phase of explosion earthquakes. Note the similar frequency content (~ 1.4 Hz) of B-type earthquakes, harmonic tremor, and ground waves from the explosion earthquakes.

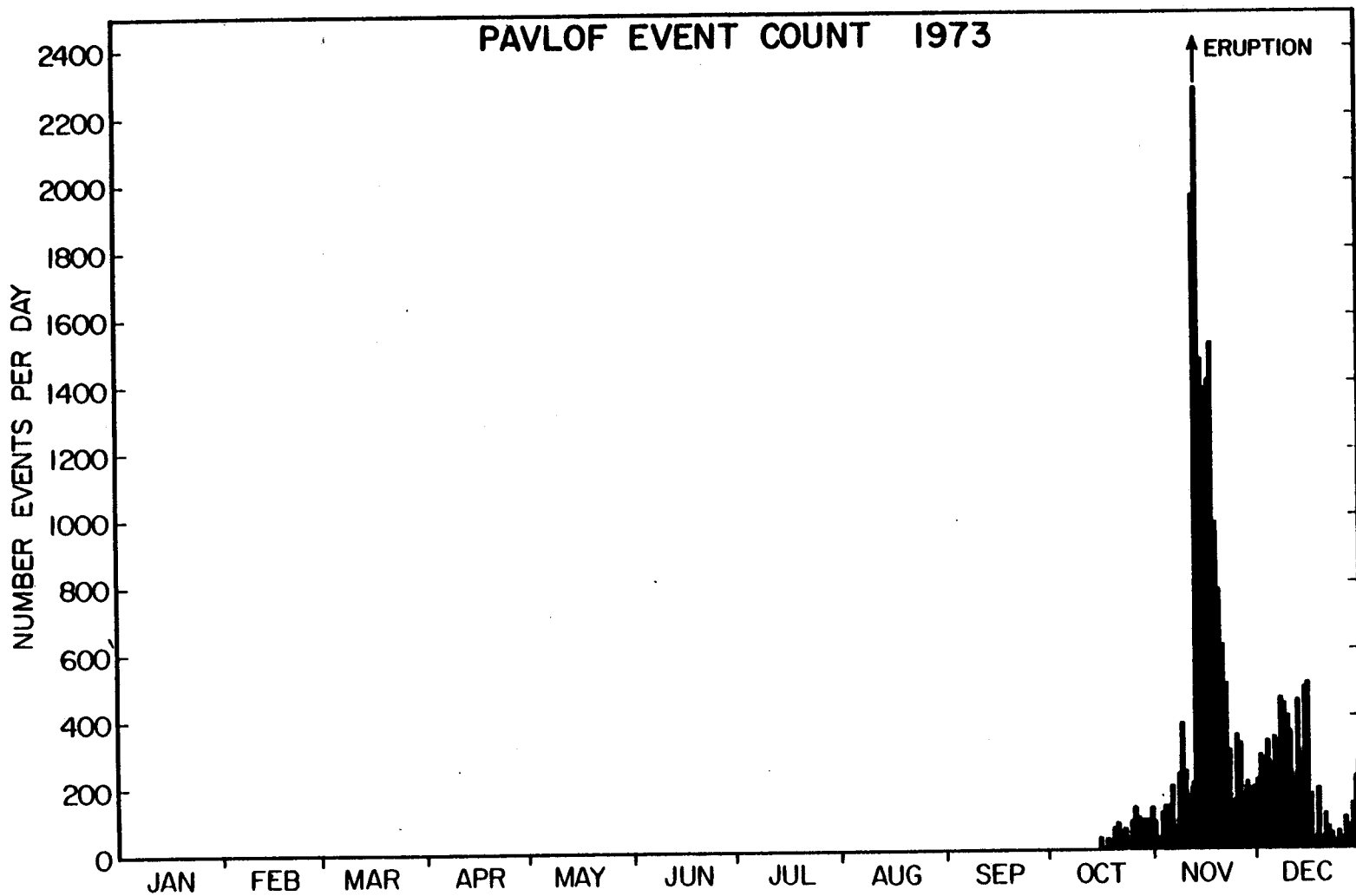


Figure 7.5.3. Number of B-type earthquakes and explosions per day.

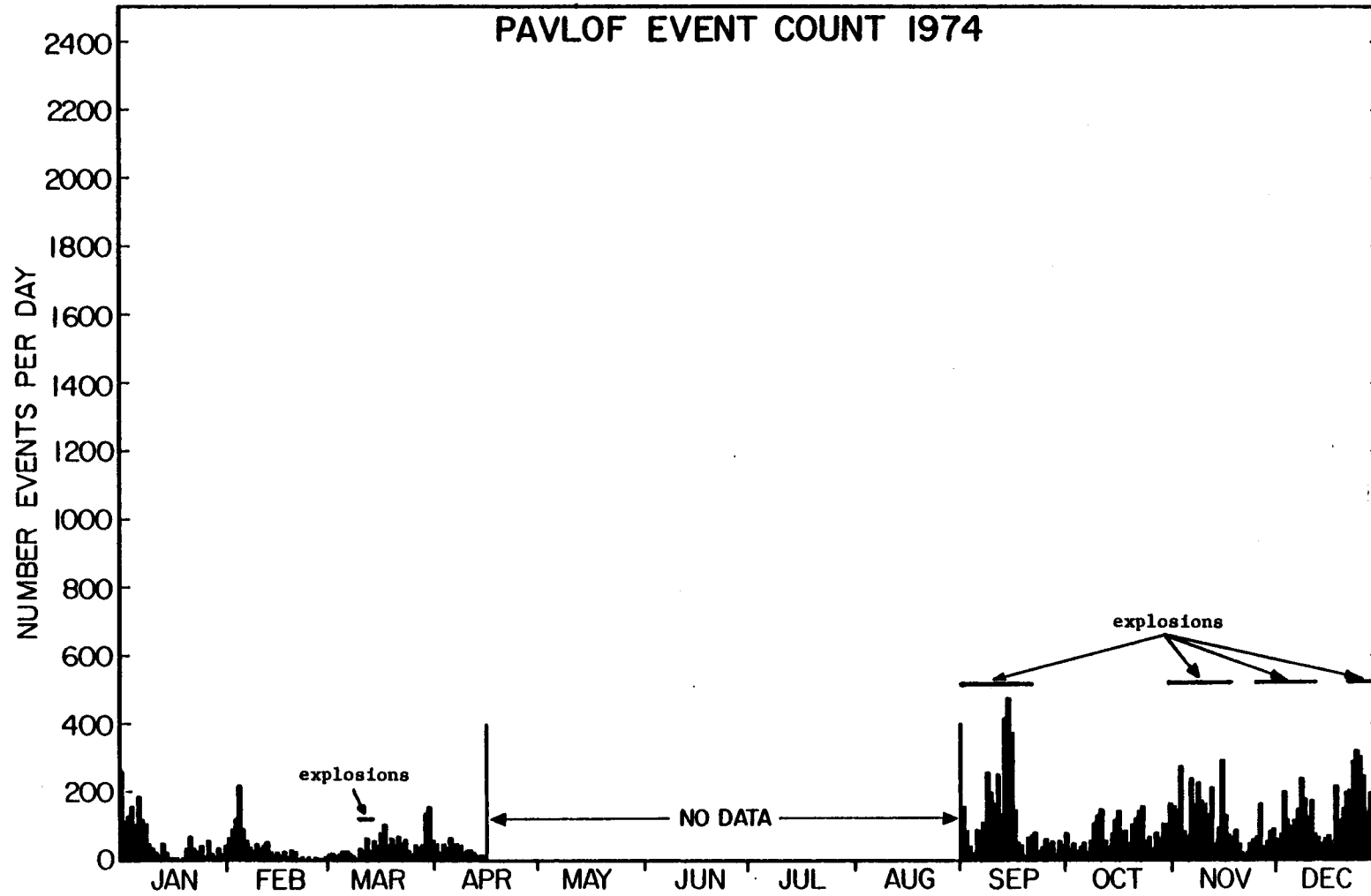


Figure 7.5.4. Number of B-type earthquakes and explosions per day.

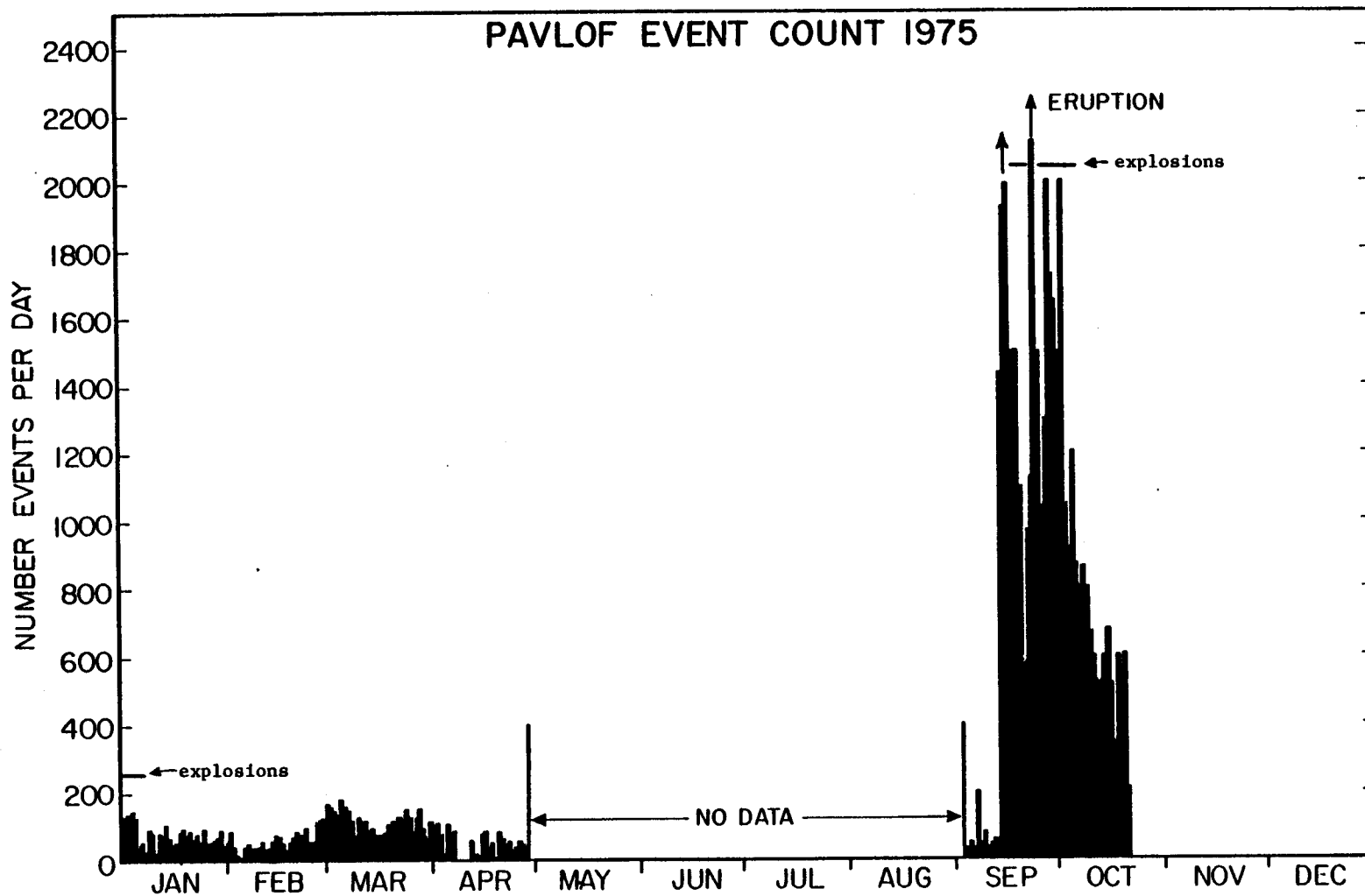


Figure 7.5.5. Number of B-type earthquakes and explosions per day.

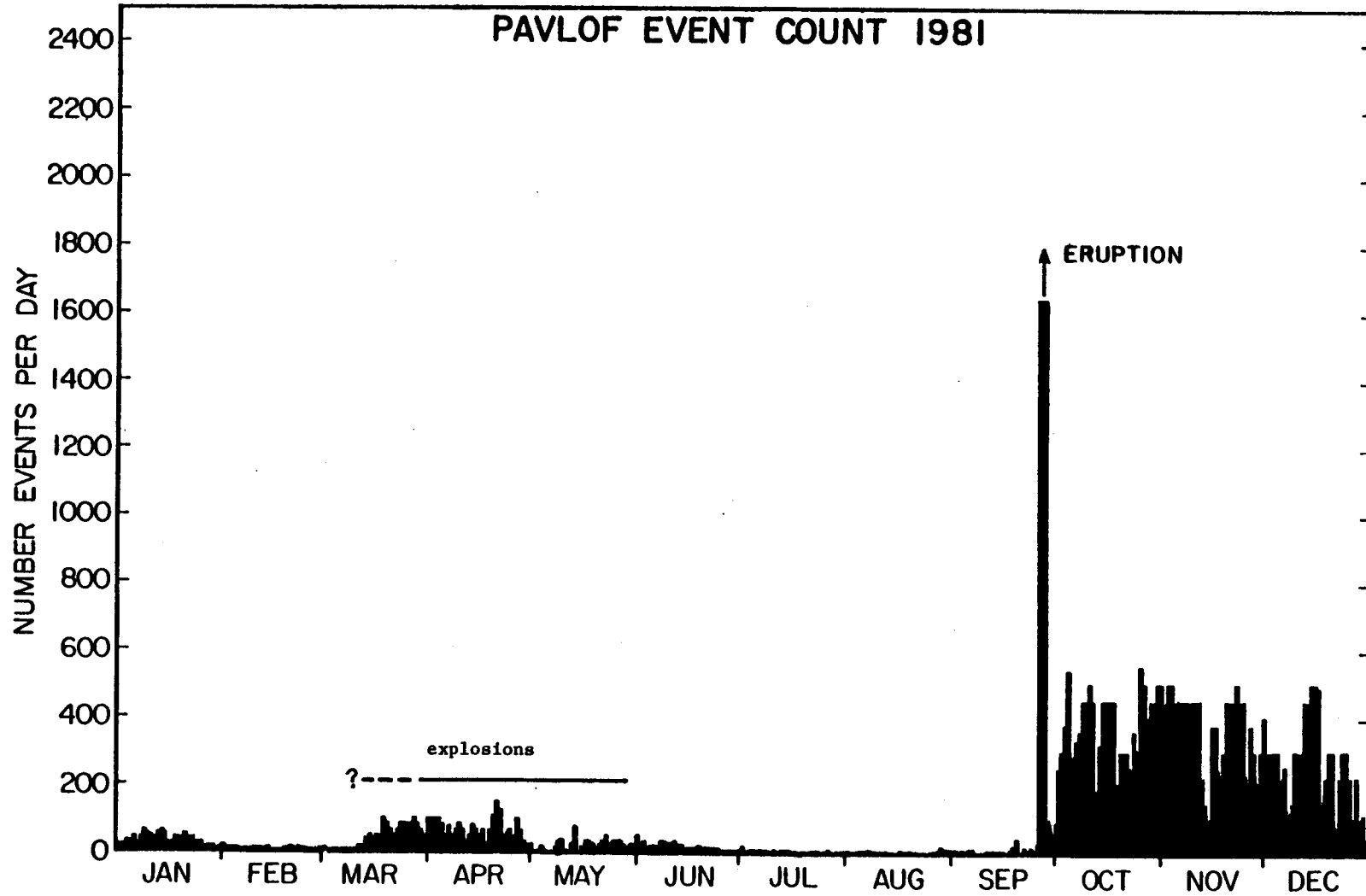


Figure 7.5.6. Number of B-type earthquakes and explosions per day.

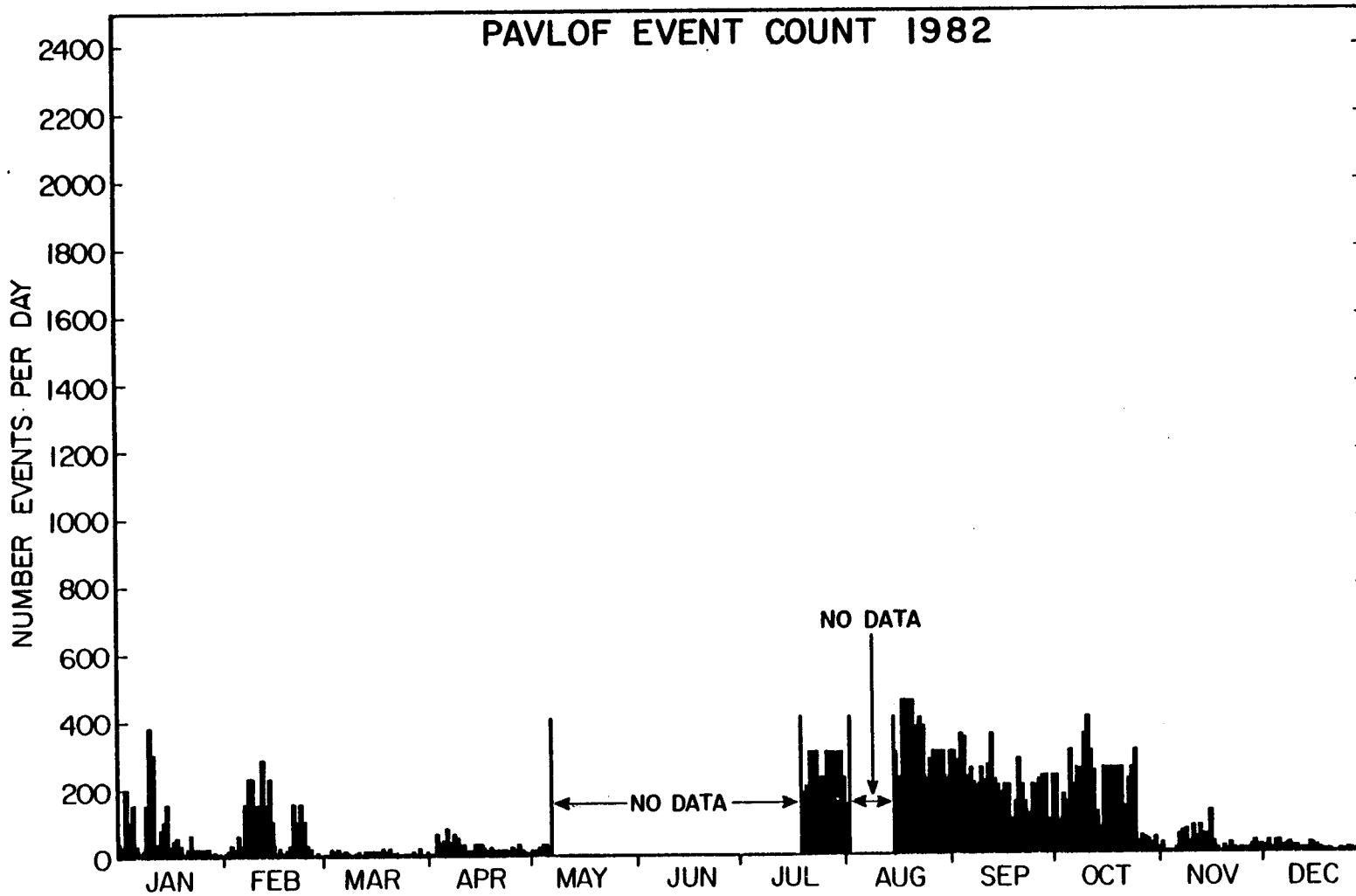


Figure 7.5.7. Number of B-type earthquakes and explosions per day.

7.6. Preliminary Risk Assessment in the St. George Basin

SEISMICITY

Historic Record

Data. The earthquake record prior to the development of sensitive seismographs in the late 1890's and early 1900's relies on observations of the effects of earthquakes on people and objects. For southern Alaska, the Aleutians in particular, these observations are most complete during the period of the Russian occupancy, generally from about 1740 to 1870. Earthquakes for this period have been catalogued by Davis and Echols (1962), Coffman and vonHake (1973), and Kisslinger et al. (manuscript in preparation); these references will be abbreviated 1, 2, and 3, respectively.

Pribilof Islands. The historic record of earthquakes in the Pribilof Islands region is summarized in Tab. 7.6.1. Because the epicenters and maximum intensities of these events are so poorly known it is not possible to compare the occurrence rate for this period, 1815-1861, to that computed below from the teleseismic record for the period 1957-1978. Significant, is the observation that the 1836 earthquake caused damage rated at Modified-Mercalli Intensity X on the Pribilof Islands themselves. This event, those of 1847 and 1954, which were felt with intensity (M.M.) V-VI, and those of 1925, 1942, 1958, and 1959 with magnitudes of 7.2, 6.75, 6.38, and 6.50, respectively (Tab. 7.6.2) demonstrate that large earthquakes have occurred in the St. George region, the Pribilof Islands in particular, and must be expected in the future. This expectation is quantified in the section below on the teleseismic record.

TABLE 7.6.1

All Events in the Greater St. George Basin Region for the Period 1925 through 1978

Date	HrMn	Sec	Lat	Long	Depth	Mag	Date	HrMn	Sec	Lat	Long	Depth	Mag
250019	1207	27.30	55 14.40	167 41.40	.00	7.20	670806	1054	15.00	55 .00	168 .00	.00	4.10
250905	1630	17.50	54 40.00	170 37.00	.00	.00	670909	315	20.00	54 12.00	168 42.00	142.00	3.90
330427	1156	6.00	55 .00	166 .00	.00	.00	671130	937	12.00	56 .00	163 .00	.00	4.30
370710	101	12.00	55 .00	165 .00	.00	.00	671213	1756	45.00	54 18.00	170 24.00	33.00	4.00
410501	707	48.00	57 36.00	166 36.00	.00	.00	680114	1331	35.00	55 .00	164 .00	.00	4.00
410806	615	4.00	55 30.00	163 .00	120.00	.00	680305	530	27.00	55 12.00	163 42.00	.00	4.00
410806	615	6.00	55 45.00	163 .00	150.00	6.75	680323	0	34.10	56 25.00	162 18.00	180.00	4.00
410806	615	12.00	55 42.00	162 24.00	200.00	.00	680530	1622	21.00	54 12.00	168 54.00	.00	4.50
410928	533	18.00	56 .00	164 .00	.00	.00	690729	539	47.00	54 48.00	165 6.00	.00	3.50
420610	108	.00	57 30.00	163 .00	.00	.00	690801	326	9.00	54 40.00	165 6.00	.00	3.50
440929	1908	14.00	57 30.00	169 .00	.00	.00	690802	438	29.00	54 48.00	165 6.00	.00	3.40
470525	1554	48.00	57 30.00	169 .00	.00	.00	690828	502	21.00	54 48.00	165 6.00	.00	3.40
511001	1011	40.00	55 .00	166 .00	.00	.00	691105	459	54.00	54 18.00	167 36.00	.00	3.50
550717	2150	23.00	54 24.00	168 18.00	.00	.00	691123	1015	20.00	55 42.00	166 .00	33.00	.00
570310	2034	.00	55 .00	165 .00	.00	.00	691127	711	37.00	55 46.20	164 .00	33.00	.00
570312	449	30.00	55 .00	164 .00	.00	.00	691129	1652	.00	54 10.00	167 36.00	.00	3.00
570323	1029	10.00	54 30.00	165 30.00	.00	.00	691130	421	2.00	56 24.00	166 48.00	.00	3.60
570328	1251	45.00	55 .00	166 15.00	.00	.00	691207	13	13.00	54 30.00	171 .00	33.00	.00
570521	1501	53.00	55 .00	164 .00	.00	.00	691212	351	1.00	55 18.00	164 54.00	154.00	4.20
570531	1619	39.00	55 .00	169 .00	.00	.00	700126	833	49.00	57 18.00	163 .00	33.00	.00
570609	2051	33.00	55 .00	167 30.00	.00	.00	700427	552	6.00	54 18.00	167 36.00	.00	3.40
580303	1618	23.00	55 37.20	166 20.40	45.00	6.30*	700703	437	.00	57 6.00	164 .00	35.00	.00
590421	1242	50.00	56 .00	162 30.00	.00	.00	701120	228	57.00	54 12.00	168 10.00	.00	3.50
590512	0457	39.20	55 9.00	160 14.40	17.00	6.50*	701202	1014	50.50	55 54.60	163 58.20	221.00	4.70
600109	1749	7.00	55 30.00	165 .00	.00	.00	701203	646	15.00	54 18.00	167 36.00	.00	3.30
601030	2156	20.60	56 36.00	167 12.00	70.00	.00	701212	345	2.00	54 18.00	167 36.00	.00	3.50
610114	1639	9.00	55 30.00	165 .00	.00	5.75	701212	1517	21.00	54 18.00	167 36.00	.00	3.50
610326	2010	31.70	55 42.60	164 .60	50.00	.00*	710005	1351	9.30	55 43.00	164 55.20	33.00	5.10
610326	2010	44.40	55 36.60	163 48.00	175.00	.00*	711231	044	47.20	54 51.00	164 23.22	33.00	4.60
620400	2209	31.40	54 48.60	165 .60	25.00	.00	720513	1309	26.10	54 54.00	166 36.60	.00	.00
630500	050	54.00	55 30.00	163 40.00	.00	5.50	730630	507	1.30	54 7.32	168 30.82	.00	.00
640311	459	45.60	54 42.00	169 54.00	33.00	4.20	730820	2226	20.60	55 47.16	166 51.70	.00	4.40
640330	1921	51.00	55 30.00	168 6.00	30.00	4.30	740509	606	40.70	54 7.00	170 40.54	.00	.00
640501	1557	20.90	56 4.00	167 36.00	33.00	4.30	740724	1016	56.30	55 40.00	162 15.00	113.00	4.10
640504	226	33.70	55 57.60	162 48.00	200.00	4.50	741019	54	44.60	54 37.62	165 10.00	.00	4.30
640827	310	19.40	54 6.00	167 24.00	33.00	4.30	750129	1854	51.36	55 50.64	170 29.04	.00	.00
640912	432	34.00	54 48.00	170 .00	33.00	4.00	750210	220	50.49	54 59.94	169 36.70	.00	4.00
650215	943	4.30	55 48.00	166 42.00	35.00	4.50	750311	1849	46.11	54 34.60	169 9.66	.00	4.50
650325	2000	19.00	55 25.20	165 6.00	33.00	4.20	751110	1303	47.16	57 30.66	170 25.00	33.00	.00
650406	1737	35.50	55 30.00	166 48.00	33.00	4.20	760930	143	27.30	56 20.00	162 32.94	75.00	.00
651022	1626	40.40	56 37.20	169 40.20	7.00	4.70	761023	025	31.00	55 2.64	165 55.32	100.40	4.70
660717	103	4.00	56 29.40	167 2.40	40.00	4.00	761025	1124	7.76	57 8.02	165 56.50	33.00	4.60
661130	56	25.00	55 .00	167 .00	.00	4.20	770327	1041	57.90	57 34.00	169 57.00	33.00	4.20
670502	1756	33.00	57 .00	164 .00	.00	4.00	700626	252	56.60	57 37.20	169 55.00	33.00	4.20
670700	922	35.30	54 37.20	166 .00	120.00	4.10	701207	16	49.20	54 40.20	165 36.00	127.00	4.60

*NB: '58 and '59 events added after analysis; both depths for '61 event inadvertently included in analysis.

TABLE 7.6.2

Shallow Events in the Limited St. George Basin Region
for the Period 1957 through 1978

<u>Date</u>	<u>HrMn</u>	<u>Sec</u>	<u>Lat</u>	<u>Long</u>	<u>Depth</u>	<u>Mag.</u>	
570310	2034	.00	55	.00	165	.00	.00
570312	449	30.00	55	.00	164	.00	.00
570323	1029	10.00	54	30.00	165	30.00	.00
570328	1251	45.00	55	.00	166	15.00	.00
570521	1501	53.00	55	.00	164	.00	.00
570609	2051	33.00	55	.00	167	30.00	.00
600109	1749	7.00	55	30.00	165	.00	.00
601030	2156	20.60	56	36.00	167	12.00	70.00
610114	1639	9.00	55	30.00	165	.00	2.22
610326	2010	31.70	55	42.60	164	.60	50.00
620408	2209	31.40	54	48.60	165	.60	25.00
630508	850	54.00	55	30.00	163	48.00	.00
640330	1921	51.00	55	30.00	168	6.00	30.00
640501	1557	28.90	56	4.80	167	36.00	33.00
650215	943	4.30	55	48.00	166	42.00	35.00
650325	2000	19.80	55	25.20	165	6.00	33.00
650406	1737	35.50	55	30.00	166	48.00	33.00
651022	1626	48.40	56	37.20	169	40.20	7.00
660717	103	4.00	56	29.40	167	2.40	40.00
661130	56	25.00	55	.00	167	.00	1.11
671130	937	12.00	56	.00	163	.00	2.22
680114	1331	35.00	55	.00	164	.00	.00
680305	530	27.00	55	12.00	163	42.00	.00
690729	539	47.00	54	48.00	165	6.00	.00
690801	326	9.00	54	48.00	165	6.00	2.22
690802	438	29.00	54	48.00	165	6.00	2.22
690828	502	21.00	54	48.00	165	6.00	.00
691123	1015	20.00	55	42.00	166	.00	33.00
691127	711	37.00	55	46.20	164	.00	33.00
691130	421	2.00	56	24.00	166	48.00	1.11
710805	1351	9.30	55	43.08	164	55.20	33.00
711231	044	47.20	54	51.06	164	23.22	33.00
720513	1309	26.10	54	54.06	166	36.66	.00
730820	2226	28.60	55	47.16	166	51.78	1.11
741019	54	44.60	54	37.62	165	10.80	.00
751118	1303	47.16	57	30.66	170	25.08	33.00
770327	1841	57.90	57	34.80	169	57.00	33.00
780626	252	56.60	57	37.20	169	55.80	33.00

Teleseismic Record

Data. The teleseismically located earthquakes compiled in Tab. 7.6.2 are derived from four sources: (1) ISC (International Seismological Center), (2) PDE (Preliminary Determination of Epicenters, published by the USGS and archived by NOAA), (3) relocations by Tobin and Sykes (1966), and (4) relocations by Sykes (1971). These events are mapped in Fig 7.6.1. We restrict this analysis to events in the crustal material containing the St. George Basin; therefore, deep events (depth greater than 110 km, shown by dashed circles in Fig. 7.6.1) are excluded. From their locations (Fig 7.6.1) it can be seen that these deep events occur within the northernmost limb of the downgoing slab of Pacific lithosphere.

Interspersed with the epicenters of the deep events are those of about 30 events, the depths of which are unknown. Since we would like to account for these events in our analysis we observe that in the same area there are 7 shallow events and 13 deep events. We will assume that the same ratio of shallow-to-deep events holds for 30 events mentioned above.

To the northwest of this band of interspersed epicenters of deep and shallow events there are 19 additional events with unknown depths. We assume from their locations that these are shallow and, for purposes of identification assign them the depth 1.11 km (Tables 7.6.2 and 7.6.3).

In Fig 7.6.1 epicenters appear to be concentrated in the immediate region of the St. George Basin. A second concentration is centered in the southwest corner of the search area; these events are in the vicinity of the Umnak Plateau and the Bering Canyon. Lastly, a few outliers occur in the northeast part of the area. We further restrict the analysis by reducing the geographic area to the immediate St. George Basin region as shown in Fig 7.6.2 and the time interval to the 22 year period 1957-1978 as shown in Figure 3B. The resultant data set (Table 7.6.3) is the basis for the analysis that follows.

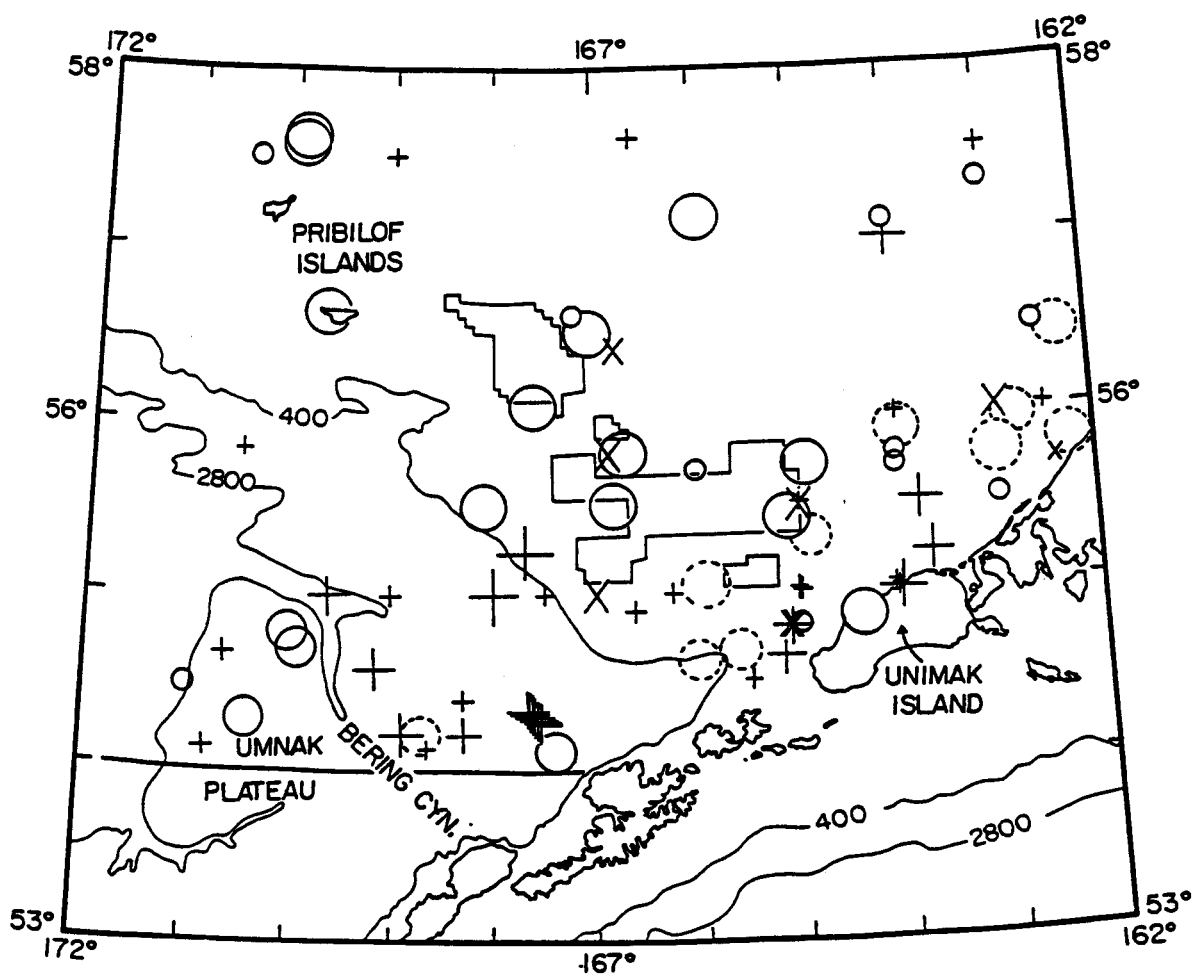


Fig. 7.6.1 Earthquake epicenters, greater St. George Basin area, 1925 through 1978. Epicenter symbols are scaled by magnitude according to height (minutes = $6.5 + 1.66 M$); crosses represent events with unknown depth; x's those with depths inferred to be shallow; solid circles, those known to be shallow ($Z < 75$ km); dashed circles, those known to be deep ($Z > 113$ km). The greater St. George Basin area is bounded on the north, east, and west by the edges of the region shown; the southern boundary is the heavy line along 54°N to its intersection with the Aleutian arc and then along the northern edge of the arc. The potential lease areas are encompassed by the light rectangular boxes. Isobaths are in meters.

TABLE 7.6.3

Frequency of Occurrence by Magnitude

<u>i</u>	<u>M</u>	<u>n</u>	<u>nr</u>	<u>N</u>	<u>log N</u>
1	5.75	1	1.606	1.606	0.206
2	5.1	1	1.606	3.212	0.507
3	4.8	1	1.606	4.818	0.683
4	4.7	1	1.606	6.424	0.808
5	4.5	2	3.212	9.636	0.984
6	4.4	1	1.606	11.242	1.051
7	4.3	3	4.818	16.060	1.206
8	4.2	5	8.030	24.090	1.382
9	3.6	1	1.606	25.696	1.410
10	3.5	1	1.606	27.302	1.436
11	3.4	<u>1</u>	<u>1.606</u>	28.908	1.461
TOTALS		18	28.908		

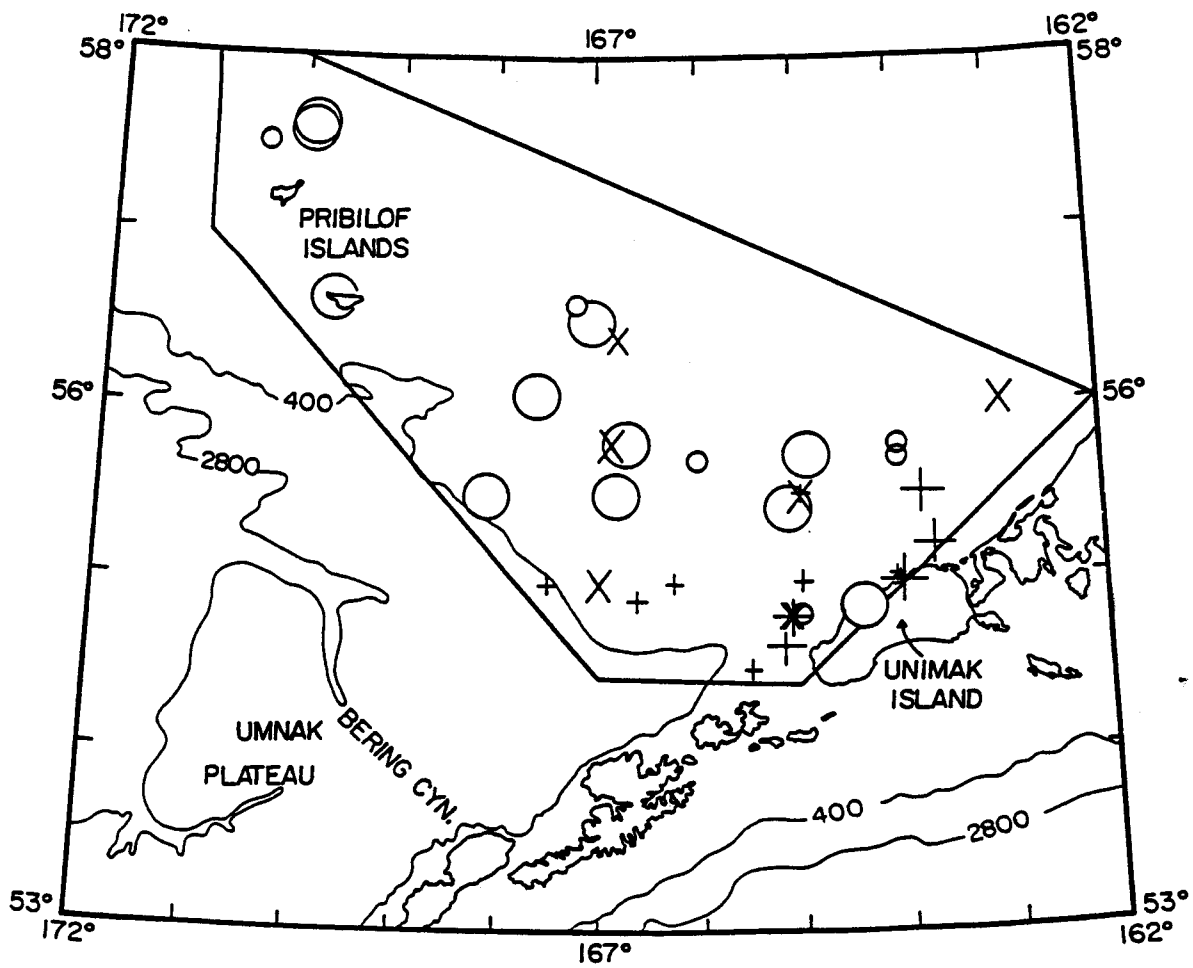


Fig 7.6.2 Epicenters of shallow ($Z \leq 70$ km) earthquakes, limited St. George Basin area, 1957 through 1978. Symbols are as in Fig 7.6.1. The limited St. George Basin area is bounded approximately by the heavy line.

Frequency of Occurrence for Events in Various Magnitude Ranges

This calculation is summarized in Tab 7.6.4. From Tab 7.6.3 we have 14 events for which both the magnitude and depth are known or inferred. Also, there are 10 events of unknown depth whose magnitudes are known. We assume that every third one of these (in order of decreasing magnitude) is shallow and for identification assign them a depth of 2.22. This results in a total of 18 events with known magnitudes that are known or inferred to be shallow. The magnitudes of these events and the number at each magnitude are listed in columns 2 and 3, respectively. In addition to these 18 events there are 6 for which only the depth is known (or inferred) and 14 for which the depth is unknown. The epicenters of the latter 14 are above the northern limb of the downgoing slab, so some of them are probably deep. We assume that the same ratio of shallow-to-deep events holds for these 14 as held for the 20 (7 shallow, 13 deep) enumerated above from the data set in Tab 7.6.2. Therefore, we infer that 4.9 of these 14 were shallow. Adding these 4.9 to the 6 known to be shallow we obtain an additional 10.9 shallow events for which to account that have unknown magnitudes. Thus, the total number of shallow events that occurred in the limited St. George basin region during the years 1957 through 1978 is 28.9. We assume that these additional 10.9 events are distributed by magnitude the same as the 18 for which magnitudes are known; therefore, since 28.9 is 1.606 times 18 we multiply the n in column 3 of Tab 7.6.4 by $r = 1.606$ to obtain the nr listed in column 4. Thus, nr is the estimated number of events at each magnitude for the specified region and time interval. We next obtain the cumulative number at successively smaller magnitudes, N, by summing the nr down column and listing the partial sums in column 5. That is:

$$N_j = \sum_{i=1}^j (nr)_i$$

Thus N_j is the number of events larger than or equal to M_j where j is the row number. The last column is simply the logarithm (base 10) of the corresponding entry in the previous one. This is computed for the b-value plot shown in Figure 7.6.4.

TABLE 7.6.4

Reports of Volcanic Activity in the Eastern Aleutian Arc from Okmok Volcano,
Umnak Island to Pavlof Volcano, Alaska Peninsula

Volcano	Report of Activity		Eruption ¹ Potential	Number of Reports ²				Remarks
	Earliest	Latest		A	E	Q	I	
Okmok	1805	- 1958	5	19	9	4	32	1878, Makushin Village destroyed
Bogoslof	1796	- 1926	5	14	12	1	27	1796,1883,1926: island-forming events
Makushin	1768	- 1980	5	22	7	2	31	two volcanoes active in 1768, Bishop Pt. mudflow 30m high at shore
Akutan	1790	- 1980	5	35	16	2	53	mud flow 1929, 1 km lava flow 1978
Akun	1828	- 1880	1	3	0	0	3	no historic eruptions, deeply dissected
Pogromni	1795	- 1965	4	9	7	1	17	
Westdahl	1826	- 1979	4	4	4	0	8	1m of ash fell on Scotch Cap forcing evacuation, damaging light, floods washed our road, 1978
Fisher	1826	- 1826	1	1	0	0	1	questionable report of eruption, 1826
Shishaldin	1775	- 1979	5	47	23	0	70	1978 Sept. 28, caused radio interference
Isanotski	1690	- 1845	3	6	4	1	11	1825: mudslides, ash to Pavlof Bay
Roundtop	none		0	0	0	0	0	no reports
Frosty	1768	- 1951	1	4	0	0	4	reports for Walrus & Morshova assigned to Frosty (3)
Amak	1700	- 1715	1	1	0	0	1	no activity since 1804 at latest
Emmons	1768	- 1953	1	4	0	0	4	reports for Medviednikof assigned to Emmons (4)
Pavlof	1790	- 1980	5	49	30	1	80	1914 eruption: 5 cm of sand on Unga
Pavlof's Sister	1762	- 1786	2	--	--	--	--	not active since major eruption in 1786

Footnotes for Table 7.6.4

(1) Eruption Potential: scale 0-5

- 0 - no historic activity
- 1 - no historic eruptions, but smoke or steam reported
- 2 - last eruption in 1700's
- 3 - last eruption in 1800's
- 4 - last eruption in 1900's
- 5 - last eruption in 1900's and $I > 25$

- (2) A = reports of activity
E = reports of activity including eruptions
Q = reports of eruptions with earthquakes
I = A + E + Q

Note that A includes E and E includes Q so that reports of earthquakes are added 3 times into the index, I, and reports of eruptions 2 times, whereas reports of activity (smoke, steam, etc.) are only counted once.

- (3) Morzhovoi = Walrus (Orth, 1967) but Walrus Peak is nonvolcanic. Waldron (1961) thinks Morshova and Frosty are the same. We tentatively agree.
- (4) Medvied = Bear; Medvednikova Zaliv = Bear Bay on Alaska Peninsula at 162°W (Orth, 1967). Since Emmons Volcano is at 162°W it seems possible that the old (≤ 1850) reports for Medviednikof refer to Emmons. Note that Emmons received its present name ~ 1940 .

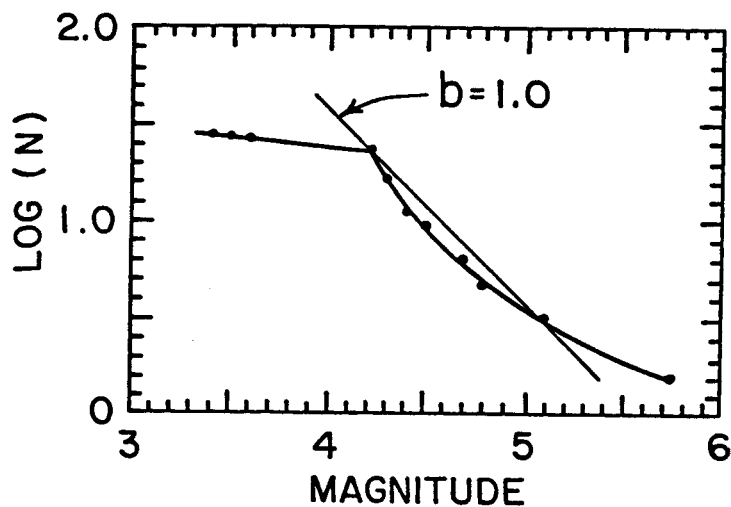


Fig. 7.6.4 Logarithm cumulative number of earthquakes vs. magnitude for the limited St. George Basin region during the period 1957 through 1978. Light line labeled $b = 1.0$ is a plot of the relation $\log N = a - bM$ with $a = 5.58184$ and $b = 1.0$. The shallow slope of the heavy curve below $M = 4.2$ indicates that the data set is incomplete below this magnitude; i.e., $M = 4.2$ is the detection threshold for this region and period. The increasing slope near $M = 5.0$ suggests that more events of $M \geq 5$ were observed than would usually be the case for this time interval.

The b-value is the absolute value of the slope of the well-known relation

$$\log N_j = a - bM_j. \quad (1)$$

We expect a b-value of about 1.0 which is the slope of the reference line plotted in Fig 7.6.4. The shape of the curve in this plot is controlled by the numbers of events actually observed at each magnitude listed in Tab 7.6.4, column 3. The shallow slope above magnitude 4.2 indicates that $M = 4.2$ is about the detection threshold for this data set. The increase in slope toward higher magnitude implies that more events with $M > 5.0$ were observed than would usually be the case for this region and interval. We note that the slope in the magnitude range $4.2 \leq M \leq 5.0$ is very close to 1.0. To determine the value of "a" in (1) it is best to use the values of M_j and N_j corresponding to the lowest magnitude above the detection threshold; viz., $M = 4.2$ and $N = 24.09$. This maximizes the number of observations used and hence minimizes the importance of observing or not observing any given event. Using the above values we obtain

$$a = \log (24.09) + 4.2 = 5.58184 \quad (2)$$

where we have assumed $b = 1.0$.

Using (1) and (2) we can compute the number of events expected within any magnitude range from

$$N (M_i, M_j) = N_i - N_j; \quad M_i < M_j. \quad (3)$$

We next assume that $N (M_i, M_j)$ is the expected value for the St. George basin region for any 22 year interval and that the number of events per unit time is distributed according to the Poisson function. We can then write (Hald, 1952, p. 732) the probability for the occurrence of one or more events in a given range $M_i \leq M \leq M_j$ and time interval $\tau = t \text{ years} \div 22$ is given by

$$P_{ij} (\text{one or more}) = 1 - P_{ij} (\text{none}) = 1 - e^{-N (M_i, M_j)\tau} \quad (4)$$

Using (1) through (4) and $t = 40$ years we find:

j	M_j	N_j	$N (M_{j-1}, M_j)$	$P_{j-1, j}$ (one or more)
1	4	38.18	----	----
2	5	3.818	34.36	1.0000
3	6	.3818	3.436	0.9981
4	7	.03818	.3436	0.4646
5	8	.003818	.03436	0.0606

The probability for the occurrence of an event of a certain size is not directly of interest: what is of more interest is the joint probability that the event will occur and that it will cause damage. We will reduce the problem to the exceedence of two specific accelerations; viz., 0.2 and 0.5g. The conditional probability that given an event of a certain size it will cause accelerations greater than or equal to α is

$$P (ij|\alpha) = \frac{\pi r_{ij}^2(\alpha)}{A} \quad (5)$$

where $r_{ij}(\alpha)$ is the radius from the site of interest within which the event must occur if the acceleration is to reach α , and $A = 80,770 \text{ km}^2$ is the total area of the limited St. George Basin region as outlined in Fig 7.63. Therefore, the joint probability that an event of a certain size will occur and it will be close enough to exceed an acceleration of α is given by

$$P (ij \text{ and } \alpha) = P_{ij} \text{ (one or more)} P (ij|\alpha). \quad (6)$$

Finally, the total (or marginal) probability that α will be exceeded is the sum of the probabilities of each of the possible cases, neglecting terms of order $(P (ij \text{ and } \alpha))^2$ and higher: i.e.,

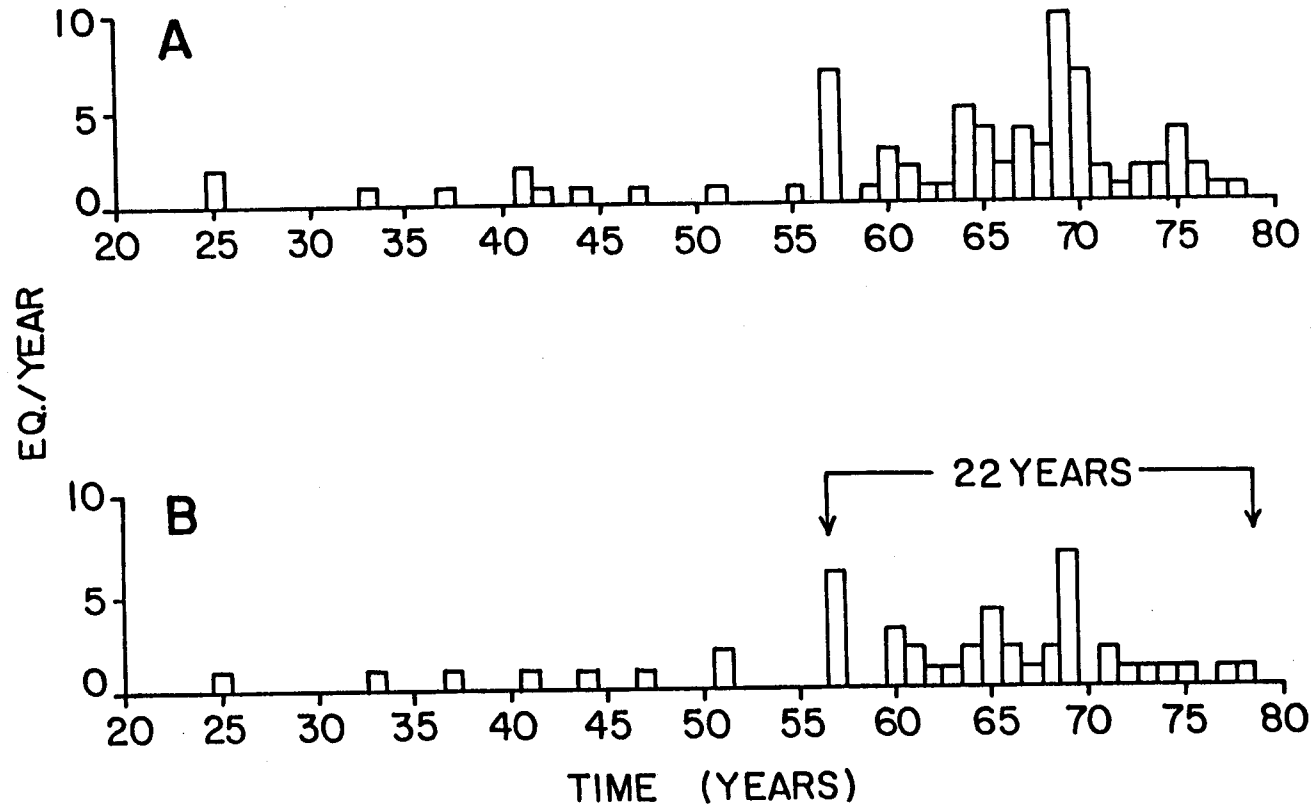


Fig. 7.6.3. Earthquakes per year for (A) the greater and (B) the limited St. George Basin region. Origin time for this histogram is the year 1900. The 22 year time span indicated for 1957 through 1978 is the period used in the computation of the probabilities that accelerations of 0.2 and 0.5 g would be exceeded at a specific site. It is clear from this figure that the detection threshold was higher in previous years, hence the restriction to the last 22 years for the analysis.

$$P(\alpha) = \sum_{j=2}^5 P_{j-1,j} \text{ (one or more) } P(j-1,j | \alpha) \quad (7)$$

where, as above, $j=1$ corresponds to $M = 4.0, 2$ to 5.0 , etc.

The radii, $r_{ij}(\alpha)$ are scaled from the plot of acceleration-vs.-distance given in Fig 7.6.5. Most of the data in this figure were compiled by Page et al. (1972) for the western U.S. The larger symbols represent data collected at Sand Point, in the Shumagin Islands. The Aleutian data show systematically higher accelerations at a given distance than do those of the western U.S. Therefore these data are used to determine the intercepts of the lines labeled 4.5, 5.5, etc., in Fig 7.6.5, while the western U.S. data are used to determine the slopes. The line labeled 4.5 is used to specify the acceleration-vs.-distance relation for earthquakes in the magnitude range $4.0 \leq M \leq 5.0$, that labeled 5.5 for the range $5.0 \leq M \leq 6.0$, etc. Thus, for example, the radius from a given site within which an earthquake in the range $6.0 \leq M \leq 7.0$ must occur if the acceleration is to exceed $0.5g$ is 30 km. From (5) the conditional probability that should such an earthquake occur in the St. George Basin region it will be close enough to a given site to cause an acceleration greater than $0.5g$ is

$$P(3,4|0.5) = \frac{\pi 30^2}{80,770} = 0.035 \quad (8)$$

Calculation of the probabilities for the ground acceleration to exceed 0.2 or 0.5 in 40 years for a site within the St. George Basin region is summarized in Tab 7.6.5. The values in this table are determined using (1) through (7) and the relations plotted in Figure 7.6.5. These calculations indicate for the limited St. George Basin region in a 40 year period the probability to exceed $0.2g$ is about 11% and that to exceed $0.5g$ is about 3%.

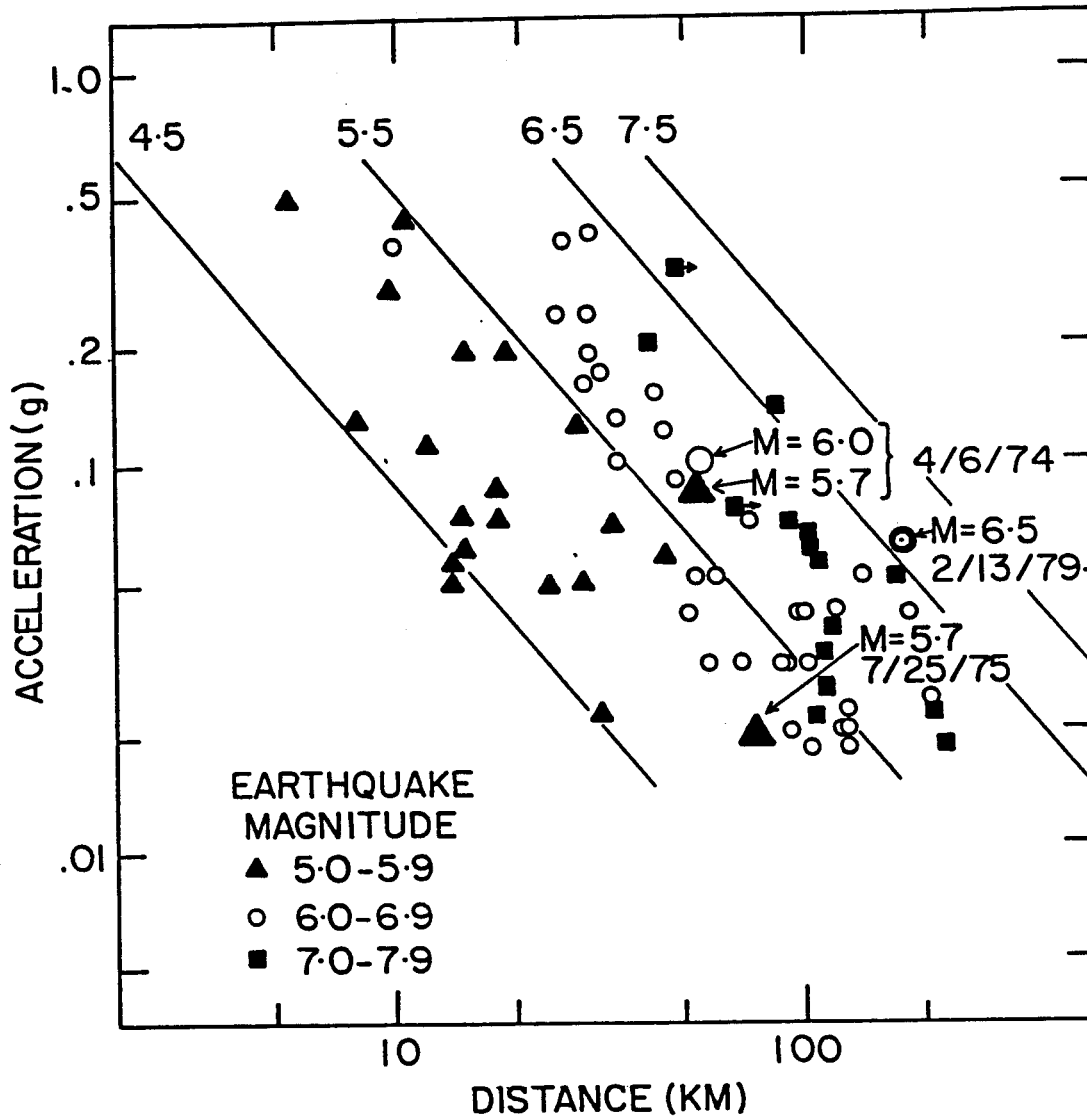


Fig. 7.6.5 Peak acceleration vs. distance for some western U.S. earthquakes (small symbols, Page et al., 1972) and eastern Aleutian earthquakes (large symbols, Davies et al., 1979 and 1976; House and Boatwright, 1980). The lines labeled 4.5, 5.5, 6.5, and 7.5 are used to define the relationship between acceleration and distance for events in the magnitude ranges 4-5, 5-6, 6-7, and 7-8, respectively. The slopes of these lines are determined by the western U.S. data and the intercepts by the Aleutian data.

Local Record

Data. A Geospace HS-10/1B seismometer was installed in the Seismic Cottage (near the National Weather Service Observatory) on St. Paul Island during October 1975. This instrument is recorded on a Helicorder with a magnification at 5 Hz of about 17,500. The magnification of the St. Paul seismograph is limited by the surf noise propagated by the alluvium on which the Seismic Cottage is located.

In an attempt to determine the azimuth of the events recorded by this station, two remote stations were installed on St. Paul Island in July 1980. None of the local events recorded since then have been impulsive enough so that arrival times could be read with any confidence. Therefore, all of the data discussed in this section were recorded by the local, short period, vertical seismograph at St. Paul Island.

Table 7.6.6 gives arrival times, distances (from S-P times), and magnitudes for events detected at St. Paul (SNP) which might have occurred in the St. George Basin; without azimuths, only the distance can be specified. Magnitudes were calculated using Richter's (1958, p. 342) local scale and a correction determined by comparing the SNP magnitudes for the larger events to those listed in the PDE. Some larger ($M = 5$) events in the Aleutian arc between the Fox Islands and the Alaska Peninsula were included for this analysis.

Comparison of Seismic Rate

Figure 7.6.6 is a plot of magnitude vs. distance which shows that the magnitude threshold at about 450 km. is approximately 4.0. In other words, an earthquake in the southern St. George Basin must have a magnitude greater than or equal to 4.0 to be detected at SNP. Therefore, in comparing seismicity rates, the analysis must be restricted to events of 4.0 and larger.

There are only 3 such events listed in Table 7.6.6., all between $M = 4$ and $M = 5$. Thus, in the nomenclature of the previous section, $N(M_4, M_5) = 3$ which can be extrapolated (assuming a b-value of 1.0) to: $N(M_5, M_6) = 0.3$, $N(M_6, M_7) = 0.03$, and $N(M_7, M_8) = 0.003$. Using (4) from that section and the above $N(M_{j-1}, j)$, the $P_{j-1, j}$ (one or more) for $j=2$ through 5 are 1.00, 0.98, 0.32, and 0.04, respectively. These are

TABLE 7.6.5

Probability for Acceleration to Exceed 0.2 or 0.5g in
40 Years for a Site Within the St. George Basin Region

j	M_j	$r_{j-1,j}(\alpha)$ (km)	$P_{j-1,j}$ (one or more)	$P\{j-1,j \alpha\}$	$P\{j-1,j \text{ and } \alpha\}$
for $\alpha = 0.2g$ and $t = 40$ years:					
1	4.0	—	—	—	—
2	5.0	5	1.0000	0.00097	0.00097
3	6.0	20	0.9981	0.016	0.01597
4	7.0	60	0.4646	0.14	0.06504
5	8.0	100	0.0606	0.39	0.02363
				$P(0.2)$	= 0.10561

for $\alpha = 0.5g$ and $t = 40$ years:

1	4.0	—	—	—	—
2	5.0	2.5	1.0000	0.00024	0.00024
3	6.0	10	0.9981	0.0039	0.00389
4	7.0	30	0.4646	0.035	0.01626
5	8.0	50	0.0606	0.097	0.00588
				$P(0.5)$	= 0.02627

TABLE 7.6.6

Events Detected at SNP in a Distance Range Such That Origin in
St. George Basin is Possible

Time Interval: May 1977 - July 1980

Date	Time	Distance (deg.)	Distance (km)	Magnitude
77 05 20	12:50	0.58	64	2.2
77 07 20	21:19	1.34	149	2.7
77 07 21	12:56	2.17	240	3.8
77 08 11	01:54	2.45	272	3.8
77 09 25	17:21	0.77	85	2.1
77 11 30	00:15	0.92	102	2.0
78 03 07	02:56	0.77	85	4.1
78 07 13	13:26	2.17	241	4.5
78 07 24	14:52	0.16	68	3.0
78 08 09	01:51	3.88	431	4.0
78 08 24	09:01	2.27	252	3.6
78 09 24	16:43	0.79	88	3.0
78 11 28	17:42	1.01	112	2.5
79 04 29	14:16	0.38	42	1.8
80 02 08	13:38	0.69	77	2.5
80 03 22	10:31	2.08	231	3.5
08 07 23	17:13	0.46	51	1.6

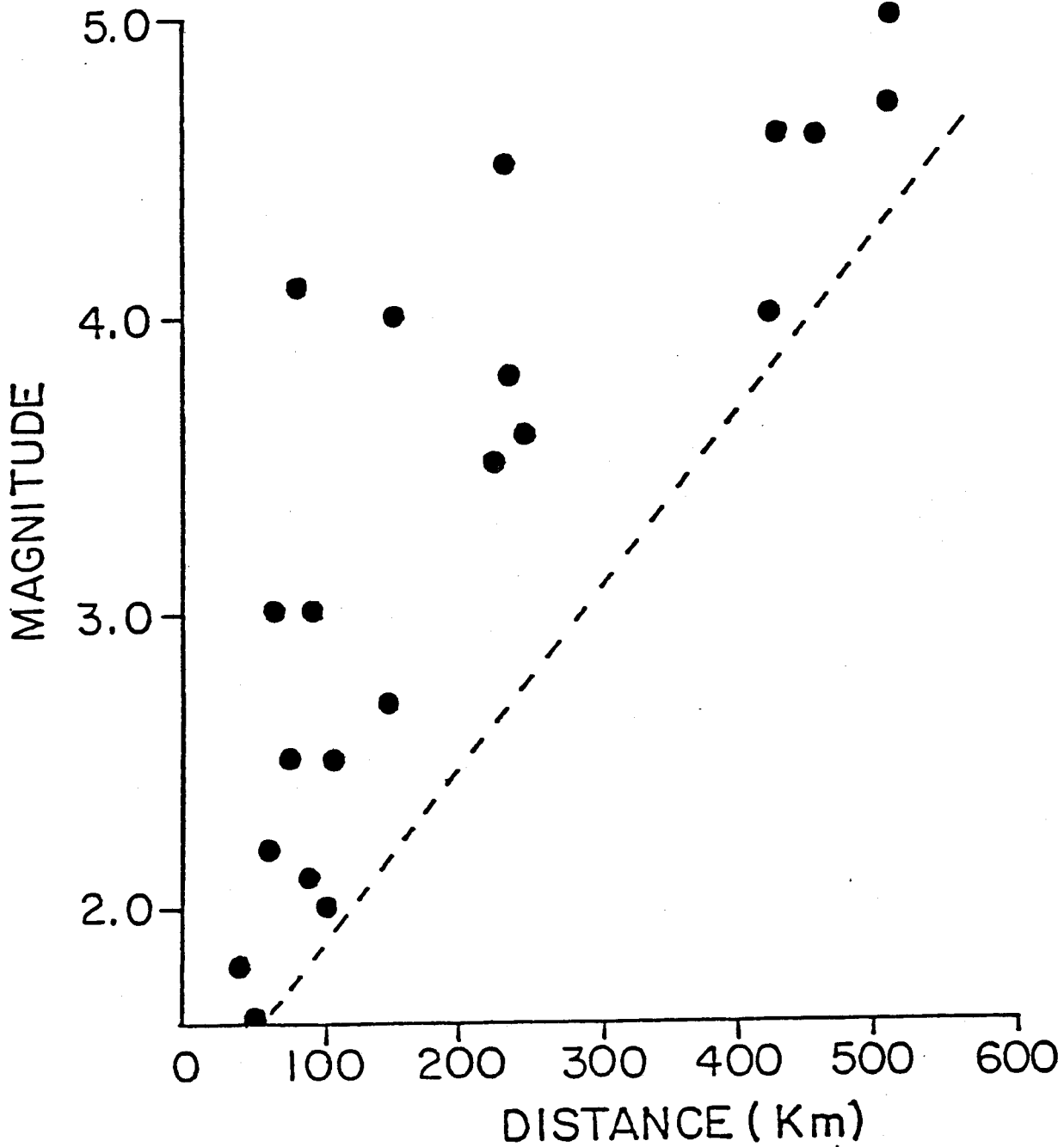


Fig. 7.6.6. Detection threshold for St. Paul Seismic station (SNP). Plotted is local magnitude (see text) vs. distance based on S-P time (the interval between the arrival of the P-wave and the S-wave). Since the southern end of the St. George basin is a little over 400 km from St. Paul is., the smallest earthquake that can be detected over the whole basin by SNP is about $M_L - 4.0$.

the probabilities that an earthquake in the respective range of magnitudes will occur within 40 years. The comparable probabilities computed from the teleseismic data are 1.00, 0.998, 0.46, and 0.06. Thus, the local data over a 3 1/6 year span indicate the same order of activity as do the teleseismic data over a 22 year span.

VOLCANIC ACTIVITY

Pribilofs. Mushketov and Orlov (1893, p. 198) report "a submarine earthquake and eruption" northeast of St. George in 1815. Barth (1956) references Landgrebe (1855) for the statement that "flames have been seen to rise from the sea northeast of the Pribilof Islands". It is likely that both of these reports are based on a report from Kotzebue around 1821 to 1828 which we have not been able to find. Barth (1956, p. 154) concludes "However, in spite of these assertions any present volcanic activity must be regarded as doubtful". Hopkins (1976) similarly concludes "The volcanic hazard is small on and near St. Paul Island and negligible elsewhere". He also states "The numerous isolated shocks in the vicinity of the Pribilof Islands are probably [emphasis ours] mostly ancient, eroded, volcanic centers... appropriate paleontological or radiometric methods [should be] used to establish their age". We conclude that volcanic activity is unlikely but suggest that Hopkins' advice be followed if any structures are to be built on or near St. Paul and St. George.

Makushin Bay. In 1878 the village of Makushin was destroyed by an earthquake (Mushketov-Orlov, 1893, p. 468). The earthquake and associated tsunami have been reported as part of a crater-forming event at Okmok Volcano (Hantke, 1951). Apparently the village was destroyed by the tsunami that swept along the north shore of Unalaska Island. Note that Makushin Bay is also exposed to Bogoslof Volcano at a distance roughly equal to that of Okmok.

Scotch Cap. The 1978 eruption of Westdahl deposited 1 m of ash on the U.S. Coast Guard light station at Scotch Cap. The ash damaged the light and forced the evacuation of the site, meltwater floods washed out the road to Cape Sarichef.

Other Volcanic Activity. Tab 7.6.7 is a summary of reports of volcanic activity (Hickman, unpublished files) in the eastern Aleutian arc from Okmok Volcano on Umnak Island to Pavlof Volcano on the Alaska Peninsula. Of the 16 volcanoes listed, 8 are rated as having a high potential for eruption (4,5 on a scale of 0-5; see footnote 1, Table 7.6.7): Okmok, Bogoslof, Makushin, Akutan, Pogromni, Westdahl, Shishaldin, and Pavlof. Isanotski is given a moderate potential (3) and the remaining seven are rated at a low to negligible potential (2-0).

For the purpose of siting a pipeline terminal/tanker facility those volcanoes with a high potential for eruption should be regarded as likely to produce the following hazards:

- (1) lavaflows, mudslides, floods, incandescent bombs, and nuee ardent on the flanks and in valleys around the volcano.
- (2) ash and sand clouds capable of depositing up to a meter of material several tens of km downwind from the volcano and a few centimeters of material at 100 to 150 km. The fine particles will produce a plume in which planes should not fly 100 to 200 km wide and 200 to 500 km long. This phase may persist for hours to days.
- (3) local tsunamis to distances of 100 to 150 km.
- (4) several hours to 10's of hours of radio interference during the eruption.

7.7 List of Publications Partially Supported by Contract NOAA 03-5-022-70

- Jacob, K.H., K. Nakamura, and J.N. Davies, Trench-volcano gap along the Alaska-Aleutian arc: Facts, and speculations on the role of terrigenous sediments for subduction, Maurice Ewing Series, 1, edited by M. Talwani and W. Pitman III, pp. 243-258, AGU, Washington, D.C. 1977.
- Nakamura, K., K.H. Jacob, and J.N. Davies, Volcanoes as possible indicators of tectonic stress orientation - Aleutians and Alaska, PAGEOPH, 115, 87-112, 1977.
- Bilham, R., A sea-level recorder for tectonic studies, Geophys. J. Roy. astr. Soc., 48, 307-314, 1977.
- Davies, J.N., K.H. Jacob, and L.R. Sykes, A comprehensive study of the seismotectonics of the eastern Aleutian arc and associated volcanic systems, Eight-Year Synopsis 1970-1978, to U.S. Department of Energy, 1978.
- Davies, J.N., and L.S. House, Aleutian subduction zone seismicity, volcano-trench separation and their relation to great thrust-type earthquakes, J. Geophys. Res., 84, 4583-4591, 1979.
- Bilham, R., and J. Beavan, Satellite telemetry of sea-level data to monitor crustal motions in the Shumagin Islands region of the Aleutian arc, in Proc. Conf. Terrestrial and Space Techniques in Earthquake Prediction Research, 1979.
- House, L., and J. Boatwright, Investigation of two high stress-drop earthquakes in the Shumagin Seismic Gap, Alaska, J. Geophys. Res., 85, 7151-7165, 1980.
- Davies, J.N., L.R. Sykes, L. House, and K.H. Jacob, Shumagin seismic gap, Alaska Peninsula: History of great earthquakes, tectonic setting, and evidence for high seismic potential, J. Geophys. Res., 86, 3821-3856, 1981.
- Sykes, L.R., J.B. Kisslinger, L. House, J.N. Davies, and K.H. Jacob, Rupture zones of great earthquakes, Alaska-Aleutian arc, 1784-1980, Science, 210, 1343-1345, 1980.
- McCann, W.R., O.J. Perez, and L.R. Sykes, 1980. Yakataga seismic gap, southern Alaska: Seismic history and earthquake potential, Science, 207, 1309-1314.
- Perez, O.J., and K.H. Jacob, 1980. Tectonic model and seismic potential of the eastern Gulf of Alaska and Yakataga seismic gap, J. Geophys. Res., 85, 7132-7150.
- Perez, O.J., and K.H. Jacob, 1980. St. Elias, Alaska earthquake of February 28, 1979: Tectonic setting and precursory seismic pattern, Bull. Seismol. Soc. Amer., 70, 1595-1606.
- Boatwright, J., 1980. Preliminary body wave analysis of the St. Elias, Alaska earthquake of February 28, 1979, Bull. Seismol. Soc. Amer., 70, 419-436.

House, L., L.R. Sykes, J.N. Davies, and K.H. Jacob, Identification of a possible seismic gap near Unalaska Island, Eastern Aleutians, Alaska, in Earthquake Prediction, An International Review, Maurice Ewing Series, 4, edited by D.W. Simpson and P.G. Richards, pp. 81-92, AGU, Washington, D.C. 1981.

Sykes, L.R., J.B. Kisslinger, L. House, J. Davies, and K. Jacob, Rupture zones and repeat times of great earthquakes along the Alaska-Aleutian arc, in Earthquake Prediction, An International Review, Maurice Ewing Series, 4, edited by D.W. Simpson and P.G. Richards, pp. 73-80, AGU, Washington, D.C., 1981.

Nakamura, K., G. Plafker, K.H. Jacob, and J.N. Davies, A tectonic stress trajectory map of Alaska using information from volcanoes and faults, Bull. Earthq. Res. Inst., 55, Part 1, 89-100, University of Tokyo, 1980.

McNutt, S.R., and R.J. Beavan, Volcanic earthquakes at Pavlof Volcano, Alaska, correlated with the solid earth tides, Nature, 294, 615-618, 1982.

Reyners, M., and K. Coles, Fine structure of the dipping seismic zone and subduction mechanics in the Shumagin Islands, Alaska, J. Geophys. Res., 87, 356-366, 1982.

McNutt, S.R., and R.J. Beavan, Correlation of the solid earth tide with volcanic earthquakes at Pavlof Volcano, Alaska, Proceedings of the 9th International Symposium on Earth Tides, New York, 1981.

House, L., and K.H. Jacob, Thermal stress in descending lithospheric slabs and implications for double seismic zones and downdip stress polarities, Nature, 295, 587-589, 1982.

McNutt, S., Seismic monitoring of volcanoes in the Aleutians, Volcano News, 11, page 7, 1982.

House, L.S., and K.H. Jacob, Earthquakes, plate subduction, and stress reversals in the eastern Aleutian arc, J. Geophys. Res., in press, 1983.

Mori, J., Dynamic stress drops of moderate earthquakes of the eastern Aleutians and their relation to a great earthquake, Bull. Seism. Soc. Am., 73, 1077-1097, 1983.

Mori, J., Short- and long-period subevents of the February 4, 1965, Rat Islands earthquake, Bull. Seism. Soc. Am., in press, 1983.

Mori, J., Duration of P- and S-wave pulses for small earthquakes in the Shumagin Islands, Alaska, submitted to Bull. Seism. Soc. Am., 1982.

Beavan, J., E. Hauksson, S.R. McNutt, R. Bilham, and K.H. Jacob, Tilt and seismicity changes in the Shumagin seismic gap, submitted to Science, 1983.

Beavan, R., R. Bilham, and K. Hurst, Coherent tilt signals observed in the Shumagin seismic gap: Detection of time-dependent subduction at depth, submitted to J. Geophys. Res., 1983.

8. REFERENCES

- Abe, K., 1979. Size of great earthquakes of 1837-1974 inferred from tsunami data, J. Geophys. Res., 84, 1561-1568.
- Abe, K., 1981. Magnitudes of large shallow earthquakes from 1904 to 1980, Phys. Earth Planet. Int., 27, 72-92.
- Aki, K., 1981. A probabilistic synthesis of precursory phenomena, in Earthquake Prediction, An International Review, Maurice Ewing Series, 4, edited by D.W. Simpson and P.G. Richards, pp. 566-574, AGU, Washington, D.C.
- Barth, T.F., 1956. Geology and petrology of the Pribilof Islands, Alaska, U.S. Geol. Surv. Bull. 1028-F, 101-160.
- Beavan, R., R. Bilham, and K. Hurst, 1983. Coherent tilt signals observed in the Shumagin seismic gap: Detection of time-dependent subduction at depth, submitted to J. Geophys. Res.
- Bendat, J.S., and A.G. Pierson, 1981. Random Data: Analysis and Measurement Procedures, Wiley-Interscience Publ., New York.
- Burke, C.A., 1965. Geologic map of the Alaska Peninsula, Geol. Soc. Am. Memoir 99, part 2, sheets 1 and 2.
- Byers, J.M., Jr., 1959. Geology of Umnak and Bogoslof Islands, Aleutian Islands, Alaska, U.S. Geol. Surv. Bull. 1028-L, 267-369.
- Carr, M.J., 1977. Volcanic activity and great earthquakes at convergent plate margins, Science, 197, 655-657.
- Coffman, J.L., and C.A. von Hake, 1973. Earthquake history of the U.S., Revised Edition (through 1970), Publication 41-1, NOAA Environ. Data Service, Boulder, Colorado.
- Cox, D., and G. Pararas-Carayanis, 1976. Catalog of Tsunamis in Alaska, U.S., 78 pp., Dept. of Commerce, NOAA/EDS, Asheville, North Carolina.
- Crandell, D.R., and D.R. Mullineaux, 1978. Potential hazards from future eruptions of Mount St. Helens Volcano, Washington, U.S. Geol. Surv. Bull. 1383-C, C1-C26.
- Davies, J.N., and L. House, 1979. Aleutian subduction zone seismicity, volcano-trench separation, and their relation to great thrust-type earthquakes, J. Geophys. Res., 84, 4583-4591.

- Davies, J., L. Sykes, L. House, and K. Jacob, 1981. Shumagin seismic gap, Alaska Peninsula: History of great earthquakes, tectonic setting, and evidence for high seismic potential, J. Geophys. Res., 86, 3821-3856.
- Davis, T.N., and C. Echols, 1962. A table of Alaska earthquakes, 1788-1961, Geophys. Inst., Univ. of Alaska, Fairbanks, Alaska, Geophys. Rep. No. 8.
- Detterman, R.L., T.P. Miller, M.E. Yount, and F.H. Wilson, 1981a. Geologic map of the Chignik and Sutwik Island Quadrangles, Alaska, U.S. Geol. Surv. Map I-1229, 1:250,000.
- Detterman, R.L., T.P. Miller, M.E. Yount, and F.H. Wilson, 1981b. Quaternary geologic map of the Chignik and Sutwik Island Quadrangles, Alaska, U.S. Geol. Surv. Map I-1292, 1:250,000.
- Donn, W.L., and D. Ninkovich, 1980. Rate of Cenozoic explosive volcanism in the North Atlantic Ocean inferred from deep sea cores, J. Geophys. Res., 85, 5455-5460.
- Drewes, H., G.D. Fraser, G.L. Snyder, and H.F. Barnett, Jr., 1961. Geology of Unalaska Island and adjacent insular shelf, Aleutian Islands, Alaska, U.S. Geol. Surv. Bull. 1028-S, 583-676.
- Duda, S.J., 1965. Secular seismic energy release in the circum-Pacific belt, Tectonophysics, 2, 409-452.
- Einarsson, P., and B. Brandsdottir, 1980. Seismological evidence for lateral magma intrusion during the July 1978 deflation of the Krafla Volcano in NE-Iceland, J. Geophys., 47, 160-165.
- Glover, D.P., 1980. Historical Seismogram Filming Project, Second Progress Report, Rpt. SE-24, August 1983, 63 pp., NOAA/EDS, Boulder, Colorado.
- Glover, D.P., and H. Meyers, 1981. Historical Seismogram Filming Project, Third Progress Report, Rpt. SE-28, World Data Center A, Solid Earth Geophysics, NOAA/OCS, Boulder, Colorado.
- Glover, D.P., and H. Meyers, 1982. Historical Seismogram Filming Project, Fourth Progress Report, Rpt. SE-33, World Data Center A, Solid Earth Geophysics, NOAA-National Geophys. Data Center, Boulder, Colorado.
- Gutenberg, B., and C.F. Richter, 1949. Seismicity of the Earth, First Edition, Princeton Univ. Press, 273 pp., Princeton, New Jersey.

- Gutenberg, B., 1956. Great earthquakes 1896-1903, Trans. Amer. Geophys. Union, 37, 608-614.
- Habermann, R.E., 1983. Teleseismic detection in the Aleutian Island arc, J. Geophys. Res., 88, 5056-5064.
- Hald, E., 1952. Statistical Theory with Engineering Applications, Wiley Publishers, New York, 97 pp.
- Hantke, G., 1951. Review of volcanic activity 1941-47 (in German), Bull. Volcan., 11.
- Hauksson, E., 1982. Some source parameters of small earthquakes in the Shumagin seismic gap, Alaska, (abstract), Earthq. Notes, 53, 40.
- Hays, J.D., D. Ninkovich, 1970. North Pacific deep-sea ash chronology and age of present Aleutian underthrusting, in Geological Investigations of the North Pacific, edited by J.D. Hays, GSA Memoir 126.
- Hopkins, D.M., 1976. Fault history of the Pribilof Islands and its relevance to bottom stability in the St. George Basin, in Environmental Assessment of the Alaska Continental Shelf, Principal Investigators Annual Reports, April 1975-March 1976, NOAA/BLM OCSEAP, Geology Volume, 13, 41-68.
- House, L., and J. Boatwright, 1980. Investigation of two high stress-drop earthquakes in the Shumagin seismic gap, Alaska, J. Geophys. Res., 85, 7151-7165.
- House, L., and K.H. Jacob, 1983. Earthquakes, plate subduction and stress reversals in the eastern Aleutian arc, J. Geophys. Res., in press.
- House, L., L.R. Sykes, J.N. Davies, and K.H. Jacob, 1981. Identification of a possible seismic gap near Unalaska Island, Eastern Aleutians, Alaska, in Earthquake Prediction, An International Review, Maurice Ewing Series, 4, edited by D.W. Simpson and P.G. Richards, pp. 81-92, AGU, Washington, D.C.
- Jacob, et al., 1983. Probabilities for future great earthquakes in the Alaska-Aleutian arc based on past moment release, in preparation.
- Joyner, W.B., and D.M. Boore, 1981. Peak horizontal acceleration and velocity from strong-motion records including records from the

- 1979 Imperial Valley, California, earthquake, Bull. Seism. Soc. Am., 71, 2011-2038.
- Kanamori, H., 1977a. The energy release in great earthquakes, J. Geophys. Res., 82, 2931-2988.
- Kanamori, H., 1977b. Seismic and aseismic slip along subduction zones and their tectonic implications, in Island Arcs, Deep Sea Trenches and Back-Arc Basins, Maurice Ewing Series, 1, edited by M. Talwani and W.C. Pitmann, pp. 1963-174, AGU, Washington, D.C.
- Kanamori, H., and K. Abe, 1979. Re-evaluation of the turn-of-the-century seismicity peak, J. Geophys. Res., 84, 6131-6139.
- Kelleher, J.A., 1970. Space-time seismicity of the Alaska-Aleutian seismic zone, J. Geophys. Res., 75, 5745-5756.
- Kimura, M., 1978. Significant eruptive activities related to large interplate earthquakes in the northwestern Pacific margin, J. Phys. Earth, 26, S557-S570.
- Kisslinger, J., J. Davies, L. Sykes, L. House, and K. Jacob, 1983. Historical earthquakes of Alaska and the Aleutian Islands: A compilation of original references, some newly translated, in preparation.
- Klein, 1978. Hypocenter location program HYPOINVERSE, part 1: Users guide to versions 1, 2, 3, and 4; part 2: source listings and notes, U.S. Geol. Surv. Open-File Rpt. 78-694, 114 pp.
- Lahr, J.C., 1980. Hypoellipse/Multics: A computer program for determining local earthquake hypocentral parameters, magnitude, and first motion pattern, U.S. Geol. Surv. Open-File Rpt. 80-59.
- Lahr, J.C., C.D. Stephens, H.S. Hasegawa, and J. Boatwright, 1980. Alaskan seismic gap only partially filled by 28 February 1979 earthquake, Science, 207, 1351-1353.
- Landgrebe, G., 1855. Naturgeschichte der Vulkane, Gotha.
- McCann, W.R., O.J. Perez, and L.R. Sykes, 1980. Yakataga seismic gap, southern Alaska: seismic history and earthquake potential, Science, 107, 1309-1314.
- McCann, W.R., S.P. Nishenko, L.R. Sykes, and J. Krause, 1980. Seismic gaps and plate tectonics: seismic potential for major plate boundaries, Pure Appl. Geophys., 117, 1082-1147.

- McNutt, S., 1981a. Pavlof volcano eruption report, EOS, Trans. AGU, 62, 13-14.
- McNutt, S., 1981b. Pavlof volcano eruption report, EOS, Trans. AGU, 62, 717-718.
- McNutt, S.R., and R.J. Beavan, 1981. Volcanic earthquakes at Pavlof Volcano, Alaska, correlated with the solid earth tide, submitted to Nature.
- McNutt, S., 1982a. Seismic monitoring of volcanoes in the Aleutians, Volcano News, 11, 7.
- McNutt, S., 1982b. Analysis of volcanic tremor from Pavlof, Fuego, Pacaya, San Cristobal, and Masaya volcanoes, Bol. de Volcanologia, Heredia, Costa Rica, in press.
- McNutt, S., and J. Mori, 1982. Analysis of B-type earthquakes and explosions at Pavlof Volcano, Alaska, abstract, EOS, Trans. AGU, 64, 45.
- Meyers, H., 1976. A historical summary of earthquake epicenters in and near Alaska, NOAA Technical Mem. EDS-NSGDC-1, National Geophys. and Solar Terrestrial Data Center, Boulder, Colorado.
- Meyers, H., and C.A. von Hake, 1976. Earthquake data file summary, key to geophysical records documentation no. 5, National Oceanic and Atmospheric Administration, Environmental Data Service, 32 pp.
- Meyers, H., R.J. Brazee, J.L. Coffman, and S.R. Lessig, 1976. An analysis of earthquake intensities and recurrence rates in and near Alaska, NOAA Technical Report EDS-NGSDC-3, National Geophys. and Solar Terrestrial Data Center, Boulder, Colorado.
- Miller, C.D., 1980. Potential hazards from future eruptions in the vicinity of Mount Shasta Volcano, northern California, U.S. Geol. Surv. Bull. 1503, 43 pp.
- Miller, C.D., D.R. Mullineaux, D.R. Crandell, and R.A. Bailey, 1982. Potential hazards from future eruptions in the Long Valley-Mono Lake area, east-central California and southwest Nevada - a preliminary assessment, U.S. Geol. Surv. Circular 877, 10 pp.
- Minster, J.B., and T.H. Jordan, 1978. Present-day plate motions, J. Geophys. Res., 83, 5331-5354.

- Mushketov, I., and A. Orlov, 1893. Catalog of earthquakes of the Russian Empire, Contr. Russian Geog. Soc., in general geography, 26, 582 pp.
- Nicholson, C., and D.W. Simpson, 1983. Routine processing for crustal earthquake locations and velocity models, in preparation.
- Orth, D.J., 1967. Dictionary of Alaska place names, U.S. Geol. Surv. Prof. Paper 567, 1084 pp.
- Page, R.A., 1968a. Aftershocks and microaftershocks of the great Alaska earthquake of 1964, Bull. Seism. Soc. Am., 58, 1131-1168.
- Page, R.A., 1968b. Focal depths of aftershocks, J. Geophys. Res., 73, 3897-3903.
- Page, R.A., D.M. Boore, W.B. Joyner, and H.W. Coultner, 1972. Ground motion values for use in the seismic design of the Trans-Alaska Pipeline System, U.S. Geol. Surv. Circ. 672.
- Pérez, O.J., and K.H. Jacob, 1980. Tectonic model and seismic potential of the eastern Gulf of Alaska and Yakataga seismic gap, J. Geophys. Res., 84, 7132-7150.
- Pérez, O.J., and K.H. Jacob, 1980. St. Elias, Alaska earthquake of February 28, 1979: tectonic setting and precursory seismic pattern, Bull. Seism. Soc. Am., 70, 1595-1606.
- Purcaru, G., and H. Berckhemer, 1978. A magnitude scale for very large earthquakes, Tectonophysics, 49, 189-198.
- Purcaru, G., and H. Berckhemer, 1982. Quantitative relations of seismic source parameters and a classification of earthquakes, Tectonophysics, 84, 57-128.
- Reyners, M., and K. Coles, 1982. Fine structure of the dipping seismic zone and subduction mechanics in the Shumagin Islands, Alaska, J. Geophys. Res., 87, 356-366.
- Richter, C.F., 1958. Elementary Seismology, W.H. Freeman and Co., San Francisco, Calif., 768 pp.
- Rose, W.I., Jr., 1972. Notes on the 1902 eruption of Santa Maria Volcano, Guatemala, Bull. Volcanol., 36, 29-45.
- Rose, W.I., Jr., A.T. Anderson, Jr., L.G. Woodruff, and S.B. Bonis, 1978. The October 1974 basaltic tephra from Fuego Volcano: description and history of the magma body, J. Volcanol. Geotherm. Res., 4, 3-53.

- Rose, W.I., Jr., S. Bonis, R.E. Stoiber, M. Keller, and T. Bickford, 1973. Studies of volcanic ash from two recent Central American eruptions, Bull. Volcanol., 37, 338-364.
- Rothé, J.P., 1969. The seismicity of the earth, 1953-1965, UNESCO, Paris.
- Sapper, K., 1905. In den Vulkanbieten Mittleamerika und Westindieu, Stuttgart, 334 pp.
- Sarna-Wojcicki, A.M., S. Shipley, R.B. Waite, Jr., D. Dzurisin, and S.H. Wood, 1982. Areal distribution, thickness, mass, volume, and grain size of air-fall ash from the six major eruptions of 1980, in The 1980 Eruptions of Mt. St. Helens, Washington, edited by P.W. Lipman, and D.R. Mullineaux, U.S. Geol. Surv. Prof. Paper 1250.
- Shimazaki, K., and T. Nakata, 1980. Time predictable recurrence model for large earthquakes, Geophys. Res. Lett., 7, 279-282.
- Simkin, T., L. Siebert, L. McClelland, D. Bridge, C. Newhall, and J.H. Latter, 1981. Volcanoes of the World, Hutchinson Ross Publ. Co., Stroudsburg, Penn., 232 pp.
- Solov'iev, S.L., 1968. Sanak-Kodiak tsunami 1788, Problema Tsunami, Nauka, Moscow, 232-237.
- Sykes, L.R., 1971. Aftershock zones of great earthquakes, seismicity gaps, earthquake prediction for Alaska and the Aleutians, J. Geophys. Res., 76, 8021-8041.
- Sykes, L.R., J.B. Kisslinger, L. House, J. Davies, and K.H. Jacob, 1980. Rupture zones of great earthquakes, Alaska-Aleutian arc, 1784-1980, Science, 210, 1343-1345.
- Sykes, L.R., and R.C. Quittmeyer, 1981. Repeat times of great earthquakes along simple plate boundaries, in Earthquake Prediction, An International Review, Maurice Ewing Series, 4, edited by D.W. Simpson and P.G. Richards, pp. 217-247, AGU, Washington, D.C.
- Sykes, L.R., J.B. Kisslinger, L. House, J. Davies, and K.H. Jacob, 1981. Rupture zones and repeat times of great earthquakes along the Alaska-Aleutian arc, 1784-1980, in Earthquake Prediction, An International Review, Maurice Ewing Series, 4, edited by D.W. Simpson and P.G. Richards, pp. 73-80, AGU, Washington, D.C.
- Sykes, L.R., and S. Nishenko, 1983. Probabilities of occurrence of large plate rupturing earthquakes for the San Andreas, San

- Jacinto and Imperial faults, California, 1983-2003, submitted to J. Geophys. Res.
- Tarr, R.S., and L. Martin, 1912. The earthquake at Yakutat Bay, Alaska, in September 1899, U.S. Geol. Surv. Prof. Paper 69.
- Taylor, P.S., and R.E. Stoiber, 1973. Soluble material on ash from active Central American volcanoes, Bull. Geol. Soc. Am., 84, 1031-1042.
- Thatcher, W., and G. Plafker, 1977. The 1899 Yakutat Bay, Alaska earthquakes, Intern. Union. Geod. Geophys., IASPEI/IAVCEI Assembly, abstract, pp. 54, Durham, England.
- Tobin, D.G., and L.R. Sykes, 1966. Relationship of hypocenters of earthquakes to the geology of Alaska, J. Geophys. Res., 71, 1659-1667.
- Utsu, T., 1962. On the nature of three Alaskan aftershock sequences of 1957 and 1958, Bull. Seism. Soc. Am., 52, 279-297.
- Waldron, H.H., 1961. Geologic reconnaissance of Frosty Peak Volcano and vicinity, Alaska, U.S. Geol. Surv. Bull. 1028T, 677-708.
- Wesnousky, S.G., C.H. Scholz, and K. Shimazaki, 1982. Deformation of an island arc: rates of moment release and crustal shortening in intraplate Japan determined from seismicity and quaternary fault data, J. Geophys. Res., 87, 6829-6852.
- Wilcox, R.E., 1959. Some effects of recent volcanic ash falls with especial reference to Alaska, U.S. Geol. Surv. Bull. 1028-N, 409-476.
- Wildenstein-Mori, A., and C.B. Crouse, 1981. Strong motion data from Japanese earthquakes compiled by Exxon Production Reserach Comp., Report SE-29, NOAA-NEIS, Boulder, Colorado.
- Winslow, M.A., 1982. Uplift and tilting in the Shumagin gap, southwestern Alaska, part I, Geologic studies, Final Report for Contract EAR 79-10608, prepared for the Geophysics Section, National Science Foundation, Washington, D.C.
- Woodward-Clyde Consultants, 1978. Offshore Alaska seismic exposure study, prepared for Alaska Subarctic Operators Committee (ASOC), March, 6 volumes.
- Woodward-Clyde, 1982. Development and initial application of software for seismic exposure evaluation, vol. II, Seismic Exposure

- Software Application, Final Report, prepared for NOAA, contract NA-80-RAC-000-91, San Francisco.
- Wyss, M., and J.N. Brune, 1968. Seismic moment, stress and source dimensions for earthquakes in the California-Nevada region, J. Geophys. Res., 73, 4681-4694.
- Wyss, M., 1979. Estimating maximum expectable magnitude of earthquakes from fault dimensions, Geology, 7, 336-340.
- Wyss, M., F.W. Klein, and A.C. Johnston, 1981. Precursors to the Kalapana M = 7.2 earthquake, J. Geophys. Res., 86, 3881-3900.
- Wyss, M., and R.E. Habermann, 1982. Conversion of m_b to M_s for estimating the recurrence time of large earthquakes, Bull. Seism. Soc. Am., 72, 1651-1662.
- Yoshii, T., 1975. Proposal of the 'aseismic front', Zishin, 28, 365-367.

[The page contains extremely faint and illegible text, likely bleed-through from the reverse side of the document. No specific content can be transcribed.]

SEISMIC RISK STUDIES, WESTERN GULF OF ALASKA

by

Hans Pulpan and Juergen Kienle

**Geophysical Institute
University of Alaska**

**Final Report
Outer Continental Shelf Environmental Assessment Program
Research Unit 251**

August 1984

[The page contains extremely faint and illegible text, likely bleed-through from the reverse side of the document. No specific content can be transcribed.]

TABLE OF CONTENTS

List of Figures	373
List of Tables	375
Acknowledgements	377
I. SUMMARY	378
II. INTRODUCTION	379
III. SOURCES, METHODS, AND RATIONALE OF DATA COLLECTION	380
High-Gain Seismic Network	380
Strong-Motion Instruments	387
IV. RESULTS AND DISCUSSION	388
Seismicity and Seismic Source Zone	388
Shallow Thrust Zone	388
Faults	393
Earthquake Activity of the Kodiak Shelf	395
Intermediate Depth Earthquake Activity	405
Seismic Exposure Studies	415
V. CONCLUSIONS	415
VI. REFERENCES	418
APPENDIX: EPICENTER PLOTS FOR 1978-1982	423



LIST OF FIGURES

- Figure 1. Aftershock zones of great earthquakes and location of seismic gaps of the Aleutian-Alaska arc system. The arrows indicate the convergence direction between the Pacific and North American plates (after Sykes et al., 1981).
- Figure 2. Layout of the high-gain seismic network as it was operated through most of the study period.
- Figure 3. Typical technical layout of part of the high-gain seismic network.
- Figure 4. Typical system response of University of Alaska stations.
- Figure 5. Plate interaction in Alaska. Motion vectors of St. Elias, Yakutat and Wrangell blocks relative to North America after Lahr and Plafker (1980).
- Figure 6. Epicenters, volcanoes, depth contours to top of Benioff zone (50, 100, 150 km), and location of projection values for cross-sections shown in Figure 7. Epicenters from local network data July 1977 to June 1981.
- Figure 7. Cross-sectional views of Benioff zone along lines A-A', B-B', C-C' shown in Figure 6. No vertical exaggeration. Land masses (solid black), the position of the trench, and location of volcanoes are also shown. Shallow thrust zone is added schematically. Dashed lines show possible position of second seismic zone.
- Figure 8. Fault map of the Cook Inlet area (after Beikman, 1980).
- Figure 9. Depth distribution of selected events of Figure 11 for which depth phases could be well discerned on seismograms. Points A and B as in Figure 11. The numbers refer to Table 1. Events 35 and 36 were not part of the set of events which were relocated by the joint hypocenter determination (JHD) method.
- Figure 10. Depth distribution of ISC locations shown in Figure 11. ISC depths are based on reported depth phases. Points A and B as in Figure 10.
- Figure 11. ISC location of 34 earthquakes that were relocated by the JHD method.
- Figure 12. Location of the 34 events of Figure 11 after relocation.
- Figure 13. Epicenters of earthquakes relocated by the JHD method using regional network data.
- Figure 14. Cross-section of seismic events mapped in Figure 13.

- Figure 15. First motion fault plane solutions of Benioff zone events in Lower Cook Inlet.
- Figure 16. First motions (open circles for dilations, full circles for compression) of one of the events situated below the main Benioff zone in Lower Cook Inlet.

LIST OF APPENDIX FIGURES

- Figure A1. Epicenters of all earthquakes located during January-March, 1978. Symbols indicate depth range of events.
- Figure A2. Epicenters of all earthquakes located during April-June, 1978. Symbols as in Figure A1.
- Figure A3. Epicenters of all earthquakes located during July-September, 1978. Symbols as in Figure A1.
- Figure A4. Epicenters of all earthquakes located during October-December, 1978. Symbols as in Figure A1.
- Figure A5. Epicenters of all earthquakes located during 1979. Symbols as in Figure A1.
- Figure A6. Epicenters of all earthquakes located during January-June, 1980. Symbols as in Figure A1.
- Figure A7. Epicenters of all earthquakes located during July-December, 1980. Symbols as in Figure A1.
- Figure A8. Epicenters of all earthquakes located during January-June, 1981. Symbols as in Figure A1.
- Figure A9. Epicenters of all earthquakes located during July-December, 1981. Symbols as in Figure A1.
- Figure A10. Epicenters of all earthquakes located during 1982. Symbols as in Figure A1.

LIST OF TABLES

- Table 1. Locations determined by the JHD method of 34 events off Kodiak Island. In addition, the table provides the location of two events (#35 and #36) for which reliable depth phases could be identified on seismograms recorded at WWSSN stations.
- Table 2. Date and locations of events for which the first motion fault plane solutions shown in Figure 14 were obtained.
- Table 3. Nodal plane parameters for events of Table 2.
- Table 4. Stress axes parameters for the events of Table 2.

1

ACKNOWLEDGEMENTS

The program was funded by the National Oceanic and Atmospheric Administration's (NOAA) Outer Continental Shelf Environmental Assessment Program (OCSEAP).

We would like to thank our program manager in Boulder, Joe Kravitz, and our program monitors in the Juneau OCSEAP Office, Rod Combellik and Laurie Jarvela, for their help and understanding during the course of this project.

Our thanks go also to George Lapiene and Mike Albertson of the Juneau Office for organizing helicopter, ship and other logistic support in the course of installing and maintaining the seismic station network. We also are indebted to the crews of the NOAA helicopters.

We owe special thanks to the management and flight crews of the U.S. Coast Guard flight station in Kodiak for valuable logistic support.

Technical work was performed by Steve Estes, Jim Benich, Ron Foster, Dick Abel, John Benevento and Jim Perry.

Data reduction and analysis were done by Dianne Marshall, Kathryn Engel, Bud Meyers and Hara Biesiot.

The program received substantial help from a concurrent one, funded by the U.S. Department of Energy (Contract No. EY-76-S-06-2229). A large portion of the seismic network was installed originally under that program. We are grateful for this support.

I. SUMMARY

This report summarizes the seismic hazard studies performed by us under the OCSEA program in the Semidi Island to Lower Cook Inlet section of the Alaska-Aleutian arc system. Central to our work was the collection of seismic data by operating a network of short-period seismograph stations in the above area. These data now permit the delineation and characterization of the seismic source zones of the area within the framework of plate tectonics. We also discuss a number of complimentary studies investigating or attempting to improve the resolution of the source zones: analysis of the location capability of the landbased network on the continental shelf area by analyzing the data obtained from the short term deployment of an array of ocean bottom seismometers on the shelf; relocation of hypocenters near Kodiak Island and Cook Inlet by the Joint Hypocenter Determination method; relocation of teleseismically recorded earthquakes in the Kodiak shelf section.

Attempts were made to collect strong ground motion data by deploying strong motion instruments at various sites during the study, but no useful records were recovered.

The contribution of this study lies in the description and characterization of the seismic source zones, thus providing important data for seismic exposure calculations. However, exposure calculations such as those performed under OSCEAP are presently limited by the rather large uncertainties associated with the occurrence times of great earthquakes along the arc system and the uncertainties in predicting strong ground motion at a particular site. Strong ground motion records and the study of the nature and mechanics of the shallow thrust zone seem to be the most important research topics for improving this situation.

II. INTRODUCTION

This study attempted to develop the scientific and technical basis for assessing the hazards associated with petroleum related developments on a portion of the Alaska Outer Continental Shelf which is subject to a very high level of seismic and volcanic activity. In many respects the Alaskan shelf is unique among the United States Outer Continental Shelf areas. The study was a data gathering program in its attempt to obtain data, pertinent to the seismic hazard problem, from a large and remote area at a resolution not previously available. It was a scientific program in its attempt to develop a better understanding of the fundamental processes underlying the seismic and volcanic activity, and it was an applied technical program in its attempt to quantify the associated risk. It was one of several such programs that covered a 1500 km long portion of the eastern Aleutian-Alaska arc system. The easternmost and westernmost portions of the area have been identified as seismic gaps (the Yakataga and Shumagin seismic gaps, respectively) and are separated by the rupture zones of the 1964 ($M_w = 9.2$) earthquakes. Our own work concentrated on the section from the Semidi Islands to lower Cook Inlet, encompassing a large portion of the 1964 rupture zone (Figure 1).

The ultimate purpose of a seismic risk analysis is to provide quantitative information about the seismic exposure a potential structure will be subjected to during its projected lifetime. This in turn requires information about (1) the location and configuration of seismic source zones, (2) the frequency of occurrence and magnitude distribution of earthquakes associated with individual source zones, (3) the nature of the motion generated at the earthquake source, (4) the modification of

that source motion as it propagates toward a particular site, and (5) the response of the structure to that input motion.

The program's principal contributions are associated with points (1) and (2), and to a more limited extent with (3). Though attempts were made to also contribute to (4) we were not successful in that task. The most important information with respect to (3) and (4) derives from strong motion recordings, still extremely limited in the various Alaskan seismotectonic environments. It is the lack of a sufficient number of such recordings in subduction zone environments that limits our understanding of the details of the earthquake rupture process and the attenuation of the strong ground motion with distance from the source. The meaningfulness of seismic hazards exposure calculations, such as were conducted in the course of OCSEAP, is therefore greatly limited. These problems have not been resolved satisfactorily in the course of the study.

The modification of strong ground motion by surficial geologic conditions (part of (4) above) is a site-specific problem and was not addressed at all in the program. Neither was the problem of the response of structures to strong earthquake ground motion.

III. SOURCES, METHODS AND RATIONALE OF DATA COLLECTION

High Gain Seismic Network

A short period, high gain seismic network was operated under this program. Earthquake hypocentral parameters were derived from the network data and assembled in the form of earthquake catalogs. These catalogs form the basis for identifying and delineating seismic source zones as well as for determining the associated magnitude-frequency relationships.

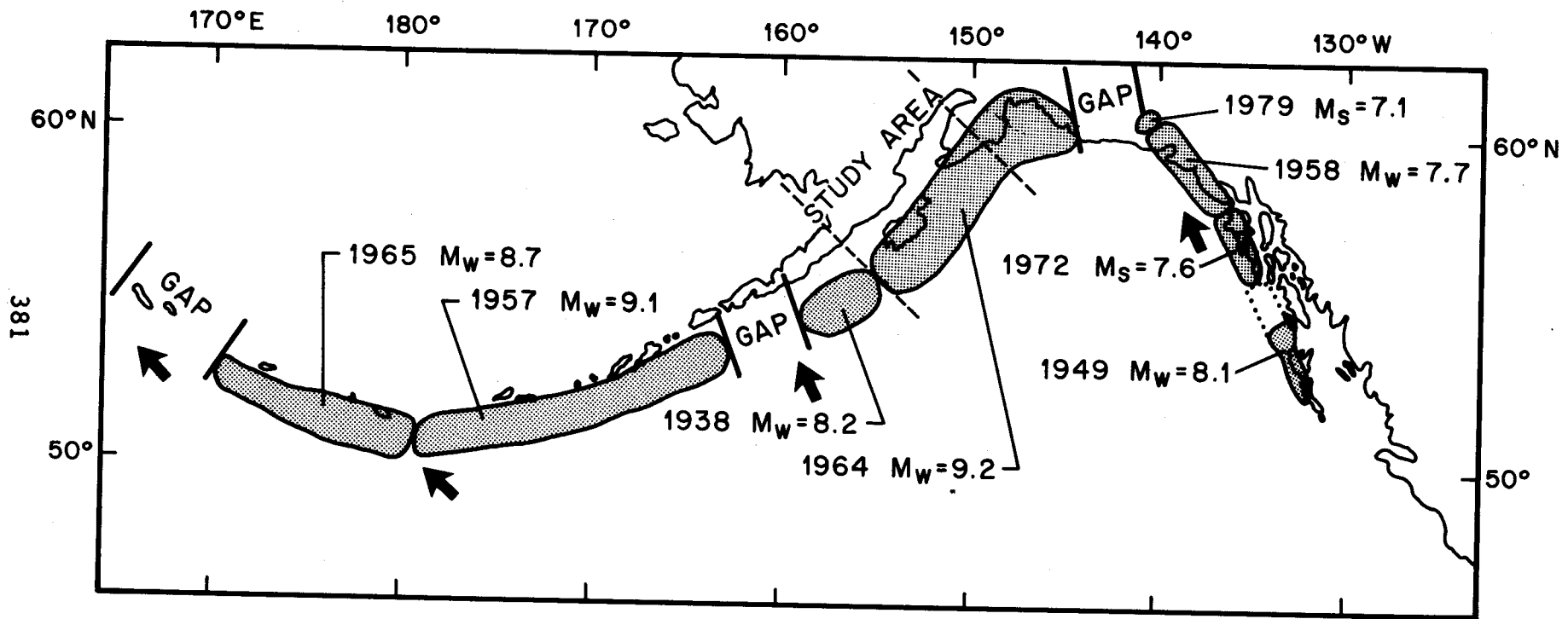


Figure 1. Aftershock zones of great earthquakes and location of seismic gaps of the Aleutian-Alaska arc system. The arrows indicate the convergence direction between the Pacific and North American plates (after Sykes et al., 1981).

Network data were also used in a variety of ways toward a better understanding of the fundamental seismotectonic processes.

Initiated as a small volcano monitoring system in lower Cook Inlet in the early seventies, the network grew under this contract to 31 stations. The configuration is shown in Figure 2. In addition to our own stations, several stations of the USGS and NOAA's Tsunami Warning System were continuously recorded under informal data exchange agreements.

Figures 3 and 4 show, respectively, general technical layout of part of the system and characteristic system response. Each station typically consists of a Geotech 18300 vertical seismometer with a natural frequency of 1.0 Hz, amplifier-voltage controlled oscillator (Monitron model 2000), and appropriate VHF (150-165 MHz) radio gear (Monitron T15F23 transmitters, Monitron R15F receivers). The stations are generally powered by "air cell" storage batteries (McGraw-Edison ST-2-1000). Data are being transmitted by a combination of VHF radio links and leased commercial telephone circuits. All data signals converge at a central recording facility for the system at Homer (see Figure 1). Data are recorded on two 16 mm, multi-channel film recorders (Geotech Develocorder Model 4000). A satellite clock (Kinematics True Time Division Model 468 DC) provides a common time standard and time code. System calibration is performed once a year in connection with the annual station service.

Changes in the recording media were initiated during the last years of the program when we began to record signals of 20 stations on digital tape. This type of recording involves an event detection system, developed in part under this contract, that discards non-useful portions of the recordings.

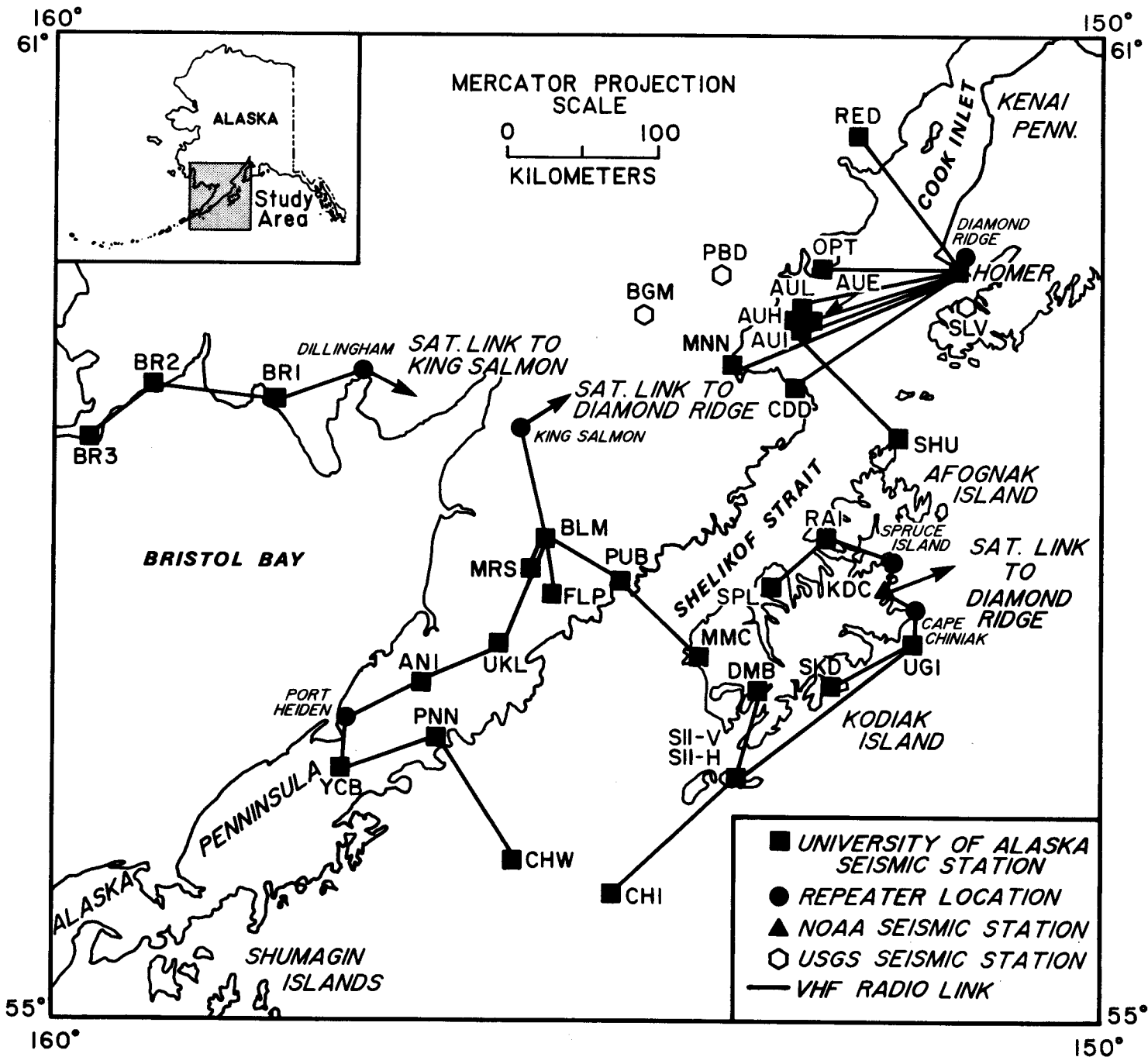
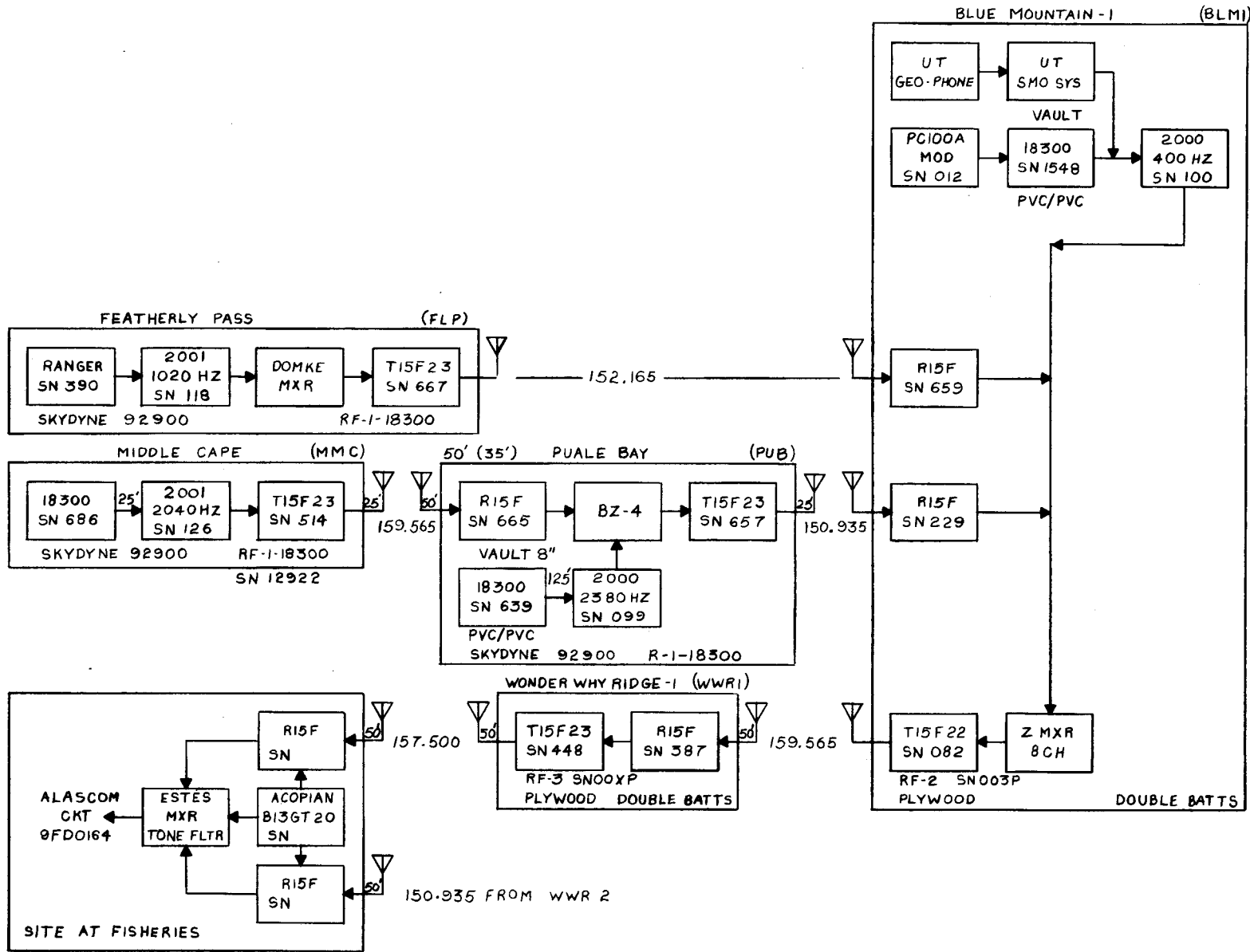


Figure 2. Layout of the high gain seismic network as it was operated through most of the study period.



REVISION	4/5/82	
REVISION	11/17/80	565
OCS2 SEISMIC NET ALASKA PENINSULA-NORTH		
GEOPHYSICAL INSTITUTE UNIVERSITY OF ALASKA FAIRBANKS, ALASKA		
DESIGN BY	OCS2	DATE 3/20/80
DRAWN BY	HELEN HIGGINS	DRAWING NO.
CHECK BY	46	1086-80-4

Figure 3. Typical technical layout of part of the high gain seismic network.

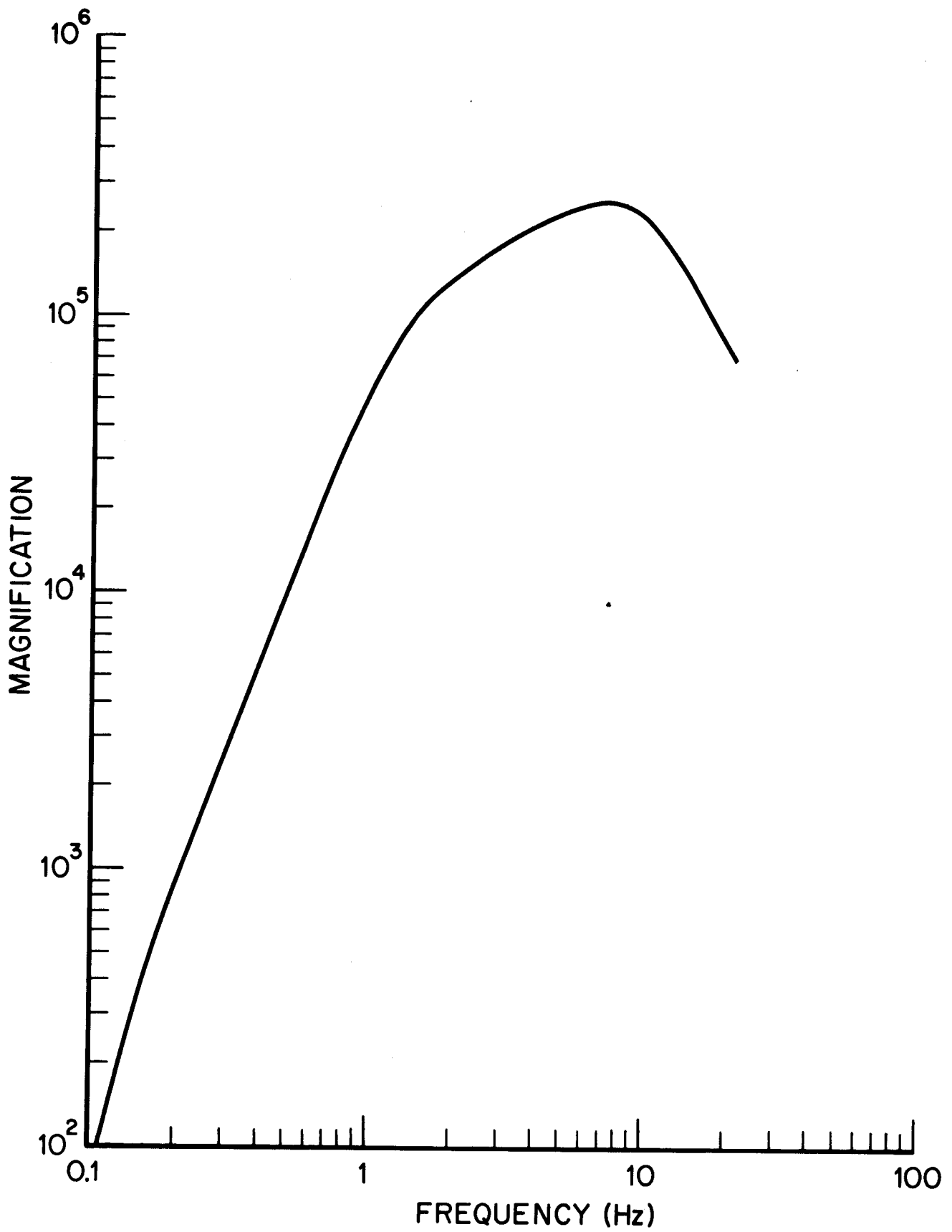


Figure 4. Typical system response of University of Alaska stations.

Routinely determined earthquake parameters are based on P-wave and S-wave arrivals. The computer program HYPOELLIPSE (Lahr, 1980) was used to obtain hypocentral parameters. Because of the large extent of the area covered by the network two different seismic velocity models were used. Travel times to stations located in the lower Cook Inlet area were calculated (regardless of the hypocenter location) for a velocity model developed by Matumotu and Page (1969) for the Kenai Peninsula area from aftershocks of the 1964 Alaska earthquake. For stations located on Kodiak Island and the Alaska Peninsula we used the model of Engdahl and Tarr (1970) obtained from refraction experiments in the central Aleutians. Routine magnitude determinations were based on maximum body wave trace amplitudes using Richter's (1958) local magnitude relationship, taking into account the stations system magnification value and the period of the maximum amplitude. Part of the routine data processing was the generation of epicenter maps, covering various time intervals for the different areas covered by the network. Figures A1-A10 of Appendix 1 are epicenter plots for various time periods from 1978 through 1982.

Magnitude detection thresholds of the system varied greatly in both time and space. With respect to time, this is due to outages of up to several months, of large portions of the system in the early years of operation and the gradual growth of the system toward its final configuration. With respect to space, differences in detection threshold are due to variation in station density. Generally speaking, the lowest threshold is in the lower Cook Inlet area, and the highest in the area between the southwest coast of Kodiak Island and the Semidi Islands.

Strong-Motion Instruments

Attempts to quantify the seismic risk in the Aleutian Alaska arc system suffer from a lack of strong ground motion records. Not only is there a lack of a sufficient number of relevant records from Alaska but also from subduction zone earthquakes in general, and great ($M_s > 7.8$) subduction zone earthquakes in particular. In the U.S., thinking with respect to strong ground motion generation is strongly guided by data from California, available because of the many strong motion networks that have been installed there over the past years. But there are fundamental questions to what extent results from that seismotectonic environment can be used in Alaska. The unusually large rupture areas associated with many great subduction zone events certainly pose questions with regard to the duration and frequency content of the strong ground motion. Thus, seismic risk analysis in Alaska is faced with rather unique problems, for which results from the remainder of the U.S. can probably only serve as starting points.

The necessity of obtaining Alaskan strong motion records was recognized during the early stages of the program. We first deployed five strong motion instruments converted by us for use at remotely located Alaskan stations. We chose five locations of the high gain network (PNN, BLM, SII, SKS and UGI, Figure 1). The converted Kinometrics SMA-1 instruments were installed using the logistic support of this program. Later on in the program, the desirability of deploying a more state-of-the-art, digital tape recording strong motion instrument, adapted for unattended operation in the Alaskan environment, was recognized. We thus began a cooperative program with the Institute of Geophysics of the University of Texas at Austin to convert ocean bottom strong motion instruments into a

version that could be used on land in Alaska. Parts delivery problems at the University of Texas led to delays in the deployment schedule, so that by the end of the contract period only three converted instruments were deployed for one year at three remote sites (SII, CHI, UGI, Figure 1). Unfortunately, no significant strong motion records were collected during this short time of deployment.

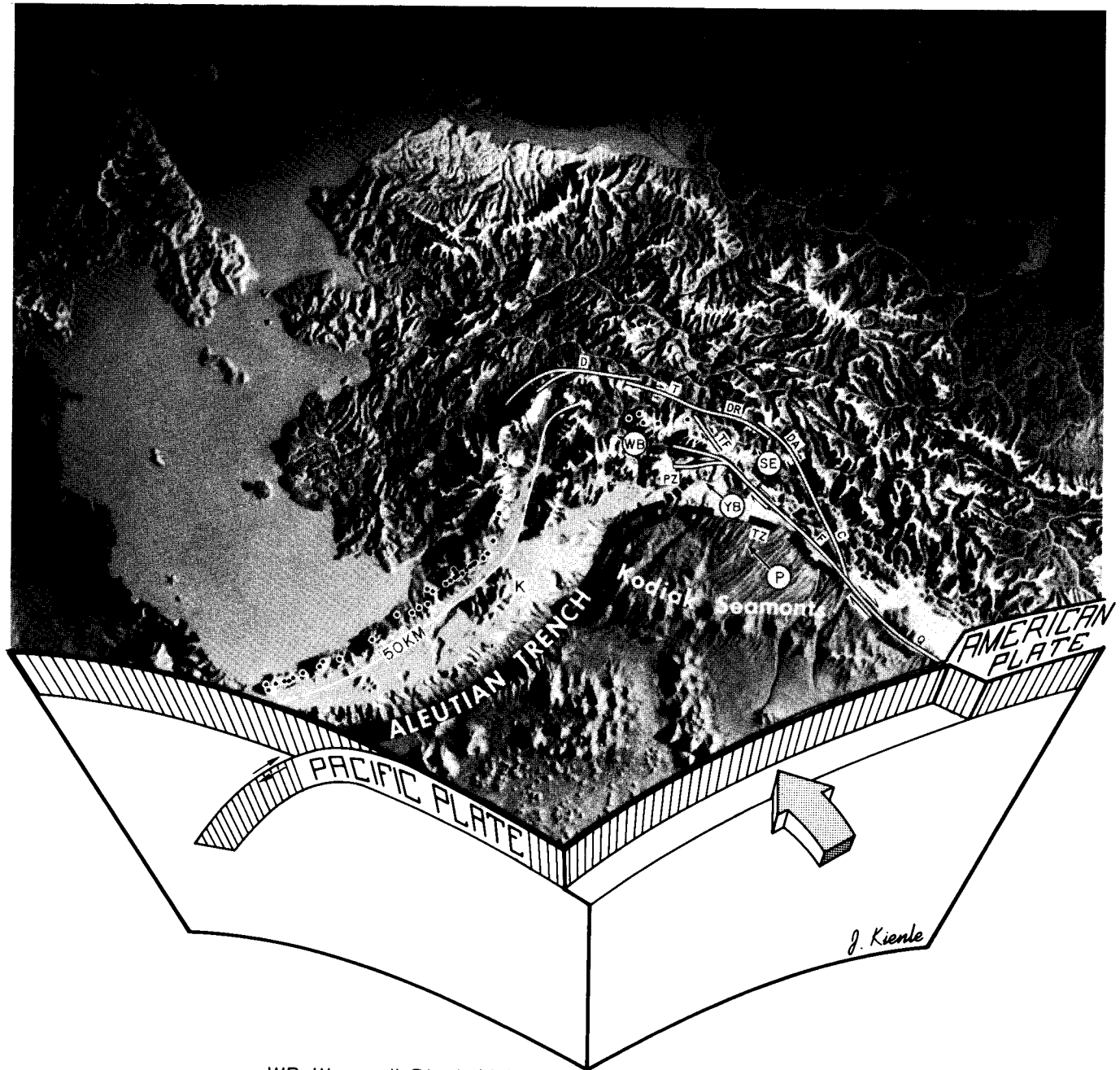
IV. RESULTS AND DISCUSSION

Seismicity and Seismic Source Zone

The tectonics of the Gulf of Alaska area are dominated by the interaction of the North American and Pacific plates (Figure 5). Along the Queen Charlotte-Fairweather fault systems the two plates are slipping past one another along a right lateral transform fault system. Along the Aleutian volcanic arc and the Aleutian-Alaska Range, up to Mt. McKinley, the oceanic Pacific plate underthrusts the continental North American plate. The Aleutian trench-axis marks the initial down-bending of the Pacific plate and the arc of active volcanoes approximately traces the 100 km depth-contour of the subducted plate. The transition zone between these two distinct tectonic regimes lies between the Denali fault and the eastern Gulf of Alaska and contains a complicated system of thrust and strike slip faults. Lahr and Plafker (1980) have proposed a model where this part of the North American plate is divided into three sub-blocks (WB, YB, SE, Figure 5), which are partially coupled to the Pacific plate. Our particular study area (Cook Inlet and western Gulf of Alaska) is dominated by the subduction process.

Shallow Thrust Zone

The dominant source of earthquakes in our study area is the shallowly dipping interface between the underthrusting and overriding plates. The



WB Wrangell Block (0.7)
 SE St. Elias Block (0.2)
 YB Yakutat Block (5.4)
 P Pacific Plate (5.8)

PZ Pamplona Zone
 TZ Transition Zone

D Denali Fault
 T Totschunda Fault (1.0)
 TF Totschunda-Fairweather
 connecting Fault (0.8)
 F Fairweather Fault (5.2)
 DR Duke River Fault
 DA Dalton Fault (0.2)
 C Chatham Strait Fault
 Q Queen Charlotte Fault (5.8)

Figure 5. Plate interaction in Alaska. Motion vectors of St. Elias, Yakutat and Wrangell blocks relative to North America after Lahr and Plafker (1980). 50 km depth contour to Benioff zone shown by solid white line. Volcanoes shown as black dots. Numbers in parenthesis after block names give rates of motion relative to fixed North American plate in cm/yr. Numbers in parenthesis after fault names indicate right lateral slip rate along faults in cm/yr.

major portion of the elastic strain accumulated along this zone by plate convergence is episodically released in the form of great ($M_S > 7.8$) earthquakes.

In our study area, the thrust zone ruptured in 1964 over an approximately 800 km long section, giving rise to the second largest ($M_W = 9.2$) instrumentally recorded earthquake ever. Rupture lengths of that length are not unusual in the Alaska-Aleutian subduction system, the rupture lengths of the 1957 (800 km, $M_W = 9.0$) and 1965 (700 km, $M_W = 8.7$) events being of similar magnitude (Figure 1). What makes the area of the 1964 event capable of producing the very largest events of the subduction system is the fact that the shallow thrust zone attains its greatest width there, producing the potentially largest rupture areas. The widening of the shallow thrust zone is associated with a general widening of the volcanic arc-trench gap from west to east. The lower edge of the large rupture zones seems to coincide with the sudden steepening of the narrow seismic zone associated with the subducting plate, which occurs at approximately 50 km depth. This lower edge and the associated steepening of the active seismic zone can be interpreted as indicating the region where the subducting plate decouples from the overriding plate. Section C-C' of Figure 7, showing a projection of hypocenters into a vertical plane approximately perpendicular to the arc in the Kodiak area (see Figure 6 for location of the cross-section) shows this situation. The shallow thrust zone dips at an angle of approximately 15 degrees arcwards from the trench. The seismicity is primarily associated with the interface between the plates and thus maps the rupture zones of future great earthquakes. At 50 km the seismic zone steepens to about 30°. This steeper zone, usually termed Wadati-Benioff zone (about 20 km thick as based upon the very best

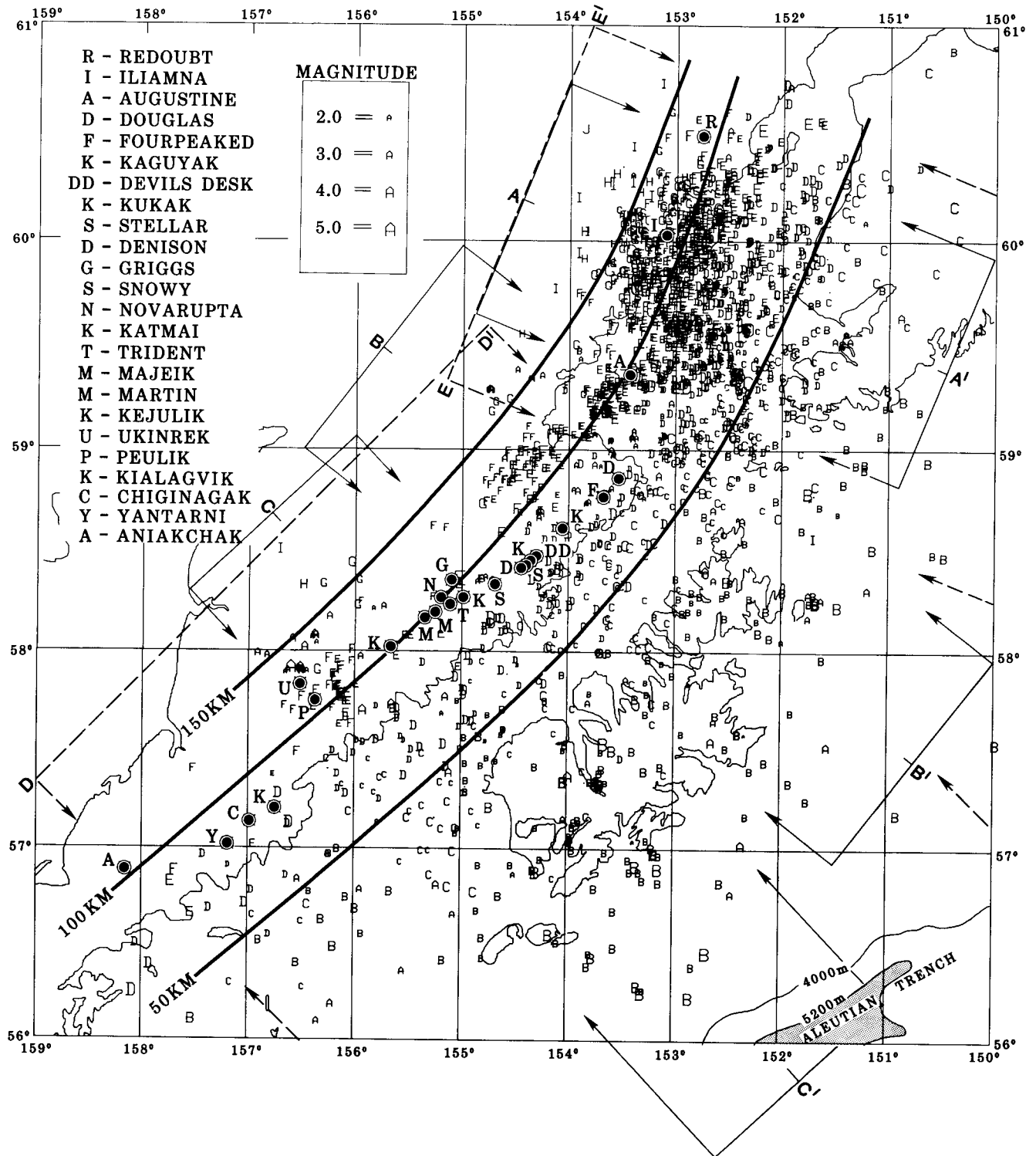


Figure 6. Epicenters, volcanoes, depth contours to top of Benioff zone (50, 100, 150 km) and location of projection volumes for cross-sections shown in Figure 7. Epicenters from local network data July 1977 to June 1981; selection criteria: recorded on at least 6 stations, RMS travel time residual $F \leq 0.4$ sec, relative vertical and horizontal location error $F \leq 10$ km. Epicenters are coded according to magnitude and depth range, A: 0-25 km, B: 26-50 km, C: 51-100 km, etc.

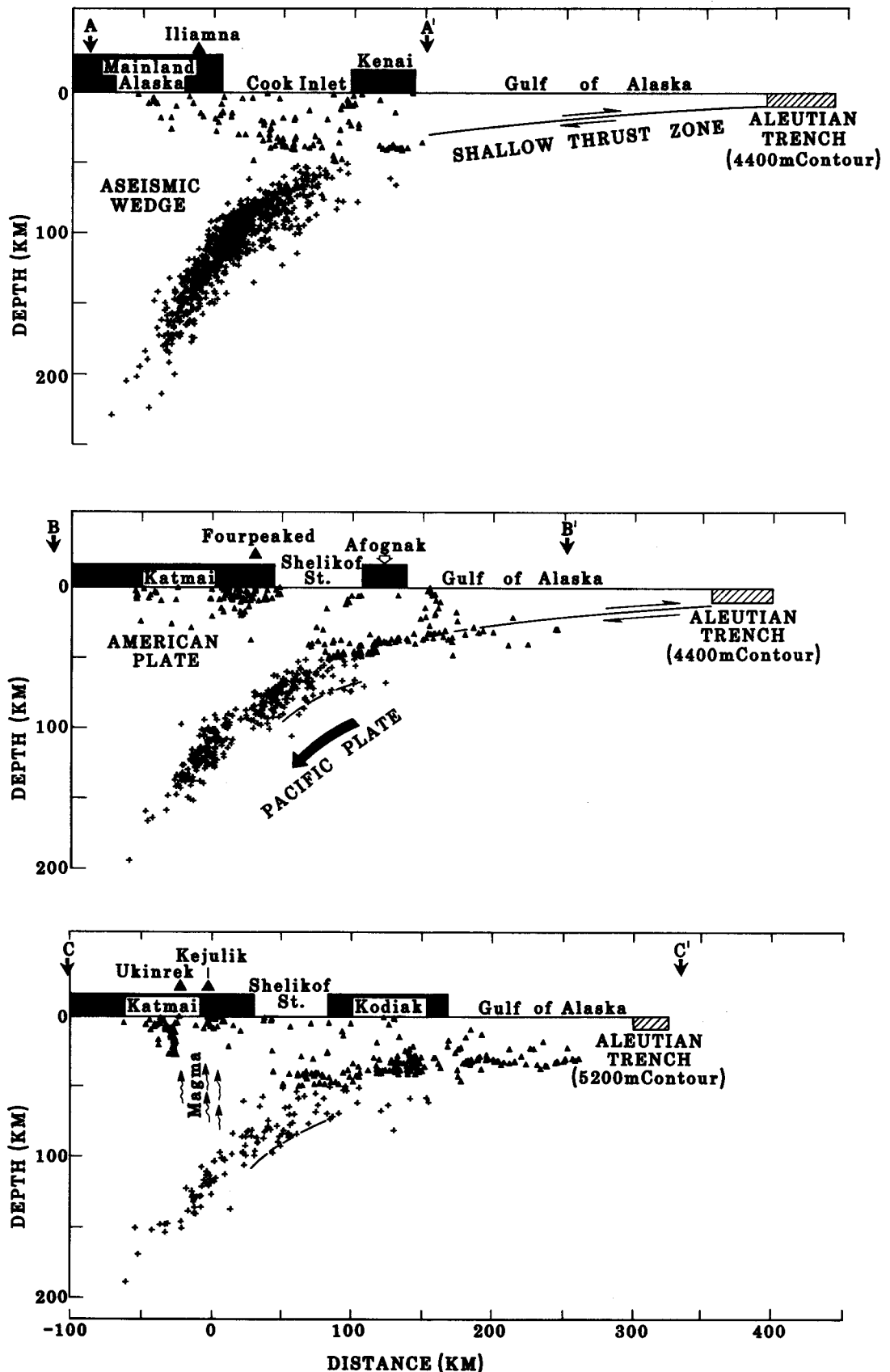


Figure 7. Cross-sectional views of Benioff zone along lines A-A', B-B', C-C' shown in Figure 6. No vertical exaggeration. Landmasses (solid black), the position of the trench, and location of volcanoes are also shown. Shallow thrust zone is added schematically. Dashed lines show possible position of second seismic zone. Selection criteria for events 0-50 km deep (triangles); recorded on at least five stations (STA \geq 5), relative horizontal and vertical location error (ERZ and ERH) \leq 10 km, RMS travel time residual \leq 0.5 sec. Selection criteria for events 50 km depth (crosses): STA \geq 6, ERH and ERZ \leq 10 km, RMS \leq 0.3 sec, and distance from epicenter to nearest station \leq 2 x depth.

hypocenter locations), represents a zone within the diving oceanic plate capable of seismic strain release. This seismic source zone, however, is not capable of producing great earthquakes and the upper magnitude limits in our area appears to be about $M_b = 6.5$.

Studies of the instrumental record (Sykes, 1971) and the historic record (Sykes et al., 1981) show that the entire Aleutian arc is capable of generating great earthquakes. The recurrence time of great earthquakes within a given segment appears to be of order 100 years. Unfortunately, the historic record as it is known so far is not sufficiently long to establish these recurrence rates within a confidence level useful for hazard analysis. The so-called seismic gap concept provides a qualitative evaluation of hazard, stipulating that those sections of the arc which have the largest time gap since the occurrence of the last great earthquake are the most likely ones to rupture in a great earthquake in the near future. Since the shallow thrust zone in our own study area ruptured in 1964, the greatest risk now appears to be associated with a highly probable great earthquake occurring in the Shumagin Gap; the source zone with the second highest risk is probably the rupture zone of the 1938 earthquake (see Figure 1). It is also conceivable that a rupture nucleating in the Shumagin Gap could propagate into the 1938 zone, and that both segments may rupture in one great earthquake.

Faults

In our study area, four major fault systems have been mapped: the Castle Mountain fault, the Bruin Bay fault, the Border Ranges fault and the Eagle River fault. These are shown for Cook Inlet in Figure 8. The trace of the Castle Mountain fault cuts the grain of the arc system at an oblique angle of 20 degrees and transects the volcano line just south of

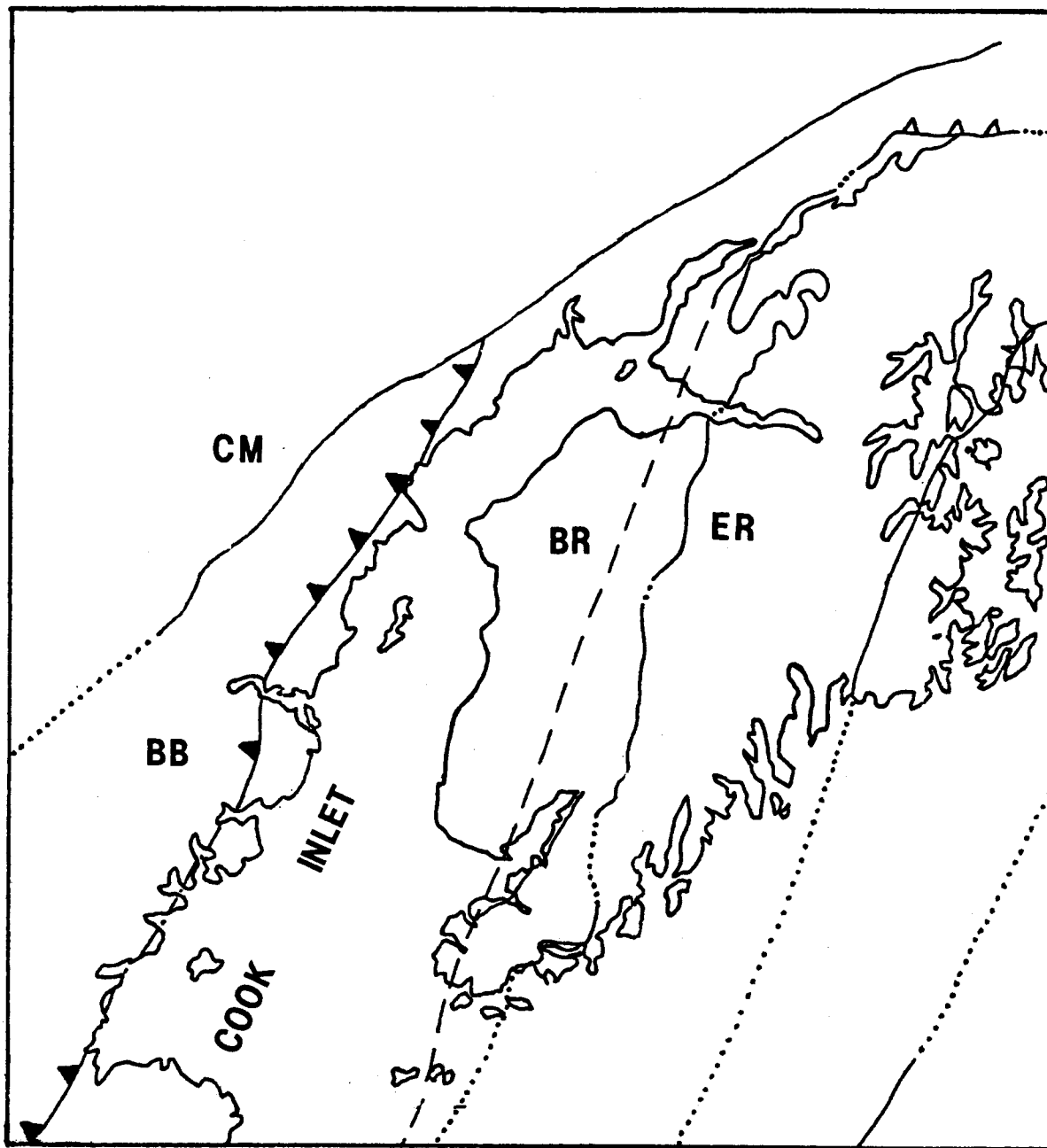


Figure 8. Fault map of the Cook Inlet area (after Beikman, 1980). BB = Bruin Bay Fault, BR = Border Ranges Fault, CM = Castle Mountain Fault, and ER = Eagle River Fault.

Mt. Spurr volcano. The relative motion along this fault is right lateral strike slip. Recent displacements have occurred along the Castle Mountain fault as indicated by offset Pleistocene glacial deposits and offset tectonic lineations (Evans et al., 1972). The Bruin Bay, Border Ranges and Eagle River faults are thrusts that essentially follow the trend of the arc structure. However, none of these faults have been active since late Mesozoic-early Tertiary time and the Bruin Bay fault is not offsetting any strata younger than 25 million years (Magoon et al., 1979). On Kodiak Island two major fault systems with their strike directions paralleling the arc have been mapped. The thrust system in the north (Figure 12) is the continuation of the Border Ranges fault system. The second, unnamed system separates Mesozoic from Cenozoic strata in the southern portion of the Island. The shallow seismicity is generally diffuse and is not preferentially associated with any of these faults (Pulpan and Kienle, 1979).

There is however a linear trend of seismic activity in the southwestern part of Kodiak Island, near the seismic station Deadman Bay (DMB on Figure 1). However, there are no mapped faults in the general vicinity of that trend, nor could we detect any tectonic lineations from satellite imagery.

Earthquake Activity on the Kodiak Shelf

The continental shelf off Kodiak Island is particularly active. Pulpan and Kienle (1979) have shown that the concentration of earthquakes between approximately 152°W and 154°W existed already before the 1964 Alaska earthquake. Aftershock activity in the first year following the 1964 main shock was also most pronounced in this region. Again in recent

years, since the installation of the seismic network on Kodiak Island, this portion of the shelf was the most active. The $M_S = 6.8$ earthquake of April 12, 1978 was the largest event to occur within the rupture zone of the 1964 earthquake during the past 10 years. Since the zone of intense activity based on teleseismically determined hypocenter locations maps out a narrow linear belt and since faulting paralleling this trend of seismicity had been documented (Hampton et al., 1979), it appeared of consequence for seismic hazards purposes to investigate potential relationships between the seismicity and the faults.

The accuracy of the hypocentral parameters of the earthquakes in question are different for local network solutions and for teleseismic solutions. The shelf events lie outside the local network, a situation that can cause location problems. On the other hand, teleseismically located events will be greatly influenced by the high velocity subducting slab, as the majority of rays will travel through it on account of the somewhat uneven worldwide seismic station distribution. In order to investigate the accuracy of locations determined by the local network for events that lie actually outside of it, we temporarily (in cooperation with RU 597) deployed a network of ocean bottom seismometers (OBS) on the Kodiak continental shelf. Thus the shelf events of interest could be located inside the combined land based-OBS network. The results of this study were:

1. Nineteen earthquakes occurring on the continental shelf of Kodiak Island were located using the combined UA-OBS network. At the present time, these are the best locations available for seismic activity on the Kodiak continental shelf.

2. The mean location of 15 earthquakes that could be determined with P-wave data from the UA network alone, shifted about 12 km when OBS data and S waves were included in the location process. However, when P- and S-wave data from more than six UA network stations were used to locate the events, the mean location fell within 1.2 km of the combined UA-OBS location.
3. The spatial pattern of earthquakes south of Kodiak Island recorded in this study, differs from the pattern reported by the ISC. The teleseismic epicenters are located 20 to 30 km north of epicenters determined with the combined UA-OBS network. The northward shift of teleseismic locations is probably caused by the presence of the landward-dipping subducting lithosphere. These observations are similar to the mislocations observed in the LONGSHOT experiment and other teleseismic relocation studies in the Aleutian Trench.

We also attempted to improve the locations of teleseismically determined events. Hypocentral parameters of these events are strongly affected by the high velocity subducting slab on rays that travel through it for a considerable distance. A further problem with teleseismic locations is the uneven azimuthal distribution of potential recording stations, with a large gap in station coverage in the Pacific Ocean region. Reasonable depth determination for shallow events requires the use of depth phase arrival times but during routine processing considerable error can occur due to depth phase misidentification. We therefore attempted to improve hypocentral parameters for teleseismically recorded events by (1) identifying depth phases from original records and (2) relocating events using the joint hypocenter determination (JHD) technique. We investigated thirty-six earthquakes in the magnitude range from $M_S = 5.0$ to 5.8 using

depth phases. For only eight of these could we identify clear phases consistent with the focal mechanism solutions at various azimuths (Figure 9). Nevertheless, these redetermined depths provide a much finer definition of the shallow thrust zone, as can be seen by comparing Figure 9 with Figure 10, which shows the location of all events based upon routine determination. The same events were also subjected to epicentral relocation by the JHD method (Frohlich, 1979) (Table 1). Upon relocation, the originally diffusely distributed events (Figure 11) collapse into two fairly narrow, subparallel groups (Figure 12). While the relocation provides reliable relative locations for these events, they may still be biased as a whole.

Four of the relocated events were also recorded well by our regional network. The locations of these events based on the local data are on the average 22 km to the south and 3 km to the west of the corresponding teleseismic JHD locations. This is in agreement with the results of the OBS study (Lawton et al., 1982), thus the actual location of the relocated teleseismic events is probably about 20 km to the south. Such a shift puts the events approximately along the shelf break (1000 m bathymetric contour).

Hampton et al. (1979) mapped a series of faults along the shelf break, some of them offsetting the sea floor by as much as 10 m. There is probably no direct relationship between the relocated events and these faults, but there may be an indirect one. The rigidity of the accreted sediments appears to be too low to permit brittle fracture at the scale indicated by the magnitude of the offsets. Focal mechanism solutions available for 11 of the relocated events (Stauder and Bollinger, 1966) all indicate that these events are associated with thrusting on a gently dipping

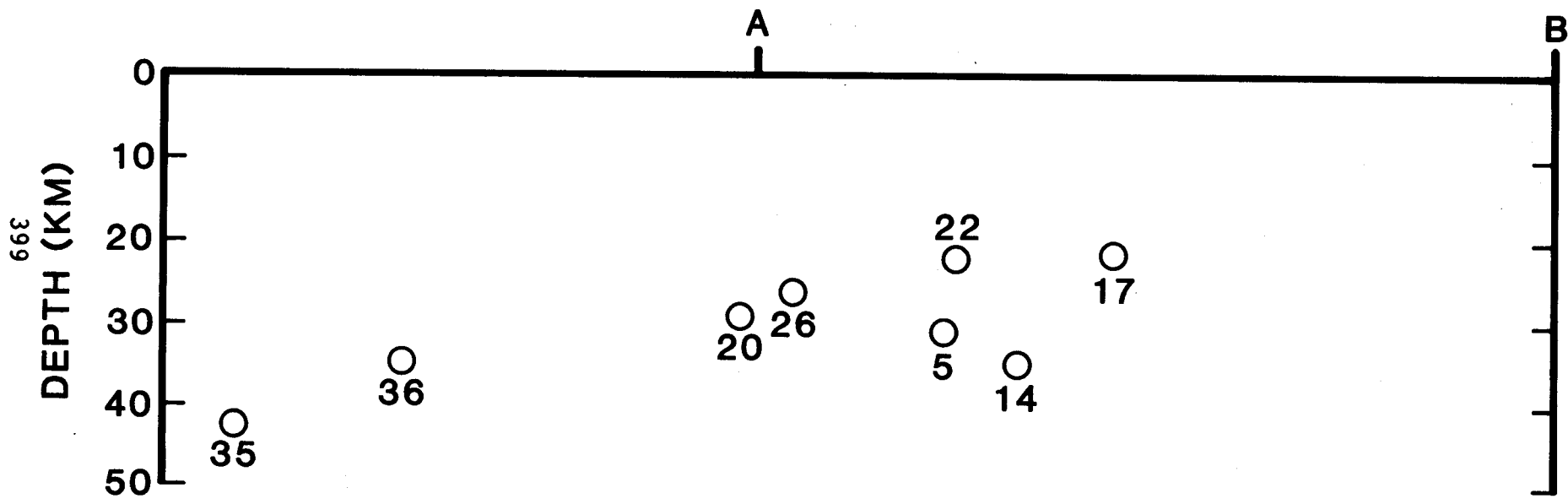


Figure 9. Depth distribution of selected events of Figure 11 for which depth phases could be well discerned on seismograms. Points A and B as in Figure 11. The numbers refer to Table 1. Events 35 and 36 were not part of the set of events which were relocated by the joint hypocenter determination (JHD) method.

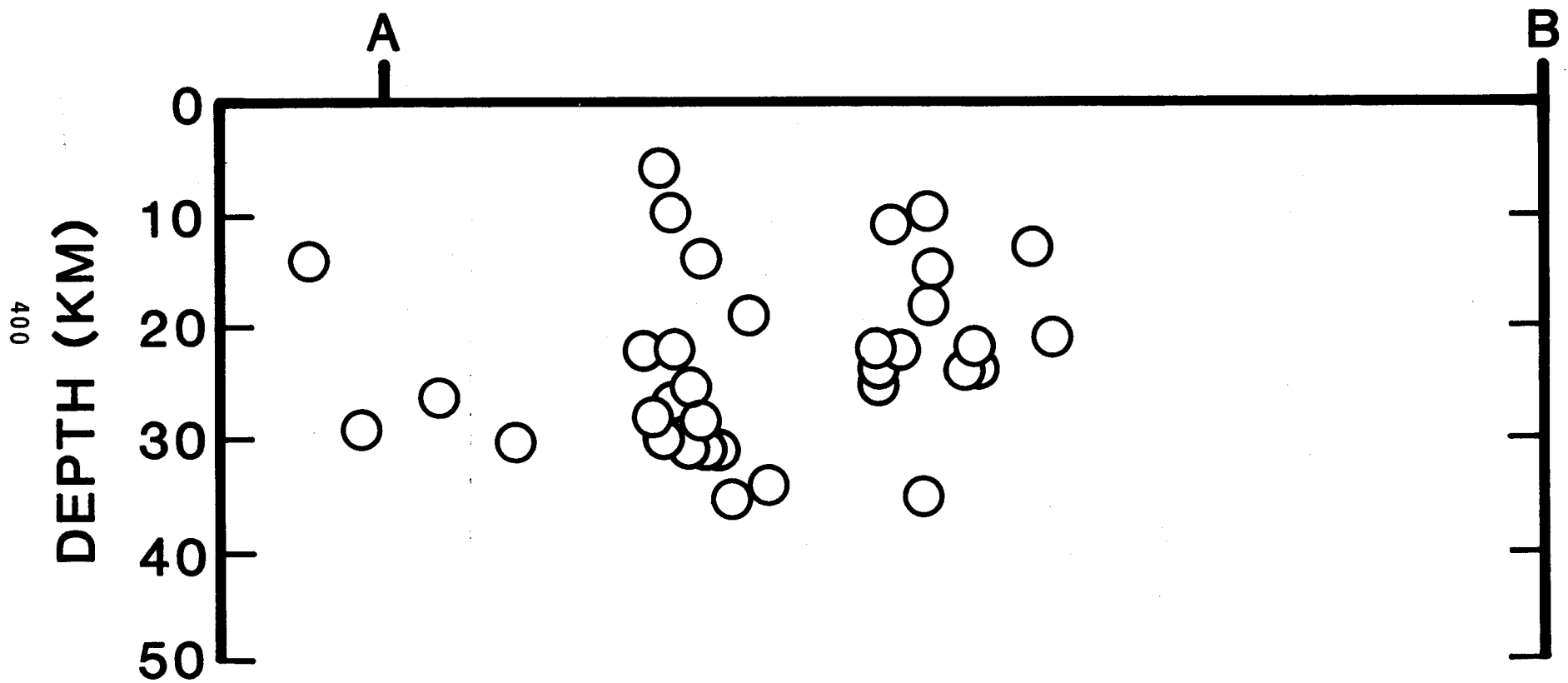


Figure 10. Depth distribution of ISC locations shown in Figure 11. ISC depths are based on reported depth phases. Points A and B as in Figure 10.

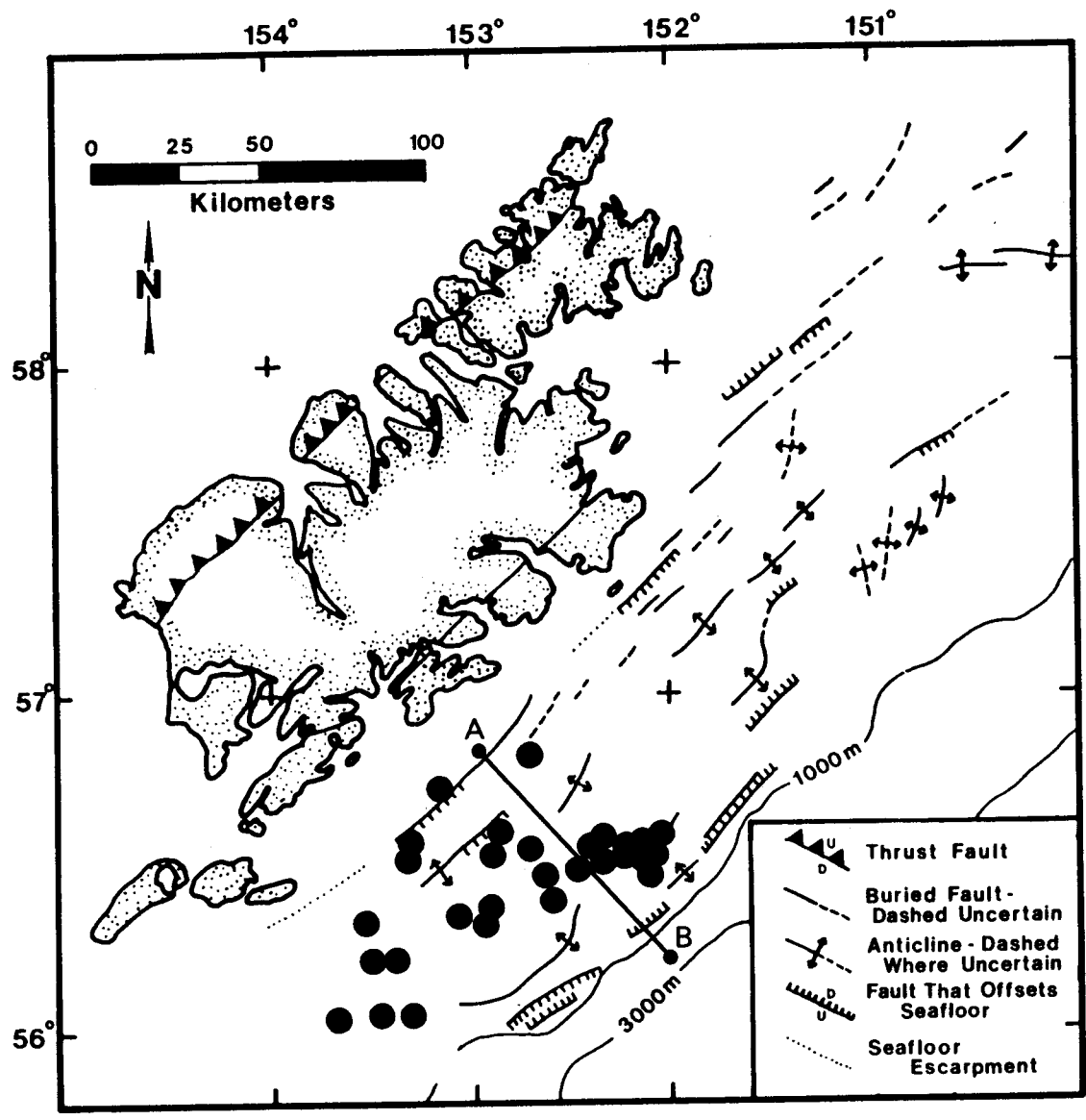


Figure 11. ISC location of 34 earthquakes that were relocated by the JHD method.

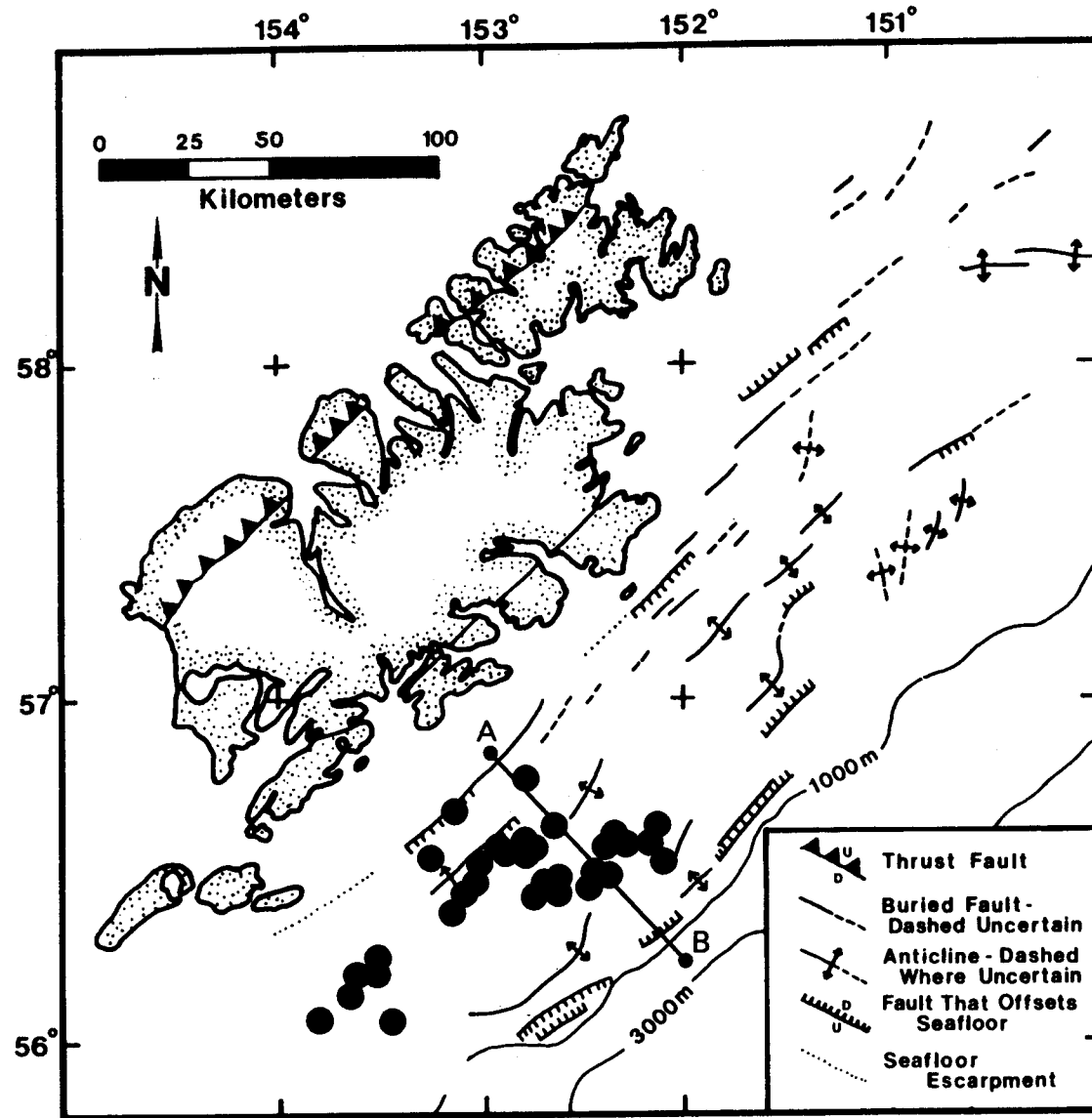


Figure 12. Location of the 34 events of Figure 11 after relocation.

TABLE 1

Locations determined by the JHD method of 34 events off Kodiak Island. In addition, the table provides the location of two events (#35 and 36) for which reliable depth phases could be identified on seismograms recorded at WSSN stations.

<u>NUMBER</u>	<u>DATE</u>	<u>LATITUDE</u>	<u>LONGITUDE</u>	<u>DEPTH</u>	<u>ORIGIN TIME</u>	<u>MAGNITUDE</u>	<u>RELIABLE DEPTH PHASES</u>
1	30 Mar 1964	56.59 N	153.00 W	22.0	0218:05.28	5.8	-
2	30 Mar 1964	56.64 N	152.27 W	18.0	1609:26.99	5.7	-
3	04 Apr 1964	56.60 N	152.75 W	19.0	0840:29.82	5.3	-
4	04 Apr 1964	56.92 N	153.01 W	14.0	0910:54.6	5.8	-
5	05 Apr 1964	56.35 N	153.48 W	30.0	0122:13.90	5.6	YES
6	05 Apr 1964	56.28 N	153.60 W	27.0	0141:43.06	5.4	-
7	12 Apr 1964	56.67 N	152.33 W	22.0	0124:30.41	5.8	-
8	16 Apr 1964	56.51 N	153.04 W	25.0	1926:56.08	5.5	-
9	17 Apr 1964	56.53 N	153.00 W	14.0	0449:28.20	5.5	-
10	06 May 1964	56.64 N	152.27 W	15.0	1526:35.99	5.5	-
11	12 May 1964	56.64 N	152.35 W	11.0	1816:42.10	5.4	-
12	27 Sep 1964	56.60 N	152.10 W	21.0	1550:53.41	5.4	-
13	23 Jun 1964	56.64 N	152.79 W	31.0	1109:15.10	5.7	-
14	22 Jan 1966	56.02 N	153.98 W	34.0	1427:07.09	5.7	YES
15	08 Apr 1966	56.69 N	152.65 W	31.00	2210:56.07	5.0	-
16	11 Apr 1966	56.65 N	152.16 W	24.00	2300:22.41	5.0	-
17	09 May 1967	56.53 N	152.60 W	22.00	1236:36.24	5.0	YES
18	13 May 1967	56.51 N	152.71 W	23.00	0518:54.21	5.0	-

<u>NUMBER</u>	<u>DATE</u>	<u>LATITUDE</u>	<u>LONGITUDE</u>	<u>DEPTH</u>	<u>ORIGIN TIME</u>	<u>MAGNITUDE</u>	<u>RELIABLE</u>	<u>DEPTH</u>	<u>PHASES</u>
19	29 Jan 1968	56.32 N	153.51 W	6.0	2052:20.75	5.2	-		
20	22 Dec 1968	56.39 N	154.07 W	29.0	1644:43.81	5.4	YES		
21	20 Nov 1969	56.61 N	153.23 W	30.0	2346:10.57	5.2	-		
22	21 Nov 1969	56.31 N	153.56 W	22.0	0014:10.71	5.1	YES		
23	24 Nov 1969	56.17 N	153.77 W	28.0	2251:48.47	5.4	-		
24	12 Jan 1970	56.71 N	152.13 W	35.0	0454:31.93	5.3	-		
25	20 Sep 1971	56.45 N	153.15 W	30.0	0644:13.65	5.1	-		
26	18 Jan 1972	56.75 N	153.12 W	26.0	0017:44.95	5.1	YES		
27	01 Aug 1974	56.56 N	152.36 W	23.0	0555:36.11	5.1	-		
28	01 Aug 1974	56.55 N	152.58 W	22.0	0759:54.92	5.1	-		
29	01 Aug 1974	56.56 N	152.45 W	10.0	0507:59.81	5.3	-		
30	07 Aug 1974	56.62 N	152.75 W	35.00	0823:36.26	5.0	-		
31	22 Oct 1976	56.17 N	153.42 W	24.0	1835:25.19	5.5	-		
32	10 Aug 1977	56.63 N	152.89 W	28.0	0935:57.55	5.1	-		
33	12 Apr 1978	56.62 N	152.87 W	10.0	0342:03.51	5.7	-		
34	12 Apr 1978	56.52 N	152.43 W	22.0	0522:29.90	5.0	-		
35	11 Mar 1970	57.39 N	153.97 W	42.0	2238:32.4		YES		
36	22 Aug 1973	57.09 N	154.12 W	36.0	1814:36.6		YES		

plane. Although the ambiguity in first motion fault plane solutions also permits dip slip faulting on a steeply dipping plane, the direction is opposite to that generally inferred for imbricate faults of the accretionary wedge, which appears to be aseismic (Chen et al., 1982). However, the relationship between the activity along the main thrust plane of the subduction zone and the observed faults might follow the model suggested by Fukao (1979). The majority of the events relocated in this study are part of the aftershock sequence of the 1964 Good Friday Alaskan earthquake. The relatively narrow belt of aftershock seismicity evident from our relocations probably reflects the brittle fracture release of stress concentrations associated with leading seaward edge of the shallow dipping rupture zone of the main shock. Since, according to Fukao's (1979) model, the main rupture does not propagate all the way toward the trench along the interface between the overriding and underthrusting plates, the wedge-shaped region of sediments between the trench axis and the leading edge of the rupture zone will be heavily stressed. These stresses will be relieved mostly in a ductile manner along slip lines curving from the tip of the main rupture zone upwards and emerging at steep dip angles on the ocean floor, generating the mapped sea floor offsets noted by Hampton et al. (1979).

Intermediate Depth Earthquake Activity

Earthquake activity below 50 km is exclusively associated with a well defined Benioff zone. While this deeper seismic source zone has much lower seismic energy release potential than the shallow thrust zone, study of its seismicity and precise location of earthquakes can provide important information concerning the details of the subduction process. For example, several recent studies have focused on earthquake locations

within subducted lithosphere and have apparently identified a second weaker zone of seismicity beneath the planar Benioff zone (Fujita and Kanamori, 1981). The combination of the usual Benioff zone together with this lower less active zone is known as a "double Benioff zone." This has been clearly observed in Japan (Hasegawa et al., 1978a, 1978b). and observed less clearly in several other areas (e.g, Veith, 1974; Lahr, 1975; Samowitz and Forsyth, 1981; Reyners and Coles, 1982). In addition, detailed delineation of the geometry of the Benioff zones from the spatial distribution of accurately determined earthquake hypocenters is important in determining the extent and nature of the lateral segmentation of the subducted lithosphere (Isacks and Barazangi, 1977). These lateral segment boundaries might control the extent of the rupture surface during great earthquakes (McCann et al., 1979; Davies and House, 1979; Davies et al., 1981). Finally, the relationships between arc volcanism and the configuration of the subducting plate have been topics of several studies (Stoiber and Carr, 1973; Carr et al., 1973; Isacks and Barazangi, 1977; Jacob et al., 1977; Kienle et al., 1983).

There are several features of the Alaska Benioff zone near Kodiak Island and Cook Inlet which suggest that the subducted plate is laterally deformed or segmented. First, the generally SW-NE striking line of volcanoes appears to undergo an abrupt change to a more northerly trend near 59°N (Figure 6). A distinct increase in the rate of seismic activity at intermediate depths occurs in Cook Inlet, just to the north of this change. Still further north, at about 63°N, the intermediate depth earthquake zone once again bends to a more easterly strike, and terminates east of Mt. Denali at 64.1°N (Tobin and Sykes, 1966; VanWormer et al., 1974; Davies, 1973; Agnew, 1979).

We used the JHD method to relocate 341 well recorded events with focal depths greater than about 40 km that occurred between 56.5°N and 60.5°N, and between 151.6°W and 156.5°W (Figure 13). These relocated hypocenters show that the Benioff zone has a dip of about 45°, its thickness varies from about 15 km in the southwestern area to about 25 km in the northeastern section (Figure 14). The strike of the Benioff zone changes by about 15° from the southern to the northern group of events. In the cross-section displaying the northern group of events, we see several events falling well below the Benioff zone. One of these events was one of the best recorded ones, so we believe their relative location to be real.

First motion focal mechanism solutions which we have obtained for twenty earthquakes (Table 2) in the Lower Cook Inlet region show that at intermediate depth the sinking slab between 59.5°N and 61°N is under horizontal north-south compression (Figure 15; Table 3 and 4). The focal mechanism solution obtained for one of the events below the main Benioff zone gave stress orientations quite different from the other solutions (Figure 16). Since differences in the principal stress directions between the upper and lower zone is characteristic for double Benioff zones, one could interpret the lower events as being part of a double Benioff zone.

Relying primarily on the observed change in strike and apparent thickness of the Benioff zone, one can interpret these data also to suggest that the subducted lithosphere separates into two distinct segments as it bends and subducts beneath Cook Inlet. Because the direction of subduction is not perpendicular to the volcanic arc the events situated beneath the Benioff zone in Cook Inlet may be part of the southwestern plate segment.

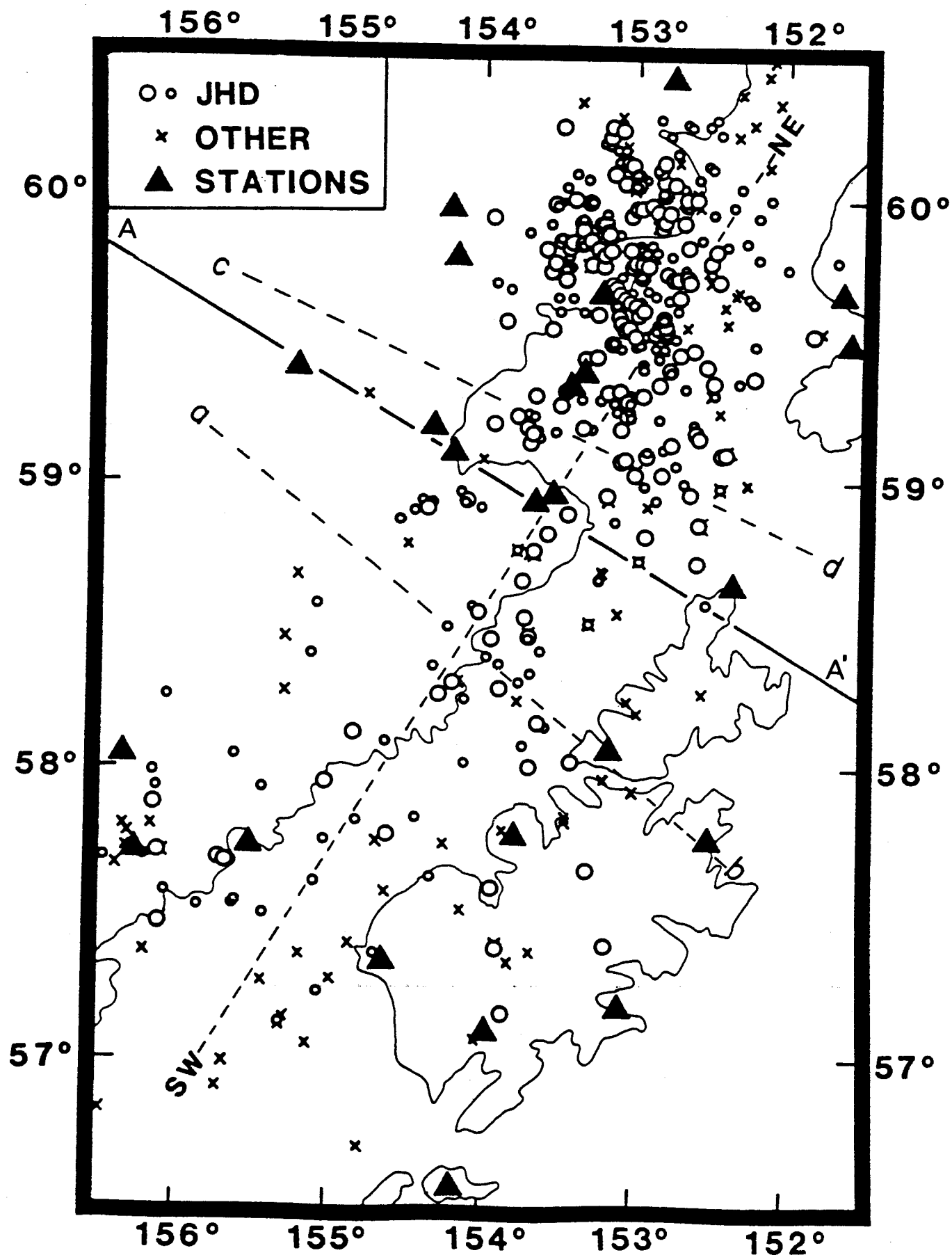


Figure 13. Epicenters of earthquakes relocated by the JHD method using regional network data. Large circles are highest quality events, smaller circles low quality events. X's are events located using station corrections determined by the JHD method.

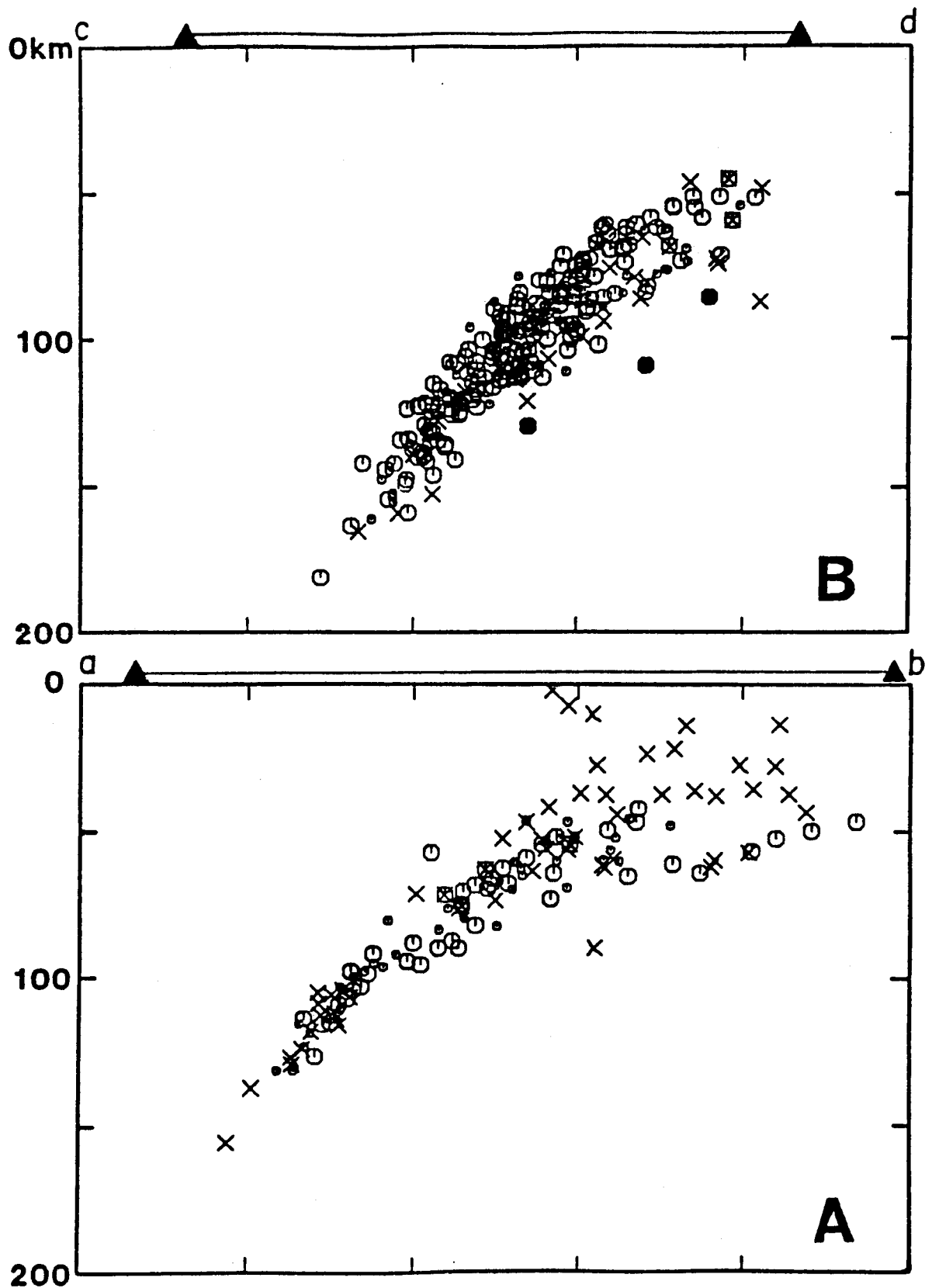


Figure 14. Cross-section of seismic events mapped in Figure 13. Section A has a trend of 50°W of N and includes events in the southwestern portion of Figure 13 (S of line A-A'). Section B has a trend of 65°W of N, and includes events in the northwestern portion of Figure 13 (N of line A-A'). In section B, note especially that a few of the events (denoted by filled circles) lie distinctly beneath the main Benioff zone.

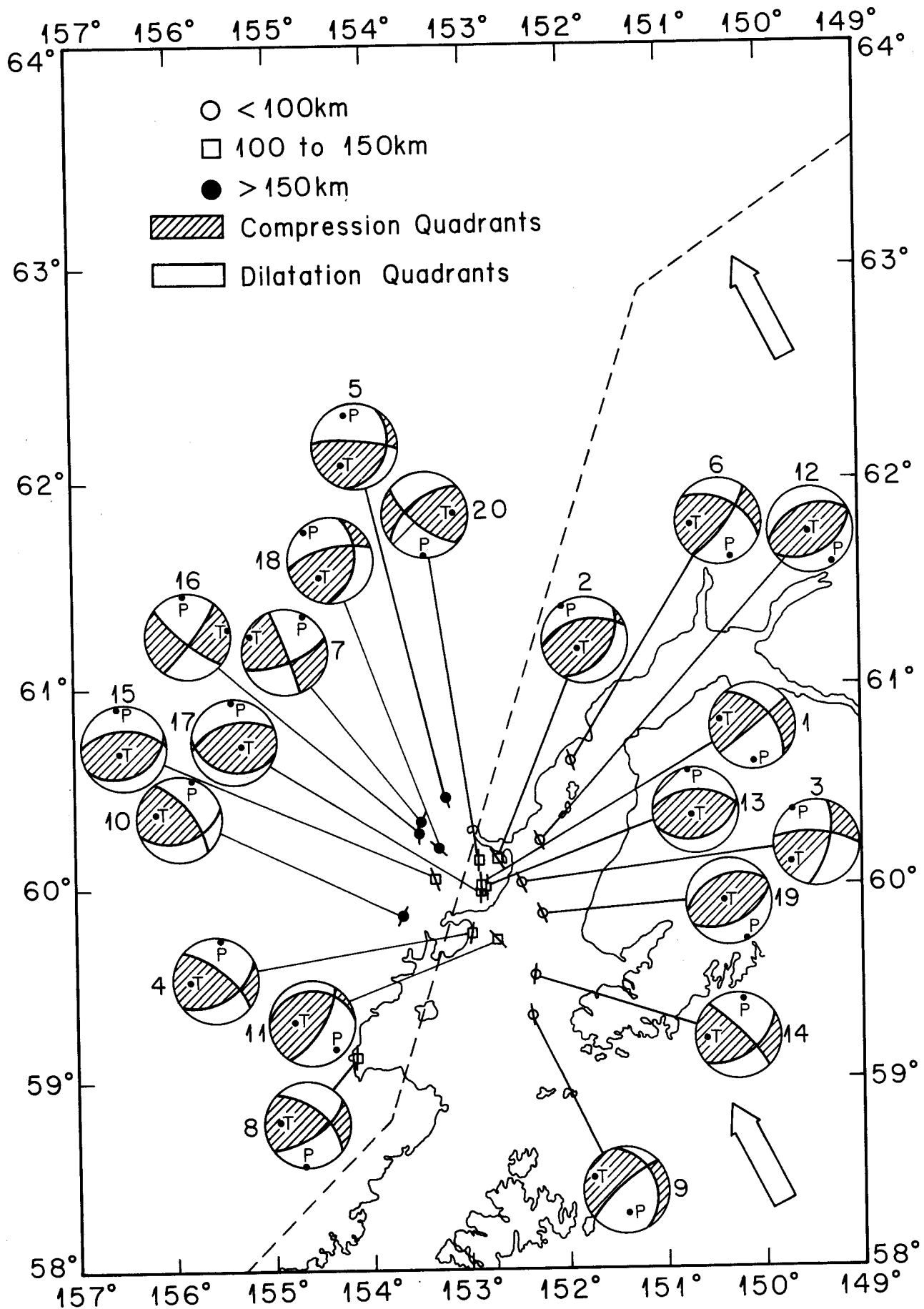


Figure 15. First motion fault plane solutions of Benioff zone events in Lower Cook Inlet.

TABLE 2

Date and locations of events for which the first motion fault plane solutions shown in Figure 14 were obtained.

<u>Event Number</u>	<u>Date</u>	<u>Hr. Min. Sec</u>	<u>Depth (km)</u>	<u>Latitude</u>	<u>Longitude</u>
1	Jan 25, 79	19 30 07.76	112.6	60°00.08N	152°51.47W
2	Feb 01, 79	12 29 06.24	119.9	60°08.39N	152°43.54W
3	Feb 09, 79	18 49 26.29	83.8	60°00.87N	152°28.37W
4	Mar 07, 79	12 10 37.45	107.6	59°40.58N	152°59.34W
5	Apr 04, 79	02 34 25.93	185.1	60°26.63N	153°13.09W
6	Apr 04, 79	04 51 37.77	91.9	60°30.79N	151°57.57W
7	Apr 04, 79	08 16 14.54	205.9	60°19.58N	153°27.22W
8	Apr 16, 79	11 10 39.22	129.9	59°07.17N	154°09.45W
9	Apr 20, 79	08 42 32.96	75.9	59°19.97N	152°21.42W
10	Jul 04, 79	08 15 38.96	150.1	59°50.13N	153°40.10W
11	Aug 15, 79	18 30 59.20	101.6	59°43.62N	152°43.60W
12	Jan 01, 80	07 03 30.84	93.1	60°13.45N	152°15.96W
13	Jun 03, 80	10 59 26.81	108.1	60°00.35N	152°49.34W
14	Jun 11, 80	04 38 06.38	59.3	59°33.38N	152°19.59W
15	Jun 15, 80	19 01 53.37	148.0	60°02.29N	153°20.39W
16	Jun 17, 80	09 16 11.45	193.8	60°16.07N	153°28.92W
17	Aug 12, 80	14 44 30.90	104.2	59°59.14N	152°52.61W
18	Sep 05, 80	05 46 13.73	167.4	60°12.25N	153°17.43W
19	Sep 13, 80	07 24 14.26	95.2	59°51.69N	152°14.81W
20	Sep 21, 80	21 00 19.39	122.5	60°08.30N	152°54.17W

TABLE 3

Nodal plane parameters for the events of Table 2

Event Number	<u>Plane 1</u>			<u>Plane 2</u>		
	Dip Direction	Angles (degrees) Dip Slip		Dip Direction	Angles (degrees) Dip Slip	
1	149	88	39	49	52	03
2	129	46	66	343	50	64
3	104	67	22	05	70	24
4	40	70	44	148	49	28
5	03	80	62	112	29	22
6	27	50	16	128	78	42
7	69	87	21	159	70	02
8	40	59	28	144	66	34
9	317	78	58	68	34	24
10	51	68	44	161	50	30
11	352	30	44	122	70	66
12	337	42	87	150	43	85
13	357	52	81	161	38	78
14	46	80	37	142	54	14
15	356	55	79	156	35	74
16	219	79	03	143	83	11
17	343	58	72	193	36	74
18	346	69	48	96	46	28
19	338	40	86	153	50	87
20	321	60	23	219	70	33

TABLE 4

Stress axes parameters for the events of Table 2

Event Number	P Axes		T Axes		B Axes	
	Trend (Degrees)	Plunge	Trend (Degrees)	Plunge	Trend (Degrees)	Plunge
1	178	24	283	27	52	52
2	330	03	59	71	327	19
3	324	01	234	30	57	60
4	08	12	266	45	110	43
5	342	30	212	48	88	28
6	161	18	266	38	51	48
7	26	12	292	16	151	70
8	180	04	275	40	85	50
9	170	48	294	26	40	32
10	18	10	279	46	120	42
11	138	22	271	59	40	22
12	154	01	260	86	64	04
13	350	07	224	80	81	07
14	09	16	268	33	121	53
15	349	10	218	77	81	10
16	353	14	83	02	177	78
17	355	11	121	72	262	14
18	316	13	211	49	58	40
19	156	06	309	84	65	02
20	181	06	86	37	281	53

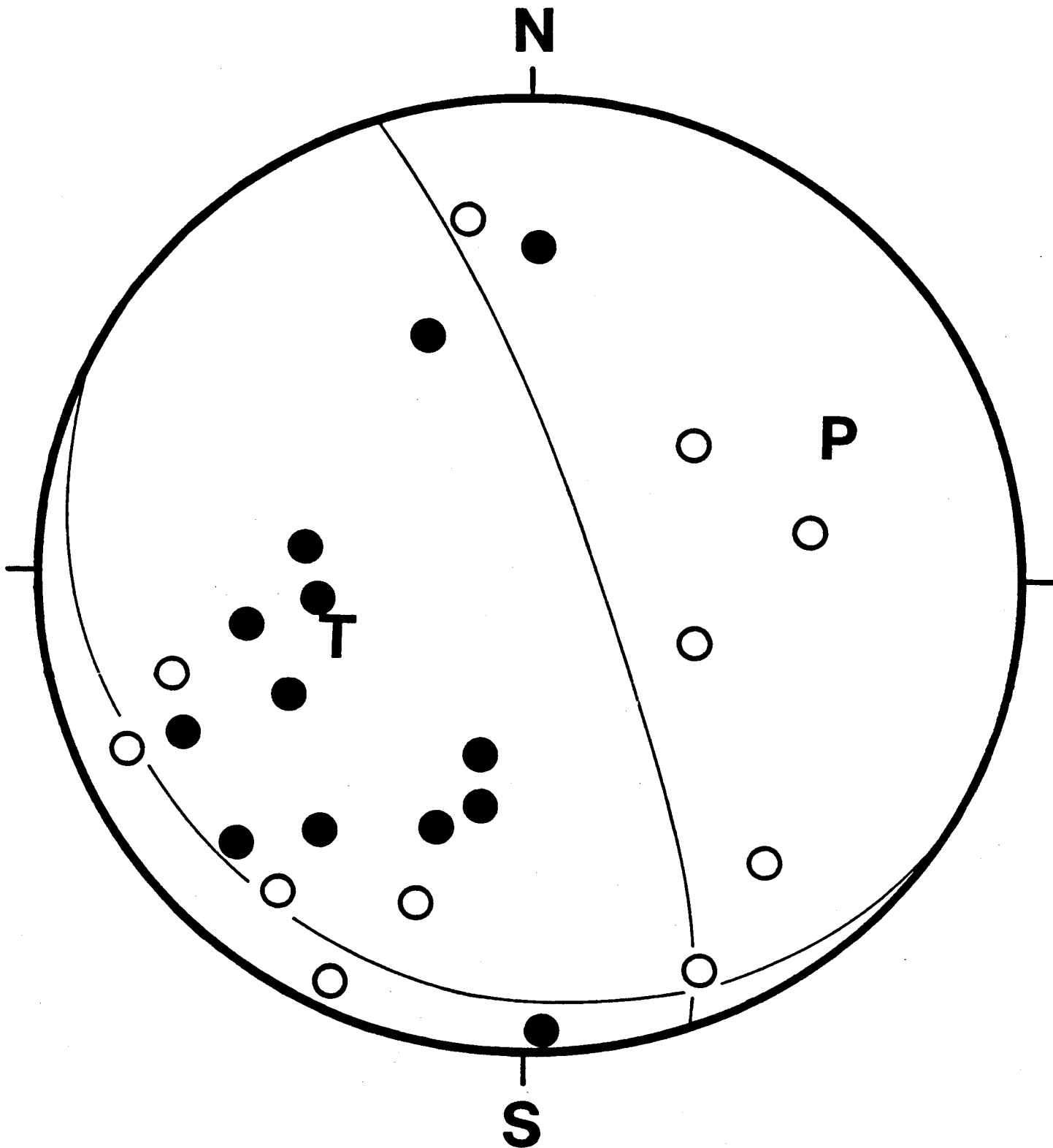


Figure 16. First motions (open circles for dilatations, full circles for compression) of one of the events situated below the main Benioff zone in Lower Cook Inlet. Note that the P and T axes differ in their orientation from those in Figure 15.

Seismic Exposure Studies

A seismic exposure study for the Gulf of Alaska region was made during the OCSEA program. The study was conducted by Woodward-Clyde Consultants with participation of the various OCSEAP Principal Investigators involved in seismic hazard studies in that area (Woodward-Clyde Consultants, 1982). Woodward-Clyde had also conducted the so-called "OASES" study (Woodward-Clyde Consultants, 1978), the first comprehensive seismic risk analysis of Alaskan offshore regions. The OCSEAP study was to update the OASES study by incorporation of the concept of seismic gaps into the analysis and by revision of the characterization of the seismic source zones on the basis of the most recent data.

Unfortunately, the Woodward-Clyde study was completed only when OCSEAP was coming to an end. Thus, while Principal Investigators participated in two workshops to discuss and specify the input data, there was no possibility to perform the crucial sensitivity studies as to how various assumptions concerning the input data would influence the exposure values. This is especially true with respect to the various transition probabilities and holding times for great earthquakes, when the occurrence of the latter is modeled as a semi-Markov process. Also, the presently available updated historic record (Davies et al., 1981) should be incorporated into specifying the initial states in the semi-Markov process. The exposure values are presently based upon distance-magnitude relationships that incorporate only few Alaskan data; the influence of changing these relationships needs to be studied.

V. CONCLUSIONS

The seismic hazard of the Aleutian-Alaska arc system is dominated by the occurrence of great earthquakes ($M_s > 7.8$) along the interface between

the subducting Pacific plate and the overriding North American plate. In our study area, along the arc from the Semidi Islands to Lower Cook Inlet, data from a network of seismograph stations operated during the course of this study delineate this interface with very good spatial resolution. The interface attains its greatest width in this and the easternmost section of the arc, making these areas the ones capable of generating the largest events of the arc system. However, since the recurrence interval for great earthquakes in the arc system is in the order of 100 years and the last one occurred in our study area only 20 years ago (in 1964), the greatest exposure in the near future is most likely associated with a great earthquake in one or both of the two seismic gaps identified to the east and west, respectively, of our study area (figure 1). In the case of the rupture of the Shumagin gap in a great earthquake it is possible that this rupture spreads into the 1938 rupture zone, the two sections breaking in a single great earthquake.

Other seismic source zones have been delineated with good resolution too, but none of these approach the seismogenic potential of the interface thrust zone.

While the results of this study provide a good quantitative description of source geometries and source potentials, two important aspects presently limit the usefulness of seismic exposure calculations: the uncertainties in predicting the time of occurrence of a great earthquake in a particular section of the arc and in predicting the characteristics of the ground motion generated at a particular site as a consequence of such an earthquake. The seismic gap concept provides a rational but only qualitative concept of likelihood of occurrence of a great earthquake. But all methods of projecting recurrence intervals on the basis of the historic record will suffer from the fact that it is too short to provide a sufficient number of cycles for a statistically

meaningful estimate. Our knowledge of the mechanical nature of the fault zone and spatial variations thereof is presently too limited for predictions, based on the plate convergence rates along the arc, to be more than rough guidelines for establishing recurrence intervals. Thus all statistical recurrence estimates for the great earthquakes which dominate the seismic hazard, presently contain large uncertainties.

Our ability to predict strong ground motion at a site is strongly linked to our knowledge of the details of the rupture process of an earthquake and the modification of the generated motion during propagation towards a particular site. The limited number of strong motion records available from subduction zone earthquakes generally, and from Alaska in particular, prevents testing of various theoretical models of the rupture process against actual data. Similarly the data are insufficient to generate with reasonable confidence empirical relationships describing the attenuation of strong ground motion with distance?. The exposure calculations performed under the OSCEAP program suffer from these deficiencies. Thus strong ground motion data and seismological studies towards the mechanical nature of the plate interface and the rupture process would be of the greatest benefit for seismic risk studies of the Alaska-Aleutian arc system.

VI. REFERENCES

- Agnew, J. Seismicity of the central Alaska Range, Proc. Alaska Sci. Conf., 30, 73, 1979 (abstract).
- Beikman, H. M., Geological Map of Alaska, U.S. Geol. Survey, 1980.
- Carr, M. J., Stoiber, R. E., and C. L. Drake, Discontinuities in the deep seismic zone under the Japanese arc, Bull. Geol. Soc. Amer., 84, 2917-2930, 1973.
- Chen, A. T., C. Frohlich, and G. V. Latham. Seismicity of the forearc marginal wedge, J. Geophys. Res., 87, 3679-3690, 1982.
- Davies, J. N. and L. House, Aleutian subduction zone seismicity, volcano-trench separation, and their relation to great thrust-type earthquakes. J. Geophys. Res., 84, 4583-4591, 1979.
- Davies, J., L. Sykes, L. House, and K. Jacob, Shumagin seismic gap, Alaska Peninsula: History of great earthquakes, tectonic setting, and evidence for high seismic potential, J. Geophys. Res., 86, 3821-3855, 1981.
- Engdahl, E. R. and A. A. Tarr. Aleutian seismicity, Milrow seismic effects, U.S. Coast and Geodetic Survey, CGS-746-102, 1970.
- Evans, C. D., F. H. Buck, R. T. Buffler, S. G. Fisk, R. B. Forbes, and W. B. Parker, The Cook Inlet--An Environmental Background Study of Available Knowledge, prepared by the University of Alaska, Resource and Science Service Center, Alaska Sea Grant Program, Anchorage, Alaska, for the Alaska District Corps of Engineers, Anchorage, Alaska, 446 pp., 1972.
- Frohlich, C., An efficient method for joint hypocenter determination for large groups of earthquakes, Computer and Geosciences, 5, 387-389, 1979.

- Fujita, K. and H. Kanamori, Double seismic zones and stresses of intermediate depth earthquakes, Geophys. J., 66, 141-156, 1981.
- Fukao, Y., Tsunami earthquakes and subduction processes near deep-sea trenches, J. Geophys. Res., 84, 2303-2314, 1979.
- Gedney, L., Tectonic stresses in southern Alaska in relationship to regional seismicity and new global tectonics, Bull. Seismol. Soc. Amer., 60, 1789-1802, 1970.
- Hampton, M. A., A. M. Bouma, R. Von Huene, and H. Pulpan, Geo-Environmental Assessment of the Kodiak Shelf, Proc. Offshore Tech. Conf., April 30-May 3, 1979, Houston, Texas, 1, 365-376, 1979.
- Hasegawa, A., N. Umino, and A. Takagi. Double-planed structure of the deep seismic zone in the northeastern Japan arc. Tectonophysics, 47, 43-58, 1978.
- Hasegawa, A., N. Umino, and A. Takagi, Double planed deep seismic zone and upper mantle structure in the northeast Japan Arc, Geophys. J., 54, 281-296, 1978.
- Jacob, K. H., K. Nakamura, and J. N. Davies, Trench-volcano gap along the Alaskan-Aleutian arc: facts, and speculations on the role of terrigenous sediments. In M. Talwani and W. Pitman (Ed.), Island Arcs, Deep Sea Trenches and Back Arc Basins, Maurice Ewing Series I. Am. Geophys. Union, 243-258, 1977.
- Kanamori, H. The energy release in great earthquakes. J. Geophys. Res., 82, 2981-2987, 1977.
- Kienle, J., S. E. Swanson, and H. Pulpan, Magmatism and subduction in the Eastern Aleutian Arc, In, D. Shimuzuru and I. Yokoyama (eds.) Arc Volcanism: Physics and Tectonics, Terra Scient. Publ. Co., (TERRAPUB), Tokyo, 191-224, 1983.

- Lahr, J. C., Hypoellipse/multics: A computer program for determining local earthquake hypocentral parameters, magnitude and first motion patterns, U.S. Geol. Survey, Open File Report, 80-59, April 1980.
- Lahr, J. C., and G. Plafker, Holocene Pacific-North American Plate Interaction in Southern Alaska: Implications for the Yakataga Seismic Gap, Geology, 8, 483-486, 1980.
- Magoon, L. B., A. H. Bouma, M. A. Fisher, M. A. Hampton, E. W. Scott, and C. L. Wilson, Resource Report for Proposed OCS Sale No. 60, Lower Cook Inlet-Shelikof Strait, Alaska, U.S. Geol. Survey, Open-File Report 79-600, 38 pp., 1979.
- Matumoto, T. and R. Page, Microaftershocks following the Alaska earthquake of 28 March 1964: determination of hypocenters and crustal velocities in the Kenai Peninsula-Prince William Sound Area. In The Prince William Sound, Alaska Earthquake of 1964 and Aftershocks, 2B., U. S. Government Printing Office, 1969.
- McCann, W. R., S. P. Nishenko, L. R. Sykes, and J. Krause, Seismic gaps and plate tectonics: seismic potential for major boundaries, Pure Appl. Geophys., 117, 1082-1147, 1979,
- Pulpan, H., and C. Frohlich, Joint hypocenter determination of teleseismically recorded earthquakes on the Kodiak Shelf, Alaska, OCSEAP Annual Reports of Principal Investigators, RU 597, 1982.
- Pulpan, H. and C. Frohlich, Earthquake relocation by the joint hypocenter determination method in Kodiak Island and lower Cook Inlet areas of Alaska (submitted for publication).
- Pulpan, H. and J. Kienle, Western Gulf of Alaska Seismic Risk, Proc. Offshore Tech. Conf., April 30-May 3, 1979, Houston, Texas, 1, 2209-2219, 1979.

- Reyners, M. and K. S. Coles, Fine Structure of the dipping seismic zone and subduction mechanics in the Shumagin Island, Alaska. J. Geophys. Res., 87, 356-366, 1982.
- Richter, C. F., Elementary Seismology, W. H. Freeman and Co., San Francisco, CA, 768 pp., 1958.
- Romanowicz, B., Depth resolution of earthquakes in central Asia by moment tensor inversion of long period Rayleigh waves, J. Geophys. Res., 86, 5963-5984, 1981.
- Samowitz, I. R. and D. W. Forsyth, Double seismic zone beneath the Mariana Island arc, J. Geophys. Res., 86, 7013-7021, 1981.
- Stoiber, R. E. and M. J. Carr, Quaternary volcanic and tectonic segmentation of Central America. Bull. Volcanologique, 73, 304-325, 1973.
- Sykes, L. R., Aftershock zones of great earthquakes, seismicity gaps, and earthquake prediction for Alaska and the Aleutians, J. Geophys. Res., 76, 8021-8041, 1971.
- Sykes, L. R., J. B. Kisslinger, L. House, J. Davies, and K. H. Jacob, Rupture zones and repeat times of great earthquakes along the Alaska-Aleution arc, In, Earthquake Prediction, Maurice Ewing Series, 4, Amer. Geophys. Union, 1981.
- Tobin, D. G. and L. R. Sykes, Relationship of hypocenters of earthquakes to the geology of Alaska, J. Geophys. Res., 71, 1659-1669, 1966.
- Van Wormer, J. D., J. Davies and L. Gedney, Seismicity and plate tectonics in south central Alaska, Bull. Seismol. Soc. Amer., 64, 1467-1475, 1974.
- Veith, K. F., The relationship of island arc seismicity to plate tectonics, Ph.D. thesis, Southern Methodist University, 1974.

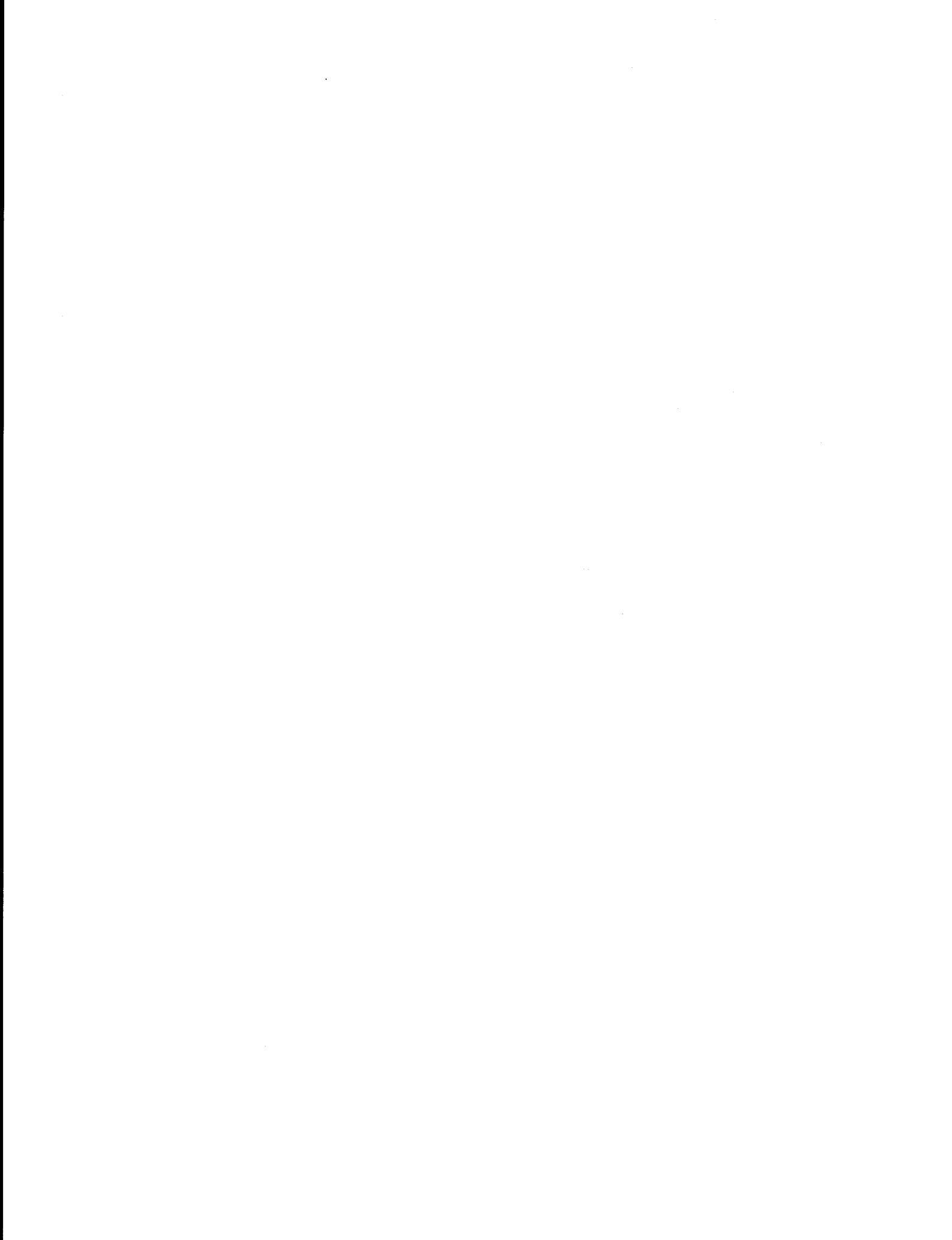
Woodward-Clyde Consultants, Offshore Alaska Seismic Exposure Study.

Report prepared for Alaska Subarctic Operators Committee, 6 volumes,
1978.

Woodward-Clyde Consultants, Development and Initial Application of Software
for Seismic Exposure Study, Report to NOAA, 2 volumes, 1982.

APPENDIX

EPICENTER PLOTS 1978-1982



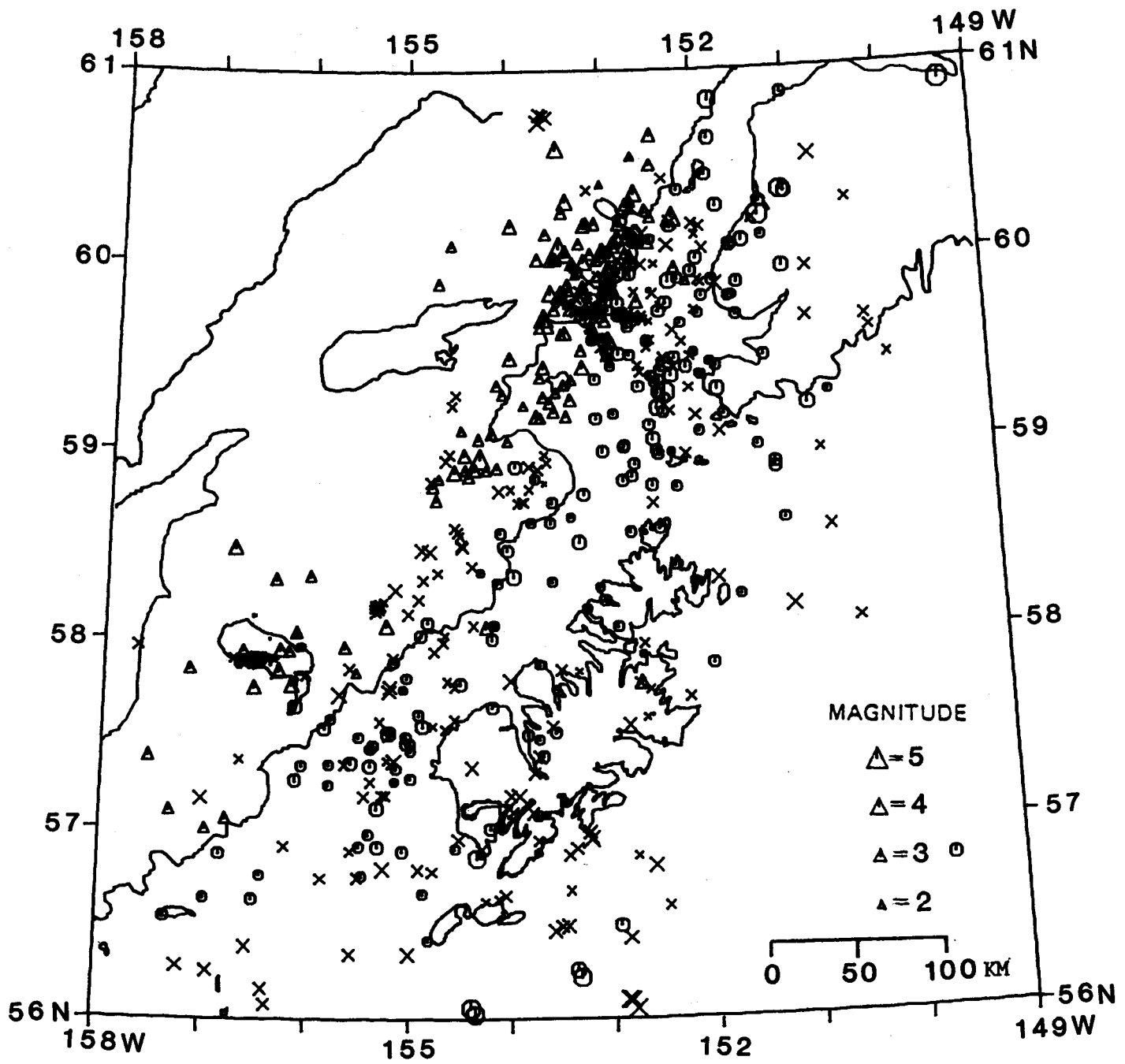


Figure A1: Epicenters of all earthquakes located during January-March, 1978. Symbols indicate depth range of events: crosses 0.35 km, circles 36 to 100 km, and triangles deeper than 100 km.

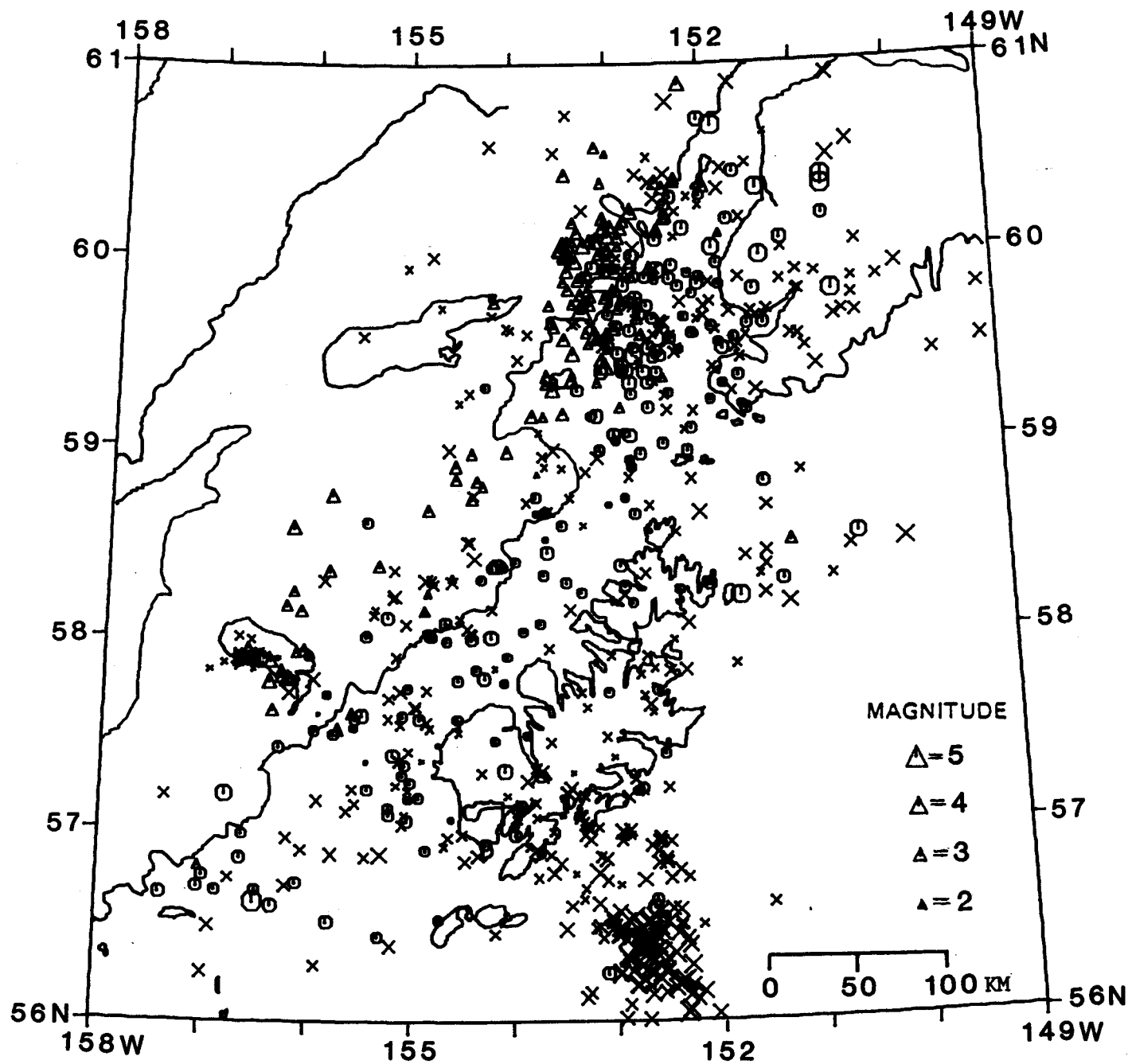


Figure A2: Epicenters of all earthquakes located during April-June, 1978. Symbols as in Figure A1.

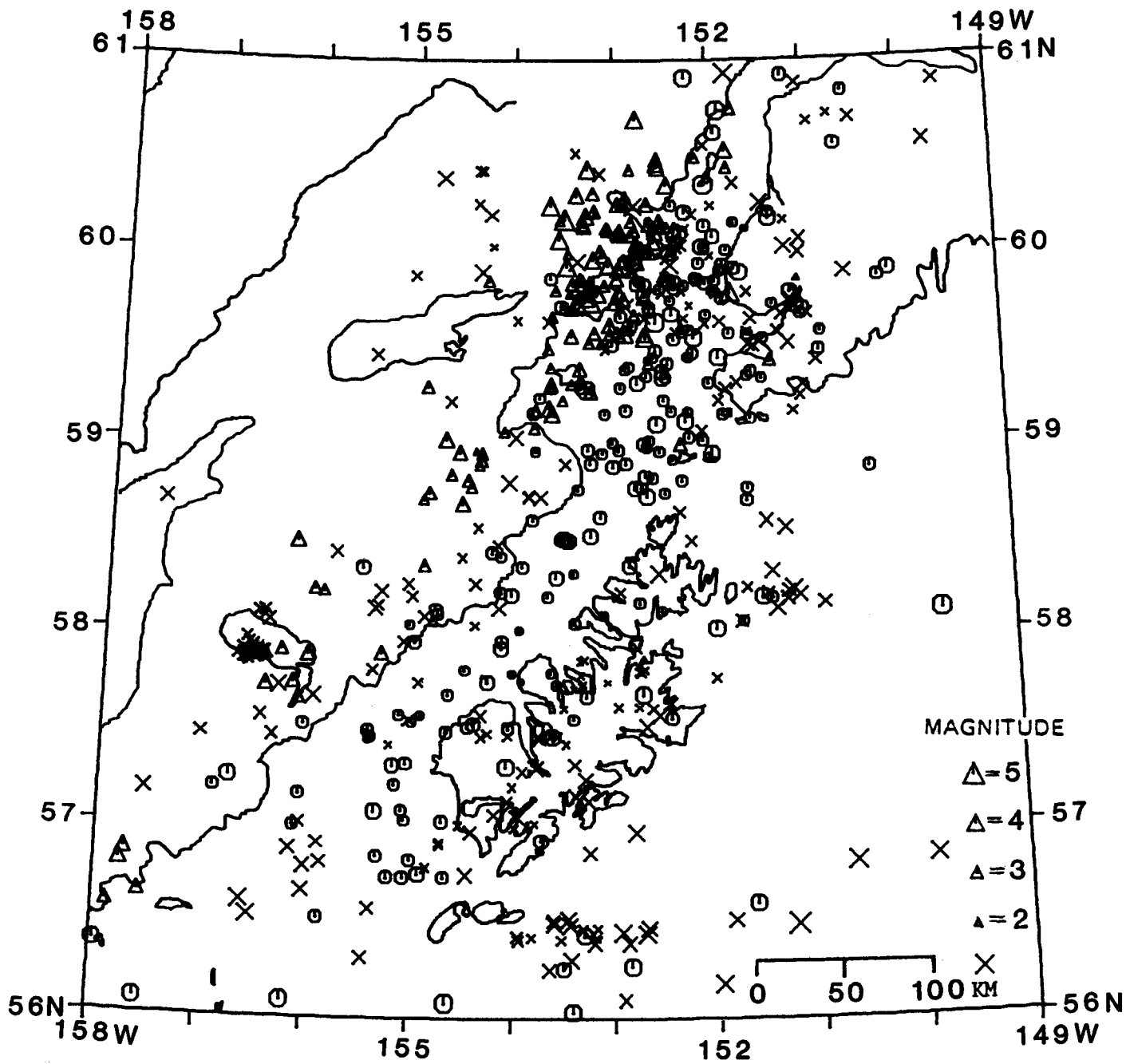


Figure A3: Epicenters of all earthquakes located during July-September, 1978. Symbols as in Figure A1.

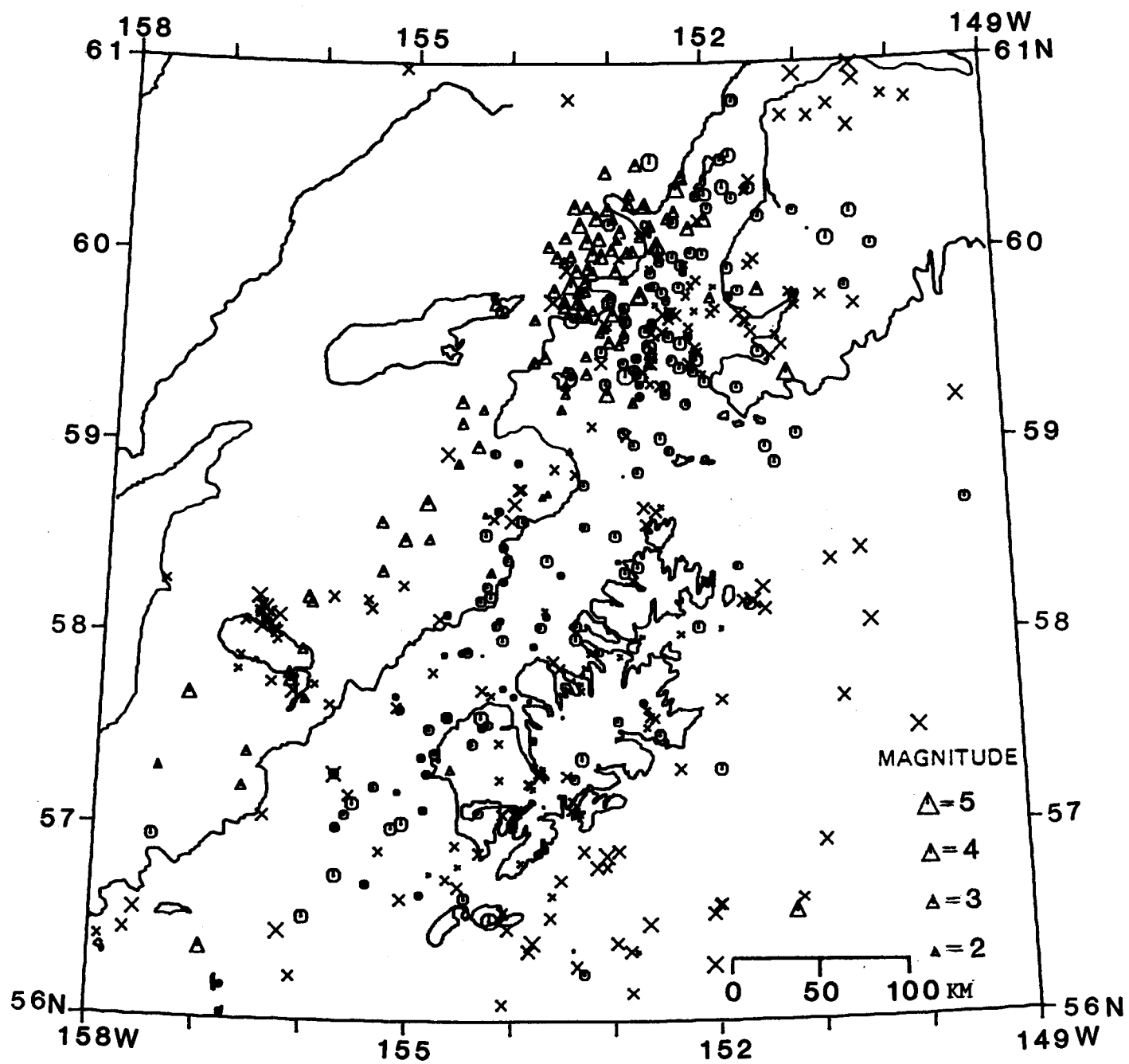


Figure A4: Epicenters of all earthquakes located during October-December, 1978. Symbols as in Figure A1.

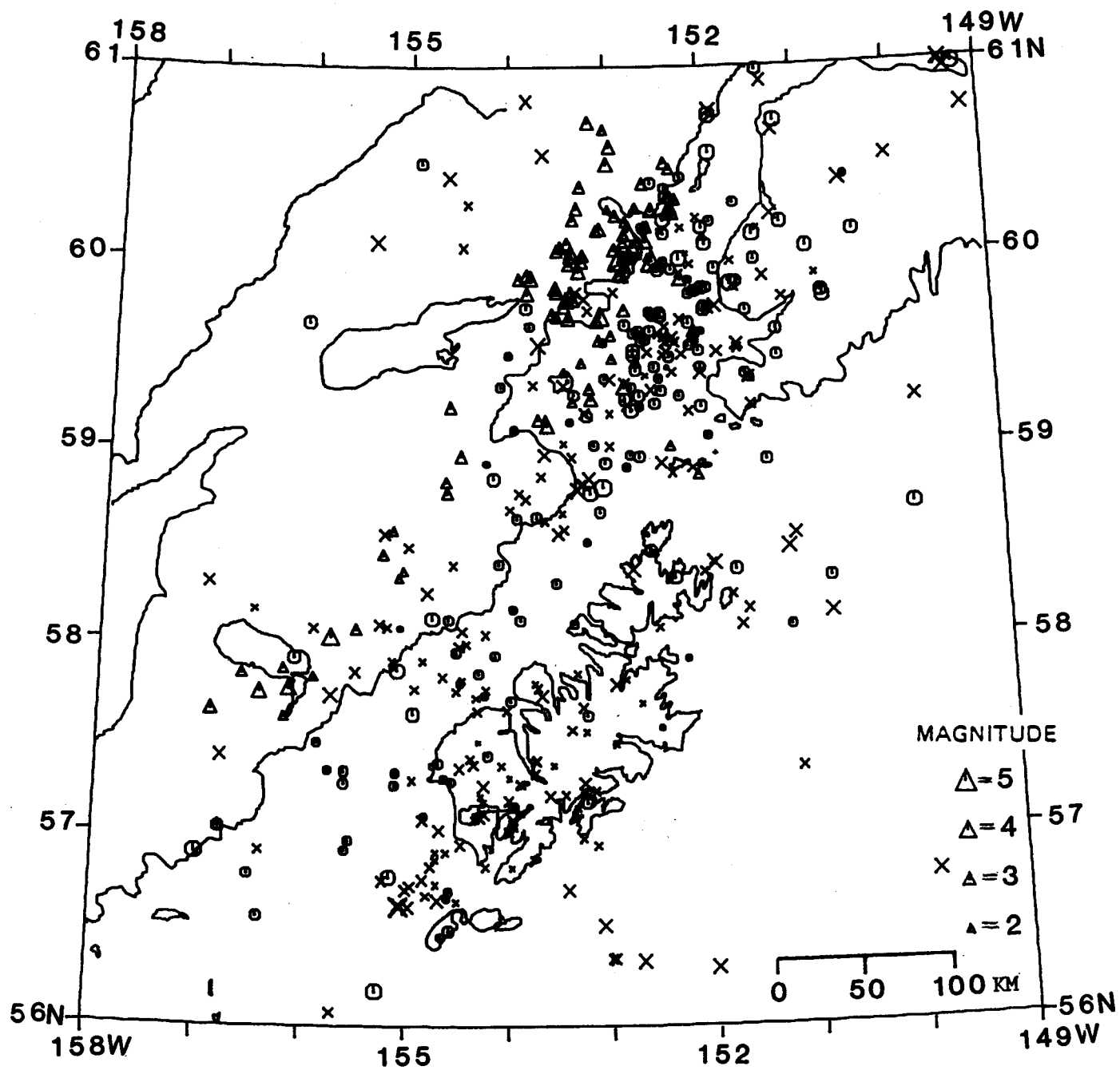


Figure A5: Epicenters of all earthquakes located during 1979. Symbols as in Figure A1.

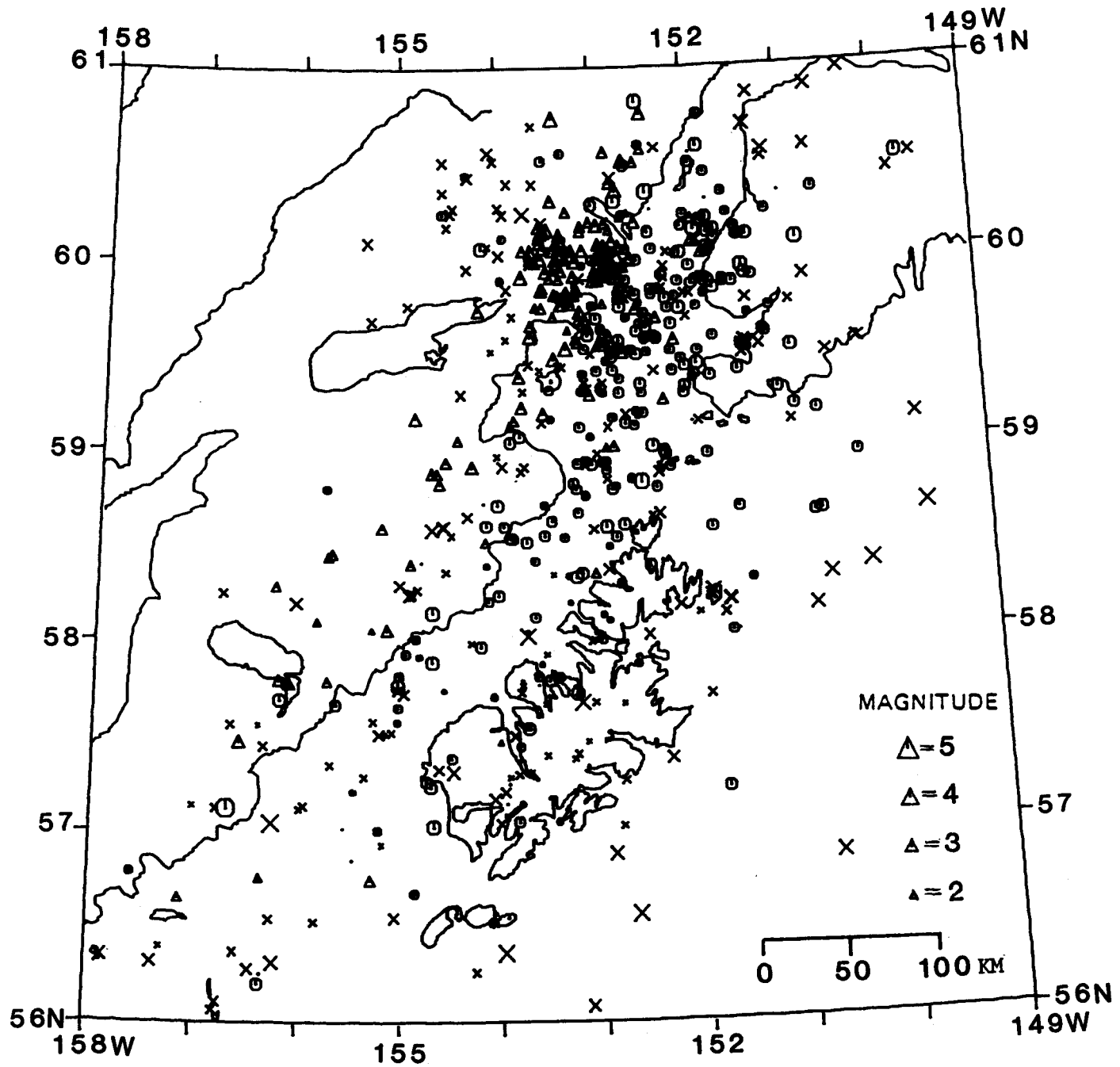


Figure A6: Epicenters of all earthquakes located during January-June, 1980. Symbols as in Figure A1.

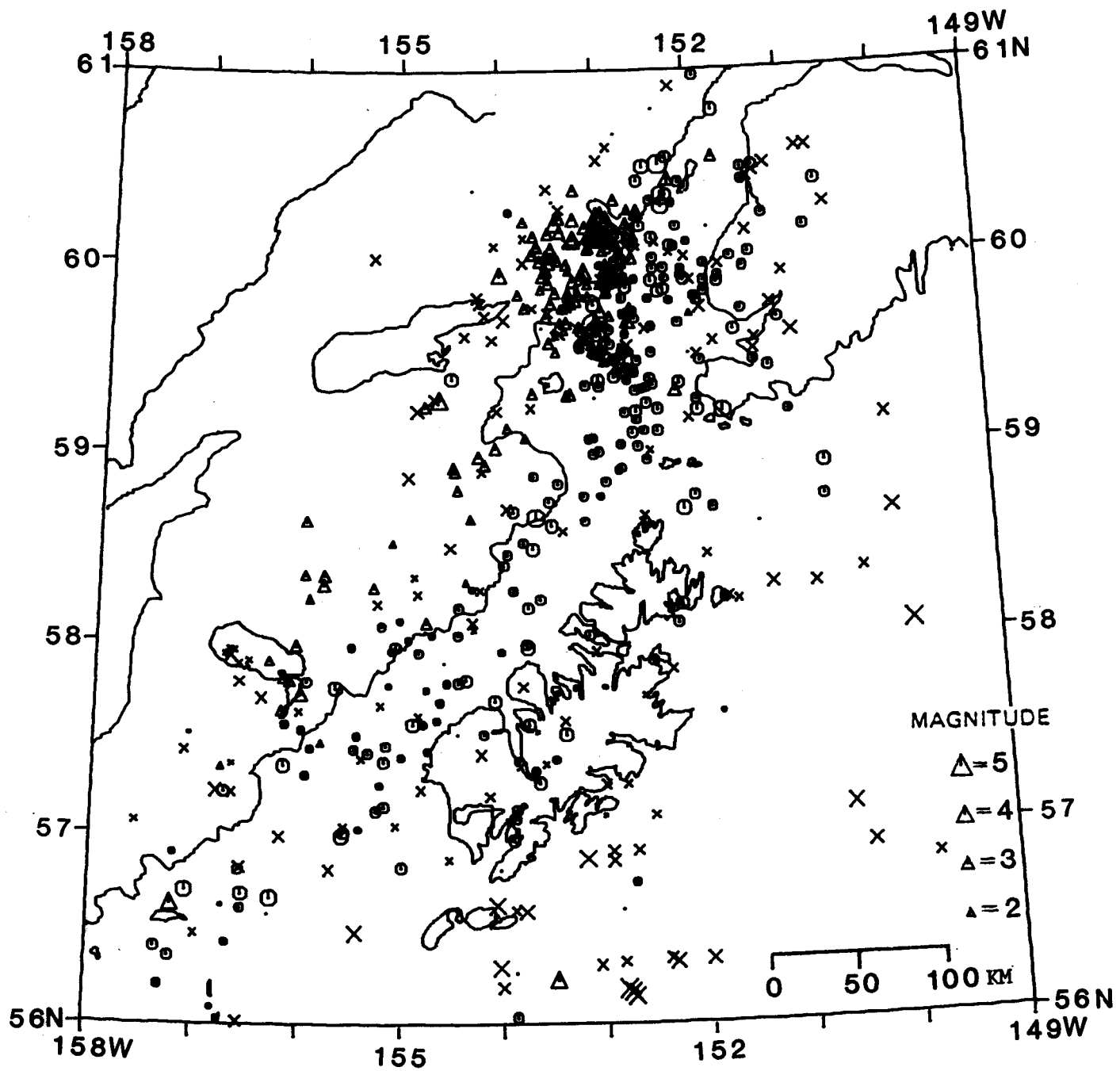


Figure A7: Epicenters of all earthquakes located during July-December, 1980. Symbols as in Figure A1.

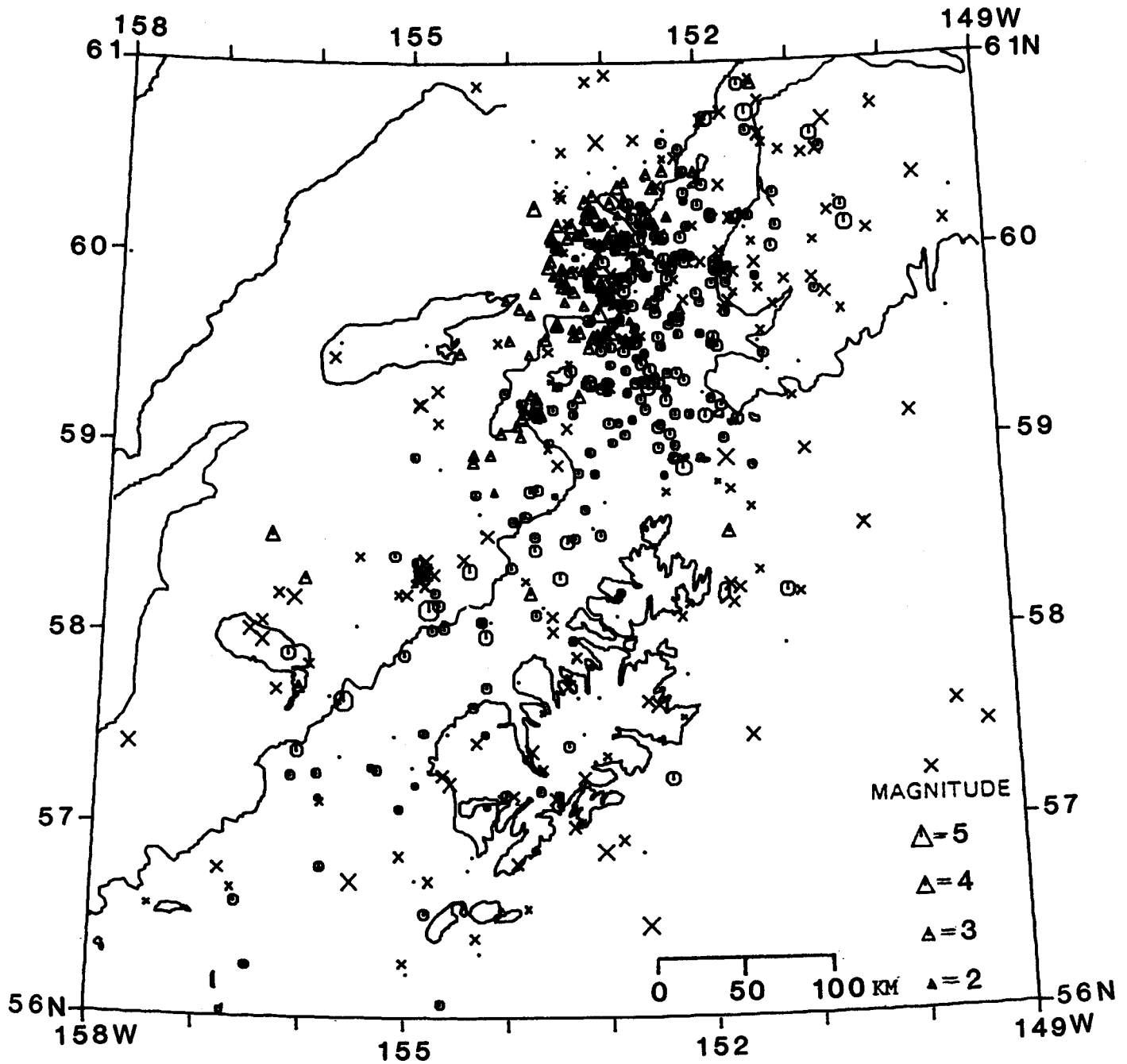


Figure A8: Epicenters of all earthquakes located during January-June, 1981. Symbols as in Figure A1.

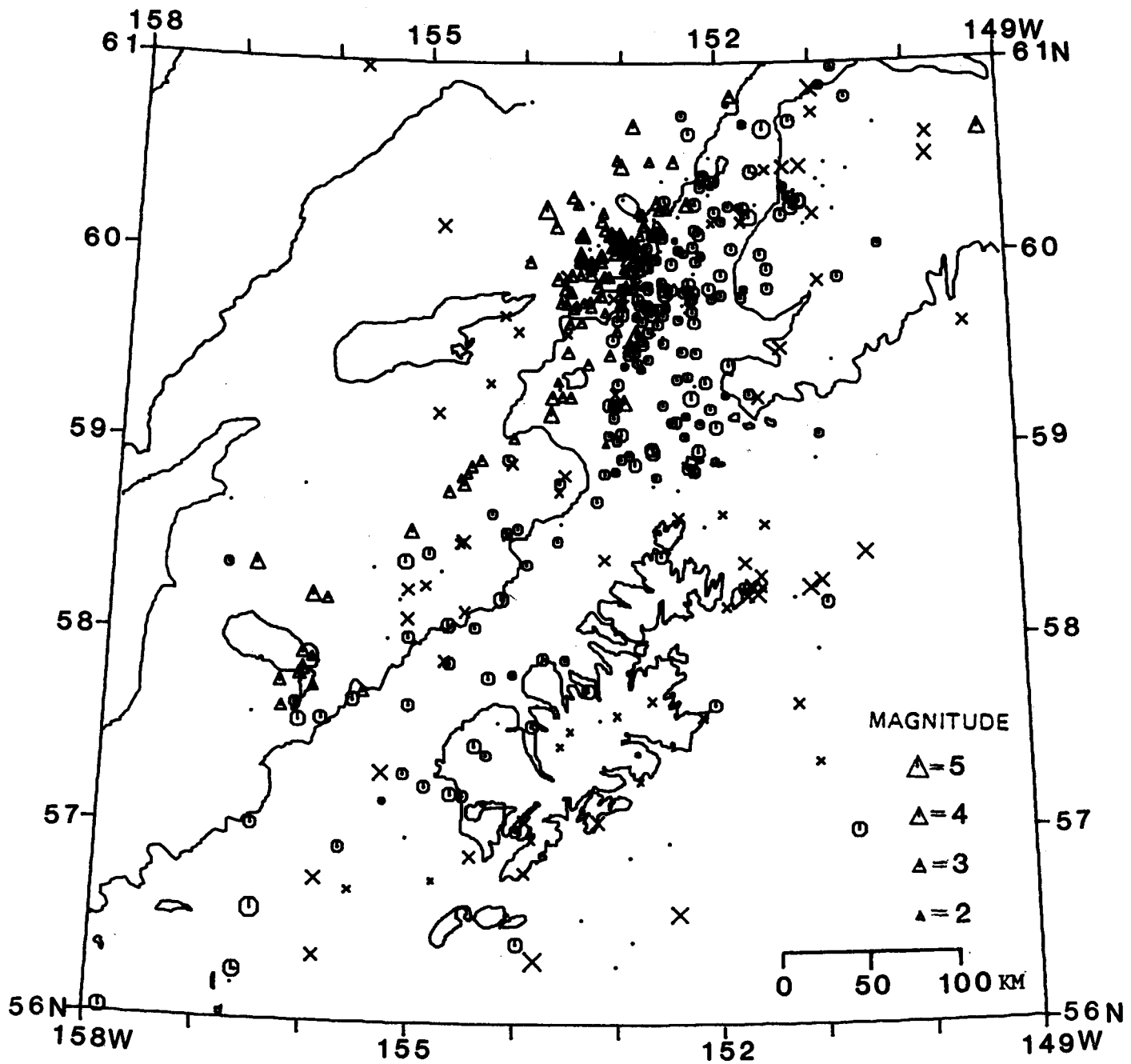


Figure A9: Epicenters of all earthquakes located during July-December, 1981. Symbols as in Figure A1.

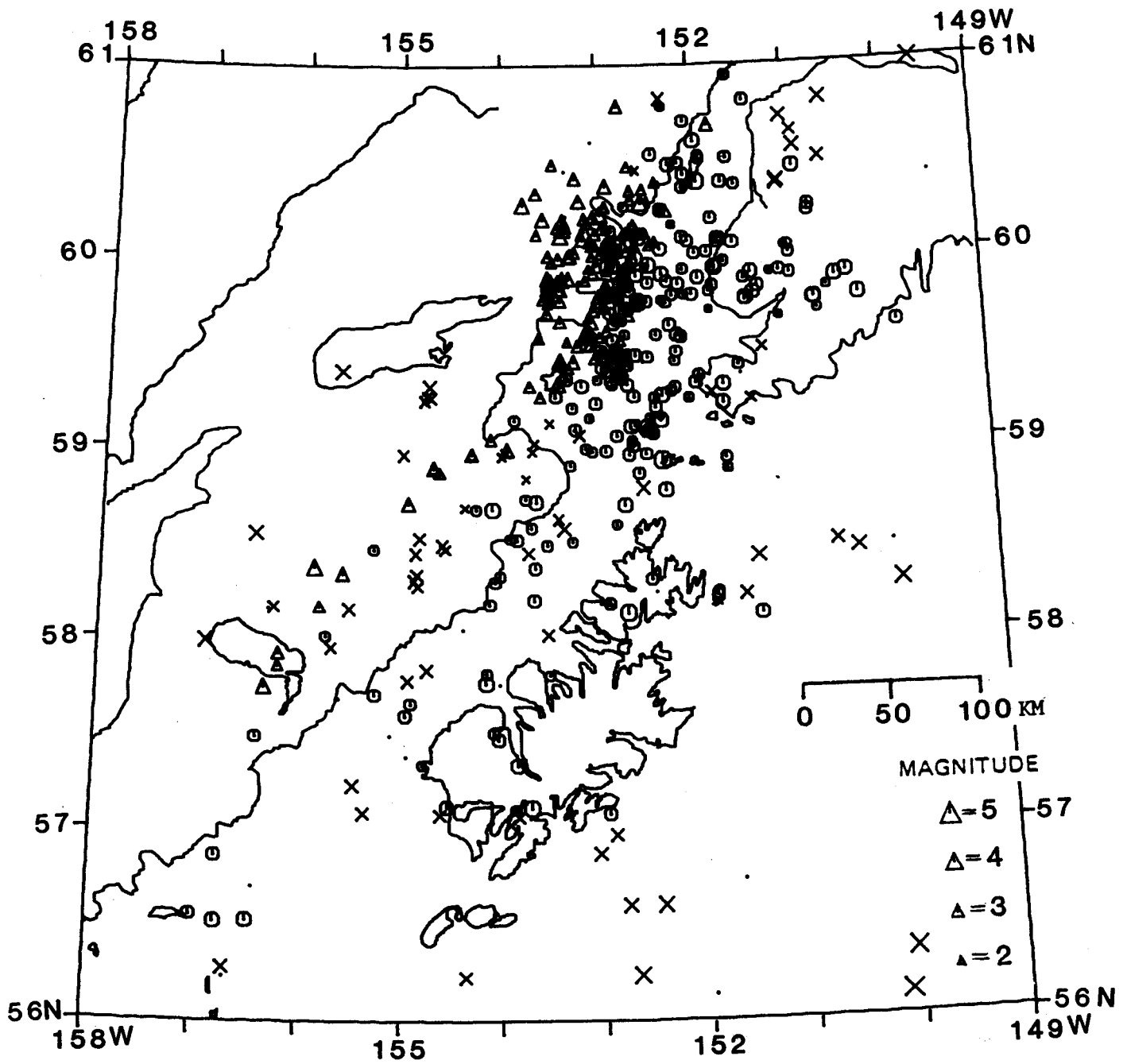


Figure A10: Epicenters of all earthquakes located during 1982. Symbols as in Figure A1.

**VOLCANIC HAZARDS FROM FUTURE ERUPTIONS
OF AUGUSTINE VOLCANO, ALASKA**

by

Juergen Kienle and Samuel E. Swanson

**Geophysical Institute
University of Alaska**

**Final Report
Outer Continental Shelf Environmental Assessment Program
Research Unit 251**

May 1980

100

100

100

100

100

TABLE OF CONTENTS

List of Figures	439
List of Tables	443
ABSTRACT	445
INTRODUCTION	446
ERUPTIVE HISTORY	450
Prehistoric	450
Discovery	451
1812 Eruption	454
1883 Eruption	456
1902 Event	460
1935 Eruption	463
1963/64 Eruption	465
1971 Event	469
1976 Eruption	472
Geophysical Precursors	472
Vent Clearing Phase	474
Effects on Augustine Island	485
February-April Eruptions	494
1976-80 Activity - Current State	509
ERUPTIVE PRODUCTS	513
Petrology	514
Chemistry	515
Chronology	517
Eruption Volumes	519
HAZARDS	524
Pyroclastic Flows	524
Debris Flow and Flood Deposits	535
Tsunamis	536
Lava Flows and Domes	538
Tephra	538
Volcanic Gases	549
HAZARD ZONES	552
Assumptions	552
Very High Risk Hazard Zone	553
High Risk Hazard Zone	556
Moderate Risk Hazard Zone	558
Low Risk Hazard Zone	558
Data Gaps	559

VOLCANIC ERUPTION PREDICTION AND MONITORING	561
ACKNOWLEDGEMENTS	563
REFERENCES	564
APPENDIX: PHOTOGRAMMETRIC MAPPING OF THE SUMMIT REGION AND NORTHEAST SECTOR OF AUGUSTINE VOLCANO	569

LIST OF FIGURES

- Figure 1. Location of Cook Inlet Volcanoes, settlements, oil pipelines and platforms.
- Figure 2. Location of Augustine Volcano in relation to already sold leases (cross hatched).
- Figure 3. Distribution of pre-1883 eruptive products.
- Figure 4. Discovery by Captain Cook, May 26 (St. Augustine's Day), 1778.
- Figure 5. Top: Sketch of Augustine Volcano as seen from the north, pre-1883 and post-1812 eruptions (Doroshin, 1870). Bottom: 1909 photograph from the north showing that the dome and spine occupying the crater prior to 1883 was probably exploded and replaced by a new dome intrusion in 1883.
- Figure 6. Crater of Augustine showing central dome in 1895 (USGS geologist is probably Becker or Purington).
- Figure 7. Distribution of 1883 eruptive products.
- Figure 8. Distribution of 1935 eruptive products.
- Figure 9. Augustine Volcano in eruption, July 7, 1964, as seen from the northeast (photograph by T. Hazard, BLM).
- Figure 10. Augustine's summit from the northeast in 1971. The 1935 and '64 lava domes are marked, P (Pinnacles) and erosional remnants of a vent breccia, L is a short lava flow.
- Figure 11. Distribution of 1963/63 eruptive products.
- Figure 12. Augustine Volcano from the south on September 3, 1971. A strong vapor plume is being fed by fumaroles on the 1964 dome during a period of intense swarms of shallow earthquake activity (photograph by Austin Post, USGS).
- Figure 13. Summary of observations during the vent clearing eruptions of January 22-25, 1976, all times in U.T. A. Ash falls at various Cook Inlet localities based on surface weather log entries. B. Damage to aircraft. C. Cloud heights, numbers 1 through 8 refer to the source of information.
- Figure 14. Lightning storm in eruption clouds of Surtsey Volcano, Iceland, December 1, 1963. Similar lightning has been reported for 1976 Augustine eruption clouds but we have no photo documentation of it (photograph taken from Thorarinnson, 1967).

- Figure 15. Area of ash fallout from 1976 Augustine eruptions.
- Figure 16. January 23, 1976, 16:19 AST, eruption seen against the twilight sky from aboard a Cessna 180 light plane flying at 3,300 m altitude, 325 km northeast of the volcano near Talkeetna. A gas jet marks the position of the volcano.
- Figure 17. Same eruption as in Figure 16 seen head-on from Homer Spit, 110 km east-northeast and downwind from Augustine Volcano. Photographs 16:20 to 16:45 AST by W. G. Feetham.
- Figure 18. NOAA-4 satellite photograph of southern Alaska, January 23, 1976, 10:10 AST, in the visible (0.6 - 0.7 μm), showing eruption plume being dispersed across the Gulf of Alaska. An eruption is in progress and the 5.8 km high eruption column casts a shadow.
- Figure 19. (a) Augustine from the east, February 1, 1976, showing new pyroclastic flow deposits on the northeast beach. (b) Close-up of the pyroclastic flow deposits, looking east, February 1, 1976; arrow points to old beach line, B marks Burr Point. Note steam rising from the deposit seaward of the old beach line. (c) Augustine from the north, June 13, 1976, showing distribution of pyroclastic flow deposits, arrow marks Burr Point cabin site. (d) Same beach as in (b) on February 27, 1976; the early February pyroclastic flow eruptions have altered the beach line significantly. Photographs a, b, and c by R. E. Wilson.
- Figure 20. Burr Point Camp before and after passage of a glowing cloud (*nuée ardente*). Note mountainward dent in smaller generator building, produced by back-eddy effect when the *nuée* passed over the small ridge protecting the camp.
- Figure 21. The main aluminum building at Burr Point dented and punctured by steep angle impact of lapilli from the side facing away from the volcano. All windows were sucked out by the Venturi effect of the passing hot cloud (photograph by H.-U. Schmincke, Ruhr-Universität Bochum, W. Germany).
- Figure 22. Charred driftwood burned by passing *nuée ardente* at Burr Point (photograph by H.-U. Schmincke).
- Figure 23. Partially melted plastic measuring cup recovered from inside the main building at Burr Point.
- Figure 24. Augustine Volcano in eruption on February 6, 1976. A *nuée ardente* is descending the northeast side (Burr Point area) of the volcano. Fresh black mudflows have melted the snow in places (photography by G. Gunkel).

- Figure 25. Same eruption as shown in Figure 24 photographed from aboard a commercial jet airplane. The eruption column is 5.5 km high. Shock wave phenomena can be seen in the atmosphere above the erupting volcano (photograph by M. F. Tollefson, National Park Service).
- Figure 26. Nuee ardente (glowing cloud) descending toward Burr Point on February 8, 1976, 14:02 AST. The nuée reached a maximum speed of 50 ms^{-1} (photograph taken from article by Stith et al., 1977).
- Figure 27. Series of historic photographs from the north, showing the evolution of Augustine Volcano.
- Figure 28. Close-up of the 1976 lava dome; 1935 dome remained unchanged; most of the 1964 dome has been removed during the January explosions.
- Figure 29. Types of glowing (pyroclastic) avalanches and associated nuées ardentes: (A) Pelee type (directed blast); (B) Soufriere type (column collapse); (C) Merapi type (dome collapse), taken from MacDonald, 1972, p. 149).
- Figure 30. Temperature profiles measured a few weeks after deposition of the pyroclastic flows east of Burr Point; temperature test site is located on new flow shown in Figure 19d near the position of the old beach line.
- Figure 31. Vertical photograph of Augustine Island, taken by the National Ocean Survey on June 11, 1976, showing distribution of the light-colored 1976 pyroclastic avalanches and debris flows (arrows and ruled area). The lines of the ruled area indicate profiles along which the topography was digitized on high-resolution vertical imagery to obtain an accurate volume estimate of the 1963/64 and 1976 deposits in that sector of the volcano.
- Figure 32. Close-up of the 1976 pyroclastic flow deposits on the northern flank of Augustine Volcano. The sulfur-stained white-appearing area at the base of the steaming 1976 dome is shown in Figure 33 (photograph by H.-U. Schmincke).
- Figure 33. "Hell's Gate" at the base of the 1976 lava dome. Pyroclastic avalanches have eroded a U-shaped channel.
- Figure 34. Distribution of the 1976 eruptive products.
- Figure 35. Close-up of the 1976 lava dome within remnant of the '64 dome. Fumarole temperature at base of summit spine of '76 dome was 754°C in August 1979 (David Johnston, personal communication).

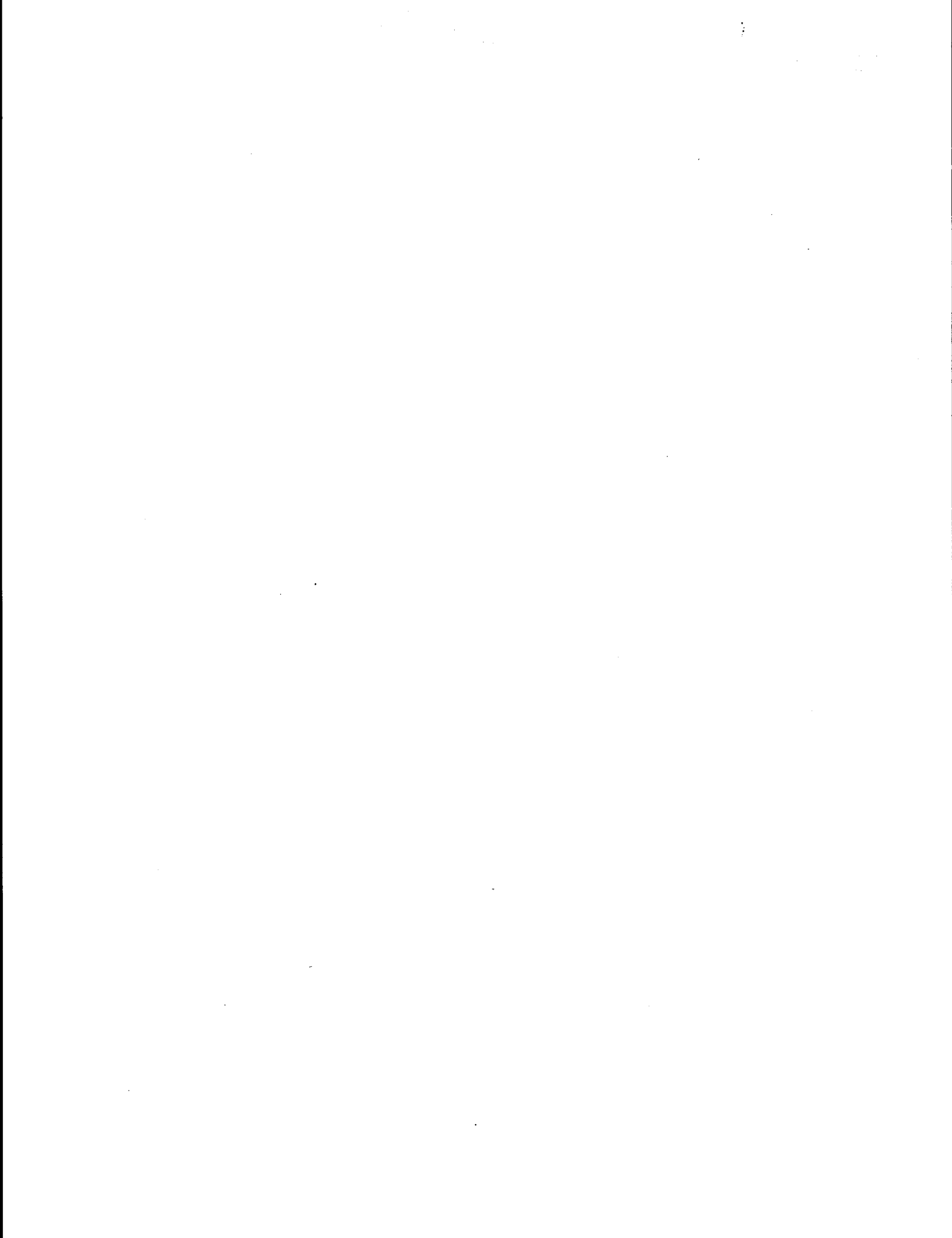
- Figure 36. An apparent shortening of repose time between eruptions for at least the past 4 Augustine eruptive cycles.
- Figure 37. Map illustrating how nuées ardentes can detach themselves from their basal pyroclastic (glowing) avalanches and proceed independently, as during the disastrous destruction of the City of St. Pierre, Martinique, Lesser Antilles, during the May 8, 1902 eruption of Mt. Pelee. The pyroclastic avalanche followed the Riviere Blanche to its mouth, while the nuee continued straight toward the city (taken from MacDonald, 1972, p. 144).
- Figure 38. Suspected offshore pyroclastic flow deposits off Augustine Island.
- Figure 39. Prevailing high altitude winds at Kodiak (from Wilcox, 1959).
- Figure 40. Prevailing surface winds at Homer and Kodiak (compiled from data given in Brower et al., 1977).
- Figure 41. Ash on the runway of Anchorage International Airport from the 1953 Mt. Spurr eruption.

LIST OF APPENDIX FIGURES

- Figure A1. Topographic map of Augustine Volcano's summit region based on aerial photography taken on June 16, 1973, i.e., post 1963/64 eruption but pre-1976 eruption. The contour interval is 10 ft. and the distance between tickmarks is 2,000 ft. (prepared for the Geophysical Institute of the University of Alaska by North Pacific Aerial Surveys, Inc., Anchorage, Alaska).
- Figure A2. Topographic map of Augustine Volcano's summit region based on aerial photography taken on August 21, 1976, i.e., post-1976 eruption. The contour interval is 10 ft. and the distance between tickmarks is 2,000 ft.
- Figure A3. Topographic map of the northeast sector of Augustine Volcano based on aerial photography taken on August 21, 1976, i.e., post-1976 eruption. The contour interval is 10 m and the distance between tickmarks is 1000 m.

LIST OF TABLES

- Table 1. Average composition of volcanic products from Augustine Volcano. Based on results of this study, Becker (1898), Detterman (1973), and Kienle and Forbes (1976). Average andesite and dacite from Nockolds (1954).
- Table 2. Volume of the 1976 Eruption
- Table 3. Summary of Augustine ash fallout collected at various Alaskan National Weather Service stations and other sources following January 23-24, 1976 eruption.



ABSTRACT

Augustine Volcano, located on an uninhabited island in lower Cook Inlet, has erupted 5 times since 1812, the first documented eruption after the discovery in 1778. Augustine is one of the most active volcanoes in the eastern Aleutian arc. Constancy of eruptive style, volume, and geochemistry has characterized the eruptions, suggesting that the feeding magma reservoir has not changed significantly during its very young eruptive history - the volcano is probably less than about 15,000 years old. Eruptions are typically Peleean, beginning with powerful vent clearing eruptions and ending with new dome intrusions. Hot pyroclastic flows are common during both stages, the first stage producing column collapse pyroclastic flows (Soufrière type), the second stage dome collapse pyroclastic flows (Merapi type). Pyroclastic flow deposits make up the bulk of the volcanic island and extend at least 4 km offshore.

The dominant hazard near the volcano on and offshore are pyroclastic flows and fast moving hot gas and dust clouds (nuées ardentes). Prevailing westerly high altitude winds govern the ash dispersal of the eruptions predominantly to the east-northeast affecting all of the Cook Inlet region (including the west shore), the Kenai Peninsula and the Gulf of Alaska. During one eruption the volcano has produced a tsunami which crossed lower Cook Inlet to the Kenai Peninsula.

INTRODUCTION

Mount St. Augustine is a very young symmetrical island volcano in Lower Cook Inlet, southern Alaska, 285 km southwest of Anchorage and 100 km west-southwest of Homer on the lower Kenai Peninsula (Figure 1). The channel that separates the island from the west shore of Cook Inlet is 10 km wide at its narrowest point. The circular island has a diameter of about 12 km and from its center rises a single symmetrical cone about 1,200 meters high. The island is uninhabited, however, from 1946 to 1949 pumice was mined on its southwest flank for use as a lightweight aggregate for construction materials (Moxham, 1951). The nearest population centers are on the Kenai Peninsula, 100 km across Cook Inlet, and at Lake Iliamna, 90 km north-northwest. There is a road from Iliamna Bay, 30 km north-northwest of the volcano, to Pile Bay on Iliamna Lake, sometimes used to portage small boats from Cook Inlet into the Lake Iliamna drainage. Otherwise, Kamishak Bay has no permanent population except for floating canneries or freezer barges during the summer fishing season.

Augustine is part of the Aleutian volcanic arc which spans 3000 km between Kamchatka and mainland Alaska. The arc is the result of convergence of the North American and Pacific lithospheric plates. The Cook Inlet volcanoes Spurr, Redoubt, Iliamna, Augustine and Douglas are nearly perfectly aligned along the strike of a very active deep seismic zone marking the site of plate subduction in Cook Inlet.

The bulk, if not all of the visible cone of Augustine, has formed in post-glacial times, perhaps as recent as 19,000 to 15,500 years ago (Johnston, 1979a). In the past 200 years since the discovery and naming of the volcano on May 20, 1778 by James Cook on his third Pacific voyage

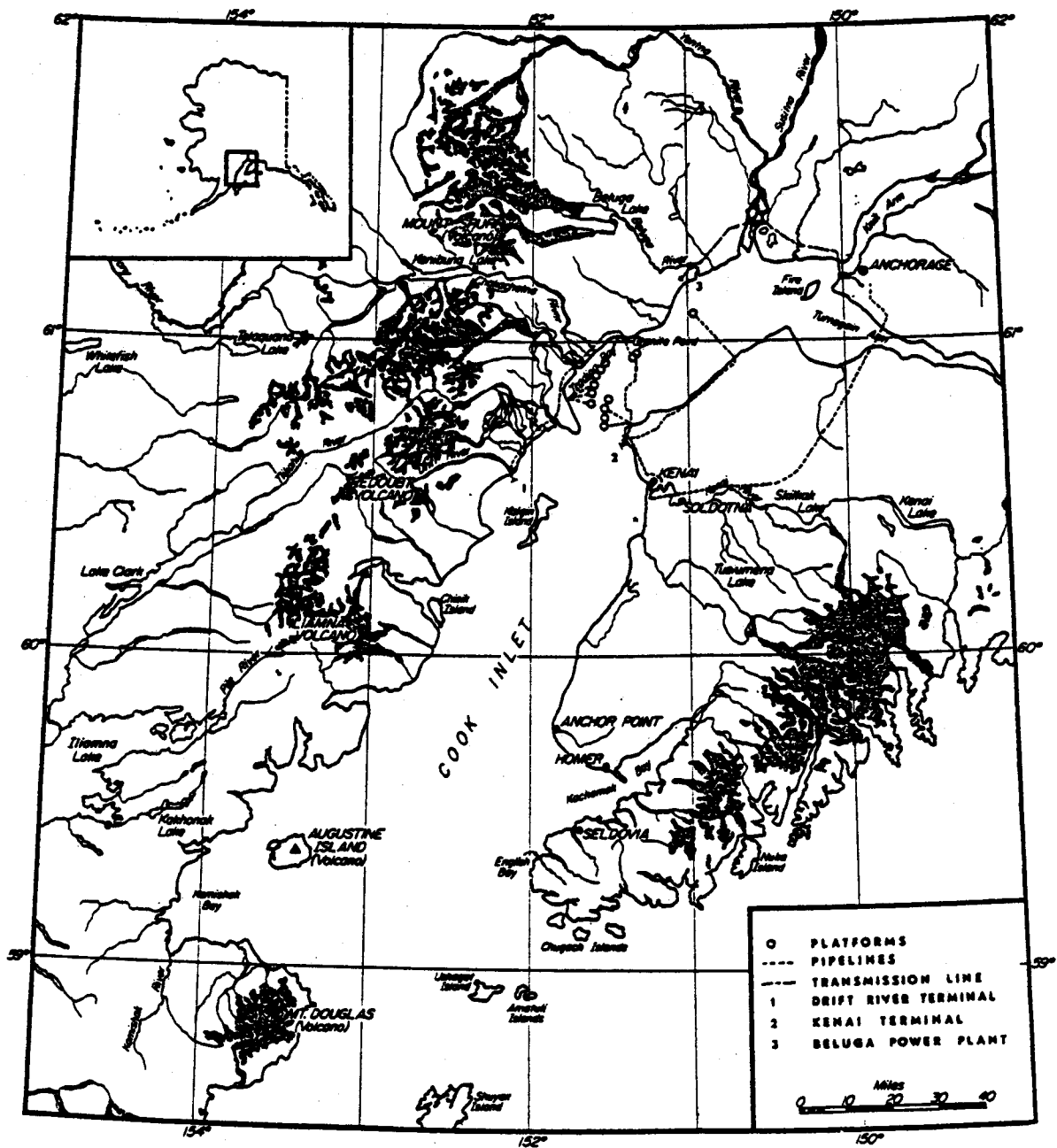


Figure 1. Location of Cook Inlet Volcanoes, settlements, oil pipelines and platforms.

(Beaglehole, 1967) Augustine has had 5 significant eruptions: 1812, 1883, 1935, 1963/64 and 1976 (Doroshin, 1870; Davidson, 1884; Detterman 1968, Kienle and Forbes, 1976; Johnston, 1978). Based on the historic record, it appears that all recent Augustine eruptions were Peléean and each greatly modified the appearance of the volcano. Typically, viscous dome intrusions ended the eruptive cycles and dome collapse produced extensive pyroclastic avalanche deposits. This style of highly explosive activity coupled with the island setting, youthfulness and short recurrence rate of eruptions make Augustine the most hazardous volcano in Cook Inlet. There is no reason to believe that similar eruptions will not occur again.

If one assumes that Augustine's eruptive style will remain that of the past 200 years, an assumption which seems reasonable based on the remarkably uniform chemistry of the eruptive products, the principal near field hazards will be pyroclastic avalanches, mudflows, glowing clouds (which can continue out to sea) and heavy bomb and ash falls. Assuming that there will never be any industrial development on the island, explosive eruptions characteristic of Augustine present hazards to lower Cook Inlet communities, to the fishing industry, to major water and air travel routes to Anchorage and, if oil development gets underway near Augustine, to offshore petroleum drilling and production platform (Johnston et al., 1977, see also Figure 2). The principal hazard in the far field, potentially affecting inhabitants on the Kenai Peninsula and in the Iliamna Lake region, will be heavy ashfalls, muddy and acid rains, and possibly tsunamis at the shores of Cook Inlet as during the 1883 eruption.

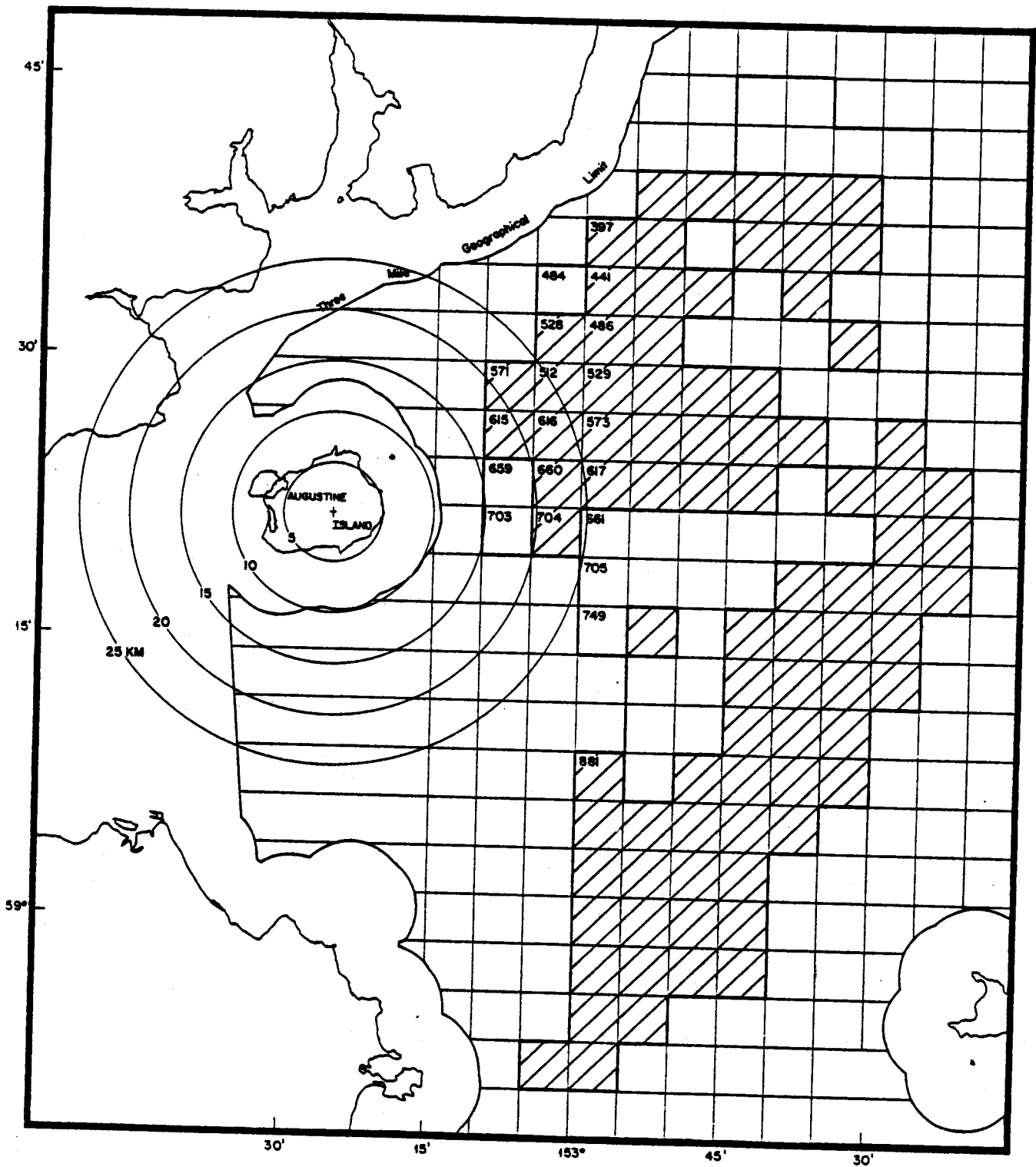


Figure 2. Location of Augustine Volcano in relation to already sold leases (cross hatched).

ERUPTIVE HISTORY

Prehistoric

Augustine is a very young volcanic center, most likely post-glacial in age. The volcanic cone is built upon an uplifted basement of Jurassic, Cretaceous and Tertiary sandstones, siltstones and shales (Detterman, 1973; Buffler, 1976 and 1980), probably heavily zeolitized at shallow depth beneath the volcano, as indicated by high seismic velocities (Kienle et al., 1979). On the southern flank of the volcano southward dipping uplifted section of marine sediments crops out at elevations up to about 300 m and is overlain by a thin layer of glacial debris and boulders (Detterman, 1973; Buffler 1976). Johnston (1979a) described a stratigraphic section on the south side of the volcano between the 260 and 320 m level that might date the onset of volcanism at Augustine. The section consists of principally non-volcanic proglacial lake deposits with layers of pumice-rich sands and basaltic hyaloclastites, implying that the initial Augustine eruptions were rhyolitic-basaltic and volcanism began while this lake existed. Because exotic glacial boulders are concentrated at the unconformable interface between the sediments and the lake deposits and because the level of occurrence of glacial debris correlates with dated shorelines at about the 230 m level in eastern Cook Inlet, Johnston deduced that the proglacial lake must have existed during the Moosehorn glacial advance. The onset of volcanism at Augustine is thus dated at 17,000 to 13,500 years B.C.

The lake deposits are horizontally layered unconformably overlying the south-dipping Mesozoic sandstones and shales which indicates that the uplifting of the basement, presumably due to intrusive activity prior to the onset of extrusive volcanism, occurred prior to the deposition

of the lake sediments (Buffler, 1980). Johnston (1979a), quoting other workers (Plafker, 1965; Detterman and Reed, 1973; and Karlstrom, 1964) thought that an additional 45 to 90 m of uplift may have occurred since Moosehorn times, assuming modern and recent uplift rates of 0.3-0.6 m/century.

Extensive areas of prehistoric mudflow and pyroclastic flow deposits occur on the lower eastern and western flanks of the volcano, and also up to at least 4 km offshore all around the island. Two C^{14} dates from a soil horizon that directly overlies the seacliff forming mudflow deposits on the eastern flank of the volcano give a minimum age for these flows of 1500 ± 155 and 1470 ± 160 years B.P.

The distribution of prehistoric deposits on Augustine Island is shown on Figure 3. Most of the older deposits on Augustine Island are buried by younger ejecta. However, around the margins of the island older deposits can be identified. The inferred distribution shown on Figure 3 revises the map by Detterman (1973) and is based on photo interpretation of newer aerial photography.

Discovery

The volcano was discovered on Saint Augustine's day (May 26) by Captain James Cook in 1778 on his third Pacific voyage (Figure 4). He named it Mount St. Augustine¹ and described it as "of a conical figure and of a very considerable height" (Beaglehole, 1967). Other early descriptions also corroborate the conical shape of the mountain topped by a "rounded dome without a peak" (Dall, 1884) and "presenting nearly

¹Map makers later omitted the "Saint"

PRE-1883

ERUPTIVE PRODUCTS

-  VENT PLUGS AND DOMES
-  DEBRIS FLOW DEPOSITS
-  PYROCLASTIC DEPOSITS (INCLUDING FLOWS AND AVALANCHES)
-  LAVA (VENT PLUGS, DOMES AND FLOWS)

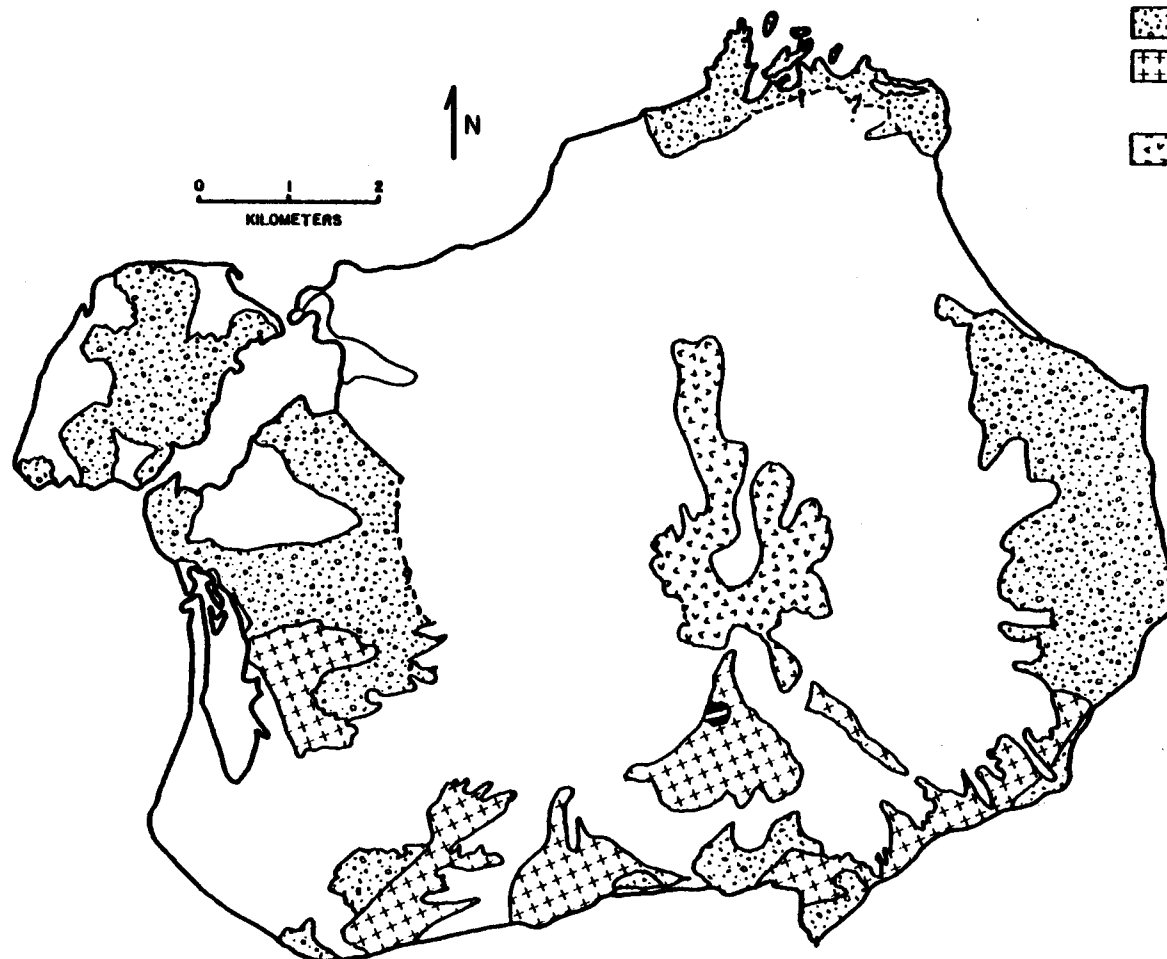


Figure 3 Distribution of pre-1883 eruptive products.



453

Figure 4. Discovery by Captain Cook, May 26 (St. Augustine's Day), 1778.

the same appearance from every point of view" (Davidson, 1884, quoting Captain Puget's description of 1794). This "rounded dome" was most likely an early vent plug (Kienle and Forbes, 1976).

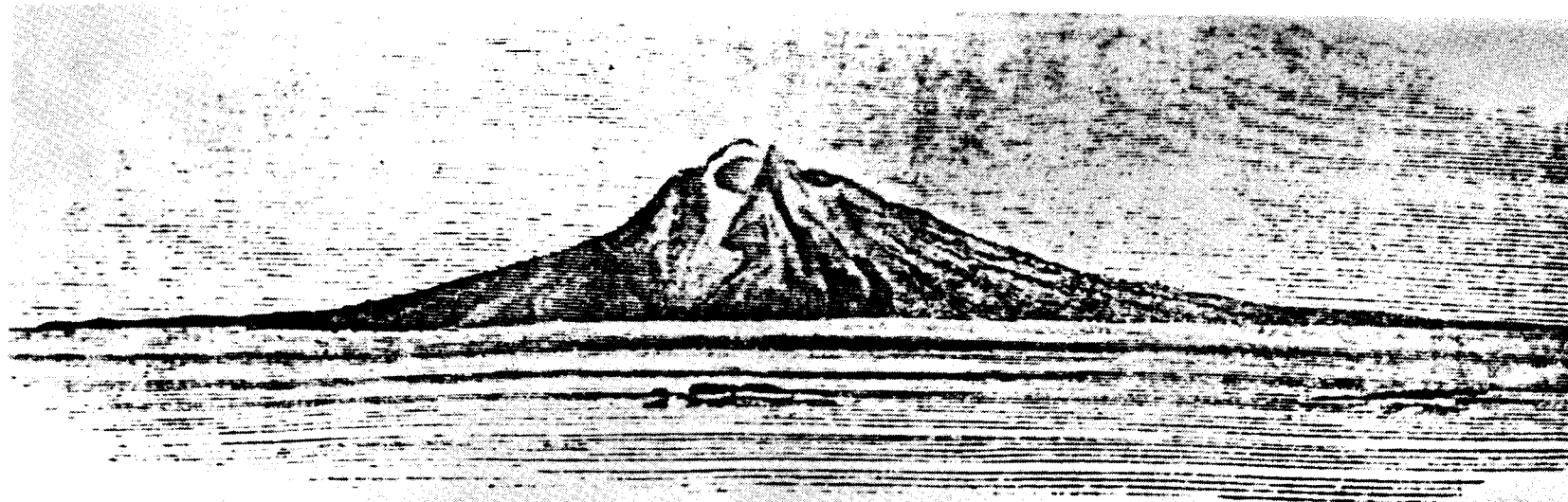
1812 Eruption

Doroshin (1870) describes Chernabura² (Augustine) as an "irregular cone with a rounded peak consisting of lava and pumice". Figure 5 (top) is a sketch of the volcano as seen from the north, given in Doroshin's publication. The sketch is remarkably similar to the first photograph we have of the volcano taken in 1909 from the same direction (Figure 5, bottom), except that the drawing shows a spine not visible in the 1909 photograph. That spine was probably destroyed in the 1883 eruption.

Doroshin (1870) reports that the volcano "burned" in 1812, "as was positively confirmed by a native of the village located in the opposite shore of the Bay [he is referring to Kenai Bay, i.e. Cook Inlet; the village could be English Bay on the lower Kenai Peninsula]. It wasn't possible to reach the island ..., because the lava [pyroclastic flows?], half of which had flown into the sea, could at any time rend the skin of the baidarkas (canoe)".

We surmise that prior to 1812 Augustine's summit was occupied by a large lava dome giving the volcano the overall rounded symmetrical appearance described by the early Pacific explorers, Cook and Puget. This dome was apparently destroyed in the 1812 eruption resulting in a new summit crater breached to the north which was only partially filled by a new dome intrusion with a pronounced summit spine (Figure 5, top). During the vent clearing eruptions in 1812, ash dispersed 210 km north-

¹Chernabura, a local corruption of the Russian name (Ostrov) Chernoburoy, meaning "black-brown" (island) - Orth (1967); other spellings found in the literature are Chernobour, Chonoborough, Chernaboura, Tchernybura and probably others.



Островъ Чернобурый.



Figure 5. Top: Sketch of Augustine Volcano as seen from the north, pre-1883 and post-1812 eruptions (Doroshin, 1870). Bottom: 1909 photograph from the north showing that the dome and spine occupying the crater prior to 1883 was probably exploded and replaced by a new dome intrusion in 1883.

east to Skilak Lake, as evidenced by an ash layer found by Rymer and Sims (1976) in the varved lake deposits. The ash is dated by counting the varves.

In 1880 Mount St. Augustine had a height of 3,800 feet (1,158 m) "as measured by angles from different stations" (Dall, 1884).

1883 Eruption

On the morning of October 6, 1883 Augustine burst again into violent eruption. Dall (1884) stated that smoke first arose from the volcano in August about two months before the cataclysmic eruptions of October 6. The initial eruption was vividly described by Davidson (1884):

"About eight o'clock of the morning of October 6, 1883, the weather being beautifully clear, the wind light from the south-westward (compass), and the tide at dead low water, the settlers and fishing-parties at English Harbor³ heard a heavy report to windward. When the heavy explosion was heard vast and dense volumes of smoke were seen rolling out of the summit of St. Augustine and moving to the north-eastward (or up the inlet... At the same time (according to the statements of a hunting-party of natives in Kamishak Bay) a column of white vapor arose from the sea near the island, slowly ascending, and gradually blending with the clouds. The sea was also greatly agitated and boiling, making it impossible for boats to land upon or leave the island...From English Harbor (Port Graham) it was noticed that the columns of smoke, as they gradually rose, spread over the visible heavens, and obscured the sky, doubtless under the influence of a higher current (probably north or northeast). Fine pumice-dust soon began to fall, but gently, some of it being very fine, and some very soft, without grit...Twenty-five minutes after the great eruption, a great 'earthquake wave', estimated as from twenty-five to thirty feet high, came upon Port Graham like a wall of water. It carried off all the fishing-boats from the point, and deluged the houses. This was followed, at intervals of about five minutes, by two other large waves, estimated at eighteen and fifteen feet; and during the day several large and irregular waves came into the harbor. The first wave took all the boats into the harbor, the receding wave swept them back again to the inlet, and they were finally stranded. Fortunately it was low water, or all the people at the settlement must inevitably have been lost. The tides rise and fall about fourteen feet."

Based on the annual report of the Russian Orthodox Missionary at Kenai, dated May 28, 1884, the waves generated by the eruption may have reached other shores of Cook Inlet:

³Near Port Graham Inlet, 85 km east of the volcano across Cook Inlet.

"Influenza Kenai, Ninilchik, Seldovia, Alexandrovsky (English Bay), nearly all children up to 2 years of age were swept away. At the same time this region suffered from inundation caused by the eruption of Chernabura Volcano which is about 60 miles across strait from Alexandrovsky. The inundation so frightened the natives of Alexandrovsky that they moved their huts to higher ground in one night".

According to Davidson (1884), the sea waves were also felt at Kodiak and the "pumice-ashes" accumulated to a depth of "4 to 5 inches" (10 to 13 cm).

From the description of dense smoke "rolling out" from Augustine's summit, a column of white vapor rising from the sea near the island and the sea being greatly agitated and boiling we deduce that during the October 6 eruptions a large hot pyroclastic flow must have rushed down the slope of the volcano and impacted into the shoal waters surrounding Augustine Island. The sudden displacement of large volumes of sea water probably gave rise to the waves that crossed Cook Inlet to English Bay. The most likely place of impact was the north or northeast shore of Augustine near Burr Point where we find the freshest terrain on the island. Whether or not the Burr Point terrain itself was created in 1883 is not clear, as there are no records of photographs that document the topography or shoreline of the north side of the island prior to the 1883 eruption. The sparse vegetation and fresh appearance of the hummocky topography do suggest that the Burr Point terrain is relatively young but perhaps a little older than 1883. We have submitted organic soils overlying the Burr Point lahar for C^{14} dating to resolve this question. If Burr Point turns out to be older than 1883, the October 6 flow most likely impacted on the northeastern shoreline of the island.

An alternate explanation for the sea waves, though less likely than impact of a pyroclastic flow, could be that they were true tsunamis, i.e., generated by the sudden displacement of the sea floor due to earthquake or other volcanic activity. Davidson, however, does not report any seismic disturbance on October 6 - except for using the term 'earthquake wave'.

Following the October 6 eruption, flames issuing from the summit of Augustine could be seen at night from English Bay while during the day vast volumes of smoke were seen "rolling" from it. The rolling motion of the cloud and incandescence during the night implies that pyroclastic flow and nuee ardente activity continued for a considerable time, probably affecting all flanks of the volcano, even though a path down the existing north-northeastern breach was most likely.

Davidson (1884) also reports that the volcano had ruptured from east to west with substantial subsidence of the northern half of the island and that a new island had formed northwest of the island, based on statements made by Captain Sands and Captain Cullie, who approached Augustine Island on November 10 on the schooner Kodiak. Apparently these statements were corroborated by a native party which hunted in Kamishak Bay during the eruptions, but studying Figure 5 (bottom) and the offshore bathymetry of Augustine Island we cannot find evidence for such major morphologic changes of the volcano. Perhaps a large floating mass of pumice was mistaken to be an island; the alleged subsidence of the northern half of the island seems to be an exaggeration of Captain Cullie (Becker, 1898).

Augustine volcanic activity must have continued for over a year after the outbreak of 1883, as interpreted from another entry in the Kenai mission log on May 27, 1885:

"Earthquakes still quite frequent here (Kenai?) and Chernabura is still smoking."

A very important narrative of the 1883 eruption which also makes reference to strong earthquake activity and tidal waves during the eruptions comes from a recently discovered field notebook from 1898 of the pioneering U.S. Geological Survey geologist, J. A. Spurr. The notebook is now in the USGS archives in Menlo Park, California:

October 17, (1898)

"Trader says here at Katmai that eighteen years ago three families from Kodiak went with families and baidarkas to St. Augustine Island to spend the winter. Built barabaras on the shore of a bay. The mountain began to shake continually and finally they took their families off, while they stayed on themselves.⁴ Finally the mountain began to shake so violently that they put all their effects in their baidarkas and started on a stormy day. Scarcely were they at the mouth of the bay when an explosion occurred, ashes, boulders and pumice began pouring down and the barabaras were buried and the bay filled up with debris. At the same time there were many tidal waves, so that the natives nearly perished with fright, yet finally escaped."

As to the dispersal of tephra from this eruption, ash from the morning eruption on October 6 accumulated to a depth of "1/4 inch" (6 mm) at English Bay (Alaska Commercial Company Records, English Bay Daily Logs, Archives, University of Alaska) and a "rain of ashes" commenced again at 11 a.m. lasting all day. Even though a considerable amount of ash seems to have fallen at Kodiak, according to Davidson (1884) (4 to 5 inches (10 to 13 cm), no ash was found in the Skilak Lake sediments (Rymer and Sims, 1976), suggesting that the wind dispersal direction was mainly east-southeasterly.

⁴The occupation and evacuation of Augustine Island by these families is also mentioned by Davidson (1884); the eruption must have been that of October 6, 1883, rather than 1880, as suggested by Spurr's reference to "18 years ago" as related by the trader.

When Becker and Purington (Becker 1898) made the first ascent of Augustine Volcano on July 22, 1895, they discovered a crater at least "1,200 feet" (370 m) in diameter with a nearly vertical inner wall, showing well-developed columnar jointing and breached to the north. An unstable inner "cone" (dome?) occupied the crater, steaming from countless crevices and separated from the outer walls by a "600 or 800 feet" (180 or 240 m) deep moat. The inner cone was nearly as high as the outer crater wall and rock avalanches frequently broke off thundering into the surrounding moat. Solfataric action blanched and reddened the surface of the cone. Figure 6 shows one of the two U.S. Geological Survey geologists, Becker or Purington, in the summit crater of Augustine, probably in 1895. Their description of the inner cone suggest that the cone was not a cinder cone as they implied but a still hot degassing vent plug. They also believed that the lava flow that can be seen in Figure 5 formed in 1883, which is clearly a misinterpretation since the flow is drawn on the sketch published by Doroshin in 1870 (Figure 5, top).

Deposits from the 1883 eruption are shown on Figure 7. The distribution of the 1883 ejecta is mapped primarily from aerial photography taken of Augustine Island in 1957. On these photographs, the most recent volcanic deposits are from the 1935 eruption while the older but still discernible, volcanic flows (debris and pyroclastics) are taken to represent the 1883 eruption. The main thrust of the debris flows of this eruption was to the north-northeast.

1902 Event

Coats (1950, quoting Sapper 1927), Detterman (1973, referring to unpublished field notes of T. W. Stanton of the U.S. Geological Survey

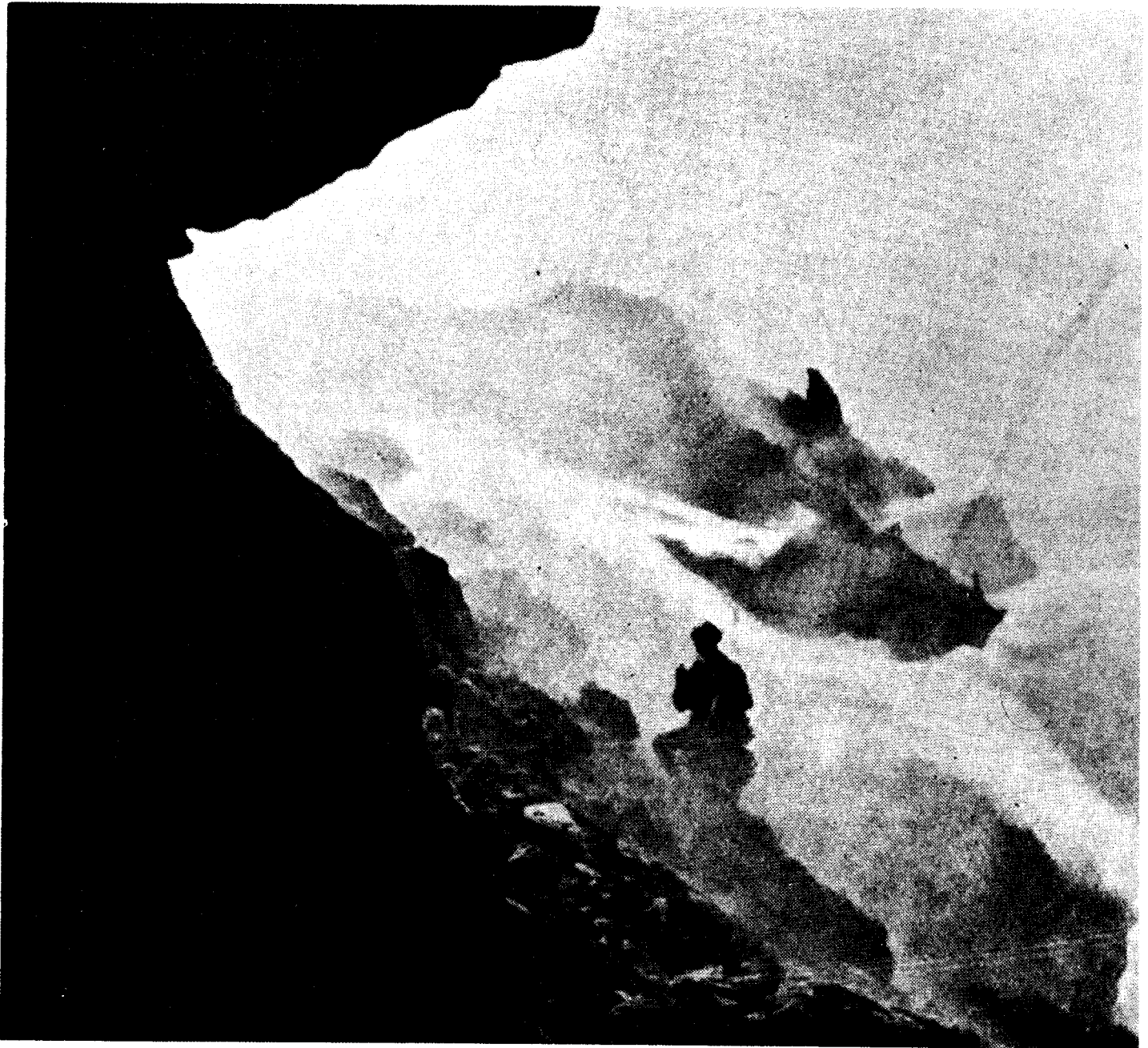


Figure 6. Crater of Augustine showing central dome in 1895 (USGS geologist is probably Becker or Purington).

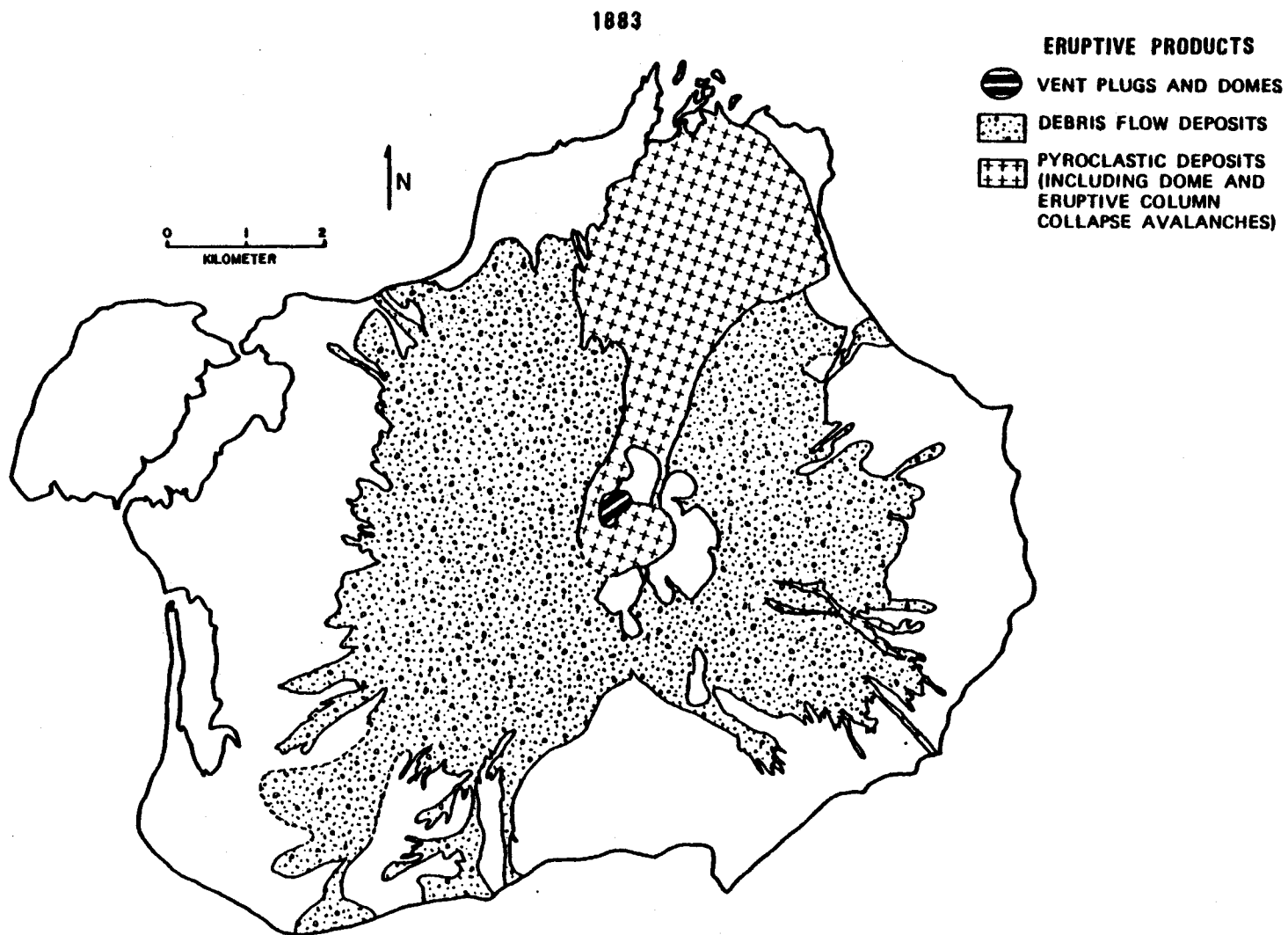


Figure 7. Distribution of 1883 eruptive products.

who visited Augustine Island on July 17, 1904) and Kienle and Forbes (1976, quoting the previous sources) report a minor phreatic explosion, partial destruction of the north crater rim accompanied by a large mudflow, and finally new dome growth and formation of a spire in 1902. Johnston (1979b) carefully reviewed the original notes and old photographs and concluded that Augustine did not have a significant eruption in 1902, except perhaps for "a large mudflow [generated] when one side of the crater broke off and slipped down, according to A. Brown who says he witnessed it from the mainland" (Stanton's field notes). Johnston (1979b) also could not identify an ash layer on Augustine Island that would correspond to a major eruption in 1902.

1935 Eruption

Detterman (1973) reports that the eruption started on March 13 and ended August 18. In mid-August a tall black eruption cloud, 10 to 30,000 feet (3 to 9 km) high, rather thin and not billowing out at the top was seen by Mr. Wahleen (personal communication) from aboard the S. S. Dellwood just after leaving False Pass on a great circle route to Seattle. Since no other eastern Aleutian volcano was active that year, it seems that Mr. Wahleen saw the final major eruption of Augustine Volcano on August 18, from a distance of about 800 km! Between March and August, minor and major eruptions were also observed from the west side of Cook Inlet. Considerable amounts of tephra were erupted, and pyroclastic flows and mudflows were concentrated on the northeastern and southwestern flanks of the volcano (Detterman, 1973; Figure 8). The 1883 dome described by Becker (1895) was presumably destroyed during the initial vent clearing eruptions, when ash spread again as far as Skilak Lake (Rymer and Sims, 1976). Finally, two new lava domes were emplaced

1935

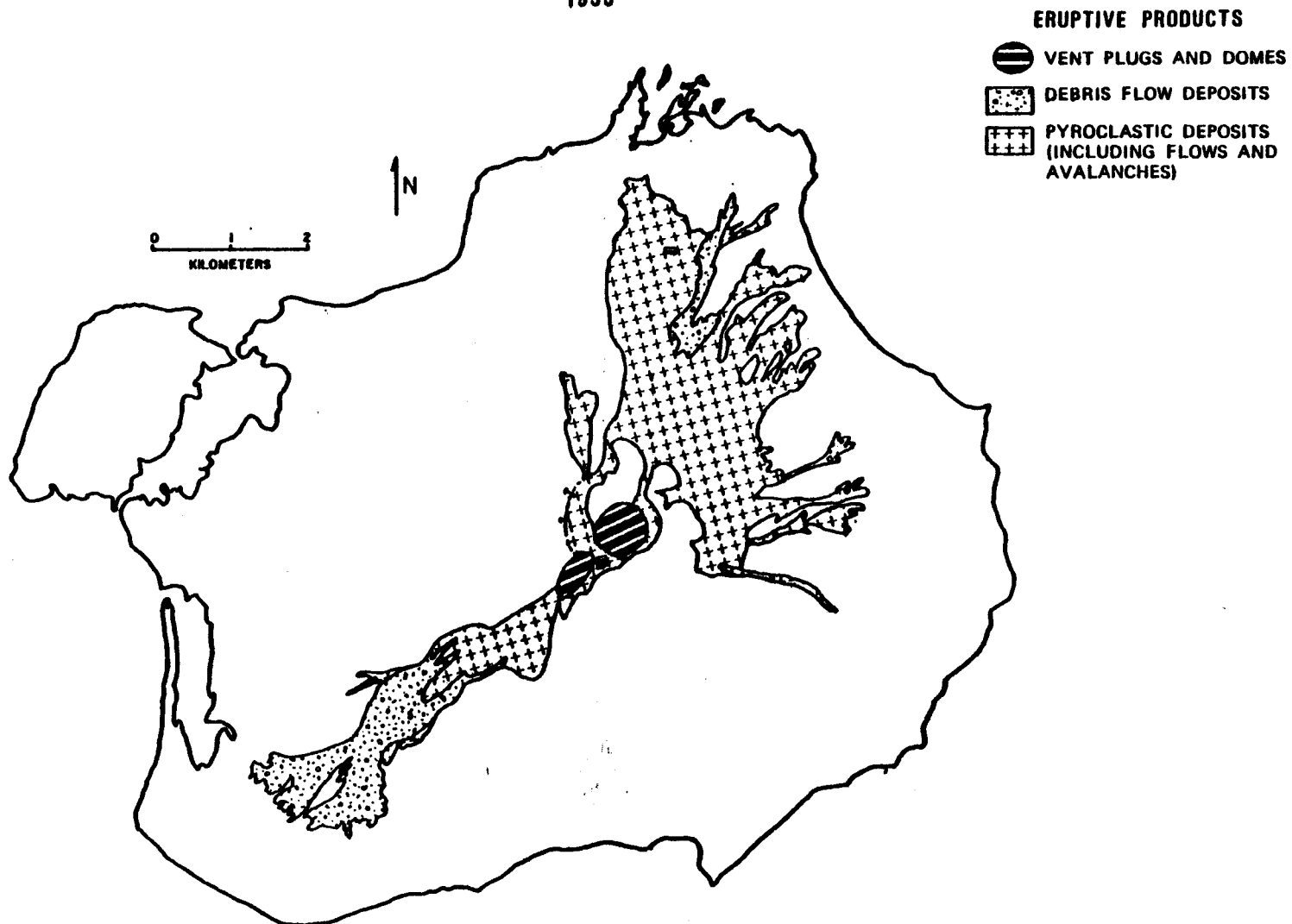


Figure 8. Distribution of 1935 eruptive products.

in the summit crater. The summit forming dome was a nearly perfect dacite tholoid, 4,025 feet high (1227 m), as determined photogrammetrically (USGS 1: 63,360 quadrangle map, Iliamna, B-2, Alaska). Thus by late 1935 the volcano had increased 498 feet (152 m) in height since Dall's first survey in 1880.

Deposits from the 1935 Augustine eruption are shown on Figure 8. Data for this figure are taken from 1957 aerial photography where the youngest volcanic features are considered to represent the 1935 eruption. The two domes emplaced during the last stages of the 1935 eruption are apparent on the aerial photographs and are also shown on Figure 8.

1963/64 Eruption

On October 11, 1963, Augustine burst into activity again, sending an ash column to about 3,000 m and a pyroclastic flow down the flank of the volcano, which set fire to brush on the lower slopes. According to Detterman (1968), the eruption continued intermittently for about 10 months, with major explosions recorded on November 17, 1963, July 5 and August 19, 1964. Presumably, during one or more of the earlier vent clearing eruptions in late 1963 ash was dispersed in a northeasterly direction and preserved in the varved sediments of Skilak Lake, 210 km distant (Rymer and Sims, 1976). Figure 9 shows an eruption photographed by Tom Hazard of the Bureau of Land Management on July 7, 1964 aboard an aircraft at 3,000 m elevation, 60 to 80 km northeast of the volcano. The eruption column reaches to about 3.5 km and tephra can be seen precipitating out of the cloud over the southwestern flank of the volcano. Many other such eruptions probably went unnoticed as there is no winter population on the shores of Kamiskak Bay and the nearest settlements are on the Kenai Peninsula, 100 km across Cook Inlet.

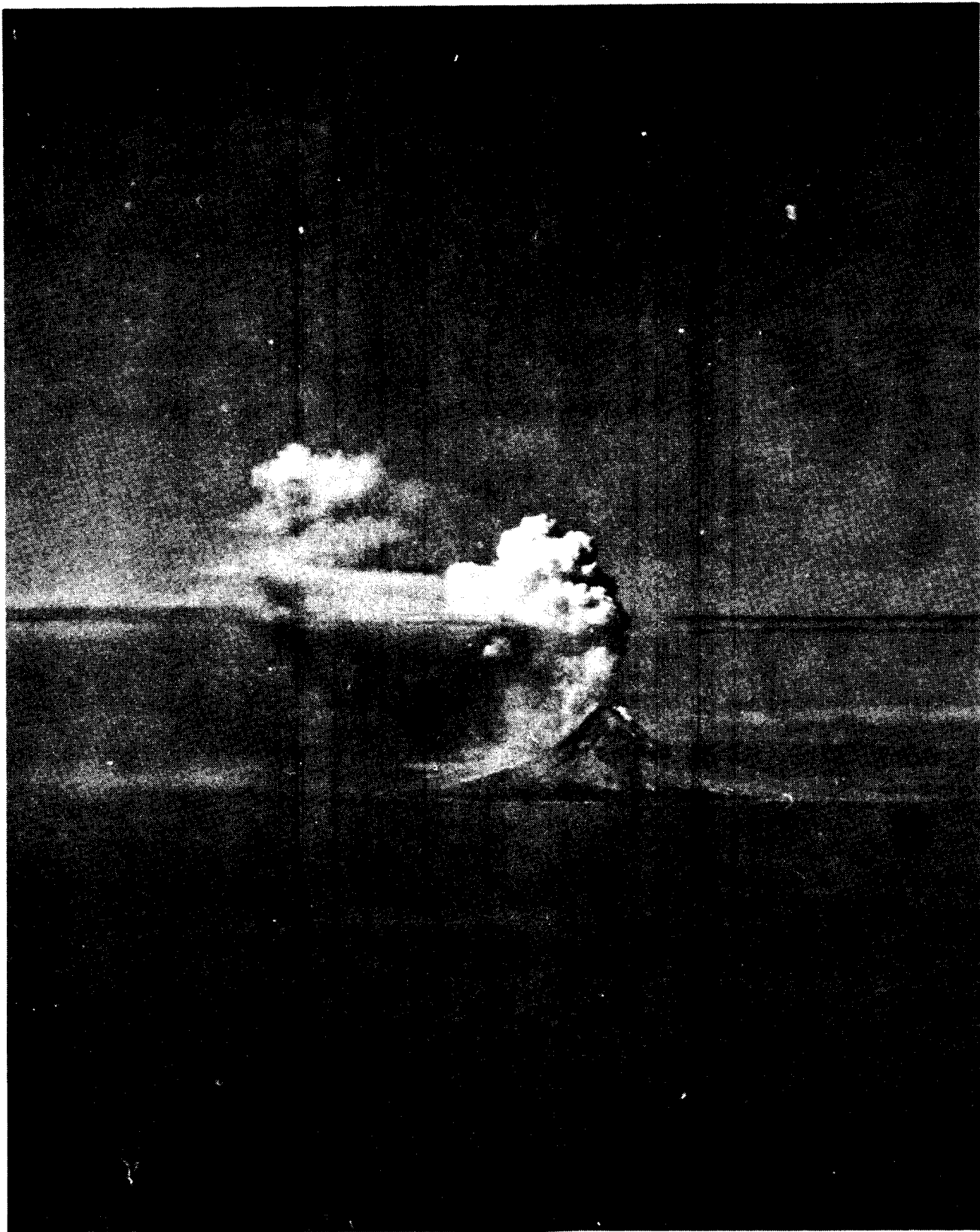


Figure 9. Augustine Volcano in eruption, July 7, 1964, as seen from the northeast (photograph by T. Hazard, BLM).

According to reports from field parties of the Pan American Petroleum Corporation (D.H. Reno, communication to R. B. Forbes) there was no unusual precursor activity during the summer 1963 field season, which terminated mid-July, but in the June-July 1964 field season the volcano was reported to be quite active and considerable ash was encountered on the mountains on the mainland up to 15 km west of Augustine. Where the ash was not disturbed it was a maximum of about 2.5 cm deep.

Detterman (1968) reports that the cone emitted smoke and steam all through 1965 and 1966, before he actually visited the island to map the deposits of the 1963/64 eruption in 1967. Detterman thought that the initial eruption was a nuee ardente eruption directed toward the southeast and originating at the base of the 1935 summit tholoid. It allegedly blew out a section of crater wall "3,200 feet long, 500 feet high and 700 feet thick".

The 1963/64 eruptions greatly altered the summit configuration and finally a new dome emerged in the new crater southeast of the remnant of the 1935 summit tholoid. By September 1964 (Figure 10) it had completely filled the crater, engulfed what was left of the eastern and southern crater rim and stood much higher than the original 1935 summit. A new summit elevation of 4,304 feet (1312 m) was determined geodetically in 1971 for the summit forming spine on top of this 1964 dome by the National Ocean Survey (J.E. Guth, written communication). Thus, at the end of the 1963/64 eruptive cycle the volcano had again increased in height by 279 feet (85 m) as compared to 1935.

The 1964 dome is an excellent example of an endogenous dome formed by internal expansion. The resulting structure is a series of inverted

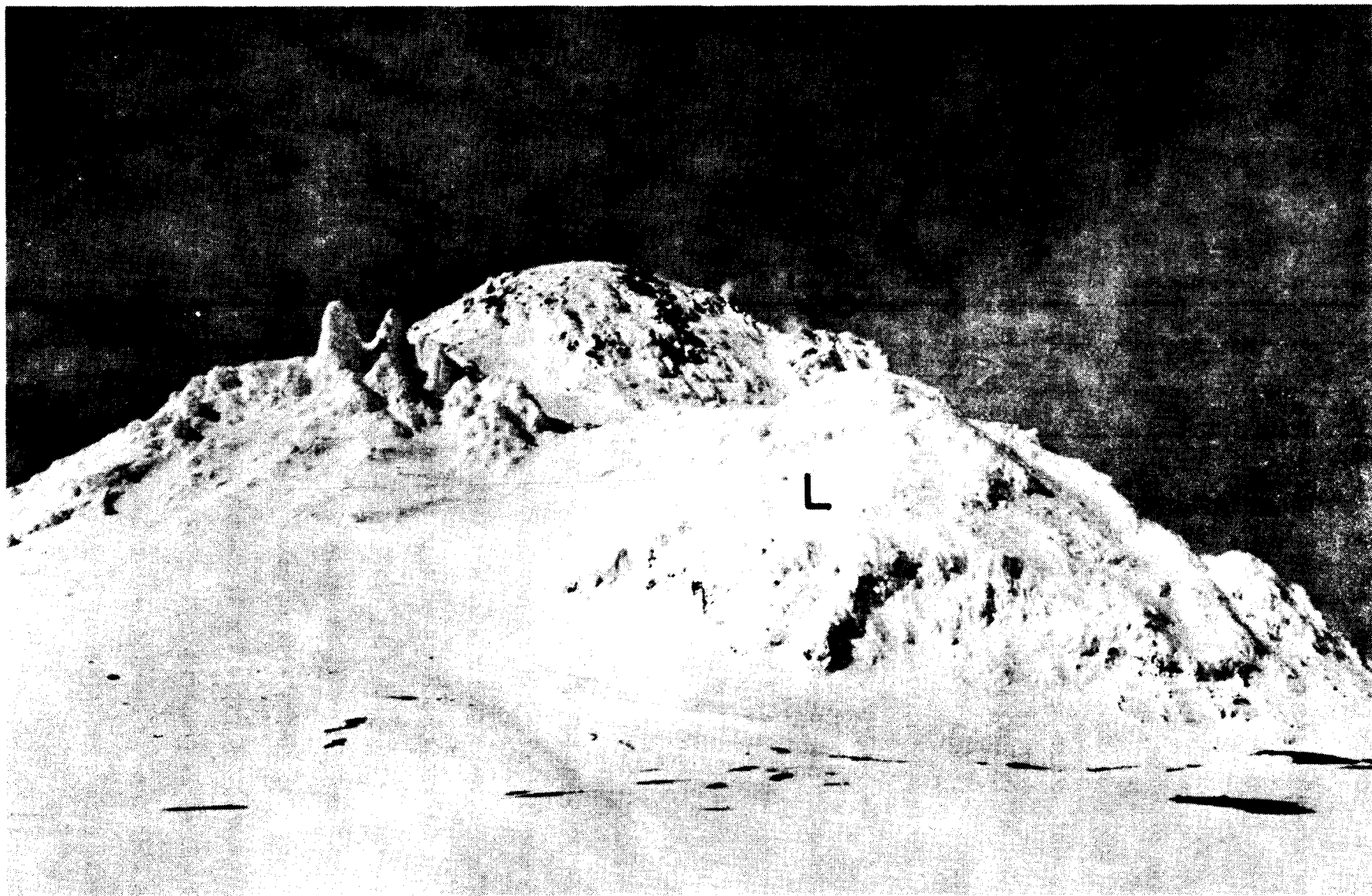


Figure 10. Augustine's summit from the northeast in 1971. The 1935 and '64 lava domes are marked, P (Pinnacles) are erosional remnants of a vent breccia, L is a short lava flow.

nested cones forming concentric moats and ridges on the surface. Much of the gas released during the cooling of the dome was released along this concentric conical fracture system.

Distribution of the 1963/64 eruptive deposits (Figure 11) is largely taken from Detterman (1968). In 1963/64 debris flows were mainly directed north, southwest and southeast. One area of Figure 11 does differ from Detterman's results and is the region occupied by the volcanic dome. The dome area shown on Figure 11 is taken from numerous photographs of the summit region between 1964 and 1976 and probably is a better representation than that given by Detterman (1968).

1971 Event

Continuous instrumental observation of Augustine Volcano began in late 1970, when the Geophysical Institute of the University of Alaska installed a radio-telemetered, vertical, short-period seismic station on its upper northern flank. Since 1970, this single station has been expanded to a 4 station island-based array and we have continuous seismic data since 1970. The only significant seismic activity prior to the precursor seismicity observed in 1975 before the 1976 eruption was an intense earthquake swarm that occurred between August 30 and September 6, 1971 (Kienle et al., 1971). The earthquakes originated within the central conduit system of the cone above sea level (Lalla, 1980) and were signaling a minor eruption. A photograph taken during the swarm by Austin Post of the U.S. Geological Survey on September 3 shows a strong plume fed by very active fumaroles on the 1964 lava dome (Figure 12). A small ash eruption and incandescence (red glow) on the flank of the volcano was seen during the late evening twilight of October 7 from a fishing boat 38 km north of the volcano. The eruption is corroborated

1963/64

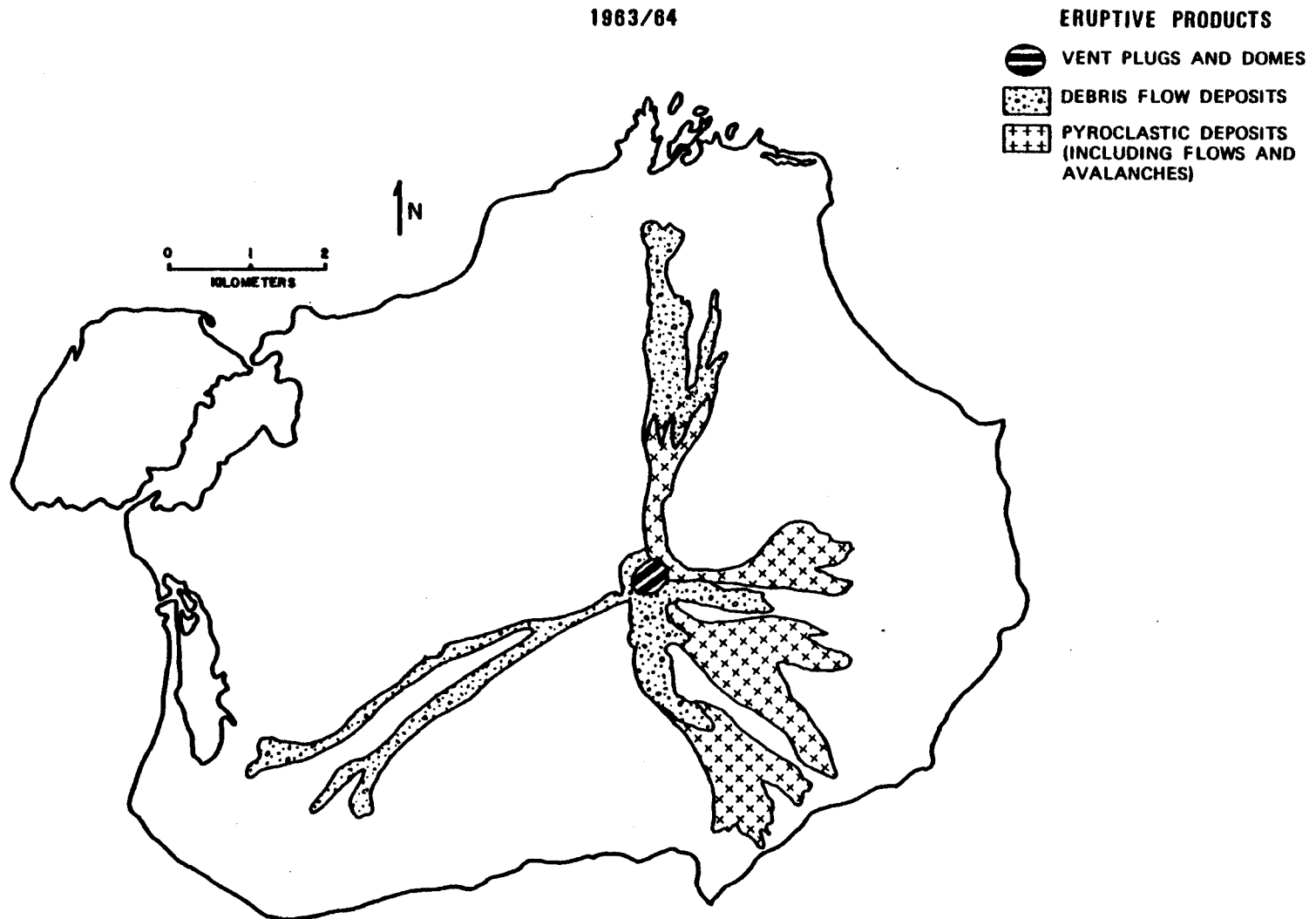


Figure 11. Distribution of 1963/64 eruptive products.

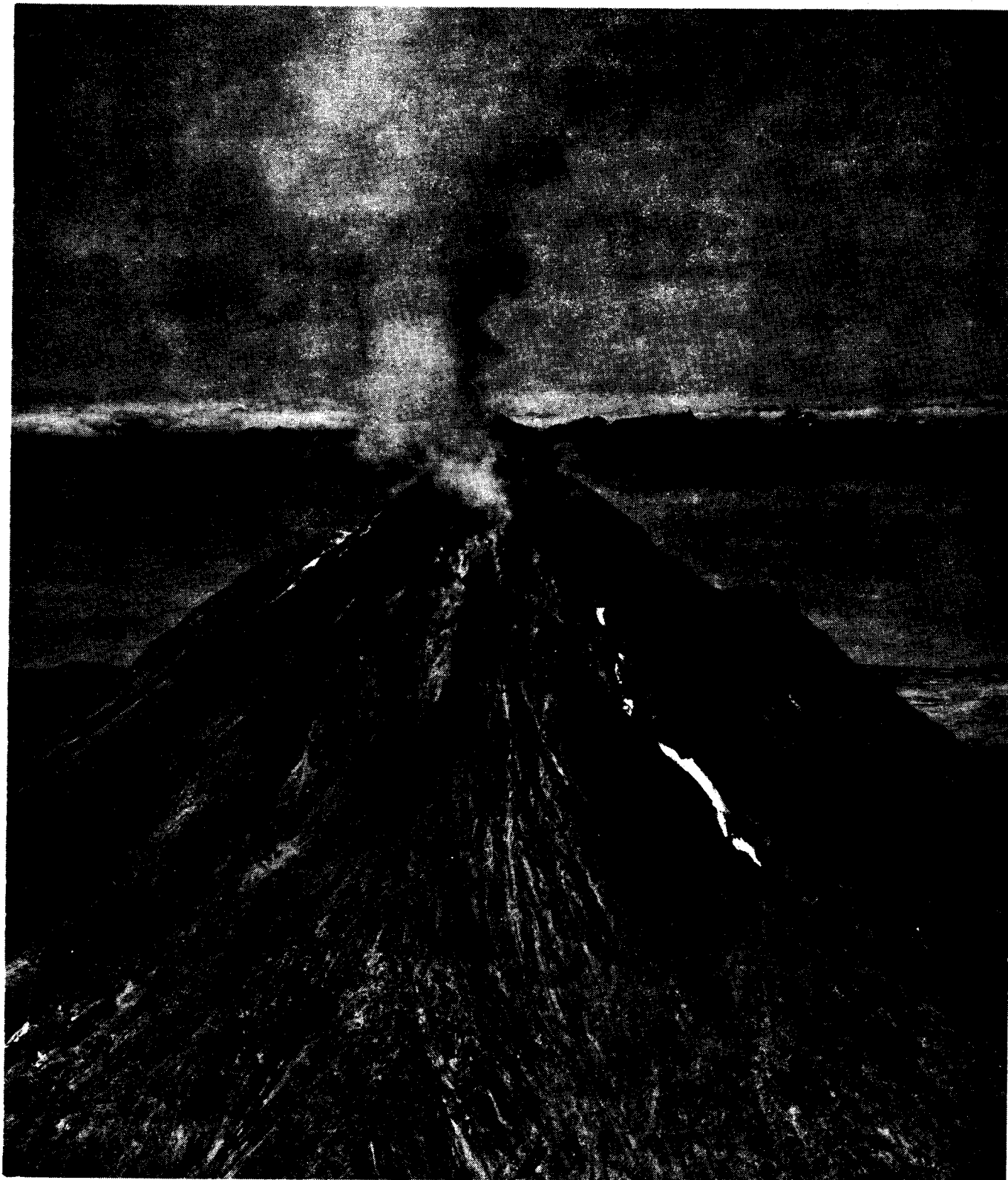


Figure 12. Augustine Volcano from the south on September 3, 1971. A strong vapor plume is being fed by fumaroles on the 1964 dome during a period of intense swarms of shallow earthquake activity (photograph by Austin Post, USGS).

by seismic eruption tremor, which was recorded on both of the then existing seismic stations between 23 and 01 hours on October 7/8.

1976 Eruption

This eruption is fairly well documented because we had intensified our geophysical surveillance of the volcano in the years prior and kept close track of the eruptive events. The 1976 sequence of events is, in our estimation, typical of what one might expect during future eruptions of Augustine Volcano and we will therefore discuss this eruption in more detail.

Geophysical Precursors

The most promising geophysical parameters monitored on other active volcanoes for the purpose of eruption prediction are:

- 1) earthquake activity - spatial and temporal variations of source region and seismic energy release,
- 2) deformation measurements - changes in distance between benchmarks and tilt,
- 3) monitoring of mass (magma) movements under ground-changes in the gravitational field,
- 4) monitoring of magnetic and electric fields-changes in these fields are caused by changes of the thermal structure (Curie isotherm), by piezoelectric effects due to pressure changes and by mass movements of conductive fluids and gases,
- 5) changes in surface and fumarole temperature,
- 6) changes in gas flux and composition.

Prior to the 1976 eruption of Augustine we had principally concentrated on (1), (4) and (5) with the following results:

a) Even though we conducted detailed geophysical experiments on Augustine's summit from late June to August 1975 and spent a lot of time in view of the mountain and camped on the summit, we did not detect any obvious signs of the impending eruption only 5 months away, except for several felt earthquakes. This was unusual as we never felt any earthquakes during the prior field seasons (1970-1974).

b) Instrumentally detected precursor earthquakes to the January 1976 eruptions were observed over a period of 8 months starting in May 1975. The events were located centrally within the volcano at depths ranging from -6 to +1 km (datum is mean sea level) but most of them occurred at depth of -1 to +1 km (Lalla and Kienle, 1978; Kienle et al., 1979; Lalla, 1980; Lalla and Kienle, 1980).

c) Two infrared radiometer surveys of the southwest face of the 1964 summit lava dome showed no change in temperature between 1974 and 1975. Snow melt pattern also stayed the same confirming this result. There was no change of heat flux between 1974 and 1975 of the hottest region on the top of the 1964 dome and all fumarole and shallow soil temperatures measured over the surface of the dome and in a fumarole field near its base were in both years below the local boiling point of 95°C (Lalla and Kienle, 1976; Kienle et al., 1979).

d) No changes were detected in the gross magnetization of the volcano between 1972 and September 1975 that would have indicated demagnetization due to heating. However, one should keep in mind that this observation is based on comparing

aeromagnetic surveys, which cannot resolve more subtle changes in the magnetization of the volcano (Barrett, 1978; Barrett et al., 1978; Kienle et al., 1979).

e) A seismic refraction survey using explosive sources failed to locate any large (>500 m) magma body at shallow depth (<1 km) beneath the volcano (Pearson, 1977; Pearson and Kienle, 1978; Kienle et al., 1979).

f) Repeated geodetic surveys since 1970 revealed no substantial (>30cm) growth of either the 1935 tholoid or the 1964 dome relative to stable reference points on the crater rim (Stone, personal communication).

In summary, the only clear precursor to the 1976 eruption was a definite increase of seismicity in the 8 months prior to the January 1976 eruptions. We judged an intense earthquake swarm on November 18 and 19, 1975 severe enough to send a reconnaissance plane to the island and to announce the event in the Homer press but the photos taken revealed no visible changes at the volcano.

Vent Clearing Phase

This phase of the eruptions was the subject of a detailed paper by Kienle and Shaw (1979). Figure 13 (taken from Kienle and Shaw, 1979) summarizes the major events of this cycle. Two preliminary explosions occurred on January 22, 1976, at 7:59 AST and in the early afternoon. The latter explosion cloud reached a height of 14 km as measured by a radar station in King Salmon (Lt. Col. Hanson, personal communication). Ash fell for the first time that evening at Iliamna, 90 km to the east-northeast.

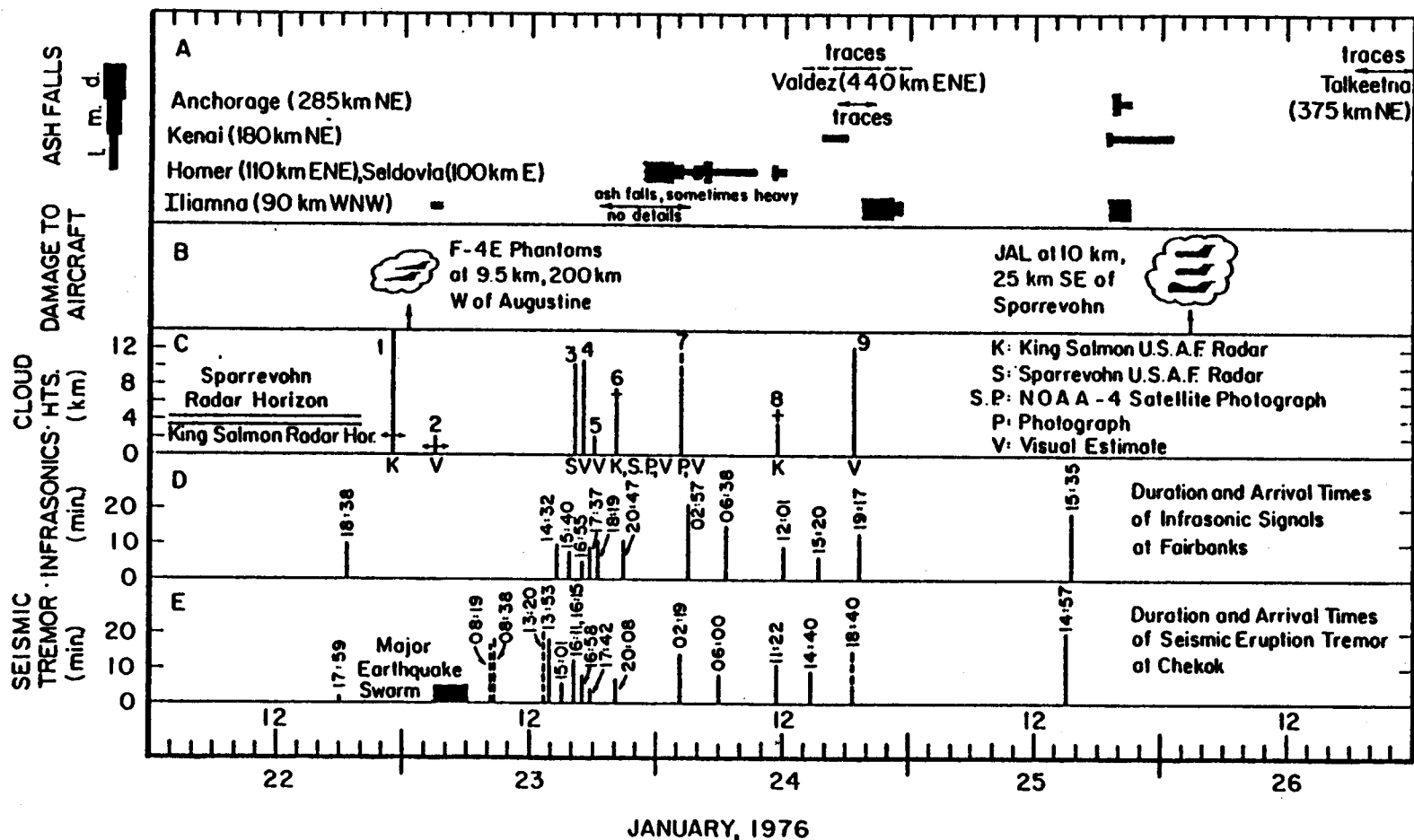


Figure 13. Summary of observations during the vent clearing eruptions of January 22-25, 1976, all times in U.T. A. Ash falls at various Cook Inlet localities based on surface weather log entries. B. Damage to aircraft. C. Cloud heights, numbers 1 through 8 refer to the source of information: 1 - Center for Short-Lived Phenomena (CSLP) event card 2367 and observations by Lt. Col. Hanson, King Salmon Radar, exact timing is not known; 2 = Iliamna Lodge residents, exact timing is not known; 3 = Sparrevohn radar; 4,5 = Federal Aviation Administration (FAA), Iliamna, M. Smith observed lightning; 6 = King Salmon and Sparrevohn radars, NOAA-4 satellite photograph indicates minimum height of 6 km, bush pilot reports a much higher (12 km) column near that time; 7 = photograph shown in Figure 16, eruption was heard 58 km north of the volcano by Chinitna Bay residents W. Byers and E. Hensley, who described the noise as a long roar, lasting a few minutes and sounding like "a gas jet at an oil well"; 8 = King Salmon radar; 9 = CSLP event cards 2367 and 2368. D,E. Arrival times and durations of infrasonic signals at Fairbanks and seismic eruption tremor at Chekok, 80 km northwest of Augustine, dashed lines indicate more questionable eruptions.

According to Lalla and Kienle (1978), an important intense earthquake swarm originating centrally within the volcanic cone near and above sea level occurred in the late afternoon of January 22: Many events were large enough ($M_L = 2.5-3.2$) to be seen on seismic stations throughout the lower Cook Inlet region (up to 150 km away). This 3 hour long earthquake swarm released two orders of magnitude more seismic energy ($5 \times 10^9 J$) than had been released during either November or December, the most active months of precursor seismicity. The swarm probably signaled the breaking up of the rock column above a shallow (probably <3km deep) magma chamber.

Ten hours later, the main sequence of vent clearing eruptions began, resulting in the destruction of the 1964 summit dome and blasting out a crater 200 m deep (as determined by a radar altimeter), 600-700 m in diameter and breached to the north (Zoller, personal communication - he overflowed the volcano after the January vent clearing eruptions on a gas and ash sampling mission with NCAR personnel aboard an Electra aircraft).

From January 22 to 25, 1976, 13 major eruptions were detected seismically and infrasonically in Fairbanks (Wilson and Kienle, 1976) and there may have been others. Some of the eruptive plumes were observed by local residents of Lower Cook Inlet communities, were seen on U.S. Air Force radars and were photographed by the NOAA-4 satellite. Frequent lightning was sighted in the clouds (Figure 14). Of the 13 eruption clouds of late January several may have penetrated the tropopause, at about 10 km at the time of the eruptions. Ash was deposited over the entire Lower Cook Inlet region, over the Kenai Peninsula, reaching as far north as Anchorage, Talkeetna (375 km north) Cordova and

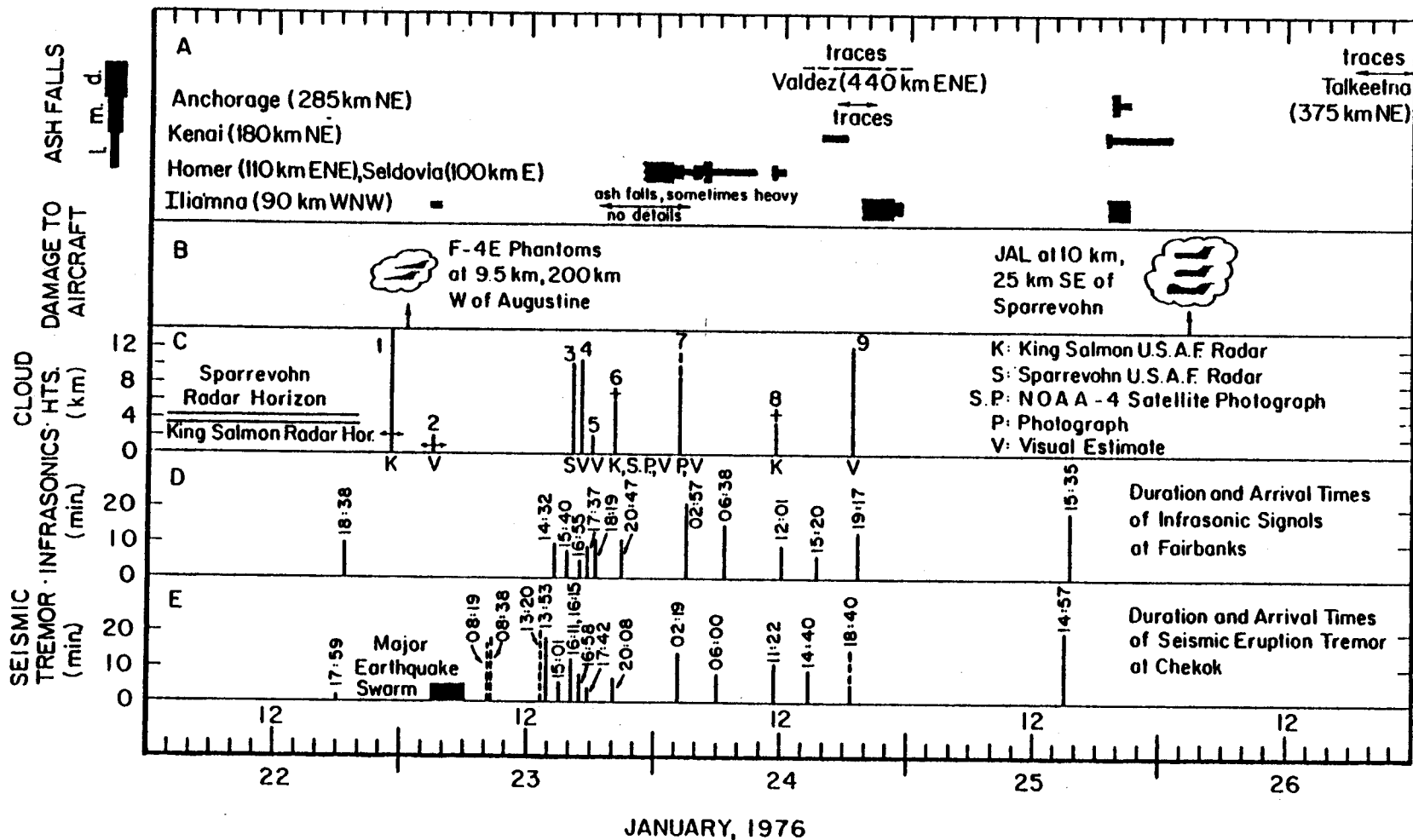


Figure 13. Summary of observations during the vent clearing eruptions of January 22-25, 1976, all times in U.T. A. Ash falls at various Cook Inlet localities based on surface weather log entries. B. Damage to aircraft. C. Cloud heights, numbers 1 through 8 refer to the source of information: 1 - Center for Short-Lived Phenomena (CSLP) event card 2367 and observations by Lt. Col. Hanson, King Salmon Radar, exact timing is not known; 2 = Iliamna Lodge residents, exact timing is not known; 3 = Sparrevohn radar; 4,5 = Federal Aviation Administration (FAA), Iliamna, M. Smith observed lightning; 6 = King Salmon and Sparrevohn radars, NOAA-4 satellite photograph indicates minimum height of 6 km, bush pilot reports a much higher (12 km) column near that time; 7 = photograph shown in Figure 16, eruption was heard 58 km north of the volcano by Chinitna Bay residents W. Byers and E. Hensley, who described the noise as a long roar, lasting a few minutes and sounding like "a gas jet at an oil well"; 8 = King Salmon radar; 9 = CSLP event cards 2367 and 2368. D,E. Arrival times and durations of infrasonic signals at Fairbanks and seismic eruption tremor at Chekok, 80 km northwest of Augustine, dashed lines indicate more questionable eruptions.

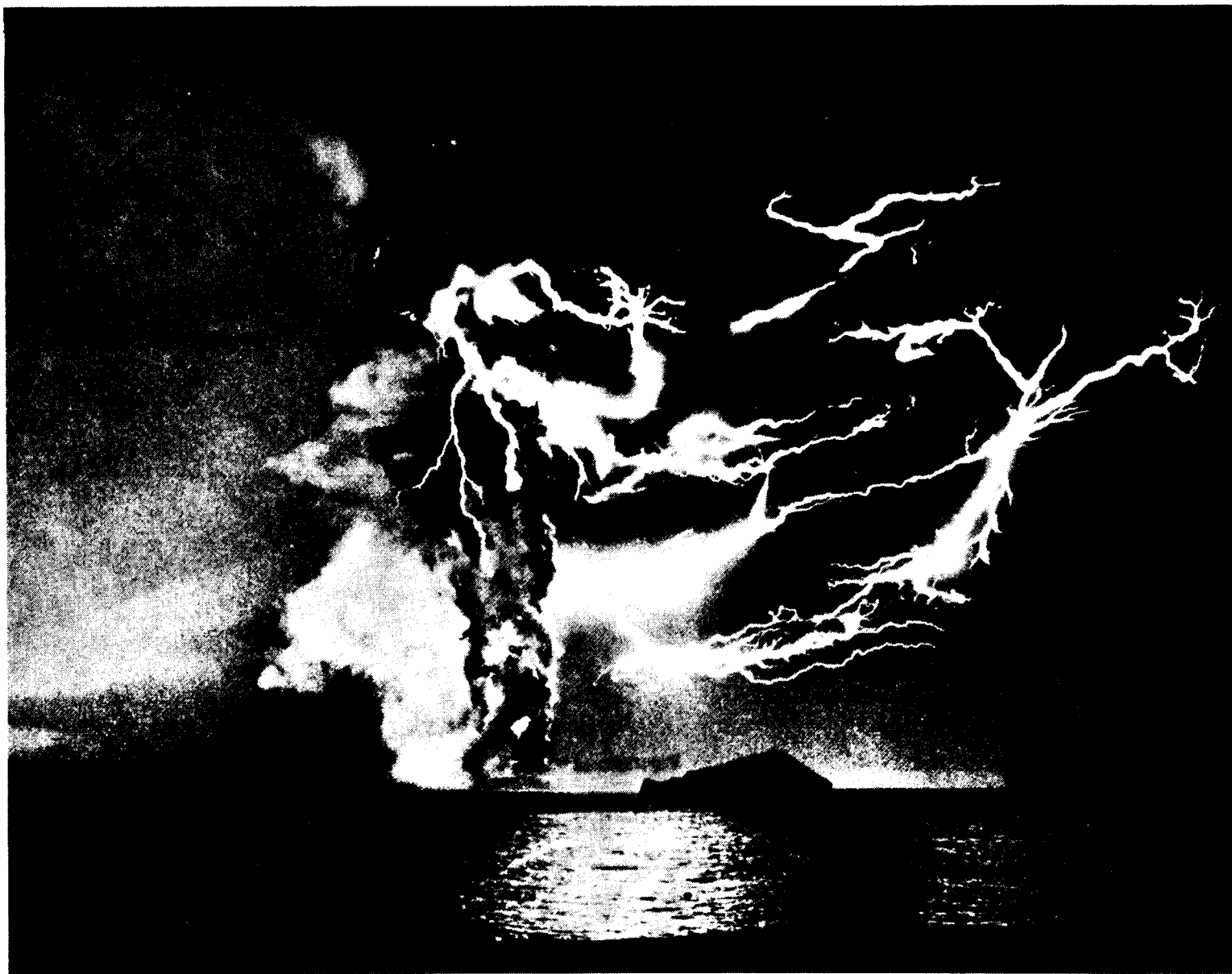


Figure 14. Lightning storm in eruption clouds of Surtsey Volcano, Iceland, December 1, 1963. Similar lightning has been reported for 1976 Augustine eruption clouds but we have no photo documentation of it (photograph taken from Thorarinsson, 1967).

Valdez, and over southeastern Alaska, where ash fell at Sitka, 1100 km distant (Figure 15).

A spectacular eruption occurred just before sunset on January 23, 1976, 16:19 AST. The anvil-shaped eruption cloud was photographed by one of us (J. Kienle) flying at 3,300 m altitude, 325 km northeast of the volcano (Figure 16). A low-lying cloud deck obscured visibility below 1,000 m. Photo-triangulation on the plume showed that most of it traveled below the 8-km level. A high-speed gas jet directly over Augustine volcano reached a height of 11 km and penetrated the tropopause. The plume was spread out horizontally over 52 km by westerly winds when the photograph was taken. Figure 17 shows a sequence of frames of the same eruption seen head-on from the town of Homer, 110 km east-northeast and downwind from the volcano. Shortly after the last frame was taken, sand-sized (millimeters) ash particles began to fall out in Homer reducing visibility to a few hundred meters. Ash dispersal throughout this eruption was mainly governed by the high altitude winds. It is interesting to note that during several eruptions high altitude and surface winds dispersed the ash in opposite directions.

The ash dispersal of the January 22-25 eruptions was mainly to the north and east and rather limited to the west and south. Even though most communities in southern Alaska (from Talkeetna south), in Cook Inlet, the Kenai Peninsula and in Prince William Sound received ash, muddy rains or ashy snowfalls, no ash fell on King Salmon or Kodiak throughout the eruptions.

The rapidly changing weather conditions between January 22 and 25 strongly affected the local ash dispersal. On the late afternoon of January 22 ash was carried to the west to the Iliamna Lake area (no

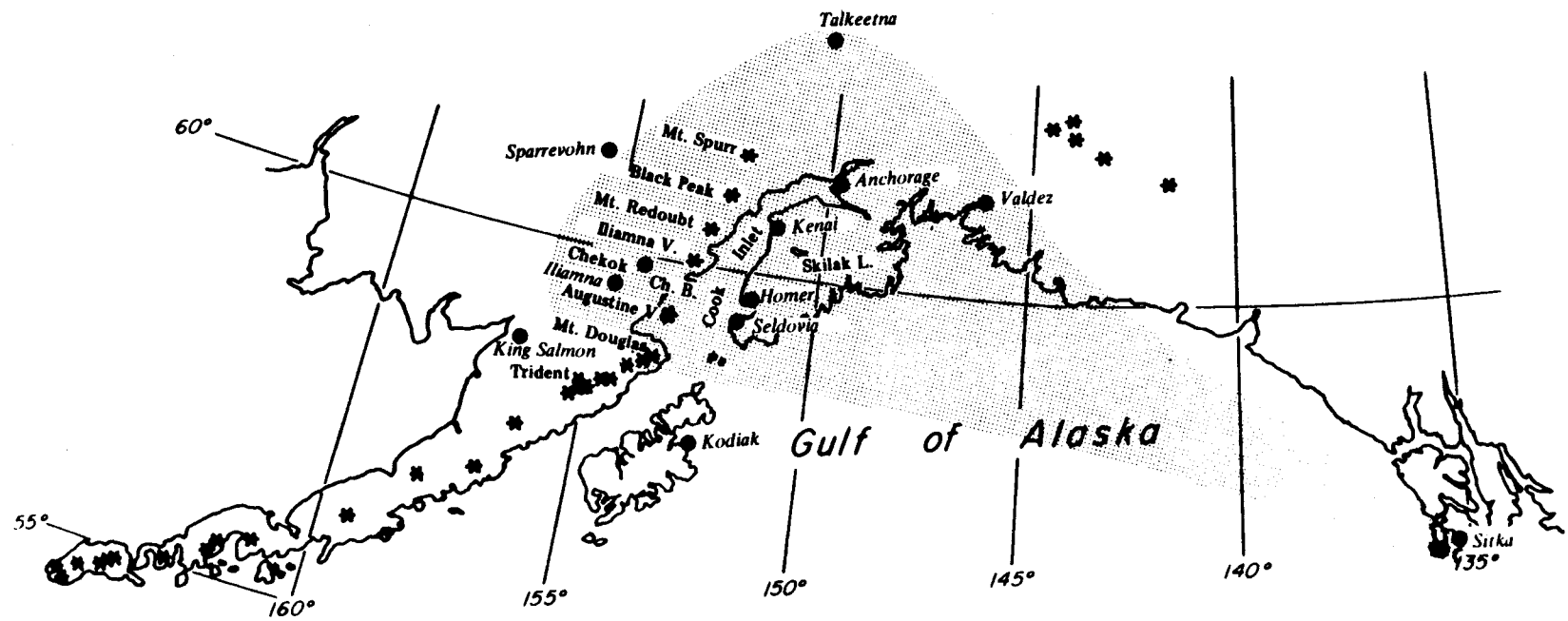


Figure 15. Area of ash fallout from 1976 Augustine eruptions.

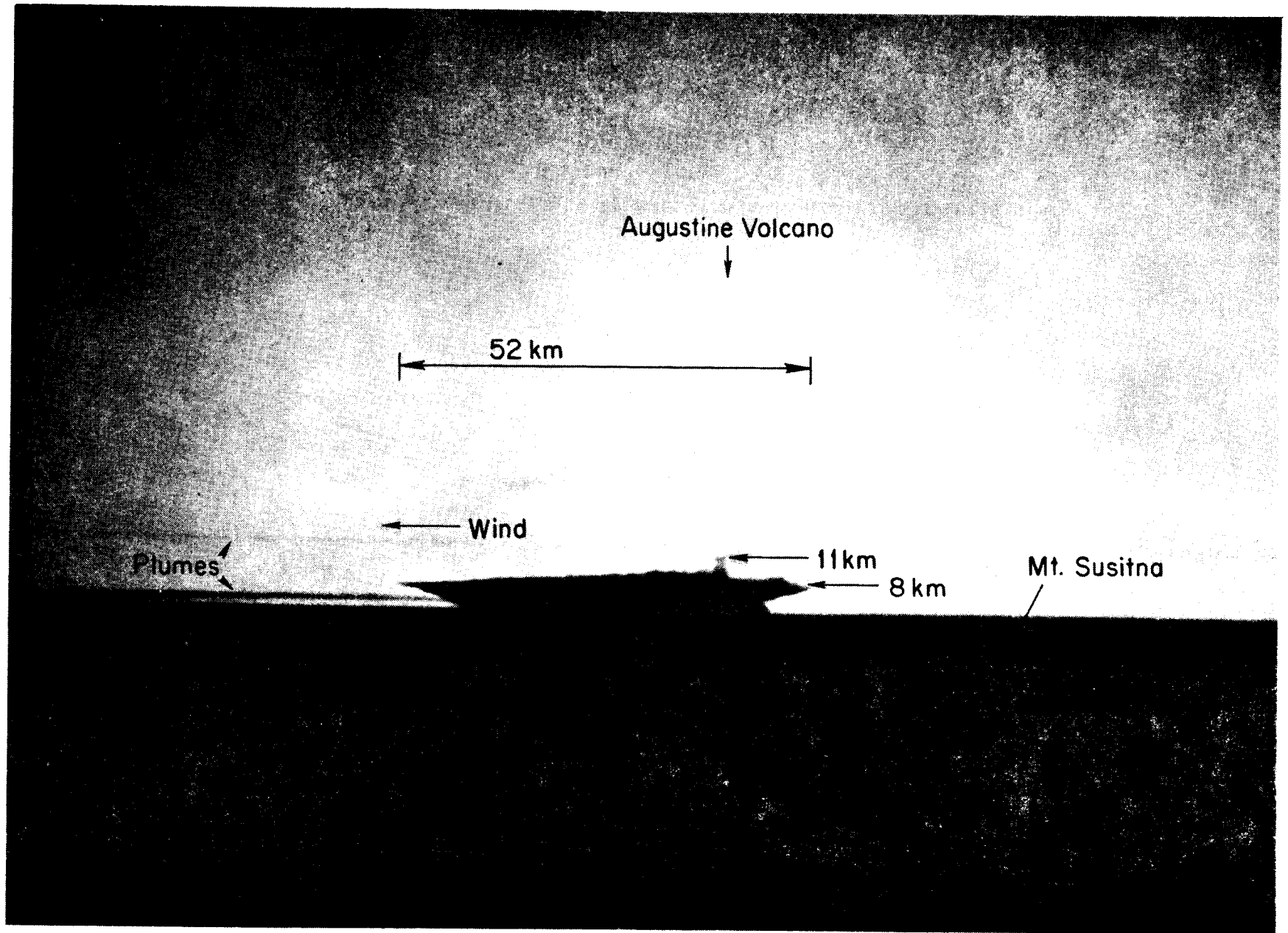
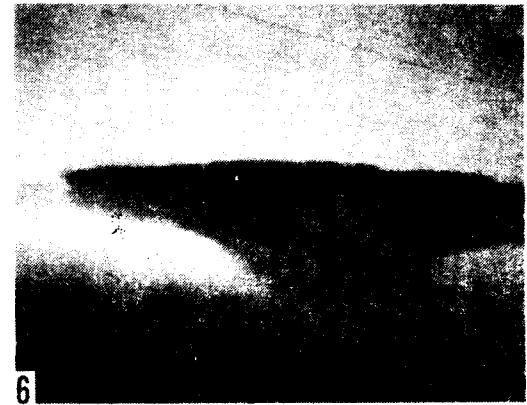


Figure 16. January 23, 1976, 16:19 AST, eruption seen against the twilight sky from aboard a Cessna 180 light plane flying at 3,300 m altitude, 325 km northeast of the volcano near Talkeetna. A gas jet marks the position of the volcano.



482

Figure 17. Same eruption as in Figure 16 seen head-on from Homer spit, 110 km east-northeast and downwind from Augustine Volcano. Photographs 16:20 to 16:45 AST by W. G. Feetham.

infrasonically or seismically detected event correlates with this ash fall, but Lt. Col. Hanson observed a huge, 14 km tall, 70 km diameter plume over Augustine on the King Salmon radar on the early afternoon which may have been the eruption that later caused the ash fall at Iliamna). A NOAA-4 satellite photograph taken on January 23, 10:10 AST, shows a string of high altitude eruption clouds from explosions at 3:53, 5:01, 6:11, 6:58, 7:52 and 10:10 AST being dispersed to the east by 60 knot winds blowing at an altitude of 6-8 km. An eruption was actually in progress when the picture was taken (Figure 18). In spite of this high altitude westerly flow, the 6:58 or 7:52 eruptions, or both, produced a dense ash fall at Iliamna 90 km to the west of the volcano reducing the visibility on the runway to less than 30 m, implying that easterly surface winds may have carried the ash that far to the west. During the daylight hours of January 23, a high pressure ridge developed over the Alaska Peninsula which resulted in a strong westerly flow over Lower Cook Inlet at 6 to 8 km altitude, where most of the ash traveled. As mentioned above, the spectacular 16:19 eruption shown in Figures 16 and 17 spread eastward over the lower Kenai Peninsula, namely Homer and Seldovia, where 185 g of sand-sized ash was deposited in a 1 m² sampling area in 1 hour as the cloud passed overhead. Ash from this eruption eventually reached Sitka during the night of January 23. Between January 24 and 25 upper level winds generally blew more from the southwest dispersing the ash toward the upper Kenai Peninsula resulting in trace amounts of ash falling as far north as Anchorage, Talkeetna, Cordova and Valdez. Major eruptions occurred on January 23, 20:00, January 24, 1:22, 4:40 and 8:40 and January 25, 4:57 AST.

In Anchorage, fine ash mixed with snow fell in the very early morning hours on Saturday, January 24, and on Sunday morning, January



Figure 18. NOAA-4 satellite photograph of southern Alaska, January 23, 1976, 10:10 AST, in the visible (0.6 - 0.7 μm), showing eruption plume being dispersed across the Gulf of Alaska. An eruption is in progress and the 5.8 km high eruption column casts a shadow (arrow).

25, another large black cloud associated with the 4:57 AST eruption reached the city at about 9 a.m., reducing the visibility from 30 to 4 km! Miller (1976) reported that only 0.5 mm of brown ash accumulated, consisting of sharp angular fragments less than 0.1 mm across, but that was enough to irritate eyes of people wearing contact lenses, ruin the cross country skiing and scour layers of corrosion off the blades of natural-gas-powered turbines, actually increasing the efficiency of the machines.

Effects on Augustine Island

The following account of eruption-related effects on Augustine Island is principally taken from a paper by Kienle and Forbes (1976):

When a field party helicoptered to the island on January 29 during a break in activity following the vent clearing set of powerful eruptions, the island was thickly mantled by ash, and pyroclastic flows, probably formed by eruption column collapse (Johnston, 1978; Sparks et al., 1978). These deposits were noted on most flanks of the volcano, but occurred predominantly on the lower northeast slope (east of Burr Point). The flows in this northeast sector had reached the sea, forming an area of 0.1 km² of new land along a stretch of beach 3 km long. A fumarole field was actively degassing on the distal end of one of the pyroclastic flows where the hot ejecta had impacted on water-saturated beach sands (Figures 19a and b). Temperatures greater than 400°C were measured 2.7 m below the surface of the upper pyroclastic flow unit east of the research station.

During that first visit we found that a small hut which had been built on the northeast flank of the volcano in earlier years of the project (Figure 20) had been severely damaged by one or more nuées

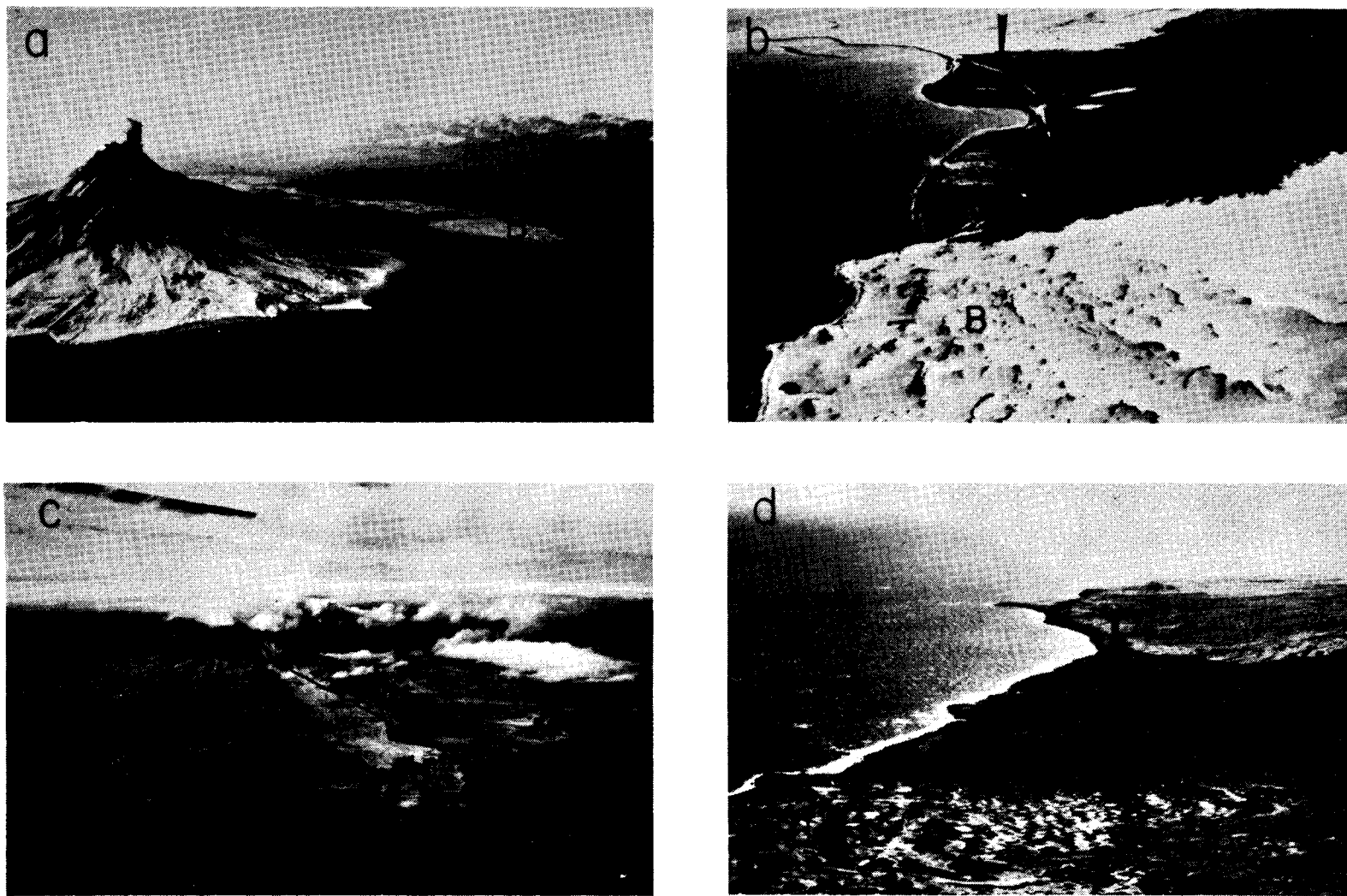


Figure 19. (a) Augustine from the east, February 1, 1976, showing new pyroclastic flow deposits on the northeast beach. (b) Close-up of the pyroclastic flow deposits, looking east, February 1, 1976; arrow points to old beach line, B marks Burr Point. Note steam rising from the deposit seaward of the old beach line. (c) Augustine from the north, June 13, 1976, showing distribution of pyroclastic flow deposits, arrow marks Burr Point cabin site. (d) Same beach as in (b) on February 27, 1976; the early February pyroclastic flow eruptions have altered the beach line significantly. Photographs a, b and c by R. E. Wilson.



Figure 20. Bury Point Camp before and after passage of a glowing cloud (nuee ardente). Note mountainward dent in smaller generator building, produced by back-eddy effect when the nuee passed over the small ridge protecting the camp.

ardentes (glowing clouds). The main research station at Burr Point (see Figure 19c for location arrow), a corrugated aluminum building, had sustained major damage from air blast and thermal effects, accompanying nuée ardente eruptions (Figure 21), although relatively little ejecta had fallen on the site (see Figure 19b for location of Burr Point - area B). The Burr Point location had been chosen for proximity to a sheltered harbor for resupply and access by sea. Additionally, the two corrugated aluminum buildings were sited on the lee side of a small hill for protection against possible blast effects - a provision which proved totally inadequate for the January nuée ardente activity. The site and the surrounding low hills were mantled by a relatively thin blanket of ash lapilli and small blocks of pumice and andesite, probably associated with the January 25 eruption. Residual clumps of charred grass projected through the ejecta blanket, and driftwood along the beach was charred on the side toward the volcano though relatively undamaged on the opposite side (Figure 22). Drums of jet fuel cached at our helicopter pad were not ignited, although paint on the barrels was discolored. The helicopter pad was not in the lee of the hill, but the barrels were nearly covered with snow prior to the eruptions. All of the windows were broken on the north side (seaward side) of the main building, which faced away from the volcano. The corrugated aluminum siding was also dented in from the same side. The siding was torn loose from the east end of the building and two mattresses were incinerated near the window opening. Mattresses in protected positions were not ignited. The roof had been pierced by falling ejecta ranging in size from lapilli to small blocks. The floor was covered by about 5 centimeters of fine ash. A vertical 2" x 4" antenna support on the roof was charred on the side away from the volcano,

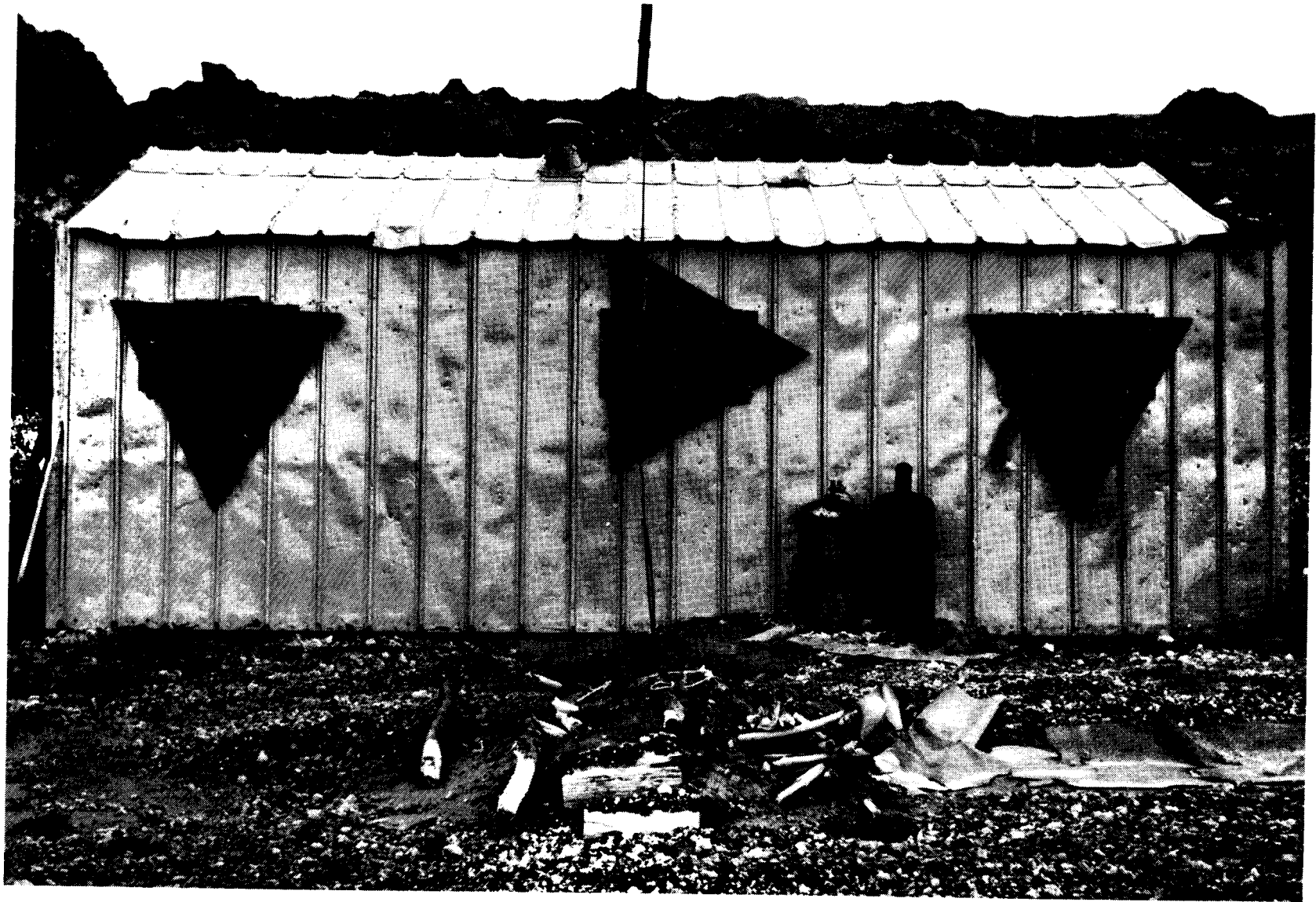


Figure 21. The main aluminum building at Burr Point dented and punctured by steep angle impact of lapilli from the side facing away from the volcano. All windows were sucked out by the Venturi effect of the passing hot cloud (photograph by H.-U. Schmincke, Ruhr-Universität Bochum, W-Germany).



Figure 22. Charred driftwood burned by passing nuée ardente at Burr Point (photograph by H.-U. Schmincke).

uncharred on the other side. Exterior covering on R-G4U coaxial cable leading to the support was also partially melted. A plastic towel holder located under the kitchen window sill showed the effects of partial fusion, and a plastic measuring cup on a shelf at window level was also partially melted (Figure 23). Some of the paper wrappings and cartons on these same shelves showed incipient charring. A battery which was sitting on the floor opposite a window also showed the effects of incipient melting.

Based on the damage discussed above, we conclude that the Burr Point camp was overrun by one or more nuées ardentes. Considering the relatively thin blanket of ejecta and the similarity of the pumice and lithic fragments to that in the lower pyroclastic flow unit in the January series of deposits east of Burr Point, we deduce the following history:

(1) One or more major explosions were accompanied by nuées ardentes down the northeast slope of the volcano. At Burr Point, Johnston (1978) distinguished at least 3 fine ash layers beneath the coarse January 25 blanket of tephra that could have formed by nuée ardente activity.

(2) The research station was not in the direct path of the basal glowing avalanches, which turned east near the head of the Burr Point high terrain but was overrun by turbulent hot gas and dust clouds (nuée ardentes), which initially formed above the avalanche but then detached from the main flow and traveled straight over Burr Point and out to sea.

(3) The dust cloud flowed at high speed over the small hill mountainward of the buildings broke the windows probably by Venturi suction (the glass was laying outside!) and then formed a back eddy which dented the aluminum siding on the seaward side of the building (Figure 20, bottom).

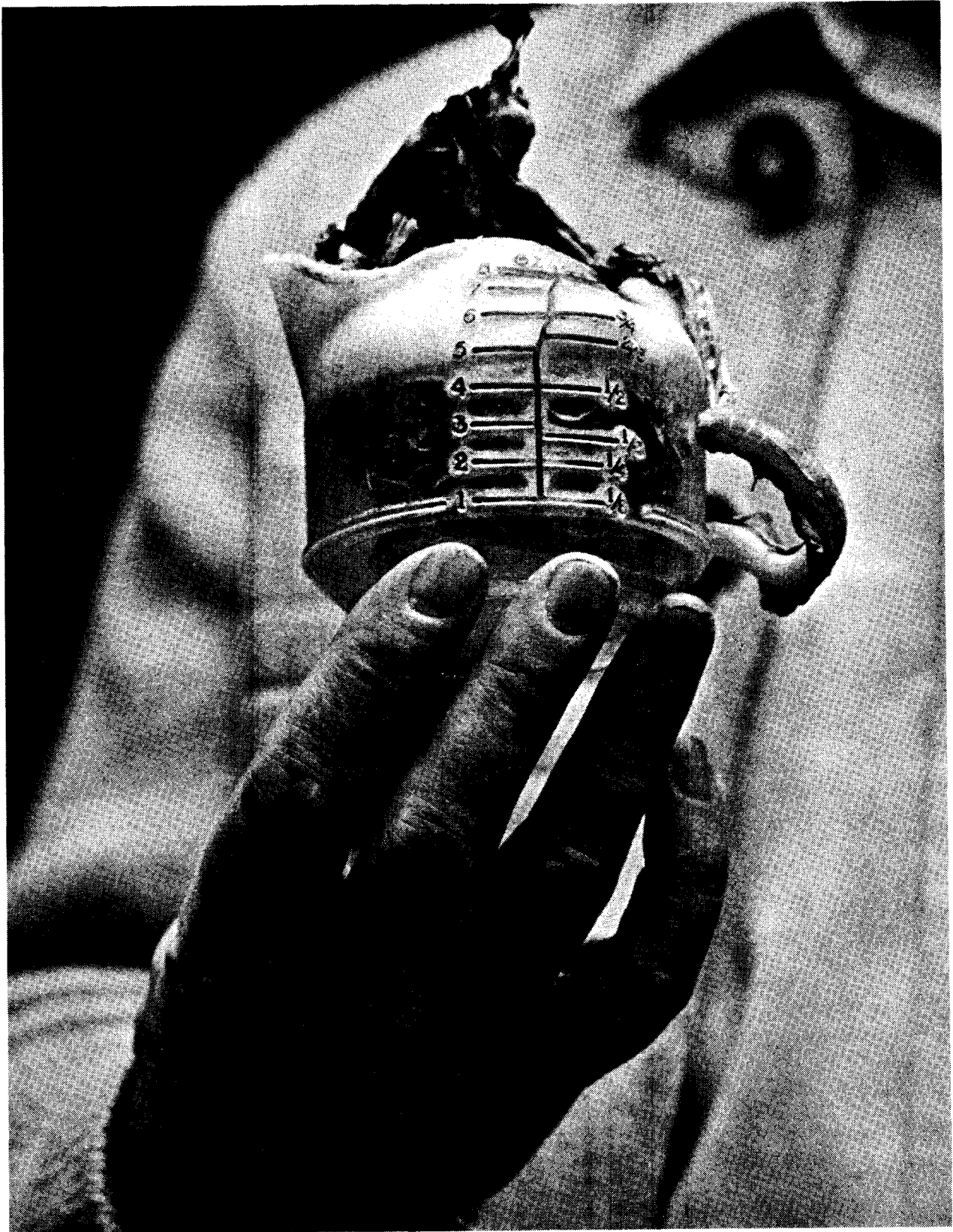


Figure 23. Partially melted plastic measuring cup recovered from inside the main building at Burr Point.

4) Gas and ash of a hot dust cloud passing over the camp flowed through the window openings, igniting mattresses and partially melted low-temperature plastics.

(5) Perforations in the roof were made by small bombs (one was however 10 to 20 cm in diameter - at a distance of 6 km from the summit!).

(6) A rain of lapilli and small bombs thoroughly dented the aluminum by high angle impact from the seaward side of the building (Figure 21).

(7) Clearly, no resident would have survived the nuées ardentes that swept through the camp. We had located the station in defilade behind a ridge for shelter from possible blast effects, and we were also misled by the fact that the site was at a relatively long distance (6 km) from the vent as compared to other potential sites on the island. Nevertheless, the glowing clouds not only reached the site, but were probably lethal on the lee side of the ridge. The nuée(s) ardente(s) must have passed the station at great speed (order 50 m/sec or 180 km/hr, as measured by Stith et al., (1977)) and their temperature was probably several 100 °C (300 to 700°C). Death to residents would have most likely occurred through inhalation of hot dust particles, burning the lung tissue as in St. Pierre in 1902 (Anderson and Flett, 1903).

In spite of this damage, the Burr Point cabin was a welcome bivouac shelter for a field crew of us, who were stranded at Augustine from February 2 to 5 because one of our helicopters had crashed due to an engine failure. During that time we were amazed to find island survivors of the eruption. Fox tracks crossed the new pyroclastic flows on the northeast sector and we saw a group of foxes at the small western island. Other wildlife was apparently not so lucky as we found the charred wing

of a seagull laying atop the new pyroclastic flow deposits on the northeastern flank of Augustine.

February-April eruptions

After 12 days of quiescence, explosive activity on Augustine was renewed at 04:43 AST on February 6, when muddy rain and ash was reported from Kenai and Soldotna on the Kenai Peninsula and the last infrasonic signal from the 1976 Augustine eruptive cycle was recorded in Fairbanks (all further eruptions were too weak to produce any more infrasonic signals that could be seen on the Fairbanks detection array). There is a suggestion that both the solid earth as well as the ocean tide may have triggered explosive activity (Kienle and Forbes, 1976). Major eruptions preferentially occurred near the peak (or maximum load) of the ocean tide as did the 04:43 February 6 eruption. On February 6 a pilot from Seldovia, Gary Gunkel, flew to the island and landed his Supercub on the beach on the west side of Augustine. Figure 24 is one of the spectacular eruption photographs he took on that day. Fresh mudflows (black) and lighter colored dry pumice and pyroclastic flows (overriding black mudflows) descended again nearly all flanks of the volcano, as can be seen from his view from the west. The eruption column had actually begun to collapse when the picture was taken and is feeding a dense nuée ardente which is descending the northeastern flank of the volcano. The same eruption was photographed shortly after noon by M. Tollefson from a commercial Wien Air Alaska airliner on its way from King Salmon to Anchorage (Figure 25). The eruption column rose to a height of about 5.5 km and a few hours later gave rise to a dense "blizzard-like" ash fall at Homer, reducing the visibility to about 1 km. This eruption is an example of an eruption that was too small to generate any seismic signal on mainland stations or generate an infrasonic signal.

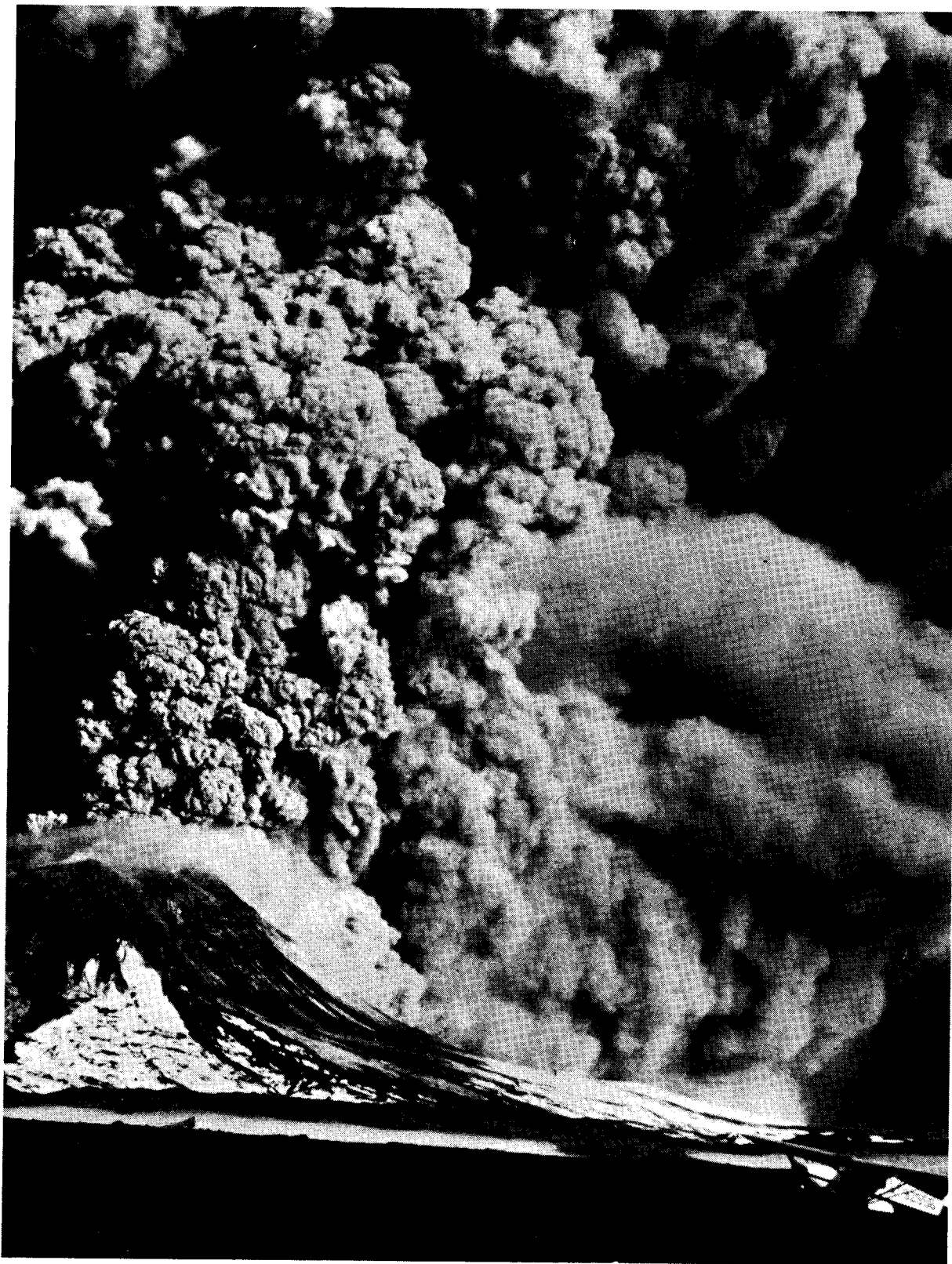


Figure 24. Augustine Volcano in eruption on February 6, 1976. A nuée ardente is descending the northeast side (Burr Point area) of the volcano. Fresh black mudflows have melted the snow in places (photography by G. Gunke1).



Figure 25. Same eruption as shown in Figure 24 photographed from aboard a commercial jet airplane. The eruption column is 5.5 km high. Shock wave phenomena can be seen in the atmosphere above the erupting volcano (photograph by M. F. Tollefson, National Park Service).

Between February 6 and 15 a crew of cloud physicists flew frequent missions over the volcano with a special aircraft (modified B-23), equipped to sample gases and small particles. They witnessed several ash eruptions, one or more northward directed blasts and pyroclastic avalanches with associated nuées ardentes (Hobbs et al., 1977; Stith et al., 1977). Figure 26 shows one of these nuées ardentes on February 8, 14:00 AST, issuing from the northern notch in the new summit crater rim and descending the northeastern flank of the volcano. According to Stith et al. (1977) who photographed the cloud with a time lapse camera, the nuée rushed down the mountain at a speed of 50 m/sec (180 km/hr) while on the upper steep ($\sim 1:3$) slopes and then slowed to about 6 m/sec (22 km/hr) near the base of the cone (slope $\sim 1:25$). The total distance traveled by this small nuée was about 5 km. Strong winds of about 25 m/sec (90 km/hr) caused the nuée to drift away from the basal pyroclastic avalanche. Stith et al. report that while most of the avalanche was still on the steep slope, a dense black cloud (nuée ardente) was billowing from it along its entire length. Later, the nuée overtook the toe of the slowing ground avalanche near the base of the volcano, while the rear portion of the pyroclastic avalanche was still speeding down the steeper inclines of the cone. Finally, a white plume rose from the place near shore where the avalanche had entered the sea. The volume of this particular avalanche was probably too small for it to continue beyond a few 100 m underwater.

The high mobility of these pyroclastic avalanches is caused by fluidization as the incandescent material within the flow autoexplodes releasing hot gases and fine particles (Sparks, 1976; Sparks and Wilson, 1976) and as air is entrained in the flow. The January pyroclastic

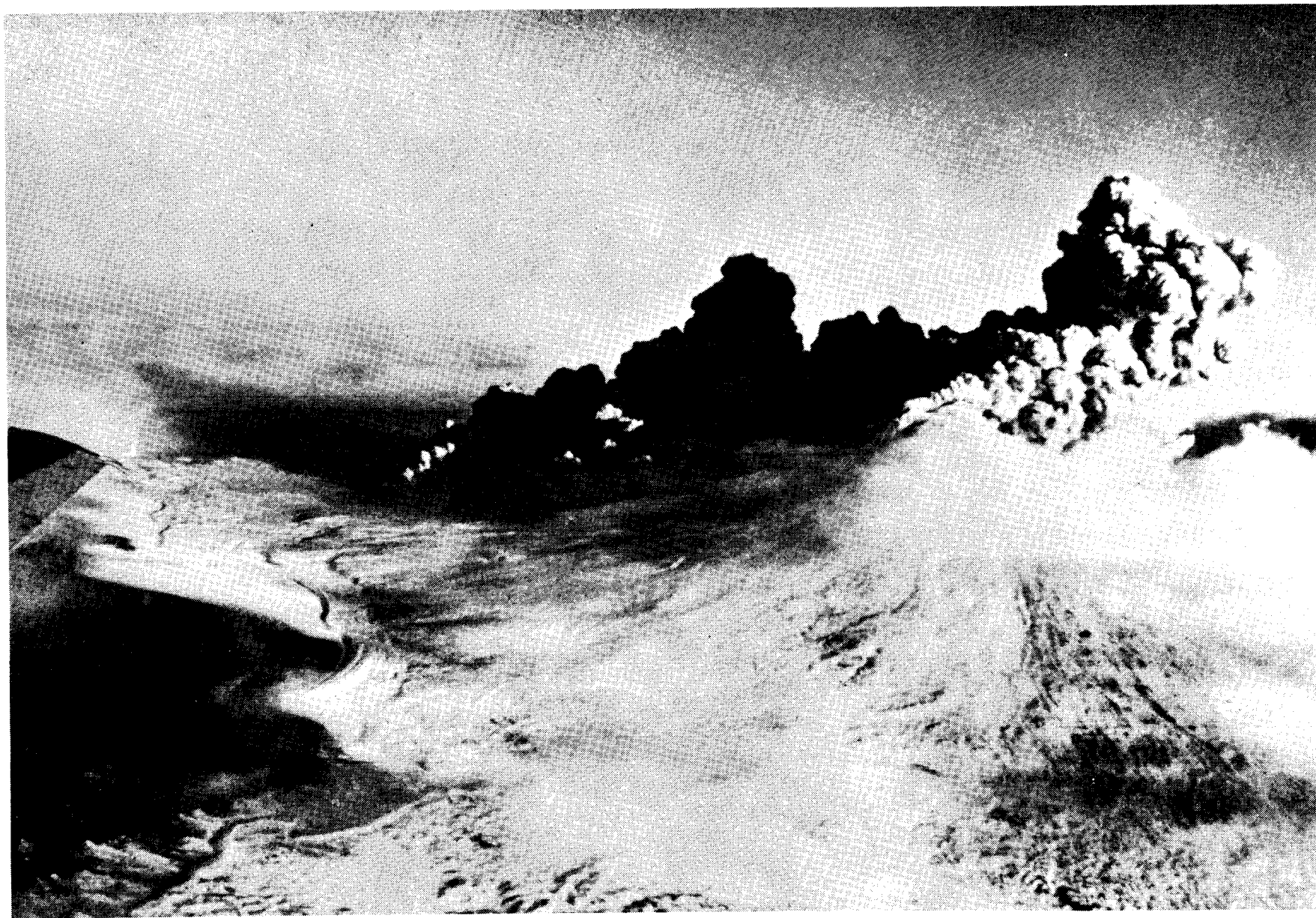


Figure 26. Nuée ardente (glowing cloud) descending toward Burr Point on February 8, 1976, 14:02 AST. The nuée reached a maximum speed of 50 ms^{-1} (photograph taken from article by Stith et al., 1977).

flows were so mobile that the avalanche producing the deposits seaward of the beachline shown in Figure 19a actually jumped the original beach bluff leaving charred blades of grass still standing when we visited the island in late January. Evidence that January avalanches higher up on the volcano became airborne can be seen in Figure 27 top right (arrow), where black avalanche deposits on the right side of the summit suddenly end on top of a small bluff created by an old lava flow, and then continue far below it.

The frequency of eruptions declined from February 6 to about 16 per day. On the most active day, February 8, Reeder and Lahr (1976) reported about 10 explosion earthquakes, detected at a seismic station (CKK) 75 km northwest of the volcano. No more ashfalls were reported from the Kenai Peninsula after February 6/7.

By February 12, a new dome began to intrude the January crater (Figure 28) and associated with this intrusion pyroclastic flow activity changed from the eruption column collapse type (Soufrière) to the dome collapse type (Merapi) (see also Figure 29).

Schmincke and Johnston (1977) report that:

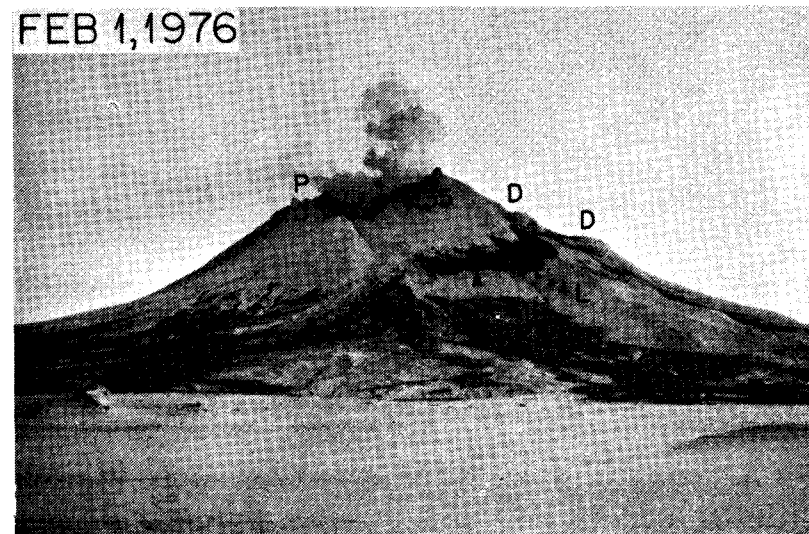
"...early deposits (January 22-25, February 5~8) are distributed radially about the island, contain abundant banded and unbanded pumices and accidental clasts, and have vesicular glass coatings on crystals, thin gradually to their margins, and are associated with extensive ash-cloud and air-fall deposits. Later deposits (February ~8-18, mid-April) were emplaced below a breach in the crater wall only, are coarser grained, nearly monolithologic (dacite), have poorly vesicular shards and glass coats, lack pumices but contain expanded bombs to 10 meter diameter, and terminate in steep lobate flow fronts.

Early pyroclastic flows probably formed by collapse of an eruption column. Abundant ash formed in the eruption column and from the flows. Decrease in gas content and/or crater widening may have lead to the gradually decreasing areal extent of the flows. Later flows appear to have formed by collapse of a dome, which first appeared in the crater [around] February 10. Little ash was produced during these eruptions..."

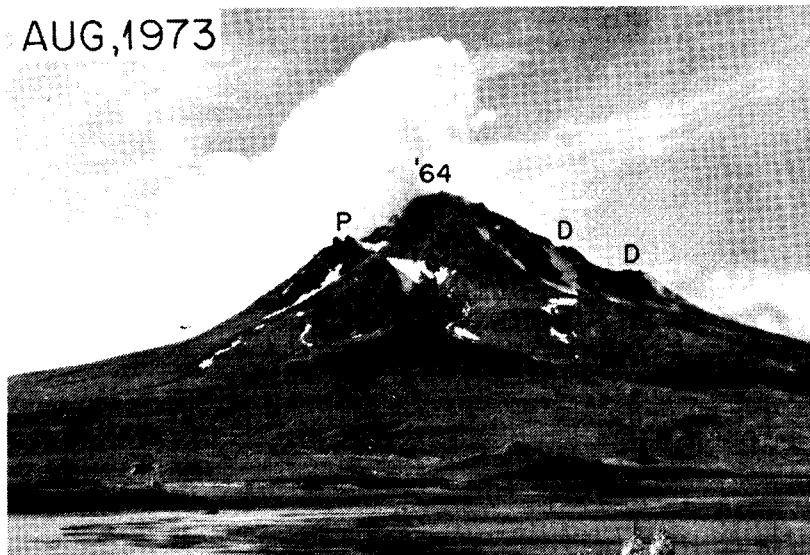
1909



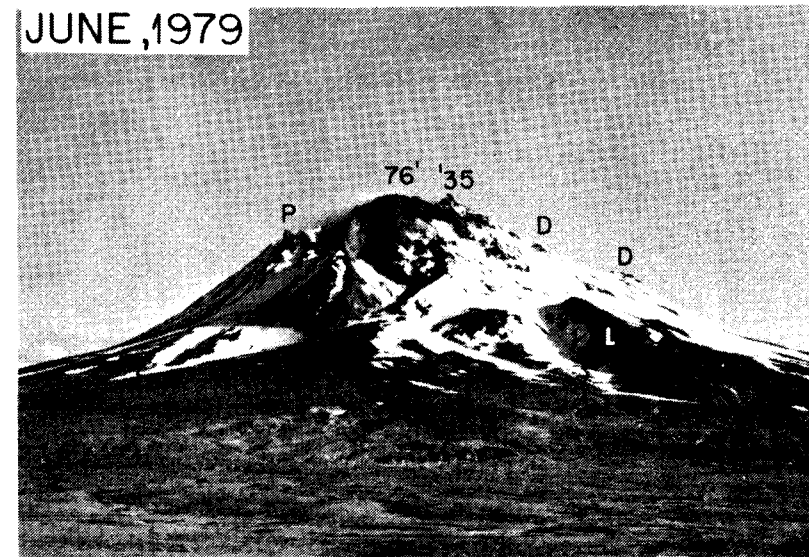
FEB 1, 1976



AUG, 1973



JUNE, 1979



500

Figure 27. Series of historic photographs from the north, showing the evolution of Augustine Volcano. Reference points for comparison are P = pair of pinnacles, D = two prehistoric lava domes, and L = lava flow. SP is the former South Peak, engulfed later by the 1963-64 lava dome. M is a mudflow erupted in 1963-64. The 1935, 1964 and 1976 lava domes are marked. Chernaburoy, meaning "black-brown" (island) (Orth, 1967). The Feb. 1, 1976 picture shows the new crater formed in January; the fresh pyroclastic flows contrast black against the snow, arrow marks the place where one flow jumped a cliff-forming old lava flow.

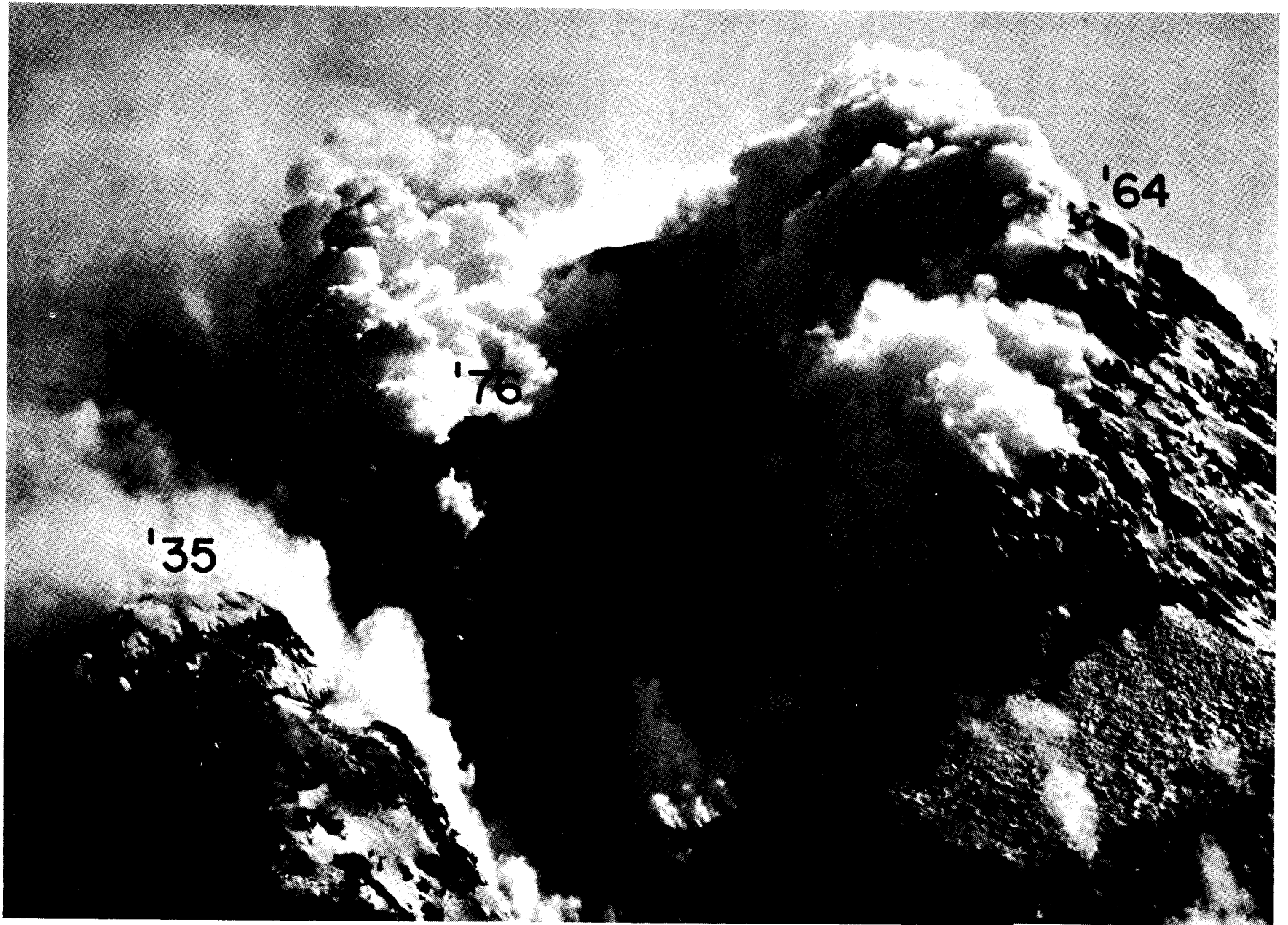


Figure 28. Close-up of the 1976 lava dome; 1935 dome remained unchanged; most of the 1964 dome has been removed during the January explosions.

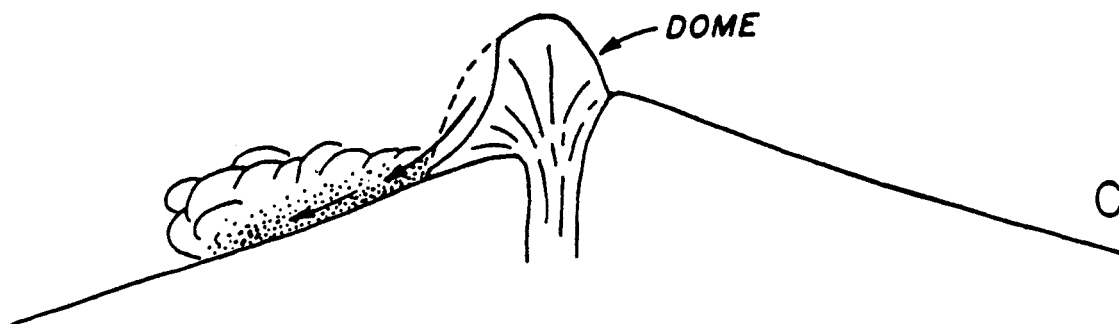
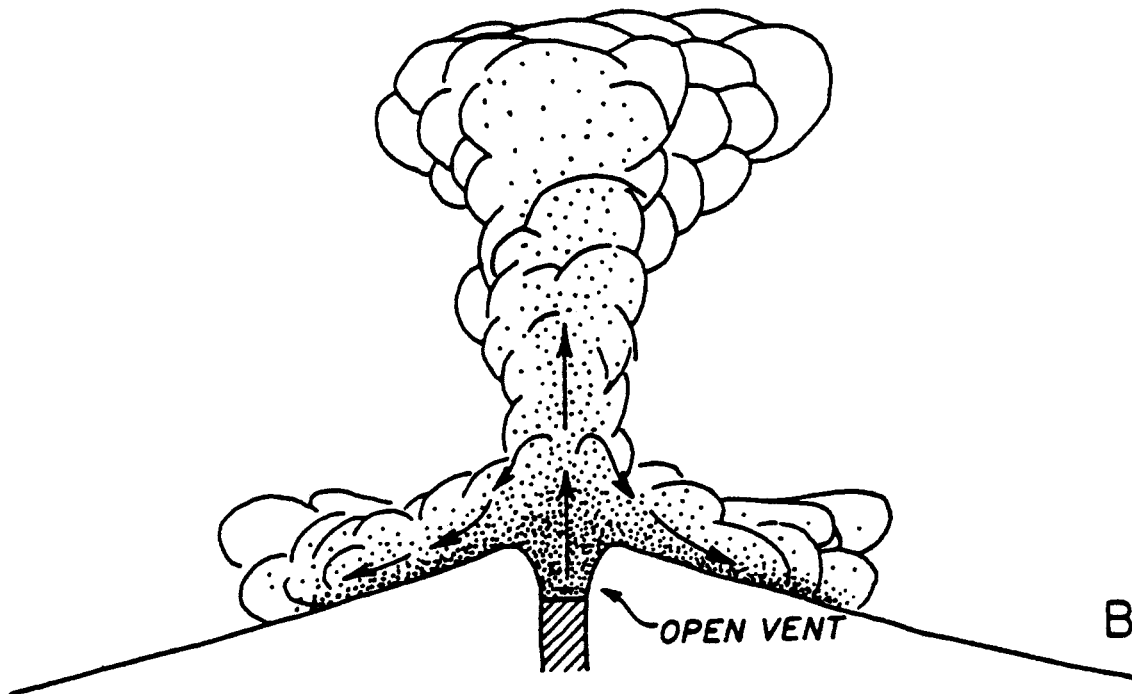
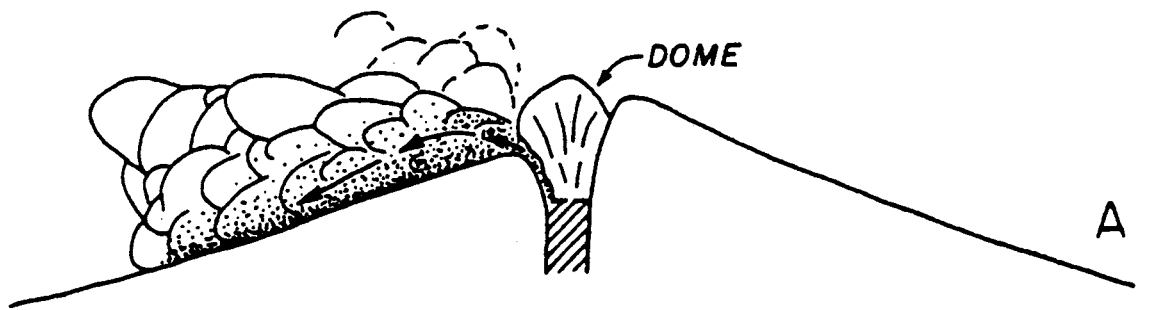


Figure 29. Types of glowing (pyroclastic) avalanches and associated nuées ardentes: (A) Pelée type (directed blast); (B) Soufriere type (column collapse); (C) Merapi type (dome collapse), taken from Macdonald, 1972, p. 149).

A University of Alaska team visited the volcano again during the period February 18-28. Although the Burr Point station had sustained no further damage, many additional pyroclastic flows of the Merapi type had been deposited along the same general path as the earlier flows. Strong fumarolic activity extended at least 2 km upslope from the beach line. Temperatures of 600°C at a depth of 5 meters were measured at a location several hundred meters up from the beach (Figure 30). The main heat source of the deposit were large juvenile blocks of the new lava dome that were entrained in the debris flow. By September 26, 1976 the bottom hole temperature had dropped to 434°C and a year later on August 2, 1977 it had cooled to 76°C, i.e. below the boiling point.

"All flow deposits were emplaced at high temperatures (>600°C), are coarse-grained ($M_d > 2\text{mm}$), have small areal extent ($< 5\text{ km}^2$) and volume (0.001 km^3), and contain abundant lapilli (degassing) pipes." (Schmincke and Johnston, 1977). The total volume of the 1976 pyroclastic flow deposits in the northeast sector of the volcano (Figure 31) was determined by digitizing the pre and post-eruption topography and is 0.05 km^3 . A similar computation for the volume of the 1964 pyroclastic flows and mudflows in the same sector yields a volume of 0.024 km^3 .

Figure 32 is a photograph by H.-U. Schmincke showing the fan of avalanches that developed on the north side beneath the collapsing new dome which was vigorously steaming in the summer of 1976. Figure 33 is a close-up of the notch carved by the February pyroclastic flows - the brightly colored area (due to active sulfur deposition) in Figure 32 at the base of the new dome. At that location the January/February dome avalanches actually eroded out a gorge in the older debris flow deposits (notice people for scale) which was again partially buried by debris from the April avalanches.

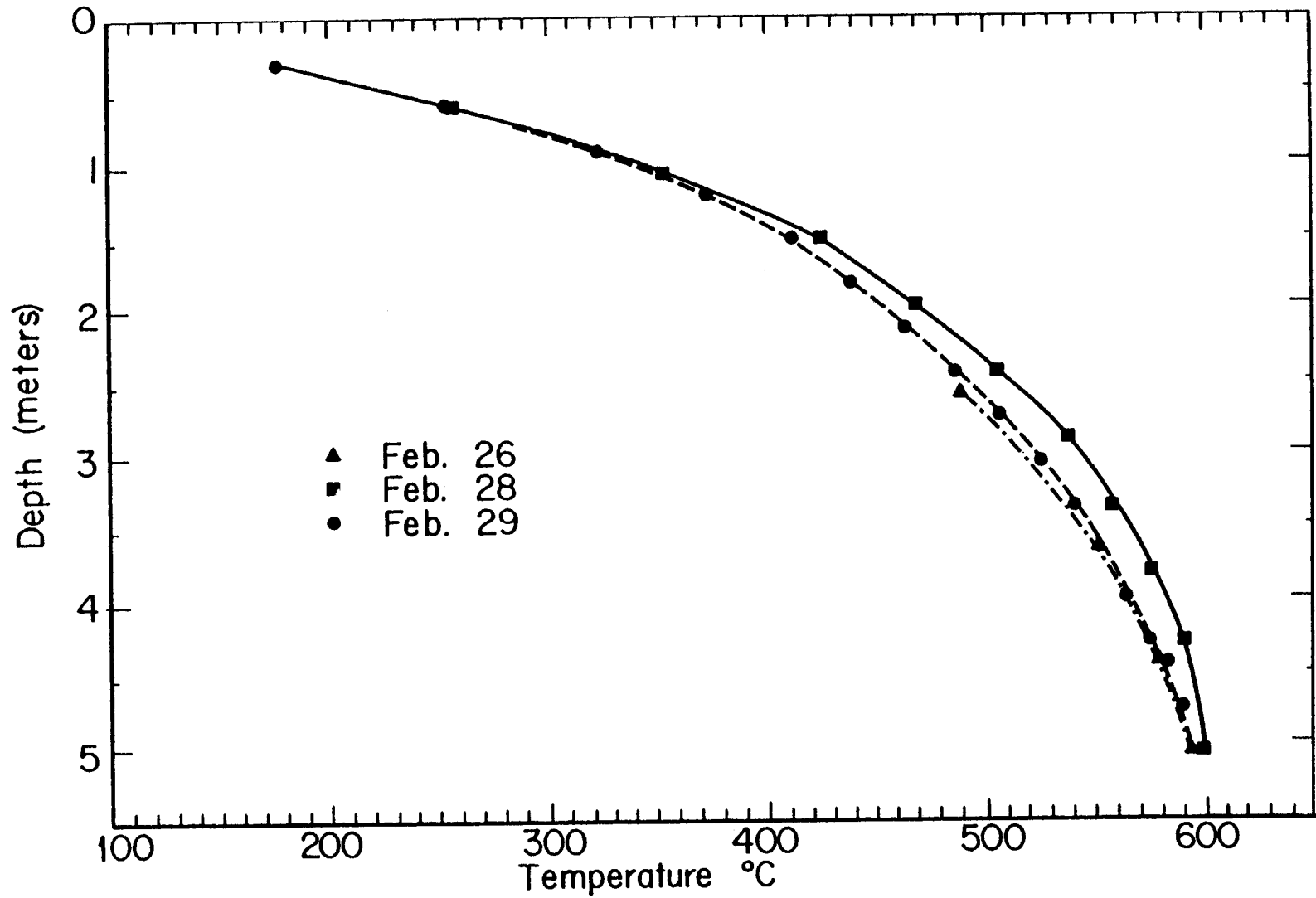


Figure 30. Temperature profiles measured a few weeks after deposition of the pyroclastic flows east of Burr Point; temperature test site is located on new flow shown in Figure 19d near the position of the old beach line.

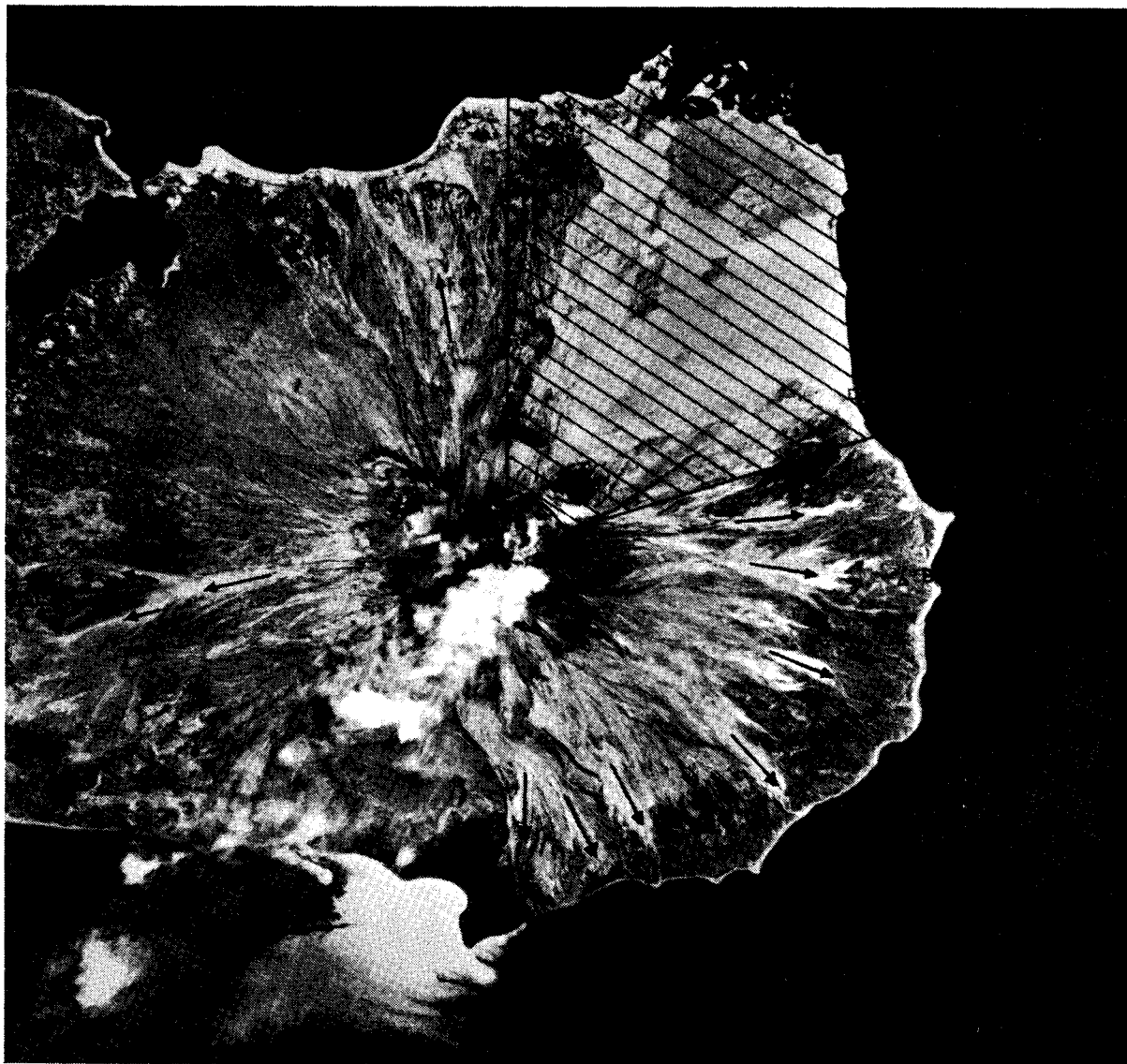


Figure 31. Vertical photograph of Augustine Island, taken by the National Ocean Survey on June 11, 1976, showing distribution of the light colored 1976 pyroclastic avalanches and debris flows (arrows and ruled area). The lines of the ruled area indicate profiles along which the topography was digitized on high resolution vertical imagery to obtain an accurate volume estimate of the 1963/64 and 1976 deposits in that sector of the volcano.



Figure 32. Close-up of the 1976 pyroclastic flow deposits on the northern flank of Augustine Volcano. The sulfur-stained white-appearing area at the base of the steaming 1976 dome is shown in Figure 33 (photograph by H.-U. Schmincke).



Figure 33. "Hells Gate" at the base of the 1976 lava dome. Pyroclastic avalanches have eroded a U-shaped channel. Two persons stand on old inversely graded pyroclastic flow deposits (the person on the left is Dr. David Johnston who completed his Ph.D. on the petrology of Augustine Volcano in 1978 and was recently killed in a tragic accident by a hot blast from Mt. St. Helens, Washington, on May 18, 1980 (photograph by H.-U. Schmincke).

During our February visit we also managed to re-establish a new three-station seismic array on the island, after all but one of the original 5 seismic stations had been buried by pyroclastic flows.

Little seismic or eruptive activity was observed from February 16 to early April, except for some shallow earthquake swarms from March 15 to 25. However, in early April, we began to record peculiar wave trains with no distinct phases and a cigar-shaped wave envelope, which we later learned to recognize as the seismic signature of pyroclastic avalanches rumbling down the mountain. The number of these events increased dramatically up to April 12. During the peak activity, avalanche after avalanche cascaded off the dome almost continuously, as it underwent renewed growth. Bill Koplín and Howard Feder from the University of Alaska's Institute of Marine Science eyewitnessed this avalanche activity on the evening of April 12 and throughout April 13 from aboard the Hawaiian research vessel "Moana Wave".

"The avalanches were glowing in a ruby-colored red sometimes splitting up in 2 or more branches and sometimes merging again as they come down at great speed the northeast sector of the volcano. Soon they would cool and become black and then split open again and glow. At dusk on April 12, avalanches succeeded each other at a rate of one every 10-15 minutes. All of these avalanches fell from the north-face of the dome as a mass of brightly-colored material falling down a vertical precipice and then following down a chute. Clouds of dust and ash would spread out like a reversed cone and then expand above the mountain. There was a tremendous amount of smoke and dust hanging over Cook Inlet and the summit had a continuous large white plume".

The seismic activity and by implication dome growth tapered off by April 19 and returned to normal by April 24.

A new photogrammetric topographic map of the summit region was produced from photography taken on August 25, 1976 (Figure A2, Appendix 1) which shows that the dome eventually grew to a height of 4,011 feet

(1,226 m). A new South Peak now makes up the summit with a height of a little over 4,100 feet (1,250 m). Thus, the volcano lost about 200 feet (61 m) in elevation since 1964.

Figure 34 shows the distribution of the 1976 eruptive deposits. The main thrust of the debris flows is again northeast and east, with some flows directed toward the northwest and southwest. Data for this figure came mainly from vertical aerial photographs taken in the summer of 1976. Numerous additional oblique photographs of the 1976 eruption were used to supplement the vertical photography. Reconnaissance field surveys of the 1976 eruptive deposits have also been done, primarily on the northern and northeastern flanks of the volcano. Johnston, shortly before his tragic recent death on Mt. St. Helens, was preparing a new detailed map of the Augustine ejecta based on field mapping between 1976 and 1979. We hope to be able to complete the map for him for the final report.

1976-80 Activity - Current State

Following the renewed growth episode of the new summit lava dome in April, 1976 only occasional minor ash eruptions occurred. Chuck Berns, an Anchorage bush pilot photographed an ash and steam explosion originating at the eastern base of the dome on April 11, 1977, at 17:15 AST. The plume rose to a height of about 300 m above the summit. David Stone overflew the snow covered volcano on April 6, 1977, and took a photograph which clearly shows that the northeastern pyroclastic avalanche deposits stayed snow free probably throughout the winter 1976/77 due to their internal heat. Bill Feetham eyewitnessed a larger ash explosion on May 14, 1977, 21:00-21:30 ADT; the plume trailed off up the inlet to a distance of about 30 km. The island was largely obscured due to ash fallout and on the following morning, May 15, a "line of smudge

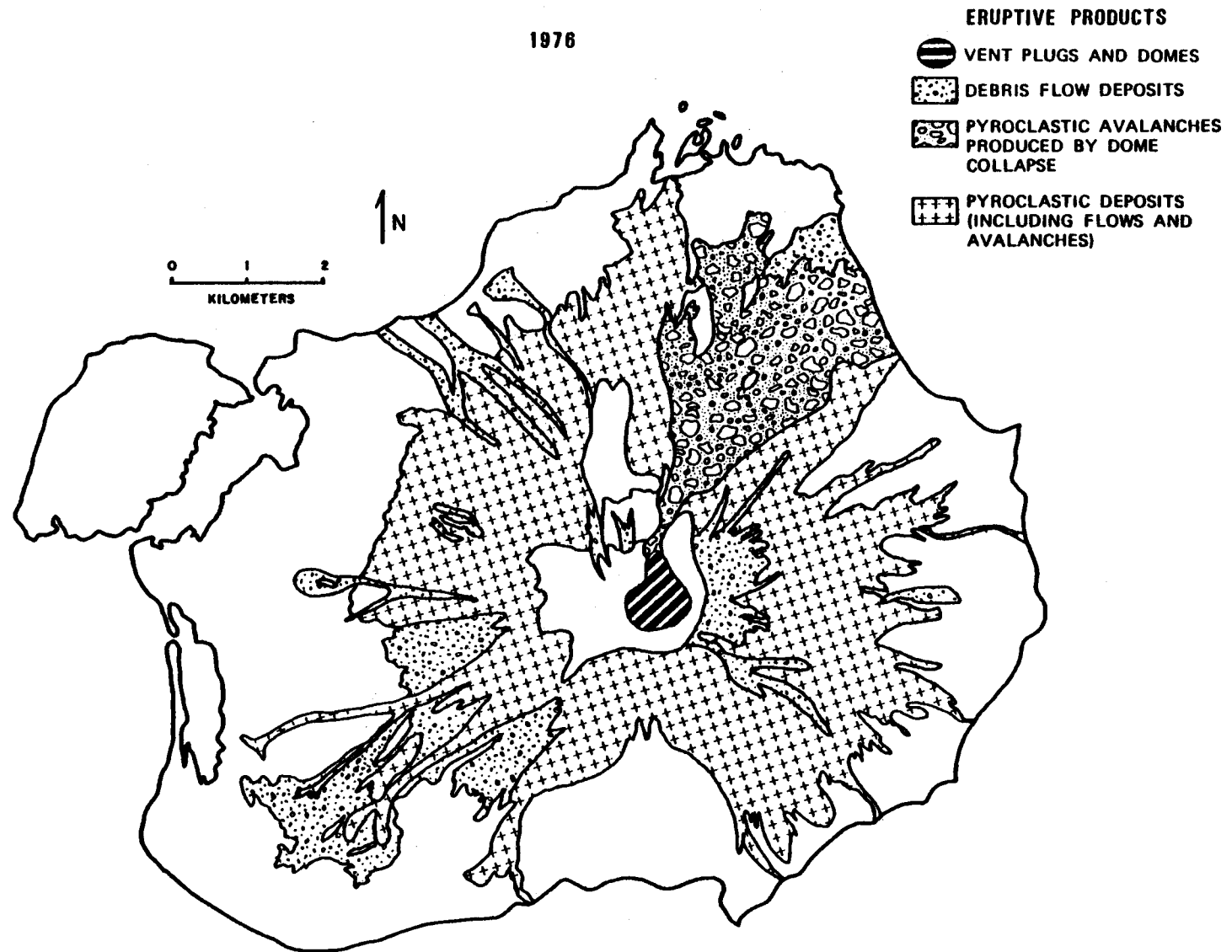


Figure 34. Distribution of the 1976 eruptive products.

and steam" extended toward Chinitna Bay at the peak level (1,200 m). The eruption also produced a seismic signal on Augustine Island stations. Undoubtedly many other such eruptions occurred in 1976 and up to 1977, but none of these caused any ash falls on the Kenai Peninsula.

In August, 1978, David Johnston made the first ascent of the new summit lava dome and estimated the temperature of the very active fumarole at the base of the apical spine (Figure 35) at about 650°C (Johnston, 1979c). His temperature measuring equipment went off scale and the temperature estimate is based on observing a faint red glow. In the following summer of 1979 Johnston (personal communication) measured the same fumarole again with appropriate high temperature equipment and found it to be still as hot as 754°C. He also collected gas which still contained abundant SO₂, CO₂, and halogens (chlorine and fluorine). Based on his Augustine gas data, Johnston (1980) discussed the volcanic contribution of chlorine to the stratosphere and its impact on the ozone layer.

No major volcanogenic earthquake swarm has been recorded since April 1976, even though we have continuous data since then. We do record occasional shallow events of small magnitude ($M_L=2$), located in the cones central plumbing system just below or above sea level.

The surface layers of the pyroclastic flow deposits have now cooled to the ambient temperature. The summit dome continues to cool and still emits a steady plume of white vapor, sulfur, carbon dioxide and halogen gases.

As a summary, Figure 27 shows 4 northern views of the volcano, illustrating how dramatically the various eruptions changed the appearance of the volcano.

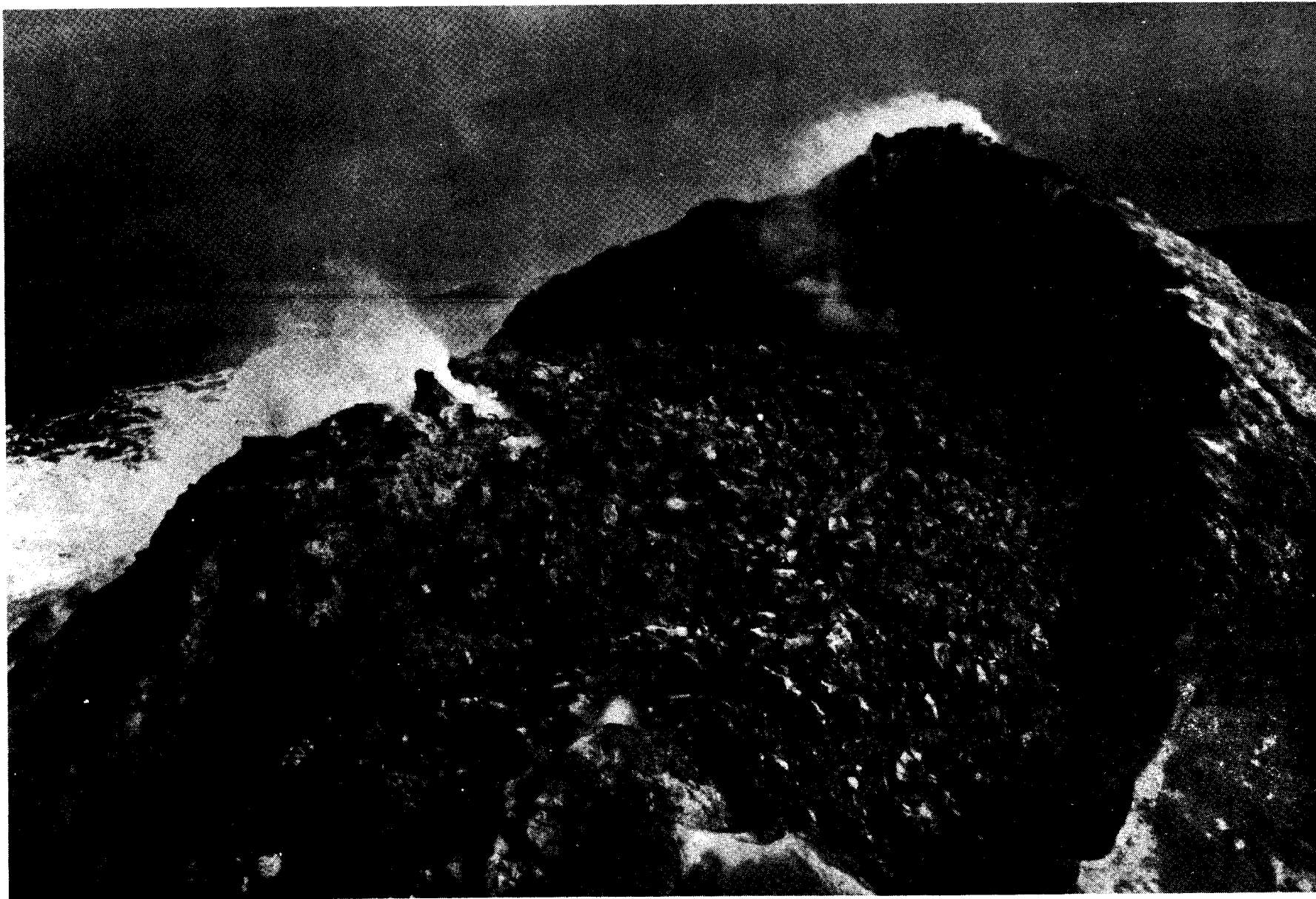


Figure 35. Close-up of the 1976 lava dome within remnant of the '64 dome. Fumarole temperature at base of summit spine of '76 dome was 754°C in August 1979 (David Johnston, personal communication).

ERUPTIVE PRODUCTS

Future eruptions of Augustine Volcano are expected to be similar to previous eruptions in terms of eruptive style and deposits. Magma composition has remained relatively constant throughout most of Augustine's history with a silica content averaging 60 percent. To a large extent, the silica content determines the style of eruption and the nature of the eruptive products. Thus, a relatively constant silica content for Augustine magmas suggests future eruptions should be similar to the ones in the past.

Silica controls the eruptive style. To quote from Francis's (1976) popular text "Volcanoes":

Composition dictates melting temperature,
temperature dictates viscosity,
viscosity dictates explosive potential of eruption,
explosiveness of eruption dictates whether lavas or pyroclastics
are produced.

Silica forms a three dimensional framework structure in magmas with oxygen and silica atoms joined in large polymers. The higher the silica content of the magma, the larger the silica polymers. Flowage of the magma is related to the size of the silica polymers, the larger the polymers the slower the flowage of the magma and hence the higher the viscosity. Silica content is also related to the temperature of a magma and this also effects magma viscosity. For any given magma, the lower the temperature, the higher the viscosity. Silica-rich magmas (70-75 percent SiO_2) melt and solidify at relatively low temperatures, while silica-poor magmas (50-55 percent SiO_2) are characterized by relatively high temperatures. Thus, silica-rich magmas have high viscosities due to low temperatures and high silica contents.

Augustine magmas have an intermediate silica content and are quite viscous. The eruptions are highly explosive and commonly produce tephra (fragmented material) and pyroclastic flows. Lava flows are not a common product of Augustine eruptions, because the viscous Augustine lavas do not tend to flow but rather form vent-filling domes. Debris flows formed by water carrying volcanic debris down the flanks of Augustine Volcano are common because of the steep slopes, an abundance of fragmental material and the moist climate.

Petrology

Andesite and dacite are the dominate volcanic rocks on Augustine Island. These intermediate lavas are in the form of pumiceous pyroclastic deposits, massive domes and a single lava flow on the northern flank of the volcano. Debris flows are composed of both pumiceous and massive varieties of andesite and dacite and are the most widespread deposits on Augustine Island. Mineralogically, the andesites and dacites are similar. Plagioclase, hypersthene and augite are the most abundant phenocrysts in the lavas. In addition, olivine and basaltic hornblende are found in the andesites. Dacites often have a glassy groundmass resulting in a vitrophyric texture. Andesites are more crystalline than dacites and have a fine-grained matrix.

Inclusions and bands of andesite within dacite are common in the Augustine lavas. Microscopic examination of the contact between andesitic bands or inclusions and the host dacite shows that phenocrysts from the andesite have been added to the dacite, suggesting mixing between the andesite and dacite. Such evidence for mixing is common in intermediate calc-alkaline volcanic rocks and is fairly common in the Augustine lavas.

Initial volcanism on Augustine Island apparently involved basaltic and rhyolitic lavas (Johnston, 1979a). On the south side of Augustine Island, Johnston describes rhyolite sands and basaltic hyaloclastites deposited on a glaciated surface of Tertiary and Mesozoic sedimentary rocks. Johnston (1979a) suggests the volcanism on Augustine Island began about 17,000-13,500 years B.P. and was initially bimodal basalt-rhyolite. However, the eruptive products quickly became more intermediate andesites and dacites with evidence of mixing between the felsic and mafic components. This pattern of hybrid intermediate magmatism has continued from early in the history of Augustine Volcano to the present.

Chemistry

The consistency in the mineralogy of the Augustine andesites and dacites is reflected in the chemistry of the volcanic rocks. Table 1 gives the average of 22 analyses of volcanic products from Augustine Volcano. Included within these 22 analyses are samples of volcanic ash and bombs, massive andesites and dacites from lava flows and domes, and pumiceous lavas from pyroclastic deposits. The analyses represent not only historical eruptive deposits but also prehistoric lavas. Despite the time span, the variety of eruptive styles and products represented in the analyses, the bulk compositions are restricted to the dacite-andesite range (Table 1). The range of compositions reported in Table 1 is about the same as the range of reported compositions from the 1976 eruption (Kienle and Forbes, 1976). Thus, magma composition appears to have remained relatively constant throughout the history of Augustine Volcano.

Average composition of the Augustine lavas is intermediate between dacite and andesite. The silica, iron and sodium contents of the average

Table 1. Average composition of volcanic products from Augustine Volcano. Based on results of this study, Becker (1898), Detterman (1973), and Kienle and Forbes (1976). Average andesite and dacite from Nockolds (1954).

	Average ¹ of Augustine Lavas	Observed Range of Augustine Lavas	Average ² Dacite	Average ² Andesite
SiO ₂	60.33	56.27-64.20	63.6	54.2
TiO ₂	0.61	0.50-0.75	0.6	1.3
Al ₂ O ₃	16.73	15.70-17.42	16.7	17.2
FeO*	6.02	4.80-7.37	5.2	9.0
MnO	0.13	0.11-0.15	0.1	0.1
MgO	4.04	2.60-4.86	2.1	4.4
CaO	7.45	5.30-8.61	5.5	7.9
Na ₂ O	3.81	2.80-5.57	4.0	3.7
K ₂ O	0.93	0.72-1.10	1.4	1.1
P ₂ O ₅	0.13	0.05-0.19	0.2	0.3

*FeO includes Fe₂O₃

¹average of 22 analyses

²from Nockolds (1954)

Augustine lava are also intermediate between dacite and andesite, titanium and aluminum contents are about the same as dacite and the magnesium, calcium and potassium contents are very similar to the average andesite defined by Nockolds (1954). These compositional relations reflect the hybrid nature of the Augustine lavas.

Chronology

As discussed earlier, Augustine Volcano has erupted in 1812, 1883, 1935, 1963 and 1976. The time interval between historic eruptions of Augustine Volcano has shortened with each successive recorded eruption (Figure. 36). Extrapolation of the trend in the recurrence interval shown on Figure 36 shows the interval between eruptions becoming zero in 1983. The significance, if any, of this projection is not presently understood. Studies of prehistoric Augustine eruptions utilizing C^{14} geochronology are currently underway and should help to evaluate the pattern of eruptive interval shown in Figure 36. Based upon the historic eruption record, Augustine has had two to three eruptions per century for the last two.

Preliminary studies of prehistoric Augustine eruptions indicate a similarly active eruptive pattern. Several stratigraphic sections have been sampled on the eastern flank of Augustine Island. The oldest exposed unit in the sections is a semi-consolidated poorly-sorted mud-flow deposit of andesite and dacite fragments in a fine-grained matrix; the flow extends offshore. A mat of contemporary tundra covers the top of the sections. Near the base of the tundra mat is a light-gray volcanic ash layer about three cm thick, representing the 1912 Katmai eruption. Between the Katmai ash and the base of the section are a series of eight volcanic ash and lapilli layers (tephra) interbedded with paleosoils.

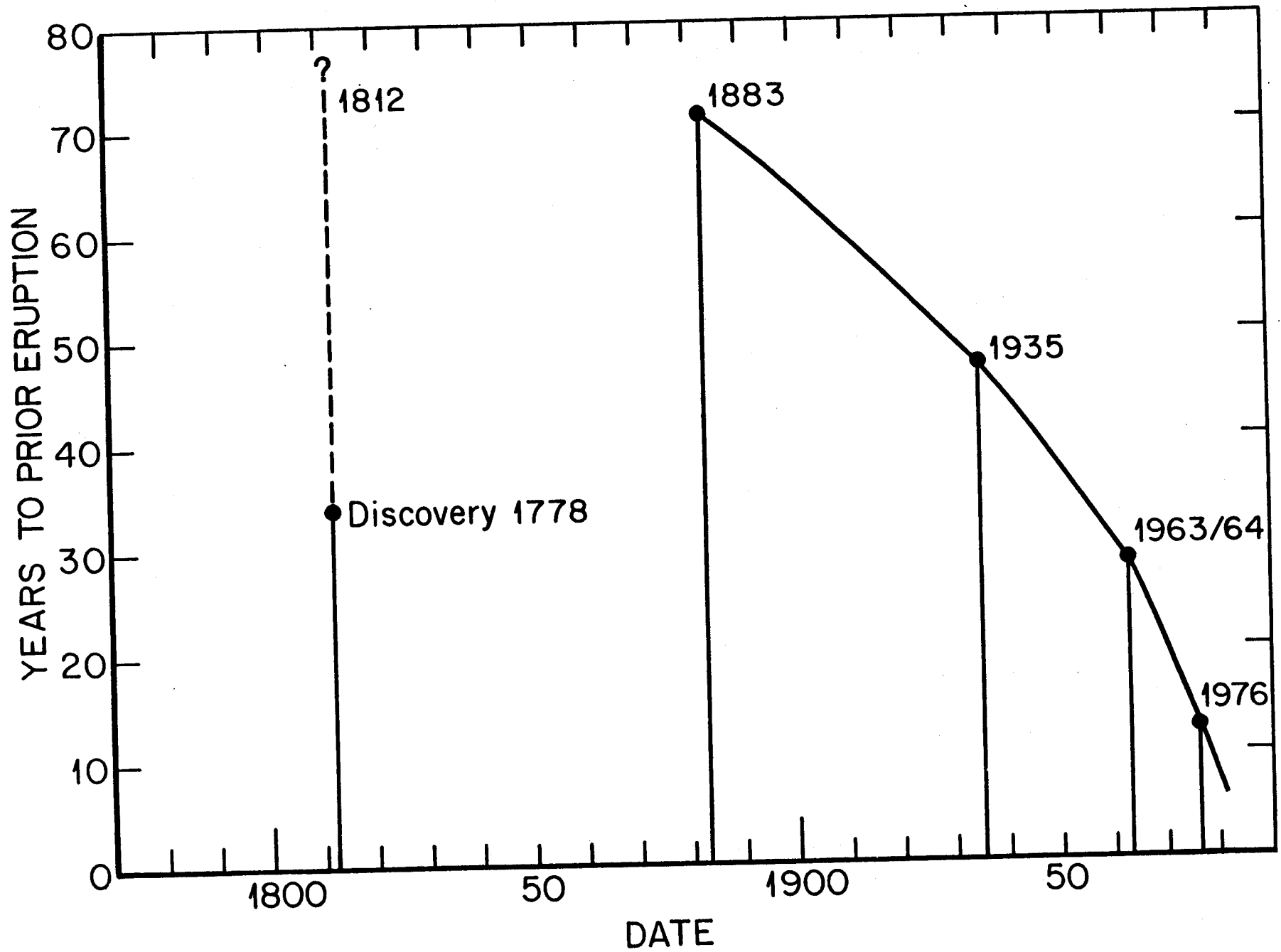


Figure 36. An apparent shortening of repose time between eruptions for at least the past 4 Augustine eruptive cycles.

Each of the ash layers is thought to represent an eruption of Augustine Volcano because the mineralogy and chemistry of the ash layers is similar to other Augustine eruptive deposits and the volcanic fragments are rather coarse suggesting a very close source. Paleosoils near the base of two different sections have been dated by the C^{14} technique and yield ages of $1,470 \pm 160$ years B.P. and $1,500 \pm 155$ years B.P. Thus, during the last 1,500 years Augustine has erupted at least eight times in the period 400 to 1912 A.D., and three times since 1912. It is extremely unlikely that the tephra layers sampled in these sections represent all of the eruptions of Augustine Volcano within the last 1,500 years. Based upon the previous discussions of volcanic eruptions and deposits on Augustine Island, it is obvious that one eruption cycle does not necessarily cover the entire island with volcanic debris. Thus, the eight eruptions in the sections studies represent a minimum and the actual number of eruptions within this 1,500 year time span may be two or three times greater. Augustine has been an active volcano for at least the last 1,500 years, probably with an average of one to three eruptions per 100 years. This pattern of active volcanism is expected to continue.

Eruption Volumes

Andesitic melts are derived from the upper mantle or the base of the crust (at 50 to 100 km depth) with subduction somehow triggering the generation of the melt. The details of this process are still not understood but the genetic relationship of island arc volcanism and plate subduction is clearly established. Once generated, the melts rise buoyantly as diapirs to shallower levels in the crust (e.g. Marsh, 1979), where they may be stored in shallow reservoirs, the shallowest of

which will probably feed the eruptions. We have geophysical evidence that such a shallow reservoir exists beneath Augustine Volcano, probably shallower than 3 km beneath the summit. Presumably, each eruptive cycle drains the chamber more or less completely and during the repose time between eruptions the chamber gets recharged by new melt from depth. Again, the details of this recharge mechanism are not yet understood. The size of the reservoir is obviously an important parameter controlling the magnitude of the eruption. Eruption volumes are an indirect indicator as to how big the eruption feeding reservoir might be and thus as to what magnitude eruption it may be able to produce. In the following we would like to demonstrate the constancy of eruption volumes at Augustine which together with the unchanging chemical composition of the ejecta over the past 1,500 years suggests a steady state plumbing system, involving a relatively small shallow storage reservoir and a fairly regular charge-discharge cycle.

In Table 2 the estimated bulk volume of the ejecta from the 1976 eruption is about 0.4 km^3 , of which 0.06 km^3 are flows on the island itself and the rest is tephra. We arrived at this estimate by digitizing the pre- and post-eruption topography of the sector most affected by debris flow activity, the northeast sector of the Island (Figure 31) and by using conservative estimates of the total thickness of tephra accumulation for the area that was affected by ash falls (Figure 15). Condensing the 0.4 km^3 of expanded material into solid rock or magma would require a storage chamber volume of about 0.2 km^3 , equivalent to a sphere of 360 m radius.

Detterman's (1968) estimate of the 1963/64 debris flow accreted on the island is 0.09 km^3 (a crude estimate that seems somewhat high, when compared to the 1976 eruption).

Table 2 - Volume of the 1976 Eruption

	<u>Area (km²)</u>	<u>Thickness</u>	<u>Bulk Volume (km³)</u>	<u>Reduction Density Ratio</u>	<u>Equivalent Solid Rock Volume</u>
Island Flows					
NE-sector	15.6	-37 to +35 m ¹	0.049		
SE-sector	2.6	~ 2 m	~ 0.005		
SW-sector	1.6	~ 1 m	~ 0.002		
NW-sector	1.0	~ 1 m	~ 0.001		
		Total	0.057	1.65 ² /2.5 ³	0.038
Mass Loss					
1964-1976 domes			-0.009 ⁴	2.3 ² /2.5	-0.008
Ash Falls, January 22-25, 1976 - later ash falls negligible					
Upper Cook Inlet & Gulf of Alaska	182,188	0.5 mm ⁵	0.091	1.36 ⁶ /2.5	0.050
Central Cook Inlet & Gulf of Alaska	55,625	~ 1 mm ²	0.056	1.36/2.5	0.030
Lower Cook Inlet	37,188	5 mm ⁷	0.186	0.99 ⁸ /2.5	0.074
Augustine Island	133	50 mm ⁹	<u>0.006</u>	0.99/2.5	<u>0.002</u>
		Total	0.339		0.16
		Total Eruption	<u>0.387</u>		<u>0.186</u>

- ¹ Near the top of the fan the flows eroded; the main accumulation was near the center and bottom of the fan.
- ² Laboratory determination of two 1964 dome samples gave 2.3 g/cm³; for flows we crudely assume 50% dome debris and 50% pyroclastics, i.e., (2.3 + 0.99)/2 g/cm³.
- ³ Mt. Hood andesite at 800°C (Murase and McBirney, 1973, p. 3572, Fig. 10).
- ⁴ $V = 1/6 \pi h (3a^2 + h^2)$, where $a = 250$ m, $h = 89$ m (4,304 - 4,011 feet).
- ⁵ Total ash thickness reported from Anchorage (Miller, 1976).
- ⁶ Laboratory determination of ash sample, 60-85 mesh or 0.175 - 0.212 mm.
- ⁷ Ash thickness, measured at Oil Bay, 35 km N of Augustine.
- ⁸ Laboratory determination of Oil Bay ash sample.
- ⁹ (Johnston, 1978.)

The total volume of volcanics making up the visible cone of Augustine is about 15 km^3 and there may be an additional 1 to 2 km^3 of volcanics offshore. Assuming that 0.05 to 0.1 km^3 of new material is accreted on Augustine Island each time the volcano erupts it would take 160 to 340 eruptions to build the visible cone and offshore flows, or given an age of the volcano of 13,500 to 17,000 years (Johnston, 1979a) about 0.5 to 1 eruptions per century. For the past 2 centuries the recurrence rate was 2.5 eruptions per century, a number which is a factor 2.5 to 5 higher than the recurrence rate derived by assuming a steady state process. The argument is no doubt over-simplified but it nevertheless demonstrates that Augustine probably never had an eruption which produced a volume greater than 1 km^3 and that repose times between eruptions may have been greater in the past.

It may be instructive to contrast these numbers to eruption volumes produced by very large eruptions such as Krakatoa in Indonesia, 1883, or Mt. Katmai, Alaska, 1912. These are relatively rare events (a few per century in the world) and involve both bulk eruption volumes (not reduced to equivalent dense rock) of order 10 km^3 or more. Katmai erupted an ashflow of $11-15 \text{ km}^3$ in volume and $\sim 20 \text{ km}^3$ of tephra in ~ 60 (!) hours (Hildreth, 1979) while the Krakatoa eruption involved about 18 km^3 of ejecta. When such large, so called paroxysmal, eruptions occur near populated areas the loss of life can be great (about 36,000 casualties due to volcanogenic tsunamis for Krakatoa) and often there are far reaching or even worldwide climatic effects (acid rain on Chicago following the 1912 Katmai eruption Griggs, 1922). The 79 A.D. Vesuvius and 1980 Mt. St. Helens eruptions produced several km^3 but probably less than 10 km^3 of ejecta.

All historic and also prehistoric Augustine eruptions have produced eruption volumes that are 2 orders of magnitude smaller than either Katmai or Krakatoa and 1 order of magnitude smaller than Mt. St. Helens or Vesuvius. In fact, a single Katmai eruption could produce the entire Augustine cone, while it takes a few hundred typical Augustine eruptions to form the same volume.

In summary, considering the youthfulness of the volcano and its apparent steady-state behavior over its short life span of no more than 13 to 19,000 years, it seems highly probable that the eruptive pattern will stay the same in the near future (few 100 years) and furthermore, it seems unlikely that Augustine in its present state of development could produce a very large, e.g. Katmai-sized eruption. Future eruptions are likely to follow the eruptive patterns of the well documented historic eruptions, with small ($\sim 0.5 \text{ km}^3$, flows plus tephra) volumes of magma being erupted 2-4 times per century.

HAZARDS

The chief hazards from future eruptions of Augustine volcano will be pyroclastic flows and nuées ardentes (glowing clouds) which may continue out to sea. Tsunamis capable of crossing Cook Inlet to the eastern shore may be generated by this process. Tephra (airborne volcanic debris) fall will affect the island and a large area offshore, the dispersal of finer airborne material depending strongly on the prevailing wind conditions. Extreme dustiness can be expected for tens of km downwind from the volcano even when the volcano is not actively erupting, as freshly fallen fine ash is easily picked up by winds. Lava flows will almost certainly be confined to the island itself. Because Augustine Island is so small (6 km radius) there are simply no sites on the island itself that would be safe to erect permanent structures unless they were underground. However, such underground structures could easily get buried.

Pyroclastic Flows

Pyroclastic flows are air-cushioned avalanches of hot, dry rock debris. They may be generated either by explosive eruptions (a directed blast as in the Pelée type or a vertical blast and subsequent collapse of the eruptive column as in the Soufrière type) or the collapse of a volcanic dome (as in the Merapi type). Cartoons of each of these three eruptive mechanisms are shown in Figure 29. Large volumes of hot air and other gases are evolved within pyroclastic flows and this, together with the force of the volcanic blast and the air cushion trapped beneath the flow accounts for their great speed (180 km/h for the small flow and nuée ardente observed on February 8, 1976; Figure 26) and mobility. Pyroclastic flows move as density currents flowing down the slope of the volcano. Generally, topography influences the velocity and direction of

the pyroclastic flows. Flows move rapidly down the steeper flanks of the volcano and slow down on gentler slopes. However, pyroclastic flows can move for considerable distances over horizontal surfaces due to the initial high velocity and the cushioning effect of the trapped air layer under the flow. Locally, pyroclastic flows may even move uphill for short distances. Miller (1977) described the spectacular mobility of large ash flows around Aniakchak and Fisher calderas on the central Alaskan Peninsula and Unimak Island:

"At Aniakchak ash flows swept down glaciated valleys on the south side, crossed a broad lowland with an altitude of less than 35 m, and continued on through passes as much as 260 m high ... into the Pacific Ocean, a distance of some 50 km".

Smaller pyroclastic flows will tend to follow topographic lows such as stream valleys.

Pyroclastic flows consist of coarse basal glowing avalanche and a high billowing hot ash and dust cloud. The majority of the material involved in pyroclastic flows is juvenile volcanic material either just erupted from the vent or from the collapse of an emerging dome. Blocks in the basal avalanche unit may be quite large (up to ten meters or more in diameter). Basal avalanches are generally confined to the bottoms of valleys while the ash cloud that rises above the avalanche spreads out both laterally and vertically. Under certain conditions the glowing ash cloud separates from the basal avalanche, as occurred on May 8, 1902, during the eruption of Mt. Pelee on the island of Martinique, West Indies. Macdonald (1972), summarizing Anderson and Flett's (1903) and Lacroix's (1904) account of the eruption, states that on that day a great black cloud of ash was erupted to several km above the volcano and simultaneously a horizontal blast was directed toward the city of St. Pierre through a notch in the crater wall. Initially, the basal glowing

avalanche and associated nuée ardente traveled together following the headwaters of Rivière Blanche, but at Morne Lenard the avalanche turned 90 degrees to the west, while the nuée detached itself and proceeded along the original course towards St. Pierre obliterating it and nearly all of its 30,000 inhabitants, all in less than 2 minutes after the eruption began (Figure 37).

The city lies 6 km from the volcano, hence the velocity of the cloud must have been of order 150-200 km/h. The hot blast that struck the city was so powerful that masonry walls 1 m thick were knocked over and a 3-ton statue was carried 12 m from its base. Most of the ships in the harbor were blown over, sunk or set afire. The bodies of people were intensely burned and many in the north end of town closest to the volcano were stripped of their clothing by the force of the blast. The nature of injuries indicated that the sudden heat was intense enough to turn water in human tissue to steam (order 600 to 1000°C) and the temperature was also high enough to soften glass. Bodies with their clothing intact were often severely burned underneath. Relatively little debris was left in the city after the cloud passed, about 30 cm, indicating that it consisted mainly of hot gas and dust.

In many respects Augustine is very similar to Mt. Pelee:

- (1) Augustine is now 4,100 feet high, Pelee 4,428 feet.
- (2) Augustine erupted in the past 200 years with an average repose time of 41 years, Pelee 44 years.
- (3) Eruption volumes and eruption style (dome growth and associated pyroclastic flow activity) and the geochemistry is very similar.
- (4) The craters of both volcanoes are breached, the breach providing the preferred avenue for pyroclastic flows.

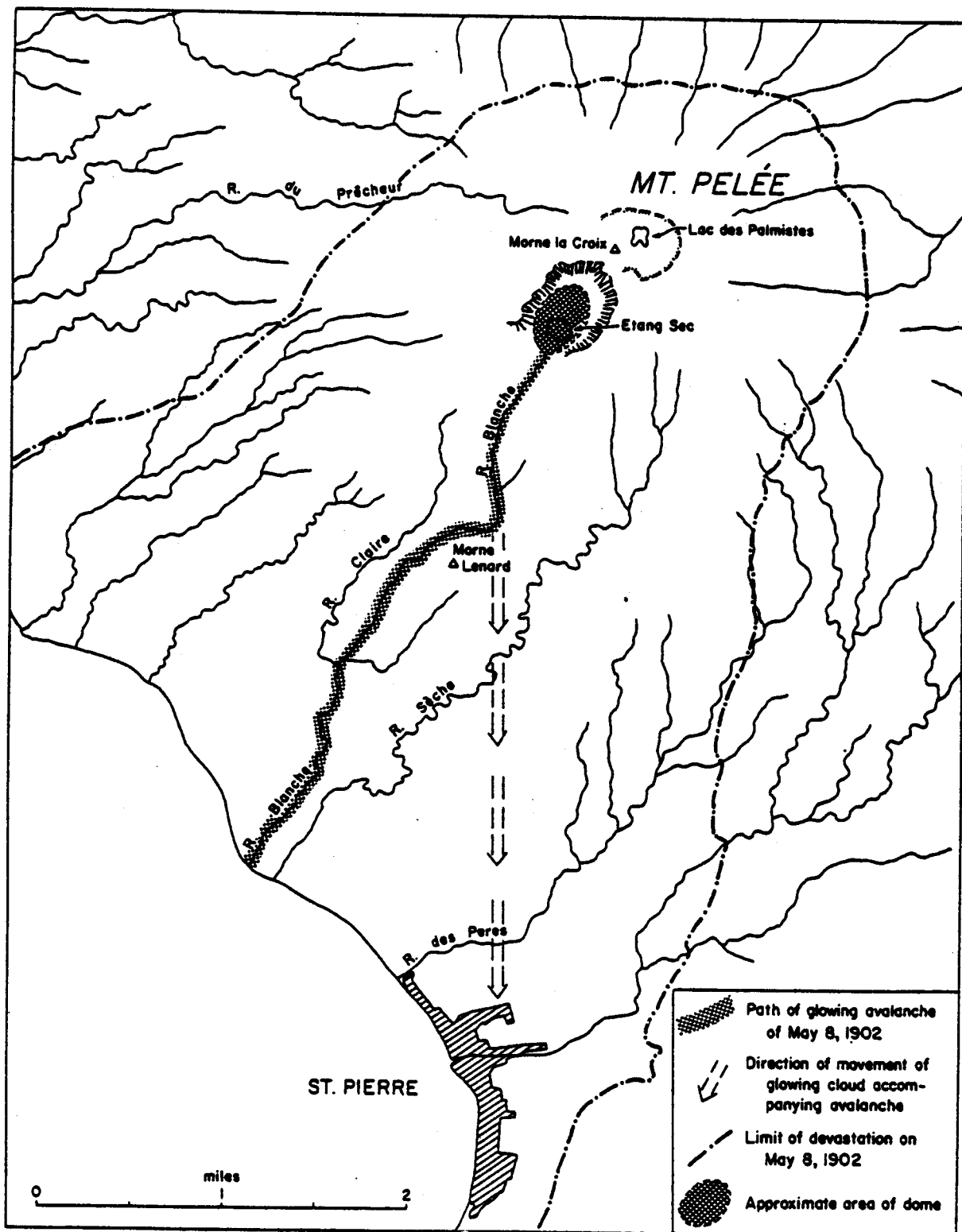


Figure 37. Map illustrating how nuées ardentes can detach themselves from their basal pyroclastic (glowing) avalanches and proceed independently, as during the disastrous destruction of the City of St. Pierre, Martinique, Lesser Antilles, during the May 8, 1902 eruption of Mt. Pelée. The pyroclastic avalanche followed the Rivière Blanche to its mouth, while the nuée continued straight toward the city (taken from Macdonald, 1972, p. 144).

- (5) The distance of the vent from the nearest seashore is 4 km for Augustine, 5 km for Pelée.

Pelée can therefore serve as a direct analogy for many eruptive phenomena at Augustine.

Other well documented glowing avalanche eruptions occurred at Mt. Lamington, Papua, in 1951 (Taylor, 1958) and Mt. Mayon, Phillipines, 1968 (Moore and Melson, 1969). The only additional phenomenon that needs to be discussed here is that the pyroclastic flows at Mt. Mayon (Soufriere type) produced a sear zone a few 100 m to 2 km beyond the flow termini. Within the seared zone all animals were killed and the tropical vegetation was charred or shriveled. Moore and Melson (1969) believe that cold shock waves, uprooting thick palm trees, preceded the hot blast of the nuée that later charred the bottom of the roots of the trees, implying that cold air is compressed and pushed forward by the rapidly advancing nuée.

Obviously, the hot ash, dust and gases in the nuée ardente are the most hazardous elements in pyroclastic flows. The high temperatures in these clouds and their great speed devastate life and property in their paths. A zone of high temperature air and gas extends out well beyond the areas of major debris deposition and greatly expands the hazard zone associated with pyroclastic flows. No structures or life would survive in the avalanche zone itself.

Eruptions of Augustine Volcano are characterized by pyroclastic flows associated with all three mechanisms, directed blasts and the collapse of a vertical eruptive column or a volcanic dome. Initially, Augustine eruptions are vent-clearing and may involve powerful low angle or vertically directed blasts. Later in an eruptive episode, a dome is commonly emplaced in the vent and subsequent collapse of portions of the

dome can produce additional pyroclastic flows of somewhat different composition as we have discussed for the 1976 eruption.

Deposits of pyroclastic flows are found on all parts of Augustine Island (Figures 3, 7, 8, 11 and 34). In fact, the island grew to its present size principally by accretion of such avalanche deposits.

Deposits from both the basal avalanche and nuée ardente associated with the pyroclastic flows are found practically everywhere on Augustine Island. Avalanche deposits are very poorly sorted and contain particles ranging in size from less than one millimeter to tens of meters in diameter. The material in these deposits is dominated by highly vesicular volcanic glass with a few percent of plagioclase and pyroxene phenocrysts.

Knowledge of damage to structures on Augustine Island caused by pyroclastic flows is limited to the effects of the 1976 eruption on research facilities at Burr Point and on a small structure on the northwest coast of the island. Both of these areas were on the edge of the paths of the 1976 pyroclastic basal avalanches and were subjected primarily to the effects of hot blasts and nuées ardentes. One of these blasts completely collapsed the small hut on the northwest coast of the island. As discussed before, the corrugated aluminum buildings at Burr Point were dented and holes, one 15 cm in diameter, were punched by falling debris in the aluminum roof. Temperatures were high enough to melt plastic objects and burn mattresses at Burr Point. Grass and tree stumps were charred along several kilometers of coast line at the northern and southwestern shores of the island.

One of the main unanswered questions at Augustine is how far across the water nuées ardentes would travel and how far the basal avalanche would proceed out to sea. Again we have to call on the Mt. Pelée

analogue, which is a particularly good one since the volcano height and distance to the shoreline are so similar to Augustine. During other eruptions besides the disastrous one of May 8, 1902 several nuées ardentes traveled as far as 8 km offshore after descending 6.5 km down the 4,428 foot high flank of the volcano. Anderson and Flett (1903) who eyewitnessed two such nuées on the evening of July 9 from a ship lying off Carbet, a small town 4 km south of the devastated city of St. Pierre, gave the following description:

First nuée: "In the rapidly-falling twilight we sat on deck..., when our attention was suddenly attracted to a cloud which was not exactly like any of the steam cauliflowers we had hitherto seen. It was globular, with a bulging, nodular surface;...darker in colour, being dark slate approaching black...Its behaviour, however, was unique. It did not rise in the air, but rested there, poised on the lip of the fissure, for quite a while as it seemed,...it was too heavy to soar up in the air like a mass of vapour, and it lay rolling and spouting on the slopes of the hill. The wind had no power over it,...slowly we realised that the cloud was not at rest but was rolling straight down the hill, gradually increasing in size as it came nearer and nearer...We helped the sailors to raise the anchor and, setting the head sails, we slipped away before the wind. By the time the mainsail was hoisted we had time to look back, but now there was a startling change. The cloud had cleared the slopes of the hill. It was immensely larger, but still rounded, globular, with boiling, pillowy surface, pitch black, and through it little streaks of lightning scintillated. It had now reached the north side of the bay, and along its base, where the black mass rested on the water, there was a line of sparkling lightnings that played incessantly. Soon, however, it seemed to lose its velocity; its surface became less agitated, it formed a great black pall, with larger, less vigorous, more globular, bulging convolutions. Evidently its violence was spent, and it was not to strike us; it lay almost like a dead mass on the surface of the sea.

For 20 or 30 minutes we sailed along with a gentle breeze from the east,...then the wind fell away, and it was practically a dead calm."....

Second nuée: "Suddenly a great yellow or reddish glare lit up the whole cloud mass which veiled the summit...Then from the mountain burst a prolonged angry growl, not a sharp detonation..."

Then in an instant a red-hot avalanche rose from the cleft in the hillside [notch in the crater], and poured over the mountain slopes right down to the sea. It was dull red, and in it were brighter streaks, which we thought were large stones, as they seemed to give

off tails of yellow sparks...The main mass of the avalanche was a darker red, and its surface was billowy like a cascade in a mountain brook. Its velocity was tremendous...The red glow faded in a minute or two, and in its place we now saw, rushing forward over the sea, a great rounded, boiling cloud, black, and filled with lightnings. It came straight out of the avalanche,...coming straight over the water directly for us, where we lay with the sails flapping idly as the boat gently rolled on the waves of the sea.

The cloud was black, dense, solid, and opaque, absolutely impenetrable, like a mass of ink. It was globular as seen end on, very perfectly rounded, but covered with innumerable minor excrescences, rounded, and filled with terrific energy. They shot out, swelled, and multiplied till the whole surface seemed boiling;... the cloud drove forward without expanding laterally to any great extent... The cloud lay on the water and sped on horizontally...

The display of lightning in the cloud was marvellous...we were at once reminded of the narratives given us by survivors in St. Vincent, in which it was stated that when the black cloud rolled down upon the sea it was filled with fire. [The Soufrière in St. Vincent erupted simultaneously with Pelée].

Nearer and nearer it came to where our little boat lay becalmed, right in the path of its murderous violence...But in a minute a slight puff of wind came from the south-east, very gentle, but enough to ripple the water and fill the sails. We had drifted out from the shore, so we gave our boatmen instructions to keep the boat close-hauled, and drawn in to the land, as the cloud was passing more to the westward. Then when we looked at the cloud again; it was changed, it showed no more the boiling, spouting, furious vigour, but the various rounded lobes in its point swelled slowly and to greater size, while fresh ones did not shoot forward,... we thought it was a mile off, or rather more.

It now lay before us nearly immobile, a gigantic wall...This lasted a few minutes, and the folds became flatter and less convex... The dust was sinking, and the pale steam...was following its own natural tendency to ascend...

The steam cloud crept southward, and was soon directly over our mast-head, traveling with a velocity of perhaps 20 miles an hour...

As the cloud reached the zenith a hail of pebbles fell in the sea and on our decks. We picked up the first that fell. It was about the size of a chestnut, and was cold to the touch, so we knew that we were safe. Then smaller pellets rattled on our decks, like a rain of peas or small shot. A little afterward the fine gray ash came in little globules moist and adherent...They were not warm, and there was a slight but noticeable smell of sulphurous acid...

The second black cloud did not differ in appearance from the first, except that it was larger, had a far greater velocity, and swept out at least twice as far across the sea...

No blast struck us -- in fact we were becalmed -- it seemed that when the black cloud ceased the blast was also over. Nor did the sea rage around us as some have described who were overtaken by the dust storm. [e.g. the account of Captain Freeman of the "Roddam", which barely escaped the May 8 disaster. He stated that a great rush of wind greatly agitated the sea; the "roaring" sea tossed ships back and forth].

Similarly, the one or more nuées ardentes that overran our Burr Point camp in January 1976 detached themselves from the basal avalanche which turned northeast a few km upslope from the camp, swept over the camp and continued out to sea (see Figure 19b and c). We have described the damage to the Burr Point camp when we discussed the 1976 eruption. Another cabin on the northeast coast of the island was completely erased by a strong blast.

Seven lobate hummocky bathymetric features, that morphologically resemble the Burr Point pyroclastic avalanche terrain, can be seen to extend up to 4 km offshore, predominantly on the north, east and south flank of Augustine Volcano (Figure 38, based on NOAA-NOS hydrographic survey H-9073, vicinity of Augustine Island, contoured by John Whitney, USGS). Whitney (personal communication) suspected these features to be submarine flows extending up to 7 to 10 km from the summit vent based on their morphology and seismic reflection profiler data. We do not know if they were emplaced subaerially or submarine but their young age of about 1500 years B.P., based on two C^{14} dates from a soil horizon that directly overlies their landward continuation on the east shore, suggests that sea level was near its present level. Even though the age is a minimum age and the flows could be a little older sea level was probably not much changed, suggesting a submarine emplacement. We will try to

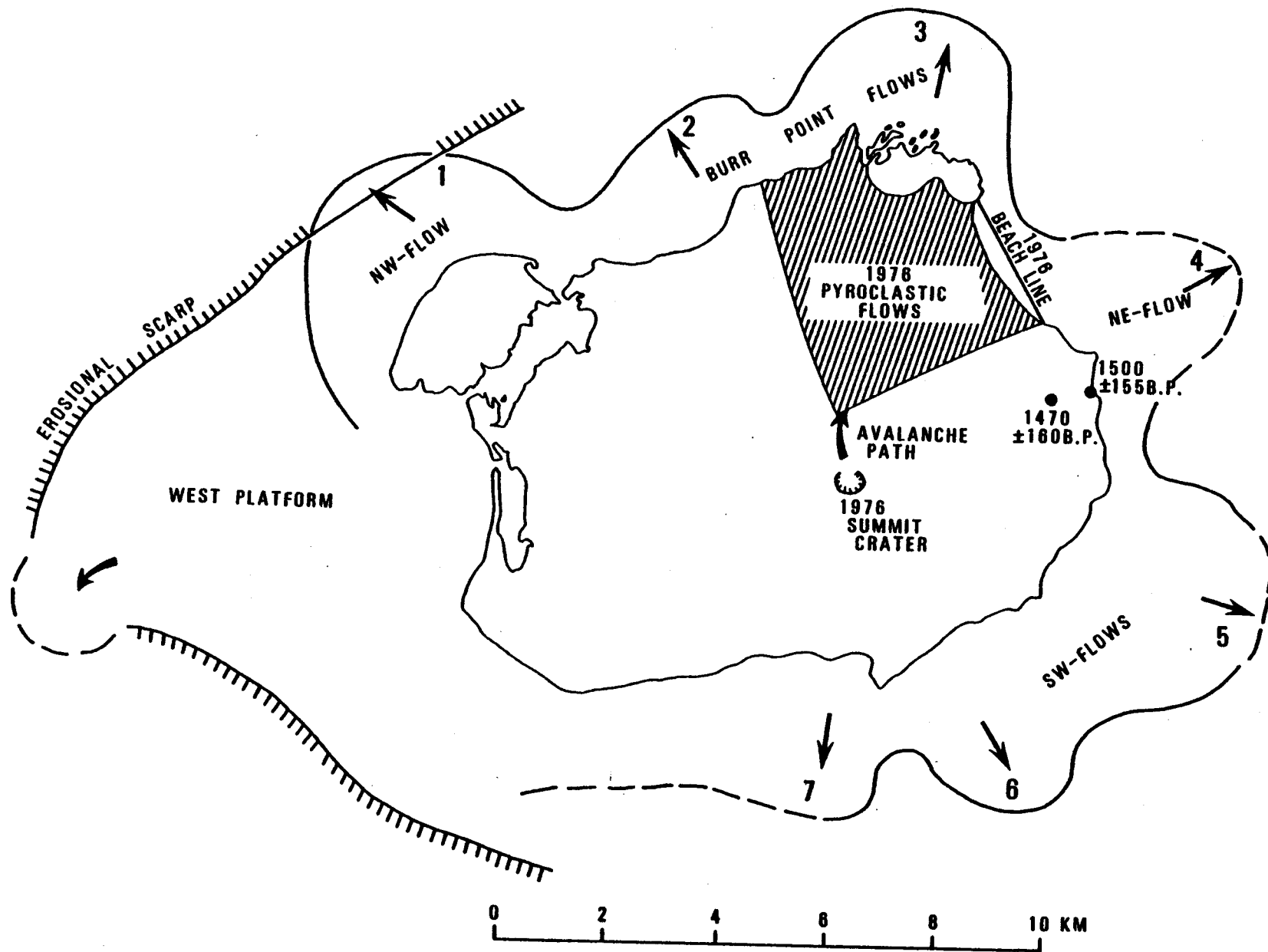


Figure 38. Suspected offshore pyroclastic flow deposits off Augustine Island.

verify the nature of these flows through direct sampling with divers this year.

Submarine counterparts of late Quaternary subaerial pyroclastic flow deposits off the western flank of the 1,400 m high volcano Morne Diablotins on the island Dominica, Lesser Antilles (the next island north of Martinique, where Pelee is located) were recently investigated by seismic reflection profiling and dredging (Sparks et al., 1980a and b). A submarine fan, consisting of block-and-ash flow deposits formed by dome collapse and a welded ignimbrite could be traced as a major ridge (2-4 km wide and 200-400 m thick) to over 13 km (!) offshore at a water depth of 1,800 m. Sparks et al. suggest that this demonstrates that pyroclastic flows can move underwater without losing their essential character and furthermore that the deposit may even be welded.

The two papers by Sparks et al. are the only ones known to us on the subject of what happens when pyroclastic flows enter the sea. The fact that they can stay intact for such long distances suggests that there is a good chance that the preliminary identification of the submerged rugged terrain offshore Augustine as pyroclastic avalanches will prove to be correct (Figure 28).

In summary, basal avalanches and associated hot air blasts and nuée ardentes are the major hazards from pyroclastic flows on Augustine Island. The basal avalanches present a hazard to any structure built on the island or in the near offshore area (at least as far as the postulated offshore flow deposits shown on Figure 38 reach). Thermal blasts and nuée ardentes present a hazard on the entire island and to a considerable distance offshore. Both can effectively carry across water for some

distance as evidenced by the destruction of ships in the harbor of St. Pierre during the 1902 eruption of Mt. Pelée. The effective range of the thermal effects is at least twice that of the actual avalanche deposits (Taylor, 1958). The avalanches are generated suddenly and reaction time is extremely short. The distance traveled and the velocity of the flows depends mainly on their volume, given the more or less fixed topography of Augustine Volcano. Small flows may spend themselves before they reach the sea, larger ones may continue offshore. At the seashore the basal avalanche will continue under water while the accompanying nuée ardente will detach itself and then surge rapidly out to sea.

Debris Flows and Flood Deposits

Debris flow and flood deposits are also common on Augustine Island (Figures 3, 7, 8, 11 and 34). Conventionally, this category of deposits would include just the classical mudflow deposits formed by water-saturated masses of debris moving downslope in response to gravity. However, experience with the 1976 Augustine eruptive deposits has shown that surface deposits of pyroclastic flows and tephra are quickly modified by running water from either snow melt or heavy rainfall and the distinction of such reworked material from original mudflow deposits is difficult, especially on aerial photographs of the older eruptive deposits. Thus, the debris flow and flood deposit category includes not only mudflow deposits but also reworked air fall deposits. Criteria for recognition of these deposits include the presence of surface flow lines, natural levees and a lobate distal end.

Debris flow and flood deposits are widespread on Augustine, even for a single eruption cycle. During the 1976 eruptions these deposits formed an almost circular apron surrounding the Augustine vent (Figures

27 top right and 34). Lack of a well defined drainage system on Augustine Island and the presence of a thick snow pack for much of the year further smoothing out the topography, act to produce these circular patterns of debris flow and flood deposits.

The deposits consist of poorly sorted volcanic fragments ranging in size from a fraction of a millimeter to several meters in diameter. Fine-grained clay-sized particles are not found in these deposits, as expected, given the fresh unaltered nature of the detritus. Some of the deposits are crudely stratified, apparently in response to a higher water content, with gradation in fragment size defining the individual beds. Variation in particle size for the pumiceous Augustine ejecta cannot be directly correlated with particle weight, since some of the more vesicular pieces can actually float on water. Thus, the presence of large particles within a particular bed does not necessarily indicate a high energy flow regime. Many of the pumiceous rocks show evidence of rounding in these deposits, not unusual considering the soft character of the pumiceous volcanic glass.

Hazards from debris flows and floods on Augustine are primarily related to burial. Mudflows, included within this category, can move with great speed (up to 85 km/h) and cover great distances (over 150 km at other taller volcanoes). Given the velocity and extent of debris flows, no cultural features would be safe from burial on Augustine Island (in 1976 we lost all but 1 of our 5 seismic stations and 2 camps). Debris flows quickly break up upon reaching the water and do not present a hazard to installations offshore Augustine Island.

Tsunamis

Sudden displacement of large bodies of water by impact of a pyroclastic flow into the sea can apparently produce volcanogenic tsunamis

at Augustine as we have discussed for the 1883 eruption. Because the waves arrived on the other side of Cook Inlet at low tide little damage was done at English Bay in 1883 even though the maximum run-up was about 10 m.

Based on our 10 year record, earthquakes associated with Augustine eruptions will most likely be too small ($M_L = 4$) to generate true earthquake-tsunamis which involve actual displacement of the sea-floor.

A submarine explosion of the scale of the 1883 Krakatoa event, which took the life of 36,000 people living along the shores of Sunda Strait when a "push-wave" tsunami radiated from the center of the explosion, is unlikely at Augustine, though possible at a much smaller scale.

If a tsunami should be generated at Augustine Volcano, platforms and vessels a few km offshore would probably only experience a relatively mild (<10 m) rise in sea level but low-lying areas of coastal communities along the eastern shore of Cook Inlet from Clam Gulch south (Ninilchik, Happy Valley, Anchor Point, Homer, Seldovia, English Bay) could expect run-ups of at least 10 m, depending on local conditions of shoaling.

Tsunami transit time depends on water depth; the velocity v of a tsunami is $v = \sqrt{g \cdot d}$, where g is the acceleration of gravity and d is the water depth. A tsunami generated at Augustine would cross Cook Inlet to English Bay and Homer in about half an hour.

Lava Flows and Domes

Volcanic domes are formed by viscous masses of magma moving up into a volcanic vent and forming a plug. Due to the high viscosity, domes show little tendency to flow. Continued upward movement of the magma mass may eventually make the dome unstable resulting in dome collapse and pyroclastic flows. Hazards from pyroclastic flows due to dome collapse at Augustine Volcano have been discussed in a previous section. Both, dome formation and partial collapse, are highly probable events during future Augustine eruptions.

Lava flows represent the rather quiet movement of lava out of the volcanic vent and down the flanks of the volcano. Lava flows may bury structures. If a hot lava flow encounters snow, melting may produce debris flows. Due to the high viscosities of Augustine magmas, lava flows are not common on the volcano. In fact, only one massive lava flow (prehistoric, on the north flank of the volcano, labeled L in Figure 27) has been identified on Augustine Island.

Tephra

Tephra, as used in this report, refers to rock of any size erupted into the air by a volcano. The rock may initially be molten magma, but this material quickly solidifies to rock upon entering the air. Based upon this definition, tephra eruptions are gradational to and include pyroclastic flows. However, the term pyroclastic flow is here reserved for the rather special glowing avalanche-ash cloud eruption, while tephra is the more general term used to describe any material thrown into the air by the volcano.

Hazards associated with tephra from Augustine Volcano include impact from falling particles, contamination of air with ash and, closer to the vent, thermal effects associated with hot ash.

Particle size in tephra ranges from less than one millimeter to several meters. Larger fragments, termed bombs (diameter greater than 5 cm) generally fall near the volcanic vent while the smaller lapilli (diameter 5 cm to 3 mm) and ash (diameter less than 3 mm) are carried further from the vent. The finest-grained ash may be injected into the stratosphere by very explosive eruptions and from there be dispersed on a global scale.

Winds strongly affect ash dispersal. As we demonstrated for the 1976 eruption, ash can be spread in opposite directions by surface winds and winds aloft. Some of the very large January, 1976 explosions penetrated the tropopause depositing very fine aerosols and sulfur gases in the stratosphere. Kienle and Shaw (1979) demonstrated an increased turbidity of the stratosphere over Mauna Loa, Hawaii, which decayed in about 5 months following the January Augustine eruption. From trajectory analysis at the 300 mbar (9 km) level Kienle and Shaw further deduced that the bulk of the January 23 plumes were transported along the base of the subpolar jet stream following a southeasterly path over western Canada, across the western United States, into Arizona and then turned northeast over the mid-western states and the Great Lakes, to southeastern Canada and out into the Atlantic. The passage of the plume was seen over Tucson, Arizona at an altitude of 7 ± 2 km in the evening twilight on January 25 (Meinel et al. 1976) and was instrumentally observed over Hampton, Virginia, at 12-14 km altitude on the evening of January 28 (Remsberg et al., 1976). This very long distance transport of ash

and sulfur compounds in the atmosphere and stratosphere occurred only for products of the more powerful initial vent clearing eruptions, which injected material to heights of up to 14 km. The later less powerful and less voluminous eruptions ejected plumes to more moderate heights of up to about 6 km, and consequently tephra fall was more localized.

Ash falls from Augustine Volcano can be expected to affect much of the Cook Inlet area from Anchorage, to Kodiak and out to the Gulf of Alaska (Figure 14 and Table 3). Ash dispersal and subsequent fall is governed by the prevailing wind direction at the time of eruption. For explosive eruptions, high altitude winds will control the ash dispersal. Figure 39 illustrates the prevailing high altitude winds at Kodiak, the point closest to Augustine Island for which such high altitude wind data is available. Prevailing high altitude winds at Kodiak are from the west and southwest. This wind pattern, transferred to Augustine Volcano, would force Augustine ash across Cook Inlet toward Homer. The lower Cook Inlet area may experience ash falls from Augustine Volcano up to a few cm in thickness. Heavy local ash falls at Iliamna and the lower Kenai Peninsula communities could be harmful to vegetation and livestock and could also contaminate surface water supplies, making them more acid. Machinery and turbines (aircraft) may suffer from severe abrasion and corrosion. For a more detailed discussion of the effects of ash falls on cultivated areas, we refer the interested reader to Wilcox's (1959) excellent discussions of this subject matter. In his paper he gives a detailed account of the effects of an ash fall over the city of Anchorage in July 1953, associated with an eruption of Mt. Spurr 125 km east of the city and he also discusses the effects of the great 1912 Mt. Katmai eruption on vegetation, livestock and man. The paper contains

SUMMARY OF AIRBORNE ASH FALLOUT COLLECTED AT VARIOUS ALASKAN NATIONAL WEATHER SERVICE STATIONS AND OTHER SOURCES
FOLLOWING JANUARY 23-24, 1976 ERUPTION

Location	Date	Time (AST)	Period of Collection	Collection Area	Weight (gm) of Accumulated Ash	Fallout gm/m ²	Fallout Rate gm/m ² -hr
Anchorage (11th and E Streets)	26 Jan. 1976	19:00	= 2 hr (1)	1 ft ²	5.1	54.9	= 27.5 (1)
Cantwell	26 Jan. 1976	15:30	--	--	trace	--	--
	28 Jan. 1976	9:45	--	--	negl.	--	--
	29 Jan. 1976	12:45	--	--	negl.	--	--
McGrath	26 Jan. 1976	?	--	--	trace	--	--
	27 Jan. 1976	?	--	--	trace	--	--
	28-30 Jan. 1976	?	--	--	negl.	--	--
Seldovia	23 Jan. 1976	(after 1st erupt., before second.)	--	= 1m ²	62.7 gm (2)	= 62.7 (2)	--
	23 Jan. 1976 (after 2nd erupt.)	18:30-19:30	1 hr	.92 m ²	171.5 gm (3)	-- (3)	185.6
	24 Jan. 1976	No observable fallout	--	--	--	--	--
Talkeetna	26 Jan. 1976	18:10	--	--	trace	--	--
	27 Jan. 1976	17:05	--	--	negl.	--	--
Valdez (downtown)	26 Jan. 1976	15:00	--	3 ft ²	.53	.63	--
Iliamna	23-24 Jan. 1976	?	--	--	--	--	--
Homer Spit	23 Jan. 1976	late afternoon (from 16:18 erupt.)	--	--	--	--	--
	6 Feb. 1976	15:00-17:00	--	--	--	--	--
Oil Point	29 Jan. 1976	15:00-18:00	--	--	--	--	--
Following February 1976 Eruption							
Homer	6-7 Feb. 1976	16:30-16:00	23.5 hr	1 m ²	12.33	12.33	.52

(1) Collector observed bulk of ash fall between 09:00-11:00 AST, 25 January 1976.

(2) First eruptive event only (see notes on observations).

(3) Second eruptive event only (see notes on observations).

TABLE 3 - (compiled by R. Motyka)

KODIAK - WIND DIRECTION AT 40,000FT

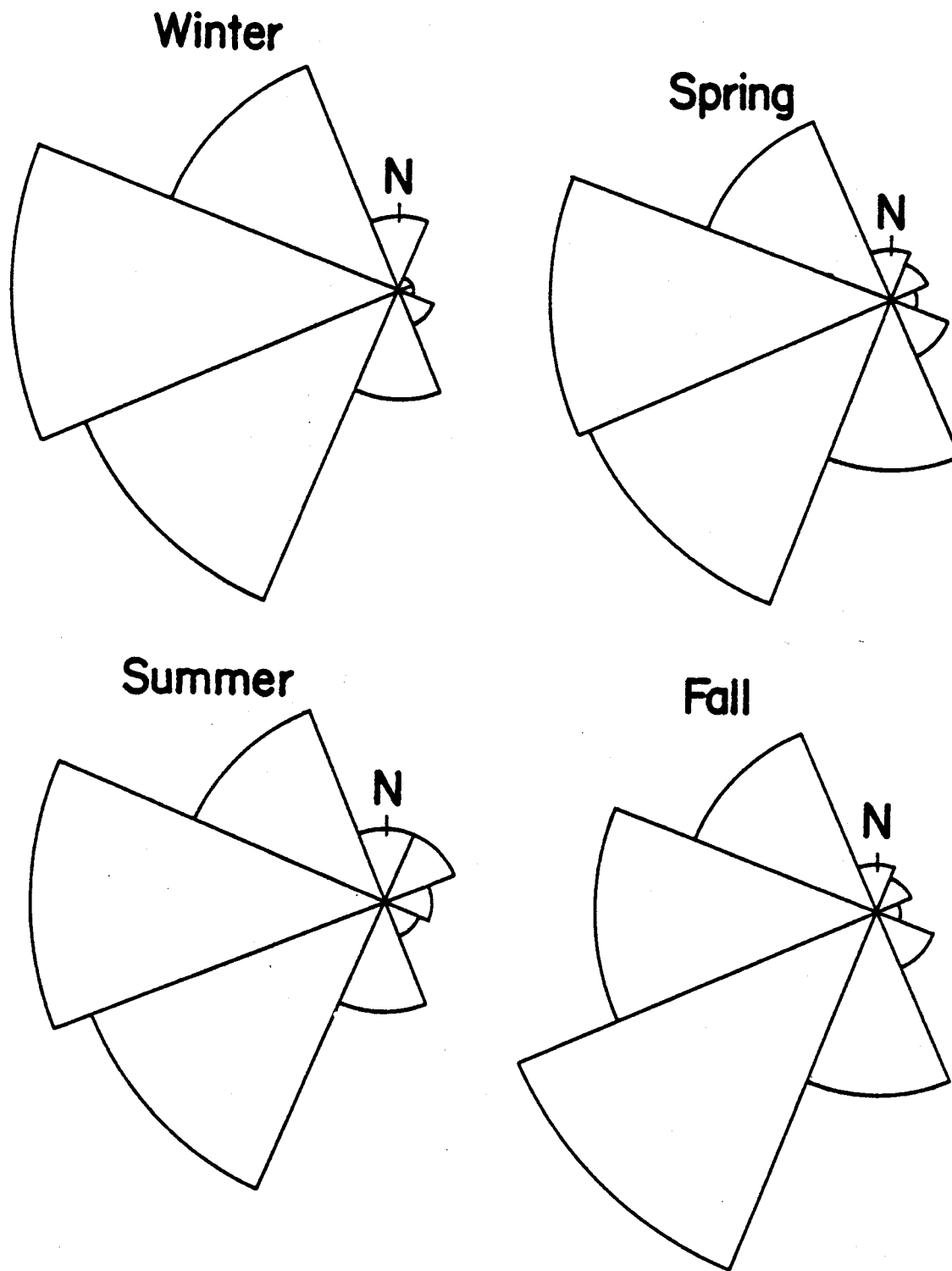


Figure 39. Prevailing high altitude winds at Kodiak (from Wilcox, 1959).

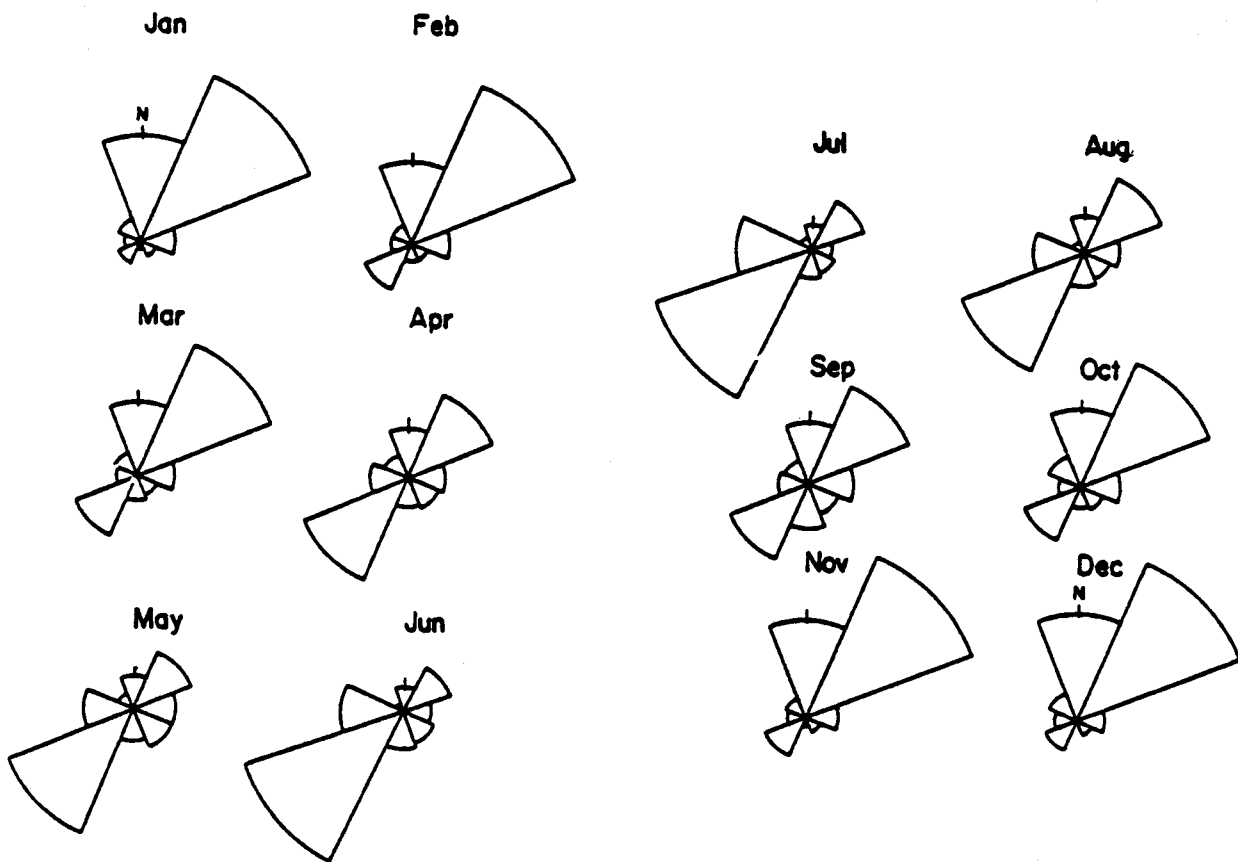
useful tables on the effect of gases on plants (p. 452) and on the effects of gases on humans (p. 443). It is worth noting that for both the Katmai and the Spurr eruptions ash dispersal was principally to the east as we observed for the 1976 Augustine eruptions, confirming the prevailing high altitude flow from the west or southwest, regardless of the seasons.

During the period of heavy ash fall, the air is charged with ash particles that could be harmful, if inhaled. A simple air filter (respirator) will remove the ash particles and render the air breathable. In January and February 1976, the air was extremely dusty in the vicinity of Augustine Island, even when the volcano was not in eruption, because strong winds picked up the dust from the island and spread it for tens of km offshore. Figure 40 (top) shows the prevailing surface winds based on Homer wind data, which may not be very representative of Augustine. Surface wind data is badly needed for the island.

Widespread fall of tephra can also have positive effects. Mathisen and Poe (1978) reported that the 1976 Augustine ash falls over the Lake Iliamna, Kvichak waters had almost immediately boosted primary production. The input of phosphorus and silica into the biologic system increased chlorophyll and phytoplankton concentrations and produced a great change in species composition enhancing the productivity of silica utilizing diatoms.

Thorarinsson (1954, p. 62) comments on the complete disappearance of cod on the coast south of Iceland for two days following the ash fall of Hekla in 1947. Perhaps such short-lived migrations of fish do occur near Augustine following extensive tephra deposition offshore, but no one has reported this yet.

HOMER WIND DIRECTION AT SURFACE



KODIAK WIND DIRECTION AT SURFACE

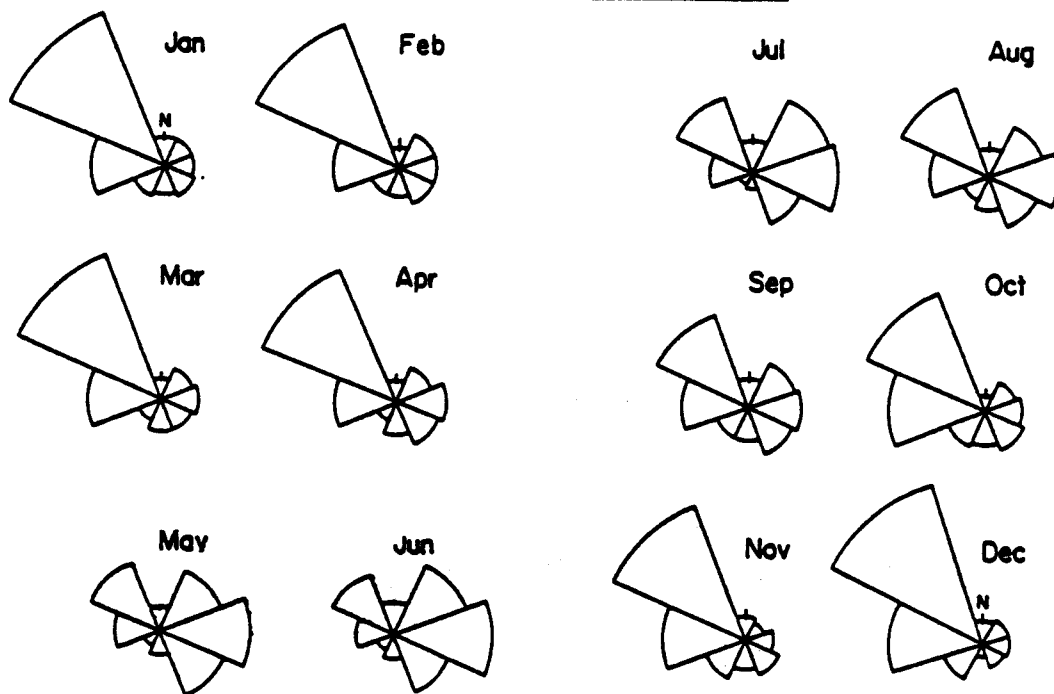


Figure 40. Prevailing surface winds at Homer and Kodiak (compiled from data given in Brower et al., 1977).

Tephra deposits are widespread on Augustine Island. Generally, the tephra layers are thin, on the order of a few millimeters to a few centimeters around the periphery of the island. Bomb distribution is restricted to the flanks of the volcano where the surface is littered with these large fragments. In 1976, bombs as large as 10 to 15 cm in diameter weighing at least 1 kg fell ballistically through the roof of the Burr Point research station 5.5 km from the summit. Theoretical ballistic considerations (e.g., Wilson, 1972; Fudali and Melson, 1972; Self et al., 1980) considering up to supersonic muzzle velocities suggest that the theoretical vacuum range $R = \frac{V_0^2 \cdot \sin 2\theta}{g}$, where V_0 is the muzzle velocity, θ the ejection angle (max. range for 45°) and g the gravitational acceleration, greatly overestimates the range attained by a projectile and that drag forces drastically reduce the range. Simple oblique ejection of the roof-piercing Burr Cabin bomb from the crater rim would, even at a supersonic muzzle velocity of order 600 m sec, not have thrown the bomb that far. We infer that the bomb must have been transported in an oblique trajectory within an eruption column to a considerable height (several km) above the summit to attain that range.

Grain size rapidly decreases with distance from the volcano. For example, the maximum grain size of pumices (density .99 g/cm³) at Oil Point 35 km north of the volcano was 15 to 20 mm. Damage and injury due to the falling of large blocks are probably restricted to within a radius of about 10 km of the volcano.

For the dispersal of finer tephra particles we may be able to use Hekla volcano as an analogy. Thorarinsson (1954, reinterpreted by Wilcox, 1959) found that at 3 km distance from the vent 80% of the material was between 0.15 and 5 cm in diameter (maximum size 6 cm), at 30 km 80% it

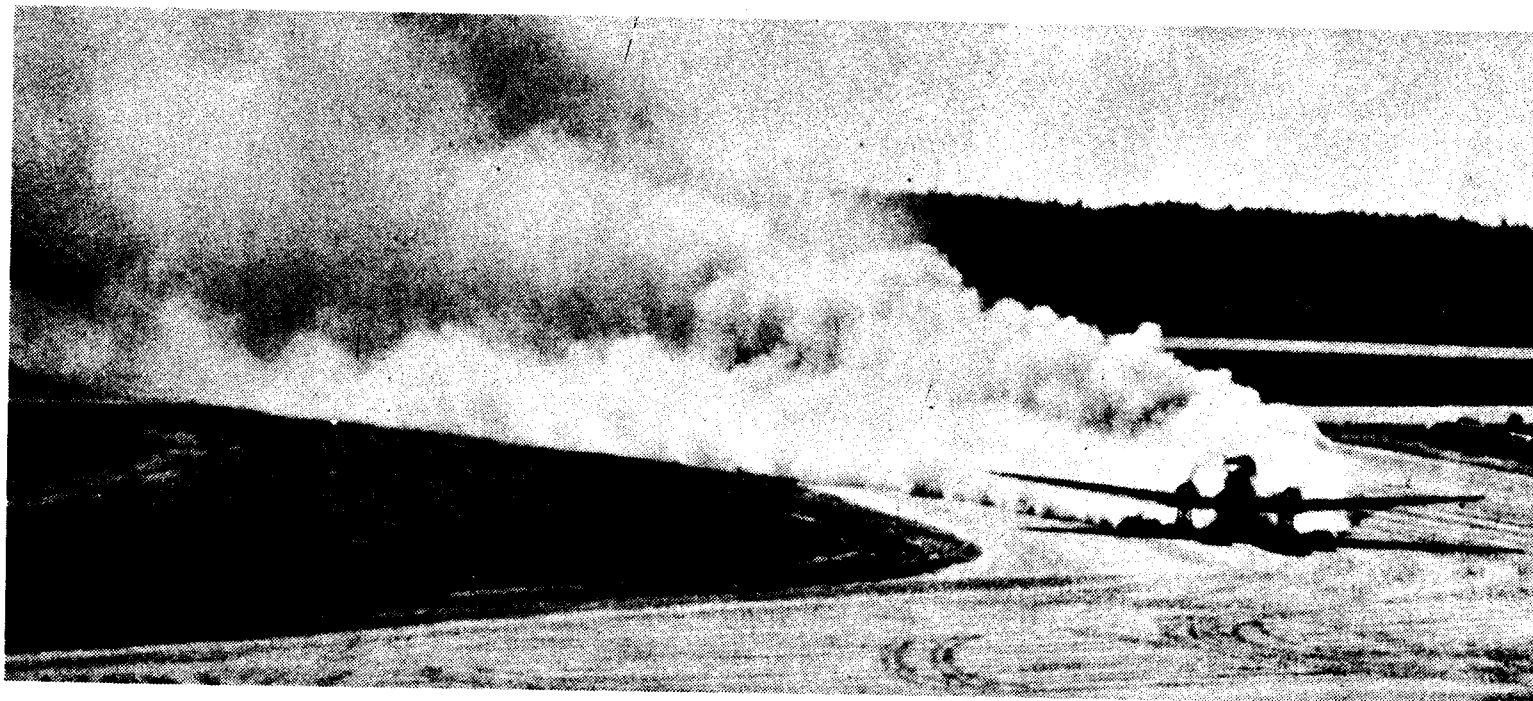
was 0.05 to 0.50 cm diameter (maximum size 1.5 cm) and at 70 km the maximum size was 0.2 cm. The exact ranges depend on local wind conditions, muzzle velocities and height of the eruption column but the example is given here to convey a rough idea of what to expect.

Hazards to aircraft flying near or over an erupting volcano can be quite substantial. Take off and landing on ash covered runways may be temporarily impaired if not completely impracticable due to very low visibility (see Figure 41). Kienle and Shaw (1979) have documented hazards to aircraft penetrating high altitude eruption clouds at large distances (> 100 km) from the erupting volcano in January 1976. One of the January 22 eruptions occurred in the midst of an air defense exercise. The following is an excerpt of a report by two F-4E Phantom Jet pilots who had taken off from Galena on January 22, 1976, bound for King Salmon and penetrated an eruption cloud:

"The two jets were flying in clouds, cruising at 31,000 feet (9 km). We were still in the weather when suddenly at 14:30 AST (January 23, 00:30 U.T.) the ordinary grey clouds slightly darkened for a moment or two, then there was instant complete darkness. There was no turbulence associated with this darkness. The two jets were flying in close formation about 10 meters apart. Had the lead plane not immediately turned on its lights, the following pilot would have lost contact; he could barely see the lead plane 10 meters away with its lights on. Upon landing in King Salmon the canopy of the aircraft was scoured, and the paint at the wing tips was sandblasted off. Very fine jewelers rouge-colored material was ingested into the cockpit through the engine air intake. The material was sticky and was found in every nook and cranny of the planes. "

A second incident concerns three Japanese Airline jet aircraft in route to Tokyo on the afternoon of January 25, 1976 (Mr. K. Noguchi, Japanese Airline, personal communication):

Cargo flight JL672 took off from Anchorage at 16:00 AST (January 26, 02:00 U.T.). The DC8 was just about to reach its cruising altitude of 33,000 ft (10 km), 25 minutes after takeoff, travelling along air route J501 when it suddenly entered an Augustine ash



547

When Mount Spurr, 40 miles northwest of Tyonek, erupted on July 9, 1953, Viola T. Mason, who now resides in Hillman, Michigan, was an air traffic controller at Anchorage International Airport. To commemorate the twentieth anniversary of the big blowup which dumped ash on Anchorage, Miss Mason provided this photo of a plane landing at Anchorage International Airport the day after the eruption. "Each takeoff and landing resulted in near-zero visibility until the dust settled," recalls Miss Mason. "Jet blowers were brought over from Elmendorf Air Force Base to blow the stuff from the runways, but the capricious winds would only blow it back."

Viola Mason

ALASKA/magazine of life on the last frontier – AUGUST 1973

Figure 41. Ash on the runway of Anchorage International Airport from the 1953 Mt. Spurr eruption.

cloud near Whitefish Lake, 25 km southeast of Sparrevohn. Upon landing in Tokyo the scoured center windshield had to be replaced and much ash had adhered to the plane. Slight abrasion damage was found on external radio parts, landing gears and the air-conditioning system, but none of these parts needed to be replaced.

Two other passenger planes, a Boeing 747 and a DC8, also bound for Tokyo and departing within one hour after flight JL672, reported ash suddenly adhering to the planes near Sparrevohn which also caused minor damage but not as extensive as that to the DC8 of flight JL672.

Passenger aircraft along air traffic routes near Augustine Volcano (e.g., Anchorage - King Salmon route) should divert from the volcano when it is in eruption. Unfortunately, diversions are frequently taken in the opposite direction, over the erupting volcano, in order to give the passengers a better view. How dangerous this can be was recently demonstrated, when during eruptions of Sakurazima Volcano in Kuyushu, Japan, on December 18 and 24, 1979, flying bombs cracked the windshields of low flying domestic aircraft. Fortunately, both planes landed safely (SEAN bulletin of the Smithsonian Institution, Vol. 5 (1), Jan. 1980, p. 8).

Large electrostatic charge buildup in active eruption columns can cause severe lightning storms, which may strike passing vessels or aircrafts or block radio communication. We frequently lost our radio VHF signals from seismic stations behind the volcano when eruption columns were well developed. Eruption clouds can easily be seen on land or ship and aircraft based radar (Kienle and Shaw 1979). During summer eruptions forest fires may be started by lightning around the shores of Kamishak Bay.

Visibility can be greatly reduced for short periods of time and at relatively large distances (> 100 km) when an ash laden eruption cloud

passes overhead as we described for the towns of Homer and Iliamna during the January 1976 eruptions. For prolonged ash falls, even at moderate ash fall rates, the lasting darkness, if combined with interrupted radio, telephone and electrical services could cause severe psychological stress, perhaps panic as was recently demonstrated during the Mt. St. Helens eruption. Near the volcano such conditions can be extreme and last for days. During many historic eruptions, survivors have reported that day becomes as dark as night. Under these circumstances, evacuation of personal from say a drilling or producing platform offshore Augustine Island may be quite difficult. Clearing of heavy ash accumulations on roofs of such structures may be necessary to avoid collapse and persons may have to wear respirators for very long periods of time (days).

Volcanic Gases

Large quantities of gas are evolved from juvenile melt during an eruption because of the great decompression that occurs when new melt actually reaches the surface, but active volcanoes also emit gases without the eruption of molten material.

Water is the most common gas, followed by carbon dioxide sulfur compounds (SO_2 and H_2S), carbon monoxide, chlorine and smaller amounts of other gases (Cl_2 , F_2 , N+ rare gases, $\pm \text{H}_2$).

The dispersal of volcanic gases is primarily controlled by near-surface winds. Gases are most concentrated near the vent but become rapidly diluted downwind. Odors can often be smelled many tens of km downwind (a table that relates the concentration of various gases to initially objectionable odor and to maximum allowable human exposure is given on p. 443, Wilcox, 1959). While SO_2 can be smelled at concentrations of only 1 ppm relative to the maximum tolerable amount of 10 ppm, chlorine

is more dangerous as only 0.35 ppm are allowable, yet it can only be smelled at concentrations as high as 3.5 ppm. Near surface wind patterns for Kodiak and Homer (the closest data points to Augustine Island) are shown in Figure 40. This data should be used with extreme care, as it probably does not apply very well for Augustine. Volcanic gases from Augustine Volcano will be spread by surface winds over the lower portion of Cook Inlet. In order to map out the most vulnerable directions we would need average surface wind data for every month of the year at Augustine. During the 1976 eruptions the gases were mainly dispersed east-northeast.

Volcanic gases may be harmful if inhaled in sufficient concentrations for a long time. Hazards from volcanic gases include suffocation, irritation of eyes and respiratory systems and corrosive effects associated with acid compounds. The presence of chlorine or one of the sulfur compounds produces irritation and a burning sensation in the eyes and lungs. However, these gases are mixed with air and if the chlorine or sulfur gas is removed by simple filtration (industrial gas masks work well) the air is safe to breathe. If a mask is not available a wet cloth over mouth and nose does wonders, especially when wetted with a dilute solution of Sodium Bicarbonate (e.g., medicinal powders sold for acid indigestion or baking soda).

Freak accidents sometimes occur in volcanic areas when odorless CO_2 pools in topographic depressions. On February 20, 1979, during eruptions of Dieng (Indonesia), 149 persons were killed by gas containing H_2S and mainly CO_2 which ponded in a low-lying area beside a road. Fleeing along the road from the eruptive activity the people passed the pool and suffocated (SEAN bulletin of the Smithsonian Institution, Vol. 4 (3), March, 1979, p. 5).

Chlorine and sulfur gases are extremely corrosive on metals. Rain water combining with chlorine or sulfur gas can produce acid rains that are harmful not only to metals, but also to vegetation. Acid rains during the 1912 Mt. Katmai eruptions spread to Seward and Cordova and even to Vancouver (B.C.) and Chicago (Griggs, 1922). The bulk of the acid in these rains is sulfuric acid, as SO_2 combines with H_2O in the atmosphere. Dilute solutions of baking soda or alkaline soap help to neutralize the acid and can be used to wash metal objects and irritated skin and eyes.

During eruptions involving new melt, as is the case for all historic Augustine eruptions, the volcano emits large amounts of sulfur dioxide and also substantial quantities of chlorine (Johnston, 1980).

In summary, gas-related hazards from Augustine Volcano are primarily related to corrosive effects of chlorine, sulfur gases and accompanying acid rains. Hazards to health or life from these gases can largely be removed by simple filtration. Corrosion of metallic structures in lower Cook Inlet will be a problem during eruption of Augustine Volcano. The concentration of the gases and hence the level of the hazard is of course greatest near the volcano.

HAZARD ZONES

All of Augustine Island and much of the lower Cook Inlet area will be affected by future eruptions of Augustine Volcano. Hazards to both human life and property are expected during an Augustine eruption. However, the approach to hazard zoning taking in this report follows the example of Crandell and Mullineaux (1978) for Mount St. Helens Volcano and does not distinguish between hazards to life and property. Instead, the hazard zones attempt to describe areas of potential danger from different eruption-related hazards and then assess the hazard in terms of magnitude and expected frequency.

Assumptions

Two key assumptions are made in the hazard zone analysis:

First, the eruptive pattern for Augustine Volcano in the future will be similar to the past eruptive history. Studies of historic Augustine eruptions reveal a similarity in eruptive style and products. Magma composition, which plays a big role in determining the mode of eruption, has been relatively constant on Augustine Volcano for at least the past 1,500 years, implying a similar eruptive style for the past 1,500 years. Augustine Volcano has erupted several times per century and this active pattern is expected to continue.

A second assumption involves the regional extent of hazard zones. Data for some types of hazards associated with Augustine eruptions are incomplete or nonexistent. Examples of such data gaps include the extent of pyroclastic flows around Augustine Island and how far the associated hot gas clouds would travel out to sea. The horizontal distances traveled by the hot gas clouds beyond the shore line have

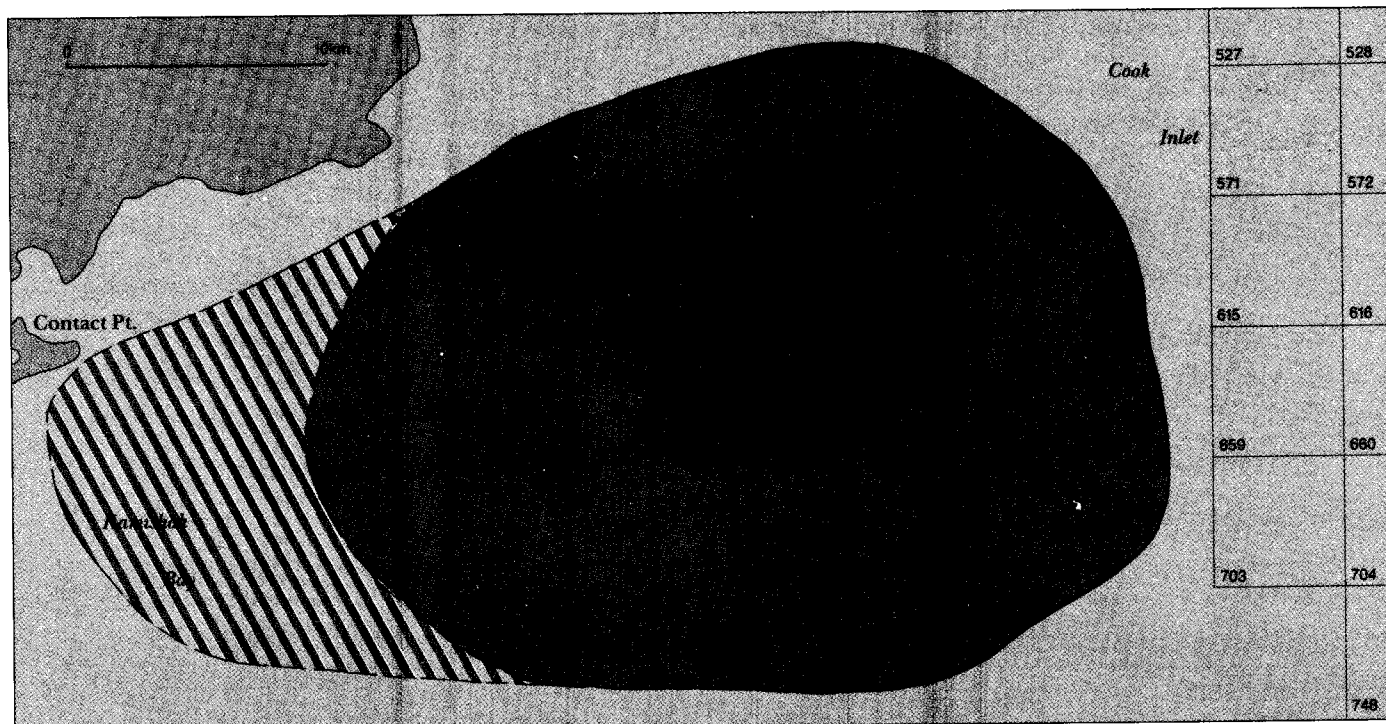
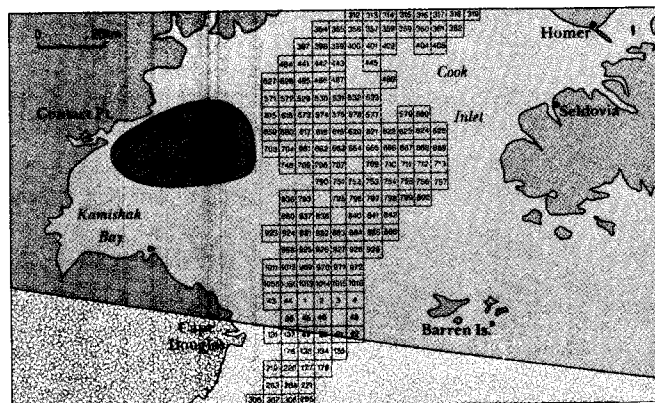
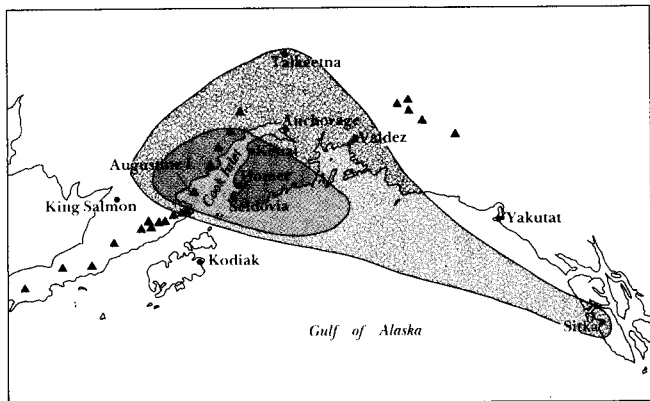
never been measured, nor has the offshore extent of the pyroclastic flows been determined. In such cases historical analogues have been selected to model the Augustine hazards. Particular reference is made to the 1902 eruption of Mont Pelee in the West Indies (Anderson and Flett, 1903) and the 1951 eruption of Mount Lamington in Papua (Taylor, 1958). Both of these volcanoes are characterized by pyroclastic flow eruptions and are similar in height to Augustine Volcano and thus should serve as good models for Augustine eruptions.

Hazards from Augustine Volcano are principally associated with pyroclastic flows and tephra fall. Hazard zones are shown on Plate 1. Four hazard zones, ranging from low risk to very high risk are distinguished around Augustine Island. Boundaries between the zone are not exact, but instead represent the authors best estimate of the effective range of a given set of hazards. Future work on Augustine eruptive products, particularly offshore deposits, may change the hazard zones shown on Plate 1.

Very High Risk Hazard Zone

A very high risk hazard zone includes all of Augustine Island and an offshore region to the northeast of the island (Plate 1). Within this zone, hazards are associated with pyroclastic flows (nuée ardentes) volcanic bomb fall, mudflows, tephra accumulation and volcanic gases.

Pyroclastic flows are a common feature of Augustine eruptions and should be expected to accompany every eruption of the volcano. Hazards accompanying the pyroclastic flows are associated with both the basal avalanches and the hot ash clouds (nuée ardentes). During historic time, pyroclastic flows have moved down all sides of the volcano, except for the southern flanks (Figs. 7, 8, 11 and 34). However, postulated



-  Area of very high risk to human life and property associated with falling volcanic bombs, pyroclastic flows, volcanic gases, thick tephra accumulation and mudflows (on or nearshore only).
-  Area of high risk to human life and property caused by pyroclastic flows, volcanic gases and tephra accumulation. (Extent uncertain in striped area.)
-  Area of low risk to human life and moderate risk to property caused by volcanic gases and tephra accumulation.
-  Area of no risk to human life and low risk to property caused by volcanic gases and tephra accumulation.
-  Extent of 1976 pyroclastic flows.
-  Extent of offshore pyroclastic deposits based on bathymetry.
-  Extent of volcanic bomb fall for 1976 eruption. (Fragments > 15cm diameter.)
-  Offshore lease blocks.
-  Volcanoes.

Plate 1

offshore pyroclastic flow deposits are found to the south of Augustine Island (Plate 1) and thus future pyroclastic flows might extend in any direction from Augustine Volcano. Due to the present crater configuration and the shape of the 1976 dome, the next eruption of Augustine Volcano is expected to initially direct pyroclastic flows down the north flank of the volcano, hence the offshore extension of the very high risk hazard zone shown in Plate 1. Volcanic risk is fairly high at lease blocks 571, 615, 659 and 703 and the latter two should probably not be reoffered for sale; the first two are already sold. Continued eruption and dome removal may subsequently change the direction of pyroclastic flow movement.

A zone of volcanic bomb hazard is shown on Plate 1 as a circle with the center at the 1976 Augustine Crater. The radius of this hazard zone is the distance from the 1976 crater to the Burr Point research station (an area that sustained volcanic bomb damage during the 1976 eruption, as previously discussed). Hazards associated with volcanic bomb fall may extend the limits shown, but the area within the circle (including most of Augustine Island) is subject to heavy volcanic bomb fall.

Mud (debris) flows accompany all eruptions of Augustine Volcano and may continue for several years following an erupting depending on availability of detritus on the slopes of the volcano. Mudflows may develop on any portion of Augustine Island and extend for short distances into offshore areas.

Accumulation of new material within the very high risk hazard zone (Plate 1) is associated mainly with the deposits of pyroclastic flows and, to a lesser extent, with ash fall from eruptive clouds. During the 1976 eruption of Augustine, pyroclastic flows deposited material tens of meters deep on the northeastern portion of the island (Fig. 34) while tephra accumulations from the normal ash fall formed deposits less than

10 cm thick at the periphery of the island. Accumulation of air fall tephra is largely controlled by the prevailing winds. For areas close to the volcano, such as the high risk zone shown in Plate 1, deposition of air fall tephra will be controlled by surface wind directions. The surface wind data available for Homer and Kodiak (Fig. 40) is probably not applicable for Augustine Volcano because in both cases the wind data might be affected by severe topography. Our experience during the 1976 eruption suggest that all sectors of the volcano will be affected by tephra fall with the northeastern and southwestern sector receiving most of the accumulation. Volcanic gas dispersal is also controlled by surface winds within the high risk area and should follow the same pattern as air fall tephra.

High Risk Hazard Zone

A high risk hazard zone characterizes the immediate offshore area of Augustine Island (Plate 1). The outer limit of this hazard zone is based on the presumed extent of offshore pyroclastic flows. On the western edge of Augustine Island a broad submarine platform (Plate 1) may represent submerged pyroclastic flow deposits or an old erosional bench. Because of the uncertainty regarding the character of this terrain, the extent of the high hazard zone in this region is uncertain. The western limit for the high hazard zone on Plate 1 is drawn assuming that this terrain represents pyroclastic flow deposits. If subsequent work reveals that the western submarine platform is not composed of pyroclastic flow deposits, the western extent of the high risk hazard zone shown on Plate 1 would be reduced.

Other offshore deposits are apparent on the bathymetry around Augustine Island (Plate 1) and their lobate form and rough topography suggests they are probably pyroclastic flow deposits. Pyroclastic flows

did travel offshore during the 1976 eruption of Augustine Volcano and Sparks et al., (1980a) documented submarine pyroclastic flow deposits offshore a volcano on Dominica in the West Indies. Thus, pyroclastic flows can travel for some distance underwater and the bathymetry outlined on Plate 1 very likely does represent pyroclastic flows from Augustine Volcano that moved offshore for some distance.

Hazards within the high risk hazard zone (Plate 1) are associated with pyroclastic flows, tephra accumulation and volcanic gases. Hazards from pyroclastic flows are related not only to the basal glowing avalanches that account for most of the deposition of debris but also to the thermal and blast effects from the *nuee ardente* that rises above the glowing avalanche. Hazards due to hot blasts from the hot ash cloud extend in a near zone well beyond the termini of glowing avalanche deposition. At Mont Pelée and Mount Lamington the hazard zone associated with the hot ash cloud extended up to twice the distance from the crater to the distal ends of the basal avalanche deposits (Anderson and Flett, 1903; Taylor, 1958). The limit of the high risk hazard zone shown on Plate 1 is taken to be three times the extent of the pyroclastic basal avalanche deposits. Tephra accumulation within the high risk hazard zone will vary in thickness from meters (basal avalanche deposits) to less than a few tens of centimeters (air fall tephra). All sectors of the volcano within this zone will be affected by volcanic gas or air fall tephra as controlled by surface wind dispersal.

Moderate Risk Hazard Zone

A zone of moderate risk hazard covers most of the lower Cook Inlet and much of the Kenai Peninsula (Plate 1, insert). Hazards within this zone are due to tephra accumulation and volcanic gases. At these distances from Augustine Volcano, tephra accumulation will result from air fall and the distribution will be controlled largely by high altitude winds. Figure 39 gives the high altitude wind pattern for Kodiak (the weather station closest to Augustine Island with high altitude wind data) and shows the dominant westerly high altitude wind flow. These persistent westerly winds account for the tephra dispersal pattern over the lower Cook Inlet shown on Plate 1. The outer limit of the moderate risk hazard zone shown on Plate 1 is approximately the limit of one millimeter of tephra accumulation during the 1976 eruption of Augustine Volcano. Moderate volcanic gas concentrations are expected within the zone of moderate volcanic risk. The major hazard associated with these relatively low concentrations of volcanic gas is the corrosive effect on metals.

Low Risk Hazard Zone

A zone of low risk hazards associated with tephra accumulation and volcanic gases from Augustine Volcano covers much of south-central Alaska (Plate 1). This hazard zone coincides with the area of trace tephra accumulation from the 1976 eruption of Augustine Volcano. Distribution of tephra and gas within this zone is controlled by the high altitude westerly winds. Tephra accumulations are expected to be less than one millimeter and low concentrations of volcanic ash and gases will result in minor corrosion to metals.

Data Gaps

Several data gaps were found during the volcanic hazard assessment of Augustine Volcano. Some of the data gaps are currently being filled while others are not being studied. Aside from the historic record, little tephrochronologic data is available on the frequency of eruptions of Augustine Volcano. Very preliminary data (Fig. 36) suggests the recurrence interval is becoming shorter. However, without confirmation in the prehistoric record this intriguing suggestion cannot be evaluated. C^{14} geochronology is currently being done on paleosoils interbedded with tephra from the northeast side of Augustine Island and this study will furnish some data on the problem of recurrence interval. To properly study prehistoric Augustine eruptions, detailed tephrochronologic studies should be done at sites in Kamishak Bay around Augustine Volcano.

Another data gap involves the extent of offshore pyroclastic and debris flows and the glacial history of Augustine Volcano. Postulated offshore flows, based on bathymetry, are shown on Plate 1. It is not certain that these offshore areas represent flows. Sampling of these offshore areas will be attempted by divers in 1980 and if successful we should be able to assess the extent of offshore flows.

Wind data is not available for Augustine Island and the dispersal of volcanic gas and ash from Augustine Volcano must utilize high altitude wind data from Kodiak (Fig. 40) or surface wind data from either Homer or Kodiak (Fig. 41). High altitude winds probably show little variation over the relatively short distances between Kodiak and Augustine Island. However, surface winds show considerable variation over relatively short distances due to the influence of surface topography and thus, the application of surface wind data from Homer or Kodiak to Augustine

Island is probably not valid. Surface wind data from Augustine Island is very much needed to assess the dispersal of low altitude ash and volcanic gas from eruptions of Augustine Volcano.

Some eruptions of Augustine Volcano, such as the 1883 eruption, produced tsunamis of considerable magnitude (Kienle and Forbes, 1976). Hazards from eruption-related tsunamis have not been studied in the current hazard assessment and warrant future work.

VOLCANIC ERUPTION PREDICTION AND MONITORING

Augustine will certainly erupt again and it is likely that the eruptions will be similar in magnitude and style to the previous ones. We base this prediction on the constancy of volume and geochemistry that has been observed for the past 5 historic eruptions and the composition of tephra back to 1,500 B. P. Pyroclastic flow activity and lava dome formation will probably accompany the next eruption with widespread ash falls affecting much of the lower Cook Inlet region, including both the eastern and western shores. The duration of eruptive activity is likely to be less than 1 year and most intense only during a few months.

We have discussed the geophysical precursors to eruptions that are commonly monitored on other volcanoes, i.e., seismicity, deformation, subterranean mass movement, changes in the electric and magnetic fields, changes in heat flux and fumarole temperatures, and changes in the geochemistry of the gases emitted from the volcano.

Since 1970, we have tried most of these methods on Augustine Volcano, except deformation, and found seismicity the most reliable predictive tool. As we discussed above, the January 1976 eruptions were preceded by eight months of low-magnitude microearthquake activity, with a major earthquake swarm of larger magnitude events signaling the main set of eruptions on January 23, 1976 that cleared the vent only hours later. A few preliminary explosions occurred before this earthquake swarm. Contrasting this sequence of events with the recent Mt. St. Helens eruptions, seismicity at Helens increased dramatically about 2 months prior to the catastrophic May 18, 1980 eruption, with March 20 marking the date of the first significant earthquake, of magnitude $M_L = 4.1$. Frequent large-magnitude events ($M_L = 4-5.5$) and occasional harmonic tremor, indicating

magma movement at depth, were recorded during the 2 months prior to May 18 but no significant seismic events signaled the cataclysmic blast of May 18, which had an extremely sudden onset. To our knowledge at this time, the only other important precursor to the May 18 event was rapid uplift of an area just below the crater on north side of the volcano, beginning in late April - as much as 6 m between April 24 and 29 (Scientific Event Alert Network - SEAN, Smithsonian Institution, Washington, D.C., 5(4):3).

For the future, in addition to continuing to operate the 4-station island-based seismic array we are planning to begin geodetic monitoring of Augustine Volcano to measure deformation. Hopefully, continued geophysical monitoring of Augustine Volcano will allow us to anticipate, if not predict the next eruption.

ACKNOWLEDGEMENTS

The authors gratefully acknowledge the contributions of Dr. David A. Johnston to the studies of Augustine Volcano. Much of the petrologic data on the 1976 eruptive products was collected by Johnston as part of his Ph.D. dissertation at the University of Washington. In addition, he contributed to the hazard studies and the collection of Augustine volcanic gases by Johnston furnish the only direct evidence on the gas composition. David Johnston lost his life during the recent (1980) eruptions of Mount St. Helens and with his passing Alaska volcanology lost a real friend.

The contributions of D. J. Lalla, R. B. Forbes, H.-U. Schmincke, D. B. Stone, J. Whitney and other students of Augustine's volcanism are gratefully acknowledged.

REFERENCES

- Anderson, T. and Flett, J. S., 1903. Report on the eruptions of Soufrière, in St. Vincent, in 1902, and on a visit to Montagne Pelée, in Martinique - Part I. Phil. Trans. Royal Soc. of London, Series A, 200:353-553, plates 21-39.
- Barrett, S. A., Stone, D. B. and Kienle, J., 1977. A three-dimensional model of Augustine Volcano. EOS, Trans. Am. Geophys. Union, 58(3): 196.
- Barrett, S. A., 1978. A three-dimensional magnetic model of Augustine Volcano, University of Alaska M.S. Thesis, 175 pp.
- Beaglehole, J. C. (Editor), 1967. The journals of Captain James Cook on his voyages of discovery, III. The voyage of the Resolution and Discovery 1776-178. Cambridge University Press, Cambridge, pp. 360-361.
- Becker, G. F., 1898. Reconnaissance of the goldfields of southern Alaska, with some notes on general geology. U.S. Geol. Survey, 18th Ann. Rep., Part III, Econ. Geol.: 28-31, 50-58, plate X.
- Brower, W. A., Jr., Diaz, H. F., Prechtel, A. S., Searby, H. W. and Wise, J. L., 1977. Climatic atlas of the outer continental shelf waters and coastal regions of Alaska: Vol. I: Gulf of Alaska. U.S. Dept. of Commerce, NOAA, Alaska OCSEAP, 439 pp.
- Buffler, R. T., 1976. Geologic map of south Augustine Island, Lower Cook Inlet, Alaska. State of Alaska, Dep. Nat. Resour., Div. Geol. Geophys. Surv., AOF-96, 3 pp. and map.
- Buffler, R. T., 1980. Geology of south Augustine Island, Lower Cook Inlet Alaska. U.S. Geol. Surv. Memoir on the Geology of Cook Inlet - ed. A. Bouma, in prep.
- Coats, R. R., 1950. Volcanic activity in the Aleutian Arc. U.S. Geol. Surv., Bull., 974-B: 35-49.
- Crandell, D. R. and Mullineaux, D. R., 1978. Potential hazards from future eruptions of Mount St. Helens Volcano, Washington. U.S. Geol. Surv., Bull., 1383-C: C1-C26 and 2 plates.
- Dall, W. H., 1884. A new volcano island in Alaska. Science, 3(51): 92.
- Davidson, G., 1884. Notes on the volcanic eruption of Mount St. Augustine, Alaska, Oct. 6, 1883. Science, 3: 186-189.
- Detterman, R. L., 1968. Recent volcanic activity on Augustine Island, Alaska. U.S. Geol. Surv., Prof. Paper, 600-C: 126-129.
- Detterman, R. L., 1973. Geologic map of the Iliamna B-2 Quadrangle, Augustine Island, Alaska. U.S. Geol. Surv., Map GQ-1068.

- Detterman, R. L. and Reed, B. L., 1973. Surficial deposits of the Iliamna quadrangle, Alaska. U.S. Geological Surv., Bull., 1368-A: A1-A64.
- Doroshin, P., 1870. "Some volcanoes, their eruptions, and earthquakes in the former Russian holdings in America". Verhandlungen der Russisch-Kaiserlichen Mineralogischen Gesellschaft zu St. Petersburg, Zweite Serie, Fünfter Band: 25-44 (in Russian).
- Francis, P., 1976. Volcanoes. Penguin Books Ltd., Harmondsworth, Middlesex, England: 132.
- Fudali, R. F. and Melson, W. G., 1972. Ejecta velocities, magma chamber pressure and kinetic energy associated with the 1968 eruption of Arenal Volcano. Bull. Volc., 35-2: 383-401.
- Griggs, R. F., 1922. The Valley of Ten Thousand Smokes. The National Geogr. Soc., Washington, 340 pp.
- Hildreth, W., 1980. Novarupta 1912: Petrology of the ejecta. EOS, Trans. Am. Geophys. Union, 61(6):66 (abstract).
- Hobbs, P. V., Radke, L. F. and Stith, J. L., 1977. Eruptions of the St. Augustine Volcano: airborne measurements and observations. Science, 195: 871-873.
- Johnston, D. A., Schmincke, H.-U. and Kienle, J., 1977. Geol. Soc. of Am., 73rd Ann. Meeting, Cordilleran Section, Abstracts with Programs, 9(4): 442-443 (abstract).
- Johnston, D. A., 1978. Volatiles, magma mixing, and the mechanism of eruption of Augustine Volcano, Alaska. Ph.D. Thesis, University of Washington, Seattle, Wash., 177 pp.
- Johnston, D. A., 1979a. Onset of volcanism at Augustine Volcano, Lower Cook Inlet. In U.S. Geol. Surv., Circular 804-B, Johnson and Williams - editors: B78-B80.
- Johnston, D. A. and Detterman, R. L. 1979b. Revision of the recent eruption history of Augustine - elimination of the "1902-eruption" In U.S. Geol. Surv., Circular 804-B, Johnson and Williams - editors: B80-B83.
- Johnston, D. A., 1979c. Volcanic gas studies at Alaskan volcanoes. In U.S. Geol. Surv., Circular 804-B, Johnson and Williams - editors: B83-B84.
- Johnston, D. A., 1980. Volcanic contribution of chlorine to the stratosphere-more significant to ozone than previously estimated., Science, in press.
- Karlstrom, T. N. V., 1964. Quaternary geology of the Kenai Lowland and glacial history of the Cook Inlet region, Alaska. U.S. Geol. Surv., Prof. Paper, 443, 69 pp.

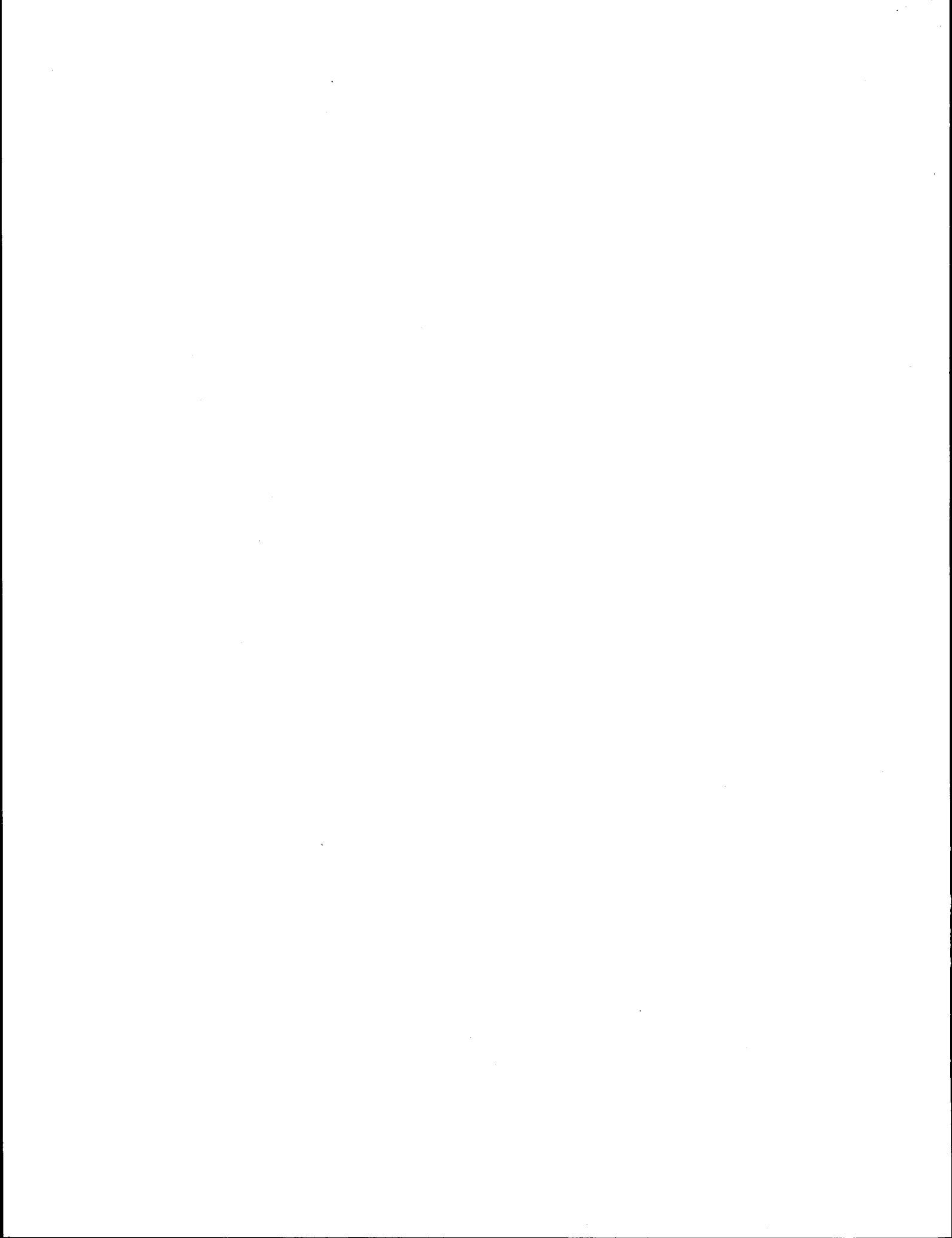
- Kienle, J., Forbes, R. B. and Marlow, D. H., 1971. Recent micro-earthquake swarm activity at Augustine Volcano, Alaska. EOS, Trans. Am. Geophys. Union, 52(11): 925 (abstract).
- Kienle, J. and Forbes, R. B., 1976. Augustine - evolution of a volcano. Geophys. Inst., Univ. of Alaska, Fairbanks, Annu. Rep., 1975/76: 26-48.
- Kienle, J., and Shaw, G. E., 1979. Plume dynamics, thermal energy and long distance transport of Vulcanian eruption clouds from Augustine Volcano, Alaska. J. of Volc. and Geotherm. Res., 6:139-164.
- Kienle, J., Lalla, D. J., Pearson, C. F. and Barrett, S. A., 1979. Search for shallow magma accumulations at Augustine Volcano. Final Report by the Geophys. Inst. of the Univ. of Alaska to DOE, 157 pp.
- Lacroix, A., 1904. La Montagne Pelée et ses éruptions. Masson et Cie, Paris, 662 pp.
- Lalla, D. J. and Kienle, J., 1976. Thermal studies on Augustine Volcano, Alaska. EOS, Trans. Am. Geophys. Union, 57(4): 347.
- Lalla, D. J. and Kienle, J., 1978. Evolution of seismicity at Augustine Volcano, 1970 to 1976 eruption. Geol. Soc. of Am., Cordilleran Section, 74th Ann. Meet., Tempe, Arizona, March 1978, Abstracts with Programs, 10(3):113.
- Lalla, D. J. and Kienle, J., 1980. Problems in volcanic seismology on Augustine Volcano, Alaska. EOS, Trans. Am. Geophys. Union, 61(6): 68.
- Lalla, D. J., 1980. Seismologic and thermal studies at Augustine Volcano, Alaska, Univ. of Alaska, Ph.D. Thesis, in prep.
- Macdonald, G. A., 1972. Volcanoes. Prentice-Hall, Inc., Englewood Cliffs, N.J., 510 pp.
- Marsh, B. D., 1979. Mechanism of igneous diapirism in island arcs. IUGG 17th. Gen. Assembly, Canberra, Australia, IAVCEI: abstract.
- Mathisen, O. A. and Poe, P. H., 1978. Effect of volcanic ash deposits on sockeye salmon lakes. Verh. Internat. Verein. Limnol. 20: 165-172.
- Meinel, A. B., Meinel, M. P. and Shaw, G. E., 1976. Trajectory of the Mt. St. Augustine 1976 eruption ash cloud. Science, 193: 420-422.
- Miller, T. P., 1976. Augustine Volcano. In Alaska's volcanoes, northern link of the ring of fire. Alaska Geographic 4 (1):17-28.
- Miller, T. P. and Smith, R. L., 1977. Spectacular mobility of ash flows around Aniakchak and Fisher calderas, Alaska. Geology 5: 173-176.

- Moore, J. G. and Melson, W. C., 1969. Nuées ardentes of the 1968 eruption of Mayon Volcano, Philippines. *Bull. Volcanol., Ser. 2*, 33:600-620.
- Moxham, R. M., 1951. Pumice deposits in the Alaska-Cook Inlet region, Alaska. *U.S. Geol. Surv., Open-File Rep.* 25 pp.
- Murase, T. and McBirney, A. R., 1973. Properties of some common igneous rocks and their melts at high temperatures. *Bull. Geol. Soc. Am.*, 84:3563-3592.
- Nockolds, S. R., 1954. Average chemical composition of some igneous rocks. *Bull. Geol. Soc. Am.*, 65: 1007-1032.
- Orth, D. J., 1967. Dictionary of Alaska place names, *U.S. Geol. Surv., Prof. Paper*, 567: 93-94.
- Pearson, C. F., 1977. Seismic refraction study of Augustine Volcano. University of Alaska, M.S. Thesis, 131 pp.
- Pearson, C. F. and Kienle, J., 1978. A seismic refraction study of Augustine Volcano, Alaska. *EOS, Trans. Am. Geophys. Union*, 59(4):311.
- Plafker, G., 1965. Tectonic deformation associated with the 1964 Alaskan earthquake. *Science*, 148: 1965-1987.
- Reeder, J. W. and Lahr, J. C., 1977. Seismological observations of the recent eruption of Augustine Volcano. *EOS, Trans. Am. Geophys. Union*, 58:1188.
- Remsberg, E. E., Browell, E. V. and Northam, G. B., 1976. Lidar measurements of stratospheric dust from St. Augustine volcano. *Bull. Am. Meteorol. Soc.*, 57:1152-1153.
- Rymer, M. J. and Sims, J. D., 1976. Preliminary survey of modern glaciolacustrine sediments for earthquake-induced deformational structures, south-central Alaska. *U.S. Geol. Surv., Open-File Rep.*, 76-373; 20 pp.
- Sapper, K., 1927. *Vulkankunde*. J. Engelhorn's Nachf., Stuttgart, 424 pp.
- Schmincke, H.-U. and Johnston, D. A., 1977. Contrasting pyroclastic flow deposits of the 1976 eruption of Augustine Volcano, Alaska. *Geol. Soc. of Am., Ann. Meeting., Abstracts with Programs*, 9(7):1161 (abstract).
- Self, S., Kienle, J. and Huot, J.-P., 1980. Ukinrek Maars, Alaska, II. Deposits and formation of the 1977 craters. *J. of Volc. and Geotherm. Res.*, 7(1/2):39-65.
- Sparks, R. S. J., 1976. Grain size variations in Ignimbrites and implications for the transport of pyroclastic flows. *Sedimentology*, 23:147-188.
- Sparks, R. S. J. and Wilson L., 1976. A model for the formation of Ignimbrite by gravitational column collapse. *J. Geol. Soc. of London*, 132:441-451.

- Sparks, R. S. J., Wilson, J. and Hulme, G., 1978. Theoretical modeling of the generation, movement, and emplacement of pyroclastic flows by column collapse. *J. Geophys. Res.*, 83(B4):1727-1739.
- Sparks, R. S. J., Sigurdsson, H. and Carey, S. N., 1980a. The entrance of pyroclastic flows into the sea, I. Oceanographic and geologic evidence from Dominica, Lesser Antilles. *J. of Volc. and Geotherm. Res.*, 7(1/2):87-96.
- Sparks, R. S. J., Sigurdsson, H. and Carey, S. N., 1980b. The entrance of pyroclastic flows into the sea, II. Theoretical considerations on subaqueous emplacement and welding. *J. of Volc. and Geotherm. Res.*, 7(1/2):97-105.
- Stith, J. L., Hobbs, P. V. and Radke, L. F., 1977. Observations of a nuée ardente from St. Augustine volcano. *Geophys. Res. Lett.*, 4:259-262.
- Taylor, G. A., 1958. The 1951 eruption of Mount Lamington, Papua. *Australia Bur. Mineral Resources, Geol. Geophys. Bull.*, 38, 117 pp.
- Thorarinsson, S., 1954. The eruption of Hekla 1947-48, II, 3., The tephra-fall from Hekla on March 29, 1947. *Soc. Sci. Islandica, Reykjavik*: 1-68.
- Thorarinsson, S., 1967. *Surtsey*. The Viking Press, New York, 47 pp. and 64 plates.
- Wilcox, R. E., 1959. Some effects of recent volcanic ash falls with especial reference to Alaska. *U.S. Geol. Surv., Bull.*, 1028-N: 409-476, plates 54-58.
- Wilson, L., 1972. Explosive volcanic eruptions - II The atmospheric trajectories of pyroclasts. *Geophys. J. R. Astr. Soc.*, 30:381-392.
- Wilson, C. R. and Kienle, J., 1976. Infrasonic signals generated by Augustine volcano during the 1976 eruption. *Am. Geophys. Union Annu. Meet., Spec. Augustine Sess.*, April 14, 1976.

APPENDIX

PHOTOGRAMMETRIC MAPPING OF THE SUMMIT REGION
AND NORTHEAST SECTOR OF AUGUSTINE VOLCANO



APPENDIX

Photogrammetric Mapping of the Summit Region and Northeast Sector of Augustine Volcano

The U.S. Geological Survey Iliamna Quadrangle Map B-2 of Augustine Island is based on aerial photography flown in 1957 and field annotated in 1958. The 1963/64 and 1976 eruptions altered the volcano, particularly the summit region, significantly. After the 1964 dome intrusion the summit was 279 ft. (85 m) higher than shown on the Quadrangle map. During the 1976 eruption 204 ft. (62 m) were lost from the summit.

With funding from these contracts a new post-1964 but pre-1976 topographic map was prepared of the Augustine summit region above the 2,500 ft. contour line, based on photography flown by North Pacific Aerial Surveys, Inc., Anchorage, on June 16, 1973. Figure A1 shows a photographic reduction of this map.

The 1976 eruption again altered the summit region dramatically. New vertical photography was acquired through North Pacific Aerial Surveys and a new topographic map of Augustine's summit above the 2,500 ft. contour line was prepared at the same scale as the previous map. Figure A2, based on August 21, 1976 photography, shows the dramatic changes that took place during the 1976 eruptions, which resulted in the removal of the 1964 lava dome, the creation of a large crater which was subsequently partially filled by a new dome intrusion which took place between February and April, 1976.

Figure A3 is a photographic reduction of a new topographic map of the northeast sector of Augustine Island, most heavily altered by pyroclastic avalanches during the 1976 eruptions. The original map has a scale of 1:10,000 and is based on photography acquired by North Pacific Aerial Surveys on August 21, 1976.

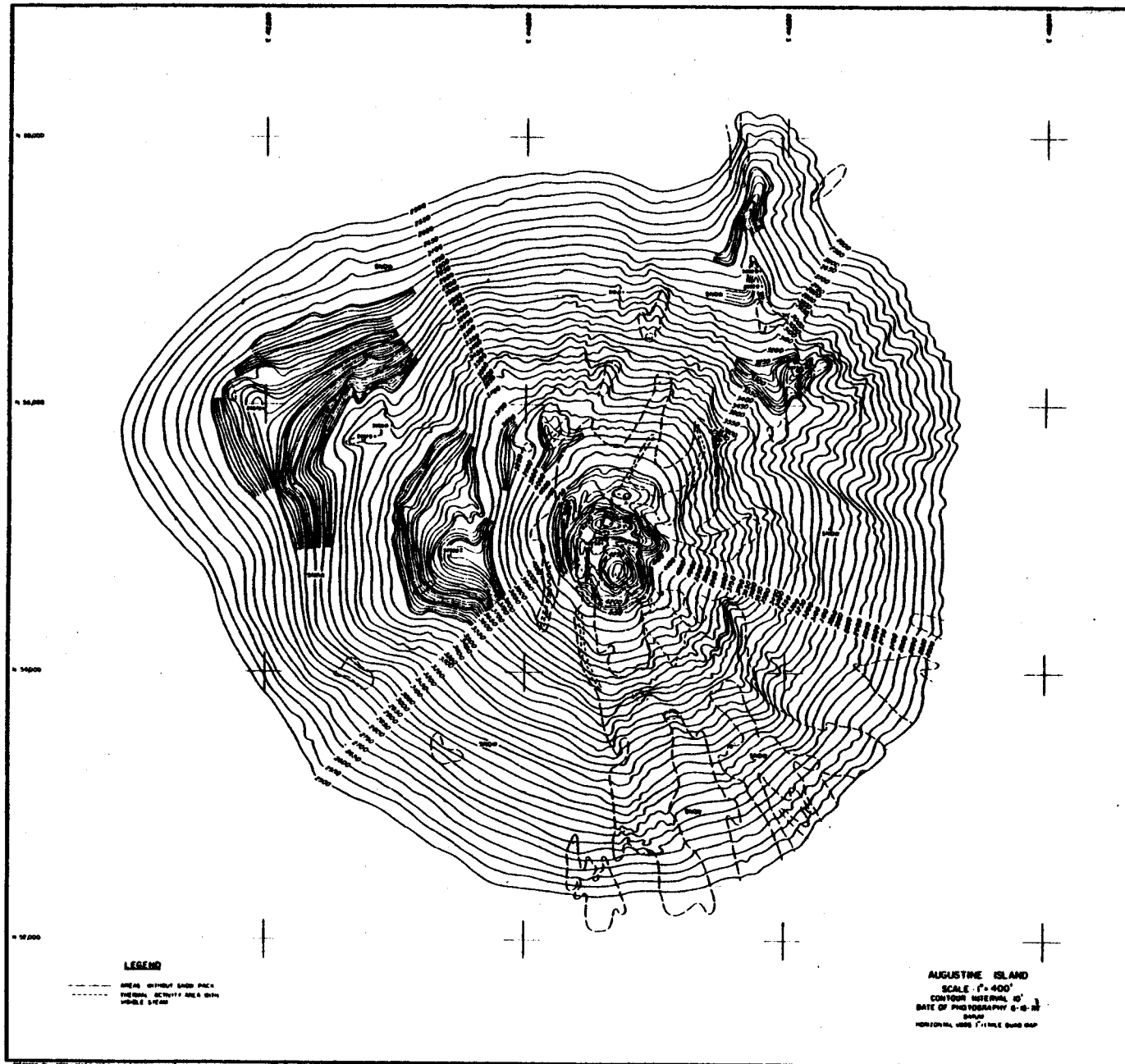


Figure A1. Topographic map of Augustine Volcano's summit region based on aerial photography taken on June 16, 1973, i.e., post 1963/64 eruption but pre-1976 eruption. The contour interval is 10 ft. and the distance between tickmarks is 2,000 ft. (prepared for the Geophysical Institute of the University of Alaska by North Pacific Aerial Surveys, Inc., Anchorage, Alaska).

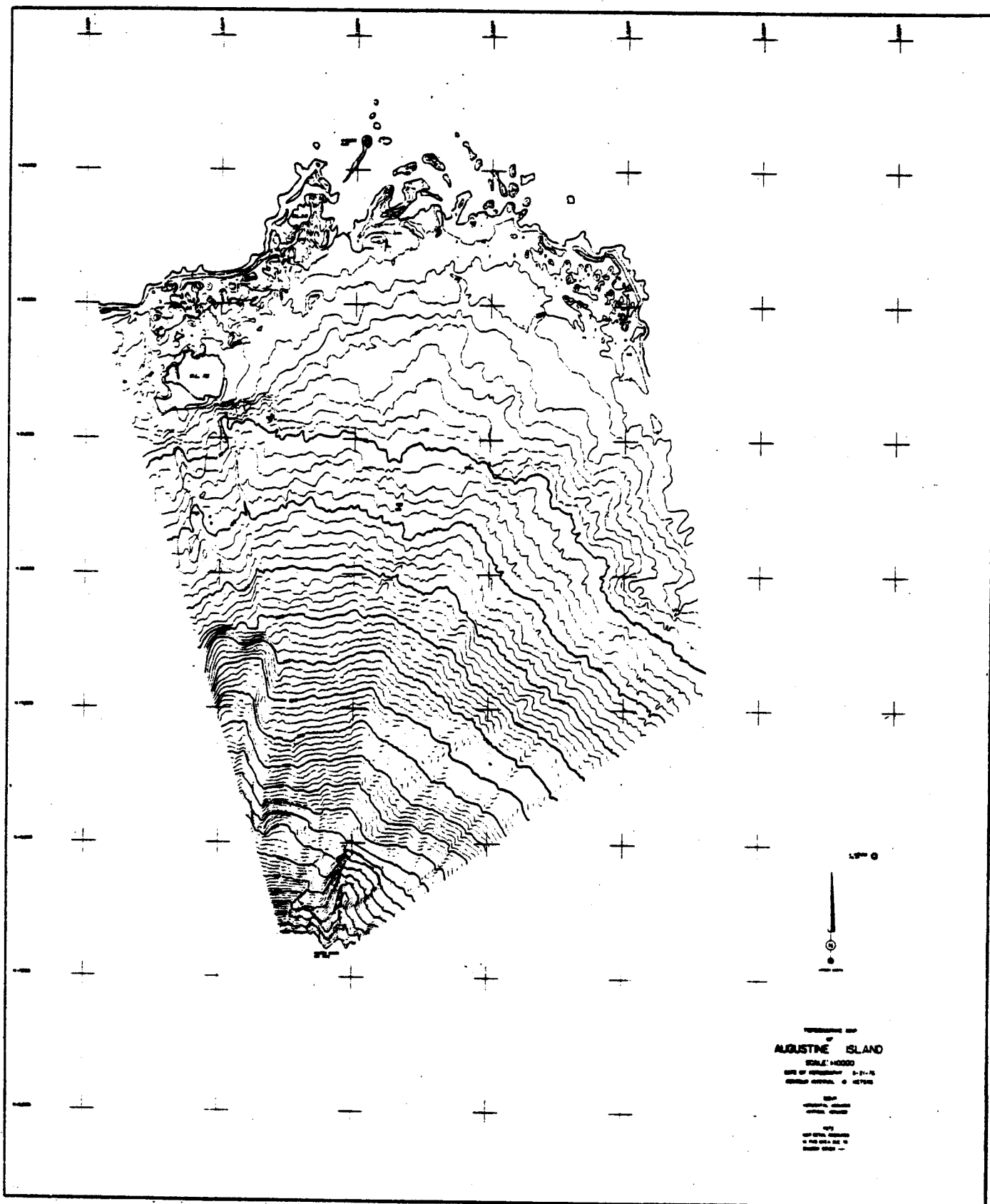


Figure A3. Topographic map of the northeast sector of Augustine Volcano based on aerial photography taken on August 21, 1976, i.e., post-1976 eruption. The contour interval is 10 m and the distance between tickmarks is 1000 m (prepared for the Geophysical Institute of the University of Alaska by North Pacific Aerial Surveys, Inc., Anchorage.

U.S. DEPARTMENT OF COMMERCE
NATIONAL OCEANIC AND ATMOSPHERIC
ADMINISTRATION
NATIONAL OCEAN SERVICE
701 C Street
Box 56
Anchorage, Alaska 99513

OFFICIAL BUSINESS
PENALTY FOR PRIVATE USE \$300

POSTAGE AND FEES PAID
U.S. DEPARTMENT OF COMMERCE
COM-210



PRINTED MATTER

CLASS OF POSTAL SERVICE

BARBARA J. SOKOLOV
ARCTIC ENVIRON INFO AND DATA CTR
UNIVERSITY OF ALASKA
707 A STREET
ANCHORAGE, AK 99501

NOAA FORM 61-13
(9-84)